INFORMATION TO USERS

This manuscript has been reproduced from the microfilm master. UMI films the text directly from the original or copy submitted. Thus, some thesis and dissertation copies are in typewriter face, while others may be from any type of computer printer.

The quality of this reproduction is dependent upon the quality of the copy submitted. Broken or indistinct print, colored or poor quality illustrations and photographs, print bleedthrough, substandard margins, and improper alignment can adversely affect reproduction.

In the unlikely event that the author did not send UMI a complete manuscript and there are missing pages, these will be noted. Also, if unauthorized copyright material had to be removed, a note will indicate the deletion.

Oversize materials (e.g., maps, drawings, charts) are reproduced by sectioning the original, beginning at the upper left-hand corner and continuing from left to right in equal sections with small overlaps.

Photographs included in the original manuscript have been reproduced xerographically in this copy. Higher quality 6" x 9" black and white photographic prints are available for any photographs or illustrations appearing in this copy for an additional charge. Contact UMI directly to order.

ProQuest Information and Learning
300 North Zeeb Road, Ann Arbor, MI 48106-1346 USA
800-521-0600

Geomorphic Form and Process of Sediment Flux within an Active Orogen: Denudation of the Bolivian Andes and Sediment Conveyance across the Beni Foreland

by

Rolf Erhart Aalto

A dissertation submitted in partial fulfillment of the
requirements for the degree of

Doctor of Philosophy

University of Washington

2002

Program Authorized to Offer Degree:

Department of Earth and Space Sciences

UMI Number: 3041003

ProQuest Information and Learning Company
300 North Zeeb Road
P.O. Box 1346
Ann Arbor, MI 48106-1346

Doctoral Dissertation

In presenting this dissertation in partial fulfillment of the requirements for the Doctoral degree at the University of Washington, I agree that the Library shall make its copies freely available for inspection. I further agree that extensive copying of the dissertation is allowable only for scholarly purposes, consistent with "fair use" as prescribed in the U.S. Copyright Law. Requests for copying or reproduction of this dissertation may be referred to Bell and Howell Information and Learning, 300 North Zeeb Road, P.O. Box 1346, Ann Arbor, MI 48106-1346, to whom the author has granted "the right to reproduce and sell (a) copies of the manuscript in microform and/or (b) printed copies of the manuscript made from microform."

Signature Rolf Eckart Aoltz

Date 20 March 2002

University of Washington
Graduate School

This is to certify that I have examined this copy of a doctoral dissertation by

Rolf Erhart Aalto

and have found that it is complete and satisfactory in all respects,
and that any and all revisions required by the final
examining committee have been made.

Chairs of Supervisory Committee:

Thomas Dunne

David R. Montgomery

Reading Committee:

Thomas Dunne

David R. Montgomery

Charles A. Nittrouer

Alan R. Gillespie

Date: 3/14/02

University of Washington

Abstract

Geomorphic Form and Process of Sediment Flux within an Active Orogen: Denudation of the Bolivian Andes and Sediment Conveyance across the Beni Foreland

by Rolf Erhart Aalto

Chairpersons of the Supervisory Committee

Professor Thomas Dunne
School of Environmental Science and Management
University of California, Santa Barbara

Professor David R. Montgomery
Department of Earth and Space Sciences
University of Washington

Mountains produce most of the sediment conveyed within continental river systems, and their associated foreland basins trap much of the material debouched from the range front. I present evidence that modern erosion rates in the Bolivian Andes are correlated with hillslope angle and basin lithology, but not associated with basin runoff. An empirical model was developed to estimate sediment production rates throughout the Amazonian Andes. When the predicted sediment efflux was compared to records from the upper mainstem Amazon River, it appears that approximately half the debouched material is intercepted by the foreland basins along the Andean range front.

To investigate sediment conveyance across a pristine foreland basin, the processes of sediment exchange and deposition were documented for the Beni River, northern Bolivia. Channel and floodplain topography and granulometry were surveyed throughout the Beni Foreland, including transects across the forested floodplains. Sediment cores taken along these transects were dated to determine accumulation rates utilizing a new method for ^{210}Pb geochronology, developed here for floodplain environments to resolve episodic sedimentation events of heterogeneous grain size.

Water and sediment discharge records gauged at the inlet and outlet of the Beni Foreland provided a hydrological framework for flux analysis. These field data were combined with a GIS analysis of four decades of channel morphology and migration. A model for meso-scale fluvial geomorphology was developed and compared to the GIS results.

The flux analysis found that sediment is mostly trapped in the Beni Foredeep, where it is conveyed overbank during exceptional floods and deposited across the broad floodplain. A smaller amount of sediment is lost in the secondary back-bulge basin, and there is no significant trapping of sediment within the Beni Forebulge. The annual exchange of sediment due to channel migration is considerably larger than the total sediment efflux from the Beni Foreland. The geochronology and stratigraphy of floodplain deposits indicate episodic accumulation, probably due to crevasse splays produced during major floods associated with cold-phase ENSO events. In responding to such climate perturbations, mountains and foreland basins dominate intracratonal mass fluxes and modulate sediment supply to lower portions of the Amazon River.

Table of Contents

List of Figures

List of Tables

Preface

This dissertation investigates the geomorphic controls on the modern rates of sediment production in the Bolivian Andes, and the processes and rates of sediment interchange, conveyance, and deposition within a foreland basin in northern Bolivia. My goal was to develop both an empirical means to predict erosion rates within a mountainous region and to investigate the quantitative fluvial geomorphology and trapping efficiency of a large foreland basin immediately downstream of the range front. Because mountains typically produce almost all of the sediment conveyed within large continental river systems and foreland basins can trap over half the sediment debouched from the range front, these two regions dominate intracratonal mass fluxes and control sediment supply to the lower portions of the river basin and to the shelf environs.

The presentation here is as chapters written as five stand-alone papers, complete with an abstract, introduction, a description of the study area, field and laboratory methods, discussion, and a summary. The rationale for this style is to spare the reader from having to read the entire dissertation in order to understand the results presented in a single chapter, and also to facilitate the timely publication of derived manuscripts. Chapter 1 presents the empirical study of geomorphic controls on Andean erosion, while Chapter 2 explores how this sediment is conveyed and stored across the Beni River foreland basin. The flux analysis in Chapter 2 relies in part upon a separate determination of the processes and rates of Beni floodplain sedimentation, presented in Chapter 5, based on a new CIRCAUS methodology for ^{210}Pb geochronology, developed in Chapter 4. An extensive GIS analysis of channel location and morphology was required to determine the sediment exchange associated with channel migration in Chapter 2, and these GIS results are presented along with topographic survey data and a conceptual model for quantitative meso-scale fluvial geomorphology in Chapter 3. Though outside the scope of this dissertation, similar results are available for the nearby Mamore River, as are measurements and observations of the geomorphic responses of the Beni and Mamore to neotectonic deformation within the Bolivian Llanos.

Acknowledgements

This research was supported by NSF research grants EAR-9903157 and EAR-9628737, and by a NASA Earth Systems Science Graduate Fellowship.

Many people contributed to the realization and success of this dissertation. Thomas Dunne and Elizabeth Safran inspired and encouraged me to think boldly and to pursue funding for a novel and ambitious research project focused on one of the few large, pristine, sand-bedded rivers left on Earth. Laurence Maurice-Bourgoin has graciously provided mission-critical scientific and logistical collaboration throughout the project. Jean Loup Guyot facilitated this international scientific collaboration between the University of Washington and IRD (Institut de Recherche pour le Développement).

Fieldwork in the remote jungle floodplains of northern Bolivia presents daunting scientific and logistical challenges. Tom, Laurence, Liz, David Finlayson, Marc Salak, David Montgomery, Pascal Fraizy, Vincent Barnaud, and Leo Soares provided valuable scientific assistance in the field. I am grateful for logistical support from Abdul Castillo, Julio Cesar Salinas, Eddy Baldellon, Fernando, and the Rurrenabaque boat crew (Carlos, Herman, and Don Teo). Air photos, maps, and depth surveys were generously supplied by Jorge Espinosa and Oscar Moreno Bello.

Charles Nittrouer provided complete access to his lab facilities and has contributed advice and encouragement vital for the development of the geochronologic method. I am grateful for extensive laboratory assistance from Kari Sauers, John Staly, Guenna Smith, and Scarlett Sherlock. James Murray and Barbara Paul generously provided additional laboratory facilities. Chris Gardner assisted with most of the GIS analysis, in facilities maintained by Harvey Greenberg and D. Montgomery.

T. Dunne, C. Nittrouer, D. Montgomery, and Alan Gillespie provided valuable advice and comments on my dissertation. Tom has supplied endless guidance, encouragement, inspiration, and support throughout a long and challenging research project. As my advisor, he has imparted an exemplary blend of the highest intellectual standards combined with frank humanism. I am appreciative to Tom and the rest of my committee for their faith, backing, and patience in giving me near-complete intellectual freedom to pursue this project.

Last and most, I am grateful to my dear family for tolerating and nurturing my lifelong fascination for landscapes, rivers, and mud. My parents and grandparents have blessed me with lifelong inspiration, encouragement, and the provisions to pursue my studies of the gorgeous and alluring natural world. Katy, August, and Tess have provided emotional nourishment and sustenance throughout the many years, travels, travails, and adventures of this dissertation.

Dedication

Eugene Arthur Aalto

1972 – 2001

In memory of my dear brother

for his grace and courage.

Chapter 1

Geomorphic Controls on Andean Denudation Rates

Abstract

Andean rivers supply over 99% of the sediment load for the Amazon River, but only a fraction of the eroded material reaches the gauged tributaries of the mainstem Amazon. The volume of rock annually removed from the Andes and redeposited as sediment within large foreland basins along the range front is poorly known. To predict erosion rates throughout the Andes, I have conducted a multiple regression analysis of sediment discharge of 47 gauged drainage basins in the Bolivian Andes. These mountainous basins are typically large (17 - 81,000 km^2, mean 11,000 km^2), often have decades of daily water- and sediment-discharge measurements, and display an extraordinary range of denudation (0.01 - 6.9 mm/yr), runoff (16 - 2,700 mm/yr), and local topographic relief (700 - 4,300m), facilitating statistical analysis, yet the underlying lithology is relatively homogeneous and anthropogenic disturbance is limited. The steep nature of the channels of these basins precludes sediment storage, and unlike previous global studies of fluvial denudation rates, based on data compilations from very large river basins (> 100,000 km^2), this analysis avoids the combined effects of sediment yields from mountain ranges and sedimentary basins. Thus, I do not find that erosion rates are correlated with either basin area or elevation. Neither of these parameters has a manifest physical effect on failure processes or sediment transport rates, yet they typically exhibit a strong, but spurious, correlation when continental-scale basins are treated as geomorphically homogeneous units. By separating regions of sediment production (e.g., steep topography and weak lithology) from zones of deposition and storage (e.g., subsiding basins with downstream-decreasing gradients), in this study sediment sources are isolated from sinks to analyze denudation explicitly. As a result, I find that lithology and average catchment slope account for 90% of the variance in

sediment yield. The data suggest that denudation is a high-order power function of basin hillslope or local relief. For the 47 mountainous basins without major sediment sinks, runoff is not significantly correlated with yield, suggesting that water-power-driven geomorphic models for basin erosion may not be appropriate for this mountainous landscape, at least on decadal timescales. Because basin runoff over geologic timescales orchestrates the process of channel network incision, however, it determines the average hillslope and, indirectly, the rate of denudation. Finally, several theoretical geomorphic models for mass wasting are tested to assess simple hill slope-scale sediment yield models for the study basins. When applied throughout the Amazonian Andes, such empirical models predict an annual Andean sediment flux to the lowland Amazon Basin of 2.3 - 3.0 Gtonnes. Since ~ 1.3 Gtonnes/yr of sediment reach the mainstem Amazon River, the intervening foreland basins appear to intercept about half of the total Andean sediment efflux.

Motivation

Since Ahnert (1970) published the first major study of mountain-basin denudation incorporating a parameterization for potential energy (local relief), numerous researchers have followed suit, each finding catchment sediment discharge proportional to some topographic index such as elevation, slope, or relief, and basin area. Milliman and Meade (1983) cataloged sediment discharge from the major rivers of the world, noting that sediment yield strongly decreases with increasing drainage basin area. Pinet and Souriau (1988) analyzed an expanded version of this data set, which Milliman and Syvitski (1992) further supplemented with data from smaller basins in their assessment of total sediment discharge to the ocean. Summerfield and Hulton (1994) investigated a large-basin subset (areas exceeding $5x10^5$ km^2) to ascertain morphometric controls on fluvial denudation rates, Hicks et al. (1996) investigated erosion in New Zealand basins, highlighting the influences of lithology and climate (runoff), and Hallet et al. (1996)

compared rates of glacial erosion and sediment evacuation to the high mountain sediment yields of Milliman and Syvitski (1992). Recent studies by Ludwig and Probst (1998) and Hovius (1998) summarize much of this earlier work, and provide extensive statistical analysis of the largest global database currently available.

These preceding studies share three noteworthy geomorphic simplifications: 1) entire basins, regardless of size, are treated as homogenous units, without considering internal zones of sediment erosion, transport, and deposition; 2) the sediment discharge for most basins, large and small alike, is measured near the river's mouth, well downstream from any internal loci of deposition in the cases of the large basins; and 3) these studies focus primarily on large rivers, where such effects are greatest. Since larger basins tend to have more extensive low-gradient zones (cratonal shields, foreland basins, and other depocenters) compared to areas of high relief (active orogeny, dissected uplands, and other sediment sources), basin area in most of these studies shows a significant negative correlation with denudation, runoff, and total sediment discharge. Because basin area itself has no apparent physical effect on erosion rate, however, it cannot have any direct causal relationship with sediment yield. Hence, the observed statistical relationships are likely to be artifacts of the ratio between sediment production area and depositional area (or length) which generally decreases with increasing basin size. By not distinguishing distinct zones of sediment production, transport, and deposition within basins, previous studies do not resolve realistic process rates within these distinct meso-scale geomorphic process zones. Rather, they provide an empirical basin-averaged proxy for the downstream area-integrated effects of erosion, transport, and deposition, and consequently afford limited quantitative insight into the contribution of each specific geomorphic process. Because the spatial distribution of these meso-scale process zones varies considerably between basins, the common procedure of grouping all the world's rivers under a single sediment yield-area relationship is of dubious value for understanding erosion and sediment transport, especially when these

general whole-basin log-log trends are cited as empirical proxies for the rates of more localized geomorphic mechanisms.

Because of these problems with basin area (Aalto and Dunne, 1996; Aalto et al., 1999), I have identified a set of mountainous basins that are largely free from significant sediment sinks. They are purely denudational basins, representative of only the meso-scale, erosional geomorphic process zone. I identified the absence of depositional zones by extensive field inspection and from the measurement of channel gradient and the absence of wide valley flats with meandering or braided channels on satellite images and 1:100,000-scale topographic maps. I was also concerned about whether sediment yields have been significantly perturbed by land use since European colonization. I examined erosion features, sediment sources, and local sediment storage throughout the region, and determined that erosion has been accelerated in a few regions, particularly near cities such as Cochabamba and Santa Cruz, and to a lesser extent La Paz and Sucre (Figure 1.1). However, these areas are surrounded by even more impressive landslides and gullies throughout vast expanses of uninhabited terrain. Despite some dramatic, qualitative descriptions of soil erosion that imply anthropogenic effects, the first detailed studies are beginning to document only local and moderate rates of erosion resulting from land use (Preston, 1998). Hence, it appears that the sometimes confounding effects of anthropogenic disturbance (Milliman et al., 1987; Walling and Webb, 1983) and changes in floodplain sediment storage (Trimble, 1976, 1977) are minimal within the study area, and that the typically large basin size effectively averages much of the small-scale stochastic sediment supply from individual hillslopes, so the decadal-scale sediment yields may reflect the long-term rate of sediment delivery from hillslopes over the Holocene.

By conducting a multiple regression analysis of how sediment yields vary with various morphometric basin parameters, I hope to attain useful insights into the geomorphic controls on denudation for rugged mountainous catchments. Then, the empirical basin-scale analysis is recast into a hillslope-scale, theory-driven, cell-based

framework, and applied to estimate erosion-dominated sediment supplies throughout the Andes.

Study basins and methods

The Bolivian Andes offer an excellent case study of erosion rates: a rugged mountain belt undergoing active crustal shortening (Norabuena et al., 1998) across a series of east-vergent, crustal-scale thrusts of the Subandean fold and thrust belt. Lithologies include arenites, argillites, lutites, and conglomerates of Paleozoic, Mesozoic, and Tertiary age, with a backbone of Mesozoic and Cenozoic granitic batholiths that form the peaks of the Eastern Cordillera Real and blankets of massive ignimbrites covering portions of the Andes east of the Altiplano. Drained by the Beni, Mamore, Grande, Pilcomayo, and Bermejo rivers, this region (Figure 1.1) features highly variable (Table 1.2) denudation rates (0.01 - 6.9 mm/yr) and substantial variation in lithology (granite to unconsolidated alluvium), basin relief (700 - 4,300m), average hill slope, average elevation (800 - 4,700m), runoff (16 - 2,700 mm/yr), seasonality, and vegetation cover (0 - 100%). Such an extraordinary range of parameters facilitates statistical identification of probable physical controls on mass wasting, once catchments with sediment sinks are identified and excluded from the analysis. Quaternary glaciation was limited to the high peaks of the Cordillera Real, affecting only the highest regions of the Beni river basin, areas of relatively minor extent.

Long term (2 - 30+ years) water and sediment discharge data were collected at 60+ locations throughout Bolivia by several governmental and scientific organizations, utilizing a variety of sampling techniques (e.g., daily surface grab samples, sediment concentration measurements correlated to river stage, and depth-integrated sediment discharge samples). At some stations, hundreds and even thousands of samples were collected. The sediment concentrations have been combined with river flow measurements in various ways (daily totals, monthly totals) to produce average annual sediment fluxes. These data, along with measurements of basin morphometry, runoff,

vegetative cover, lithologic index, and other geomorphic parameters were augmented and collated by Guyot (1993) and Guyot et al. (1989b). Most of the flux estimates were based on surface-sampled suspended load and cannot presently be calibrated for the depth-dependence of sediment concentration. However, at shallow river depths and steep Andean river gradients, the resulting underestimate of suspended sediment discharge should be relatively minor (10 - 30%) for the majority of fine particles (Aalto, 1995; Guyot, 1993). As suspended load typically represents well over 90% of total solid flux (Collins and Dunne, 1989), these data therefore represent a conservative estimate of total sediment discharge. The various methods of combining concentrations and discharges also yield conservative estimates of flux (Walling and Webb, 1981). As a first step in quality control, I culled those flux data of downstream stations for which the sum of sediment input from nearby gauged upstream stations exceeded the downstream load. These discrepancies might simply reflect errors of measurement or significant sediment sinks, and were therefore discarded.

The best currently available topographic database of Bolivia, a 30-arc-second (~ 900 m) digital elevation model (DEM) (Bliss and Olsen, 1996), was used to perform basin-scale morphometric analyses (average elevation, average slope), to calculate local slope for the "hillslope-scale" flux models, and for assisting with landscape visualization. While the scale of the DEM does not accurately represent topographic details, the dramatic relief and enormous valleys typical to the Bolivian Andes compensate in part for this coarse resolution. However, the degree to which the DEM provides only an index of the topography is indicated by the discrepancy between that average hillslope gradient measured from different topographic databases. The area-weighted average hillslope gradients (S_{avg}), calculated from a 3x3 DEM neighborhood using the average-maximum technique, derived from the 30-arc-second DEM lie in the range of 2 - 14 degrees. A 25m-resolution DEM obtained from the SIR-C shuttle mission for a representative high-relief basin (of the Zongo river, with a 1km-DEM S_{avg} of 10 degrees) yields an average hillslope of 31 degrees, a number much closer to my

own field measurements. Not only is the 30-arc-second DEM vastly coarser than the 25 m DEM, but the corresponding DEM slope is further smoothed by using the standard average maximum technique, which calculates the steepest descent of the best-fit plane within a 3x3 DEM neighborhood (therefore generating a slope DEM sampled at ~ 1,800 m pixel resolution). Nevertheless, these 30-arc-second elevation data provide a consistent means to quantify basin relief and an index of average slope. I have also used 1:50,000 scale topographic maps of parts of the study area, as well as the 25m NASA SIR-C DEM (where available), and edited portions of the 1km DEM to correct errors in the river network. The 900-meter DEM is fairly accurate in depicting total basin relief, but systematically under-represents average hillslope angle by about a factor of 2 - 3, for the reasons discussed above. For each basin, I have also determined an average mean local relief (the maximum elevation difference observed within a 5-km search radius of each measurement point, as defined by Ahnert (1970)), a value that should be largely independent of DEM resolution (Montgomery and Aalto, 2001; Polidori et al., 1991). From this corrected 900-m DEM, I next generated longitudinal river profiles to identify reaches where channel gradient and hence sediment transport capacity decreases rapidly (e.g., large synclinal valleys in the Subandean fold and thrust belt). These locations were then flagged as potential sediment sinks to be evaluated further with Landsat imagery and by visual inspection in the field.

I have obtained spatially and temporally extensive Landsat TM and MSS satellite images spanning 1972 - 2000 for most of the study region, enabling evaluation of channel shifting, bar deposition, and other characteristics of active deposition over the last ~ 30 years. Landsat band ratios and linear mixture analysis (Mertes et al., 1993) were used to classify Landsat pixels as water, vegetation, and active (unvegetated) gravel bars. Reaches with comparatively high rates of channel migration across a broad valley floor, extensive active bars, and substantial changes in slope were identified as potential sediment sinks. Stations downstream from these sinks may no longer represent purely erosional basins, and were therefore flagged for further scrutiny. By measuring grain-

size distributions and observing geomorphic processes in the field at many of these locations, I have evaluated the significance of the suspected sedimentation. For example, I visited a large intramontane basin within the Beni River system every year for four years to study the morphology of channel bed and floodplain deposition, ultimately deciding that the observed gravel bar deposition is thin and amounts to only a small fraction of the total sediment flux. I then made rough estimates of the magnitude of sediment deposition within these sinks, discarding stations with substantial (> 20% of the total load) upstream deposition. Because of the narrow valleys, steep channels, and high sediment fluxes, only two Andean stations were discarded. Both of them were in small, recently de-glaciated catchments with low sediment yields, where clasts generated by hillslope failures primarily accumulate as talus at the bottom of the cliffs, distant from the active channel in the center of these classic glacial valleys. My field inspection and image analysis of erosion processes throughout Beni river basin suggest that deposits of loose material produced by Quaternary glaciation do not significantly contribute to modern sediment yields: such stores may have previously been evacuated during deglaciation, leaving only small remnants that are of little significance within large, modern, rapidly eroding basins. The sediment loads of all stations within or downstream of the foreland basin are affected by extensive upstream deposition, and were therefore discarded. Thus, the dataset contains no major sediment sinks and represents hillslope erosion processes. I next utilize the remaining 'erosional' discharge stations in my statistical analysis of present-day Bolivian denudation rates.

I defined the lithology of each study basin by digitizing a 1:1,000,000-scale geologic map of Bolivia (Pareja and Ballón, 1978). I also measured the compressive rock strength of lithologies at 50 sites using a Schmidt hammer (Table 1.1) and made field observations of the associated morphology of mass wasting. On the basis of these measurements, I applied a lithologic scaling index similar to that of Probst (1990) to classify basic rock types throughout the study area. I next used a geographic information system (GIS) weighted-area-averaging routine to generate an area-weighted Probst

lithologic index (PLI) for each basin (Table 1.1) (concordant to those reported by Guyot (1993)), and then grouped the study basins by this average value into one of three distinct lithologic classes: igneous, strong-sedimentary (including meta-sedimentary), and weak-sedimentary rock. As a result, I have characterized the effective lithologic composition of each study basin, as determined by the area-weighted average of the PLI predicted susceptibility to erosion of each rock type present (Table 1.2). In practice, basins within the intrusive batholiths and extrusive ignimbrites are igneous, much of the lower Andes and sub-Andes are classified as "strong-sedimentary," and basins containing significant expanses of Plio-Pleistocene fanglomerates, river and floodplain deposits, and other weakly consolidated strata are "weak-sedimentary."

Basin flux analysis

The remaining 47 Andean stations (Table 1.2) were entered into a forward stepwise multiple regression analysis (tol = 0.05, F-statistic = 2.0) to determine statistically significant controls of average annual basin sediment flux. Of the tested parameters (Table 1.3), area (A), lithology (PLI), and average slope (S_{avg}) were found to be statistically significant and were therefore selected for further analysis. Data from each of the three general lithologic classes define sub-parallel lines when basin yield is plotted against S_{avg} (Figure 1.2a). Mean local relief can effectively replace average slope in this relationship (Figure 1.2b), although the explained variance declines significantly. While this mean local relief relationship is probably more transportable between DEMs of varying resolution and quality, for the purposes of the current study (which uses a consistent DEM) I will focus on the better statistical relationship for the S_{avg}.

To determine the average contribution to basin erosion for each lithologic class, it is useful to assume that their associated best-fit lines are in fact parallel (because their regression slopes are statistically similar) and to then compare the ratio of their intercepts, thereby deriving a new lithologic index (L). For the mean slope relationship, the observed ratio (Figure 1.2a) of 46 : 7 : 1 once the slopes are fixed (at the slope of the

largest intermediate class, strong sedimentary) expresses the expected increase in sediment production for basins composed of weak sedimentary and strong sedimentary rocks as compared to granitic basins of the same average hillslope, accounting for 92% of the total variance in flux (Table 4a). In Bolivia, lithologic variation therefore accounts for an observed 46-fold range in short-term denudation rates. This range corresponds roughly with the findings of Meybeck (1987) and Probst (1990) for a similar range of lithologies studied elsewhere in the world. Interestingly, in-situ compressive strength varies over only a factor of ~ 4 for fresh rock (Table 1.1), so the complex geomorphic process of converting solid "laboratory" rock to river sediment by means of dramatic landscape-scale erosional processes apparently multiplies these material differences by approximately an order of magnitude. I use the fitted relationship of sediment flux to S_{avg} and lithology (L) depicted in Figure 1.2a to normalize sediment discharge (according to the equations in Table 1.4a), and plot this value versus basin area in Figure 2c. Since the resulting exponent on area is ~ 1, this suggests that area is significant only as a scaling factor, the only physical meaning that it can have. Consequently, the physical sampling effects of area are evidently minimized for the Bolivian dataset. It is therefore defensible to divide both sides of the second equation in Table 1.4a by area and rock density to obtain an estimate of contemporary basin denudation rate based on average basin slope and lithology.

Geomorphic controls on modern sediment yield

While it may appear unusual that runoff is not statistically related to denudation rate for suspended sediment, several previous yield studies have reached similar conclusions (Ahnert, 1970; Pinet and Souriau, 1988), as has a recent comparison of erosion rates for seven small monolithologic Sierra catchments, as estimated for the last few thousand years using cosmogenic nuclides (Riebe et al., 2001). However, even the classic studies of climatic effects on sediment yield by Langbein and Schumm (1958) and Fournier (1960) proposed non-monotonic relationships of undocumented statistical

power between sediment yield and rainfall statistics. Other studies that have found a relationship between denudation and runoff (Milliman and Syvitski, 1992; Summerfield and Hulton, 1994) have analyzed fluxes from large basins ($> 5 \times 10^5$ km^2), and consequently may suffer from the divergence between erosion rate and sediment yield that occurs in large basins, which tend to have greater areas of low relief. Besides serving as sediment sinks, these flat areas lack the higher orographic precipitation of mountainous regions and some of the large interior basins in the data sets are distant from oceanic moisture sources (Aalto and Dunne, 1996). As a result, the aforementioned erosion studies find that runoff decreases significantly with increasing basin area, demonstrating how an increasing fraction of lowlands in a basin imbues the area parameter with a spurious physical significance, confounding the effects of rainfall and denudation rates. Since sediment yield also decreases with increasing basin area (Milliman and Syvitski, 1992), it necessarily follows that in such large-scale datasets, sediment yield increases with runoff, as both increase together with decreasing basin area. For example, the Andes represent only 10% of the total Amazon basin area, yet they supply almost all of the sediment and their lower portions have some of the highest rainfall rates; in contrast, lowland Amazonia contains mostly sediment sinks, irrespective of rainfall. Hence, while the sampling effects of increasing basin area may be ignored in some cases to provide simple estimates of total sediment discharge to the oceans from river mouths, the resulting statistical relationships may not be causal and cannot be applied elsewhere because this apparent "area effect" probably scales differently between basins.

It is perplexing that this and some other studies have found denudation rates statistically uncorrelated to runoff or rainfall. Geomorphic models of landscape evolution are often based on stream-power-driven channel incision and sediment transport (Tucker and Slingerland, 1994) or precipitation-driven surface erosion and mass failure (Chase, 1992; Masek et al., 1994). However, given the enormous variation in runoff (17-2,660 mm/yr) and sediment yield (34-18,300 tonnes/km^2 a), it is evident

that the two are not very well correlated in the Bolivian Andes (Figure 1.3a). In the multiple regression analysis, the variance in yield explained by runoff is better explained by S_{avg}, due in part to the fact that runoff and average hillslope are themselves correlated (Figure 1.3b). The fact that slope captures far more variance in sediment yield than does runoff or rainfall, but that slope and runoff are weakly correlated, precludes the recognition in a multiple regression analysis of any association that might exist between runoff and sediment yield. A second complication in recognizing possible associations between precipitation, runoff, and erosion in the data set is that I am in a position only to test for monotonic relationships. I have no *a priori* basis for proposing a non-monotonic regression model, as suggested by the data of Langbein and Schumm (1958), for such a steep mountainous landscape with deep gullies and active mass wasting.

For the study basins, yields range well over an order of magnitude higher than those in classic erosion studies (Langbein and Schumm, 1958), yet stations in the drier Grande basin, where erosion occurs by surface wash, deep gullying, and mass wasting, exhibit a range of erosion rates similar to those in the wettest part, the Beni basin (Guyot et al., 1989a), where erosion is dominated by mass wasting, including very large rockslides and deep gullies. Hence, in this steep, rapidly-eroding study area, the erosive effects of increasing rainfall may in part be balanced by protective effects of additional vegetation cover, and also by the observed correlation (Figure 1.3b) that wetter basins tend to have steeper average hillslopes (perhaps masking the variance explained by runoff in the multiple regression analysis). However, my analysis finds that the product of runoff and S_{avg} (a measure of the energy expenditure rate of runoff) does not offer a statistical improvement in explaining erosion. Hence, geomorphic mass-flux models which ascribe a predominant role to the erosive power of water may not apply directly on large spatial scales to the hillslopes that compose most of the landscape – the "unit power of water discharge" concept used for modeling river incision or hillslope erosion does not obviously apply here to hillslope mass wasting. In the Bolivian Andes, so many hillslopes are undercut by streams and stand near their threshold angle of stability that

variations in slope, associated with lithological differences, do not appear to control the intensity of landsliding or gullying, if runoff is sufficient to carry away the debris supply.

However, in the very arid Pilcomayo basin to the south, both modern and late Neogene erosion rates are considerably lower (Gubbels et al., 1993; Guyot et al., 1990; Horton, 1999), suggesting that there may indeed be a runoff limit below which denudation rates (and, implicitly, channel incision) do ultimately decrease for desert basins (the four runoff values < 100 mm/yr in Figure 1.3a which also show anomalously-high slopes in Figure 1.3b). However, for the wet extreme, humid basins (runoff > 1000 mm/yr) do not show remarkably higher rates of erosion (Figure 1.3a depicts only a weak positive relationship which is explained by the associated increase in slope in Figure 1.3b), so I do not find any strong runoff-erosion relationship similar to the correlation that Hicks et al. (1996) found for mountainous New Zealand basins of uniform lithologies, similar to Bolivia. This may be because their humid basins display a larger amount of rainfall, 710 - 11,200 mm/yr, so perhaps they may realize different rates or types of "humid" geomorphic processes than typically observed in Bolivia, or that their wettest basins lie in recently deglaciated mountains with significant erosion of stores of loose glacial sediment. Upon inspection of the New Zealand dataset, I note that the statistical correlation between runoff and average hillslope angle is particularly strong, so S_{avg} can by itself explain much of the observed variance in basin erosion.

Implications for landscape denudation over geologic timescales

The positive correlation between runoff and average hillslope angle (Figure 1.3b) is intriguing, because it suggests a potential positive feedback mechanism over geologic time between higher precipitation and rougher landscapes: more rain would imply a higher erosive stream power (e.g., Seidl and Dietrich, 1992), favoring more robust channel network incision and the resulting excavation of deep valleys with steep hillslopes. Furthermore, I speculate that these large valleys might then, in turn, topographically funnel and trap additional moisture through orographic precipitation and

the creation of macro-scale atmospheric turbulence, a potential positive feedback mechanism that might enhance upslope moisture conveyance.

It is important to emphasize that because wetter landscapes tend to have steeper slopes, runoff may indeed play a critical indirect role in "adjusting" a landscape over geologic timescales via enhanced or diminished rates of channel network incision to generate "wet" or "dry" hillslope conditions, which in turn control sediment delivery to the channels (e.g., incision rates decrease with runoff, decreasing average basin hillslope, and consequently denudation). In the extreme case of 'desert' basins (here defined as having runoff < 100 mm/yr), not only is the stream power of water greatly reduced, but the sediment conveyance capacity of the channel network may be insufficient to remove much of the material supplied by hillslope mass wasting. In field studies in the arid Andes of southeastern Bolivia, I have observed that many channels are completely mantled by sediment (to an unknown depth), which would prevent or retard the further incision of the channel network into bedrock. Hence, transport-limited desert basins would be expected to have extremely low sediment yields, due to 1) low rates of channel network incision, 2) the resulting low-angled hillslopes, and 3) the possible trapping of significant volumes of sediment supplied from hillslopes within the wide valley floors.

A probable explanation for the lack of a strong role for runoff in the wetter basins of the dataset is that many of the landscapes in the humid Beni River drainage basin of northern Bolivia may have reached "steady-state" rates of hillslope mass wasting and river incision which are in long-term equilibrium with local uplift rates (Burbank et al., 1996; Schmidt and Montgomery, 1995). In this scenario, a "constant" rate of mass wasting may exist such that in these basins the average hillslope has locally adjusted to the lithologic strength such as to yield an effectively constant rate of exhumation equal to the tectonic input (i.e., a dynamic equilibrium such that there is no change in the average surface elevation), regardless of regional variations in rainfall. However, while such a "steady-state" argument may be made for many of the 16 stations within the Beni basin (as modeled for the Beni by Safran (1998)), which has seen significant uplift and

exhumation, few of the 31 other stations farther to the southeast appear to have reached a similar sort of dynamic equilibrium. Here, due to a more arid climate sustained over geologic timescales, total exhumation and evacuation of sediment has been considerably less, leading to a substantial increase in the width of the Andean orogen (Horton, 1999; Montgomery et al., 2001). Furthermore, because the foreland basin trap efficiency for the arid fluvial megafans along the Chaco Plain (along the Subandean range front in southern Bolivia) is near 100% (Horton and DeCelles, 2001), in contrast to the 40 - 55 % trap efficiency observed for the Beni and Mamore foreland basins (Guyot, 1993), sediment not stored within the Subandes is likely to be deposited near the range front. Thus, for arid regions, most eroded sediment would be readily reincorporated back into the orogen via crustal shortening, while the more humid northern basins would export the majority of their fluvially-mobilized rock mass to depocenters far removed from the orogenic system. In conclusion, while basin runoff does not show obvious statistical significance in determining modern erosion rates in Bolivia, over geologic timescales it may play a key role in orchestrating channel network incision and sediment evacuation, thereby setting the basin conditions for hillslope and relief.

Cell-based models for hillslope mass wasting

The watershed-averaged parameters of hillslope angle and local relief apply only to discrete basins. To estimate erosion elsewhere throughout the Andes, I next develop a flux model which estimates mass wasting on the hillslope scale (1 - 3 km, the scale of several DEM pixels) based on available parameters: cell slope and the lithologic index (L). Previous workers have proposed landscape evolution models which calculate cell-flux as linear, power, or threshold functions of local slope (e.g., Anderson, 1994; Howard, 1994; Kirkby, 1987). Granger et al. (1996) found that an exponential function of the average hillslope gradient best describes erosion rates within a small catchment. Accordingly, to explore general empirical models applicable to the humid Andean basins that drain into the Amazon basin to the north, I have tested such theoretical mass flux

models against a dataset of all of the Bolivian basins for which the annual runoff exceeds 100 mm/yr (41 basins, after discarding 6 arid basins from southern Bolivia). I examined statistical models of the form indicated in Table 1.4b.

For all parameter values (variable *n*, Table 1.4b, tested between 0.1 and 20.0 in steps of 0.1), versions of each flux model were applied on a cell-by-cell basis throughout the DEM and then summed for each study basin. Values of the parameter L for average basin lithology were set to 46, 7, or 1, as derived from the foregoing analysis. After thus controlling for lithology, I regressed the slope function against observed sediment flux to determine which n and k best explained the observed variance in sediment discharge. I found that all three slope-driven cell flux models offer similar R^2 values (Table 1.4b). Because pixel size is approximately 870m x 930m, calculated slope (3 x 3 average maximum) represents a valley-wall-scale slope, not the steepest local slopes where mass failures typically occur. It therefore seems problematic to apply a threshold failure model to a DEM of this resolution because 1) pixel scale is generally larger than failure scale, and 2) without maximum slope values accurately observed at the failure scale, the selection of an appropriate S_{max} is somewhat arbitrary. Until we develop a higher-resolution DEM and lithologic dataset for the Andes, simpler power and exponential functions of slope, with correction for lithology, appear to be the most practical candidates for a general mass-flux model applicable throughout the Amazonian Andes.

Given previous work that estimates an annual Andean sediment input of at least 1.3 Gtonnes to the lower mainstem Amazon River (Dunne et al., 1998), it is interesting to estimate the total sediment efflux from the Andes to the Amazon basin. Lacking appropriate geologic maps for the entire range, I employ the best-fit power and exponential equations for mass flux (Figure 1.4, Table 1.4b) for an estimated range of 'average' L values from 7 to 9 (L = 8 is the average for Bolivia). When the GIS procedure is applied to the 30-arc-second DEM throughout the Amazonian Andes, these equations generate flux estimates of 2.3—3.1 Gtonnes/yr to the range front, depending on which equation and average lithologic value is assumed for the Andes. Evidently, the

intervening foreland basins along the Andean range front intercept approximately half of the total mass flux out of the Andes, a fraction similar to that measured for the foreland basins of Bolivia (Guyot, 1993). Because water surface measurements of suspended-sediment concentration used for this study underestimate total sediment flux, the best-fit equations and flux calculations represent conservative estimates. In contrast, Dunne et al. (1998) utilized depth-integrated measurements of sediment concentrations. Therefore, my assessed values for Andean sediment production and the foreland basin trap efficiency are probably significantly lower than their actual rates.

Conclusion

A new procedure is presented for mass flux analysis in large, continental-scale basins. By separating the Amazon Basin into geomorphic process zones, I specifically focused attention on the process of denudation in the rapidly eroding mountainous regions that supply essentially all of the Amazon's sediment load: the Andes of Bolivia, Columbia, and Peru. After selecting Bolivian basins free from major sediment sinks and, consequently, the non-physical scaling effects of basin area, I performed a multiple regression analysis to determine which morphometric parameters best predict decadal-scale denudation rates derived from river sediment yields: average lithology (L) and average hillslope angle. That runoff is not statistically significant in determining modern erosion rate is both intriguing and enigmatic, suggesting a complex relationship between runoff, channel network incision, valley slope morphology, lithology, mass wasting, and sediment transport in active orogens. Therefore, I evaluated several hillslope-scale mass flux models to develop a technique based on lithology and slope that is transferable to other basins. Simple slope-driven power and exponential models perform well to estimate observed sediment flux, and can therefore be applied to predict flux rates for ungauged basins throughout the greater Andes. By utilizing higher-resolution DEMs and more extensive lithologic data, enhanced versions of these mass-flux models might be flexible enough to be applied globally to predict denudation rates elsewhere in the world.

Table 1.1. Results from in-situ measurements of compressive rock strength with a N-type Schmidt hammer at 50 sites throughout Bolivia. A Probst Lithologic Index (PLI), which represents the relative rates of chemical erosion expected for each rock type (Probst, 1990), is assigned for each lithology, with the basin-averaged values reported in Table 1.2. For this analysis, the "Strong Sedimentary" lithologic class (common throughout the Andes) is combined with the "Meta-Sedimentary" group (found topographically deeper within the major valley bottoms and therefore probably extensive at depth within the mountains, although of more limited spatial extent higher on the valley walls). This new group is henceforth referred to as "meta-seds" and is assigned a common PLI of 4.

Rock Type	Granite	Ignimbrite	Quartzite	Slate	Schist	Massive Sandstone	Massive Greywacke	Greywacke	Phyllite	Weathered Sandstone	Colluvium & Alluvium
Lithologic Class	Igneous		Meta-Sedimentary			Strong Sedimentary		Weak Sedimentary			Unconsolidated
Compressive Strength (N mm^{-2})	80 ± 14	51	83 ± 7	77 ± 4	63 ± 14	51 ± 10	54 ± 9	19 ± 6	23 ± 5	7 ± 2	0
Assigned Probst Lithologic Index (PLI)	1	2	4	4	4	4	4	10	10	10	40

Table 1.2. Bolivian river gauging stations without major sediment sinks, including most of the morphologic parameters used in the regression analysis. Water and sediment discharge are reported (flux data and abbreviated station names from Guyot, 1993, and Guyot et al., 1990), along with the associated basin runoff, sediment yield, and denudation rate. For each station, we list the number of sediment concentration measurements used to develop the relationship of sediment concentration to water discharge, which is measured daily. For each basin, average slope (S_{avg}) is the mean of all DEM slope values, average local relief (R_a) is the mean of all local relief values (defined at each DEM pixel as the maximum difference in elevation observed within a 5 km search radius), maximum relief is maximum basin elevation minus the station elevation, relief ratio is the maxim relief divided by the trunk stream length, Probst lithologic index (PLI) is the area-weighted PLI average for the basin, and soil carbon, a proxy for vegetation coverage and root density, is the area-weighted soil carbon content (as derived from a global vegetation map). Additional regression parameters were tested, but are not depicted in this table because they are not available for all stations and are not statistically significant. These include basin seasonality (fraction of the annual discharge conveyed during the rainy season), percent of vegetation cover, and hillslope "power" of water (runoff x S_{avg}).

Station Code	Basin Area (km^2)	Station Altitude (m)	Average Annual Discharge (m^3/s)	Average Altitude (m)	Avg Slope (deg)	Average Local Relief (m)	Max DEM Relief (m)	Trunk Stream Length (km)	Relief Ratio (m/m)	Probst Lithologic Index (PLI)	Assigned Lithologic Class	Soil Carbon (tonnes/ ha)	Number of Sediment Concentration Records	Runoff (mm/yr)	Sediment Flux (Mtonnes/ yr)	Yield (tonnes/ km^2 yr)	Basin Denudation Rate (mm/yr)
SIR	270	1640	12	3565	13.7	1815	3235	40	0.080	3.8	igneous	89	194	1400	2.00	7420	2.800
TAM	950	1185	52	3561	13.1	1826	3862	56	0.069	3.8	igneous	71	320	1730	2.40	2520	0.952
VBA	1900	1050	67	2937	11.8	1621	4172	85	0.049	3.8	igneous	75	353	1110	7.80	4110	1.550
HUL	17	3620	0.1	3922	6.0	1113	1048	10	0.108	30.0	weak sed.	5	349	190	0.07	4060	1.534
ACH	38	3580	0.2	4188	7.4	1124	1345	12	0.113	34.0	weak sed.	7	131	170	0.20	5300	1.999
LUR	810	2550	10	4053	5.0	780	2366	56	0.042	15.4	weak sed.	9	39	390	6.41	7910	2.984
POR	240	2500	3	4065	8.5	1256	2143	28	0.083	6.2	meta sed.	11	36	380	0.80	3310	1.250
VER	140	2830	5	4729	5.0	930	1818	23	0.080	2.0	igneous	14	146	1130	0.01	80	0.030
MIG	380	1980	17	4284	7.8	1232	2693	34	0.080	2.0	igneous	37	87	1490	0.05	130	0.049
CAJ	6500	760	99	3498	9.3	1332	4214	159	0.027	14.0	weak sed.	30	332	480	119.03	18310	6.910
COT	5600	1270	84	3389	9.7	1355	4299	148	0.029	4.2	meta sed.	24	105	470	40.56	7240	2.733
MIS	350	3700	4	4264	5.3	724	920	26	0.036	4.0	igneous	9	153	400	0.01	30	0.013
VIN	50	3700	1	4442	5.2	802	676	9	0.076	4.0	igneous	8	1141	510	0.00	60	0.023
LOC	200	1700	15	3121	12.3	1838	3133	23	0.136	4.0	igneous	47	1000	2370	0.67	3350	1.264
SPE	320	1040	27	2921	12.0	1836	3576	28	0.126	5.7	meta sed.	59	190	2660	3.50	10940	4.127
ICO	2300	600	130	2556	8.3	1248	3974	87	0.046	5.1	meta sed.	84	188	1780	11.40	4960	1.870
BER	480	900	4	1491	4.6	582	1229	39	0.031	4.6	meta sed.	184	2220	280	0.60	1250	0.472
ANG	1420	650	11	1462	4.3	574	1798	72	0.025	4.4	meta sed.	177	3027	240	2.90	2040	0.771
ELV	64	650	1	1247	5.7	860	1025	13	0.077	4.8	meta sed.	182	2162	250	0.03	470	0.177
EPS	203	550	3	883	3.6	532	1046	25	0.043	12.6	weak sed.	209	2186	400	0.42	2070	0.781
AMO	9200	1850	59	3304	5.7	834	2927	170	0.017	14.0	weak sed.	10	580	200	126.05	13700	5.170
HUR	11200	1600	70	3589	7.6	948	3334	258	0.013	5.0	meta sed.	10	282	200	14.12	1260	0.476
ARC	23700	1500	130	3314	6.9	911	3511	300	0.012	6.8	meta sed.	13	868	170	154.25	6510	2.456
PNA	31200	950	220	3059	6.7	901	4024	428	0.009	6.1	meta sed.	19	938	220	206.89	6630	2.502
MIZ	10800	950	47	2390	5.1	742	3544	247	0.014	4.6	meta sed.	32	897	140	14.11	1310	0.493
PAZ	4360	1080	32	2200	5.3	789	3061	151	0.020	6.2	meta sed.	57	557	230	2.20	510	0.191
SAN	7500	550	79	1264	3.2	484	2705	228	0.012	18.8	weak sed.	127	642	330	19.42	2590	0.977
AT	6340	2500	20	4021	5.5	764	2565	186	0.014	5.6	meta sed.	7	1088	98	12.00	1890	0.714
NU	1600	2300	8.5	3497	7.7	954	2231	95	0.024	7.3	meta sed.	6	48	168	1.10	690	0.259
VQ	13200	2000	49	3644	5.9	809	3164	269	0.012	6.6	meta sed.	6	552	117	22.00	1670	0.629
SL	4200	3100	6.5	4084	5.2	696	2272	113	0.020	4.0	igneous	10	57	49	0.50	120	0.045
EP	20100	2300	10	3870	3.6	557	3420	389	0.009	10.8	meta sed.	8	584	16	2.40	120	0.045
CH	42900	2100	53	3734	4.5	649	3734	453	0.008	7.5	meta sed.	8	549	39	14.00	330	0.123
SJ	47500	800	82	3646	4.8	688	4977	563	0.009	7.2	meta sed.	10	309	54	31.00	650	0.246
VI	81300	340	260	3263	5.2	739	5441	697	0.008	6.9	meta sed.	22	745	99	72.00	890	0.334
CAB	230	2100	1.5	2801	4.7	734	1319	27	0.049	5.4	meta sed.	7	444	206	0.05	220	0.082
OB	920	1900	3.8	2653	5.1	803	2263	47	0.048	12.1	meta sed.	10	192	130	0.40	440	0.164
TO	460	1900	9	2594	7.0	1148	2805	36	0.078	12.0	meta sed.	11	584	617	1.50	3261	1.231
SA	290	1200	5.9	2214	4.4	701	1700	35	0.049	4.4	meta sed.	44	181	642	0.06	207	0.078
PA	220	1200	4.6	2068	5.3	860	2143	34	0.063	4.6	meta sed.	72	182	660	0.11	500	0.189
AQM	9400	500	420	2678	4.3	734	5294	147	0.036	14.0	weak sed.	80	351	1410	36.80	3900	1.472
SRC	4700	440	260	2212	7.8	1142	5052	125	0.040	3.8	igneous	106	49	1750	7.10	1500	0.566
AIN	29900	400	840	2606	7.6	1132	4994	360	0.014	8.0	meta sed.	79	157	890	115.00	3800	1.434
AB	67500	280	2170	2227	5.7	870	5596	446	0.013	8.9	meta sed.	94	456	1010	219.00	3200	1.208
LBE	2880	350	12	1077	3.1	433	2088	155	0.013	14.5	weak sed.	179	1684	130	2.30	799	0.301
PEI	4160	280	21	832	2.1	301	2160	193	0.011	21.4	weak sed.	163	3900	160	1.00	240	0.091
AP	59800	450	290	2522	6.0	828	4685	604	0.008	7.2	meta sed.	53	851	150	125.00	2100	0.792

Table 1.3. Pearson correlation matrix (r values) for the log values of the basin parameters depicted in Table 1.2. Sediment yield is most strongly correlated with average slope (of the "topographic" variables) and lithology (PLI). Other parameters with apparent relevance to sediment yield (e.g., runoff) are no longer statistically significant once the first independent variables have been incorporated into the multiple regression analysis.

	Basin Area (km^2)	Station Altitude (m)	Average Annual Discharge (m^3/s)	Average Altitude (m)	Avg Slope (deg)	Average Local Relief (m)	Max DEM Relief (m)	Trunk Stream Length (km)	Relief Ratio (m/m)	Probst Lithologic Index (PLI)	Soil Carbon (tonnes/ha)	Runoff (mm/yr)	Sediment Flux (Mtonnes/ yr)
Station Altitude (m)	-0.48												
Average Annual Discharge (m^3/s)	0.85	-0.62											
Average Altitude (m)	-0.01	0.71	-0.04										
Avg Slope (deg)	-0.16	0.22	0.14	0.51									
Average Local Relief (m)	-0.25	0.26	0.08	0.54	0.98								
Max DEM Relief (m)	0.78	-0.45	0.88	0.15	0.32	0.29							
Trunk Stream Length (km)	0.99	-0.49	0.82	-0.04	-0.19	-0.29	0.76						
Relief Ratio (m/m)	-0.90	0.40	-0.60	0.15	0.46	0.57	-0.45	-0.92					
Probst Lithologic Index (PLI)	0.07	-0.13	-0.12	-0.25	-0.39	-0.35	-0.05	0.10	-0.18				
Soil Carbon (tonnes/ha)	0.02	-0.79	0.29	-0.78	-0.08	-0.10	0.12	0.02	0.04	-0.11			
Runoff (mm/yr)	-0.37	-0.17	0.16	-0.03	0.55	0.62	0.10	-0.42	0.64	-0.34	0.46		
Sediment Flux (Mtonnes/ yr)	0.85	-0.50	0.84	-0.02	0.14	0.05	0.83	0.84	-0.66	0.24	0.10	-0.12	
Yield (tonnes/ km^2 yr)	0.17	-0.25	0.35	-0.03	0.48	0.46	0.46	0.17	0.04	0.35	0.17	0.30	0.66

Table 1.4. Tested sediment flux models with best-fit statistics. A: Results of a forward stepwise multiple regression of basin-averaged parameters. Independent variables listed in order of statistical significance. B: Cell flux models tested for all values of n between 0.1 and 20.0 for 41 basins, excluding the 6 most arid basins in Table 1.2. The negative terms for the exponential and threshold models are to force a zero flux for zero slope. Variable include average annual sediment discharge (Q_s), lithology (L), basin area (A), and average basin slope (S_{avg}, in degrees). For the flux models in B, DEM cell-based slope (S) is measured in units of gradient (m/m), not degrees, and sediment flux has been normalized to L = 1, the hypothetical flux for granite (e.g., before regression analysis, the recorded sediment fluxes from basins of meta-sedimentary and weak-sedimentary lithology are reduced by factors of 7.2 and 46, respectively). All regression p-values are less than 0.001.

A: Multiple Regression Analysis for Basins	**Units**	**R^2**
$Yield = 0.46\ L\ S_{avg}^{3.36}$	tonnes/km^{2}yr	0.77
$Q_s = 0.00055\ A^{1.04} L\ S_{avg}^{3.36}$	Mtonnes/yr	0.92
B: Cell-based Flux Models Applied to DEM	**Best *k*, *n***	**R^2**
$Q_s = \sum kS^n$	0.0115, 1.6	0.82
$Q_s = \sum k(e^{nS} - 1)$	0.00076, 3.6	0.81
$Q_s = \sum k\left(\frac{1}{S_{max} - S^n} - \frac{1}{S_{max}^n}\right)$	0.0071, 3.7	0.81

Figure 1.1. Shaded topographic map of Bolivia with marked gauging stations (yellow triangles with red dots), DEM rivers (in blue), and lithology (classified by color scheme).

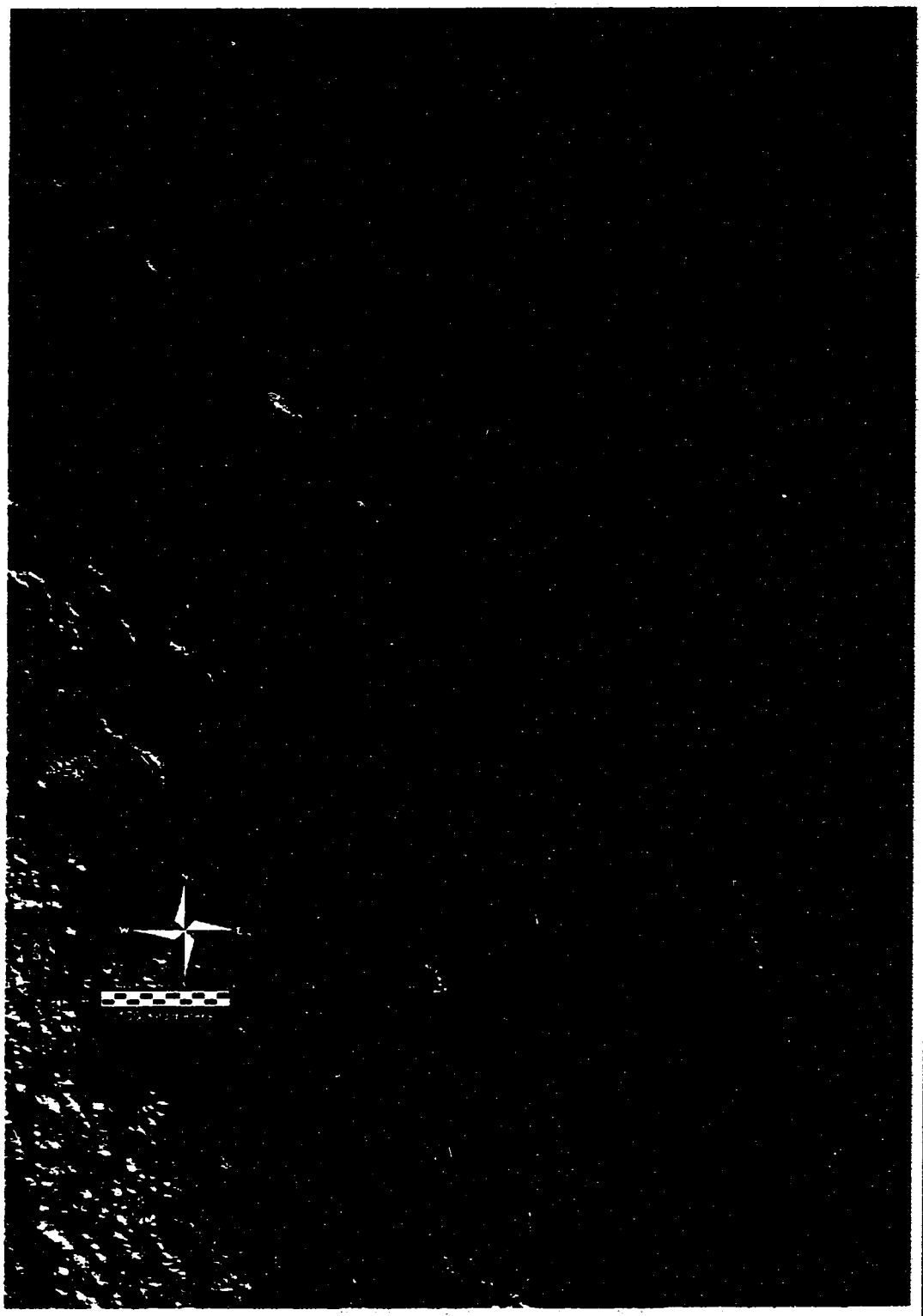

Figure 1: Shaded topography of Bolivia with marked gauging stations, DEM rivers, and lithology:
■ - Igneous Intrusive ■ - Igneous Extrusive ■ - Strong Seds ■ -Weak Seds ■ - Alluvium

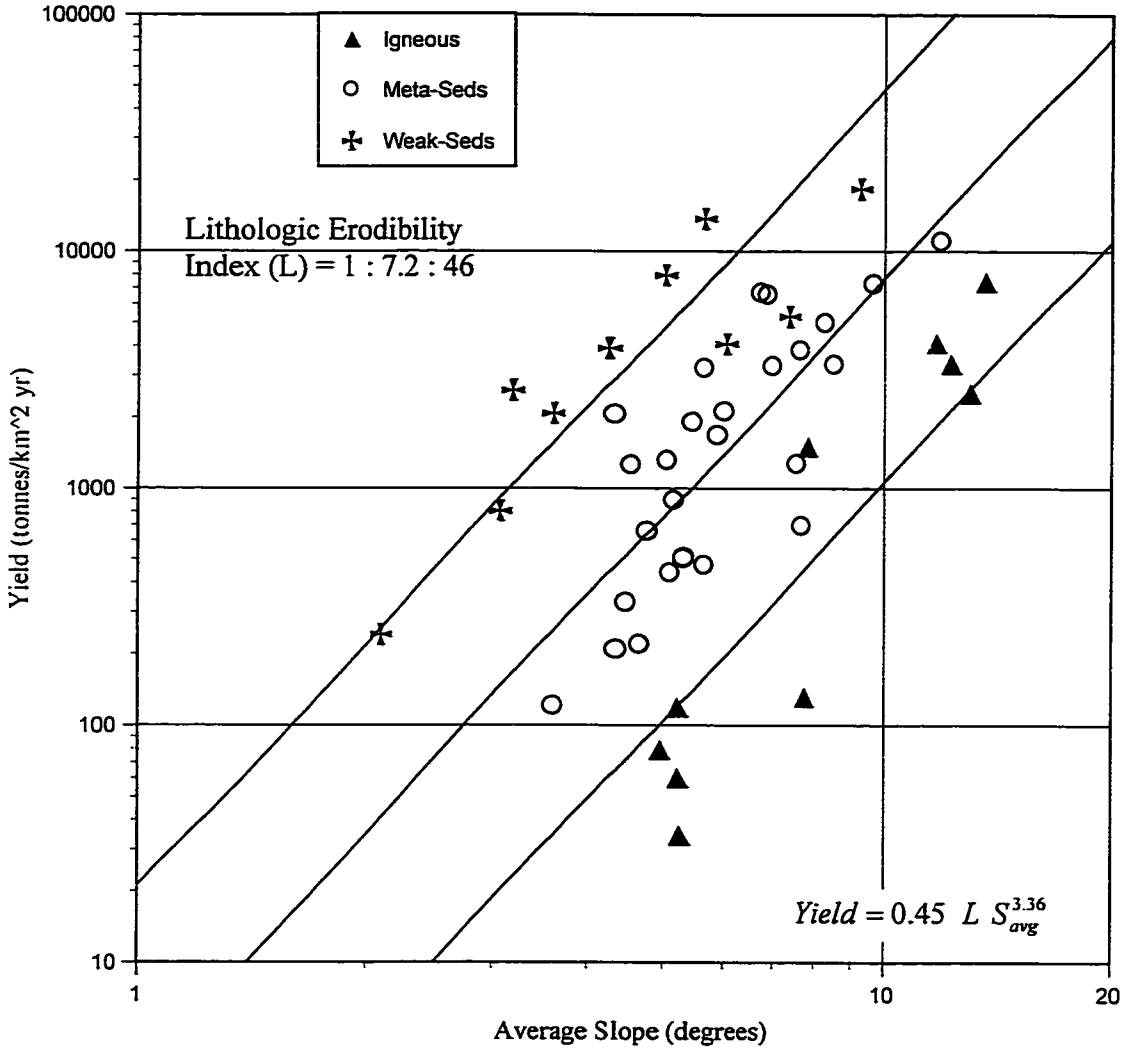

Figure 1.2a. Plot of basin yield versus average basin slope (S_{avg}) for the 47 Andean study basins, with basins classified according to their GIS-averaged PLI (Table 1.2). Slopes for the weak-seds (N=10) and igneous (N=10) lithologic groups were similar (at p=0.04) to that for the larger meta-seds (N=27) group (p=0.09 and p= 0.04), so all were fitted with the slope of the meta-sed group (3.36 +/- 1.13, p=0.05) to facilitate comparison of the intercepts (0.454 +1.93/–0.367, 3.29 +13.0/-2.63, and 20.65 +63.5/-15.6; p=0.05). The ratio of intercepts for each lithologic class defines a new lithologic erodibility index (L): 1 : 7.2 : 46. Best-fit lines for igneous, meta-seds, and weak-seds lithologic classes have respective R^2 values of 0.72, 0.67, and 0.55 ($p < 0.00001$ for all).

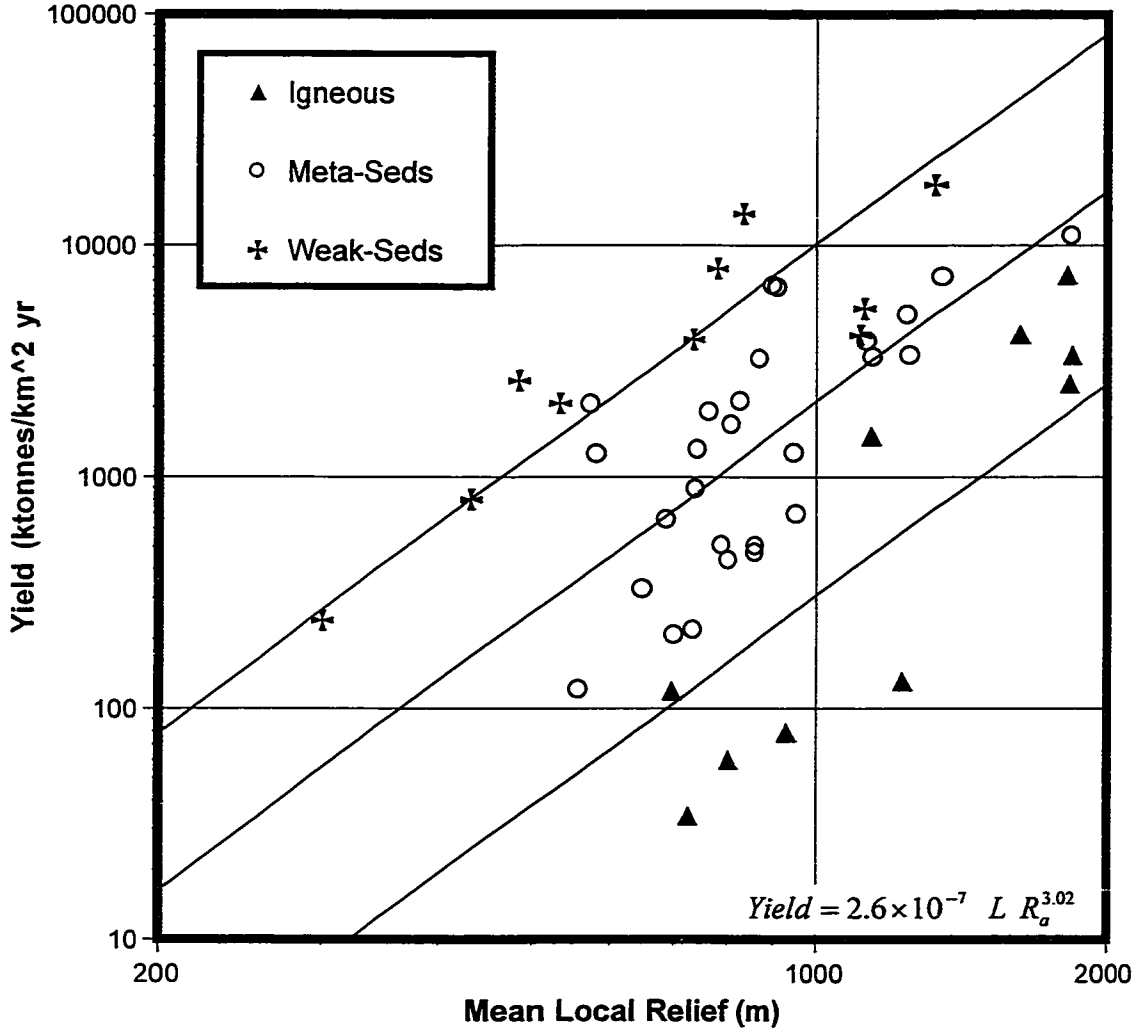

Figure 1.2b. Plot of basin yield versus average local relief (R_a) for the 47 Andean study basins, with basins classified according to their GIS-averaged PLI (Table 1.2). Slopes for the smaller groups were again somewhat similar to that for the larger meta-seds group (p=0.16 and p= 0.03), so all were fitted with the slope of the meta-sed group (3.02 +/- 1.28, p=0.05) to facilitate comparison of the intercepts (2.60E-7, 1.79E-6, and 8.57E-6). Ratio of intercepts for each lithologic class defines a slightly different lithologic erodibility index than in Figure 1.2a: 1 : 6.9 : 33. Best-fit lines for igneous, meta-seds, and weak-seds lithologic classes have respective R^2 values of 0.56, 0.49, and 0.49 ($p < 0.01$ for all).

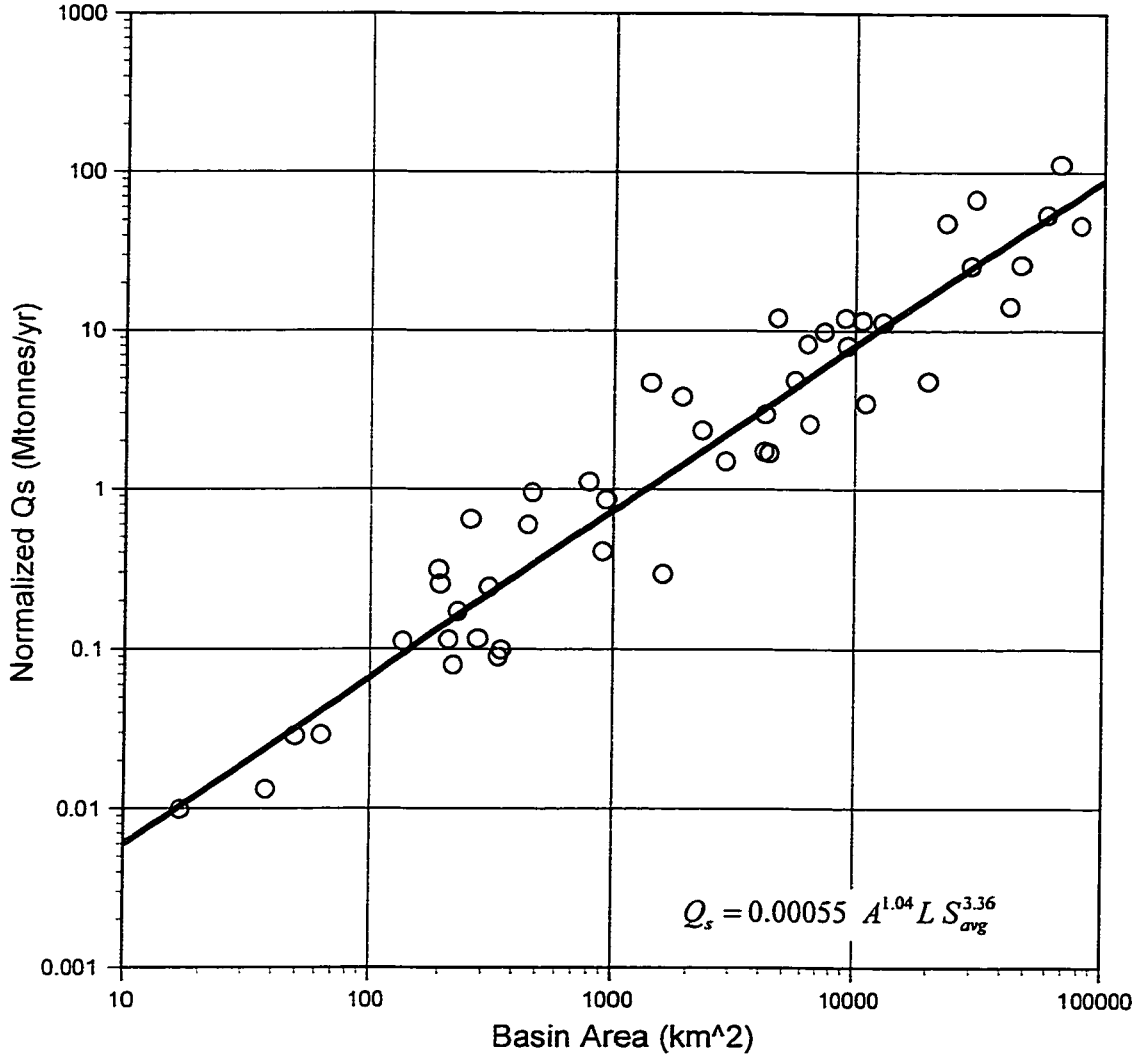

Figure 1.2c. Plot of area versus study basin flux normalized (per the depicted equation) to the explained lithologic and slope variance as depicted in Fig. 1.2a. Best-fit line has slope 1.04 +/- 0.096 and $R^2 = 0.92$ ($p < 0.00001$).

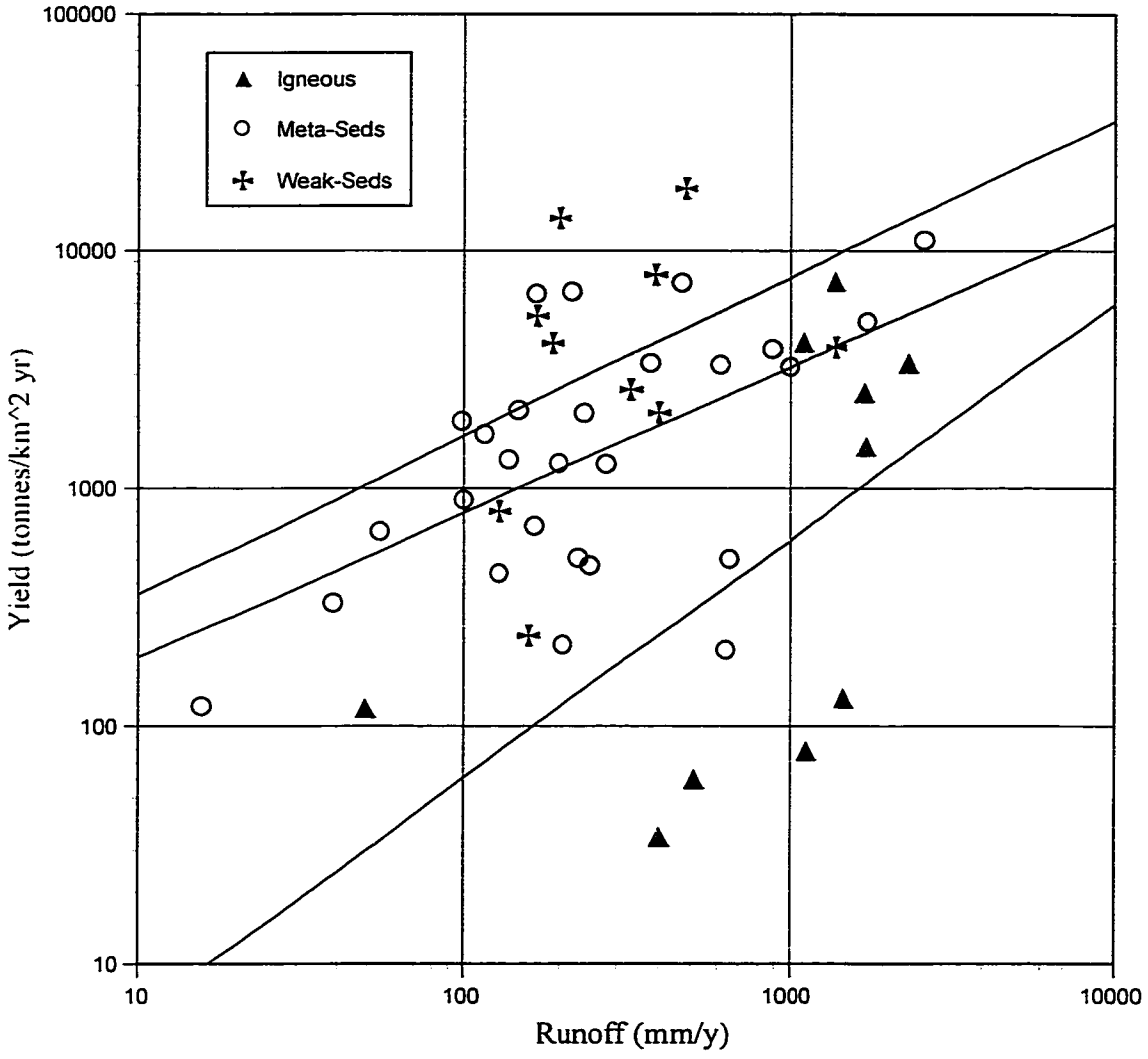

Figure 1.3a. Relationship between runoff and erosion for all 47 study stations, showing a positive correlation mainly for the extremes in rainfall (< 100 and > 1000 mm/y). Best-fit lines (no assumptions for slope) for igneous, meta-seds, and weak-seds lithologic classes have respective R^2 values of 0.31, 0.32, and 0.13 (p=0.047, 0.001, and 0.15).

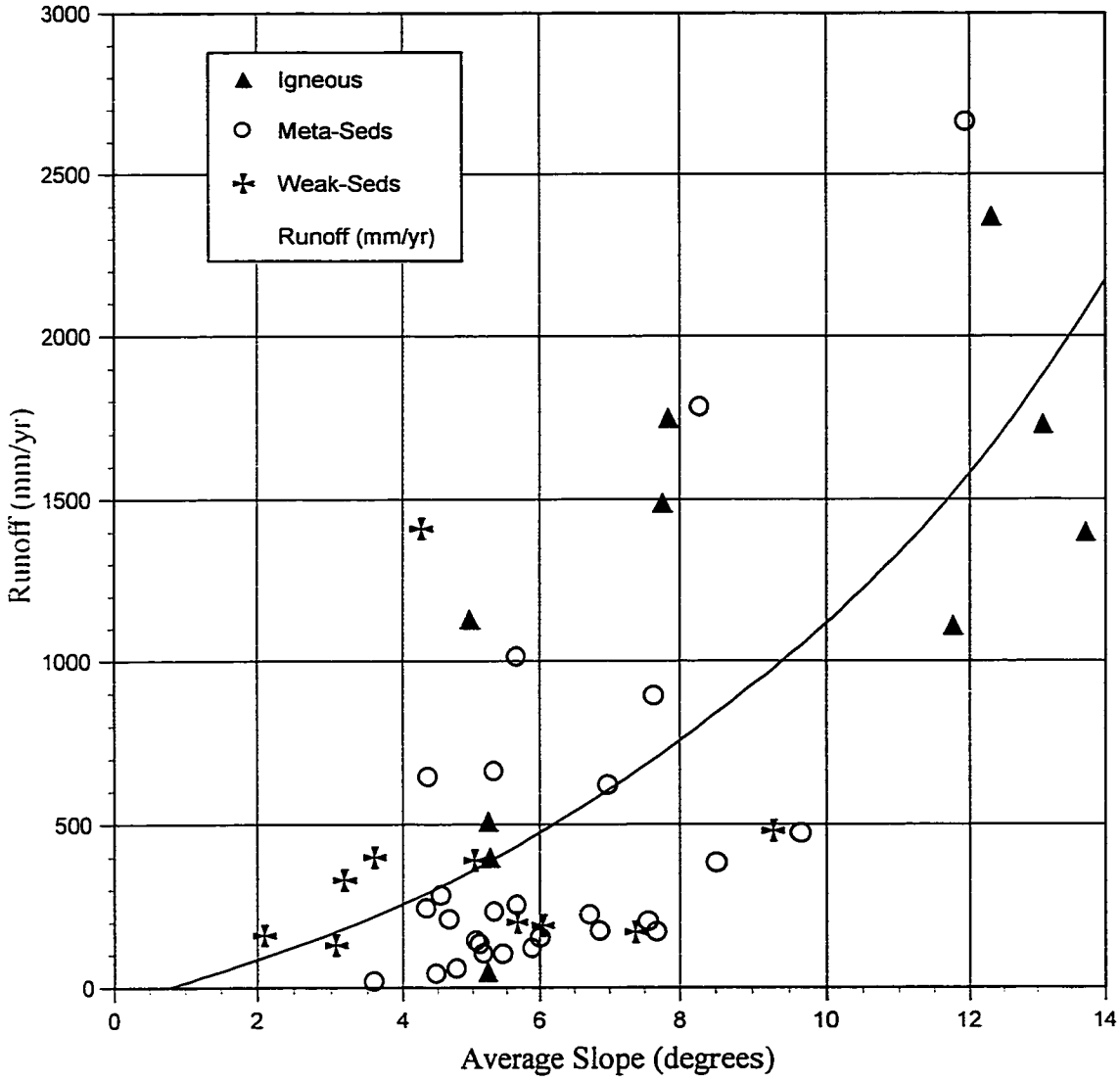

Figure 1.3b. Relationship between rainfall and average slope (S_{avg}). Best-fit exponential curve to entire dataset has $R^2 = 0.50$ ($p < 0.00001$).

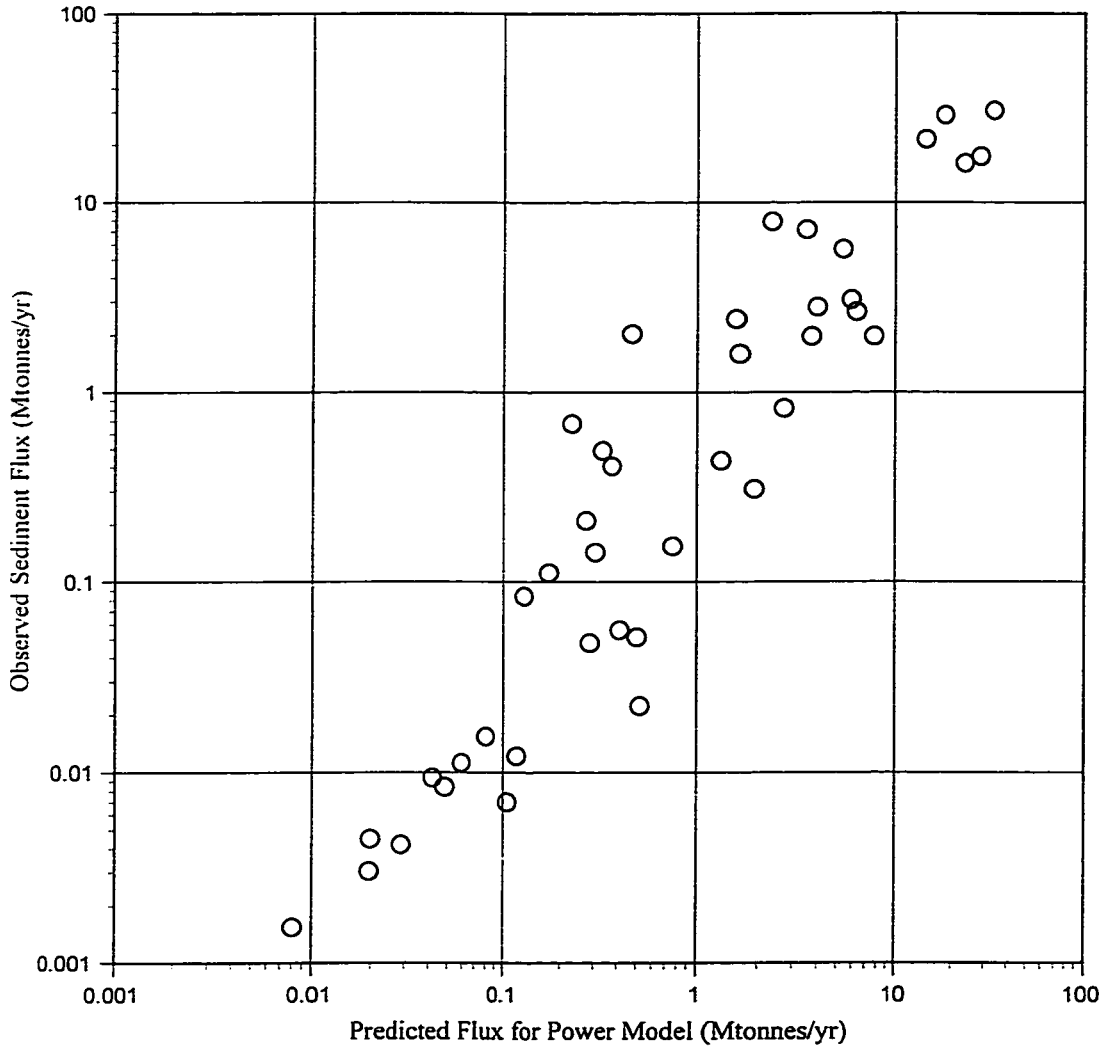

Figure 1.4. Plot of predicted versus observed sediment flux for all 41 study basins for which the annual runoff exceeds 100 mm/yr, the results of the DEM cell-based power law depicted in Table 1.4b. As listed in Table 1.4b, $R^2 = 0.82$ ($p < 0.00001$).

Chapter 2

Beni River morphology, migration, and sediment exchange between the river and its floodplain

Abstract

Decadal-scale sediment transport and deposition, lateral migration, and floodplain-channel interaction within large, sand-bedded rivers is a topic of considerable global relevance. The Beni River, which drains 70,000 km^2 of the northern Bolivian Andes into the Amazon Basin, offers a unique opportunity to study a pristine river that interacts dynamically with its floodplain, depositing ~ 100 Mtonnes of sediment annually as it traverses a large foreland basin. This study combines field surveys of bank and channel topography, channel slope, and granulometry with floodplain sedimentation rates measured using ^{210}Pb geochronology, and analysis of four decades of channel migration data derived from Landsat and aerial images. The resulting model of sediment interchange between the channel and floodplain quantifies fluxes at the scale of 10-km reaches, and concurs with four decades of gauging records (calibrated to account for the non-uniform concentration of suspended sediment with river depth) and an observed downstream decrease in ^{210}Pb activity. While the annual mass of sediment eroded from cut banks and redeposited into point bars is very large, greater than the total sediment throughput of the Beni River, the net change in floodplain sediment storage associated with this process is small. The majority of the net sediment efflux is into the distal floodplain as large crevasse splay deposits, while proximal floodplain and channel bed deposition, lateral migration, and the formation of cutoff lakes all play a secondary role. Supplemented with observations of floodplain morphology and accumulation rates determined via sediment coring and ^{210}Pb geochronology, this flux analysis suggests that much of the Beni channel and proximal floodplain are aggrading at 2–5 cm per year, consistent with the observed bank granulometry and the Beni River's geological history

of repeated major channel avulsions. Large natural levees are present, and may facilitate the crevasse splays that account for most floodplain deposition. On the scale of the foreland basin, sediment accumulation occurs mostly in the foredeep, with a smaller amount deposited within the back-bulge secondary basin and almost nothing in the forebulge. Downstream of the gravel-sand transition, granulometric analysis of bedload suggests constant grainsize across the foredeep, followed by a slight fining of coarse suspended load downstream of the tectonic forebulge, either as a result of selective transport, or of less energetic secondary circulation for meander point bars. Cross-channel granulometry transects also support the estimated floodplain accumulation rate. This analysis shows that sediment exchange and transport by a large sand-bedded river within a foreland basin is dominated by channel-floodplain interaction and suggests that similar floodplain processes may also be or once were important for sand-bedded rivers elsewhere, before they were altered anthropogenically to reduce flooding, channel migration, and breaching of natural levees.

Introduction

Throughout the world, large rivers occupy lowland floodplains, which are both constructed and destroyed by channel migration. Sediments are continually eroded from the outer cut banks of meander apexes, mixed with waterborne sediment, and re-deposited onto the inner point bars and, during flooding, onto the floodplain itself via diffuse and channelized overbank flows. To determine the total annual sediment exchange and net accumulation of channel sediment on the floodplain, these processes must be investigated and quantified on at least a decadal-to-century temporal scale, so as to record and account for annual variations in channel migration and sediment conveyance. To establish a sediment budget for the sediment exchanged between the channel and floodplain within any large river-floodplain system, it is necessary to analyze floodplain destruction by channel migration and construction by bar deposition and floodplain accumulation. Ideally, all forms of sediment exchanges between the

channel and the floodplain must be quantified, preferably on a reach-by-reach basis so as to account for down-valley variation in the rates of these processes, as they are controlled by varying hydraulics, hydrology, and sediment availability. Only then can we "close" the mass balance, accounting for all exchanged sediment and net accumulation within the channel-floodplain system.

Whereas previous studies of such complex systems have investigated the individual processes of erosion, transport, or deposition, two prior studies have explored all of them simultaneously so as to construct a detailed mass balance for the system. For the lower Mississippi River and its floodplain, Kesel et al. (1992) estimated rates of bank erosion, point bar growth, and estimated the overbank sediment flux from surveys of deposit thickness. For the mainstem Amazon River in Brazil, Dunne et al. (1998) quantified a range of exchanges of sediment, including bank erosion, point bar growth, and overbank conveyance of sediment calculated from a flood routing analysis and an assumed floodplain trap efficiency of 90%. However, both of these prior studies are for the lower reaches of large rivers, regions which exhibit relatively minor net trapping of riverborne sediment as compared to the more active foreland basin depositional systems more proximal to the range front (e.g., < 15% for the mainstem Amazon, as compared to ~ 50% for the foreland basins in northern Bolivia).

Potter (1978) described several 'archetypical' fluvial environments, the behavior of which were controlled by the interactions of sediment supply, basin tectonics, and sediment transport capacity in foreland basins. Some rivers cross them; others run along them; others flow through and out of them and continue long trajectories along these structural down-warps in Earth's crust. The functioning of the foreland basin is a first-order determinant of the sediment budgets of continental-scale rivers, dictating how much sediment passes from an active orogen to distal lowlands, estuaries, and marine depocenters far from the mountain range. For example, Guyot (1993) demonstrated that of the 600 million tonnes of sediment leaving a gauged area of 175,000 km^2 in the Bolivian Andes, at least 60% was trapped in the foreland basin of the Beni-Mamore

lowland. Since the sediment supply of the Amazon River, to which this area drains, is derived almost entirely from Andean sources (Dunne et al., 1998; Gibbs, 1967; Meade et al., 1985), the influence of the foreland basin as an abstractor of sediment from a river system extends far downstream, affecting the floodplain geomorphology (Mertes et al., 1996), estuarine sediment supply (Dunne et al., 1998), the subaqueous delta of the Amazon continental shelf (Nittrouer et al., 1995), and ultimately the sediment supply to the coastal ocean (Milliman and Meade, 1983; Milliman and Syvitski, 1992).

In this chapter, I quantify a full range of exchanges of sediment between the channel and the floodplain along an 800 km sinuous section of the Beni River as it traverses a 450 km wide foreland basin. The gravel-sand transition in the Beni is ~ 10 km downstream of the range front, so almost the entire channel is sand-bedded. I measured decadal-scale rates of channel migration and the associated bank erosion and bar deposition, and quantified floodplain accumulation rates using a new procedure for ^{210}Pb geochronology. Because the river migrates rapidly, the floodplain is very active, and the effective foreland basin trap efficiency is ~ 50%, this study of a large river-floodplain system provides insight into the processes of sediment transport, exchange, and accumulation within a foreland basin.

Study area

The Bolivian Llanos is an excellent region to study active river-floodplain systems and foreland basins. First, the water and sediment fluxes, channel-floodplain interchanges, and net sediment sinks are all enormous (not subtle or hard to discern) and well-recorded for many stations throughout the basin (Guyot, 1993; Maurice-Bourgoin, 2001), facilitating geomorphic interpretation, flux measurement, and calculation of differences in mass flux. In particular, the Beni River gauging station near the piedmont town of Rurrenabaque (Figure 2.1) has been recording discharge on a daily basis since 1967, and the Beni station upstream of the lowland Amazonian city of Riberalta, at the other side of the Beni foreland, also has years of gauging records. Second, the tectonic

setting is relatively simple and well understood (Jordan, 1995; for a review of adjacent Andean tectonics see Beck et al., 1996; and Masek et al., 1994). It is the type example of a large, overfilled retroarc foreland basin with substantial basement depression (2–7 Km). Modern basin architecture is the result of continuous, eastward migration of the coupled orogenic wedge and foreland basin system since the Late Cretaceous-Paleocene, and consists of a continuous system of wedge-top, foredeep, forebulge, and back-bulge depozones (Horton and DeCeiles, 1997). Third, Horton and DeCelles (2001) and Horton et al. (2001) have investigated the preserved Mesozoic and Cenozoic foreland lithology deposited by several large fluvial megafans debouching from arid Andean basins ~1000 km to the south, proposing a stratigraphic model that may apply in part to the larger Beni River system. Fourth, the Beni basin is essentially pristine, without artificial levees, dams, roads, significant deforestation or cultivation (no mixing of the floodplain to affect the geochronology), or other anthropogenic complications detracting from the study of natural fluvial process. Fifth, the Bolivian Llanos, traversed by the Beni and Mamore Rivers, are significant in many globally important ways: the Beni River is the principal sediment supplier to the Madeira River (Guyot, 1993), which emerges from the far side of the basin and accounts for half of the sediment flux input into the mainstem Amazon River (Dunne et al., 1998); the basin is representative of the vast expanse of Andean-Amazonian foreland basins to the north; and the Llanos are rich in fluvially orchestrated biodiversity (e.g., Rasanen et al., 1987).

This study focuses on the reach of river between Rurrenabaque and Riberalta, Bolivia (Figure 2.1, pocket material), which traverses the entire foredeep, forebulge, and secondary back-bulge basin. At Rurrenabaque, the Beni has a drainage area of 68,000 km^2 and a mean annual discharge of 2,200 m^3/s (Guyot, 1993), with recorded flood discharges of > 20,000 m^3/s and regularly in excess of 15,000 m^3/s (Maurice-Bourgoin, 2001). From an elevation of 190 m (above mean sea level) at Rurrenabaque, the Beni flows along ~ 800 km of channel as it crosses its foreland basin and descends to about 120 m elevation at Riberalta, where it has a total basin area of 119,000 km^2. This reach

is remarkable in that there is only one major tributary, the Madidi River, along its entire course, greatly simplifying the modeling efforts: the many observed changes in river and floodplain morphology and mechanics are due primarily to transport mechanics and neotectonics, rather than to major tributary effects. For example, there are no sudden increases in water and/or sediment discharge; the Beni gradually increases its water discharge from the cumulative influence of dozens of minor "blackwater" floodplain tributaries, which transport virtually no sediment. Furthermore, the lower Beni and upper Madeira Rivers cross several hundred kilometers of upwarped hard crystalline cratonic basement (realized as a series of massive rapids) near the Brazilian border, effectively isolating the Bolivian foreland basins from the rapid and dramatic variations in sea level during the Quaternary.

I conducted system-wide field surveys of topography and granulometry, and undertook an extensive GIS (geographical information system) analysis of channel migration over the past four decades. Combined with my measurements of floodplain accumulation rates along the Beni River (Chapter 5), these surveys help quantify rates of sediment exchange between the channel and floodplain, and net sediment deposition within the Beni foreland. In this paper, I present an overview of the study methods and results, with a particular focus on the mechanisms of sediment exchange and accumulation within the Beni foreland. Besides a summary of results relevant to sedimentation along the Beni, this includes a complete accounting for all processes that affect sediment mass flux within the river-floodplain system. It includes a detailed model for sediment fluxes resolved at a 10-km scale, and a comparison of that model to long-term gauging records at Rurrenabaque and Riberalta. This description of Beni River morphology, granulometry, sedimentation, and flux analysis sets the stage for additional detailed analyses of the meso-scale geomorphic controls on channel morphology (Chapter 3), and the timing and rates of floodplain accumulation (Chapter 5).

Field and laboratory methods

After preliminary inspection of long-term gauging records and Landsat imagery, a primary site visit was conducted in June of 1998, during which limited topographic data and floodplain cores were collected within 100 km of Rurrenabaque. The principal sampling excursion occurred during August and September of 1999, during the dry season when the river and floodplain are the most accessible and the river stage is relatively constant. The lower Beni upstream of Riberalta was surveyed in September of 2000, and additional samples at Rurrenabaque and Riberalta were collected during a rainy season campaign in February, 2001. Because there is no road access for the entire river, all sampling was conducted from boats equipped to travel for long distances without resupply. Topographic surveys and sediment sampling were conducted both in the river and on the floodplain.

The basic sampling strategy was to stop at regular intervals, generally on the apex of a point bar. At 25 locations (Table 2.2), chosen for their representative position in the foreland basin or for other morphometric reasons (e.g., to sample a variety of channel-floodplain geometries), I surveyed transects across the channel and into the floodplain on both sides of the river. On these transects, sediment samples were collected 50 m –1.2 km into the forested floodplain (Figure 2.2), well past the edge of the unvegetated point bar. For such detailed transects, I would systematically sample the point bar, cut bank, and floodplain (Figure 2.2, Table 2.1), including topographic surveys, granulometric samples taken from 10 cm pits dug into the bare surfaces of the bar (Figure 2.3a) and cutbank (Figure 2.3b), and sediment cores extracted 65–160 cm deep into the vegetated floodplain (Figure 2.3c). On more regular intervals, I would briefly stop to record water-surface elevation, to collect granulometry samples at a consistent location on the point bar (the "MB" location, Table 2.1), and to survey bar and cutbank height and channel bed topography.

Water surface elevations, bar and floodplain locations, and boat locations on cross-channel transects were all recorded with a Trimble Pathfinder ProXRS DGPS

system, differentially corrected with the RACAL satellite DGPS service for South America. Depending on GPS satellite geometry and forest canopy interference, real-time DGPS accuracy approached 1 m horizontal and 2 m vertical. Short-term precision, specified by the instrument, was typically decimeters or better, but repeated DGPS measurements taken hours apart with different satellite geometries and atmospheric conditions suggest that the effective accuracy is worse. To obtain the best possible DGPS results, all sample locations were averaged for 3 – 6 minutes, and water surface elevations were averaged on a custom "river sand" stand for 30 minutes to several hours. For all such longer occupation times, DGPS data were post processed to discard data recorded during periods of poor satellite geometry, considerably improving the observed precision and estimated accuracy of the enhanced dataset to ± 2 m or better. On the cross-section surveys, cutbank, bar, and terrace heights, channel widths, and sometimes floodplain topography were also measured with a survey-grade laser rangefinder (Laser Technology IMPULSE 200LR). Water depth was measured with a hand-held sonar rangefinder with a multiple return function to distinguish logs and large fish from the actual channel bottom. In some cases, stadia rod and eye-level surveys were conducted with a survey tape to independently measure floodplain, bank, and bar topography.

Sediment grab samples and floodplain cores were collected across the channel in standardized locations (Figure 2.2, Table 2.1). For grab samples, the top 10 cm of sediment was removed from the site and then ~ 80 grams of material was sealed into a screw-top polypropylene container. At some transects, a pipe dredge was dragged along the channel thalweg to collect a sample of the sediment at the bottom of the channel. In the gravel-bedded reaches of the river near Rurrenabaque, sub-surface pebble counts were conducted on 1 m^2 patches to quantify the bar granulometry immediately adjacent to the channel. For the core samples, dry leaf litter on the forest floor was brushed aside, revealing a surface of floodplain sediment. Then, core samples were extracted by soil probe or auger to depths of 65 - 200 cm, as discussed in Chapter 5. For some cases of large grab and auger samples, several hundred grams of sample were collected into

taped, double-bagged, 6-mil Ziploc freezer bags. All sample material was sealed, securely packed into wood crates, and flown back to the University of Washington laboratory, where it was stored at 5° C until ready for analysis.

All sediment grab samples were analyzed for grain size distribution. First, ~ 60 g of sample was removed and dried in aluminum sample pans at 80° C for 24 hours. The material was next dry-sieved with a roto-tap shaker for 15 minutes, and the resulting mass fractions were recorded at 354, 250, 180, 125, 88, 75, 63, and < 63 microns. For samples with more than a third of their mass in the < 63 micron range, silt and clay size distributions for this fine material was analyzed in detail using a Micromeretics Sedigraph 5100 calibrated for river sediment. All resulting size distributions were plotted in semi-log space analyzed to determine the best-fit median grain size (D_{50}) for each sample.

Prior to cutting for analysis, all floodplain cores were photographed at two angles (orthogonal) with a large X-ray machine (Faxitron Cabinet X-ray Model 43855C). These images allowed me to evaluate sedimentary structure and potential disturbance within each of the floodplain cores. After imaging, the cores were cut at discrete depth intervals and the resulting samples were analyzed for sediment granulometry, using a combination of wet-sieving at 63 microns (to determine sand fraction) and Sedigraph analysis of the silt and clay distributions. To determine floodplain accumulation rates, these samples were also analyzed for ^{210}Pb activity and clay fraction, as discussed in Chapters 4 and 5.

Satellite images for the entire study area were obtained for 1999, 1996, 1993, 1986, and 1975, and aerial photographs of the Beni River were acquired for 1994 and 1960. For these images, the vector locations were digitized for the edge of the vegetation (right and left banks), for the unvegetated point bars and mid-channel bars, and for the perimeter of two dozen oxbow lakes, entering the results into a GIS (geographic information system) model for the Beni River. These vector data are plotted on the 1999 ETM+ base maps for the Beni River: examples are shown in Figures 2.4 (a-b), with

additional site maps presented in Appendix A, and plotted for the entire channel in the three large maps (pocket material). For the GIS analysis, the Beni river was divided into 10-km reaches of UTML (universal transverse mercator projection latitude). Because the Beni flows approximately due north across the foreland basin, this is a convenient means to subdivide the river in ARC/INFO and to plot results. All results were corrected for the actual river and valley lengths within each 10 km UTML interval. Additional aspects of the GIS analysis, the dynamic relationships between channel migration and morphology, and other details of planform channel morphology are explored at length in Chapter 3. For the purposes of the flux analysis presented here, I report only the mean (averaged from 1960 – 1999) channel reach sinuousity, width, length, and the lateral erosion rate due to channel migration.

Results from topographic surveys

The heights above the low-stage water surface were measured for cut banks, bars, and terraces at numerous locations along the Beni River (Figure 2.5, Table 2.2). Bar heights were categorized as unvegetated bar tops, also referred to as sand "berms" (TB location in Figure 2.2), and as "forested" bar (FB in Figure 2.2) floodplain (typically covered with young vegetation 2-4-m high), typically 50 m from the edge of the vegetation. The elevation increase for the forested bar floodplain is noteworthy, and is typically realized as a sharp ~ 2m rise right at the edge of the vegetation. For the running averages (Figure 2.16), cut bank heights are generally higher than vegetated bar heights, with a gradual downstream increase in both heights towards ~ 8,590 km UTML, where a rapid increase is realized coincident with the appearance of terraces. These high cliffs are weathered a distinctive shade of red, are composed of cemented silt and clay, and are not inundated by river floodwaters, whereas the floodplain sediment had an olive-drab color and was composed of unconsolidated silt and clay.

A high-resolution dataset for channel depths was surveyed for the entire Beni River in 1969, at a low stage similar to that observed in 1999 (Semena, 1969). I

averaged all of the 750 recorded depths into 10-km UTML reach means for the 1969 channel (Figure 2.6). Because I conducted depth measurements at only a few dozen cross-sections, my surveyed depths span a wider range than the average values from 1969. Except for some regions of minor shoaling (e.g., around 8,440 km UTML), curved channel depths are fairly constant at 5.5 m along the upper Beni, increasing to ~ 6.5 m downstream of 8,600 km UTML.

The elevation of the water surface was surveyed across the entire basin. To account for a few minor variations (< 1 m) in water level during a brief precipitation event in late September, 1999, and a handful of larger (1–3 m) differences during the high stage campaign in February, 2001, I corrected a subset (14 out of 72) of these elevations by the measured local stage change due to these higher discharge conditions. The resulting plot of low-stage water-surface elevation versus UTML (Figure 2.7) exhibits several distinctly different reaches of channel. The gravel-bedded portion of the Beni has a mean UTML "valley" slope of approximately 7×10^{-4} m/m, with the mountainous reaches somewhat steeper than those downstream of Rurrenabaque. After a short low-gradient reach near 8,450 km UTML, UTML slope averages 2×10^{-4} m/m until 8,610 km UTML, with the upper reaches of this section slightly steeper than the lower reaches. Then, UTML slope declines dramatically to $< 3 \times 10^{-5}$ m/m until 8,700 UTML, where it temporarily increases to $\sim 3 \times 10^{-4}$ m/m, declining to 1×10^{-4} as it crosses the secondary basin. In Figure 2.7, I have marked these reaches according to my proposed tectonic associations to the wedge-top, foreland, forebulge, and back-bulge secondary basins. Note that the actual water surface slope for the river is considerably less (by a factor of 1.3–4.5) than the UTML "valley" slope, because the river is sinuous and the river valley does not necessarily run exactly south to north (Figure 2.12). Further data, analysis, and discussion concerning the interplay between the fluvial geomorphology and valley slope are presented in Chapter 3.

The Beni River builds natural levees along its channel. Logistical constraints thwarted the extensive topographic survey of decimeter-resolution vertical transects

across kilometers of floodplain, but transects surveyed by hand level away from the channel depicted a typical floodplain slope of 2–8 x 10^{-3} m/m away from the cut bank (Figure 2.8). DGPS data (of insufficient vertical accuracy to cleanly resolve floodplain slopes over such short distances) and the common visual impression of generally descending on the floodplain as I walked away from the active cut bank are consistent with these estimates for levee slope. Sustained over distances of a 0.5–1 km, such slopes would imply that the flooded channel (inundating the natural levees) may lie 5 meters or more above the surrounding forested floodplains, which can extend 10 km or farther from the channel. Consequently, the potential energy slope of the water surface during flooding is approximately 10 times steeper into the floodplain than it is down the river valley. Such a difference may facilitate levee breaches and channel avulsion.

Results from granulometric surveys

Bed and bar granulometries were measured in the thalweg or on the bar immediately adjacent to the low stage channel ("MB" location, Figure 2.1). A down-channel plot of these results is presented for the Beni River in Figure 2.9. Results concur with the data of Guyot et al. (1999), who observed a large decrease in mean bed grainsize from 3000 to 150 μm at the gravel-sand transition, located near 8,415 km UTML. The data here also support their observation that bed D_{50} thereafter remains roughly constant, although here this trend is evident for only the first ~ 180 km of river valley. Farther downstream, where prior data are more limited, my larger dataset depicts a general fining trend beginning at 8,610 km UTML, the proposed start of the Beni forebulge. This trend may be due to selective deposition of coarser bed material within the Beni foredeep, although the data show no evidence for fining upstream of the forebulge. Alternatively, the channel downstream of 8,610 km UTML generally exhibits lower slopes (Figure 2.7) and sinuosity (Figure 2.13) than in the foredeep, which would tend to reduce the strength of the secondary flow around meander bends. This in turn would diminish the average inward conveyance velocity, and possibly the average size of the particles transported

laterally and ~ 7 m upwards from the channel thalweg (~ 6 m depth) to the sampling location on the exposed berm ("MB" locations are typically at ~ 1 m height). Data supporting this mechanism are presented later in this section.

Sediment granulometry was measured for all grab samples of all transects (Appendix B, Table 2.2). Such data offer insight into meander flow mechanics and total system aggradation as the channel crosses the floodplain. For example, Figure 2.10a depicts a granulometric profile for a transect across a meander bend apex (Site 60, Figure 2.4c). All samples from the cutbank (samples designations ending in "C") are fine, with a D_{50} averaging ~ 40 microns, while the bed and unvegetated bar samples exhibit an average D_{50} of ~ 150 μm. However, only ~ 5 m distance into the vegetation on the bar, the D_{50} drops to 50 μm, similar to that for the surface sediment on the cutbank floodplain. Apparently, even young vegetation provides sufficient roughness to impede the lateral transport of coarser suspended sediment onto the floodplain. Of course, this observation also reflects the fact that vegetation only grows on bar surfaces that are high enough and sufficiently distant from the main channel to limit basal scour during flooding. In a cutbank exposure that can be interpreted as trading space for time, Figure 2.10d depicts a vertical profile of an excavated point bar, which was deposited and vegetated at this location around 1983. This remarkable transition from medium sand to silt occurs over a vertical distance of less than a centimeter, and underscores the important role that vegetation plays in impeding the conveyance of sand onto the floodplain. Such vegetation effects and grain-size distributions across meander apexes are typical for all actively migrating meander apexes throughout the Beni foredeep. In some cases, a meander has impinged against a hard clay plug, developing a sharp kink and an unusually fine grain size distribution on the bar.

With few exceptions, the point bar granulometry is much coarser than at the corresponding elevation on the cut bank (see Appendix B for more transects and details). This observation suggests that cutbank cliffs are generally composed of vegetated floodplain deposits (on the vegetated bar, forested cutbank, or distal from the channel),

not channel or unvegetated point bar deposits. However, because the Beni river migrates rapidly across its floodplain, all of the floodplain must be underlain at some depth by either point bar deposits or infilled abandoned channels (oxbow lakes). In only two cases, the cutbank material was unusually fine (< 20 μm), clay-rich, and obviously resistant to erosion (a hard clay cliff, with a large scour pool in front of the cutbank, and a distorted meander stable over the 40-year GIS analysis), and therefore probably of oxbow lake origin. But for all other meander apex transects, I did not observe granulometry profiles representative of point bar deposits. Therefore, the Beni River must aggrade sufficiently (relative to the bar deposits) as it migrates across its floodplain such that a ~ 6-m cutbank exposure will display only fine deposits; this requires 4–5 m of floodplain accumulation above the point bar deposit. Given a mean lateral migration velocity of ~ 20 m/yr (from the GIS analysis), the river would take ~ 500 years to migrate across an assumed meander-belt width of 10 km (a typical value observed on the maps) and reoccupy the same planform location. Consequently, such a channel-floodplain system would have to aggrade at least 1 cm/yr to produce the observed granulometric results. For a single floodplain location that has been close to the channel, the profile in Figure 2.10d suggests a higher rate of average accumulation of > 10 cm/yr since the start of fines deposition associated with vegetation, which was first observed at the site in the mid 1980s. Because the channel is most likely to migrate into the closest parts of its floodplain (within a few km of the channel, and the location of all of the sample sites), the reoccupation interval is probably much shorter and the corresponding accumulation rates much higher for much of the proximal floodplain. Therefore, based on the observation that channel cutbanks are composed of floodplain deposits, I propose minimum system-wide accumulation rates proximal to the river channel of 2–5 cm/yr.

While much of the cut bank erosion and bar deposition occurs near meander apexes, it is informative to consider other granulometric distributions and their mechanics. The particularly active meander in Figure 2.4c exhibits a cross-channel granulometry similar to Figure 2.10a for a considerable distance upstream (site 61,

Appendix B) and downstream (site 63, Appendix B) of the apex. However, at the extreme upper (Figure 2.10b) and lower (Figure 2.10c) limbs of the meander, the bar granulometry is considerably finer, much closer in size to that of the cutbank sediment. The channel thalweg for all these transects is composed of a medium sand in the 130 – 150 um range, so there is no difference in the bedload being transported through this meander. I interpret these data to reflect the mechanics of secondary circulation, which is strongest near the meander apex and weakest along the straighter sections of the meander limbs. In straighter reaches (both meander limbs and straight sections of channel), where secondary circulation is weak, I consistently observe fine bank sediment. Slack-water deposits are another mechanism for sedimentation of silts and clays. For example, Figure 2.10e depicts a nascent oxbow lake that cut off during a large flood in March of 1999. As such, all sampled surface locations were essentially free from significant vegetation. Beyond the high sand berm at the edge of the cutoff channel, the surface slopes gradually down into the new lake. Grab samples across this deposit show it to be fine grained in nature, except for some samples closest to the channel. This and numerous other examples of slack-water deposits along the Beni River are composed primarily of silt and clay, with only small amounts of sand.

I have discussed representative transects across the river channel, illustrating how coarser sandy deposits (80–100 % sand) are found primarily within the channel and unvegetated bars. Due to the flow-impeding roughness of vegetation and the distance from and elevation above the main channel (enhancing slack-water conditions), forested floodplains generally accumulate a mixture of silt and clay, with limited sand (0–20 %, Table 2.3). To further investigate floodplain granulometry, I have cored hundreds of locations throughout these floodplains and measured detailed granulometric profiles down 78 of these cores, with additional results presented in Appendix C and Chapter 5. Here, I present a summary Table (2.3) of mean floodplain granulometry for all survey transects across the forested floodplains. Floodplain sediment is primarily silt, with various quantities of clay and sand. Deposits on the forested point bar are generally

coarser than those on the cut bank side of the channel. There is also a downstream fining trend towards the forebulge, with floodplain sediment containing more silt and clay and less sand.

Before they were cut for analysis, all floodplain cores were X-rayed to assess sedimentary structure and core coherency. Almost all cores depict an intact, undisturbed floodplain, with sedimentary structures well preserved (Figure 2.11). Except for the occasional root or rare void, the only typical disturbance is minor fracturing to limited portions of some cores, apparently during sampling and transport. Most of these sedimentation features are delicate horizontal laminations, which would be destroyed by even a few millimeters of bioturbation. Accordingly, I conclude that the soil in this tropical rainforest floodplain is not subjected to any detectable bioturbation. This is astonishing, because of the large numbers of ant, termites, birds, and other animal life throughout the floodplain. However, the ^{210}Pb analysis presented in Chapters 4 and 5 also supports this interpretation, because there is no apparent transport of the meteoric radionuclide below the top 5–10 cm. And, after sampling more than 300 floodplain cores along the Beni and Mamore rivers and inspecting hundreds of kilometers of freshly-eroded river banks, I cannot recall having ever seen an earthworm, evidence for burrowing insects, or observed more than a handful of rodent burrows. Strangely enough, one of the most verdant and productive habitats on Earth exhibits very little bioturbation of the soil. I suspect that the large number of termites (there are a half dozen or more termite nests in trees within a 10 m radius of any location on the floodplain) rapidly consume all dead plant material before it has a chance to become incorporated into the floodplain. Therefore, there is little organic material in the ground for earthworms or other creatures to eat, and consequently virtually no bioturbation.

Inspection of the X-radiographs indicates that most cores exhibit fine horizontal lamina, faint ripple lamination, or massive deposits (Figure 2.11b & c), indicative of a medium-to-low-energy depositional environment. Only recent deposits from the unvegetated point bar tops exhibit significant cross-bedding (Figure 2.11a), and these are

rare and exhibit much coarser granulometry than found on the vegetated floodplain. The geochronologic analysis in Chapter 5 demonstrates that these deposits are typically formed during single depositional events, after which many decades can pass without any additional observable accumulation (< 5 cm) on the floodplain. The deposits are usually at least 40 cm thick, often encompassing the whole 65 cm core, and blanket entire floodplain transects hundreds of meters in length.

I interpret these deposits, which account for the vast majority of floodplain accumulation on the higher cutbank side of the river, as crevasse splay deposits, formed when the flooded channel breaches a natural levee and debouches enormous volumes of sediment-laden water far into the lower surrounding floodplain. Because of the dense rainforest vegetation throughout the floodplain, the energy of this flow is moderated enough to preclude cross-bedding or basal scour over most of the deposit. Flow is rapid enough to transport silt and clay, but only limited amounts of fine sand are transported and ultimately found in such deposits (Table 2.3, Appendix C). Such non-channelized overbank deposits, as documented here for the modern Beni River, are directly analogous to the thin, laterally continuous nonerosional sandstones of the lower Carmargo formation (a Paleogene foredeep deposit preserved in southern Bolivia), for which upward-thickening assemblages are interpreted to represent the progradation of crevasse splay complexes and/or the increased proximity to active channels (Horton and DeCelles, 2001). Similar deposits are also observed in the main Potoco formation, a Paleogene foredeep deposit now located in the central Altiplano (Horton et al., 2001). I further discuss the evidence for the splay-deposit hypothesis in Chapter 5, including extensive geochronological evidence supporting this mechanism.

Once the splay deposit is formed, aggrading the local floodplain relative to the river, the levee break fills in, restoring the high natural levees and preventing floodplain sedimentation until the next large levee break. I hypothesize that channels are considerably more likely to break their natural levees when the surrounding floodplains are relatively low, because the higher local energy slope into the floodplain would tend

to promote scour and the excavation of a levee breach. Conversely, a floodplain that has recently aggraded as a result of crevasse splay deposition would be much closer in elevation to the crest of the natural levee, making it significantly less likely to experience another splay deposit in the immediate future. As time progresses, the channel bed and adjacent natural levees would continue to aggrade as the channel migrates across the Beni foredeep, gradually raising the levees with respect to the surrounding floodplains, and ultimately building a sufficiently high energy gradient to again breach the levee and debouch another crevasse splay deposit to blanket the previous one. This concept does not apply to the recently deposited point bar side of the river, for which I have limited granulometric, topographic, and geochronologic data. Such point bar locations would probably receive sediment during moderate flooding, because they are both topographically lower and are characteristically surrounded by and close to the river channel; inundation of vegetated point bar surfaces with sediment-laden river water would likely be both a regular and measured (non-catastrophic) process.

Thus, for any hypothetical location on the high (cutbank) forested floodplain farther than a few hundred meters from the river, I propose that the average time interval between the arrival of successive crevasse splay deposits is inversely proportional to the rate of channel-levee aggradation (relative to the floodplain). The appeal of such a conceptual relationship is that it could be developed into a stochastic model of floodplain accumulation by repeated, large, discrete crevasse splay events. Otherwise, it is not possible to model such floodplain deposition with standard geomorphic schemes for advecting excess water laden with sediment onto the floodplain (Dunne et al., 1998) or routing 2-D diffusive flood waves over raster grid approximations for vegetated floodplains (Nicholas and Walling, 1997a, b), because accumulation by splay deposits has little to do with the frequency and depth of floodplain inundation. In fact, the popular mechanistic conception of the diffusive transport of river sediment onto the floodplain (Dietrich et al., 1999; Pizzuto, 1987) may not be particularly useful for the Beni River, because crevasse splays are clearly advective phenomena. Even the

infrequent large floods that account for almost all of the splay deposits (Chapter 5) only do so on an infrequent basis at any specific floodplain location, with no discernible floodplain accumulation occurring during most other large flood events. For the Beni River, and presumably other rivers like it, crevasse splay deposits are the primary mechanism for sediment accumulation within the foredeep depositional basin.

Results from the GIS analysis

Following the GIS procedures previously discussed, I measured static and dynamic morphometric parameters derived from the planform fluvial geomorphology of the Beni River as depicted in a series of images from 1960 to 1999. These results and their relationships to each other and to valley slope are discussed in greater detail in Chapter 3. Here, I present only a summary of the basic channel morphology, as these results are relevant to the mass flux analysis.

Figure 2.12 depicts average channel sinuosity across the foreland basin, along with river valley length per 10 km UTML increment (distances are comparable to those in Figure 2.7). The river shows low sinuosity through the gravel-bedded reaches and across the wedge-top basin, becoming far more sinuous after 8,450 km UTML. Sinuosity declines gradually across the foredeep, and then drops to very low values at the forebulge (8,600 km), with the channel nearly straight until 8,700 km UTML. Sinuosity climbs again in the secondary back-bulge basin, although there are also some straighter reaches. These data provide estimates for total channel and valley length per 10 km UTML interval, as needed for the flux analysis.

Average channel width is narrow through the canyons at the sub-Andean range front (~ 250 m), but increases to ~ 450 m in the wedge-top basin (Figure 2.13). It then steadily declines from 400 m to 300 m across the foreland basin to the forebulge at 8,600 km UTML, where it jumps back to 400 m downstream of the confluence with the Madidi River. At 8,690 km UTML, near the proposed start of the back-bulge basin, channel width again increases to ~ 450 m. There are zones of width instability near 8,430 km

UTML and from 8,560–8,590 km UTML: these are regions of rapid change in channel slope and channel instability and are discussed further in Chapter 3. The channel+bar width is the more consistent and functional measurement, representing bankfull channel width, so it is used for the mass flux analysis. A plot of total bar area (Figure 2.14) illustrates the expected trend that 10 km UTML reaches with more sinuous channels and/or greater total valley length tend to contain a greater area of bars.

The average channel lateral migration velocity is presented in Figure 2.15. This parameter, derived by using the previously-discussed GIS determination of eroded bank area per unit time, provides a 40-year estimate of the rate of channel migration across the floodplain. Measured rates are highest downstream of the gravel-sand transition, near 8,450 km UTML, and decline steadily across the foredeep. Migration is slow across the forebulge and the secondary basin, with notable local exceptions at 8,610 and 8,680 km UTML, probably associated with the sudden changes in channel slope near the boundaries of these features (Chapter 3). For the analysis here, these average channel migration rates are critical, because they are used to determine the average annual erosion of cutbank material and deposition of point bar sediment associated with channel movement.

Finally, to investigate the processes of oxbow lake infilling, I have tracked the changes in planform area for 23 oxbow lakes that have formed since 1960 (Table 2.4). Only one of these lakes appears to have a sustained history of infilling, with three more exhibiting some decrease in lake area in the years after meander cutoff (these were all partially connected to the river at the time of the image in 1993). The rest show little change in water surface area once the cutoff process has been completed, with a GIS analysis of 11 of the older lakes (formed prior to 1993) identifying 13 time intervals during which lakes **increased** in area (possibly due to a higher river stage at the time of the image) and only 7 intervals when lakes decreased in area. Hence, the 40 years of record show little evidence for steady infilling of older oxbow lakes, at least at a rate rapid enough to be resolved with the GIS analysis.

To understand such apparent lake stability, I next studied the nature of the connection between the lakes and the main channel: of the 23 total, 20 had their tie channels rapidly infilled with sediment and apparently lost channelized communication with the Beni River. Two more had just cut off during a recent large flood, so their tie channels had not yet had a chance to infill. The only tie channel with long-term persistence connects to an oxbow lake that also receives discharge from a small floodplain tributary; this is also the lake that exhibit the most consistent history of infilling. Because tie channels can serve as principal conduits for sediment transport into off-river water bodies (Dietrich et al., 1999), this remarkable lack of preserved tie channels along the Beni River offers an explanation for why ~ 90% of the oxbows show no evidence for decrease in area over time. It also supports the idea that general broad flooding does not occur across the Beni floodplain, because regular cycling of water between the channel and the floodplain would tend to maintain the tie channels.

Because the Beni carries a large sediment load and accumulation is especially high closest to the river (Figure 2.18 and Chapter 5), I propose that the river tends to rapidly suture any breaks in the large natural levees, including tie channels. This hypothesis is supported by my field observations of 800 km of Beni river channel, during which I found only a few faint remnants of tie channels from recent cutoffs (during the late 1990s), preserved as small notches in the natural levees high above the low stage water surface. Considering this evidence, as well as the plethora of well-preserved older stable oxbows (centuries in age?) common throughout the Beni floodplain, it appears that oxbow lakes on the Beni floodplain do not accumulate sediment at a rate substantially higher than that of the surrounding floodplain (e.g., the rates depicted in Figure 2.18). As such, I see no compelling reason to consider them as a separate sediment sink in the flux analysis for the Beni foreland.

Calculation of sediment fluxes across the Beni foreland

By combining all of the preceding data from the GIS analysis, topographic surveys, granulometric measurements, and the results from the ^{210}Pb geochronologic analysis presented in Chapter 5, it is possible to quantify the total exchange and accumulation of sediment within the Beni foreland basin. I first present each major component of the flux analysis, and then combine them to calculate sediment flux across the entire system.

First, I take the raw data from the topographic surveys presented earlier, average them into 10 km UTML "bins," and use these values to construct 10 km UTML running averages for vegetated and unvegetated bar ("berm") heights, cut bank heights, and channel depths (Figure 2.16). When a channel migrates, it excavates a wall of sediment equal in total height to the cut bank height plus the channel depth. Likewise, on the bar side it deposits a wall of sediment equal in total height to the vegetated point bar height plus the channel depth. These two heights can be multiplied by the average lateral migration velocity (according to analysis in Chapter 3, the channel is in long-term steady-state, such that the average depositional bank migration velocity equals the average erosional bank migration velocity) and the average channel length to produce the total annual volume of sediment eroded and deposited due to channel migration within each 10 km UTML reach. Because I have measured sediment density throughout the Beni foreland, these volumes can be directly converted into quantitative values for the erosional and depositional masses of the sediment (Figure 2.17).

The cut bank erosion flux and the bar deposition flux mirror each other and Figure 2.15 closely across the Beni foreland, with the highest rates in the upper foredeep declining towards the forebulge, and increasing again in the back-bulge secondary basin. The offset between the two fluxes is a function of the differences in bank heights, depicted in Figure 2.16. Summed across the entire foreland, both the erosional and depositional flux values are very large: 230 and 222 Mtonnes/yr respectively, greater than the total annual sediment efflux from the Beni Foreland. However, the difference

between the two is small, representing a loss of net floodplain sediment storage (NFSS) due to channel migration of only 8 Mtonnes/yr, less than 4% of the total annual cutbank erosion. This differs from the results of Dunne et al., 1998, who estimated that < 25% of the total eroded mass due to channel migration of the Amazon river was redeposited into the unvegetated channel bars, equivalent to a remarkable loss of NFSS greater than 75% of the total annual cutbank erosion. To investigate a probable cause for this difference, I reran the flux analysis using the surveyed heights for the "berm" top: the center of the wide, flat, sandy unvegetated point bar top which are 2–6 m lower than the point bar heights 5–50 m into the young floodplain vegetation (Figure 2.16). This berm location is significant, because it represents the bar height used for the Amazon flux analysis – the field surveys did not extend into the vegetated portions of the large Amazon River point bars. For the Beni River, I calculate a berm depositional flux of only 160 Mtonnes/yr, resulting in a NFSS loss of 70 Mtonnes/yr, more than 30% of the total annual cutbank erosion. This percentage would be even higher still if I had used the heights of the point bar berm rise immediately adjacent to the low stage channel, which are significantly lower than the berm tops. Hence, the topographic location one interprets as representing the total height of the unvegetated point bar can make a substantial difference in the accounting of the sediment transfer due to channel migration versus the sediment deposited overbank in the forested point bar. Either approach can properly account for the incorporation of the same total sediment mass into the floodplain, but the presumed depositional processes and thus the representative grain size may be different.

An uncertainty therefore lies in interpreting the mechanism responsible for the deposition of several meters of sediment on the bar near the edge of the vegetation. For the Beni River, this rise was typically recognized as a slope of fine sandy or silty river sediment, either unvegetated or sparsely vegetated with short grasses. At the top of the rise, the vegetation becomes much denser and taller, and the sediment is noticeably finer (e.g., more cohesive, clayey, and often rife with mud cracks). Although no sediment grab samples were collected on the topographic rise itself, 65-cm sediment cores were

taken at the nearby "VB" location (~ 5 m into the vegetation past the top of the rise) for all transects. In the X-radiographs, most of these "VB" cores exhibit a distinct transition at a depth of 15 - 35 cm from horizontal silt and clay laminations to cross-bedding composed of sand and silt. Several of these cores have been cut and analyzed for granulometry (e.g., transect 60 in Appendix C), and show evidence for an increase in grain size at a depth of 10–30 cm. Consequently, I have assumed here that the sediment within this rise is more similar in size to the coarser material on the unvegetated bar rather than to the finer sediment on the vegetated floodplain.

To calculate floodplain deposition by overbank flows into the older (cutbank) floodplain, first I must borrow a figure from Chapter 5, a plot of measured average accumulation rate versus distance from the channel (Figure 2.18). These measured values represent minimum floodplain accumulation rates by crevasse splay deposition, as dated by ^{210}Pb geochronology keyed to the measured minimum thickness depicted in the floodplain cores. There are no accumulation data from distances greater than 3 km from the Beni River (at the time of deposition), so it is necessary to extrapolate the average minimum 2–3 km rates to calculate a total sedimentation flux to the most distal floodplain (3–10 km from the channel) by episodic deposition. This may overestimate floodplain accumulation rates farther than 3 km from the Beni River, but measured rates do not decline significantly from 1 to 3 km from the channel and the accumulation rates within 3 km of the channel are probably underestimated (Chapter 5), balancing the error. The few cores that I have from the forebulge and secondary basin exhibit lower rates of deposition (Chapter 5), and the field and GIS inspection of the floodplain in this region seem to indicate a less dynamic environment; I therefore assume that all floodplain accumulation rates downstream of 8,620 km UTML are half that depicted in Figure 2.18. As part of the GIS analysis, I have characterized floodplain width and valley and channel length for each 10 km UTML increment, subdividing the floodplain into four regions associated with their respective distances from the channel (0–300 m, 300–1000 m, 1–2 km, and > 2 km).

Combining these two datasets, I then multiply the measured sub-area of each floodplain distance class by its representative accumulation rate such as to calculate the total Beni River floodplain accumulation rates for each 10 km UTML increment (Figure 2.19). For the highest accumulation rates on the floodplain most proximal to the channel (0–300 m), the 300-m width is multiplied by the total average channel length for each reach. In contrast, because the accumulation rates are much lower (Figure 2.18) and the amount of channel "edge" is less of a factor because the channel is more distant, the areas of all the other sedimentation regions are represented by the multiple of their observed width and the average valley length. The foredeep, where the floodplain is wide, exhibits the highest calculated rates of floodplain accumulation or NFSS. Across the forebulge, the river is constrained between high terraces, so floodplain accumulation is limited to small areas on either side of the river. In the secondary basin, NFSS increases again, as the floodplain widens and provides more area to accommodate sediment deposition. The Beni foredeep accounts for almost 90% of the total mass of floodplain sediment accumulated across the entire Beni foreland.

In Figure 2.20a I synthesize all previously calculated mass fluxes into one summary plot for the entire Beni foreland. Here I have added one additional flux calculation for the NFSS due to channel bed deposition: the product of the measured channel area for each 10 km UTML reach multiplied by the floodplain accumulation rate at 300 - 1000 meters distance into the floodplain (I assume that the channel must aggrade at least at the same rate as the floodplain within 1 km distance, except where it runs over "bedrock," where no deposition can occur). I again depict the berm NFSS calculation, not used in the final accounting, to illustrate the effects of the topographic survey location and procedure for defining bar height, and to elucidate how I account for the associated depositional flux in this study. Figure 2.20b presents the summed NFSS calculation for all processes, illustrating the importance of the Beni foredeep as the principal abstractor of sediment from the river system within the foreland basin.

As an independent internal check of the mass flux analysis, I present a summary of a detailed analysis (Chapter 4) of the modeled clay-normalized ^{210}Pb activity in river sediment (Figure 2.21). This radionuclide is primarily adsorbed by clay, and I have determined the clay fraction and ^{210}Pb activity for bar and floodplain deposits and eroded cut banks throughout the Beni Foreland. Sediment ^{210}Pb activity is high at Rurrenabaque, but diminishes across the Beni Foreland as a result of (1) the deposition of higher-activity river sediment into point bar and channel bed deposits and onto the floodplain, and (2) the excavation of lower-activity (radiometrically older) floodplain sediment from the cut banks due to channel migration. Consequently, is it possible to multiply the sediment fluxes depicted in Figures 2.17 and 2.20a by their representative clay content and ^{210}Pb activity (both are empirically defined as functions of UTML latitude) to construct a mixing model for the activity in fresh river sediment as a function of UTM latitude. When all sediment fluxes are assumed to be at their mean average values, the model predicts a river sediment ^{210}Pb activity very similar to the measured sediment activity as determined from channel-proximal floodplain samples (Chapters 4). Therefore, the geochronological measurements and modeling independently confirm my mass flux results for the Beni Foreland.

This flux analysis predicts a total annual increase in NFSS of 97 Mtonnes/yr. There is obviously much potential for error in such an analysis. For example, I have only limited data for floodplain accumulation rates beyond 2 km distance from the channel, and nothing beyond 3 km (see Chapter 5). Therefore, I must make a critical and unsupported (although I believe reasonable) assumption that all accumulation rates for regions of floodplain greater than 3 km distance from the channel (in the Beni foredeep) average ~ 1 cm/yr. Also, the floodplain deposition rates in Figure 2.18 are minimum estimates, because much of the time the 65-cm cores are not deep enough to resolve the bottom of discrete crevasse splay deposits (see Chapter 5). Obviously, it would be informative to measure the rates and processes of sediment accumulation on the distal floodplain, at greater depth, and to collect more data in the secondary basin, where I have

done only limited fieldwork. I have illustrated the importance of the differential between cut bank and vegetated bar height in determining the change in NFSS associated with channel migration; future work should endeavor to survey these topographic differences as frequently as possible (e.g., my dataset is sparse in places).

For this analysis, I also discounted the importance of oxbow lakes as a sediment sink, because I saw no evidence that they infilled faster than the surrounding floodplain. However, oxbow lakes might alternatively be considered a sediment source to the channel in the accounting scheme adopted here, because a large lake that does not fill in represents a large void or "mega-pore" in the floodplain. Such megapores were initially formed when the channel extended in length, excavating floodplain sediment and conveying it away from the growing gooseneck meander. After cutoff, if the nascent oxbow escapes obliteration by future channel migration, it appears to infill only slowly, partially by crevasse splay deposition like the rest of the floodplain and partially by local diffusion of nearby sediment into the lake, effectively "deflating" the surrounding floodplain to a lower average elevation. This concept is particularly well suited for the Beni, because the river has preferentially migrated and avulsed to the northwest over geologic time, leaving a train of abandoned oxbows in its wake. Such megapore formation proximal to the channel and relaxation over geologic time provides a sort of temporary faux aggradation of the floodplain near nascent oxbow lakes, ultimately culminating in the deflation of the surrounding floodplain to a lower, more uniform elevation. To illustrate the potential significance of this effect for the decadal-scale NFSS, the four decades of record for the Beni foreland show 26 effective oxbow cutoffs (out of 30 total, 4 filled immediately at cutoff), or about 0.67 cutoffs/yr. From Table 2.4 I determine that an average oxbow lake might be 1.4 km^2 in area, which multiplied by an estimated average bed-to-floodplain rise of ~ 8 m and a typical sediment density of 1.45 tonnes/m^3 gives a total sediment mass displacement per oxbow of 16 Mtonnes. Multiplying this mass by cutoff frequency, I estimate an annual NFSS loss due to oxbow formation across the Beni foreland of 10.8 Mtonnes/yr, greater than the change in NFSS

due to channel migration or bed deposition. Therefore, the proposed processes for the geomorphology of oxbow "megapores" may indeed play a significant role in the modulation of NFSS across the Beni foreland.

Estimation of sediment flux at Rurrenabaque and Riberalta

In the preceding section, I estimated an increase in NFSS across the Beni foreland of 97 Mtonnes/yr (with the discussed uncertainties in my analysis), a total loss of riverborne sediment which I can compare to the measured decrease in the average annual sediment discharge observed between long-term gauging stations located in Rurrenabaque and Riberalta.

A gauging station has been maintained at or near Rurrenabaque since 1967, recording daily values for river discharge and regular measurements of the concentration of suspended sediment in surface waters. To determine total sediment flux, rating curves have been developed to predict sediment concentration as a function of water discharge (Guyot, 1993; Maurice-Bourgoin, 2001). For example, Figure 2.22a depicts a typical plot of surface suspended sediment concentration versus water discharge at the Rurrenabaque gauging station, and Figure 2.22b illustrates the daily record of water and sediment discharge from 1995 to 2001. Over this time period the average annual sediment discharge was estimated to be 174 Mtonnes/yr. For the discharge record spanning 1969 – 1989, Guyot (1993) used a concentration-discharge relationship developed from 456 surface concentration measurements to estimate a total annual sediment discharge at Rurrenabaque of 219 Mtonnes/yr. This second value for flux has been increased by 10% to reflect an observed increase of water turbidity between the water surface and the channel bed (Guyot, 1993), so the uncorrected flux would also be 199 Mtonnes/yr. Because optical turbidity meters primarily "see" clays and very fine silts, this 10% estimate may not account for the significant vertical gradient in suspended-sediment concentration expected for the considerable fraction of sand and coarser silt transported by the Beni River.

To investigate the calibration needed to determine the depth-integrated sediment discharge, I used a custom-designed sampling apparatus to collect large sample volumes of water from the surface (64.0 liters) and at depth (24.5 l), ~ 0.1 m off the bed of the channel. My device consisted of a variable-speed pump attached via a thin, flexible, polyethylene hose to a finned sampling nozzle. To minimize Stokes sampling bias, inlet nozzle diameter and pump speed were adjusted to match the average current velocity during the flood-stage sampling campaign in February, 2001. Particle-size distribution for the samples collected at Rurrenabaque (Table 2.5) was determined using a combination of dry-sieving, wet-sieving, and Sedigraph 5100 analyses as previously described. Concentration increases from 6,050 mg/l at the water surface (7.6 m) to 14,465 mg/l near the bottom (0.1 m), with essentially all of the increase occurring in the sand and coarse silt fractions. To model this effect numerically, I applied a two-layer Coleman sediment concentration model modified to account for the differences in sediment diffusion within turbulent eddies as a function of particle size (Aalto, 1995). Using the observed surface concentration and size distribution, flow depth, and internal shear velocity (derived from measured velocity profile and in close agreement with the value predicted from the surveyed channel slope and depth), I predicted a theoretical suspended-sediment concentration profile for all 21 particle size classes (Figure 2.23a). Combining all size classes into total sediment concentration, I observe a predicted sediment concentration at 0.1 m above the river bed of 14,236 mg/l (Figure 2.23b), almost identical to the observed concentration. Multiplying this modeled concentration by the flow velocity at each depth, I calculate a total profile section discharge of 130 kg of sediment per meter channel width per second. Compared to the lower profile discharge of 97 kg/ms for the case of uniform concentration with depth, the concentration-profile correction increases the estimate for total sediment discharge of the depth profile by 33%. Because the majority of the sediment in the Beni River is transported during high-stage conditions, I speculate that this profile correction factor may be conveniently applied to the gauged annual flux (of surface sediment) to provide a

depth-corrected estimate for the average annual suspended sediment discharge at Rurrenabaque of 248 Mtonnes/yr. This figure does not include the bedload flux, which is likely to be small, but all such gravel transported past Rurrenabaque is deposited within a short distance downstream and therefore of little consequence to the flux model.

At Riberalta, the flux data are considerably more limited. Guyot (1993) has used 91 measurements of suspended sediment and discharge records from 1983 – 1989 to calculate a total sediment flux of 100 Mtonnes/yr upstream of Riberalta. Maurice-Bourgoin (2001) has compiled ~ 70 measurements of surface suspended sediment concentrations and discharges from 1998 – 2001, but the data have not yet been analyzed. In February, 2001, sediment was sampled from the water and floodplain upstream of Riberalta during a period of rising, moderately-high river stage. A surface sediment concentration of 2,100 mg/l was measured and the depth was estimated. I had previously surveyed the channel slope, thereby providing an estimate for the internal shear velocity. Logistical constraints prevented me from using the sediment sampling apparatus at depth, so at this juncture I must rely entirely upon my previous modeling approach which I employed for Rurrenabaque. My calculations for the vertical sediment concentration profiles (Figure 2.24a) and the total profile sediment flux (Figure 2.24b) produce a predicted profile correction factor of 52%. This factor is larger at Riberalta because the internal shear velocity is considerably smaller than at Rurrenabaque (the channel slope is 6 times less), resulting in steeper vertical sediment concentration profiles despite the fact that the suspended sediment is finer (e.g., settles more slowly and therefore would tend to be more uniformly mixed for the same internal shear velocity). Assuming as before that this correction is representative, I estimate that the average sediment discharge (there is no gravel bedload) of the Beni River upstream of Riberalta is 152 Mtonnes/yr.

Comparing these two flux estimates derived from river gauging records, I observe that the difference is 96 Mtonnes/yr, which would correspond to the net annual accumulation of sediment within the Beni foreland basin between Rurrenabaque and

Riberalta. This value is comfortably close to the separately-derived value of 97 Mtonnes/yr, and is certainly well within the potential errors in these flux estimates.

Summary

This study quantifies sediment interchange and transport within a large channel-floodplain system spanning a foreland basin, presenting several key findings:

(1) I present a detailed flux analysis for a sand-bedded river which deposits an large mass of material within its foreland basin. In contrast, previous models for sediment transport within foreland basins represent the fluvial transport system with excess-shear-stress bedload routing schemes appropriate only for gravel-bedded rivers (Heller and Paola, 1992; Paola, 1989; Robinson, 1998), or as simple power-law functions of slope or distance (Flemings and Jordan, 1989). The field data and quantitative flux analysis presented in this chapter illustrate that large rivers like the Beni require a new modeling approach, as presented here in its empirical form and developed theoretically in Chapter 3.

(2) The flux analysis and calculation of net sediment accumulation within the Beni Foreland concurs with two independent measurements: the net annual sediment loss across the foreland as determined from a re-calibration of the long-term sediment discharge records collected at two gauging stations, and the measured and modeled downstream decay in the ^{210}Pb activity of fresh river sediment.

(3) The annual sediment exchange between the cut banks and point bars due to channel migration is larger than the total annual sediment efflux from the Beni Foreland. This observation suggests that similar processes of sediment exchange may also be or once were important for sand-bedded rivers elsewhere, before they were stabilized to limit channel migration.

(4) Oxbow lakes cut off in rapidly-migrating reaches typically do not infill, effectively functioning as large floodplain voids as the river migrates away from and abandons them; this process may serve to accelerate local channel and

floodplain aggradation over the timescale of channel migration away from the site (which has a strong directional bias in this basin).

(5) I have estimated minimum rates of channel aggradation within the Beni Foreland of 2–5 cm/yr by employing two separate techniques: measuring the channel-proximal sediment accumulation rates on the floodplain (assumed to be equal to that of the channel bed) and determining the minimum channel bed aggradation necessary to explain the observed granulometric distributions across meander apexes.

(6) The surprising lack of regular floodplain sedimentation during most large floods, copious crevasse splay deposits, and high natural levees describe a system quite different than other floodplains commonly described in the literature. This may be in part because the Beni floodplain is covered with a dense tropical rainforest, providing considerable vegetation roughness to slow the advective or diffusive transport of sediment into the surrounding floodplain. In contrast, the floodplains of most other sand-bedded rivers have been extensively deforested and cultivated, removing this natural impedance to overbank flow. Consequently, anthropogenic influences may have fundamentally changed the mechanics of floodplain sedimentation for many other large rivers.

Table 2.1. Standard sediment sample locations, listed for survey transects across meander apexes (e.g., Figure 2.1). In addition to the location code in the table, "R" or "L" is appended before other letters to denote right or left side of river. Floodplain transects were typically completed to 100 m on the cutbank side and 50 m on the point bar side, although "FC" transects frequently extended 300 m or farther (up to 1200 m) and some "FB" transects reached 100 m. All sample locations were surveyed by DGPS, some also by hand surveys. Most cutbank and berm heights and associated sample locations were also measured with a survey-grade laser rangefinder/inclinometer. Channel depths were determined with a hand-held sonar unit coordinated with a DGPS survey of channel location.

Code	Location	Nature	Comments
FB100	Forested floodplain, bar side (100 m from unvegetated sand)	soil core	occasionally done
FB50	Forested floodplain, bar side (50 m from unvegetated sand)	soil core	usually done
FB5	Forested floodplain, bar side (5 m from unvegetated sand)	soil core	
VB	Sand bar, at edge of vegetation (~ 1 m into veg)	grab	often a rise to here
TB	Sand bar top, halfway between EB and VB	grab	"berm top" location, flat!
EB	Sand bar, top edge of "berm" rise near low-stage water	grab	often flat past TB to near VB
MB	Sand bar, middle of "berm" rise near low-stage water	grab	large sack samples here
WB	Sand bar, bottom of "berm" at low-stage water	grab	Long occupation DGPS here
Dredge	Channel bottom (thalweg)	grab	occasionally done
WC	Cutbank, just above water (often covered by slump blocks)	grab	
MC	Cutbank, halfway up cliff	grab	sometimes extra locations
TC	Cutbank, near top of coherent cliff (~ 1 m from top)	grab	sometimes extra locations
VC	Cutbank, at vegetation (~ 1 m back from cliff edge)	grab	
FC5	Forested FP, cutbank side (5 m into vegetation from bank)	soil core	
FC50	Forested FP, cutbank side (50 m into vegetation from bank)	soil core	
FC100	Forested FP, cutbank side (100 m into vegetation from bank)	soil core	usually done
FC150	Forested FP, cutbank side (150 m into vegetation from bank)	soil core	occasionally done
FC200	Forested FP, cutbank side (200 m into vegetation from bank)	soil core	occasionally done

Table 2.2. List of all floodplain sampling locations for the Beni River, including the 25 survey transect locations where samples were collected and topography was measured over long distances (usually on both sides of the river, spanning the point bar and the channel). Maps of these locations are presented in Figure 2.4a-c, and in Appendixes A, and in the pocket material.

			Water	Floodplain Survey Length		
Transect #	East (UTM 19s)	North (UTM 19s)	Elevation (m)	Cutbank (m)	Bar (m)	Description
1	672533	8503591	163	50	50	short transect
2	678338	8508874	159	100	50	short transect
3	675573	8519691	155	1250	50	very long transect on fp
4	690003	8539939	155	50	50	short transect
6	713201	8554524		5	5	banks of blackwater tributary
7	712524	8565731	150	50	50	short transect
8	722828	8584404		300	none	single core on high terrace
9	722010	8586316	148	50	50	short transect
10	719996	8599633	144	100	50	transect
11	722743	8603551	142	300	50	longer transect
14	723343	8622025	138	150	50	transect
18	729247	8672095	138	300	50	longer transect
25	651369	8373045	217	50	none	single core on floodplain
27	658467	8383200	211	50	none	single core on floodplain
34	656742	8411877	185	10	none	two cores on high terrace
41	656200	8414890	182	600	none	meander neck transect
48	678224	8499947		1000	none	core from oxbow lake limb
49	674889	8494758	163	5	none	vertical transect
50	677119	8491756	164	50	100	transect
51	669443	8485943	164	300	50	longer transect
52	667855	8481240	165	700	none	survey around oxbow cutoff
54	659492	8475573	168	50	5	transect
55	660703	8461648	174	50	5	transect
56	661496	8453645	173	50	50	transect, very large sand bar
57	662197	8444955	173	50	50	transect
59	660427	8426380	177	50	50	transect
60	664551	8420047	178	300	100	longer transect
61	664551	8420047		200	50	transect
62	664551	8420047		200	50	transect
63	664551	8420047		200	50	transect
64	664551	8420047		200	50	transect

Table 2.3. List of mean granulometry (percentage clay, silt, and sand) of cutbank floodplain cores from all survey transect locations along the Beni River. Total sand fraction is typically < 10%, in contrast to unvegetated bar deposits which contain 80 – 100 % sand by mass. Clay is defined as particles < 4 μm.

Transect #	Description	average % clay	average % silt	average % sand
1	short transect	19.3	77.3	3.4
2	short transect	30.7	64.7	4.6
3	very long transect on fp	39.7	57.7	2.6
4	short transect	37.7	57.3	5.0
6	banks of blackwater tributary	37.9	43.2	18.9
7	short transect	16.2	76.8	7.1
9	short transect	22.0	75.7	2.3
10	transect	30.7	66.6	2.8
11	longer transect	36.9	61.9	1.1
14	transect	25.8	58.3	17.4
18	longer transect	51.1	42.6	6.3
41	meander neck transect	37.0	55.2	7.8
50	transect	26.0	57.7	16.8
51	longer transect	36.4	57.4	6.2
54	transect	17.0	80.5	2.5
55	transect	15.4	78.9	5.7
56	transect	17.2	73.4	9.4
57	transect	22.4	69.8	9.9
59	transect	38.4	60.7	0.8
60	longer transect	21.3	65.1	13.9
61	transect	29.0	69.7	1.3
62	transect	25.5	62.7	11.8
63	transect	21.6	72.5	6.0
64	transect	20.1	62.8	17.4

Table 2.4. Historical data for 23 oxbow lakes that have formed since 1960. GIS area data are currently available for only 15 of these lakes, 11 of which formed prior to 1993, and hence have more than one time interval of record. Also listed is the condition of the tie channel, if any, which connects each oxbow lake to the main river channel.

Lake	Lake Lati-		Tie channel			Oxbow lake area (km^2)			
#	tude (deg)	Cutoff Date	condition	Infilling History	notes	1975	1986	1993	1999
1	13.01	1975-1986	filled	no infilling			1.43	1.65	1.49
2	13.07	1975-1986	filled	no infilling			0.07	0.63	0.97
3	13.14	1960-1975	filled	no infilling			1.15	1.16	1.17
4	13.20	1960-1975	filled	no infilling		3.43	3.50	3.57	3.67
5	13.24	1993-1999	recent cutoff	not enough time					1.84
6	13.27	1993-1999	recent cutoff	not enough time	connected to river				0.99
7	13.31	1986-1993	filled by 1999	filling after 1993	connected to river			2.75	0.36
8	13.35	1960-1975	yes, open!	steady filling	floodplain tributary	0.88	0.48	0.32	0.42
9	13.48	1960-1975	filled	no infilling			0.13	0.10	0.12
10	13.52	1986-1993	filled by 1999	filling after 1993	connected to river			1.08	0.54
11	13.56	1986-1993	filled	no infilling	very close to river			1.61	1.58
12	13.64	1975-1986	filled	no infilling			1.14	1.65	1.66
13	13.71	1993-1999	filled	not enough time					1.41
14	13.72	1986-1993	filled	no infilling				1.60	2.47
15	13.78	1993-1999	filled	filled at cutoff					0.21
16	13.80	1993-1999	filled	not enough time		Area results not yet available			
17	13.86	1993-1999	filled	filled at cutoff					
18	13.87	1975-1987	filled	no infilling					
19	13.92	1975-1987	filled	filled at cutoff					
20	14.02	1987-1993	filled	filling after 1993	distal ends near river				
21	14.19	1993-1999	filled	not enough time					
22	14.21	1987-1993	filled	no infilling					
23	14.37	1975-1987	filled	filled at cutoff					

Table 2.5. Particle size distribution and equivalent concentration for river surface (7.6 m) and bottom (0.1 m) suspended sediment samples collected at Rurrenabaque during a flood-stage sampling campaign in February, 2001.

	River Top Sample			River Bottom Sample			Comparative Change		
Diameter (microns)	Concentration (mg/l)	% of total	Cumulative % smaller	Concentration (mg/l)	% of total	Cumulative % smaller	mg/l Increase with Depth	% Increase with Depth	Estimated % Error
354	2	0.04	99.96	82	0.57	99.43	79	3416	373
250	10	0.17	99.79	662	4.58	94.86	652	6230	47
180	52	0.86	98.92	2636	18.22	76.64	2583	4939	12
125	135	2.23	96.69	2985	20.64	56.00	2850	2114	10
88	314	5.20	91.49	1880	13.00	43.00	1566	498	14
75	266	4.40	87.09	829	5.73	37.27	563	212	29
63	240	3.97	83.12	525	3.63	33.64	285	119	41
50	48	0.79	82.33	178	1.23	32.41	131	274	139
40	126	2.08	80.26	327	2.26	30.15	201	160	69
30	317	5.23	75.02	488	3.37	26.77	172	54	39
25	244	4.03	70.99	290	2.00	24.77	46	19	59
20	322	5.32	65.68	334	2.31	22.46	13	4	48
15	490	8.10	57.58	411	2.84	19.61	-79	-16	35
10	980	16.20	41.38	557	3.85	15.76	-422	-43	20
8	636	10.51	30.87	295	2.04	13.72	-341	-54	34
6	625	10.34	20.52	389	2.69	11.03	-236	-38	31
5	241	3.99	16.54	238	1.64	9.39	-3	-1	65
4	196	3.24	13.30	250	1.73	7.66	54	28	70
3	173	2.87	10.43	253	1.75	5.91	79	46	74
2	161	2.66	7.77	265	1.83	4.08	104	65	74
<2	470	7.77	7.77	590	4.08	4.08	120	26	30
Total	6047	100		14465	100		8418		

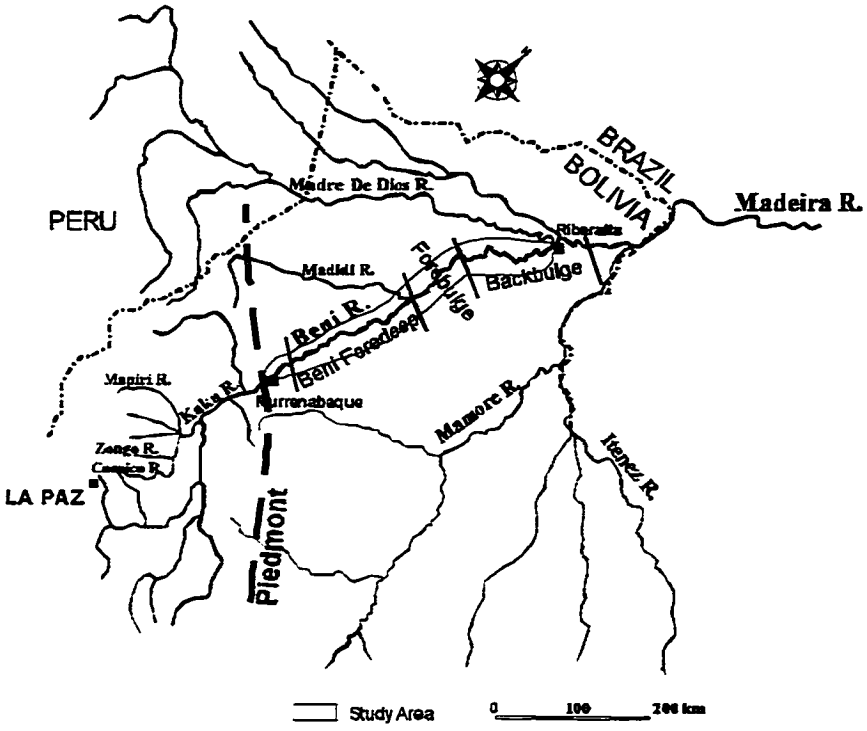

Figure 2.1. Hydrographic map of major Madeira River tributaries, depicting the Beni River, the study focus area for floodplain sampling, and principal long-term river gauging stations at Rurrenabaque and Riveralta. Approximate location of the foredeep, forebulge, and backbulge secondary basin are depicted, as determined by DGPS surveys of river gradient.

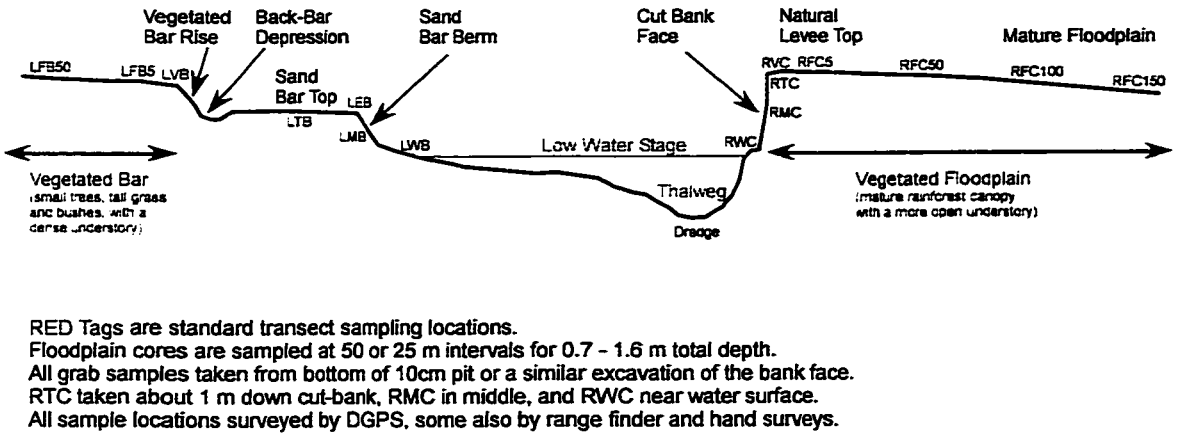

Figure 2.2. Sketch of a typical survey transect across a Beni River meander apex. All grab samples taken from the bottom of a 10 cm pit or a similar excavation of the bank face. Floodplain cores were sampled at 50- or 25-m intervals for 65–130 cm total depth. All sample locations surveyed by DGPS, and many also by laser or hand level surveys.

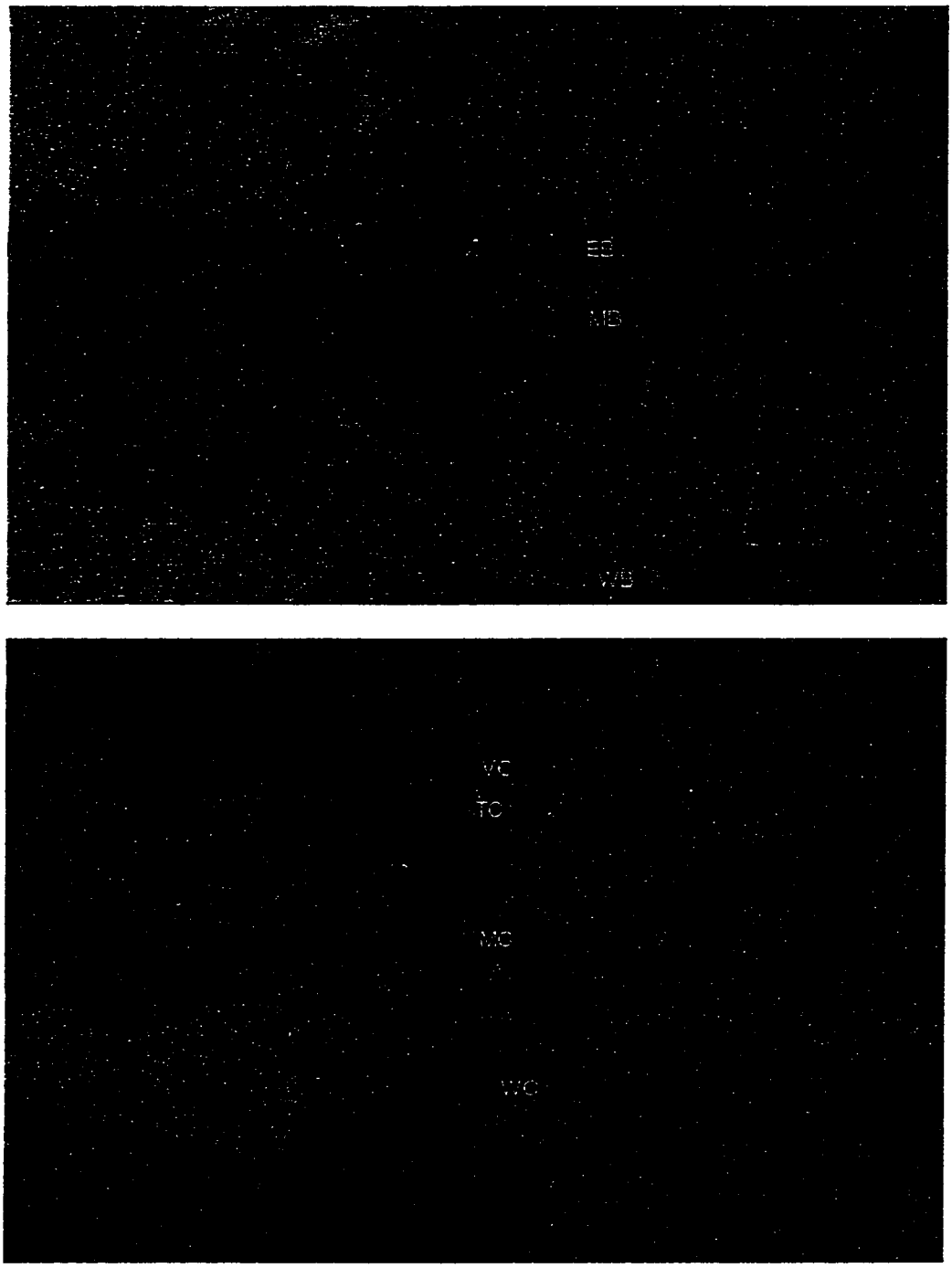

Figure 2.3. (a) Representative point bar deposit, showing a large sand "berm" which usually occurs near the water's edge, and typical sample locations. Person is ~ 1.8 m tall. (b) Representative cut bank, showing steep 6 m cliff at the water's edge. Standard sample locations are marked.

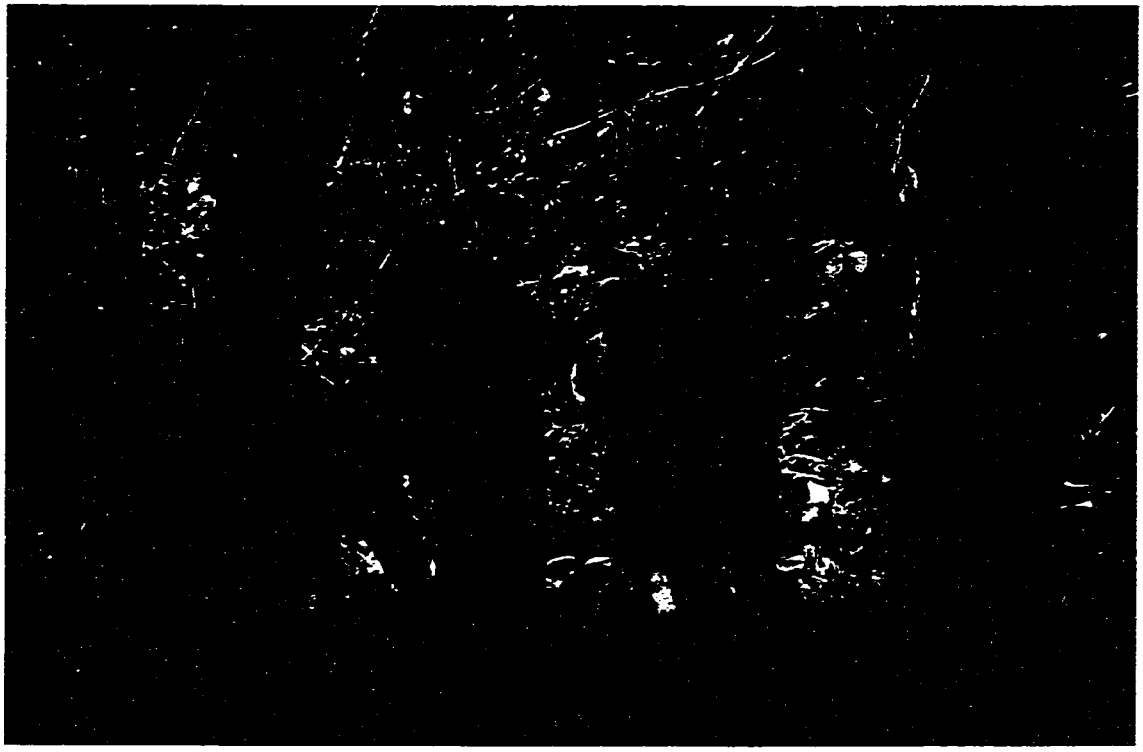

Figure 2.3. (c) Sampling location on the Beni forested floodplain, depicting the usual verdant rainforest vegetation. People are 1.7 – 1.8 m tall.

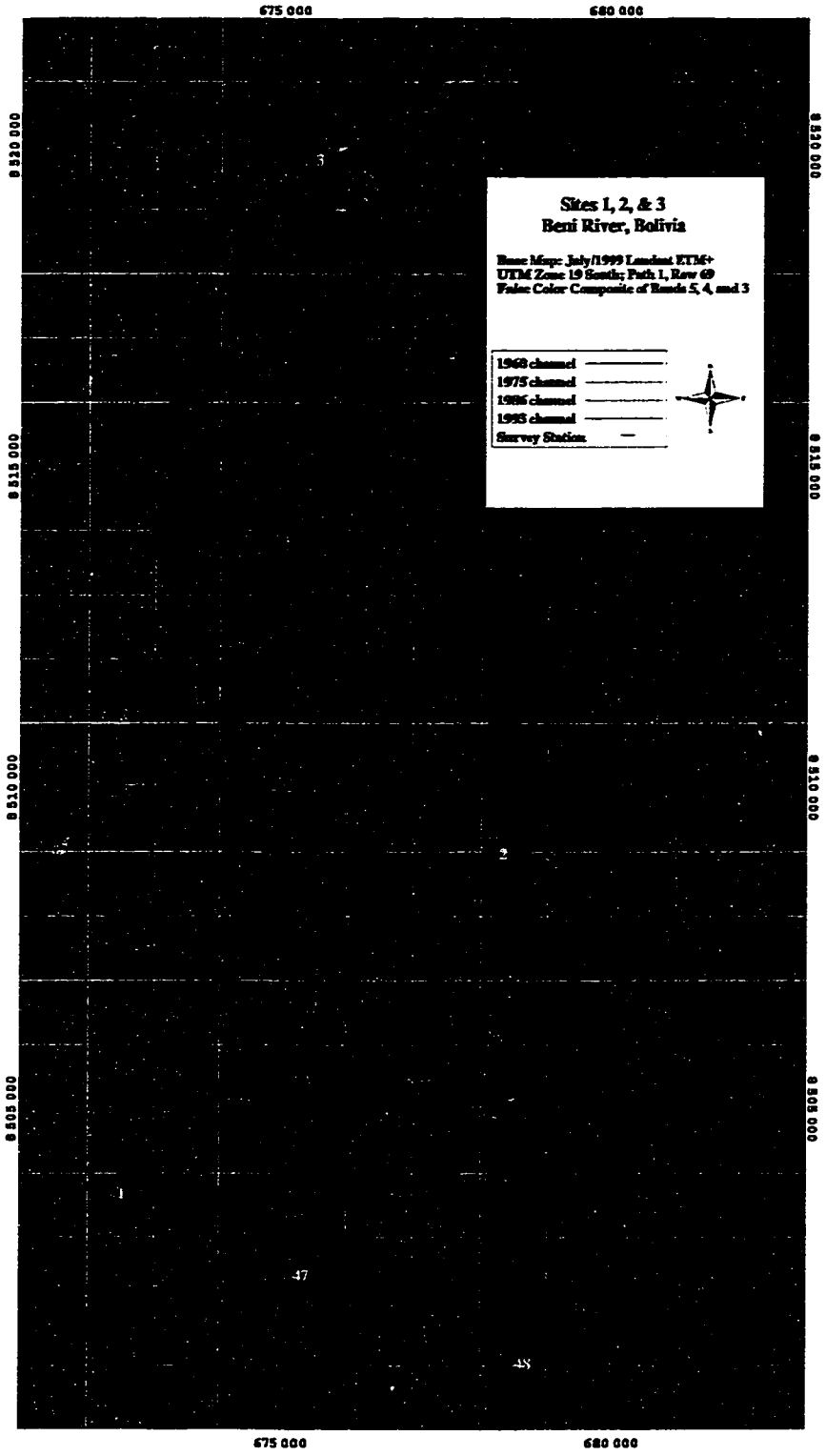

Figure 2.4. (a) GIS map of survey transects at sites 1, 2, and 3.

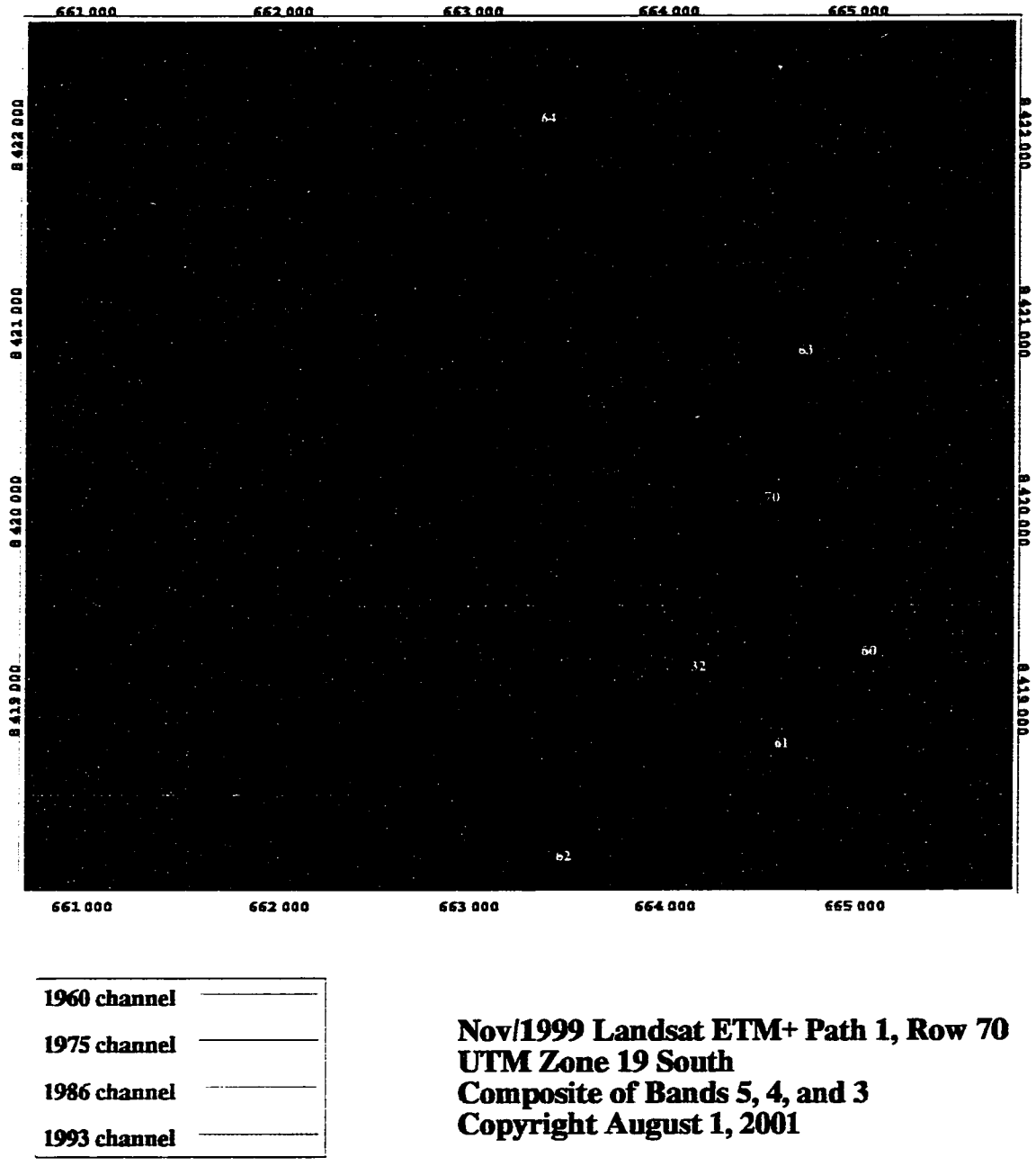

Figure 2.4. (b) GIS map of sites 60 to 64, depicting previous channel locations superimposed on 1999 ETM+ LANDSAT image. In image, bare sand or earth (band 5) is red, vegetation (band 4) is green, and water (band 3) is blue.

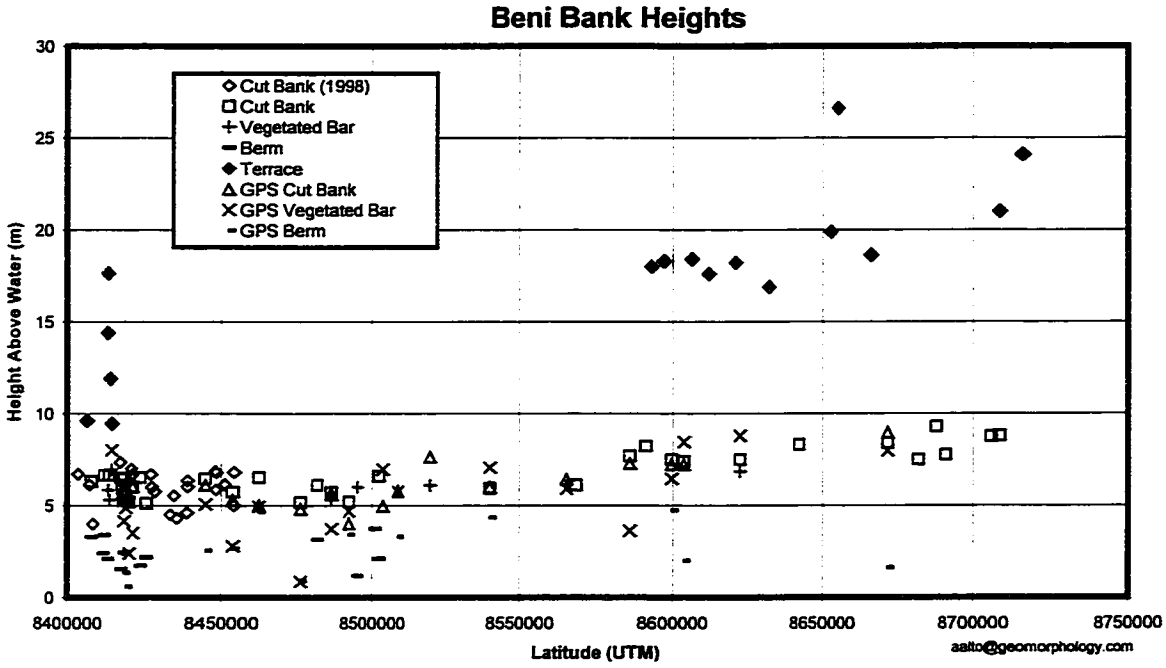

Figure 2.5. Surveyed heights for vegetated bars, cut banks, bar tops (berm), and terraces along the Beni River plotted by UTM latitude (zone 19s). Heights surveyed with DGPS are plotted separately from those surveyed by laser or hand level.

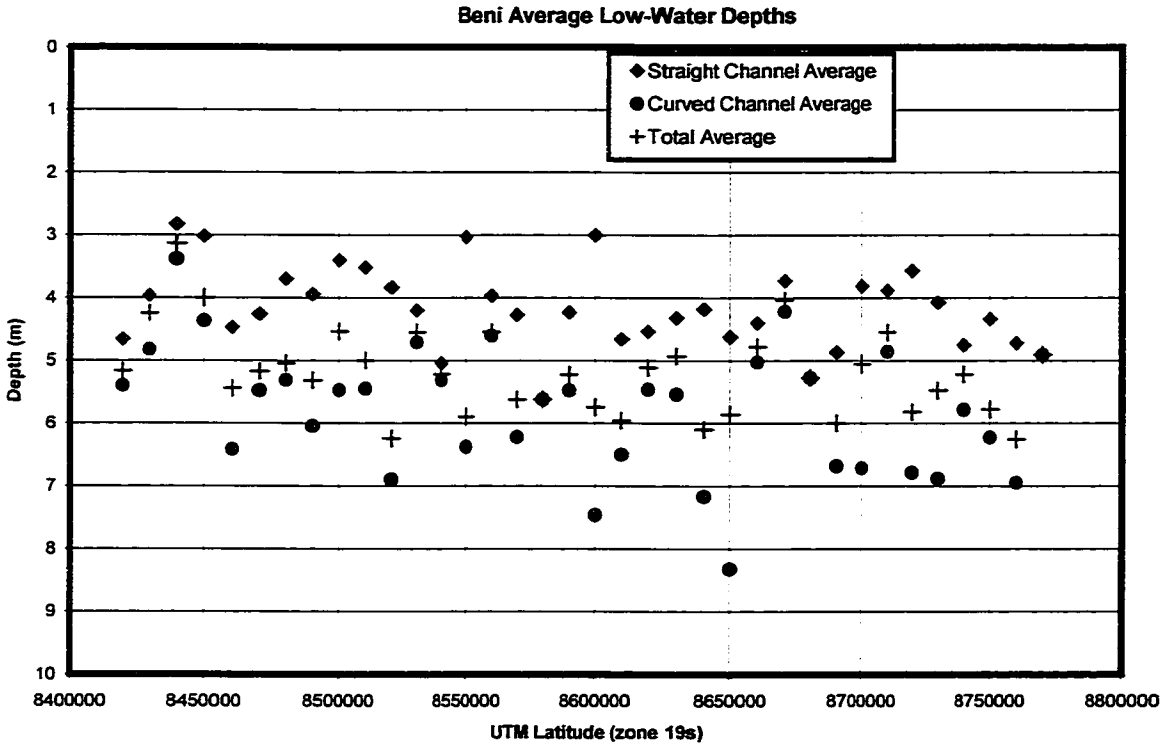

Figure 2.6. Channel depths for the Beni River measured in 1969 (Senema, 1969). For each 10 km latitude river reach, I separately report the average depth of all straight and all curved sections of channel, along with the combined average depth for the entire channel. Because the principal erosion and deposition occurs in curved meanders, not the straight channel reaches, for the mass flux analysis I used the average channel depth in the curved reaches.

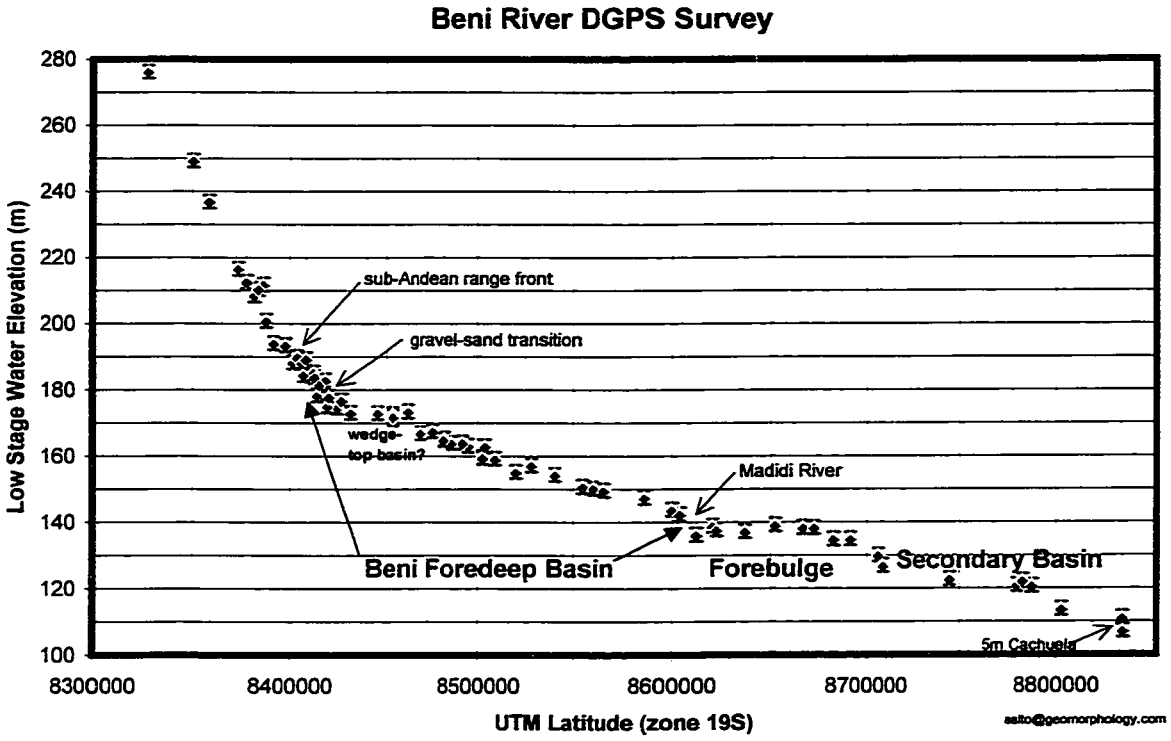

Figure 2.7. Longitudinal profile of low stage water surface elevation for the Beni River versus UTML. Locations of the range front, gravel-sand transition, confluence with the Madidi River, and the first large rapids (5 m Cachuela) are marked in black. Red letters indicated the proposed (in Chapter 6) locations of tectonic features, including the foreland, forebulge, and back-bulge secondary basin. For the water surface elevations, DGPS elevation was post-processed to an accuracy of ± 2 m or better (2 m error bars are depicted). Note that UTML "valley" slope is 1.3–4.5 times steeper than the slope of the river water surface.

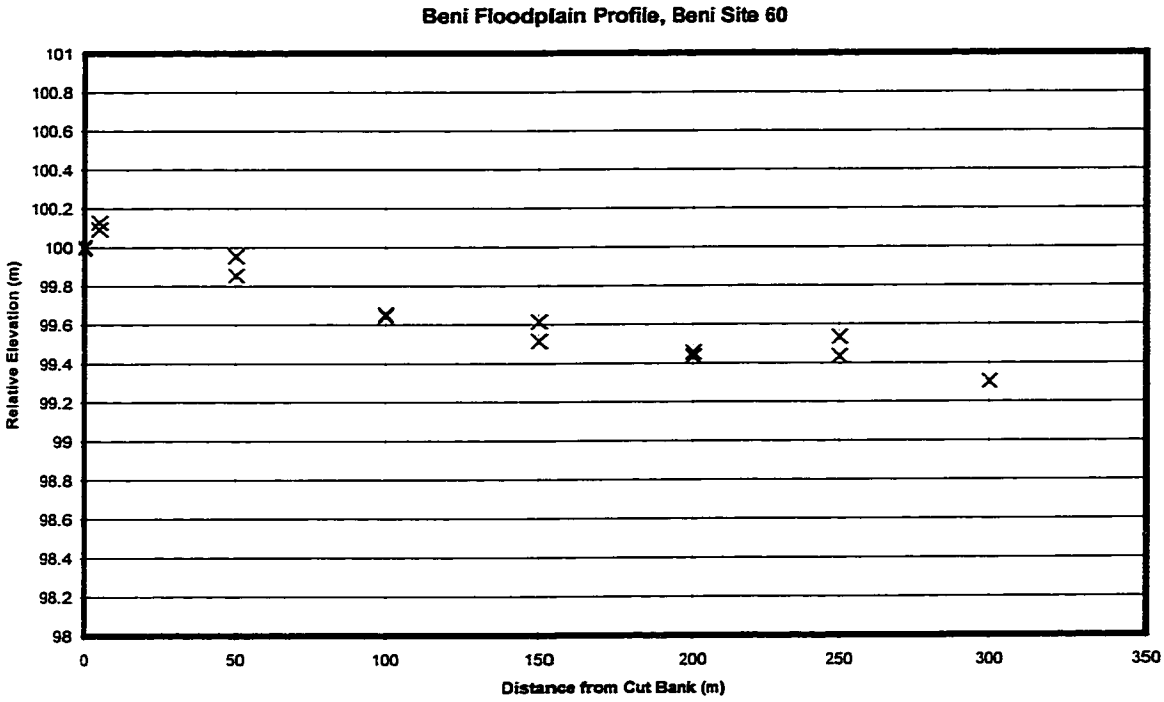

Figure 2.8. Representative topographic profile across a natural levee, Beni River transect 60. Elevations were measured with a hand level and stadia rod, with the survey starting and ending at the edge of the cut bank (elevations are shown for both the outbound and return surveys, to close the loop).

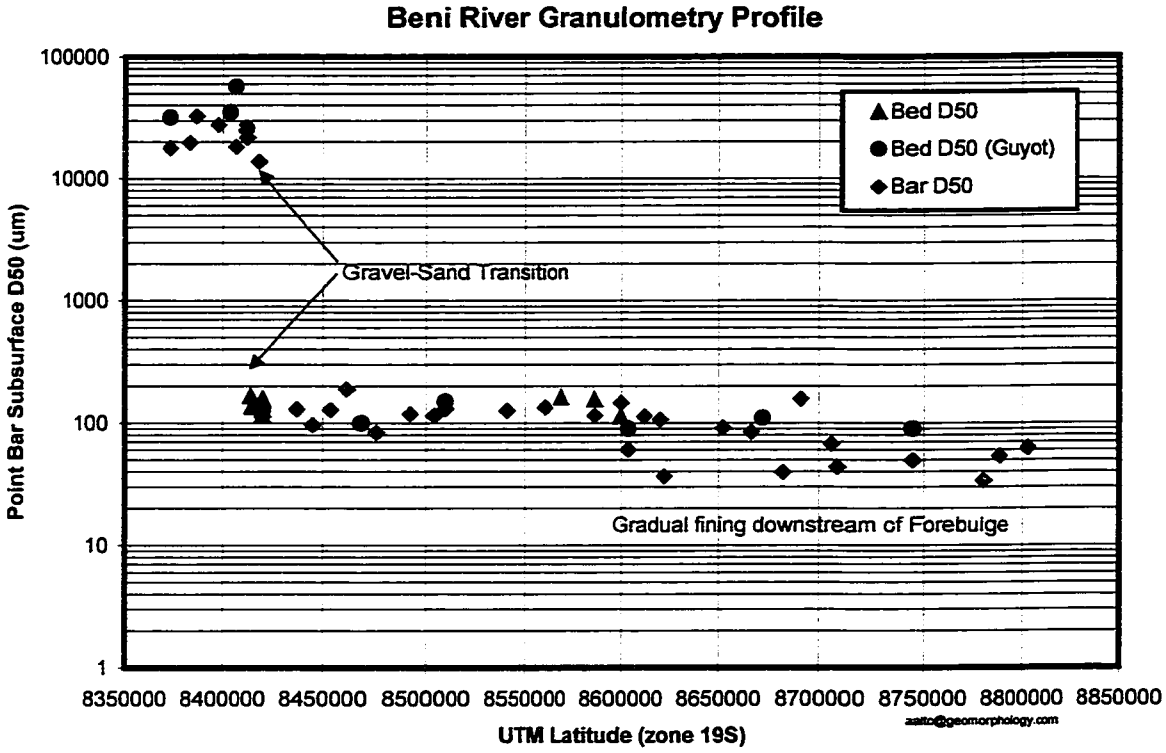

Figure 2.9. Down-channel plot of Beni River granulometry versus UTML. Bar D_{50} is determined from pebble counts or grab samples, both taken from the bar apex immediately adjacent to the low stage channel. Bed D_{50} is sampled with a pipe dredge. Plotted in green are Bar D_{50} values from Guyot et al., 1999, sampled using a different methodology for samples taken in 1988-89.

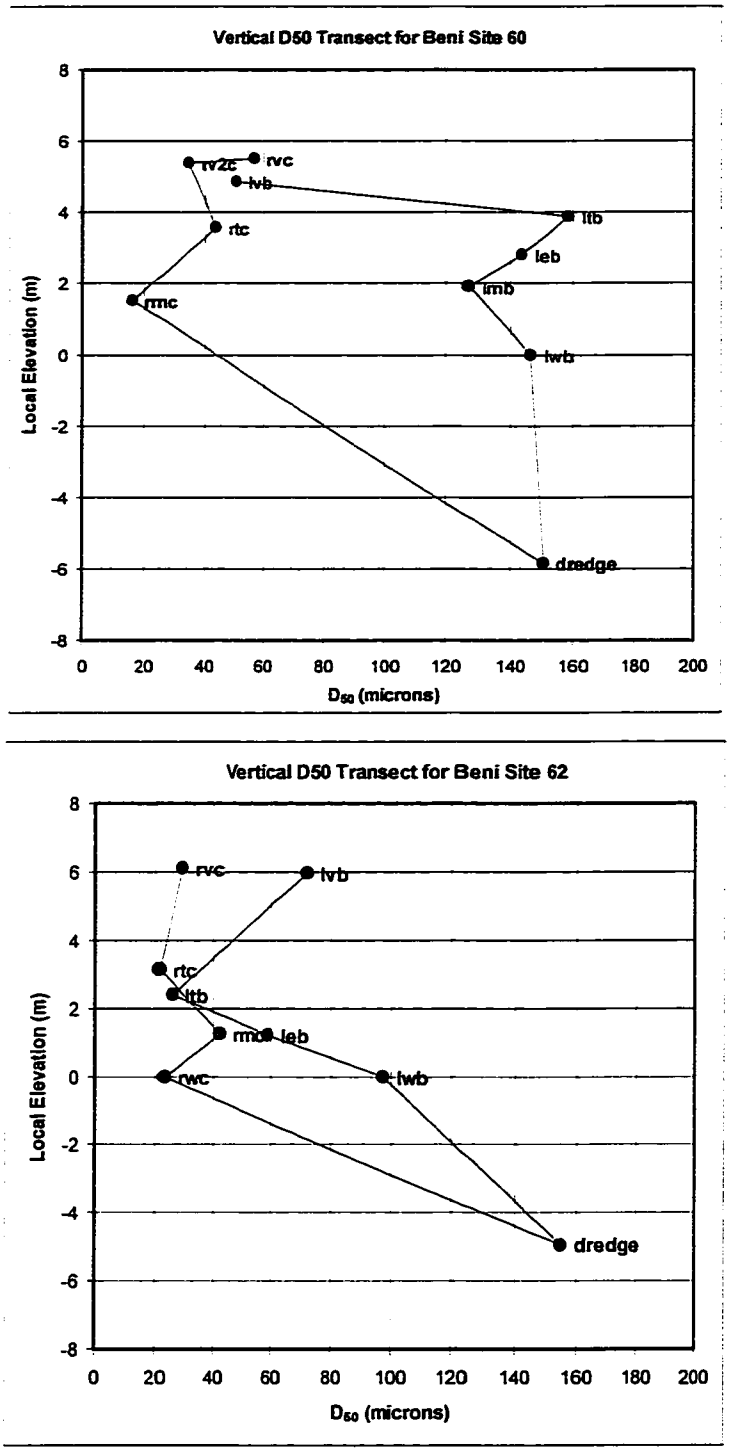

Figure 2.10. (a) Local elevation versus sediment D_{50} for survey transect across a meander bend apex, site 60. (b) Local elevation versus sediment D_{50} for survey transect upstream of a meander bend apex, site 62. For (a-c), see Figure 2.4b for locations.

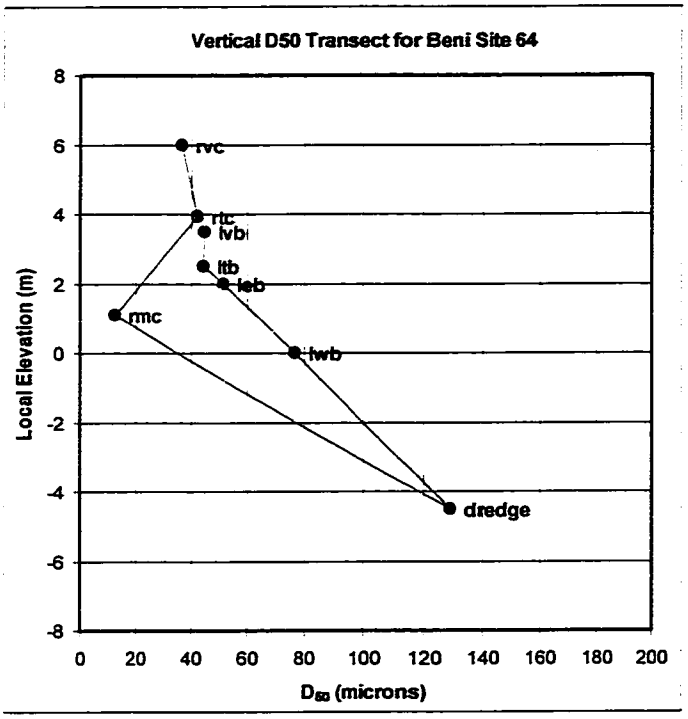

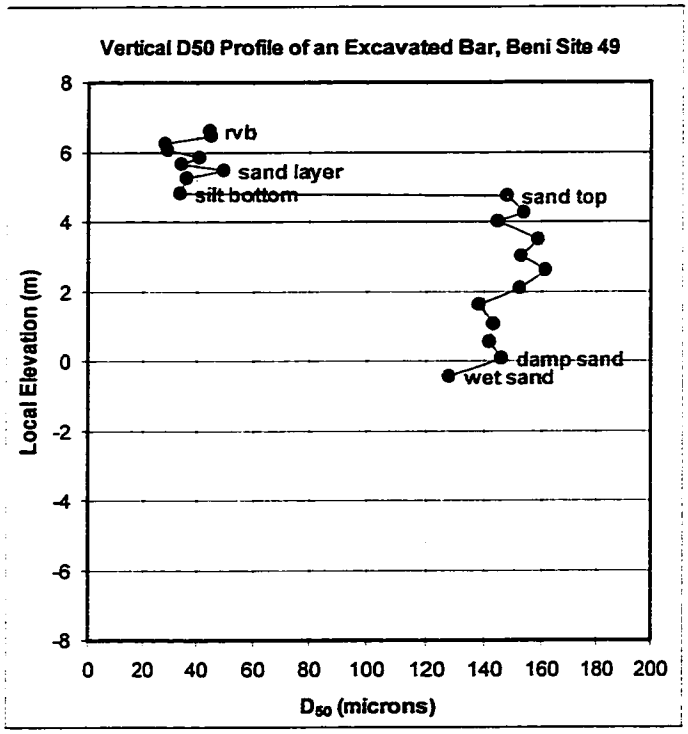

Figure 2.10. (c) Local elevation versus sediment D_{50} for survey transect downstream of a meander bend apex, site 64. (d) Local elevation versus sediment D_{50} for a vertical profile of an excavated point bar deposit, site 49.

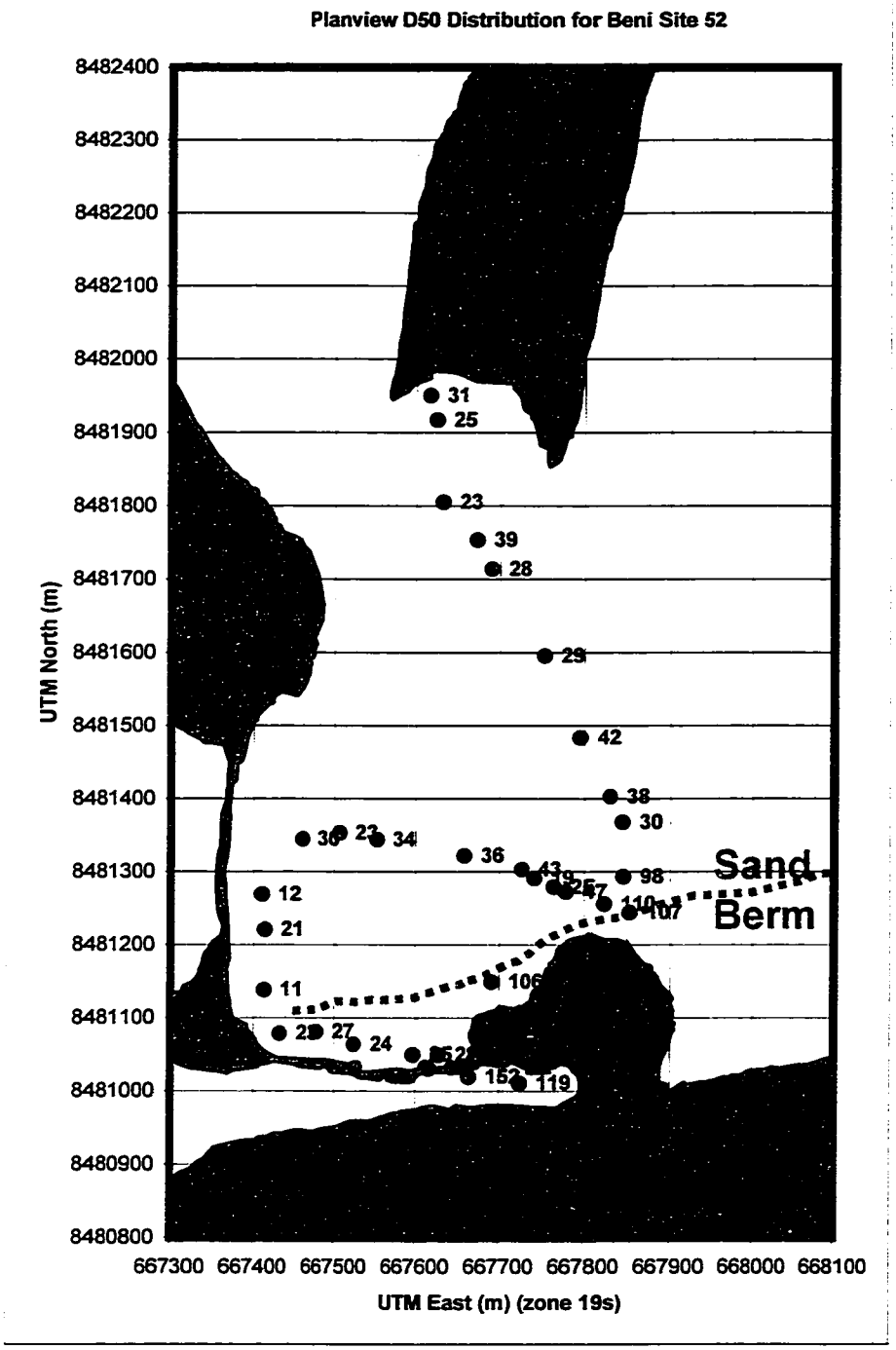

Figure 2.10 (e) Planform plot of sediment D_{50} for a recent channel cutoff, site 52.

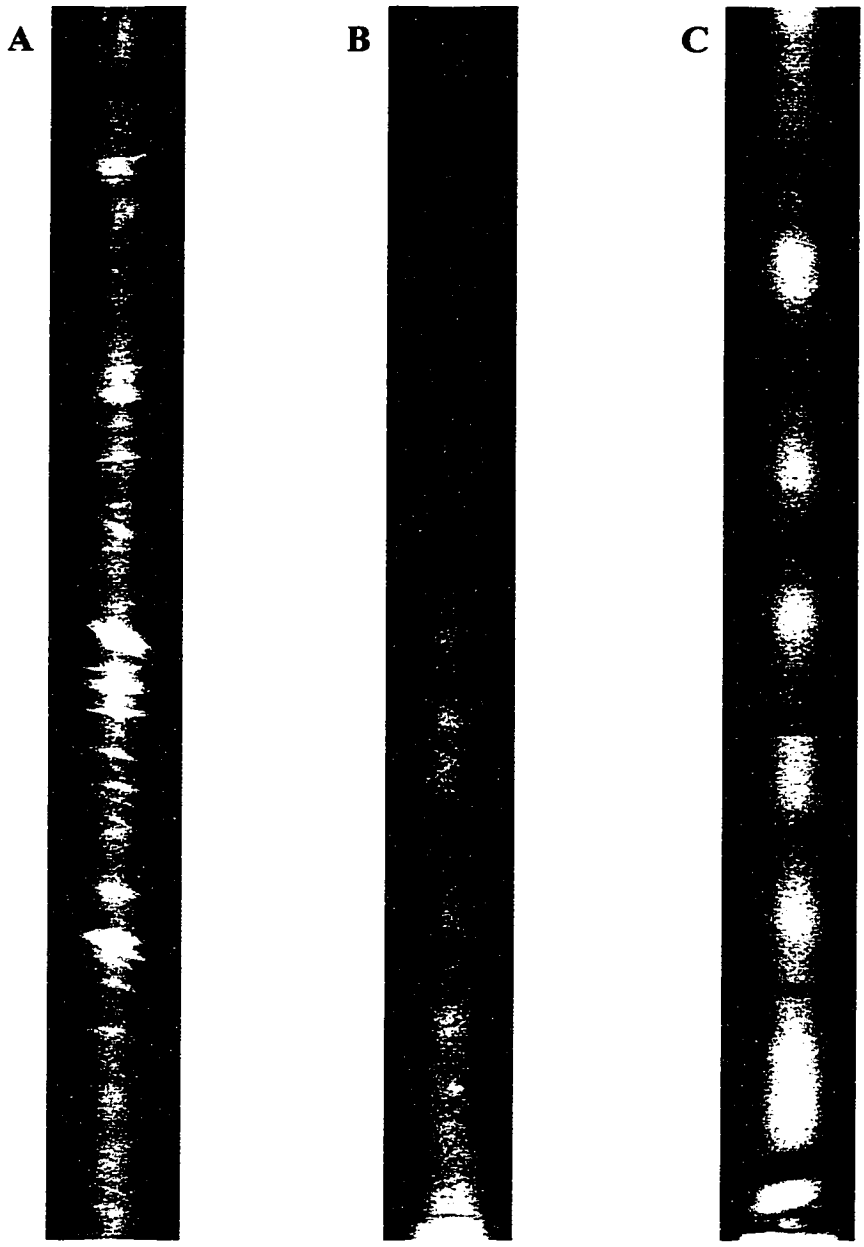

Figure 2.11. (a) X-ray image of a core located 5 m from the edge of the vegetation on a point bar deposit, site 49. Note the well-defined cross-bedding, which reflects the energetic depositional environment. (b) X-ray image of a core located on the forested floodplain 3 km from the river at the time of deposition, site 60. Fine horizontal lamina and massive silty deposits suggest a medium-to-low-energy depositional environment. (c) X-ray image of a core located on the forested floodplain 50 m from the river at the time of deposition, site 51, depicting massive banding and fine horizontal lamina. Images are approximately half of life size.

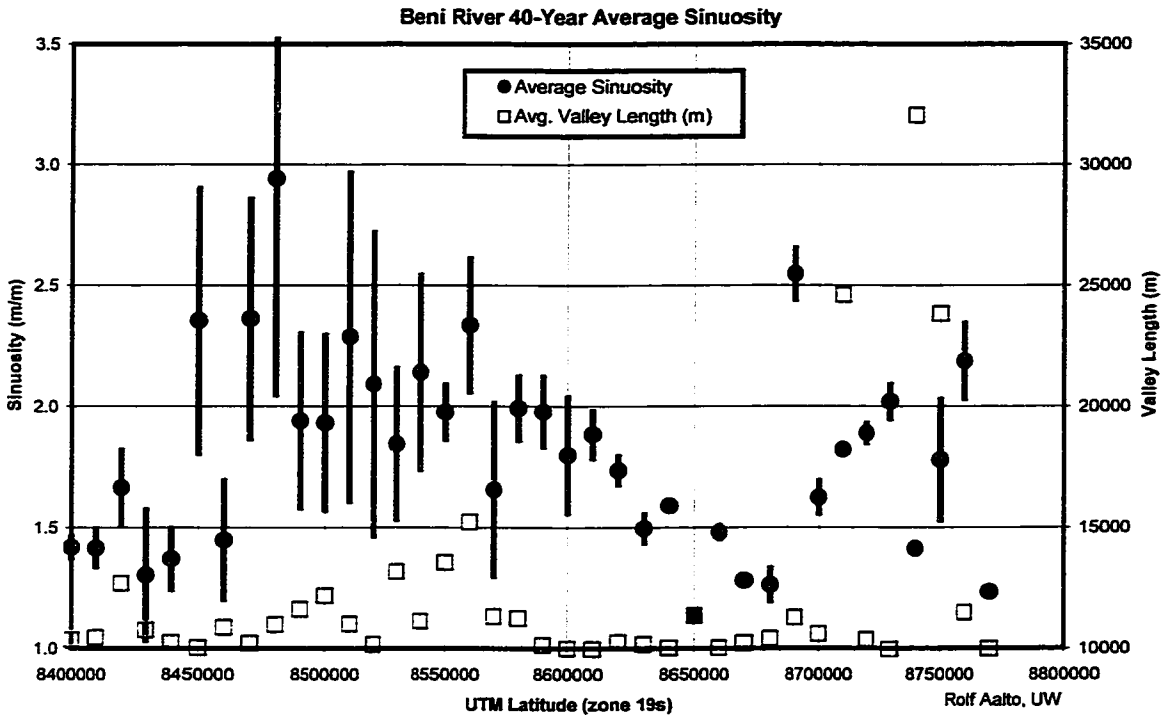

Figure 2.12. Beni River sinuosity and valley length versus UTML. Depicted is the average value since 1960, with the bars showing the standard deviation among the 4 measurements for each reach. Values for valley length above 10 km indicate a valley that lies at an angle across the 10 km UTML "box"; that is, does not follow a south-north path.

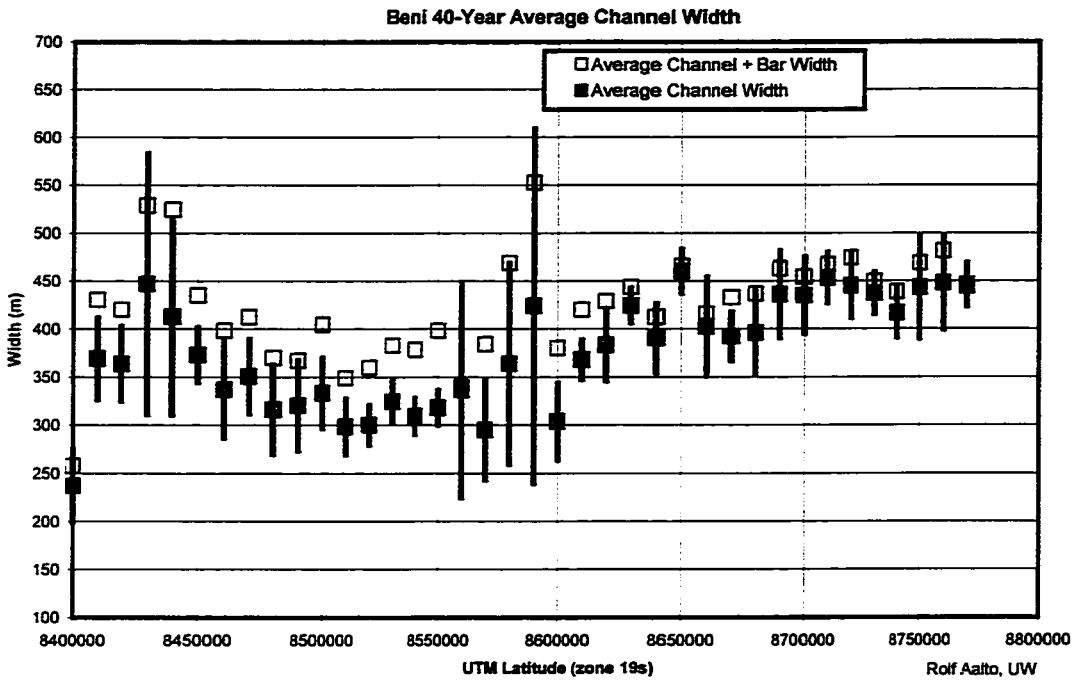

Figure 2.13. Beni River width versus UTML. Depicted is the average value since 1960, with the bars showing the standard deviation among the 4 measurements for each reach. Channel width is reported with and without bars (bar area and hence "wetted channel" width varies significantly with river stage). Total channel+bar width is used for the analysis, because this best represents bank-full width during flooding.

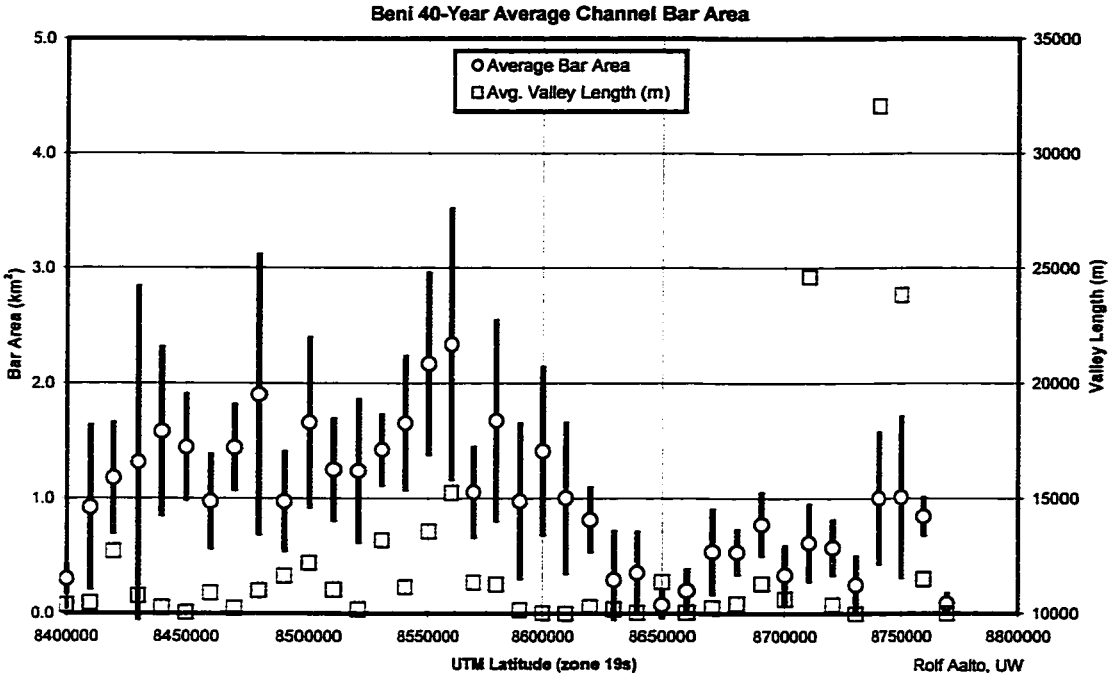

Figure 2.14. Beni River bar area and valley length versus UTML. Depicted is the average value since 1960, with the bars showing the standard deviation among the 4 measurements for each reach. Bar area varies significantly with river stage, increasing the observed variance. Values above 10 km indicate a valley that lies at an angle across the 10 km UTML "box," that is, does not follow a south-north path.

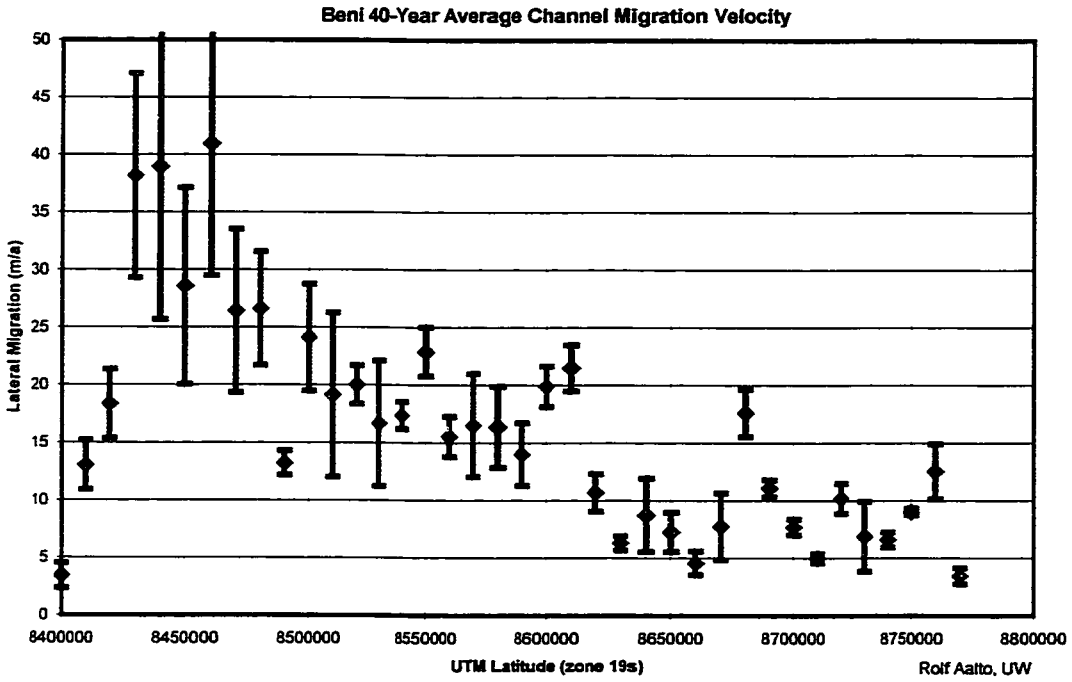

Figure 2.15. Beni River lateral migration velocity versus UTML. Depicted is the average value since 1960, with the error bars showing the confidence interval.

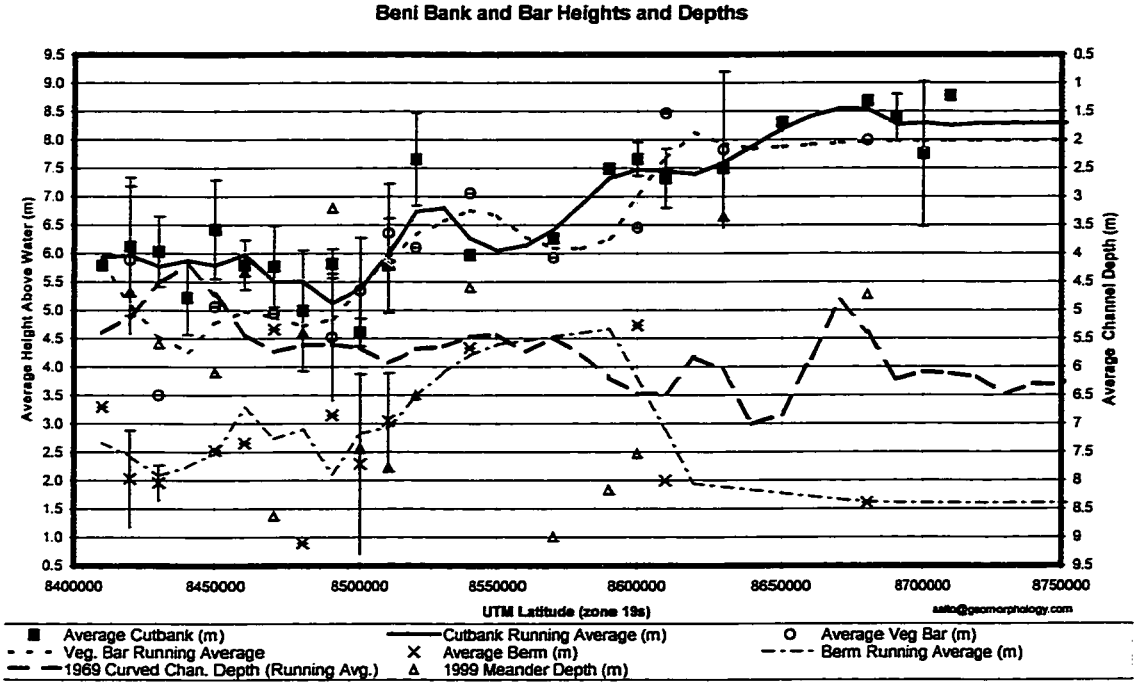

Figure 2.16. Summary of Beni River topographic survey results. Depicted are 10 km UTML average cutbank, vegetated bar, and berm heights (unvegetated bar top), along with 1999 channel depths. Also shown are running average values (30 km UTML averaging windows) for these heights, including those for the 1969 curved channel depths, which are used in the flux analysis.

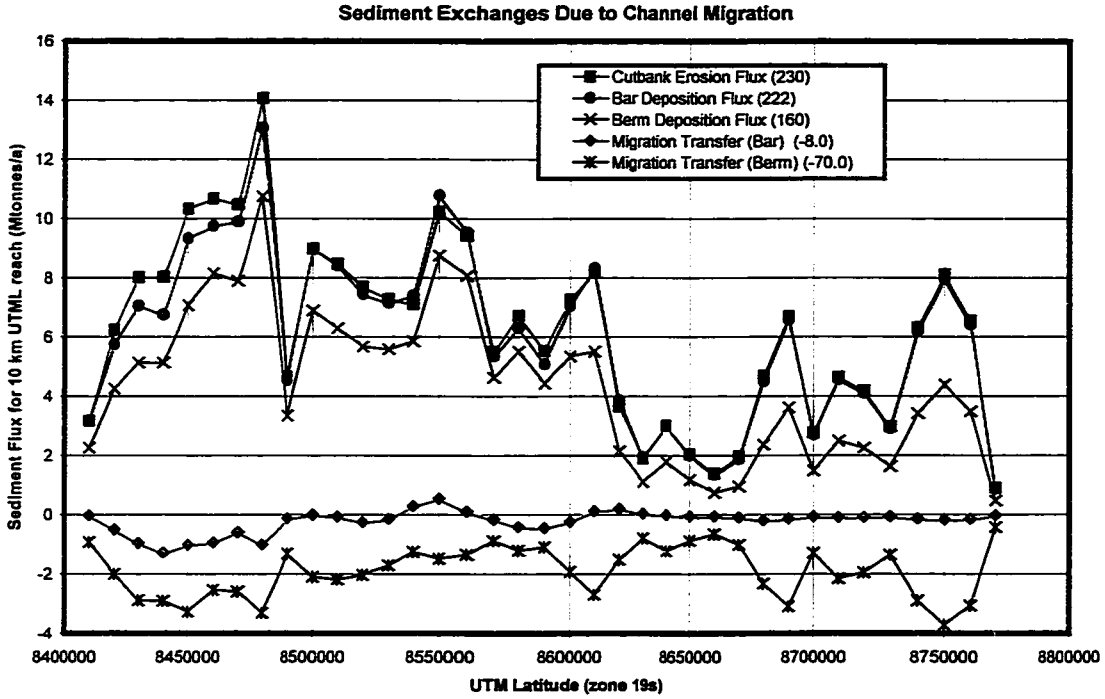

Figure 2.17. Sediment exchanges due to channel migration, plotted for 10 km UTML increments. Bar and berm deposition flux are the masses of sediment deposited due to channel migration, for the vegetated point bar ("bar") and the unvegetated point bar top ("berm"). Cutbank erosion flux is the mass eroded into the channel due to migration, a loss of floodplain material to the channel. However, here it is inverted and plotted as positive value to facilitate comparison with the bar and berm fluxes. The net change in the floodplain storage of sediment due to channel migration is plotted for the "bar" and the "berm" values – here, a negative value indicates a loss of floodplain sediment to the channel.

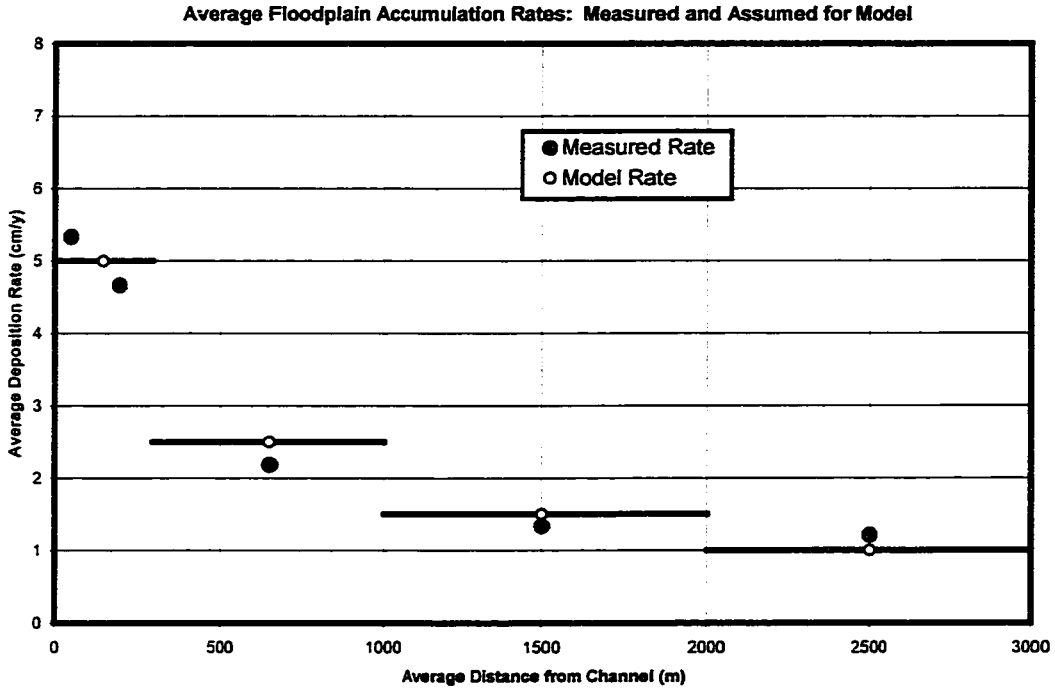

Figure 2.18. Average floodplain accumulation rates as a function of distance from the channel (from the geochronologic analysis presented in Chapter 5). The red circles indicate the average measured minimum accumulation rates. The yellow circles depict the floodplain deposition rates assumed for this flux analysis, including the distance intervals (black horizontal bars) over which these rates are assumed.

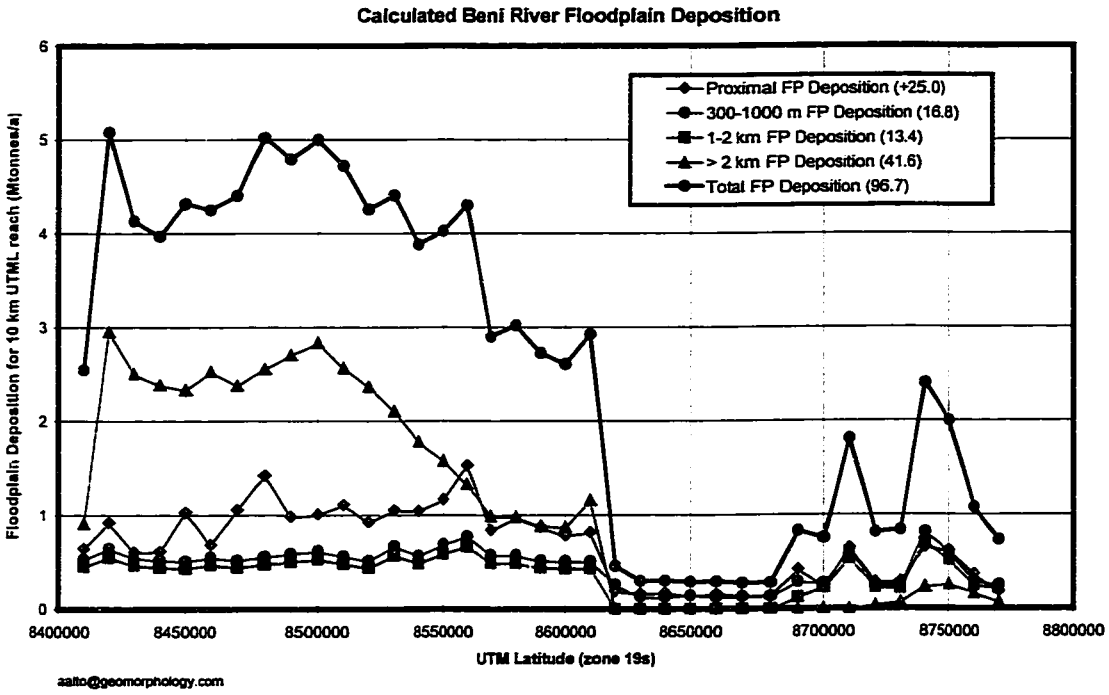

Figure 2.19. Calculated Beni River floodplain accumulation rates, plotted for 10 km UTML increments. Using measured floodplain widths, valley and channel lengths, and channel morphology from the GIS analysis, accumulation rates are calculated as a function of channel distance per the assumed rates in Figure 2.18. Downstream of the forebulge (8,620 km UTML), the floodplain becomes very narrow and I assume that all deposition rates decrease by half.

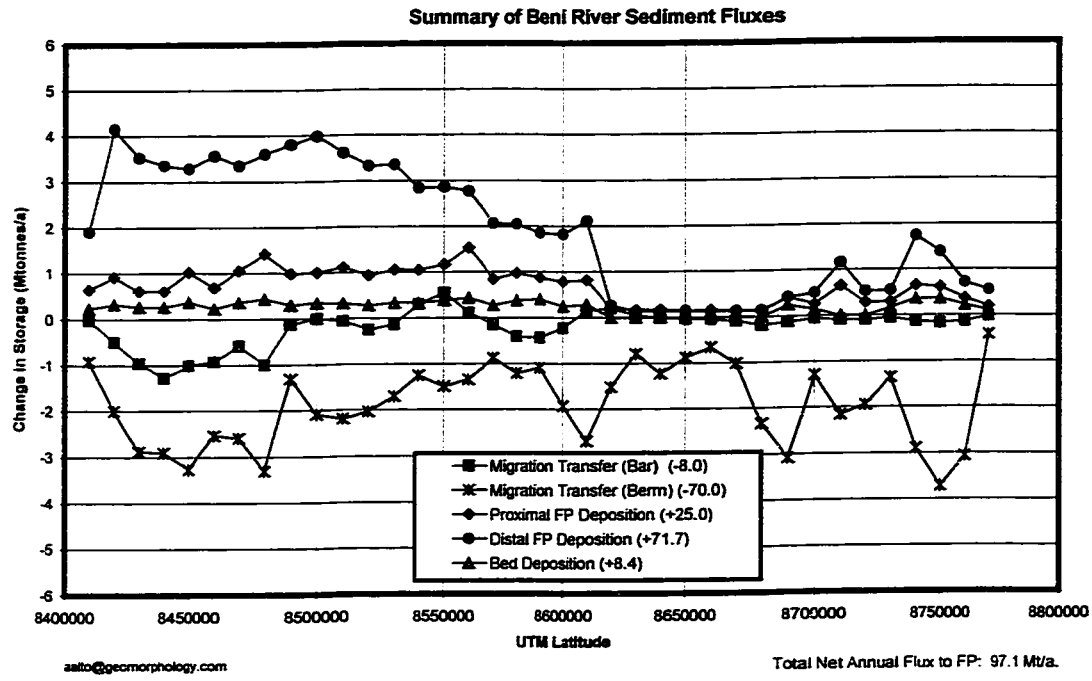

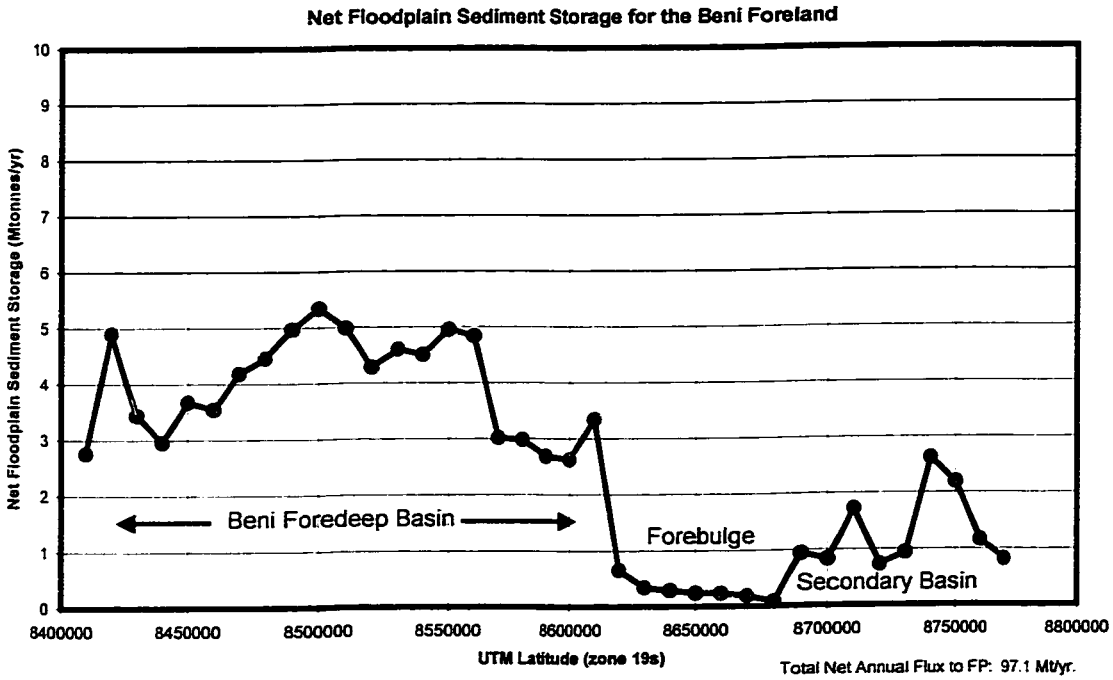

Figure 2.20. (a) Summary of all Beni River sediment fluxes, plotted for 10 km UTML increments. Along with the values in Figures 2.17 and 2.19, I include an estimate for channel bed deposition, assumed to be equal to the 1 km floodplain accumulation rate. (b) Plot of the net floodplain sediment storage from the sum of all fluxes in (a).

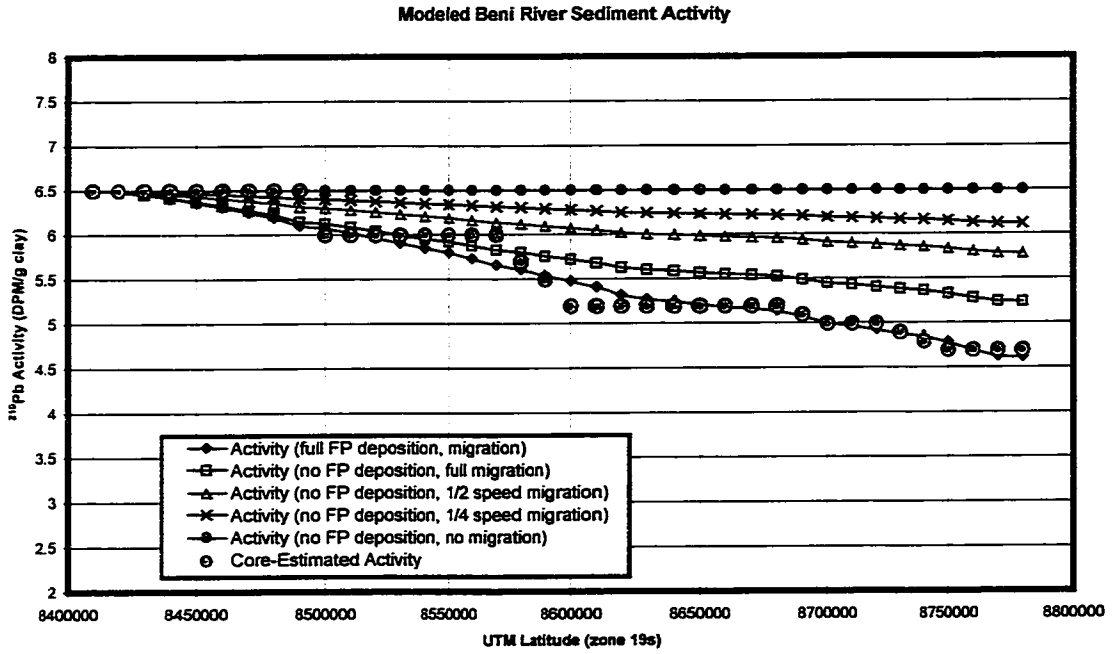

Figure 2.21. Modeled clay-normalized ^{210}Pb activity in river sediment plotted versus UTML, based on the exchanges of clay associated with the mass fluxes presented in 2.20a. Red line represents full flood conditions, with all exchange and depositional processes occurring at their mean annual rates. Grey circles depict measured sediment activity from channel-proximal floodplain samples. The full data and analysis are presented in Chapter 4.

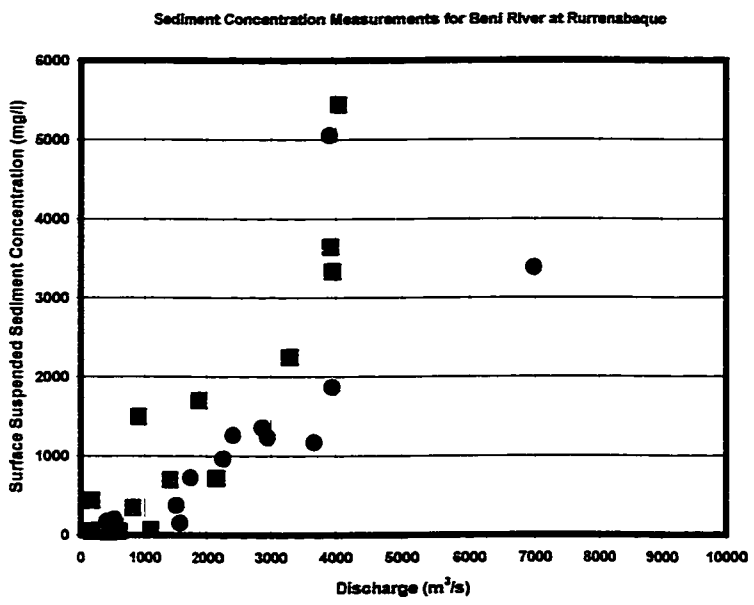

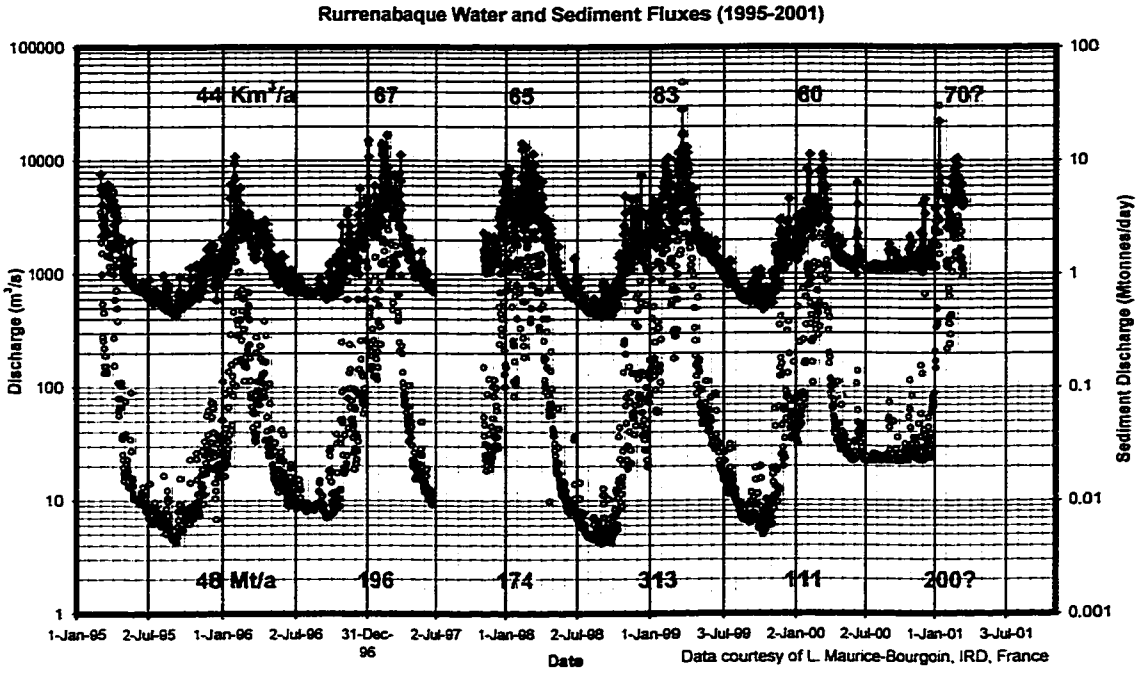

Figure 2.22. (a) Plot of surface suspended sediment concentration versus water discharge at the Rurrenabaque gauging station, data from Maurice-Bourgoin, 2001. Concentrations show a positive hysteresis, with higher values on the rising limb of the hydrograph. A two-stage rating curve is used for predicting sediment concentration as a function of water discharge. (b) Daily record of water (blue) and sediment (red) discharge at Rurrenabaque from 1995 to 2001, data and sediment flux calculations by Maurice-Bourgoin, 2001. The approximate annual fluxes for 2000 have been estimated.

Figure 2.23. (a) Predicted suspended sediment concentration profiles for 21 resolved particles sizes (listed in caption, in μm), as modeled (Aalto, 1995) from the surface concentration, depth, and slope measured during flood-stage at Rurrenabaque.

Predicted Rurrenabaque Sediment Concentration Profiles for all Size Classes

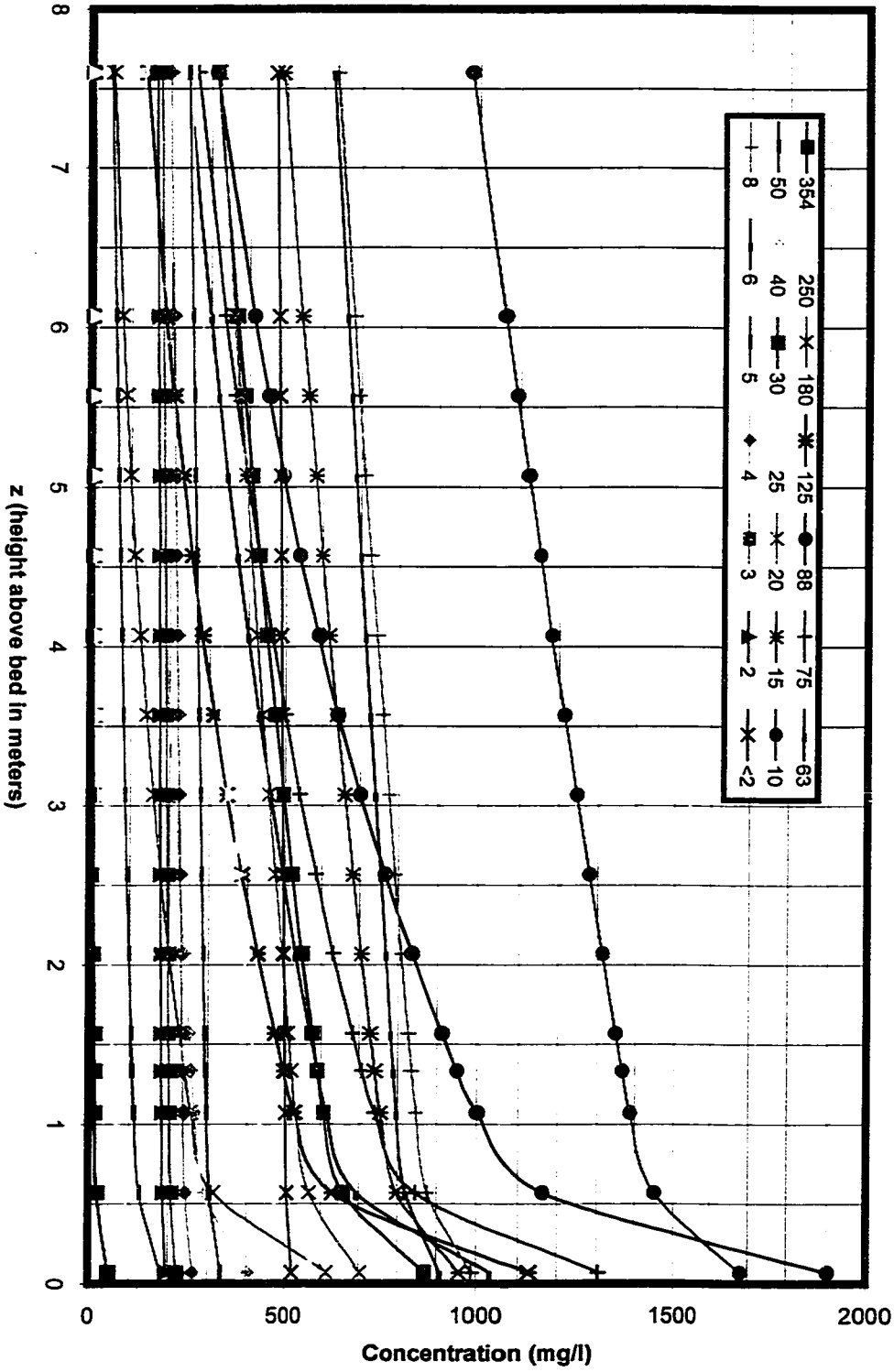

Figure 2.23. (b) Predicted concentration profile for all suspended sediment (blue line). Total incremental flux (per m^2 window) is also depicted for two conditions: 1) total sediment concentration is uniform with depth (green line), and 2) sediment concentration increases with depth (red line) as portrayed in the figure. Total depth-integrated flux per meter channel width is listed for each condition.

Predicted Rurrenabaque Total Sediment Concentration and Depth-Integrated Flux Profiles

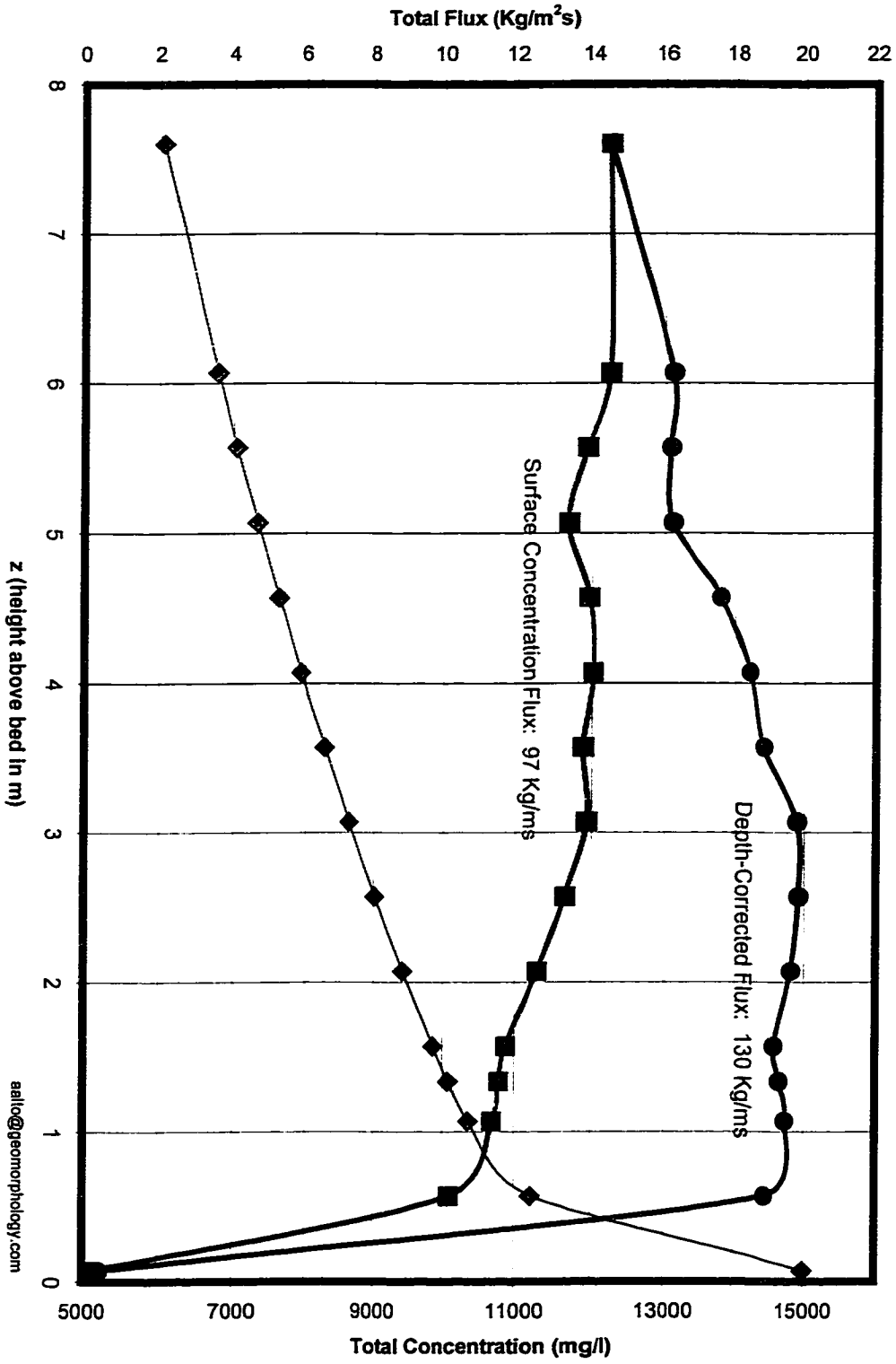

Figure 2.24. (a) Predicted suspended sediment concentration profiles for 21 resolved particles sizes (listed in caption, in μm), as modeled (Aalto, 1995) from the surface concentration measured at moderate stage at Riberalta, estimated depth, and the surveyed channel slope.

Predicted Riberalta Sediment Concentration Profiles for all Size Classes

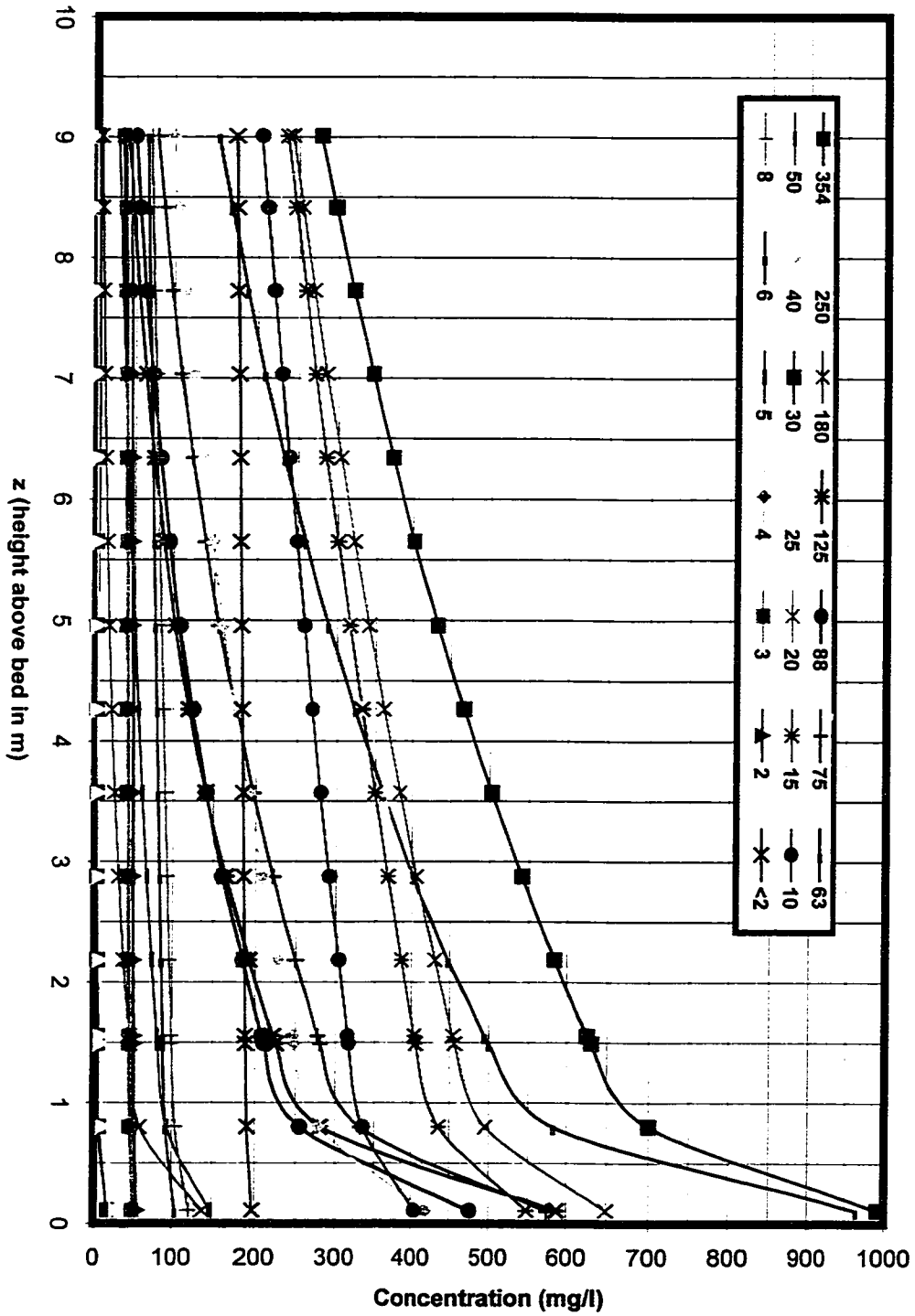

Figure 2.24. (b) Predicted concentration profile for all suspended sediment (blue line). Total incremental flux (per m^2 window) is also depicted for two conditions: 1) total sediment concentration is uniform with depth (green line), and 2) sediment concentration increases with depth (red line) as portrayed in the figure. Total depth-integrated flux per meter channel width is listed for each condition.

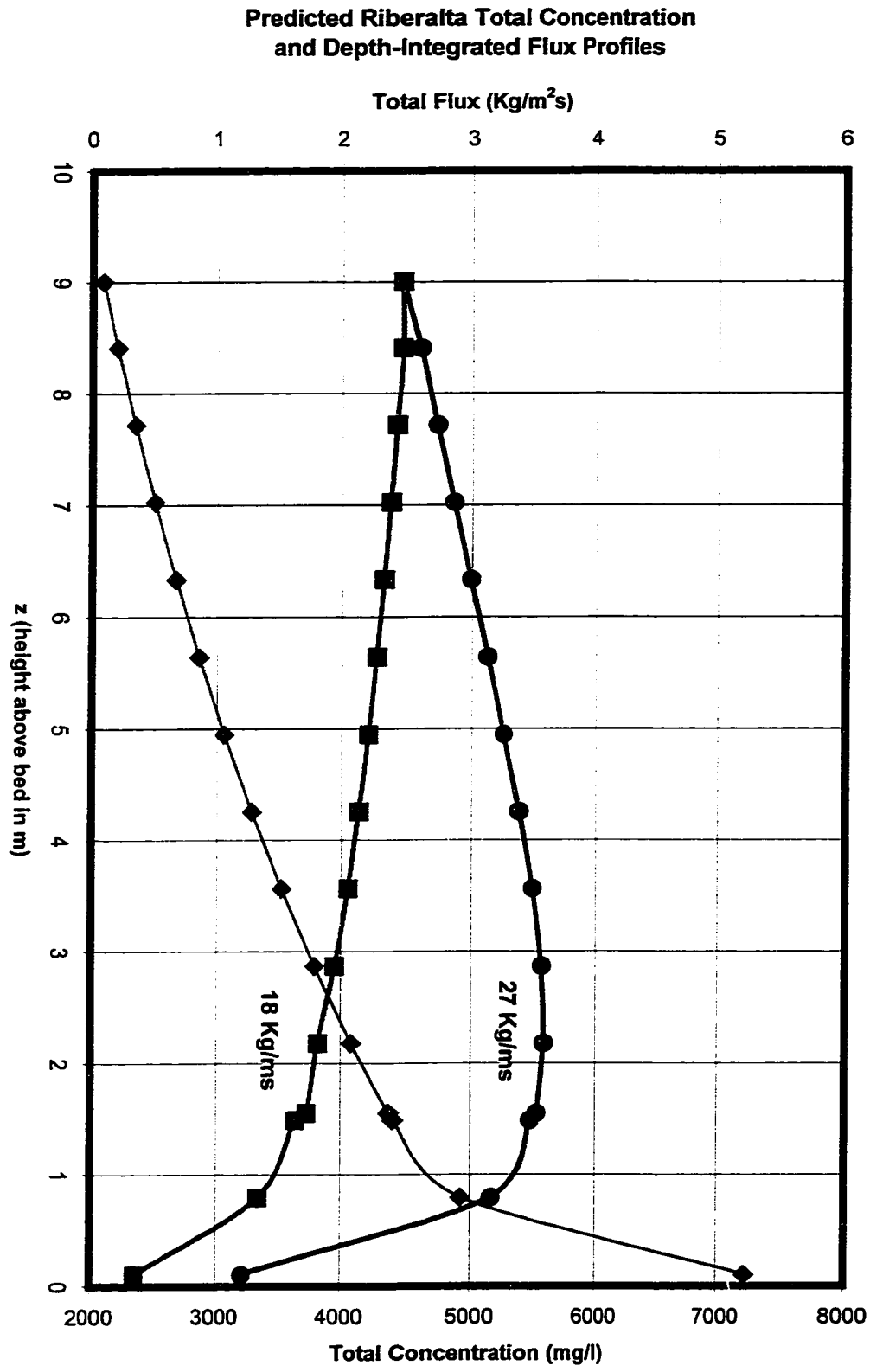
Predicted Riberalta Total Concentration
and Depth-Integrated Flux Profiles
Total Flux (Kg/m²s)
0
1
2
3
4
5
6
z (height above bed in m)
0
1
2
3
4
5
6
7
8
9
10
18 Kg/ms
27 Kg/ms
2000
3000
4000
5000
6000
7000
8000
Total Concentration (mg/l)

Chapter 3

Quantitative meso-scale fluvial geomorphology: theory and observations

Abstract

To study the natural mechanics of large sand-bedded rivers in a pristine condition, I investigated the interplay between sediment and water transport and active lateral migration of a dynamic, sinuous river in the northern Bolivian Llanos, the Beni River. A simple theoretical comparison of flow routing through both meandering and straight reaches suggests that the meandering reaches should exhibit deeper flow during flooding, interacting more with their floodplains by means of overbank flooding and lateral migration. Furthermore, for a given water and sediment discharge, for any floodplain with varying valley slope, the channel will adjust its sinuosity as necessary to maintain an constant energy slope to dissipate potential energy loss in a quasi-uniform fashion. To test the theoretical models, field observations of valley and channel slope and floodplain deposition are combined with five decades of planform channel morphology derived from Landsat and aerial imagery. The morphological characteristics measured were sinuosity, width, lateral migration rate, bar area, and valley and channel length, and were compiled on the spatial scale of 10-km UTM latitude increments (corresponding to 10–20-km valley lengths) and the temporal scale of 40 years.

The data suggest that in both static and dynamic cases, sinuous reaches are the same width and depth as straight ones (and probably even narrower and shallower), and they have high rates of lateral migration, which decline as their channels become more and more sinuous. As channels become more sinuous, the area of active points bars increases, emphasizing the importance of secondary flow and increased depth of flooding. Sparse data for floodplain deposition rates, as measured with ^{210}Pb geochronology, and cut-bank heights generally support the prediction that sinuous

reaches have higher rates of floodplain aggradation. Field surveys of channel and valley slope across the Bolivian foreland basin and the forebulge illustrate that river sinuosity and lateral migration rates are a strong function of valley slope: steeper valleys contain more sinuous channels with higher rates of lateral migration. The data provide evidence for negative feedback processes that maintain constant river slopes over decadal timescales: river reaches that are temporarily too straight tend to migrate rapidly and become more sinuous, whereas reaches that are too sinuous tend to form neck cutoffs and thereby reduce their sinuosity. Hence, the theoretical predictions of channel response to changes in sinuosity and valley slope are corroborated by a variety of field observations from a large river system, providing useful empirical and theoretical insights that may be applied elsewhere to other large rivers in a less pristine condition.

Introduction

Large, sinuous, actively-migrating rivers characterize lowland floodplains throughout the world. Extensive research has focused on the hydraulics of such rivers, especially in regard to re-engineering them to be straighter and more stable, with more controlled flows and less channel-floodplain interaction. However, only limited attention has been paid to the mechanics and morphology of large sand-bedded rivers in a pristine condition, especially those which traverse noteworthy foreland basins, interacting dynamically with their floodplains and depositing a significant fraction of their annual load within these tectonic structures. But sediment transport through and deposition in foreland basins are a first-order determinant of the sediment budgets of continental-scale rivers, dictating how much sediment passes from an active orogen to distal lowlands, estuaries, and marine depocenters far from the mountain range (Chapters 2 and 5).

Existing models for sediment transport within foreland basins represent the fluvial transport system with excess-shear-stress bedload routing schemes appropriate only for gravel-bedded rivers (Heller and Paola, 1992; Paola, 1989; Robinson, 1998), or

as simple power-law functions of slope or distance (Flemings and Jordan, 1989). Similarly, there exist numerous methods to route coarse bedload material through ideal 'flume-like' channels (e.g., Ackers and White, 1973; Bagnold, 1980; Meyer-Peter and Muller, 1948; Parker et al., 1982), and a smaller number of 'total load' transport functions (e.g., Bagnold, 1966; Einstein, 1950; Engelund and Hansen, 1972; Yang, 1972) that also estimate sediment discharge for sand-sized suspended load. However, such 'total load' schemes are actually total flux equations for material found in the bed and therefore do not predict 'wash load' flux, which consists of fine materials that are not found in significant abundance in the river bed. Since the instantaneous flux of 'wash load' depends mainly on the supply from the watershed and not on the river hydraulics, it is impossible to predict 'wash load' flux based on the site hydraulic geometry of a particular river cross-section (Yang, 1996). However, for most rivers, bedload flux represents only a few percent of total flux (Collins and Dunne, 1989; Reid and Dunne, 1996), and for larger sand-bedded rivers, essentially all of the bed material can be transported as suspended load (Dunne et al., 1998), meaning that total load flux calculations are primarily suspended sediment routing problems. Furthermore, in most large rivers, the finer 'wash load' accounts for the vast majority of the total solid flux (e.g., Meade et al., 1985). The failure of available models to account for this 'wash load' flux limits their application to the study of channel bed geometry and bed load transport, making them inappropriate for total mass flux modeling and the role of floodplains in sediment routing. Additionally, natural rivers are complex systems that actively meander, transfer sediment to and from the floodplain (Dunne et al., 1998; Chapter 2), change their longitudinal profiles in response to changes in storage and tectonic flexure (Adams, 1980; Schumm, 1986; Schumm and Khan, 1972), and otherwise do not behave like laboratory flumes. If we wish to study the total sediment flux transported by fluvial systems of appropriate scale for problems of continental mass-flux routing, a new, more realistic meso-scale approach of process-based analysis is needed for rivers.

Here, I propose a theoretical and conceptual foundation for such a meso-scale model for the geomorphic controls on fluvial mechanics and morphology: the theoretical framework is presented first, followed by extensive quantitative results from a combined GIS and field study of a large pristine river which I use to test and calibrate the model. This conceptual framework provides a context for parallel studies of all major sediment fluxes within the Beni Foreland (Chapter 2) and investigation of the timing, mechanism, and rates of floodplain accumulation (Chapter 5).

Meso-scale theoretical model

To study mass transport on a reach scale for a large river, it is important to focus attention on processes and relationships that are important in regulating channel mechanics and morphology at the meso-scale: the average state of the channel-floodplain system at the spatial scale of valley reaches 10 km or more in length and the temporal scale of 30–100+ years. Numerous flume and site-scale field studies of sediment transport (e.g., Dietrich, 1982; Einstein and Chien, 1954; Parker, 1990; Smith and McLean, 1977) provide important analytical insight into what key processes control sediment transport and deposition, but this perspective needs to be scaled to match the problem of sediment flux of all particle sizes in a large river on an effective reach scale of 10 - 50 km. To achieve these goals, the approach and tools must differ significantly from those of previous flume and site-scale studies. Although it is possible to model sediment transport on a site-scale using the familiar tools of diffusion, advection, and mass-flux balance, here I will outline an analytical framework within a meso-scale perspective that provides more scale-appropriate insight into to the problem.

I feel the term 'wash load' is misleading, because fine suspended material follows physical laws describing its vertical and horizontal distribution in a river (Aalto, 1995) and mechanics of overbank deposition (Dunne et al., 1998). The term is only appropriate for channelized sediment transport and is inappropriate for reach-scale transport involving significant exchange of flow and sediment between a channel and its

floodplain. Since 'wash load' does not passively wash though a fluvial system and because I can model its transport and storage in a process-based sense (Chapter 2), I will hereafter refer to this material as 'fine suspended load,' where the relative term 'fine' will still be defined in terms of the absence of these grain sizes in the bed material. Since I am studying continental-scale sediment production (Chapter 1) and transport, I can both measure and model the upstream influx of fine suspended load into a reach and use the derived reach-scale sediment fluxes (Chapter 2) to characterize the meso-scale mechanics of transport, migration exchange, and net accumulation.

The proposed meso-scale sediment transport perspective entails a fluvial reach of length L_v with valley slope (S_v), floodplain valley width (B_v), channel sinuousity (s), bankfull water discharge (Q_t), and bankfull channel width (B_c), as depicted in Figure 3.1a. The ratio of channel width (B_c) to valley width (B_v) is defined as β, channel length $L_c = sL_v$, and channel slope, $S_c = S_v/s$. Downstream, cross-stream, and vertical directions are defined as x, y, and z, and time is t. I define bankfull depth (H_c), velocity (U_c), discharge (Q_c), basal shear stress ($\tau_{ch} = \rho g H_c S_c$) and shear velocity ($U_{*c} = (gH_sS_c)^{1/2}$) for the channel. For the floodplain, I define the mean inundation depth (H_f), effective cross-valley width (B_f), down-valley velocity (U_f), discharge (Q_f), basal shear stress (τ_f), and shear velocity (U_{*f}), as depicted in Figure 3.1b. For all these preceding terms, a "0" added to the subscript denotes the end member case where s = 1 (ie. τ_{ch0} is the basal shear stress for a straight channel). Using this geometry and simple algebra, I calculate the ratio of channel edge to floodplain area,

$$\frac{2sL_v}{B_f L_v} = \frac{2sL_v}{B_v(1-s\beta)L_v} = \frac{2s}{(1-s\beta)B_v} \qquad (1)$$

dimensionless excess total water momentum (non-directional) for bankfull discharge (since $Q_c = Q_{c0}$),

$$\frac{\rho s L_v B_c H_c U_c}{\rho L_v B_{c0} H_{c0} U_{c0}} - 1 = (s-1) \qquad (2)$$

and dimensionless excess cross-valley channel width due to meandering:

$$\frac{s\beta B_v}{\beta B_v} - 1 = (s-1) \tag{3}$$

Using the observations that meander wavelength $\lambda \approx 11B_c$ and that mean meander path length $L_m \approx \lambda\pi/2$ (Leopold and Wolman, 1960) and approximating the length of the active scour pools along the outer limbs of two successive meanders as $\approx \lambda/3$ yields an "active meander edge" to floodplain area ratio of

$$\frac{sL_v / 3}{B_f L_v} = \frac{s}{3(1-s\beta)B_v} \tag{4}$$

Next, I use the Manning formula to calculate hydraulic relationships between the hypothetical straight channel (geometry with "0" subscripts) and the sinuous channel. This formula is widely calibrated for a broad range of rivers, and offers the additional advantage (unlike the Chezy or Darcy-Weisbach formulas) that for deeper flows ($H_c >$ 0.5m) the channel roughness coefficient "n_c" does not change substantially with channel depth or flow velocity (Chang, 1992; Wolman, 1955):

$$U_c = \frac{R^{2/3} S^{1/2}}{n_c} \quad \text{where R} \approx \text{H for wide channels} \tag{5}$$

For bankfull discharge $Q_c = Q_{c0}$, since bankfull discharge both defines the channel geometry and does not inundate the floodplain. The assertion that $B_c \approx B_{c0}$ follows from extensive field evidence that the water discharge is the primary control on bankfull channel width (e.g., Chang, 1992; Leopold and Maddock, 1953), which means that B_c can be plausibly derived for large, sand-bedded rivers as a power function of Q_c and perhaps mean bedload particle size (D_{50}) (e.g., Bray, 1982; Robinson, 1998). From the above comments, (5), and the relationship that $S_{c0} = S_v = sS_c$, I derive the following hydraulic relationships for the channel in a sinuous floodplain:

$$H_c = H_{c0} s^{3/10} \tag{6a}$$

$$U_c = U_{c0} s^{-3/10} \tag{6b}$$

$$\tau_{ch} = \tau_{ch0} s^{-3/10} \tag{6c}$$

$$U_{*_c} = U_{*_{c0}} s^{-3/20} \qquad (6d)$$

The sinuous channel is deeper, slower, and has less 'excess' (after the frictional loss of rounding bends on the longer path) kinetic energy available to entrain, suspend, and transport material than a straight channel with equivalent bankfull discharge. If n_c increases ~ 10% with sinuosity (Chow, 1959), H_c will show a corresponding increase.

I can extend this reasoning to overbank flow as well, using the geometry fixed in (6) by the bankfull flow and total channel depth ($H_c + H_f$). Assuming that for channel flow during flooding $Q_{cf} = Q_{cf0}$ yields the relationship that $H_f = H_{f0} s^{3/10}$, or that the sinuous channel floodplain is more deeply inundated than the straight channel. However, the assumption that $Q_{cf} = Q_{cf0}$ is in fact not likely to be true, as different amounts of discharge will flow overbank during floods for the straight and sinuous channels; in reflection, H_f is likely to be controlled by floodplain deposition processes which are more active in the sinuous river and therefore tend to build a higher floodplain, increasing bankfull height of the channel (this will be discussed in the next sub-section). Therefore, $H_f = \alpha H_{f0}$, where $0 << \alpha <= 1$. From (5) and (6),

$$Q_{cf} = \gamma Q_{cfo} \quad \text{where} \quad \gamma = \left(\frac{\alpha H_{f0} + H_{c0} s^{3/10}}{H_{f0} s^{3/10} + H_{c0} s^{3/10}} \right)^{5/3} \qquad (7)$$

For a valley with $H_{c0} = 3$m, $H_{f0} = 1$m, $\alpha = 0.8$, and $s = 3$, $\gamma = 0.8$, indicating that for the sinuous channel, 20% more discharge goes overbank than for the straight channel. In extreme cases, 40-50% additional discharge will flow overbank in the case of the sinuous channel, suggesting a substantial increase in the channel-floodplain interchange of sediment and water for the sinuous channel. (For this hypothetical example and the following case study of the Beni River, the influence of direct precipitation onto the floodplain, local 'clear-water' runoff, and other 'perirheic' processes (Mertes, 1997) is not considered to be important.) Since $Q_{tf} = Q_f + Q_{cf}$, equation (7) can also be rewritten as $Q_f = Q_{tf} - \gamma Q_{cfo}$, where Q_{tf} and Q_f are total flood discharge and total floodplain

discharge. This equation can be combined with (5) and (7) and solved to determine a value for floodplain roughness, n_f, which is otherwise difficult to measure in the field:

$$n_f = \frac{H_f^{5/3} B_v S_v^{1/2} (1 - s\beta)}{Q_{tf} - Q_{cf}} \qquad \text{where } Q_{cf} = \frac{H_c^{5/3} \beta B_v S_v}{n_c \sqrt{s}} \qquad (8)$$

Note that Q_{tf} can be determined both from upstream gauging stations, where the entire flow is within a confined channel, and from Muskingum-Cunge flood routing.

The mean thickness of floodplain deposition $H_{fd} = H_{cb} - H_{pb}$ (Figure 3.1b), where H_{cb} is the mean height of the cut bank above the channel bed and H_{pb} is the equivalent height for the freshly-deposited bedload on the point bar (this assumes that channel aggradation is insignificant in the short term, and a floodplain in steady-state). Combining this with the mean lateral migration rate, M, and the sediment porosity, ϕ, gives an equation for the approximate volume of finer floodplain sediment eroded per unit time and returned to the channel for downstream transport and redeposition:

$$Eroded\ Volume\ of\ Floodplain\ Material = \frac{s H_{fd} L_v M}{1 - \phi} \qquad (9)$$

The rate M is maximized for sinuous point bar rivers where $R_m/B_c \approx 3$ (Nanson and Hickin, 1983), where R_m is the average meander radius of curvature. In aggrading systems, reach sinuousity should be closely related to lateral migration rate, which in turn must be related to deposition rate (Dunne et al., 1998) through the flow-forcing mechanics of point bar deposition (Dietrich and Smith, 1983). Equation (9) has been combined with models or measurements of overbank deposition (Chapter 5) to construct the net mass balance for all sediment on a reach scale (Chapter 2).

There are several significant advantages to using this reach-scale perspective to formulate a conceptual model. First, key terms like s, β, and S_v, and B_v are much easier to measure as reach-scale averages than at individual field sites. Second, it is relatively straightforward to derive reach-scale geometry and processes from these terms – I have depicted a small set of practical physical relationships which can be later expanded to incorporate other geomorphic processes or to entertain other models or assumptions as

necessary. Third, this meso-scale framework is appropriate to the scale of the problem I am attempting to address.

As a separate meso-scale hypothesis, I conjecture that the numerous processes and equations for suspended sediment and wash load transport and deposition (e.g., Einstein, 1950; James, 1985; Nicholas and Walling, 1997; Yang, 1972) may be approximated to a first order by a simple power law transport model (inspired by Lane, 1955) for fluvial systems of the approximate form

$$Q_s = \frac{k_{qs}\psi Q_t^a}{D_{50}^c}\left(\frac{S_v}{s}\right)^b \qquad (10)$$

where k_{qs}, k_ψ, and a - f are positive empirical constants, D_{50} is mean particle diameter, Q_s is total sediment flux, Q_t is total water discharge (which can in turn be approximated as a power function of contributing area (Leopold and Maddock, 1953)), and a coefficient ψ which can either be assumed to be unity or cast separately as a hypothetical function of channel morphology:

$$\psi = \frac{k_\psi M^d \beta^e}{s^f} \qquad (11)$$

These equations can also be normalized to B_v so as to express (10) in terms of net transport efficiency for a fluvial valley system per unit width, thereby facilitating the practical application of (10) to a wide variety of valley systems outside the present study of a large foreland basin. For example, (10) implies that for constant sinuosity, Q_s should decrease and sedimentation rates should accordingly increase at concave inflections in valley slope (Lane, 1955), a relationship that can be explored in the field. If, however, the system is 'at grade' where Q_s is roughly constant along the valley (Mackin, 1948), sinuousity (s) should vary directly with valley slope (S_v) and discharge (Q), and vary inversely with D_{50}.

These simple models provide a meso-scale conceptual framework which can be explored using an extensive dataset of topographic field surveys and channel morphology derived from GIS analysis of river images taken over the past four decades.

Study Area

The Bolivian Llanos (Figure 3.2) is an excellent locale to study active river-floodplain systems and meso-scale fluvial mechanics and morphology within foreland basins. The water and sediment fluxes, channel-floodplain interchanges, and net sediment sinks are all enormous (not subtle or hard to discern) and well-recorded for many stations throughout the basin (Guyot, 1993; Maurice-Bourgoin, 2001), facilitating geomorphic interpretation, flux measurement, and calculation of differences in mass flux. The tectonic setting is relatively simple and well understood (Jordan, 1995; for a review of adjacent Andean tectonics see Beck et al., 1996; and Masek et al., 1994) – a good example of a large, overfilled retroarc foreland basin with substantial basement depression (2 - 7 Km). Modern basin architecture is the result of continuous, eastward migration of the coupled orogenic wedge and foreland basin system since the Late Cretaceous-Paleocene, and consists of a continuous system of wedge-top, foredeep, forebulge, and back-bulge depozones (Horton and DeCelles, 1997). Most importantly for this study, the Beni basin is essentially pristine, without artificial levees, dams, roads, significant deforestation or cultivation (no mixing of the floodplain to affect the geochronology), or other anthropogenic complications detracting from the study of natural floodplain and fluvial processes.

This study focuses on the reach of river between Rurrenabaque and Riberalta, Bolivia (Figure 3.2, pocket material), which traverses the entire foredeep, forebulge, and secondary back-bulge basin. At Rurrenabaque, the Beni has a drainage area of 68,000 km^2 and a mean annual discharge of 2,200 m^3/s (Guyot, 1993), with recorded flood discharges of > 20,000 m^3/s and regularly in excess of 15,000 m^3/s (Maurice-Bourgoin, 2001). From an elevation of 190 m (above mean sea level) at Rurrenabaque, the Beni flows along ~ 800 km of channel as it crosses its foreland basin and descends to about 120 m elevation at Riberalta, where it has a total basin area of 119,000 km^2. This reach is remarkable in that there is only one major tributary, the Madidi River, along its entire

course. Thus, the many observed changes in river and floodplain morphology and mechanics are primarily due to transport mechanics and neotectonics, not major tributary effects (e.g., sudden increases in water and/or sediment discharge – rather, the Beni gradually increases its water discharge from the cumulative influence of a dozens of minor "blackwater" floodplain tributaries), which transport essentially no sediment.

Numerous survey transects along with sediment cores have been collected on the Beni floodplain, as well as system-wide surveys of topography and granulometry (Chapter 2). These data have been used to quantify rates of sediment exchange between the channel and floodplain, and net sediment deposition within the Beni foreland (Chapters 2 and 5). In this analysis, I present a brief summary of the study methods and focus primarily on the planform morphology, channel slope, and channel-floodplain geometry across the Beni Foredeep. This investigation explores fundamental morphometric relationships and the implied meso-scale geomorphic controls on channel morphology and sediment transport.

Field and GIS methods

The principal sampling excursion occurred during August and September of 1999, the lower Beni upstream of Riberalta was surveyed in September of 2000, and additional samples at Rurrenabaque and Riberalta were collected during a rainy season campaign in February, 2001. Water surface elevations, bar and floodplain locations and topography, and boat locations on cross-channel transects were all recorded with a Trimble Pathfinder ProXRS DGPS system and complemented with a survey-grade laser rangefinder or a stadia rod and eye-level for local measurements. Sediment grab samples and floodplain cores were collected across the channel in standardized locations, both in the river and on the floodplain, as described further in Chapters 2 and 5.

Satellite images for the entire study area were obtained for 1999 (Landsat – ETM), 1996 (JERS-1), 1993 (Landsat —TM), 1986 (Landsat – TM), and 1975 (LANDSAT – MSS). Aerial photographs of the Beni River were acquired for 1994

(DMA, 1995) and 1960 (Naval, 1960). Landsat TM has a pixel size of 30 m (ETM+ also has a 15 m panchromatic band), whereas MSS and JERS-1 are of a coarser 90-m resolution. The 1999 ETM+ image was acquired in July, within a month of the main sampling campaign on the Beni. Landsat ETM+ images are georeferenced: my DGPS field surveys of the channel generally agree with the 1999 image to 30 meters or better, with only a few locations off by ~ 100 m. As such, the 1999 ETM+ images were used as *de facto* basemaps to which all other images were georeferenced. The "rubber-sheeting" procedure was to search an older image and a more recent georeferenced image to find 8-12 common locations, such as small, stable floodplain tributaries, distant oxbow lakes with no apparent infilling, and identifiable anthropogenic features. These control points would then enclose a common channel reach, which was then warped to match the georeferenced image using a cubic-convolution routine in ERDAS Imagine. In the case that the resulting transformation exhibited a high RMS error, the control points would be reviewed so as to identify and correct the digitizing error. Once all the images were transformed into a common coordinate system, I next digitized the location of the channel, bars, and lakes.

For the 1999, 1993, 1986, 1975, and 1960 images, the vector locations were digitized for the edge of the vegetation (right and left banks), for the unvegetated point bars and mid-channel bars, and for the perimeter of two dozen oxbow lakes, entering the results into a GIS (geographic information system) model for the Beni River. Because vegetation, sand, and water all have very distinct spectral signatures, it was straightforward to recognize and delineate these features. On the lowland rainforest floodplain, vegetation is verdant and growth rapid, such that migrating meander complexes exhibit rapid colonization of their depositional point bars by numerous plant species. Only the outer portions of point bars are unvegetated – their lower topographic elevation and proximity to the rapid flow of the main channel probably afford sufficient scour during flooding to suppress vegetation by removing and redepositing sediment so as to preclude vegetation. Except for outer point bars and a few rare mid-channel bars,

the rainforest extends to the very edges of the low-water main channel and, similarly, to the edges of all floodplain tributaries and lakes. These vector data are plotted on the 1999 ETM+ base maps for the Beni River: examples are shown in Figures 3.3 (a-c), with additional site maps presented in Appendix A, and plotted for the entire channel in the three large maps (pocket material).

For the GIS analysis, the Beni river was divided into 10-km reaches of UTML (universal transverse mercator projection latitude). Because the Beni flows approximately due north across the foreland basin, this is a convenient means to subdivide the river in ARC/INFO and to plot results. All results were corrected for the actual river and valley lengths within each 10 km UTML interval. Because the sinuous river sometimes flows southwards out of a reach, only to reenter it farther downstream, the river was considered to have entered a new 10 km UTML reach the first time its right bank intersected that reach. Dynamic channels sometimes presented long-term complications to this rule, and in all cases were categorized for the greatest spatial and temporal consistency.

For each time increment for each reach, total channel bank length (left and right) was quantified, along with channel area and bar area. Valley length was determined as the distance between the mean entry and exit points of the right channel bank from a UTML reach for all images. Next, right bank locations between successive image years were intersected, defining a series of arcuate polygons. These polygons were classified as erosional or depositional, depending on whether they represented cut banks or point bars (because bar area varies greatly with river stage, for this exercise all unvegetated bars were considered part of the channel). The same procedure was completed for the left channel bank, providing a total eroded and deposited area for each reach during the time increment between images. Images depicting a channel neck cutoff required an area adjustment associated with the formed oxbow lake, so that this area is not improperly ascribed to channel migration. Dividing these swept areas by the average channel length and the associated time gives an estimate of the annual distance of lateral erosion and

deposition due to channel migration within each reach. When erosion is greater than deposition, the channel grows in length and/or the bars grow in area. Here, I report the mean (averaged from 1960 – 1999) channel reach sinuousity, width, length, and the lateral erosion rate due to channel migration, and then explore the static and dynamic relationships between channel migration and morphology, and other details of planform channel morphology.

Down-channel Beni River morphology

Figure 3.4 depicts average channel sinuosity across the foreland basin (refer to Figures 3.2 and 3.10), along with river valley length per 10 km UTML increment. The river shows low sinuosity through the gravel-bedded reaches and across the wedge-top basin, becoming notably more sinuous after 8,450 km UTML. Sinuosity declines gradually across the foredeep, and then drops at the forebulge, with the channel nearly straight until 8,700 km UTML. Sinuosity climbs again in the secondary back-bulge basin, although there are also some straighter reaches. These data provide measurements of total channel and valley length per 10 km UTML interval.

Narrow through the canyons at the sub-Andean range front, average channel width (Figure 3.5) declines steadily from 400 m to 300 m across the foreland basin to the forebulge at 8,600 km UTML, where it increases to 400 m downstream of the confluence with the Madidi River. Across the forebulge, channel width increases gradually to 450 m at 8,690 km UTML, near the proposed start of the back-bulge basin. There are zones of width instability near 8,430 km UTML and from 8,560 – 8,590 km UTML, consisting of reaches of rapid change in channel slope and channel instability and corresponding to "physio-tectonic" features discussed later. For this plot, "wetted channel width" is determined for any specific image by dividing the digitized water surface area during low river stage by the associated channel length. Because point bars (and the occasional mid-channel bar) are often low and relatively flat, small changes in river stage can lead to large perceived changes in channel area. This phenomenon is important for the GIS

analysis presented here, because the channel+bar width is the more consistent and functional measurement; the correlation of various morphometric interrelationships improves substantially when the measured channel area and width includes the bars. More importantly, my survey transects across the channel and floodplain found a substantial topographic rise at the edge of the vegetation (Chapter 2), so the channel+bar width corresponds to the bankfull width. Because such a classification of bankfull width has a well-defined physical meaning, corresponding to the term (B_c) used in the meso-scale model, and results in better statistical relationships, it is hereafter implied in all discussions of channel width. A plot of total bar area (Figure 3.6) illustrates the expected trend that 10 km UTML reaches with more sinuous channels and/or greater total valley length tend to contain a greater area of bars.

The average 10 km UTML lateral migration velocity is presented in Figure 3.7. This parameter, derived by using the previously-discussed GIS determination of eroded bank area per unit time, provides a 40-year estimate of the rate of channel migration across the floodplain. Measured rates are highest downstream of the gravel-sand transition, near 8,450 km UTML, and decline steadily across the foredeep. Migration is slow across the forebulge and the secondary basin, with notable local exceptions at 8,610 and 8,680 km UTML, probably associated with the sudden changes in channel slope near the boundaries of these features (Figure 3.11). These average channel migration rates are used to determine the average annual erosion of cutbank material and deposition of point bar sediment associated with channel movement (Chapter 2).

A high-resolution dataset for channel depths was surveyed for the entire Beni River in 1969, at a low stage similar to that observed in 1999 (Semena, 1969). Because the 1999 channel depth survey is limited to only a few dozen cross sections, it was better to average the 750 recorded depths for 1969 (Figures 3.8 and 3.9). Except for some regions of minor shoaling (e.g., around 8,440 km UTML), curved channel depths average around 5.5 m along the upper Beni, increasing to ~ 6.5 m downstream of 8,600 km UTML.

The heights above the low-stage water surface were measured for cut banks and bars along the Beni River (Chapter 2). Bar heights were categorized as unvegetated bar tops and the vegetated bar floodplain (typically covered with young, 2–4-m tall vegetation). For the running averages (Figure 3.9), cut bank heights are generally higher than vegetated bar heights, with a gradual downstream increase in both heights towards ~ 8,590 km UTML, where a sudden increase is realized coincident with the appearance of terraces (these high cliffs are weathered a notable shade of red, are composed of cemented silt, and are not inundated by river floodwaters).

The elevation of the water surface was surveyed across the entire basin (Chapter 2). The resulting plot of low stage water surface elevation versus UTML (Figure 3.10) exhibits several distinctly different reaches of channel. The gravel-bedded portion of the Beni has a mean river valley slope of approximately 6×10^{-4} m/m, with the mountainous reaches somewhat steeper than those downstream of Rurrenabaque (Figure 3.11). After a short low-gradient reach near 8,450 km UTML, valley slope declines from 2×10^{-4} m/m to 1.2×10^{-4} m/m, before suddenly increasing and decreasing around 8,600 km UTML. At 8,620 km UTML, valley slope declines dramatically to $< 4 \times 10^{-5}$ m/m until 8,700 UTML, where it increases again to $\sim 2.5 \times 10^{-4}$ m/m, declining to 5×10^{-5} as it crosses the secondary basin. In Figure 3.10, I have marked these reaches according to my proposed tectonic associations to the wedge-top, foreland, forebulge, and back-bulge secondary basins. The most remarkable result in Figure 3.11 is that the surveyed water surface slope for the river is virtually constant across the entire Beni Foredeep; the average 10 km UTML reach sinuosity is closely matched to variations in valley slope such as to maintain a constant river slope for each physio-tectonic region: sub-Andean gravel-bedded (data not shown), foredeep, forebulge, and back-bulge. At the transitions between each region, river slope (and valley slope) exhibits a sharp increase for a limited UTML distance of ~ 30 km (a convexity in the longitudinal channel profile). Such slope increases would imply associated intensifications of river stream power, possibly in response to tectonic uplift at the sub-Andean range front and forebulge. Further analysis

and discussion concerning the interplay between the fluvial geomorphology and foreland neotectonics will be discussed elsewhere. Here, I will explore the fundamental static and dynamic interrelationships between slope, sinuosity, and channel morphology.

Static morphometric relationships for the Beni River

The down-channel UTML planform morphology and surveyed topography portrayed in the preceding section facilitate a number of comparisons between channel morphology, sinuosity, and slope. Unlike the previous figures, which generally presented GIS values averaged over the four decades of record, the following data are measured at discrete dates from each available image.

First, to test the internal consistency of the GIS analysis, I plot normalized channel area against sinuosity (Figure 3.12a), depicting the expected one-to-one correspondence. Next, a plot of normalized bar area versus sinuosity (Figure 3.12b) illustrates the result that sinuous channels have relatively more bar area than straight ones, although the plot is noisy because of the variations in river stage and resulting bar inundation between channel images. To examine the relationship between bankfull channel width and sinuosity, I plotted these data for the entire Beni Foreland (Figure 3.13a) and a subset restricted to the Beni Foredeep (Figure 3.13b). In both cases, width decreases from ~ 500 m to ~ 350 m as the channel sinuousity increases from 1 to 4. The change in bankfull width is not associated with a change in unvegetated bar area (Figure 3.13c). This implies that sinuous channel reaches are narrower than straight reaches, a relationship relevant to the proposed meso-scale conceptual framework. The foredeep subset provides critical geomorphic insight, because it represents the Beni River in a dynamic river-slope equilibrium as it crosses a single physio-tectonic region, without any major tributaries or tectonic perturbations.

Figures 3.14a and 3.14b plot channel depth against sinuosity, both for the entire foreland basin and for the foredeep subset. Depth shows no correlation to sinuosity, implying that sinuous reaches are neither deeper nor shallower than straight ones – this

also has implications for the proposed meso-scale theory. Cutbank height shows no obvious relationship to sinuosity (Figure 3.15), especially when the data are separated for the foredeep. Finally, within the Beni Foredeep, river sinuosity shows a very strong correlation to valley slope (Figure 3.16), a result expected from the relatively constant river slope depicted in Figure 3.11. These slope data support the previously stated meso-scale hypothesis that, within tectonic limits, large sand-bedded rivers dynamically adjust their average sinuosity to maintain a uniform energy slope despite changes in valley slope.

Dynamic morphometric relationships for the Beni River

The preceding relationships are for morphologic comparisons of static river channels, that is, data "snapshots" taken at specific dates from an aerial image or field campaign. Because there are a series of such snapshots, it is possible to quantify morphometric changes between dates and to thereby investigate the geomorphic relationships associated with dynamic channel change. It is important to point out that these changes are for successive image increments for each specific reach, so the observed relationships are real site-scale geomorphic responses, not general down-channel channel changes across the entire Beni Foreland (e.g., regional-scale morphologic changes due to tectonics, tributaries, or changes in granulometry).

As before, to test the internal consistency of the GIS analysis, I plot the normalized change in channel area against change in sinuosity (Figure 3.17a), depicting the expected excellent correspondence (because there are significant width changes and minor GIS errors associated with different channel sinuosities and different areas digitized on different images, this relationship is not perfect like in Figure 3.12a). Comparing changes in bar area to changes in sinuosity for the Beni Foreland, Figure 3.17b depicts a dynamic version of the previous observation (Figure 3.12b) that river reaches generally gain more relative bar area as they become more sinuous. For the change-in-width versus change-in-sinuosity relationship, Figure 3.18 illustrates that river

channels tend to decrease in width as they increase in sinuosity, and vice versa. These results support the previous static relationships depicted in Figures 3.13a and 3.13b.

These preceding results are best understood within the context of dynamic channel response to sinuosity and valley slope. For the Beni Foredeep where the river is maintaining a constant slope, Figures 3.19 and 3.20 illustrate that channels that are unusually straight (due to a temporary perturbation) tend to migrate more rapidly than more sinuous channels, such as to increase their sinuosity until a value of ~ 2.5, where the net average change in sinuosity becomes negative (i.e., the river is in the process of straightening). After that point, migration rates continue to decline with increasing sinuousity, but the average absolute change in sinuosity continues to increase, indicating greater morphologic instability. This indicates the increased likelihood of oxbow cutoffs at ever higher sinuosities, as reflected in the increasingly negative values for the net average change in sinuosity in Figure 3.20. Conceptually, if the river is "too straight" (e.g., the water surface slope is relatively steep), it responds by cutting its banks and migrating more rapidly, thereby increasing its sinuosity. As the river approaches a sinuosity of about 2.5, these migration rates decline substantially, and the slower channel migration becomes increasingly likely to reduce sinuosity rather than to increase it.

To investigate how such dynamic behavior relates to valley slope, I plot average migration velocity (four decade averages) versus valley slope across the entire Beni Foreland (Figure 3.21). Ignoring a few outliers in distinctive tectonic locations, the observed relationship provides compelling evidence that the rate of channel migration increases directly with local valley slope. Combined with the previous plots and Figure 3.16, this implies that the Beni River responds to along-channel increases in valley slope by becoming progressively more sinuous and migrating more rapidly, both responses that have strong implications for the meso-scale conceptual model. These results therefore provide a clear insight into how the Beni river dynamically responds to perturbations and maintains an average constant river slope in the face of varying valley slopes. Although a few previous researchers have demonstrated the effects of tectonics on the longitudinal

profiles and morphology of large rivers (Adams, 1980; Burnett and Schumm, 1983), this is the first study for a river to 1) present evidence that sinuosity is precisely adjusted to maintain a uniform river slope, and 2) provide data supporting the requisite negative feedback mechanisms to both positive and negative perturbations necessary to return reach sinuosity to a certain value.

Implication of results for the meso-scale model

I have presented results for the Beni Foreland that support the general hypothesis of a large sand-bedded river which dynamically adjusts to tectonic perturbations in valley slope, maintaining an optimum average sinuosity and river slope. Across the foreland, there is persuasive evidence that these average values are adjusted to the local tectonics on a 10 km UTML reach scale. Furthermore, Figures 3.18 – 3.21 present quantitative evidence for the explicit mechanistic responses of individual river reaches to perturbations away from optimal river slope and sinuosity, providing the necessary geomorphic negative feedback to return the channel to well-adjusted conditions. Note that the Beni is not "at grade" in the traditional sense of constant sediment transport (Mackin, 1948), because the river deposits enormous quantities of sediment as it crosses its foredeep (Chapter 2).

Such results present a cogent argument for the utility of a meso-scale conceptual model for sand-bedded rivers. For the Beni Foreland, traditional site-scale models would perceive an incomprehensible heterogeneity of channel geometries, migration rates, sinuosities, and slopes, with many dynamic 1 – 5 km river reaches far removed from any obvious equilibrium state. However, at the scale of 10 km UTML reaches (15 – 40 km of channel length) considered over a timescale of four decades, the system is homogeneous and predictable, following well-defined mechanisms to regulate its slope. Therefore, such a meso-scale spatial and temporal conceptual framework is inherently the best means to interpret the quantitative geomorphology of such large, sand-bedded rivers.

As an example, I have previously predicted that more sinuous river reaches would inundate their floodplains more deeply during floods (equation 7), assuming that certain features are held constant. The GIS analysis provides evidence that sinuous channels are about the same average depth as straight ones, and that they are likely to be narrower. As such, the underlying assumptions for equation 7 are apparently justified by the GIS measurements. Figure 3.15 shows no evidence for an increase in bank height with increasing sinuosity, so (7) implies that floodplains adjacent to sinuous reaches must be subjected to deeper inundation during flooding, and accordingly, exhibit a higher floodplain accumulation rate.

In Chapters 5 and 2, I have measured and modeled floodplain deposition rates, and have produced a subset of nine dated sedimentation intervals sampled adjacent to straight sections of channel within the Beni Foredeep (cores from sites 3 and 51, Table 3.1, as modified from Chapter 5). Comparing deposition rates between straight and sinuous channels, I observe that the minimum mean floodplain sedimentation rate for straight reaches is 0.73 cm/yr, as compared to an average of 3.61 cm/yr for all floodplain locations throughout that part of the upper Beni Foredeep (note that most sampling locations are at or near meander apexes, so the average value reflects sedimentation rates near meanders). While more floodplain cores would help to establish whether these differences are significant, the available evidence supports the concept of lower sedimentation rates along straight channel reaches, as predicted by the theoretical conceptual model expressed in Equation 7.

The meso-scale concepts expressed here can easily be expanded to incorporate the specific mechanics of crevasse splay deposition, which is thought to dominate floodplain sedimentation across the Beni Foreland (Chapters 5 and 2). Crevasse splays form when the stream power of discharge over a natural levee into the distal floodplain is sufficient to incise a splay breach into the densely-vegetated levee. Such levee breaches would preferentially occur when the water height during flooding is significantly higher than the top of the natural levee, because for a given slope away from the channel into

the distal floodplain, the basal shear stress and total discharge (per unit levee width) of the flow will be higher. Comparison of channelized flow in a sinuous reach versus a straight reach (7) suggests that sinuous channels tend to inundate to a higher elevation during floods, thereby promoting such levee scour. Also, in sinuous reaches, lateral cutbank erosion is primarily focused on the outer limbs of river meanders (in contrast to the straight connections between successive meanders), rapidly cutting away at the natural levees along these meander edges and thereby limiting their vertical growth. Therefore, the outer meander limbs in sinuous reaches would tend to exhibit lower levee elevation in comparison to the floodplain surfaces adjacent to straight stable channel segments (which have typically had many decades to build high levees proximal to the channel). Finally, during flooding the rapid flow of water around a meander will generate strong outward centrifugal forces near the apex, further elevating the water surface such as to augment discharge out of the channel and across the levee at this location. Combined, these three complementary processes could act in concert to promote the formation of levee breaches and splay deposits near the outer apexes of river meanders in anomalously sinuous channel reaches. The frequency-integrated depth of such floodplain sedimentation events might reasonably be modeled as the stochastic interplay between major cold-phase ENSO floods (Chapter 5), short-term differences in distal floodplain and channel bed aggradation rates (Chapter 2), channel-proximal levee growth (Chapter 5), and the recurrence interval for positive perturbations away from the slope-optimal average reach sinuosity viewed within the perspective of a meso-scale quantitative model for fluvial geomorphology.

Summary

I have presented a conceptual framework for interpreting processes within sand-bedded rivers, supplemented with a field and GIS dataset of substantial spatial and temporal extent. The proposed meso-scale perspective offers a number of useful quantitative insights into the fluvial geomorphology of a large sand-bedded river:

(1) The Beni River maintains a uniform water slope within three separate physio-tectonic zones: the foredeep, forebulge, and back-bulge. In particular, the river slope across the Beni Foredeep is remarkably uniform, despite regular variations in local valley slope. The Beni evidently achieves this regularity across the foredeep by maintaining an average sinuosity for each reach adjusted to compensate for the effects of valley slope.

(2) Any given river reach within the foredeep may be in a temporary state of perturbation from average conditions, providing a site-scale view of a dynamic, heterogeneous system. In contrast, a meso-scale temporal and spatial perspective will exemplify the well-adjusted fluvial geomorphology, underscoring the utility of such an approach.

(3) Perturbations away from an optimal sinuosity beget negative feedback processes to restore the channel to its average state. If a channel is temporarily straightened by a cut off, it migrates more quickly, cutting its banks and becoming more sinuous. If a channel has become more sinuous than its long-term average, migration rates slow and further migration is increasingly likely to result in natural cut-offs and an associated reduction in sinuosity.

(4) In general across the Beni Foreland, valleys with steeper gradients contain channels which on average are both more sinuous and migrate more rapidly. Therefore, variations in both the static and dynamic meandering behavior of rivers can indicate fundamental changes in valley slope.

(5) The meso-scale conceptual model can be developed to make quantitative predictions regarding reach-scale process geomorphology. For example, I have demonstrated that a sinuous channel would flood more deeply than a straight one, a process that would be expected to result in increased rates of floodplain sedimentation. Available field measurements in straight reaches and at meander apexes support this concept.

Table 3.1. Summary of results from all dated cores, including sample depths, associated dates, and corresponding GIS channel distances. Minimum accumulation rates are determined by dividing the representative thickness of the deepest sample by its age (see Chapter 5 for details). Average rates are reported for various spatial subsets, with a highlighted subset for this Chapter (in red) of distal sites (< 100 m from river) adjoining straight reaches of channel within the Beni Foredeep.

Site	Site Name	deepest sample (cm)	partial depth (when not entire core) (cm)	CIRCAUS Date of Deposition	Corresponding GIS Channel Distance (m)	CS rate (cm/a)	Accumulation Rate (cm/ yr, minimum, all)	Bounded Accumulation Rate (cm/yr)
41	41RFC200	115		49	200		2.25	
	41RFC300	43		70	500		1.43	
	41RFC450	49		76	350		2.04	
	41RFC523	50		70	250		1.67	
60	60LFB5	52		98	5		26.00	
	60RFC5	56		98	150		28.00	
	60RFC50	25		88	700		2.08	
	60RFC100	48		88	750		4.00	
	60RFC150	50		72	2000		1.79	
a	60RFC200		15	74	2000		0.58	0.58
b	60RFC200	25		47	2800		0.19	
a	60RFC250		80	74	2000		3.08	3.08
b	60RFC250	120		49	2900		0.78	
	60RFC300		40	82	1300		2.22	2.22
61a	61RFC100		30	89	620		2.73	2.73
b	61RFC100	52		50	2400		0.44	
	61RFC200	53		77	1650		2.30	
62a	62RFC5		30	87	160		2.31	2.31
b	62RFC5	49		83	325		1.12	
	62RFC50	43		83	210		2.53	
	62RFC100	53		73	900		1.96	
	62RFC150	48		50	1500		0.96	
a	62RFC200		40	75	1000		1.60	1.60
b	62RFC200	59		50	1600		0.38	
63	63RFC5	53		77	1700		2.30	
	63RFC100	62		70	1800		2.07	
a	63RFC200		35	97	300		11.67	11.67
b	63RFC200	53		88	675		1.50	
64	64RFC5	33		90	260		3.30	
	64RFC50	43		73	480		1.59	
	64RFC100		37	82	575		2.06	2.06
	64RFC150	42		72	550		0.18	
	64RFC200	43		77	480		1.87	
59	59RFC50	48		55	50		1.07	
cb2	CB2 - 1998	156		87	300		12.00	
57	57RFC50	43		73	150		1.59	
cb1	CB1 - 1998	165			250	1.9	1.90	1.90
56	56RFC50	43		74	2500		1.65	
55	55LTC50	63		98	50		31.50	
54	54LFC50	53		97	225		17.67	
51	51RFC50	43		88	50		3.58	

Table 3.1. (continued)

a	51LFC5		40	84	5		2.50	2.50
a	51LFC50		44	84	50		2.75	2.75
b	51LFC50	53		74	50		0.35	
	51LFC100	53		73	100		1.96	
a	51LFC200		30	56	200		0.68	0.68
b	51LFC200	46		17	200		0.19	
a	51LFC300		25	55	300		0.56	0.56
b	51LFC300	53		43	300		0.49	
50	50RFC5	35		76	925		1.46	
	50RFC50	118			250	1.15	1.15	1.15
	50RFC50	118		49	800		2.31	
1	1LFC50	52		83	750		3.06	
2	2RFC50	53		74	225		2.04	
3	3A-1200M	50		54	1200		1.09	
	3B-1150M	43		55	1150		0.96	
a	3D-900M		23	49	900		0.45	0.45
b	3D-900M	43		14	1000		0.23	
	3E-20M	30		48	20		0.58	
a	6LVB5		40	83	2500		2.35	2.35
b	6LVB5	65		49	2000		0.49	
	6RVC5	54		82	2500		3.00	
7	7RFC50	58		88	400		4.83	
8	8RFC400	50		49	400		0.98	
9	9RFC50	53		75	400		2.12	
a	10LFC50		35	88	550		2.92	2.92
b	10LFC50	53		48	1000		0.35	
11	11LFC50	27		56	2000		0.61	
a	11LFC100		50	83	750		2.94	2.94
b	11LFC100	57		48	2000		0.13	
	11LFC150	63		88	675		5.25	
	11LFC200	53		88	725		4.42	
	11LFC250	53		87	775		4.08	
a	11LFC300		53	89	825		4.82	4.82
b	11LFC300	60		54	2200		0.15	
14	14RFB5	53		71	55		1.83	
a	14RFB50		35	71	100		1.21	1.21
b	14RFB50	43		44	100		0.14	
	14RFB100	50		74	150		1.92	
a	14RFB150		43	71	200		1.48	1.48
b	14RFB150	53		56	200		0.23	
18a	18RFC5		30	97	5		10.00	10.00
18b	18RFC5	53		56	100		0.52	
	18RFC50	117		42	150		2.02	
	18RFC100	51		42	200		0.88	

Average Distance	Measured Rate
50	5.34
200	4.67
650	2.20
1500	1.35
2500	1.22

	CS rate (cm/a)	Sed. Rate (min., all, cm/yr)	Bounded Sed. Rate (cm/yr)
All samples	1.53	3.20	2.82
Foredeep		3.36	2.59
Foredeep to #3		3.61	2.41
Foredeep from #6		2.47	3.26
Straight Foredeep (51, 3)		0.73	0.56
Forebulge		2.02	4.23

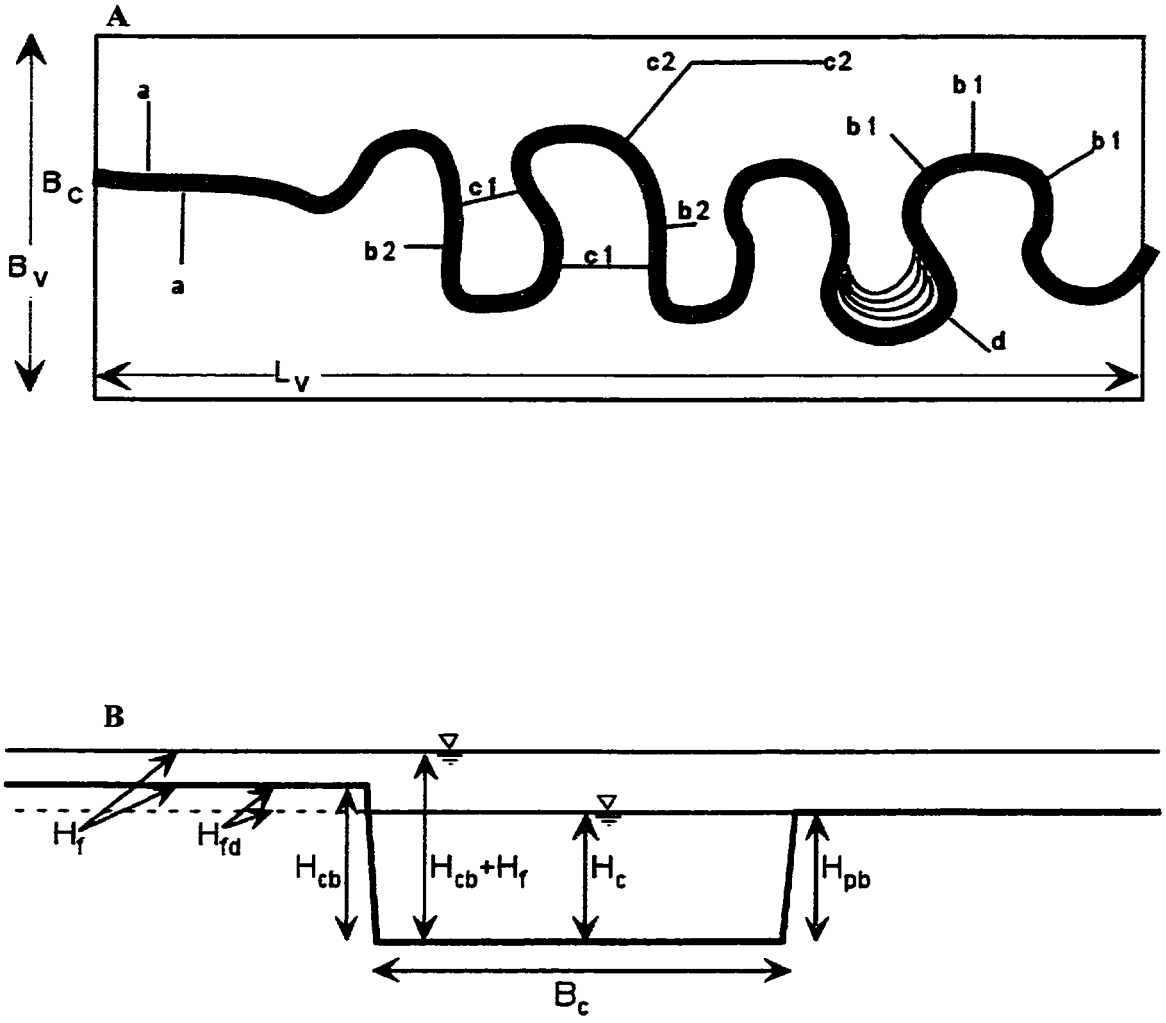

Figure 3.1. (a) Planform sketch of a sinuous river channel in a simplified rectangular valley reach with uniform valley width (B_v), slope (S_v), and channel width (B_c). Representative floodplain transects "a-d" are discussed in Chapters 2 and 5. (b) Cross-sectional diagram of a river channel, denoting bankfull channel depth (H_c), flooding depth on floodplain (H_f), and thickness of floodplain sediment (H_{fd}). Height of the cutbank (H_{cb}) equals the height of unvegetated point bar (H_{pb}) plus H_{fd}. For this simple conceptual model, $H_c \sim H_{pb}$, and the floodplain is assumed to be flat without natural levees.

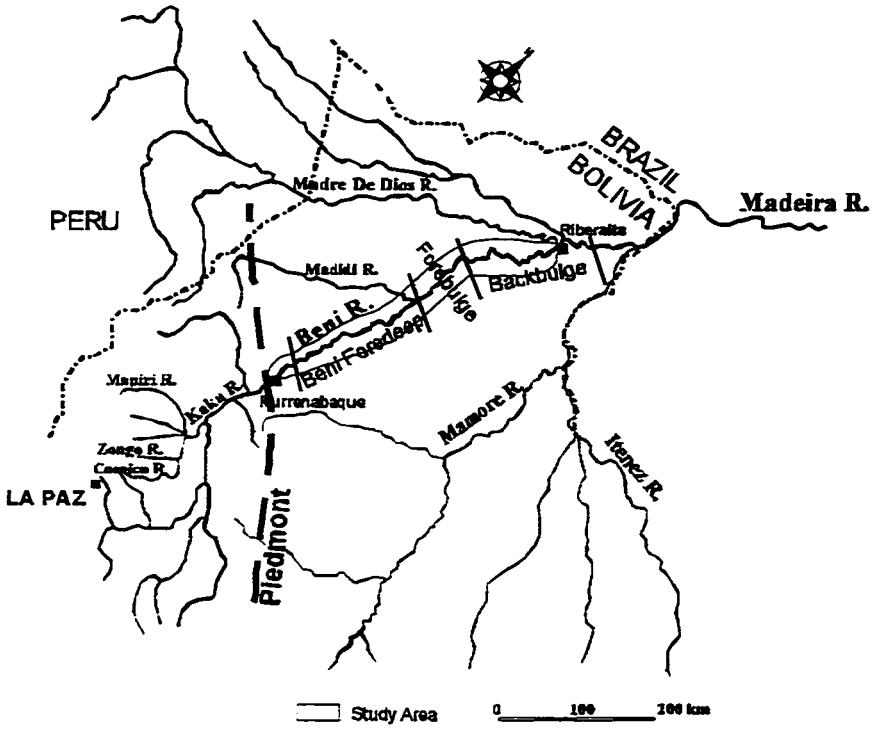

Figure 3.2. Hydrological map of major Madeira River tributaries, depicting the Beni River, the study focus area for floodplain sampling, and principal long-term river gauging stations at Rurrenabaque and Riveralta. Approximate location of the foredeep, forebulge, and backbulge secondary basin are depicted, as determined by DGPS surveys of longitudinal river gradient.

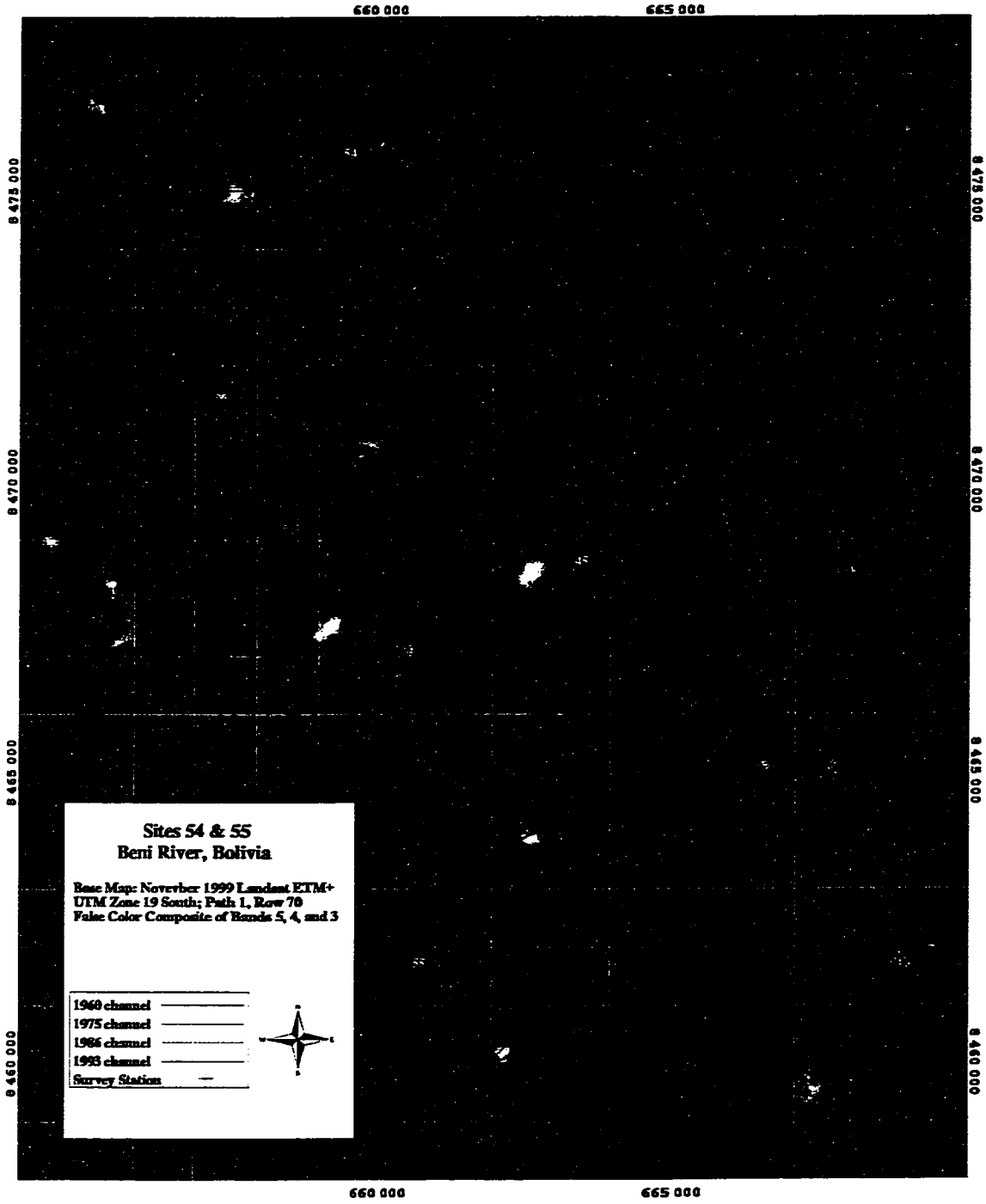

Figure 3.3. (a) GIS map of survey transects at sites 54 and 55, depicting previous channel locations superimposed on 1999 ETM+ LANDSAT image. This upper foredeep location contains several remarkable oxbow lakes. In image, bare sand or earth (band 5) is red, vegetation (band 4) is green, and water (band 3) is blue.

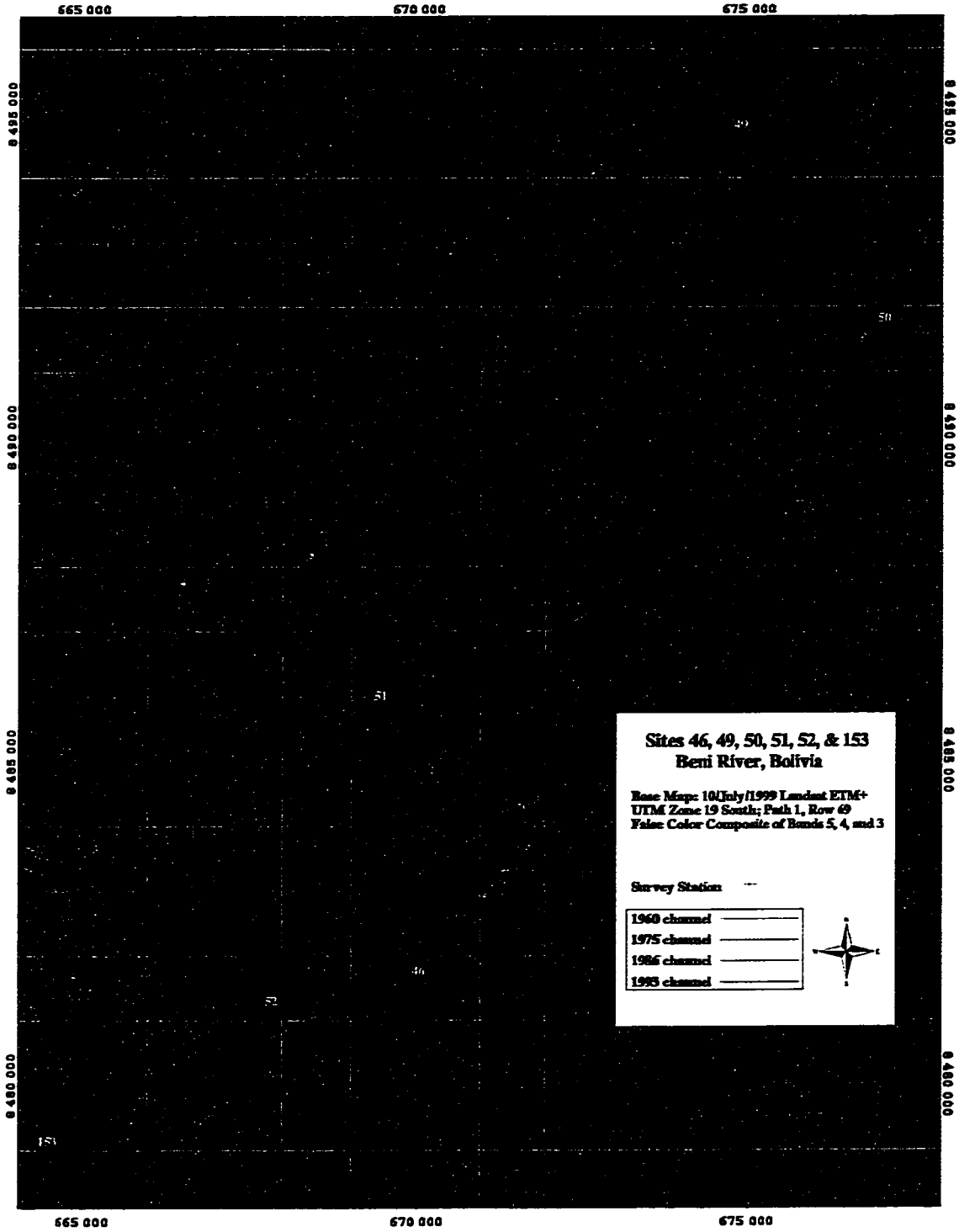

Figure 3.3. (b) GIS map of sites 46 to 53, middle Beni Foreland.

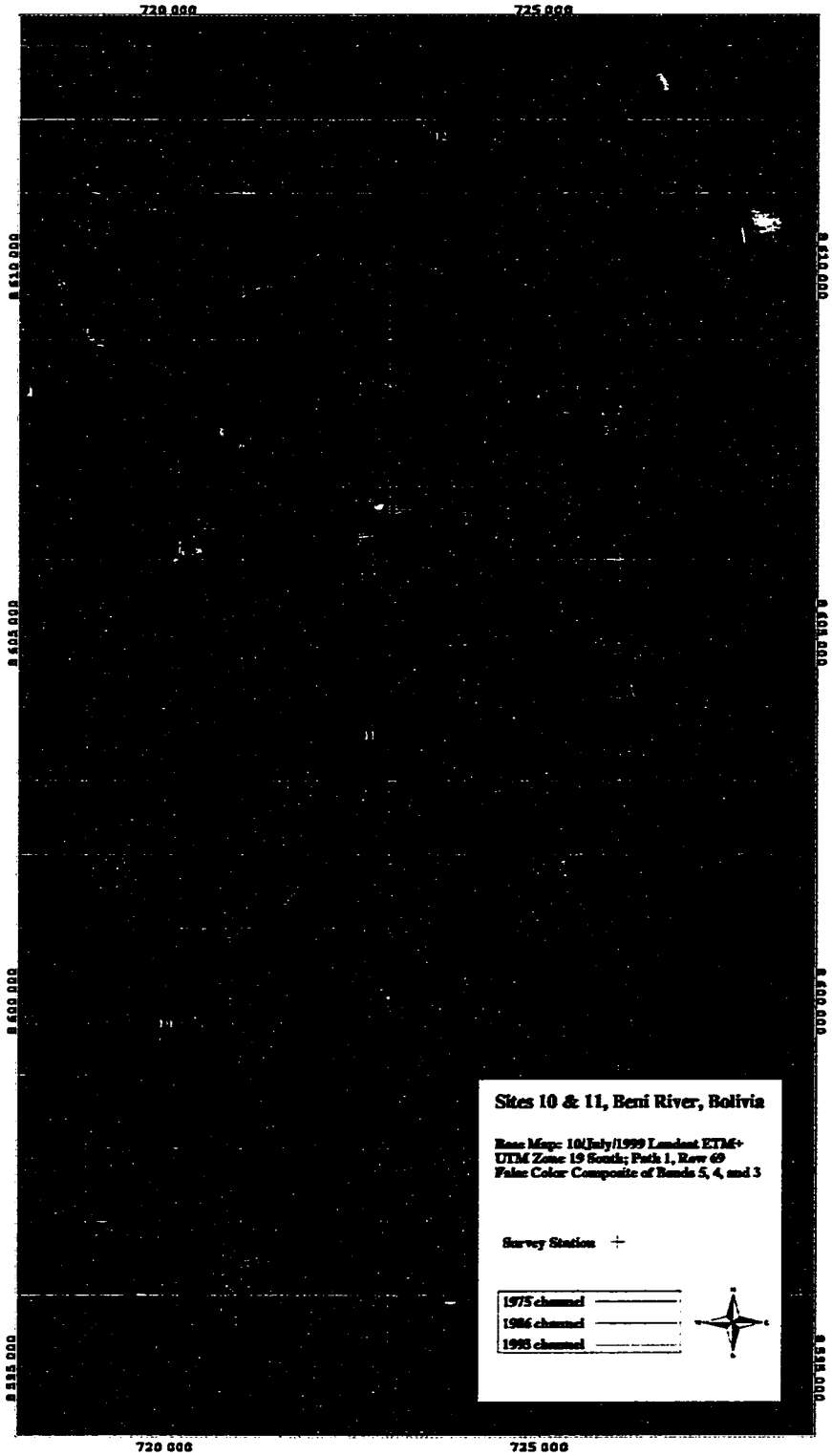

Figure 3.3. (c) Sites 10 and 11, near Madidi confluence and Beni Forebulge.

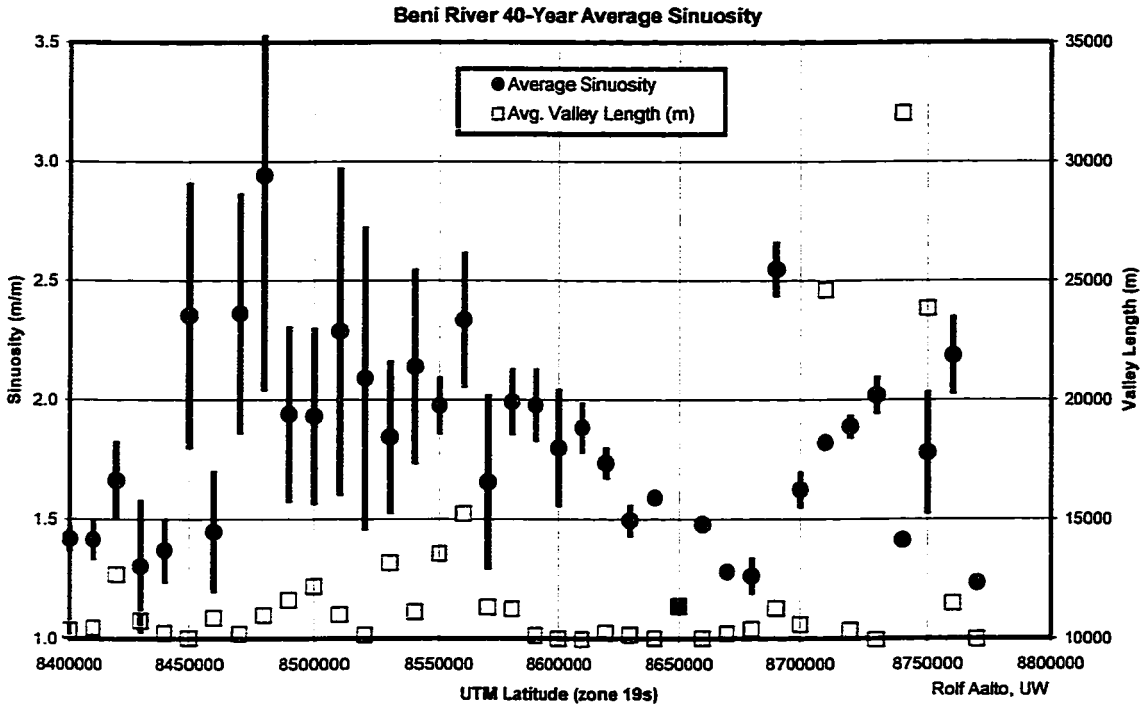

Figure 3.4. Beni River sinuosity and valley length versus UTML. Depicted is the average value since 1960, with the bars showing the standard deviation among the 4 measurements for each reach. Depicted are bankfull width (channel+bar) and wetted width (channel). Values for valley length above 10 km indicate a valley that lies at an angle across the 10 km UTML "box"; that is, does not follow a south-north path.

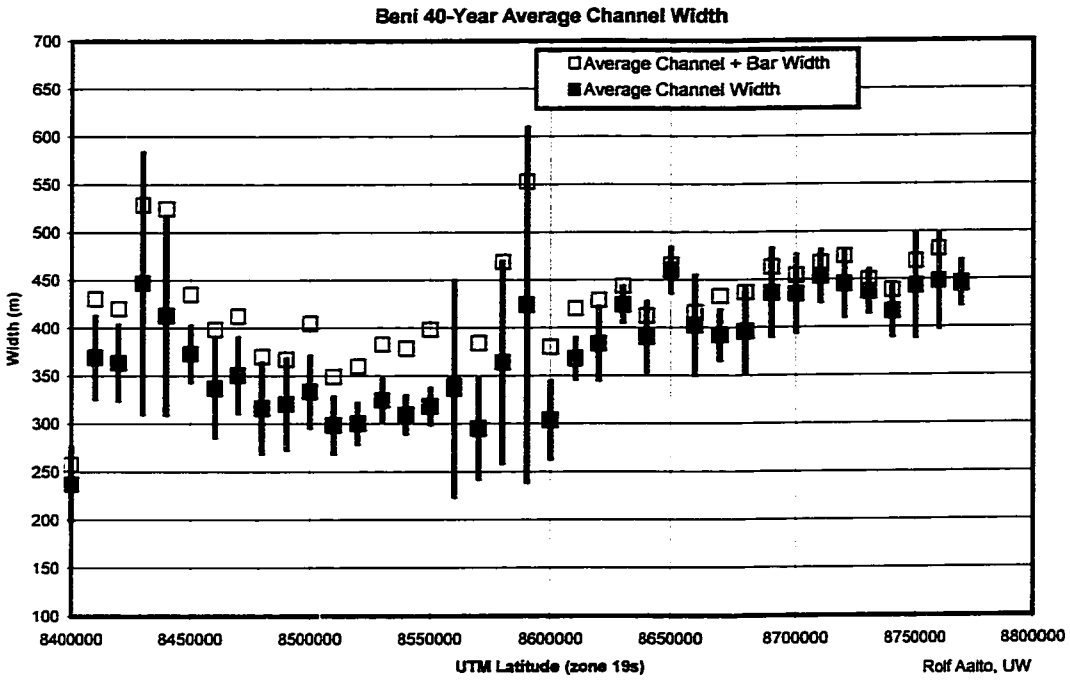

Figure 3.5. Beni River width versus UTML. Depicted is the average value since 1960, with the bars showing the standard deviation among the 4 measurements for each reach. Channel width is reported with and without bars (bar area and hence "wetted channel" width varies significantly with river stage). Total channel+bar width is used for the analysis, because this best represents bank-full width during flooding.

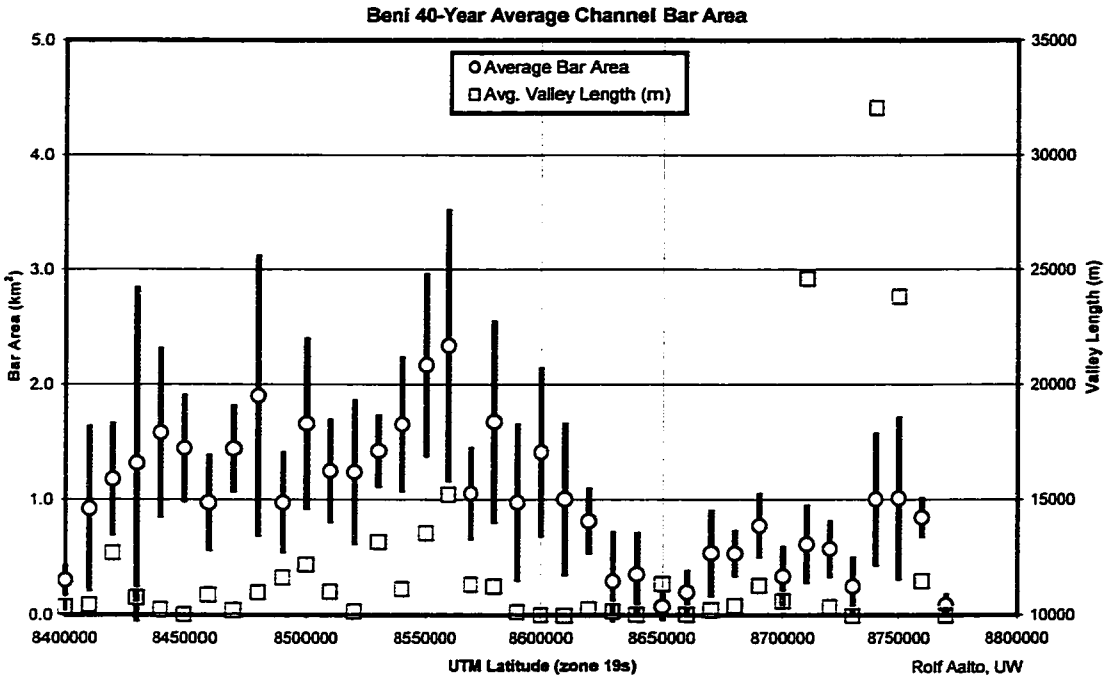

Figure 3.6. Beni River bar area and valley length versus UTML. Depicted is the average value since 1960, with the error bars showing the standard deviation among the 4 measurements for each reach. Bar area varies significantly with river stage, increasing the observed variance. Values above 10 km indicate a valley that lies at an angle across the 10 km UTML "box," that is, does not follow a south-north path.

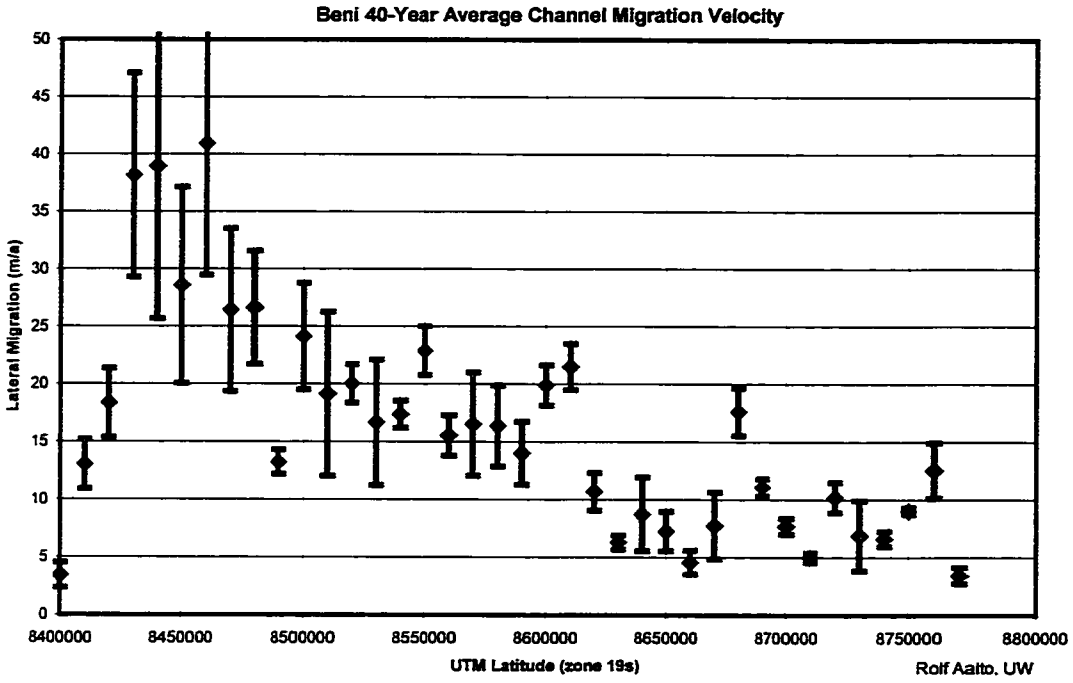

Figure 3.7. Beni River lateral migration velocity versus UTML. Depicted is the average value since 1960, with the error bars showing the confidence interval.

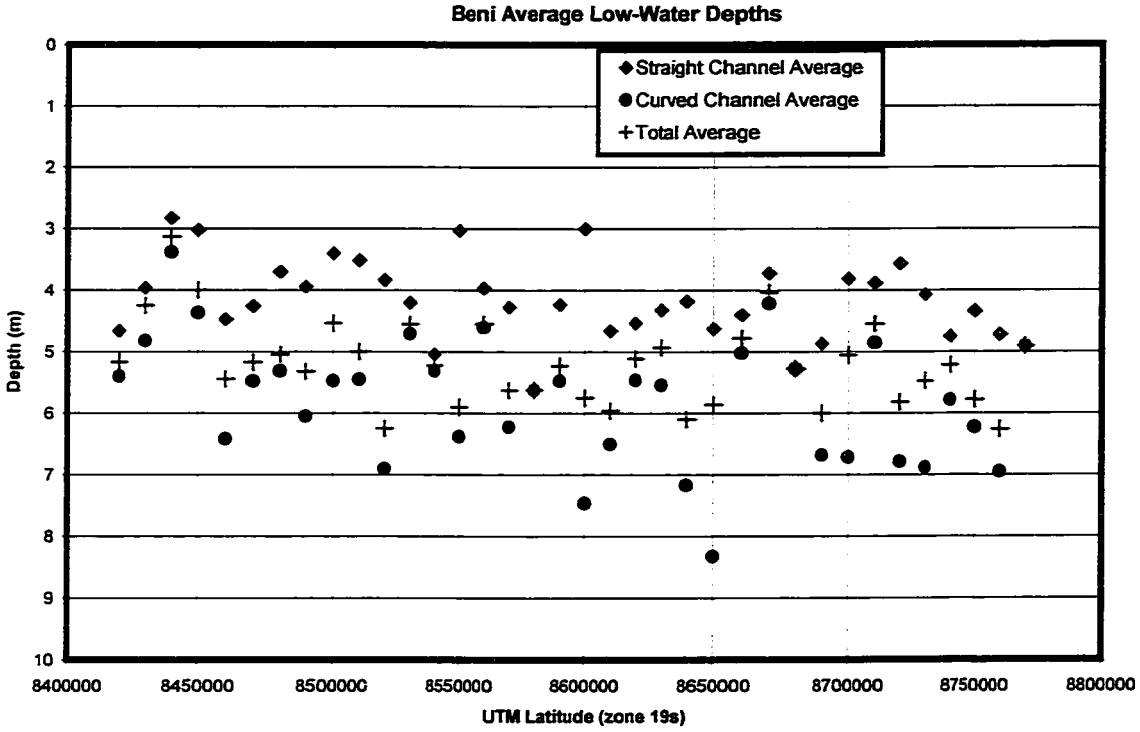

Figure 3.8. Channel depths for the Beni River measured in 1969 (Semena, 1969). For each 10 km latitude river reach, I separately report the average depth of all straight and all curved sections of channel, along with the average depth for the entire channel.

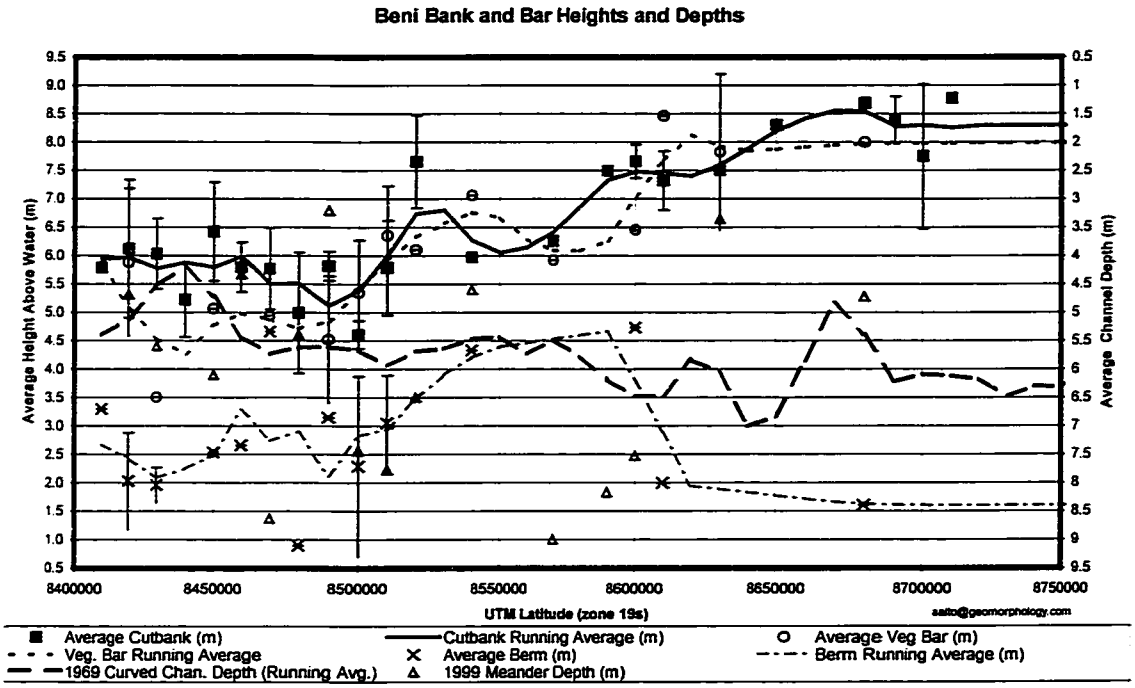

Figure 3.9. Summary of Beni River topographic survey results. Depicted are 10 km UTML average cutbank, vegetated bar, and berm heights (unvegetated bar top), along with 1999 channel depths. Also shown are running average values (30 km UTML averaging windows) for these heights, including those for the 1969 curved channel depths.

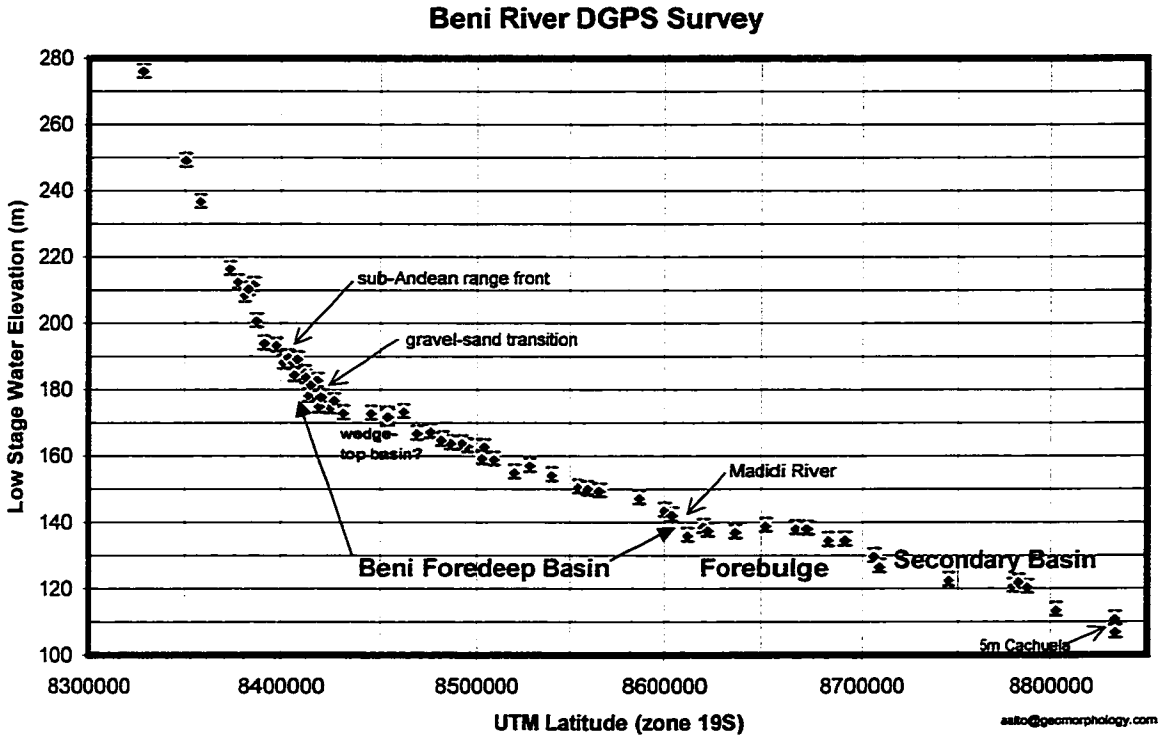

Figure 3.10. Longitudinal profile of low stage water surface elevation for the Beni River versus UTML. Locations of the range front, gravel-sand transition, confluence with the Madidi River, and the first large rapids (5 m Cachuela) are marked in black. Red letters indicated the proposed (in Chapter 6) locations of tectonic features, including the foreland, forebulge, and back-bulge secondary basin. For the water surface elevations, DGPS elevation was post-processed to an accuracy of ± 2 m or better (2 m error bars are depicted). Note that UTML "valley" slope is 1.3 – 4.5 times steeper than the slope of the river water surface.

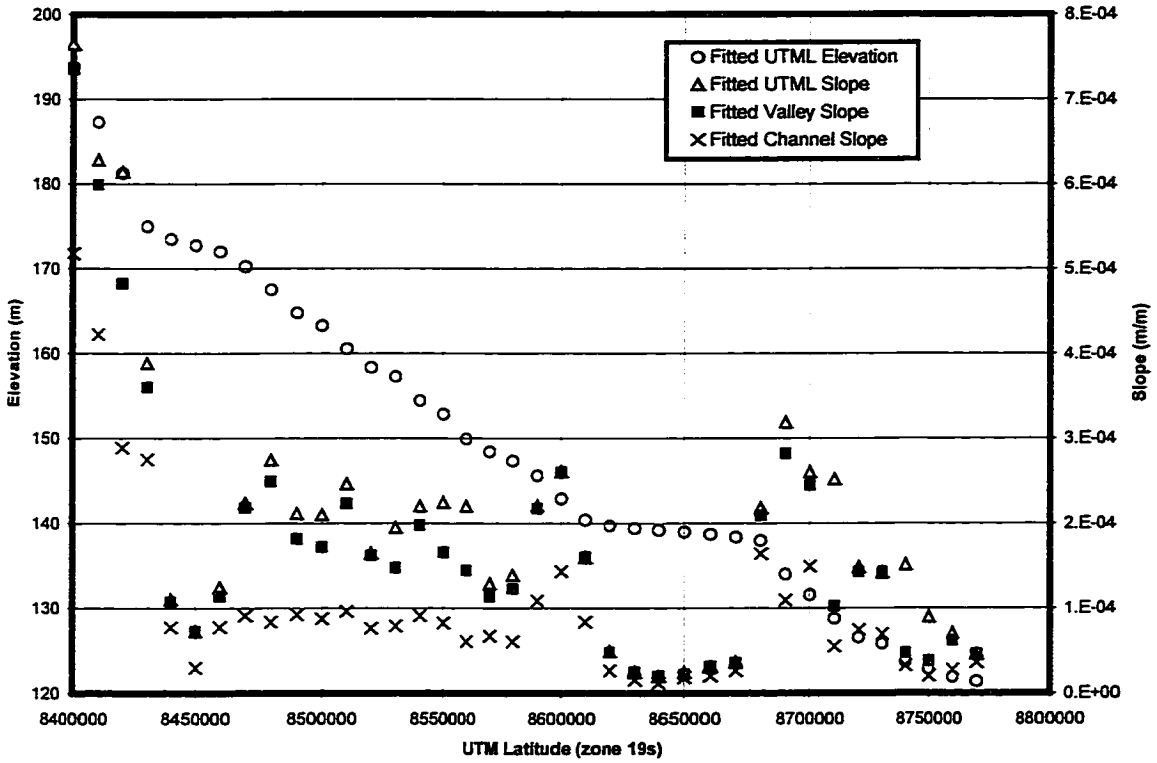

Figure 3.11. Best-fit 10 km UTML binned water elevations, derived from Figure 3.10. From these elevations are calculated UTML, valley, and river slopes. Because the river valley does not always run exactly south to north (Figure 3.4) and the channel is sinuous, the valley and river slopes are reduced by the corresponding correction for each 10 km UTML reach (mean valley length and channel sinuosity are determined from the GIS analysis of four decades of channel imagery).

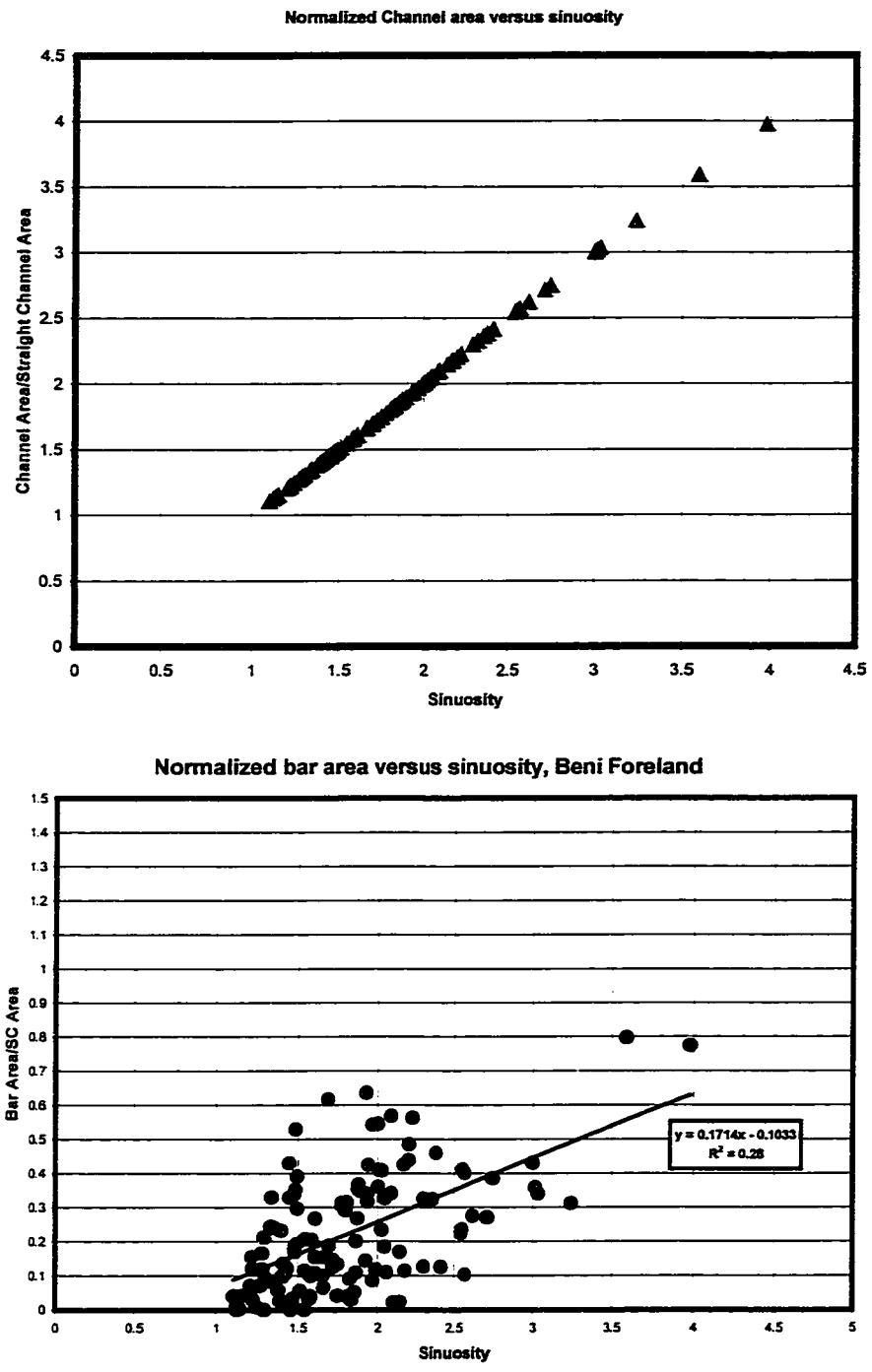

Figure 3.12. (a) Normalized channel area versus sinuosity. Channel area is divided by the area of a straight channel of corresponding width. Fit is perfect. (b) Normalized bar area versus sinuosity. Area normalizations are to the equivalent area of a straight channel (s = 1) across each 10 km UTML reach. Despite the low R^2 value, due to variations in river stage and resulting bar inundation between the channel images, the trend is highly significant ($p < 10^{-9}$) due to the large number of data points (n = 121).

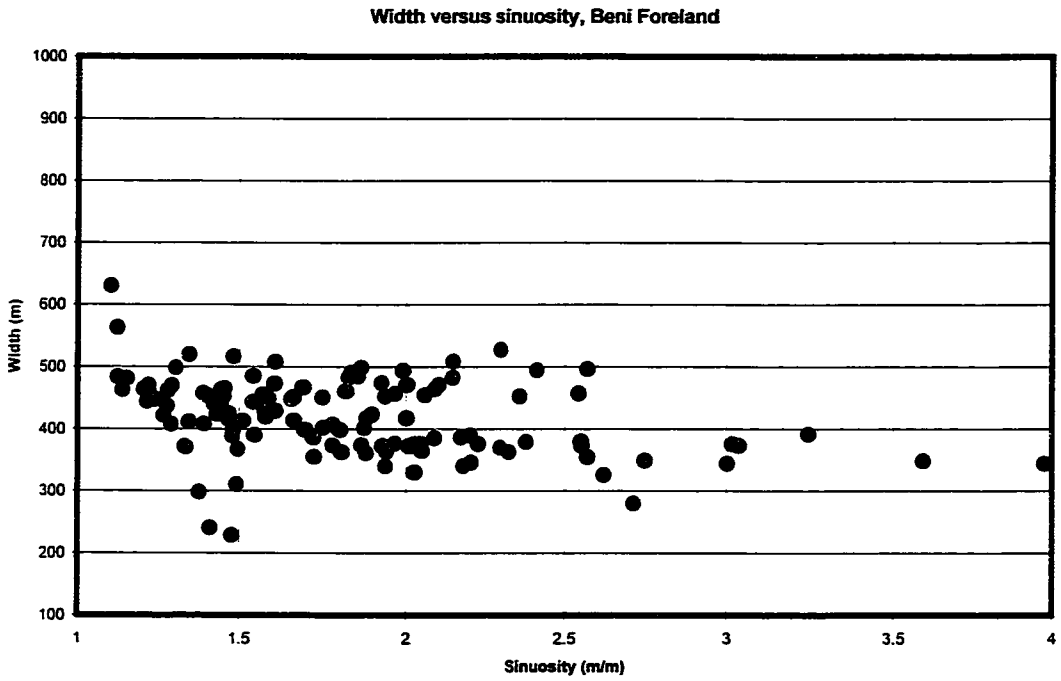

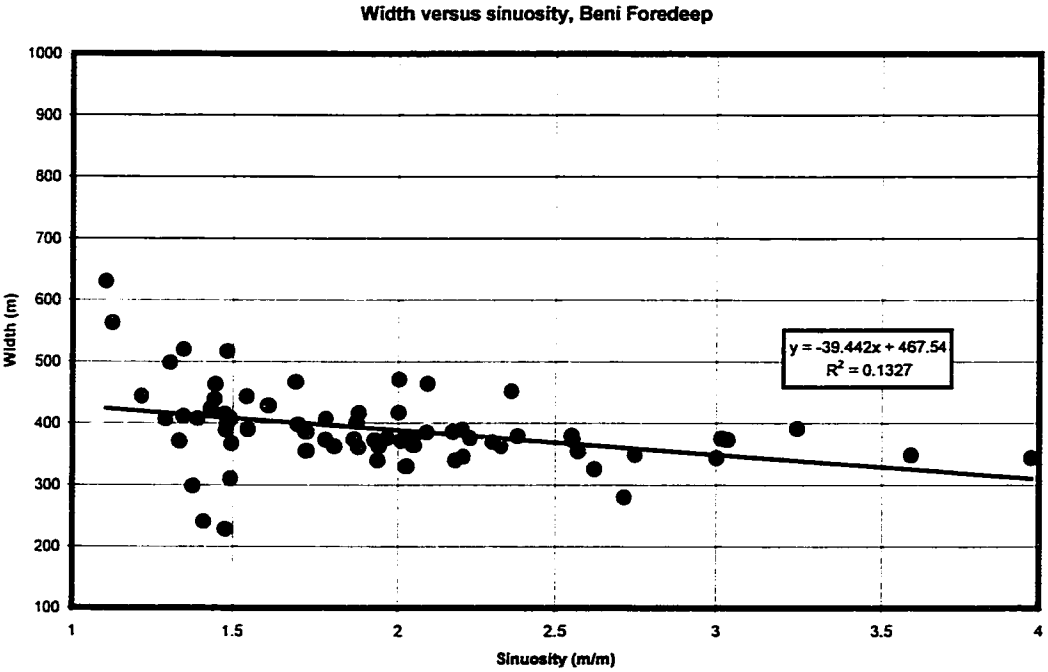

Figure 3.13. (a) Bankfull width versus sinuosity, Beni Foreland. (b) Bankfull width versus sinuosity, Beni Foredeep. Despite the low R^2 value, the trend is significant ($p < 0.001$) due to the number of data points ($n = 71$).

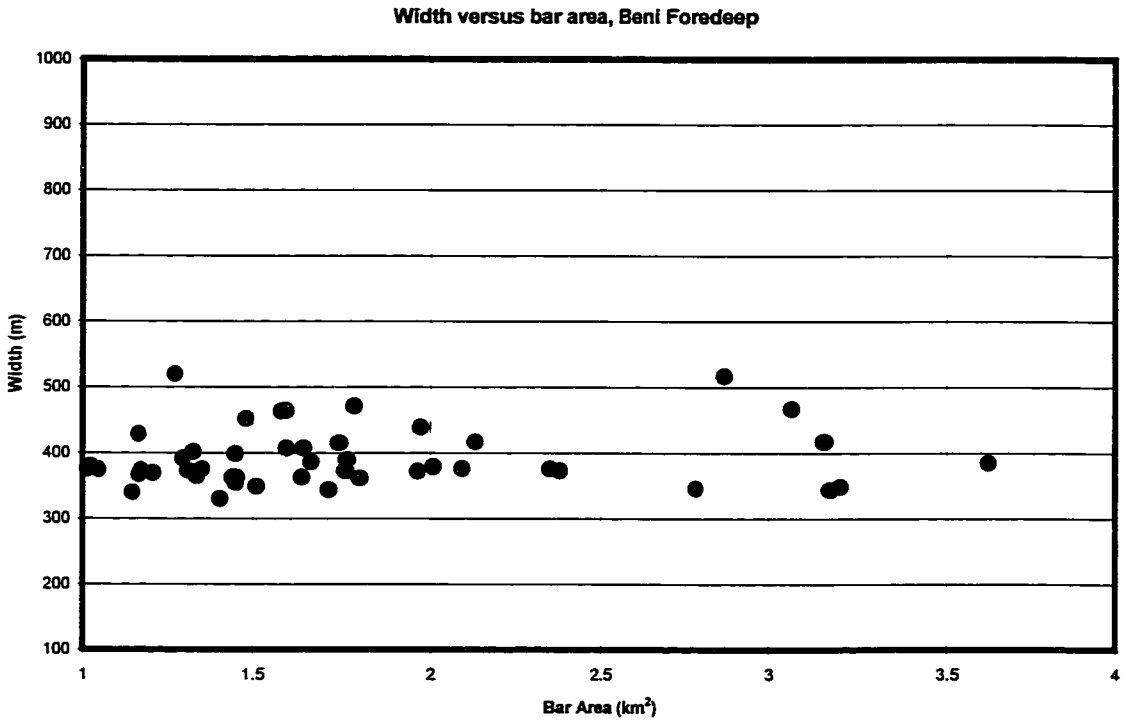

Figure 3.13. (c) Bankfull width versus bar area, Beni Foredeep. There is no statistically significant relationship between the two ($p = 0.42$).

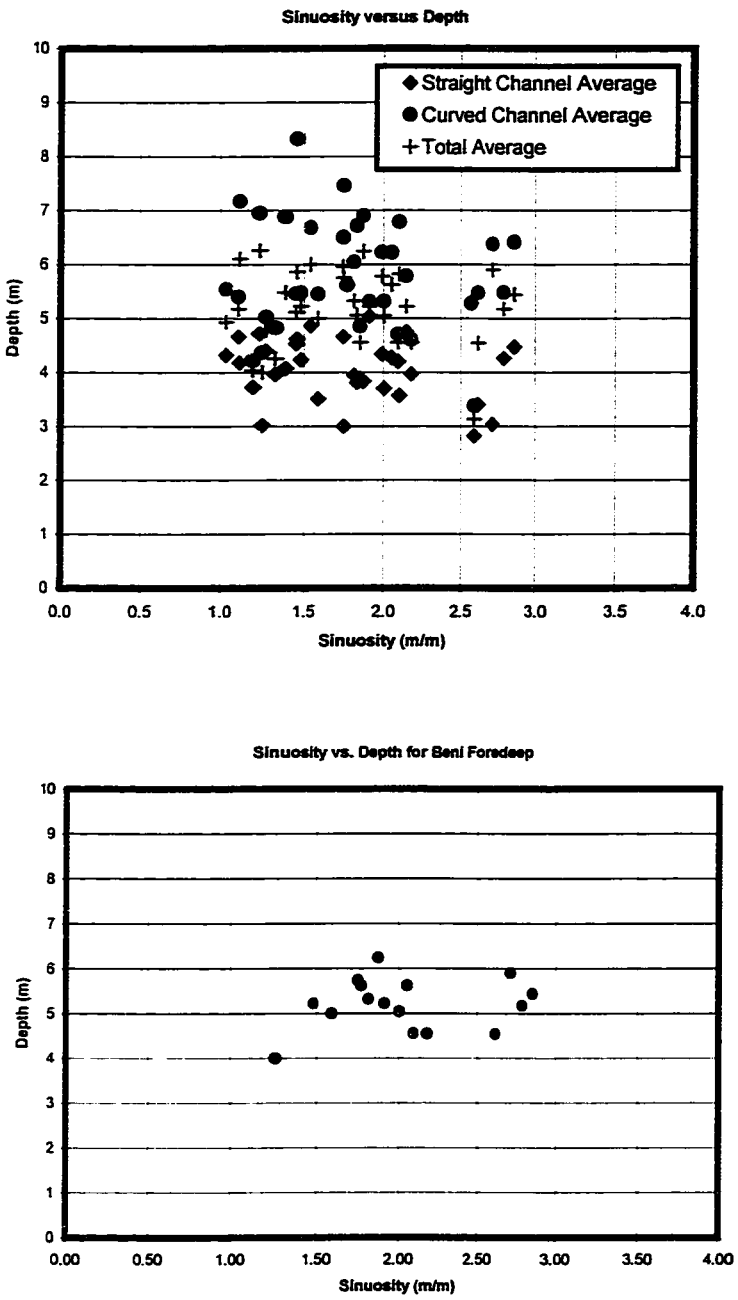

Figure 3.14. (a) Channel depth versus sinuosity, Beni Foreland. Channel depths were measured in 1969 (Semena, 1969), and sinuosity is estimated from the 1960 and 1975 images. For each 10 km latitude river reach, I report the average depth of all straight and all curved sections of channel separately, along with the average depth for the entire channel in that 10 km reach. (b) Average channel depth versus sinuosity, reported for each 10 km UTML reach in the Beni Foredeep. Although the channel appears to become slightly deeper with increasing sinuosity, there is no statistically significant relationship between the two ($p = 0.27$).

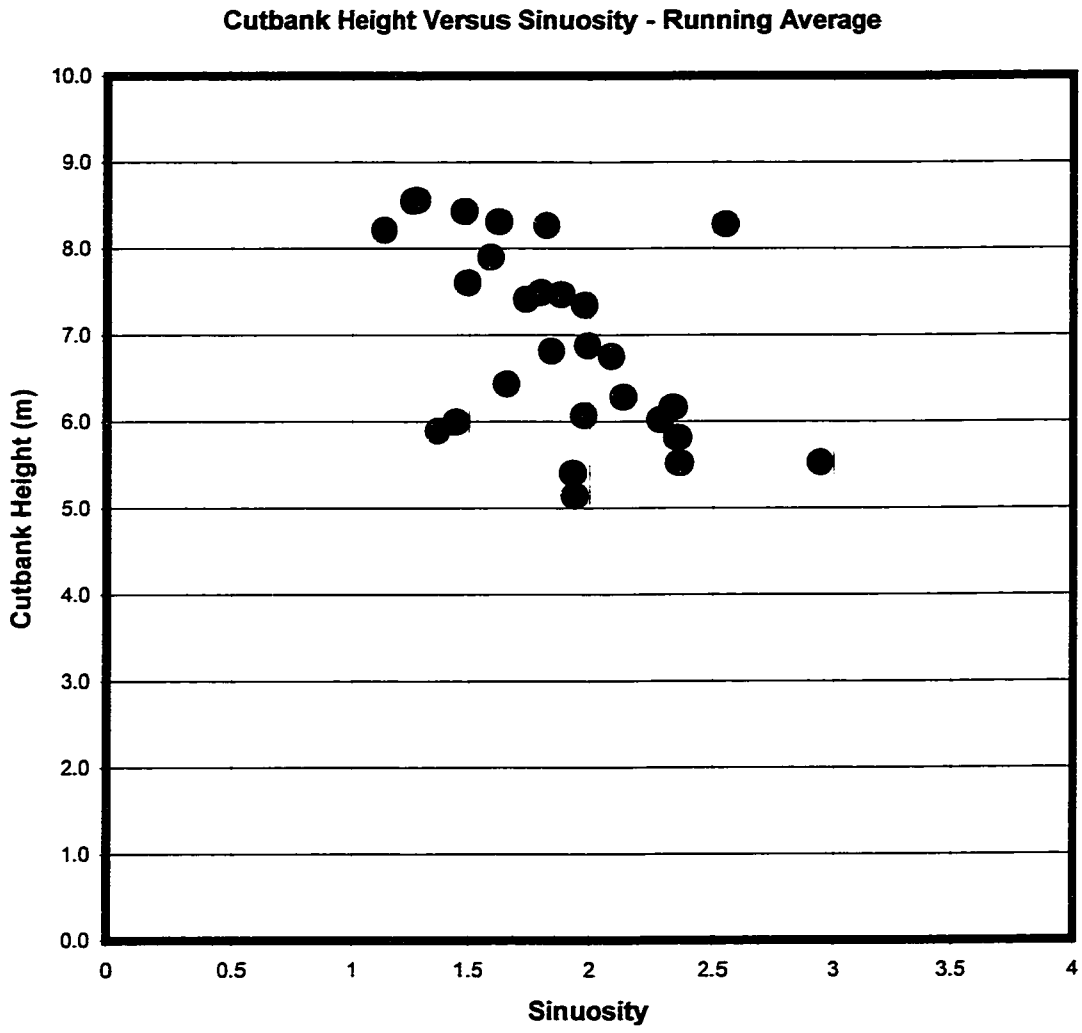

Figure 3.15. Channel cutbank height versus sinuosity, Beni Foreland. Data from the Beni Foredeep are marked in purple, the rest of the foreland locations are marked in black.

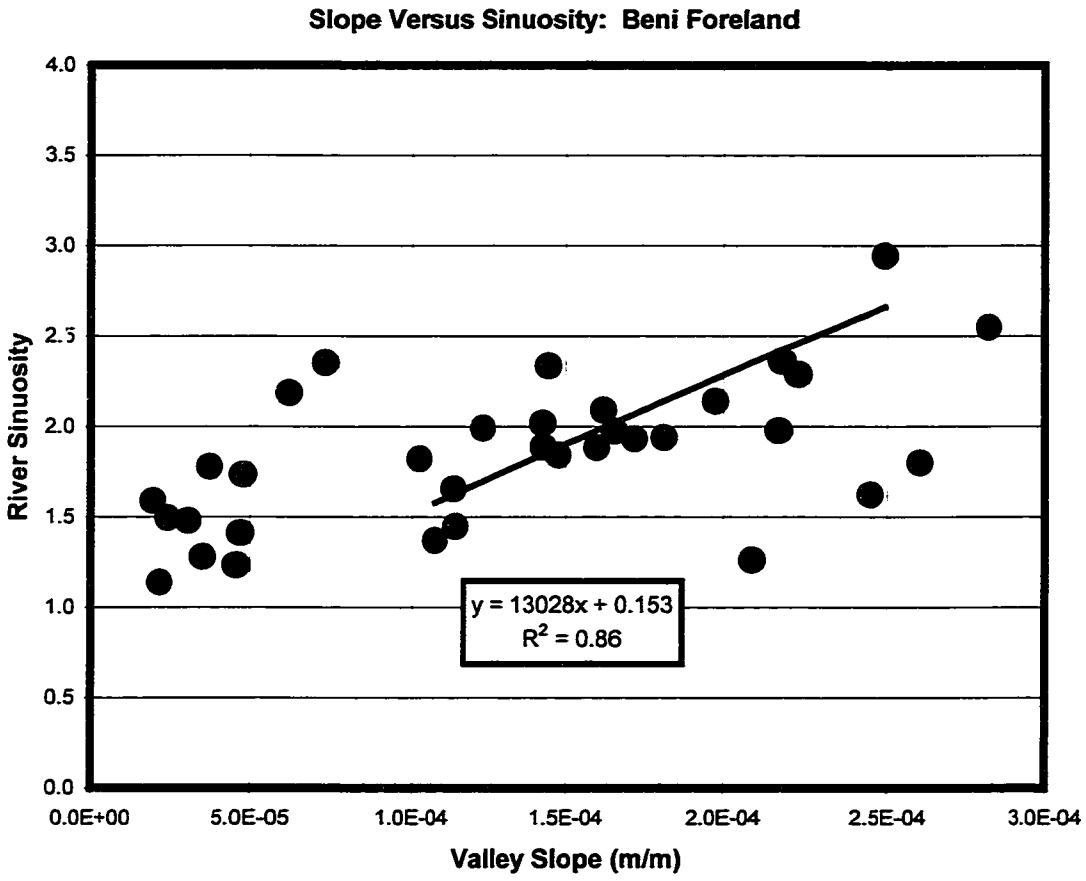

Figure 3.16. River sinuosity versus valley slope, Beni Foreland. Data from the Beni Foredeep are marked in purple, with a corresponding best-fit equation ($p < 10^{-6}$).

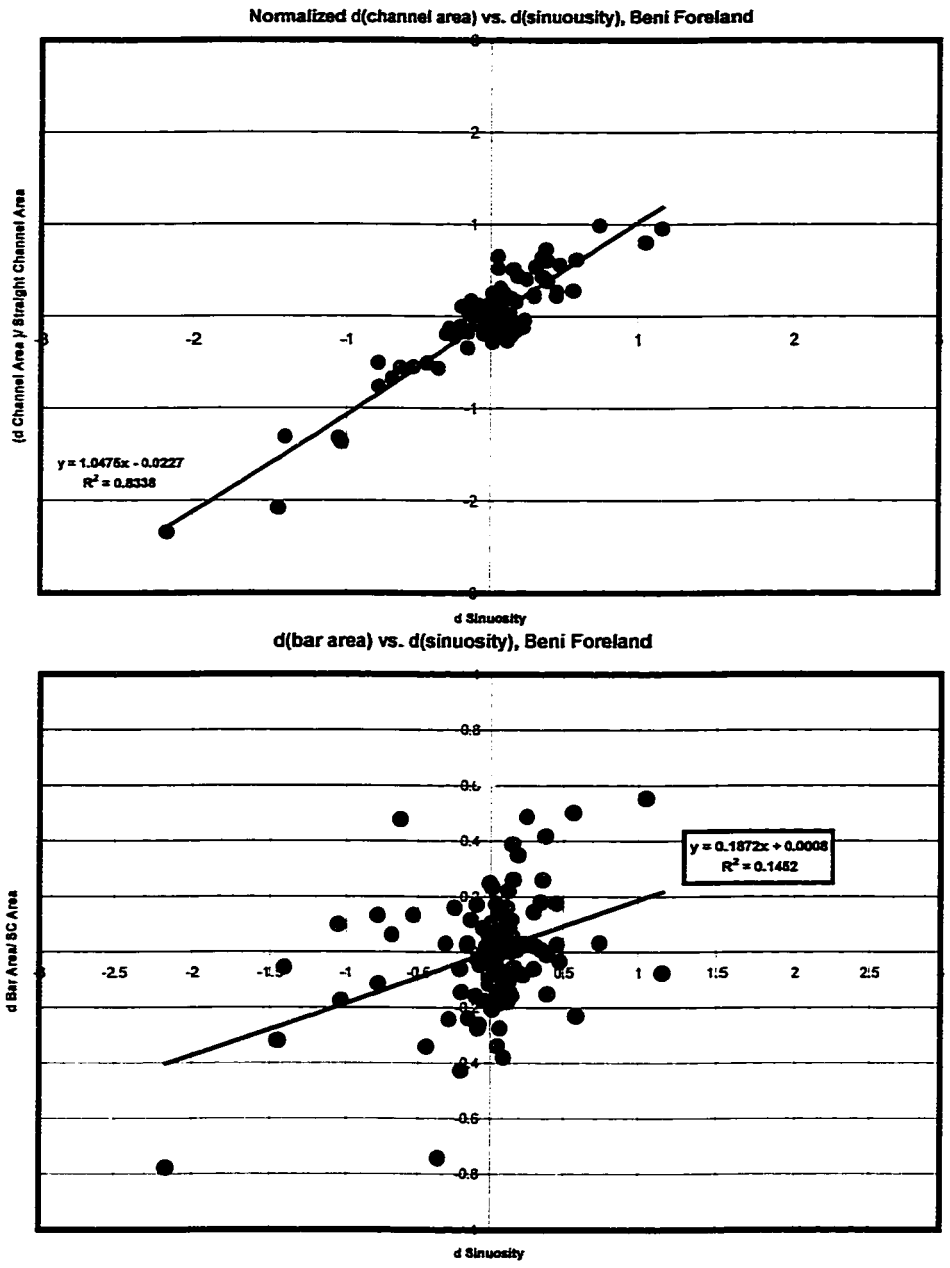

Figure 3.17. (a) Change in normalized channel area versus change in sinuosity, Beni Foreland ($p < 10^{-47}$). (b) Change in normalized bar area versus change in sinuosity, Beni Foreland. Area normalizations are to the equivalent area of a straight channel ($s = 1$) across each 10 km UTML reach, for the state of the channel *before* the change. Despite the low R^2 value, due to variations in river stage and resulting bar inundation between the channel images, the trend is highly significant ($p < 10^{-5}$) due to the large number of data points ($n = 121$).

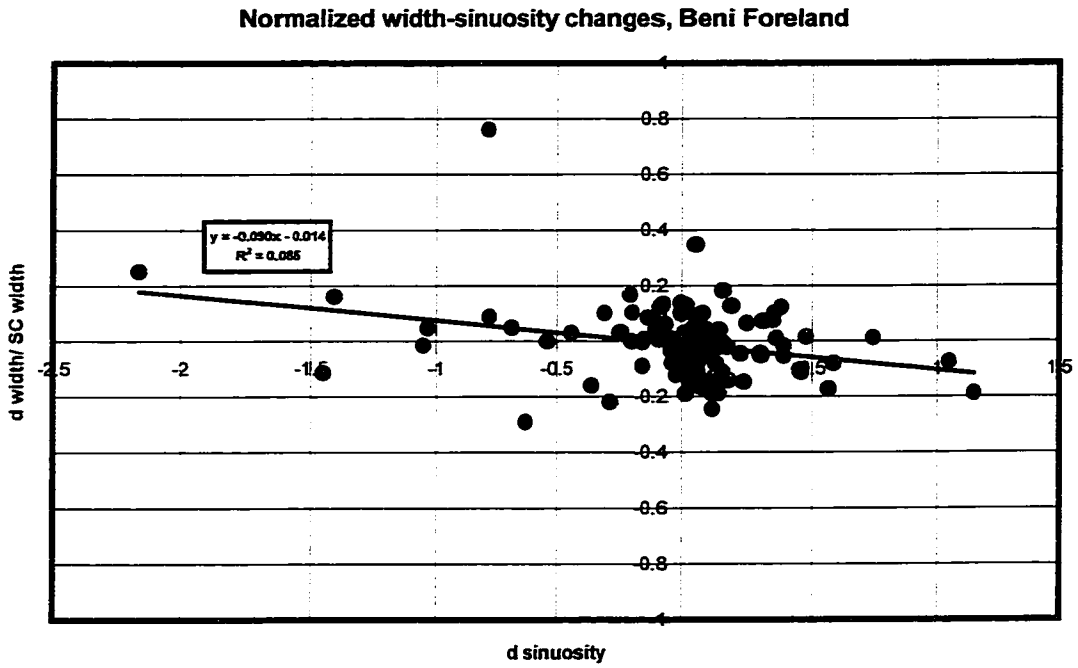

Figure 3.18. Change in normalized channel bankfull width versus change in sinuosity, Beni Foreland. Width normalization is to the initial channel width prior to the change. Despite the low R^2 value, the trend is significant ($p < 0.0006$) due to the large number of data points ($n = 121$).

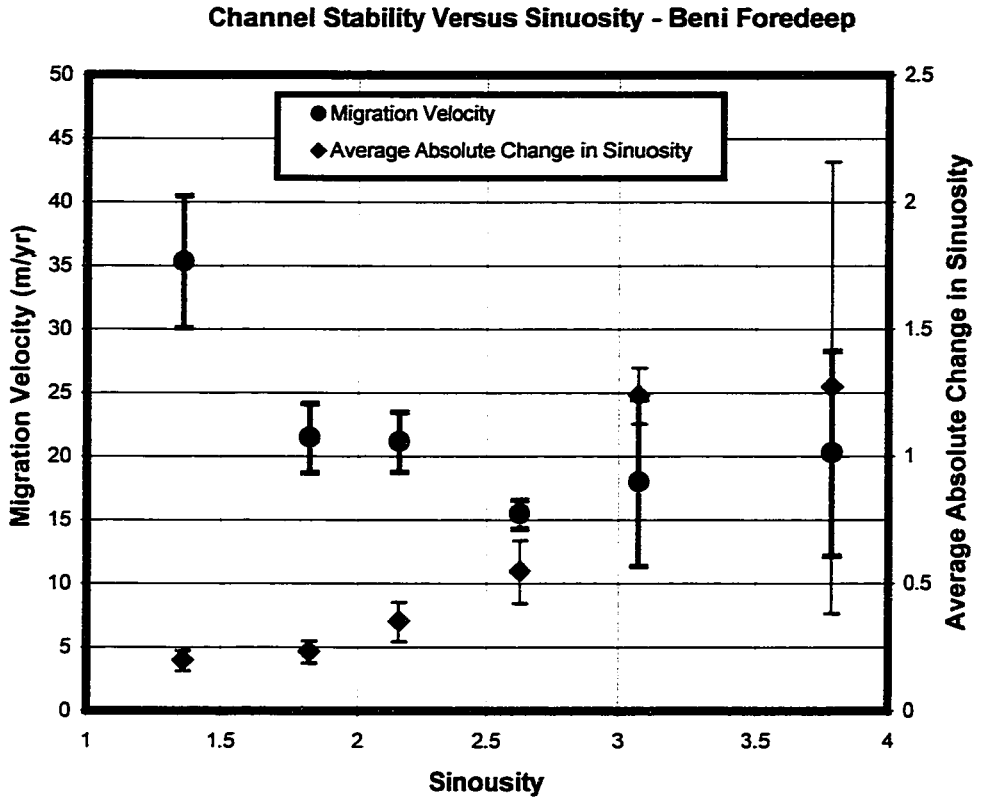

Figure 3.19. Channel migration velocity and average absolute change in sinuosity versus channel sinuosity, Beni Foredeep. Data have been averaged in 0.5 sinuosity bins, and plotted according to average bin center. Error bars represent bin confidence interval.

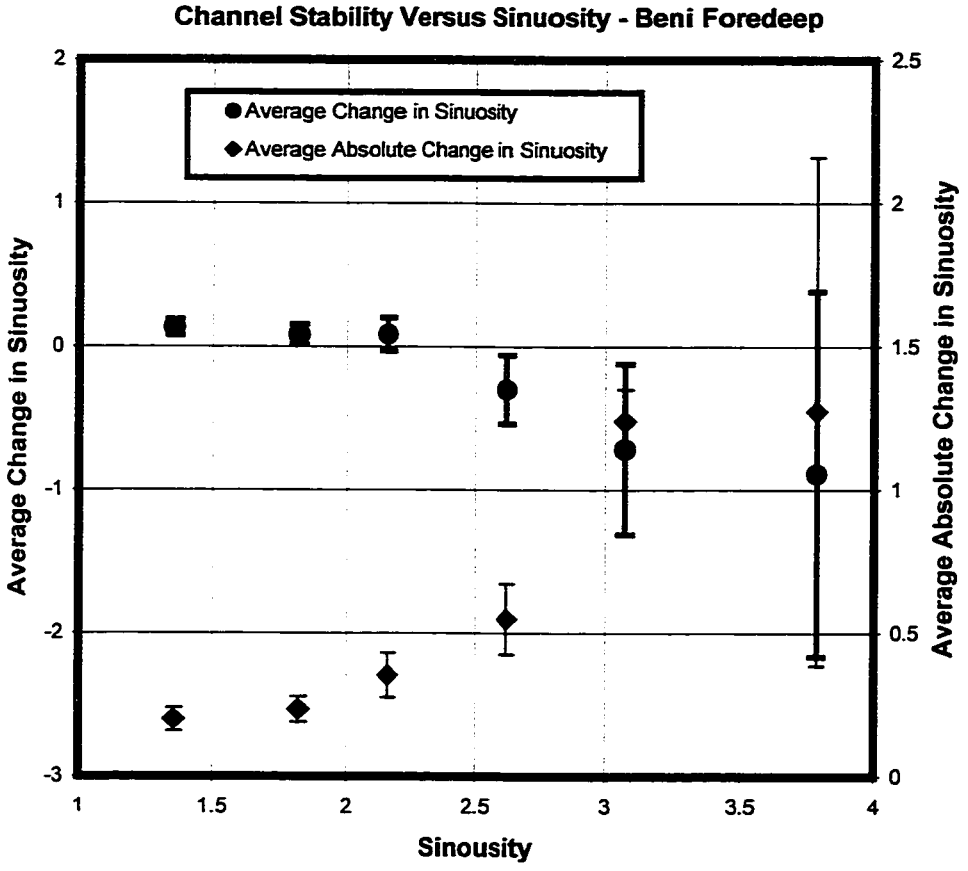

Figure 3.20. Channel average absolute and net average change in sinuosity versus channel sinuosity, Beni Foredeep. Data have been averaged in 0.5 sinuosity bins, and plotted according to average bin center. Error bars represent bin confidence interval.

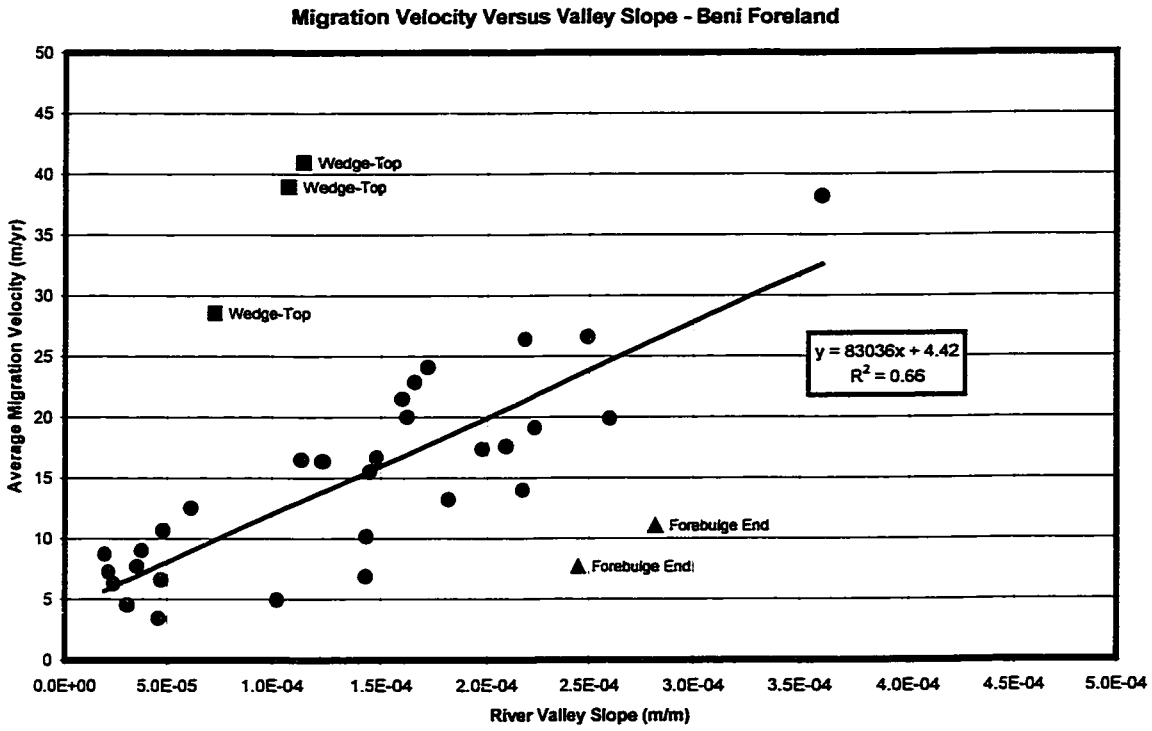

Figure 3.21. Channel migration velocity versus river valley slope, Beni Foreland. Outliners are from the low-gradient wedge-top basin proximal to the range front, where the channel is embayed behind a tectonic high, and the slope inflection at the end of the forebulge, where the channel is constrained between high terraces resistant to erosion. Best-fit relationship is depicted for the rest of the data ($p < 10^{-7}$).

Chapter 4

Application of fallout ^{210}Pb geochronology to river-floodplain systems: a flexible new methodology

Abstract

Lowland floodplains store suspended sediment carried over bank during floods. Because floodplain sedimentation may account for the majority of the net sediment deposition within large sand-bedded river-floodplain systems, it is important to develop a means to quantify this process. Several recent studies have demonstrated that the natural radionuclide ^{210}Pb, previously used to date lacustrine and marine sediments, can be used to determine floodplain deposition rates over decadal-to-century timescales. These studies determine deposition rates with a recently proposed Constant Input Concentration and Constant Sedimentation rate model (CICCS), and have been conducted on disturbed floodplains (grazed or farmed) and on very small (a small patch of floodplain) or very large (the Bengal Delta) spatial scales.

To investigate the application of the CICCS method to a large, dynamic, pristine river system with extensive forested floodplains, 139 vertical cores were collected throughout the floodplain along 800 km of the Beni River in northern Bolivia. The sampling strategy was devised to quantify rates of floodplain accumulation within 3 km of the channel, as they vary with both channel geometry and distance from the river. Rather than measuring bulk-averaged down-core ^{210}Pb activity to estimate average deposition rate according to the standard CICCS procedure, the cores were instead sectioned vertically to obtain detailed activity profiles. Because there is little bioturbation or other floodplain disturbance in this area, these cores record a high-resolution record of sediment and ^{210}Pb deposition. Over 95% of these profiles depict a history of episodic deposition over decadal recurrence intervals, with only a few exhibiting the steady-state deposition assumed by the CICCS model. Because these

discrete accumulation events are large, few of the cores ever reach supported background ^{210}Pb activity at depth, another requirement of CICCS. Furthermore, there is compelling evidence that the input activity of ^{210}Pb is not constant, both at a site and down-channel, as illustrated both by samples of fresh river sediment and with a flux model of ^{210}Pb 'aging' in river sediment by transfer of 'old' sediment from the cut banks to the point bars during channel migration. The ^{210}Pb content of sediment varies directly with fines content, which is highly variable within many of the cores, so all measured ^{210}Pb activity were first normalized to the clay content of each sample at each core depth. Without a discretely sampled, clay-normalized ^{210}Pb activity profile available for any given core, it is difficult to evaluate the suitability of CICCS for that core.

To accommodate these complexities, a more labor intensive approach is proposed for dating sedimentation using discrete down-core, clay-normalized measurements of ^{210}Pb activity, coupled with a geomorphic model of input concentration of ^{210}Pb in sediment during large floods. Combined with a field determination of supported ^{210}Pb activity, collection of multiple terrace cores to determine the meteoric input of ^{210}Pb, and a proposed technique for independently dating the "meteoric cap" above discrete depositional events, this approach to ^{210}Pb geochronology provides a convenient, reliable, and internally verifiable approach to dating floodplain sediment.

Introduction

Large lowland rivers construct floodplains through the deposition of sediment conveyed overbank by turbid waters during flooding. To determine the average annual accumulation of riverborne sediment (including associated nutrients and pollutants) across such floodplains, sedimentation processes must be investigated for a wide expanse of floodplain locations and quantified on at least a decadal-to-century temporal scale, so as to resolve annual variations in the spatial distribution and amount of sediment conveyed from the channel to the floodplain. However, until recently there was no available technique to quantify floodplain accumulation rates over such longer

periods of time. Researchers could only document the apparent accumulation of fresh sediment deposited during a single flood, either during the event itself (sediment traps) or immediately thereafter (surveys of sediment deposits). Without a prolonged logistical effort spanning decades (e.g., repeated benchmarked topographic surveys at the same site (Leopold, 1973)), it is unclear how to integrate the results from a single event into a century-scale estimation of floodplain accumulation rates.

One recent approach to this challenge is to determine a datable surface at some depth within the floodplain, with the bomb-derived fallout nuclide ^{137}Cs offering the most widespread applicability (Allison et al., 1998; Goodbred and Kuehl, 1998; Walling and He, 1997; Walling et al., 1992). However, such ^{137}Cs radionuclide geochronology presents a number of limitations. First, maximum depth of penetration is typically keyed to the peak of weapons testing in 1963, giving less than four decades of temporal coverage. Second, the flux of both atmospheric and particle-sorbed ^{137}Cs to a floodplain location may be highly variable, although ^{137}Cs concentrations in river sediment have been sometimes interpreted as steady-state since the early 1970's (Goodbred and Kuehl, 1998; Smith et al., 1987). As a result, both the total penetration and inventory (Goodbred and Kuehl, 1998) methods can only be used to estimate average deposition rate, not employed to effectively resolve changes in rates or discrete sedimentation events within the 40-year geochronological window (this technique is discussed later). Third, some floodplain environments may exhibit little or no ^{137}Cs activity, due to global variations in fallout and dilution since the 1963 peak for catchments with high erosion rates. And fourth, ^{137}Cs is measured using a laboratory procedure that requires substantially larger samples and is typically a slower process than that for the ^{210}Pb radioisotope, another fallout radionuclide.

^{210}Pb is a naturally-occurring fallout radionuclide, a result of the atmospheric decay of ^{222}Rn, which diffuses from the lithosphere as a daughter of the ^{238}U decay series. Like ^{137}Cs, ^{210}Pb deposition is primarily due to meteoric fallout, and it adsorbs quickly and tenaciously to the surfaces of fine sediments (primarily in the interlayer sites

of hydrous clays, where it is chemically immobile (Comans et al., 1991; Cremers et al., 1988; Francis and Brinkley, 1976)) and undergoes beta decay to ^{210}Bi with a half-life of 22.3 years. However, as a natural process, ^{210}Pb fallout is functionally uniform throughout time at any given location (He and Walling, 1996b; Walling et al., 1992), facilitating application to temporal scales of ~ 100 years. While the background production rate of ^{210}Pb has remained essentially uniform, there may be regional-scale differences in these rates, and therefore the general rate of direct atmospheric fallout should be determined from reference inventory cores for each general study region. In-situ ^{210}Pb produced by the decay of ^{222}Rn within the soil or sediment is referred to as "supported" activity, in contrast to "unsupported" ^{210}Pb activity from meteoric fallout. For a floodplain sample, ^{210}Pb is derived from three sources: in-situ production from ^{222}Rn decay, local atmospheric fallout, and catchment-derived input from deposited sediment. It is the latter, dominant source that facilitates measurement of rates of floodplain deposition.

^{210}Pb radioisotope geochronology is commonly applied to lacustrine (Appleby and Oldfield, 1978, 1983; Oldfield and Appleby, 1984) and marine (Nittrouer et al., 1979) environments, which often meet the assumptions of grain size homogeneity and steady-state nuclide fluxes underpinning common aquatic models: CRS (constant rate of supply), CFCS (constant flux and constant sedimentation rate), or CIC (constant initial concentration). However, on floodplains, neither the annual inputs of unsupported ^{210}Pb to the sediment nor the annual sedimentation rates can be assumed to be constant (He and Walling, 1996b), because the episodic fluxes of particle-sorbed radionuclides in fluvial systems reflect the strong spatial and temporal variability of overbank flooding (Goodbred and Kuehl, 1998). These and other heterogeneities of floodplain-river systems preclude the straightforward application of conventional ^{210}Pb models for aquatic geochronology.

A promising new ^{210}Pb dating method for floodplains has recently been developed by He and Walling (1996b), who recognized that total unsupported

inventories are derived from meteoric fallout at a floodplain site and the catchment-derived input of sediment. Thus, the fallout component can be subtracted from the whole-core radionuclide inventory to determine catchment input, reflecting the time-averaged accumulation rate, R (g cm^{-2} yr^{-1}),

$$R = \lambda_{Pb} \frac{I_{total} - I_{atm}}{A_{catch}} \quad (1)$$

where λ_{Pb} is the ^{210}Pb decay constant (yr^{-1}), I_{total} is the total core nuclide inventory (DPM cm^{-2}), I_{atm} is the local fallout inventory (DPM cm^{-2}), and A_{catch} is the assumed constant concentration of ^{210}Pb in catchment-derived sediment (DPM g^{-1}). The accuracy of this CICCS model (constant initial concentration and constant sedimentation rate) depends on several important assumptions: 1) the mean ^{210}Pb activity of river-derived sediment is constant; 2) although variable on an annual timescale, the sedimentation rate is roughly constant over decadal timescales; 3) atmospheric fallout is constant over decadal timescales; and 4) the total depth of coring is sufficient to reach background supported ^{210}Pb activity, such that I_{total} is properly determined. The CICCS procedure appeared viable in initial tests at a small, intensively documented location (a ~ 100 m x 100 m patch of grassy floodplain) along the River Culm (channel width ~ 12 m), U.K. However, the ideal ^{210}Pb activity profiles characterize a floodplain study location of extraordinary regularity and homogeneity (Figure 4.1), conditions that are not typically prevalent elsewhere.

To explore the application of CICCS to a large, dynamic, and heterogeneous fluvial system, Goodbred and Kuehl (1998) measured accumulation rates across a large floodplain/delta complex in the Bengal Basin using ^{137}Cs and ^{210}Pb geochronology. With their 60 sample cores, they were able to distinguish variations in sedimentation rate for the fluvial braidbelt, the distal floodplain, and the low-lying bils (bottomland basins). Comparing results from the two radionuclides and realizing that ^{210}Pb is primarily adsorbed by the clay fraction of sediment (Cremers et al., 1988; Goodbred and Kuehl,

1998; He and Walling, 1996a), they proposed a revision to (1) to account for natural spatial and temporal variations in the clay content of sediment:

$$R_{Pb} = \lambda_{Pb} \frac{I_{total} - cI_{atm}}{f_{clay} \rho A_{clay}} \quad (2)$$

Here, R_{pb} is the sedimentation rate (cm yr^{-1}), f_{clay} is the clay fraction of sediment, ρ is the bulk sediment density (g cm^{-3}), A_{clay} is the assumed constant activity of clay-sorbed ^{210}Pb in river sediment (DPM g^{-1}), and c is an empirical focusing factor to account for differences in the floodplain deposition of meteoric ^{210}Pb. Goodbred and Kuehl (1998) present compelling evidence that the clay fraction in floodplain sediment varies significantly across the Bengal Basin and that the modified CICCS approach in (2) provides a good agreement between accretion rates determined independently with ^{210}Pb, the ^{137}Cs total penetration method, and the ^{137}Cs inventory method. Their CICCS results are most persuasive for floodplain locations distal from the main channel; braidbelt and channel-proximal floodplain ^{210}Pb activity profiles do not exhibit clean monotonic declines in activity to a supported background level (Figure 4.2), suggesting that the CICCS model may not be appropriate for such dynamic locations.

A benefit of the CICCS model for ^{210}Pb geochronology is that entire core samples are homogenized to determine bulk-averaged ^{210}Pb activity, requiring the measurement of only one sample activity per core. However, such an assumption of quasi-continuous sedimentation downcore to a supported ^{210}Pb activity precludes the recognition of 1) large discrete deposition events spanning much of the core, and 2) cases where background activity is not reached within the core. Consequently, it not clear if the CICCS model is indeed appropriate for the majority of such homogenized cores, and therefore the reported rates of sediment accumulation are suspect, particularly those for dynamic environments near the active channel. Furthermore, the assumption of constant initial concentration of ^{210}Pb in river sediment (or in the clay fraction of that sediment) has not been explored in much detail, despite concerns that it may vary significantly between floods (He and Walling, 1996a). These prior studies have made significant

contributions towards developing a new framework for the application of radioisotope geochronology to floodplains, but further work is needed to ascertain if the CICCS model is appropriate for dynamic, heterogeneous environments near channels.

Building upon this previous research, this paper presents lessons learned during an extensive study (Chapters 2 and 5) of floodplain sedimentation with ^{210}Pb radioisotope geochronology along a 800 km sinuous section of the Beni River as it traverses 450 km across a large foreland basin. Hundreds of core samples have been collected throughout the floodplain, for a wide variety of channel-floodplain geometries, distances from the channel, and locations across the Beni foreland basin. Because these cores were all sampled at discrete depths, and not bulk-homogenized, all results are in the form of clay-normalized ^{210}Pb activity profiles, facilitating the evaluation of the CICCS model for this large, important fluvial system. The data suggest that the fundamental assumptions of the CICCS model are inappropriate for the Beni foreland. In its stead, a new procedure for ^{210}Pb geochronology is proposed which offers results with higher temporal resolution, better model verification and error-control, and greater flexibility for quantifying rates and processes of sedimentation within dynamic channel-floodplain systems.

Study area

The Bolivian Llanos (Figure 4.3) is an excellent locale to study active river-floodplain systems and floodplain sedimentation within foreland basins. Besides the availability of well documented sediment fluxes and neotectonics (Chapters 2 and 6), the basin is essentially pristine, without levees, dams, roads, significant deforestation or cultivation (no mixing of the floodplain to affect the geochronology), or other anthropogenic complications detracting from study of natural floodplain and fluvial processes.

This study focuses primarily on the reach of river between Rurrenabaque and Riberalta (Figure 4.3, Pocket Material), which traverses the entire foredeep,

forebulge, and secondary back-bulge basin. At Rurrenabaque, the Beni has a drainage area of 68,000 km^2 and a mean annual discharge of 2,200 m^3/s (Guyot, 1993), with recorded flood discharges of > 20,000 m^3/s and regularly in excess of 15,000 m^3/s (Maurice-Bourgoin, 2001). From an elevation of 190 m (above mean sea level) at Rurrenabaque, the Beni flows along ~ 800 km of channel as it crosses its foreland basin and descends to about 120 m elevation at Riberalta, where it has a total basin area of 119,000 km^2. This reach is remarkable in that there is only one major tributary, the Madidi River, along its entire course.

Numerous survey transects were established across the Beni floodplain, including core samples and topographic measurements approximately every 50 m (an example site is depicted in Figure 4.4). These data were combined with system-wide surveys of topography and granulometry (Chapter 2), and an extensive GIS analysis of channel migration over the past four decades (Chapter 3). Together, these data can help quantify rates of sediment exchange between the channel and floodplain and net sediment deposition within the Beni foreland (Chapter 2). This paper presents the motivation for and development of the CIRCAUS methodology for ^{210}Pb radionuclide geochronology employed elsewhere (Chapter 5) to determine rates and processes of sediment accumulation across the Beni floodplain.

Field and laboratory methods

The principal sampling excursion occurred during August and September of 1999, during the dry season when the river and floodplain are most accessible and the river stage is relatively constant. Cores and sediment grab samples were collected across the channel and onto the floodplain in standardized locations along with topographic surveys, as discussed in detail in Chapters 2 and 5.

For the core samples, dry loose leaf litter on the forest floor was brushed aside, revealing a surface of floodplain sediment. Then, a 65-cm steel sampling probe was inserted, collecting a 2.5-cm-diameter soil core within an internal clear polyethylene tube

(slightly oversized such as to allow easy entry of the cut soil core). The cutting tip of the soil probe sometimes jammed with a hard plug of sediment, preventing further entry of sediment into the probe. Therefore, the resulting sample sometimes was shorter than the expected 65 cm. Field observations and laboratory X-radiographs led me to conclude that this "jamming" does not lead to substantial core compaction. In some cases, a hole was augered to a 65 cm depth adjacent to the first sample, cleaned, and then a second 65 cm core was taken from 65–130 cm depth for a combined total core depth of 130 cm. Since the sediment is cohesive there was little or no sidewall collapse. At a few additional locations, samples were collected to > 200 cm depth using a soil auger and extension rods. Grab samples were also collected down the cut banks at most transect sites, providing vertical activity profiles to an effective depth of 3 – 6 m into the floodplain. Further details, including the collection and analysis of the sediment grab samples, are discussed in Chapter 2.

Prior to cutting for analysis, all floodplain cores were photographed at two angles (orthogonal) with an X-ray machine (Faxitron Cabinet X-ray Model 43855C) designed for imaging sediment cores. These images allowed evaluation of the sedimentary structures and identification of potential disturbances within each of the floodplain cores. After imaging, the cores were cut at discrete depth intervals (typically at 2 cm intervals within the top 10 cm, and 2.5 cm intervals at depth) with a cleaned narrow-kerf saw, dried in aluminum sample pans at 80° C for 24 hours, weighed, and then two ~ 5 gram samples (dry weight) from each depth interval were separated for further analysis. Organic debris (twigs, roots, leaves, etc.) were removed, although most floodplain samples are free of such material. One of these resulting samples was analyzed for sediment granulometry, using a combination of wet-sieving at 63 microns (to determine sand fraction) and detailed analysis of the silt and clay distributions using a Micromeretics Sedigraph 5100 particle analyzer calibrated for river sediment. I have optimized the laboratory procedures for the best possible determination of the sediment clay fraction (particles smaller than 4 microns). (Modifications include extended

ultrasonic agitation times, prolonged wet sieving with large volumes of liquid followed by additional desiccation and agitation, higher volumetric sediment concentrations (6%) for Sedigraph analysis, duplicate Sedigraph runs with settings adjusted for river sediment, frequent machine and procedural calibrations, and an aggressive error-checking process that triggers reruns for all questionable samples). To determine the ^{210}Pb activity using the ^{210}Po method (Benniger et al., 1979; Nittrouer et al., 1979), the second 5 g sample was spiked with ^{209}Po and put through a series of sequential acid leachings (HNO_3 and HCL) over a hot plate. Ionic polonium was then autodeposited onto a silver planchet suspended in the leachate for ~ 24 hrs. Resulting samples are counted in an alpha spectrometer (EG&G Ortec) for 48 – 100+ hours (as long as is needed to record at least 1000 decays of ^{210}Po). Supported levels of ^{210}Pb were determined by measuring the down-core asymptote of clay-normalized ^{210}Pb activity in numerous floodplain and terrace cores. All necessary corrections for radioactive decay were made to account for the time intervals between sample collection in the field, ^{210}Po plating, and alpha counting, and error bars were determined for all samples. Direct gamma assays of ^{210}Pb and ^{137}Cs activities were also measured for a number of samples using two identical LEGe detectors (Canberra model GL2020R), but ^{137}Cs activities were found to be insufficient for reliable geochronologic application.

^{137}Cs may be absent from the study location for a number of reasons. First, the remote southern hemisphere location is far from bomb test sites. Second, precipitation and moisture recycling are intense over the Amazon Basin, so any remaining ^{137}Cs would be scavenged as the contaminated air is carried by the prevailing winds over 1000s of kilometers of intervening tropical rainforest between the South Atlantic and the study location. Third, the Beni headwaters in the Andes exhibit extremely high erosion rates (Chapter 1), with many regions expected to lose 5 – 10 cm of soil or more during the 3 decades since ^{137}Cs meteoric fallout ceased. As such, most of the ^{137}Cs deposited in Andean soils may have already left the watershed. Furthermore, the enormous sediment interchanges and transport across the Beni Foreland (Chapter 2) would further

dilute any remaining ^{137}Cs signal. But whatever the reason, if ^{137}Cs is functionally absent from one of the largest tributaries to the Amazon River, it suggests this radionuclide might be of limited use elsewhere within the Amazon basin.

The ^{210}Po method for determining ^{210}Pb activity using alpha counting offers several significant advantages over direct gamma assays. First, 24 samples are prepared at a time and up to 24 can be counted simultaneously in the UW laboratory, as compared to only 2 samples for the gamma spectrometers. Multiple-bank alpha spectrometers are both low-cost and low-maintenance. Second, alpha samples require only 5 grams of mass, and may be as little as 2 grams, far less than the 50 – 80 grams required to fill a typical container used for gamma assay. This allows for shorter depth intervals (2 cm) within smaller cores (2.5 cm diameter), greatly simplifying the logistics of field sampling campaigns across remote jungle floodplains. Third, the acid leaching process utilized for the ^{210}Po method removes the radionuclide only from the surfaces of the sediment for alpha assay, the same ^{210}Po which is in secular equilibrium with the unsupported and supported ^{210}Pb accounted for by the conceptual model. In addition to this surface activity, gamma assay will also record any ^{210}Pb activity trapped within sediment particles themselves, adding noise to the resulting measurements. Fourth, gamma assay is fraught with a number of instrument sensitivity and sample geometry calibrations, including the correction for self-shielding within the sediment itself (Cutshall et al., 1983), which depends on the sediment grain size, density, and the mineralogy (this can be quite variable, depending on clay abundance). Because it simply determines the activity ratio between ^{210}Po and a known spike of ^{209}Po, the ^{210}Po method offers few such problems, and is therefore used almost exclusively throughout this study.

Core results: sedimentation not constant and supported background not reached

For the floodplain locations surveyed across the Beni Foreland, X-radiographs (Figure 4.5) for all 139 cores typically indicate a moderate-to-low-energy depositional environment (Chapter 5). Core lithology frequently exhibits fine horizontal laminations

and other micro-structures at a sub-millimeter scale, suggesting that the floodplain sediment has not been significantly disturbed since deposition and that bioturbation is negligible at most locations (Chapter 2). These results indicate an ideal environment for the application and interpretation of radionuclide geochronology at a high vertical resolution, because there are no complications associated with sediment mixing due to crop ploughing, grazing, and bioturbation prevalent in previous studies (Goodbred and Kuehl, 1998; He and Walling, 1996b).

For many of the 78 floodplain cores cut and analyzed to date for ^{210}Pb geochronology (Appendix C), grain size changes significantly over the depth of the core. Because ^{210}Pb activity is almost entirely contained within the clay fraction of sediment (Goodbred and Kuehl, 1998), this means that the sediment activity (A_{sed}) must also change in proportion to clay. For the case of a dynamic river which migrates across its floodplain, the clay fraction within floodplain sediment is probably some approximate function of the distance from the channel – therefore, as the river migrates towards a particular floodplain location, any deposited sediment will become increasingly coarse with closer proximity to the channel (Figure 4.7 depicts a good example of such an upwards-coarsening pattern). Because the Beni River has migrated towards many of the sample sites over the past few decades (Appendix A) and because of the heterogeneous nature of crevasse splay deposits and of floodplain sedimentation in general, many cores exhibit a considerable variation in clay fraction with depth. Therefore, the core-averaged clay normalization strategy depicted in equation (2) is not applicable to such a dynamic granulometric environment, because the clay fraction can vary significantly throughout the core. For example, consider the case of two 100 cm floodplain cores, the first with a uniform clay fraction of 50%, and the second with 20% clay for the top 50 cm and 80% clay for the bottom 50 cm (both having a bulk-averaged clay content of 50% over the entire core). For both cores, assume that the top 50 cm contains clay with an unsupported ^{210}Pb activity of 6 DPM per gram clay, the bottom 50 cm contains clay with an activity of 3, and below the 100 cm core depth the unsupported activity is zero.

Following a normalization procedure equivalent to that expressed in (2), the first core would have a bulk sediment activity of 2.25 DPM/g, and a clay-normalized ^{210}Pb activity of 4.5 DPM/ g clay. However, the second core exhibits a much lower bulk activity of 1.8 DPM/g and a clay-normalized ^{210}Pb activity of 3.6 DPM/g clay, which would result in a significantly lower average deposition rate for the 100 cm interval according to either equations (1) or (2). However, both these cores have identical radiometric sedimentation histories: 50 cm of sediment was deposited, followed by a hiatus in sedimentation during which the ^{210}Pb activity decayed, and then a second 50 cm of sediment was deposited. Although the preceding example is for a simplified case of two sedimentation events, cores containing many events (quasi-annual sedimentation) would exhibit the same fundamental problem with bulk-averaging if the clay fraction of the sediment varies throughout the core.

One approach that might account for variations in sediment clay fraction is to utilize a discrete normalization procedure for each separate sample depth, with all reported sediment activities, A_{csed}, normalized to the associated sediment fraction < 4 μm (e.g., ^{210}Pb activities are reported as DPM per gram clay):

$$A_{csed} = \frac{A_{sed}}{f_{clay}} \qquad (3)$$

This concept is akin to considering that clay is the only focus of the ^{210}Pb radionuclide geochronology, with the sand and silt traveling along. Given the very strong affinity of ^{210}Pb for clay particles (Goodbred and Kuehl, 1998; He and Walling, 1996a) and the lack of floodplain disturbance in the Beni Foreland, it is therefore appropriate to utilize clay as a datable tracer suspended within a matrix of other coarser material. This approach and the determination of ^{210}Pb activity at discrete floodplain depths offers the most flexible and robust approach for dating sediment within river floodplains, because it both provides correction for heterogeneous core granulometry and presents full representation of discrete depositional events. In a practical sense, it typically produces the smoothest ^{210}Pb activity profiles, those which exhibit a monotonically-decreasing abundance with

increasing sample depth. Consequently, all cores were processed with this enhanced procedure, so as to offer the best possible insight into the processes and rates of floodplain sedimentation.

Of the 78 cores processed to date, fewer than 5% show any evidence for constant sedimentation (Table 4.2, Figures 4.6a-d). Rather, most cores exhibit one or two regions of relatively constant clay-normalized ^{210}Pb activity, termed 'plateaus,' separated by rapid changes in activity. The top 5 – 15 cm of many cores exhibit a considerable increase in activity, a 'meteoric cap' due to the wet fallout of atmospheric ^{210}Pb (discussed later). With just one or two discrete depositional events accounting for the entire core depth over a period typically spanning several decades (Appendix C, discussion in Chapter 5), it is not appropriate to consider floodplain sedimentation as constant. Furthermore, only one of the floodplain cores reaches the supported background activity of 1.4 DPM/g clay, as determined from the terrace cores (note that all plots depict total ^{210}Pb activity; unsupported ^{210}Pb activity is equal to this total amount minus the supported activity of 1.4). This suggests that because of very high sedimentation rates across the Beni Foredeep (Chapter 5), the 65 – 160 cm cores were not deep enough to reach background supported activity (and neither were deeper samples taken 3 – 6 m down the cutbank at two dozen locations). As such, even in the case of uniform down-core granulometry, any attempts to determine I_{total} by bulk averaging and application of the CICCS method would result in a substantial underestimate of the average annual accumulation rates. And without discrete down-core samples, the CICCS approach also does not provide a means to evaluate its own viability, so it is therefore unclear whether its prior application has always been appropriate.

There are a few floodplain locations sampled within the Beni Foreland which do indeed appear to be characterized by quasi-annual sedimentation. For example, Figure 4.7 depicts a site which has received ~ 1.9 cm of sediment annually over the recorded depth of 160 cm. However, in this case the CICCS model would still not apply, because

the clay fraction declines up-core by a factor of five and the lowest ^{210}Pb activity (2.4 DPM/ g clay) is well above the supported background. Despite these complications, the observed activity profile is straightforward to reconstruct using the discrete depth approach for the ^{210}Pb activity of clay (model line depicted in Figure 4.7), given the following assumptions: 1) sedimentation is steady-state; 2) the ^{210}Pb activity of clay in freshly-deposited river sediment is constant over time for that particular reach of channel (6.5 DPM/ g clay); 3) the meteoric fallout of ^{210}Pb is constant (44 DPM/cm^2), and 'grows' into the surface sediment across a depth window of 5 cm (a common depth by which most of the meteoric ^{210}Pb has been adsorbed in stable terrace cores). This approach, termed constant initial reach clay activity and constant sedimentation (CIRCACS), generally provides an excellent model fit for the few study cores which exhibit the steady monotonic decline in ^{210}Pb activity associated with constant sedimentation, including faithful depiction of the characteristic activity spike typically observed at 5 – 10 cm depth in such cores. Therefore, the assumption of constant sedimentation is sometimes appropriate, but a more labor-intensive approach than CICCS may be required to model the resulting ^{210}Pb activity profiles.

Results of the river sediment survey: initial concentration not constant

The CICCS model assumes that the input concentration of ^{210}Pb is constant for river sediment. As recognized by Goodbred and Kuehl (1998) and previously discussed, ^{210}Pb activity must be normalized to clay abundance at each site to account for spatial variations in floodplain granulometry. Here, I have suggested that this adjustment also should be made down-core for discrete samples, so as to account for temporal variations in the granulometry of river sediment conveyed to each floodplain site. Having thus decided that it is most appropriate to measure ^{210}Pb activity in terms of DPM per gram clay, it is imperative to investigate if this clay-normalized activity is both spatially and temporally constant for fresh river sediment.

Figure 4.8 depicts a variety of activity measurements for fresh river sediment, plotted versus UTM latitude (as discussed in Chapter 2 and 3). The activity of Beni River sediment clearly declines downstream across the foreland basin. This trend is particularly compelling for the grab samples taken from topographically high locations on point bars (the vegetated "VB" locations discussed in Chapter 2). These locations would principally receive sediment during higher flood stage, when the discharge conditions are liable to achieve greater homogeneity. The open circles represent samples from other locations across the bars (and some high cutbank locations), which are inherently more variable, due to the vagaries of sediment input by bank collapse during falling river stage, variable upstream sediment sources during moderate stages, or lack of recent sediment supply at some of the highest cutbank locations. Three sediment samples were filtered from the water during a moderate stage event, and depict only a minor decrease in activity. Finally, the gray circles portray the average clay-normalized ^{210}Pb activity as determined from floodplain cores using the empirical CIRCA technique (developed in the next section). These values represent river sediment conveyed onto the high cutbank floodplain by crevasse splay deposits during infrequent floods of extraordinary magnitude (Chapters 2 and 5), which probably epitomize the most uniform conditions for radionuclide homogeneity during floodplain deposition. Consequently, as all three data sources attest, clay-normalized ^{210}Pb activity is not constant for the Beni River system, but instead exhibits a rather marked downstream decrease over 800 kilometers of channel. Even the best-case scenario of a very large flood does not support the concept of constant initial concentration of ^{210}Pb for fresh sediment, and the lower stages exhibit far more temporal and spatial variability. Therefore, for the Beni River system, a new geochronological approach is needed to quantify sedimentation within such a dynamic fluvial environment.

Modeling and measuring constant initial reach clay activity

To develop a geochronological model appropriate for rivers and their floodplains, it is important to consider and model the processes responsible for the conveyance and exchange of clay-associated radionuclides. The key to most effective methods of radionuclide geochronology is determining the initial concentration. Figure 4.8 suggests that, despite some noise in the grab samples, there appears to be a monotonic down-channel decrease in activity associated with geomorphic processes, one that may be modeled with a study of sediment fluxes within the Beni Foreland.

As presented in Chapters 2 and 3, the Beni river migrates rapidly across its floodplain, excavating enormous quantities of sediment from the cutbank side of meanders and redepositing most of this material onto the point bars (Figure 4.9). The significance of this process has implications for the down-channel budget of ^{210}Pb, because the cutbanks contain material which is radiometrically older than the river sediment. Therefore, the process of channel migration orchestrates a continuous downstream dilution of the ^{210}Pb activity of riverborne clay – a similar process has been documented in a subaqueous environment for the Wilmington Submarine Canyon (Sanford et al., 1990). Because these migration fluxes have been quantified, along with measurements of the clay percentages of all classes of river sediment and the approximate radionuclide content of the cutbanks across the Beni Foreland (Figure 4.10), it follows that the sediment budget of clay and the associated downstream decline in ^{210}Pb activity can be determined.

For the purposes of this exercise, I will assume that the input concentration of ^{210}Pb from the Andes at Rurrenabaque is relatively constant during the largest floods. In reality, there is probably some variation in this input activity depending on the geomorphic source of the sediment eroded upstream in the source basin. For example, during the early rains, erosion of surface soils high in ^{210}Pb activity (adsorbed from meteoric fallout) is likely to dominate the signal, especially from areas recently deforested or cultivated (this mechanism is supported by field observations of erosion

and records from gauging stations throughout the basin, which tend to show high sediment concentrations with the early rains). As the wet season progresses, hillslopes become more saturated, typically leading to deeper mass wasting of colluvium, and river stages rise, remobilizing previously-stored alluvium (such processes are readily apparent and quite impressive during the rainy season). These large volumes of stored material, which might be expected to have lower activities (because they are shielded from fallout ^{210}Pb and are geochronologically older), would both serve to decrease and to stabilize the ^{210}Pb concentration at Rurrenabaque. This homogenization effect would probably be greatest at the height of the wet season during infrequent catastrophic storms, when hillslope and fluvial processes throughout the entire 68,000 km^2 contributing basin are all simultaneously realized – at such a time, the myriad heterogeneous ^{210}Pb contributions of individual failures or disparate processes would all tend to integrate and average together throughout this large Andean basin, as sediment discharges approaching 70 Mtonnes/day occur at Rurrenabaque during major cold phase ENSO events (Chapter 5). Once the storm passes and river stage falls, the sediment discharge then drops back to levels where individual massive hillslope failures (of frequent occurrence in this basin) and other stochastic processes might more easily affect the concentration of ^{210}Pb in river clay at Rurrenabaque. While speculative at this juncture, this conceptual process of the homogenization and stabilization of ^{210}Pb activity during large floods is in agreement with the available data. Near Rurrenabaque, channel samples illustrate that the input concentration varies from 5.5 – 8 DPM/g clay (Figure 4.8), and a single assumed value of 6.5 DPM/g clay during all the largest floods is found to match the floodplain samples (Figure 4.12b).

Assuming this input concentration and applying the mass fluxes determined in Chapter 2 (Figure 4.9) along with their associated clay content and the measured ^{210}Pb activity of the cutbank deposits (Figure 4.10), it is a straightforward accounting exercise to quantify the exchange of clay within each 10 km UTM latitude river reach (Figure 4.11a). The volume of material eroded from the cutbank by channel migration is

multiplied by its associated density and clay fraction to determine the mass of clay returned to the channel. The mass of clay deposited within the 10-km UTML reach is calculated in a similar way for sediment deposition on the bar, bed, and floodplain. Because the channel migration, sediment input, and floodplain deposition rates are decadal averages (Chapters 2 and 5), I must assume here that, while they are augmented during large floods, these various process rates exhibit approximately the same ratio as the long-term averages. This assumption is reasonable, because the decade-averaged values for sediment input at Rurrenabaque and the processes of floodplain deposition and channel migration are all known to be dominated by extreme events (Chapter 5). Given these clay fluxes for any particular 10-km reach, the measured activity of the eroded cutbank clay (Figure 4.10), and assuming that all deposited clay in that reach has the same activity as the clay input from immediately upstream, it is a simple mass balance and mixing exercise to calculate the resulting clay flux out of the reach and its associated ^{210}Pb activity (Figure 4.11b). The predicted downstream decline in ^{210}Pb activity closely matches that determined empirically from the floodplain cores. To pursue this model further, Figure 4.12a depicts the same procedure for a range of declining channel migration rates without floodplain sedimentation. This example illustrates the effects of changing the migration rate, and therefore can be utilized to explain much of the variation observed in the grab samples (Figure 4.12b). The rest of the observed downstream variability in the ^{210}Pb activity of clay is probably due to a combination of 1) variation in the input concentration at Rurrenabaque and 2) accelerated cutbank erosion rates during flooding. For the Beni River, rapid cutbank collapse may be a significant process during the period of falling river stage after large floods; this has been observed in the field and is also a common phenomenon for other large sinuous sand-bedded rivers like the Beni (Dunne, 2001). As such, the ^{210}Pb activity of river sediment would be diminished by the large input of cutbank material during these times, as apparently reflected in the grab samples (Figure 4.12b). Despite these temporal heterogeneities, the modeled clay activity provides a practical

understanding of the downstream variation in the ^{210}Pb activity of clay, reflecting more homogeneous conditions present during the largest flooding events, those which also orchestrate sediment deposition across the floodplains (Chapter 5). Therefore, these model results for the constant, initial reach-averaged clay activity offer a practical means to date river sediment deposited on floodplains, because a constant initial concentration can be dated with standard radionuclide geochronology. This flux-based modeling approach is termed the numerical technique for determining the constant initial reach clay activity, or 'numerical CIRCA,' in contrast to 'empirical CIRCA,' discussed next.

The problem with the numerical CIRCA approach is that it is time-consuming to determine all river sediment fluxes for a large system like the Beni, not to mention the effort required to measure cutbank activities throughout the system. Fortunately, there is a much simpler empirical means to determine the same down-channel decrease in ^{210}Pb activity that relies on a few simple principles. First, one must establish the radionuclide boundary conditions with a limited number of fresh floodplain samples from channel-proximal locations of *moderate* height above the channel (not too high or low), or preferably, from river sediment filtered directly from floodwaters. Second, a brief consideration of channel stability will ascertain the fundamental importance of channel migration in terms of the expected down-channel decline in ^{210}Pb activity. For stable channels, no significant decline would be anticipated. For mobile channels, the CIRCA can be projected to decline monotonically in a downstream direction, with the rate of decline a direct function of channel migration. The third and final step is to collect floodplain cores throughout the study area and to analyze them. During the course of this work, it will soon become evident that there are optimal input concentrations of ^{210}Pb that provide dates for sedimentation events that are consistent with independent means of dating. In this study, I have compared the dates of discrete sedimentation events to the independent dates of meteoric caps, but ^{137}Cs geochronology, known dates of major floodplain deposition, or other alternative means could just as easily be employed. Furthermore, for the Beni Foreland there were a number of floodplain

locations which had received fresh river sediment during the large flood of the preceding rainy season – these cores provided a lower bound for the possible ^{210}Pb values of river sediment at those reaches (and necessarily, all reaches farther upstream). In practice, the first two principles will have already provided a relatively narrow range of allowed ^{210}Pb activities for each reach, which this third step will further constrain to produce a well-defined empirical determination of CIRCA. *Because the same values are used consistently for all cores within each reach, there is no "fine-tuning" of the geochronology method on a core-by-core basis.* The more floodplain cores that are analyzed, the less significant is this tuning effect on any individual dated core. For the Beni River, this empirical CIRCA method produces values that are a close match to the numerical CIRCA method (Figures 4.11 and 4.12), that concur with an independent means of dating, and provide compelling results in a strong temporal association with major floods (Chapter 5). Consequently, such an empirical approach to determining CIRCA may be useful for dating floodplain sediment in other river systems with Unknown Sedimentation, that is, a CIRCAUS method for ^{210}Pb geochronology.

Identifying and dating activity plateaus

As previously discussed, most floodplain locations across the Beni Foreland exhibit one or two regions of relatively constant clay-normalized ^{210}Pb activity, separated by rapid changes in activity (examples in Figures 4.6a-d). Whenever activity is constant over a substantial vertical distance, the CIRCA assumption implies that all of this sediment is of the same radiometric age. Because these features are so prevalent, they are termed activity 'plateaus,' which are interpreted as single sedimentation events. A plateau will typically be bounded by an up-core rise in activity and a down-core drop, with a zone of constant activity across the plateau. The basic dating procedure is to average the value of all activities within the plateau and then to date this average:

$$T_{sed} = -\ln\left(\frac{A_{csed} - A_{csup}}{A_{CIRCA} - A_{csup}}\right) \Big/ \lambda_{Pb} \qquad (4)$$

Here, sediment age in years (T_{sed}) is determined as a simple decay function of unsupported clay-normalized ^{210}Pb activity (clay-normalized sediment activity, A_{csed}, minus clay-normalized supported activity, A_{csup}) and the corresponding unsupported clay-normalized CIRCA value (A_{CIRCA} - A_{csup}). The accuracy of the resulting date depends in large part on how well the plateau is defined by the number and consistency of the constituent points. Environments with more bioturbation would tend to exhibit smearing of the plateau edges, but the centers should remain well-defined so long as the effective mixing distance is less than half of the total plateau depth. Because the CIRCAUS method assumes nothing about the nature of floodplain sedimentation, the analytic approach is iterative by necessity. This proves to be a strength of the method, because core sections initially thought to represent plateaus can be selected for additional sampling at greater densities to better investigate these suspect plateaus (the first laboratory run for any core typically consists of only 5 – 8 discrete points along the entire core). As a result, plateaus can be ultimately defined to a depth resolution limited only by the site bioturbation, core diameter, and the enthusiasm of the researcher. As a matter of accuracy, it is important to choose points which best define the limits of the plateau, as well as enough points across the center to verify that the ^{210}Pb activity is indeed relatively constant.

Figure 4.13 presents an example of the power of the approach. In this core, ^{210}Pb has been determined at every possible depth interval, allowing for full visualization of sedimentation processes. At first glance, sedimentation seems well-described by a CIRCACS model with an annual sediment accumulation of 0.9 cm/yr. However, further inspection reveals a plateau (dated 1983) from 18 to 41 cm and a second plateau of lower activity (dated 1949) from 41 to 65 cm. From 0 to 18 cm lies a meteoric cap, dated 1982 (see discussion in the next section). This core provides an example of how two distinct sedimentation events separated by 34 years can combine with a 27-year-old meteoric cap (ingrown during the time since the last sediment was deposited at this site) to provide a false impression of constant sedimentation. A lower resolution sampling of this core

would likely support the CS interpretation, but the full dataset illustrates that sedimentation occurs only every few decades. This example illustrates that the veracity of the CIRCAUS method relies in large part upon the vigilance of the researcher, both in 1) selecting the appropriate sample points to test all significant sedimentation hypotheses for each core, and 2) in maintaining suitable laboratory procedures to resolve clay-normalized ^{210}Pb activity at the necessary accuracy and vertical precision.

Identifying and dating meteoric caps

For any given floodplain location, meteoric ^{210}Pb falls out of the atmosphere at an approximately constant annual rate, rapidly adsorbing to the first fine particles that it contacts. If a surface is aggrading, this meteoric activity is incorporated into the most recently deposited sediment, as previously discussed. If a floodplain surface is stable, without aggradation, the meteoric ^{210}Pb will adsorb into the clay nearest the surface, forming a 'meteoric cap.' The best examples of these caps are on elevated river terraces, where no deposition has occurred for hundreds of years.

Terrace cores (Figures 4.14 a-b) provide several very important pieces of information. First, they provide a means to determine the supported background activity of river sediment using the same alpha counting technique that is employed for the rest of the core samples (as previously discussed, gamma counting adds a suite of potential errors). Because the old river sediment on terraces is mineralogically similar to the modern river sediment, this approach provides an ideal means to determine unsupported activity. There is some conceptual question as to why supported activity should be normalized to clay content, but in practice such an adjustment often results in smoother plateaus of more uniform activity (preferential adsorption by clay evidently applies to supported activity as well as unsupported activity). Second, all unsupported ^{210}Pb activity in a terrace core is in dynamic equilibrium with meteoric fallout such that decay exactly equals input. Therefore, for any such stable locations (older than 5 half-lives), total ^{210}Pb inventory (not clay-normalized) equals the meteoric rain rate (I_{atm}). Third, the

shape of the meteoric cap provides essential insight into the adsorption mechanics and soil disturbance in nearby floodplain cores. For terrace locations, almost all of the unsupported activity is accounted for within the top 10 cm of core, with most of that amount being adsorbed in the top 5 cm. Consequently, it follows that ^{210}Pb adsorbs very rapidly upon entering the soil, and that it is thereafter immobile. Furthermore, there is very little soil mixing at these locations; the meteoric cap has not been noticeably spread out over depth. All of these observations for terrace cores also can be applied to any surface that has been stable for some period of time, even if only for a decade.

Consider the case of a floodplain sedimentation event. A fresh pulse of material arrives from the river, blanketing the core location to a depth of several tens of centimeters with sediment of a uniform clay-normalized activity as approximated by the CIRCA method. As years pass without further sedimentation, two processes affect the ^{210}Pb profile. First, the activity of the entire event plateau decays identically across the entire deposit, "lowering" the plateau height. Second, meteoric fallout grows an ever-larger meteoric ^{210}Pb cap in the top ~ 10 cm of the deposit. The total activity of this meteoric cap above that of the plateau represents the total inventory of atmospheric ^{210}Pb fallout within the cap, I_{cap} (DPM/cm^2). Assuming a relatively constant annual fallout, the age of this cap, T_{cap} (yr) can be expressed as:

$$T_{cap} = -\ln\left(1 - \frac{I_{cap}}{I_{atm}}\right) \Big/ \lambda_{Pb} \qquad (5)$$

Such a procedure can be used to date meteoric caps up to about a century in age. Because the process of cap growth is entirely independent from the CIRCA determination of the initial sediment activity used to date the plateau in equation (4), this proposed new technique for dating meteoric caps can be used to verify the CIRCA values. Effective cap dating requires three fundamental conditions. First, the meteoric fallout must be established and relatively uniform. Second, clear evidence for a plateau must exist to a depth well beyond that of the apparent meteoric cap, and all indications (activity, granulometry, X-radiographs, et cetera) must point to a single depositional

event of uniform age without any further sedimentation. Bioturbation may occur to a limited depth, so long as both the cap and the plateau remain clearly identifiable such that I_{cap} can be determined with good confidence. Third, because most of the cap activity is typically within the top five centimeters, the floodplain surface cannot have been disturbed in any way such as to remove even 1 – 2 cm of sediment, and the coring and analytical techniques must similarly preserve this surface material. In practice across the Beni Foreland, it is this third condition that was most commonly violated, because the initial field and laboratory techniques did not always faithfully record the top few cm of core. As a result, the ages determined for meteoric caps are sometimes younger than those of the underlying activity plateau. However, many cores do show close agreement between the two ages, including for cores sampled more recently (using improved field and laboratory techniques) from another large, dynamic river system, the Mamore (Figure 4.15). Consequently, the proposed procedure for dating meteoric ^{210}Pb caps shows promise for use as an independent radioisotopic geochronometer.

An interesting question regarding meteoric cap mechanics is why they are not apparently preserved at depth on top of older sedimentation plateaus within cores with two or more sedimentation events (e.g., Figures 4.6d and 4.13). One likely hypothesis is that most of the limited number of cases of two sedimentation events (Table 4.1) do not yet have enough sampling resolution to properly depict these buried caps (e.g., Figure 4.6d). For the few cores that do have the necessary resolution (Figure 4.13), there are two possible answers. First, the elevated fallout activity (but decayed since burial) of the meteoric cap on the top of the older activity plateau could be mistaken for part of the overlying younger plateau, implying a ~ 10 cm zone of uncertainty at the transition between two plateaus. Second, limited basal scour by the crevasse splay during the deposition of the overlaying sediment may have removed a few centimeters of floodplain surface material, erasing the previous meteoric cap. Regardless of the explanation, the identification and dating of activity plateaus would not be significantly compromised.

Summary

The proposed CIRCAUS approach to ^{210}Pb geochronology consists of several elements which together offer an effective means to date floodplain sedimentation in the vicinity of dynamic, heterogeneous river systems. First, the approach realizes that both the floodplain clay content and sedimentation rate may be highly irregular, necessitating the determination of clay-normalized ^{210}Pb activity (per equation 3) at discrete depths down each floodplain core. This is an iterative, adaptive process, with the researcher choosing additional sample points to properly resolve and date sedimentation events. Second, both a numerical and empirical means are provided to determine CIRCA across large river systems, along with insight into the potential and processes for variation in the ^{210}Pb activity of fresh river sediment. This approach allows appropriate recognition of the geomorphic processes that affect CIRCA, such that each river system can be evaluated for its suitability for the application of ^{210}Pb geochronology. Third, procedures are provided to date both episodic sedimentation events (equation 4) and cases of constant floodplain sedimentation (CIRCACS). This offers the flexibility needed to investigate environments with a wide range of sedimentation processes and rates. Fourth, there is a separate approach for dating meteoric caps above activity plateaus (equation 5), such that the dates of discrete sedimentation events can be independently verified. This provides an iterative, adaptive approach that can resolve sedimentation processes in heterogeneous floodplain environments.

Table 4.1. Unsupported ^{210}Pb activity for different sediment size fractions within floodplain soils, Bengal Basin (after Goodbred and Kuehl, 1998). Data suggest that ^{210}Pb is found only within particles smaller than 2 μm, especially for those particles < 0.5 μm.

Size Fraction (um)	Modal Diameter (um)	^{210}Pb Activity (DPM/g)
> 62.5	-	0.0
30-62.5	31.9	0.0
10-30	15.4	0.0
2-10	6.1	0.0
0.5-2	1.6	1.9
0.1-0.5	0.4	3.0

Table 4.2. Summary of results from all dated cores (Appendix C), including sample depths, associated dates, accumulation rates, and corresponding GIS channel distances. Minimum accumulation rates are determined by dividing the representative thickness of the deepest sample by its age (see Chapter 5 for details, Appendix A and pocket material for locations). For this chapter, the highlighted cores (in red) represent the only three locations which could legitimately be interpreted has having constant sedimentation. All of the other floodplain locations are characterized by episodic deposition of thick sediment deposits, followed by years to decades of no sediment accumulation.

Site	Site Name	deepest sample (cm)	partial depth (when not entire core) (cm)	CIRCAUS Date of Deposition	Corresponding GIS Channel Distance (m)	CS rate (cm/a)	Accumulation Rate (cm/ yr, minimum, all)	Bounded Accumulation Rate (cm/yr)
41	41RFC200	115		49	200		2.25	
	41RFC300	43		70	500		1.43	
	41RFC450	49		76	350		2.04	
	41RFC523	50		70	250		1.67	
60	60LFB5	52		98	5		26.00	
	60RFC5	56		98	150		28.00	
	60RFC50	25		88	700		2.08	
	60RFC100	48		88	750		4.00	
	60RFC150	50		72	2000		1.79	
a	60RFC200		15	74	2000		0.58	0.58
b	60RFC200	25		47	2800		0.19	
a	60RFC250		80	74	2000		3.08	3.08
b	60RFC250	120		49	2900		0.78	
	60RFC300		40	82	1300		2.22	2.22
61a	61RFC100		30	89	620		2.73	2.73
b	61RFC100	52		50	2400		0.44	
	61RFC200	53		77	1650		2.30	
62a	62RFC5		30	87	160		2.31	2.31
b	62RFC5	49		83	325		1.12	
	62RFC50	43		83	210		2.53	
	62RFC100	53		73	900		1.96	
	62RFC150	48		50	1500		0.96	
a	62RFC200		40	75	1000		1.60	1.60
b	62RFC200	59		50	1600		0.38	
63	63RFC5	53		77	1700		2.30	
	63RFC100	62		70	1800		2.07	
a	63RFC200		35	97	300		11.67	11.67
b	63RFC200	53		88	675		1.50	
64	64RFC5	33		90	260		3.30	
	64RFC50	43		73	480		1.59	
	64RFC100		37	82	575		2.06	2.06
	64RFC150	42		72	550		0.18	
	64RFC200	43		77	480		1.87	
59	59RFC50	48		55	50		1.07	
cb2	CB2 - 1998	156		87	300		12.00	
57	57RFC50	43		73	150		1.59	

Table 4.2. (continued)

cb1	CB1 - 1998	165			250	1.9	1.90	1.90
56	56RFC50	43		74	2500		1.65	
55	55LTC50	63		98	50		31.50	
54	54LFC50	53		97	225		17.67	
51	51RFC50	43		88	50		3.58	
a	51LFC5		40	84	5		2.50	2.50
a	51LFC50		44	84	50		2.75	2.75
b	51LFC50	53		74	50		0.35	
	51LFC100	53		73	100		1.96	
a	51LFC200		30	56	200		0.68	0.68
b	51LFC200	46		17	200		0.19	
a	51LFC300		25	55	300		0.56	0.56
b	51LFC300	53		43	300		0.49	
50	50RFC5	35		76	925		1.46	
	50RFC50	118			250	1.15	1.15	1.15
	50RFC50	118		49	800		2.31	
1	1LFC50	52		83	750		3.06	
2	2RFC50	53		74	225		2.04	
3	3A-1200M	50		54	1200		1.09	
	3B-1150M	43		55	1150		0.96	
a	3D-900M		23	49	900		0.45	0.45
b	3D-900M	43		14	1000		0.23	
	3E-20M	30		48	20		0.58	
6a	6LVB5		40	83	2500		2.35	2.35
6b	6LVB5	65		49	2000		0.49	
	6RVC5	54		82	2500		3.00	
7	7RFC50	58		88	400		4.83	
8	8RFC400	50		49	400		0.98	
9	9RFC50	53		75	400		2.12	
a	10LFC50		35	88	550		2.92	2.92
b	10LFC50	53		48	1000		0.35	
11	11LFC50	27		56	2000		0.61	
a	11LFC100		50	83	750		2.94	2.94
b	11LFC100	57		48	2000		0.13	
	11LFC150	63		88	675		5.25	
	11LFC200	53		88	725		4.42	
	11LFC250	53		87	775		4.08	
a	11LFC300		53	89	825		4.82	4.82
b	11LFC300	60		54	2200		0.15	
14	14RFB5	53		71	55		1.83	
a	14RFB50		35	71	100		1.21	1.21
b	14RFB50	43		44	100		0.14	
	14RFB100	50		74	150		1.92	
a	14RFB150		43	71	200		1.48	1.48
b	14RFB150	53		56	200		0.23	
18a	18RFC5		30	97	5		10.00	10.00
18b	18RFC5	53		56	100		0.52	
	18RFC50	117		42	150		2.02	
	18RFC100	51		42	200		0.88	

Average Distance From Channel (m)	Measured Minimum Rate (cm/yr)
50	5.3
200	4.7
650	2.2
1500	1.4
2500	1.3

	CS rate (cm/yr)	Sed. Rate (min., all, cm/yr)	Bounded Sed. Rate (cm/yr)
All samples	1.5	3.2	2.8
Foredeep		3.4	2.6
Foredeep to #3		3.6	2.4
Foredeep from #6		2.5	3.3
Straight Foredeep (51, 3)		0.7	0.6
Forebulge		2.0	4.2

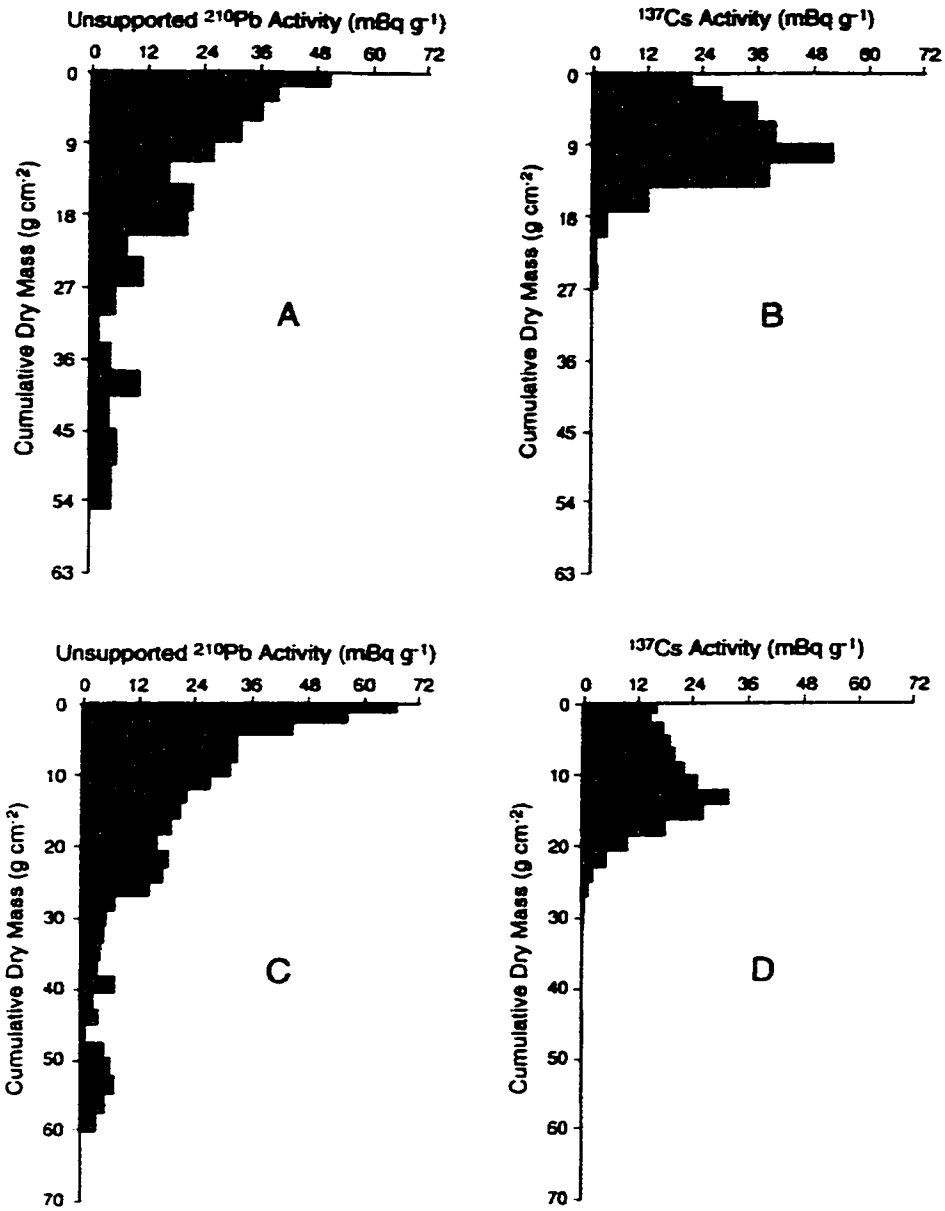

Figure 4.1. Example of the unsupported ^{210}Pb and ^{137}Cs profiles of two sediment cores from the Culm River floodplain (A and B) and the Exe River floodplain (C and D) (from He and Walling, 1996b). Following the CICCS method, most other study cores were bulk-averaged.

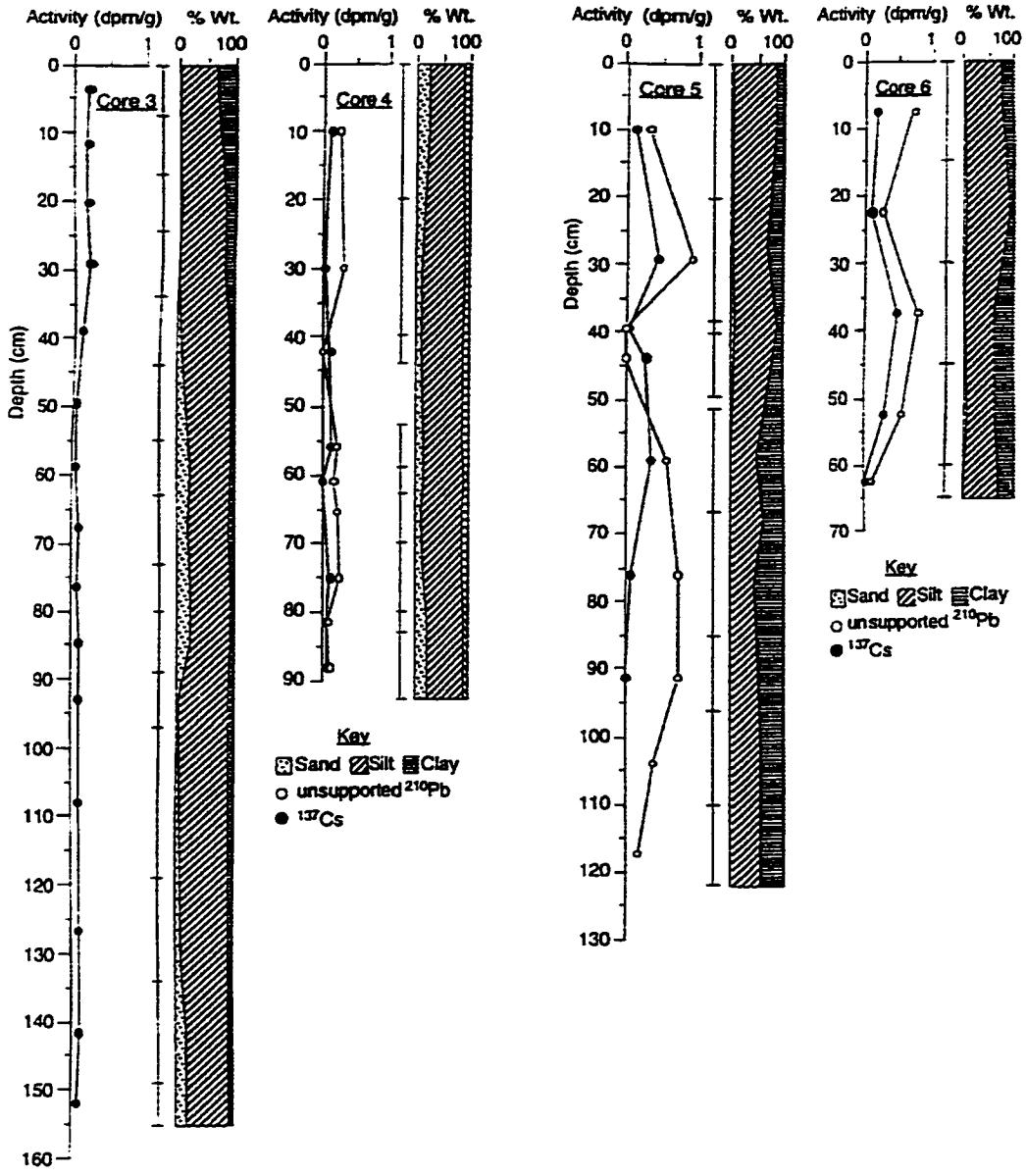

Figure 4.2. Example of the unsupported ^{210}Pb and ^{137}Cs profiles of four sediment cores from the Brahmaputra River braidbelt (cores 3 and 4) and the proximal floodplain (5 and 6) (from Goodbred and Kuehl, 1998). Vertical bars alongside the plot indicate sampling intervals. Profiles are erratic, without a clean downward monotonic decline in activity, suggesting a heterogeneous environment with sporadic deposition. Following the CICCS method, most other study cores were bulk-averaged.

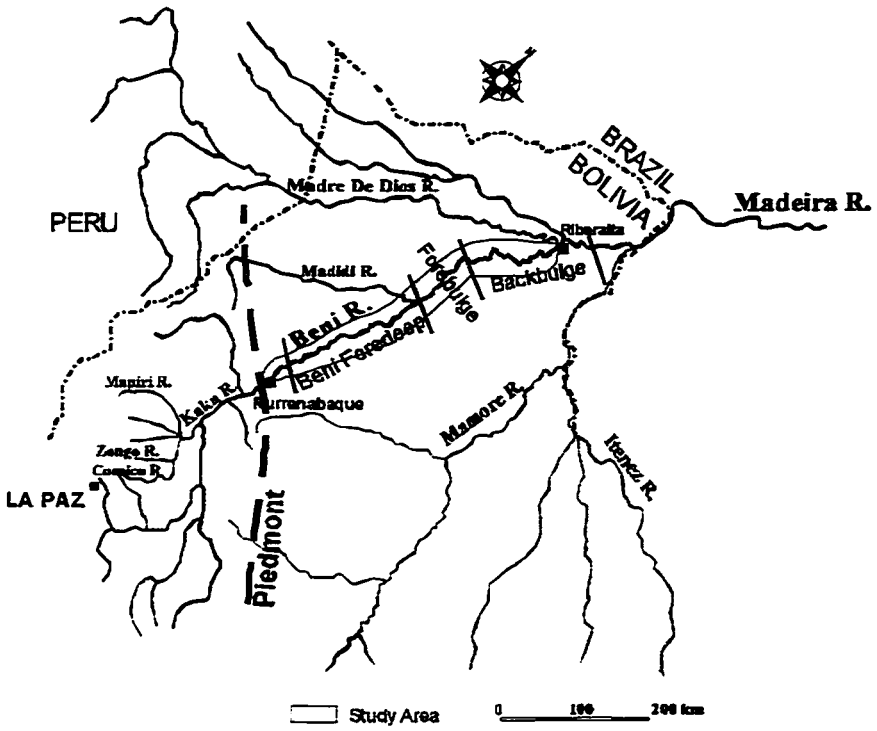

Figure 4.3. Hydrological map of major Madeira tributaries, depicting the Beni River, the study focus area for floodplain sampling, and principal long-term river gauging stations at Rurrenabaque and Riberalta. Approximate location of the foredeep, forebulge, and backbulge secondary basin are depicted, as determined by DGPS surveys of longitudinal river gradient.

Figure 4.4. Example of a GIS detail map for a Beni floodplain survey site. This site was chosen to measure sedimentation rates along a series of five transects spaced along an active meander: 60, 61, 62, 63, and 64. In the image, bare sand or earth (band 5) is red, vegetation (band 4) is green, and water (band 3) is blue. Additional GIS detail maps are presented in Appendix A, and the GIS procedure is discussed in Chapter 3.

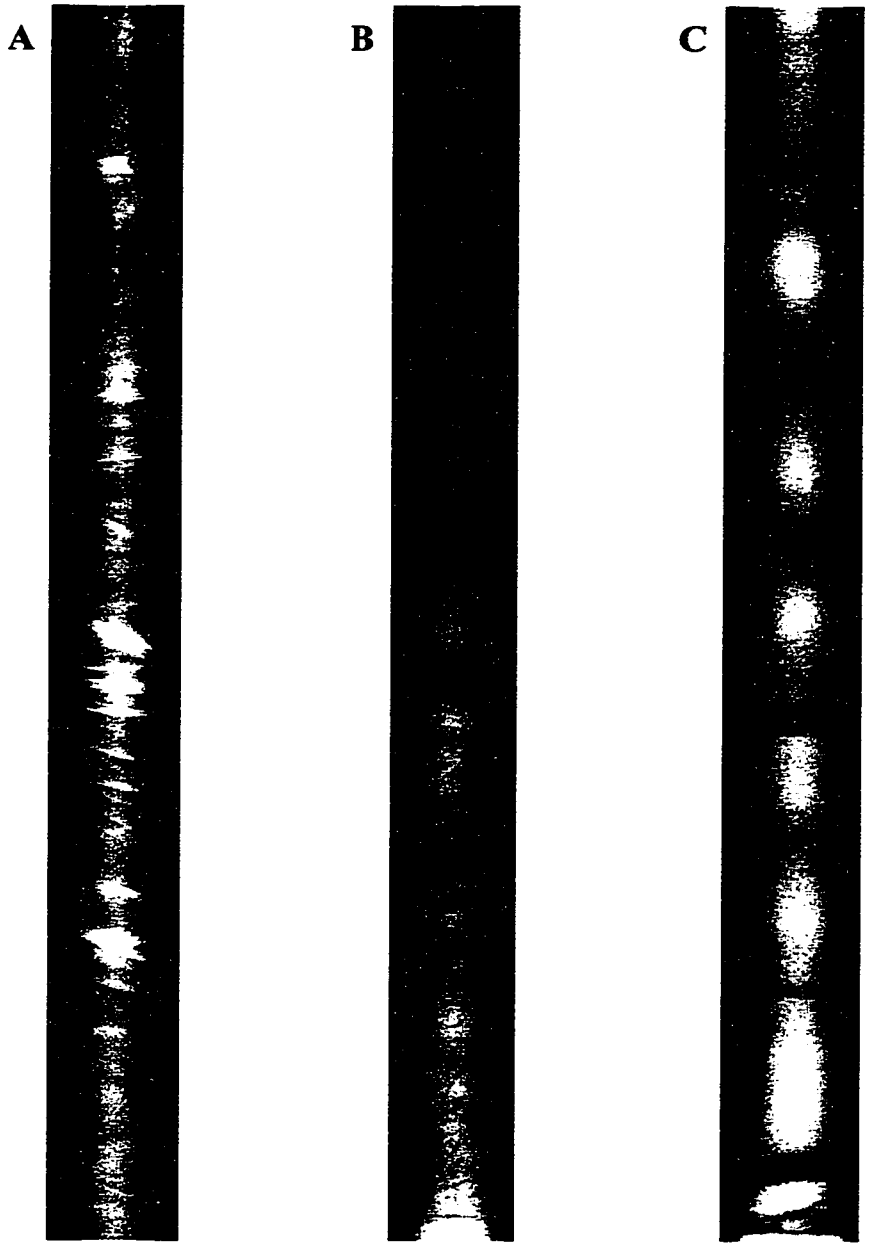

Figure 4.5. (a) X-ray image of a core located 5 m from the edge of the vegetation on a point bar deposit, site 49. Note the well-defined cross-bedding, which reflects the energetic depositional environment. (b) X-ray image of a core located on the forested floodplain 3 km from the river at the time of deposition, site 60. Fine horizontal lamina and massive silty deposits suggest a medium-to-low-energy depositional environment. (c) X-ray image of a core located on the forested floodplain 50 m from the river at the time of deposition, site 51, depicting massive banding and fine horizontal lamina. Images are approximately half of life size.

Figure 4.6. Floodplain core depicting clay-normalized activity, granulometry, summary of the X-radiograph, and interpretation of results from the CIRCAUS geochronology: any date(s) of activity plateau(s) and the date of the meteoric cap (if any). (a) Site 3-A, located 1200 m from the channel when the sediment was deposited in 1954.

Beni Core 3A - >1km from River

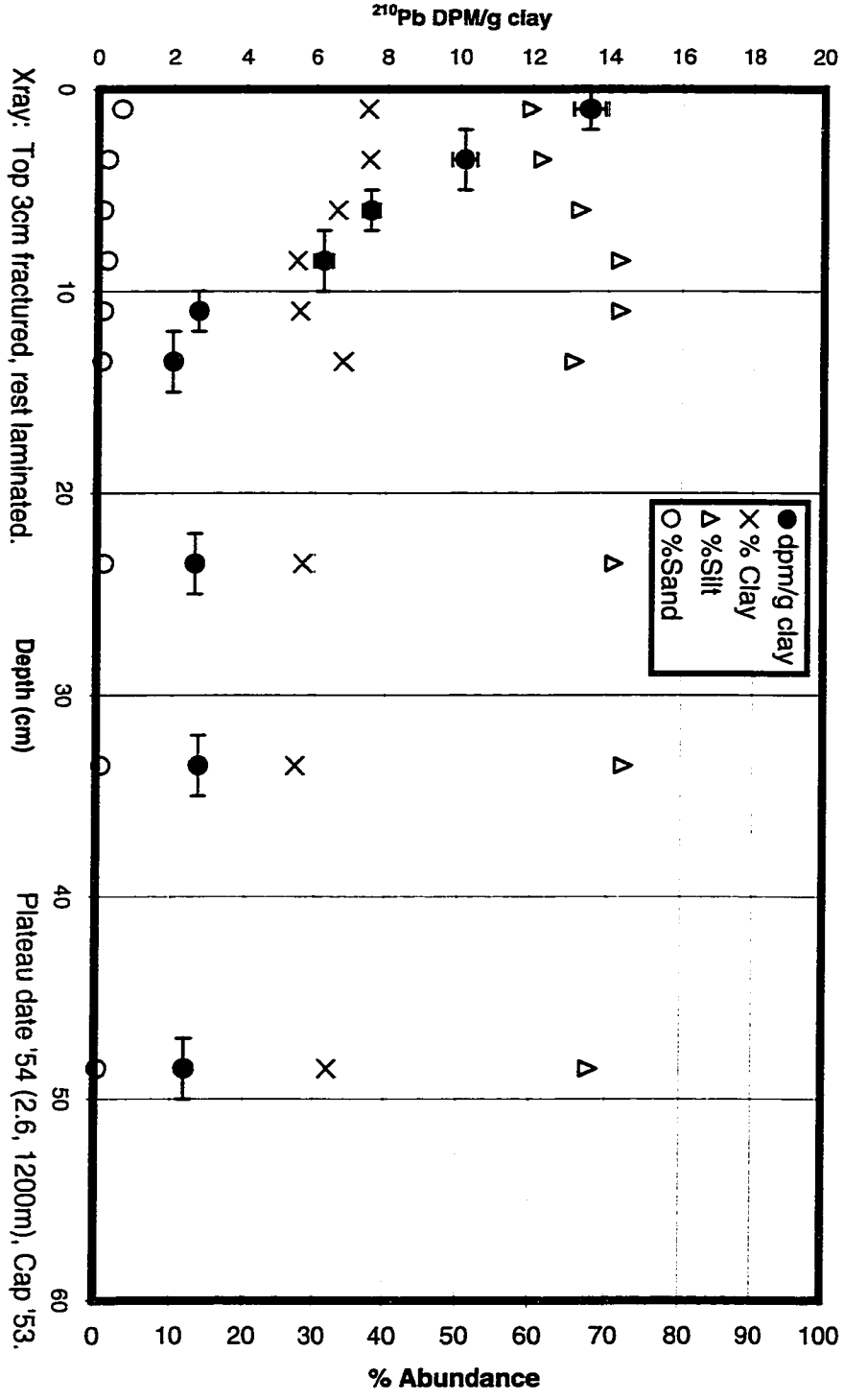

Figure 4.6. Floodplain core depicting clay-normalized activity, granulometry, summary of the X-radiograph, and interpretation of results from the CIRCAUS geochronology: any date(s) of activity plateau(s) and the date of the meteoric cap (if any). (b) Site 3-B.

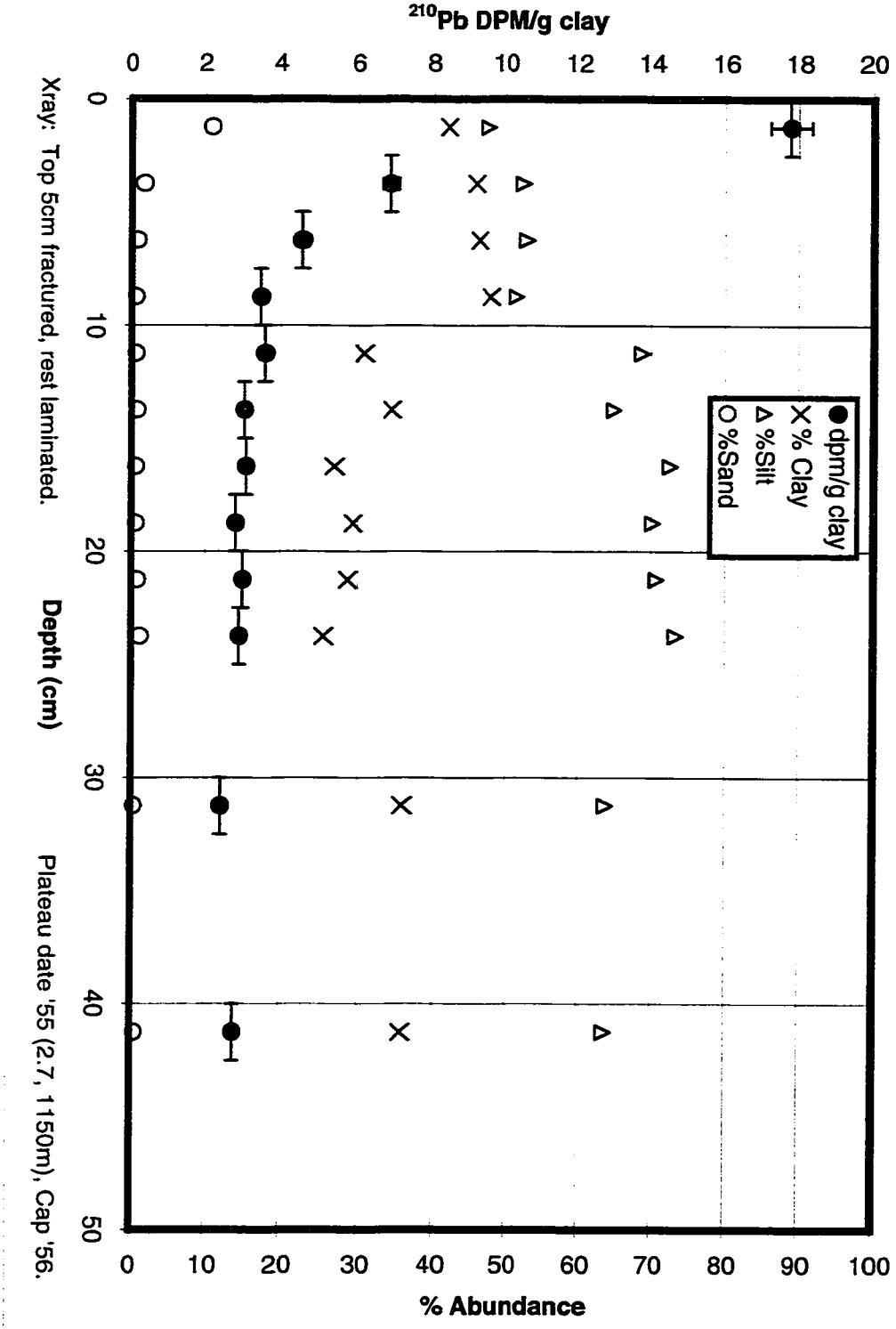
Beni Core 3B - Edge of Forest
^{210}Pb DPM/g clay
0 2 4 6 8 10 12 14 16 18 20
Xray: Top 5cm fractured, rest laminated.
Depth (cm)
0 10 20 30 40 50
dpm/g clay
% Clay
%Silt
%Sand
0 10 20 30 40 50 60 70 80 90 100
% Abundance
Plateau date '55 (2.7, 1150m), Cap '56.

Figure 4.6. Floodplain core depicting clay-normalized activity, granulometry, summary of the X-radiograph, and interpretation of results from the CIRCAUS geochronology: any date(s) of activity plateau(s) and the date of the meteoric cap (if any). (c) Site 62 RFC-100m, located 900 m from channel when the sediment was deposited in 1973.

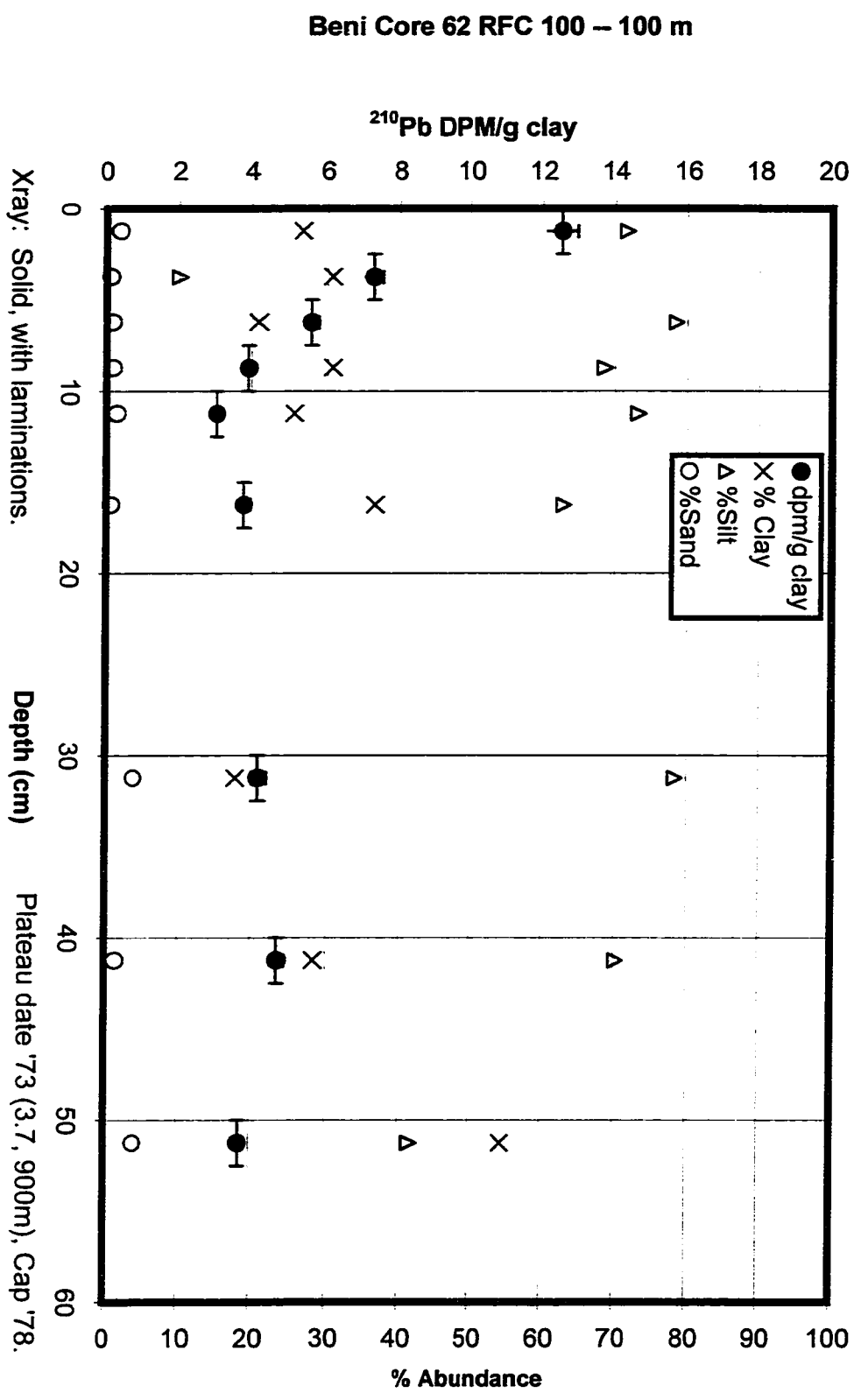
Beni Core 62 RFC 100 -- 100 m
^{210}Pb DPM/g clay
0 2 4 6 8 10 12 14 16 18 20
dpm/g clay
% Clay
%Silt
%Sand
Xray: Solid, with laminations.
Depth (cm)
Plateau date '73 (3.7, 900m), Cap '78.
0 10 20 30 40 50 60
0 10 20 30 40 50 60 70 80 90 100
% Abundance

Figure 4.6. Floodplain core depicting clay-normalized activity, granulometry, summary of the X-radiograph, and interpretation of results from the CIRCAUS geochronology: any date(s) of activity plateau(s) and the date of the meteoric cap (if any). (d) Site 60RFC-250m, depicting two depositional events in 1974 and 1949.

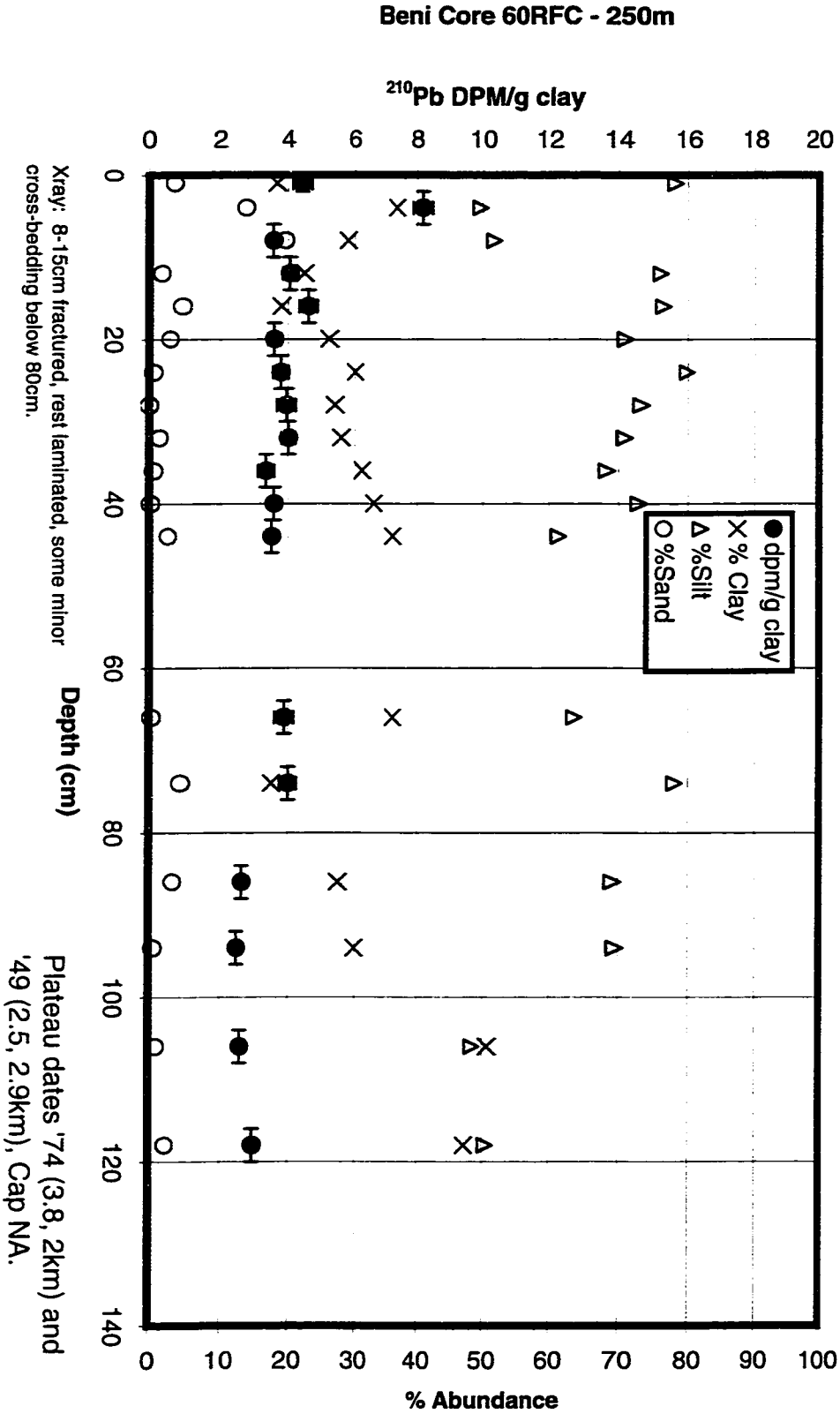
Beni Core 60RFC - 250m
^{210}Pb DPM/g clay
0 2 4 6 8 10 12 14 16 18 20
0 20 40 60 80 100 120 140
Depth (cm)
dpm/g clay
% Clay
%Silt
%Sand
0 10 20 30 40 50 60 70 80 90 100
% Abundance
Xray: 8-15cm fractured, rest laminated, some minor cross-bedding below 80cm.
Plateau dates '74 (3.8, 2km) and '49 (2.5, 2.9km), Cap NA.

Figure 4.7. Site CB-1, depicting evidence for constant accumulation. Because the supported ^{210}Pb activity of 1.4 DPM/g clay is not reached in this core, the CICCS model would underestimate the sediment accumulation rate. Red line represents best-fit CIRCACS model, as discussed in the text.

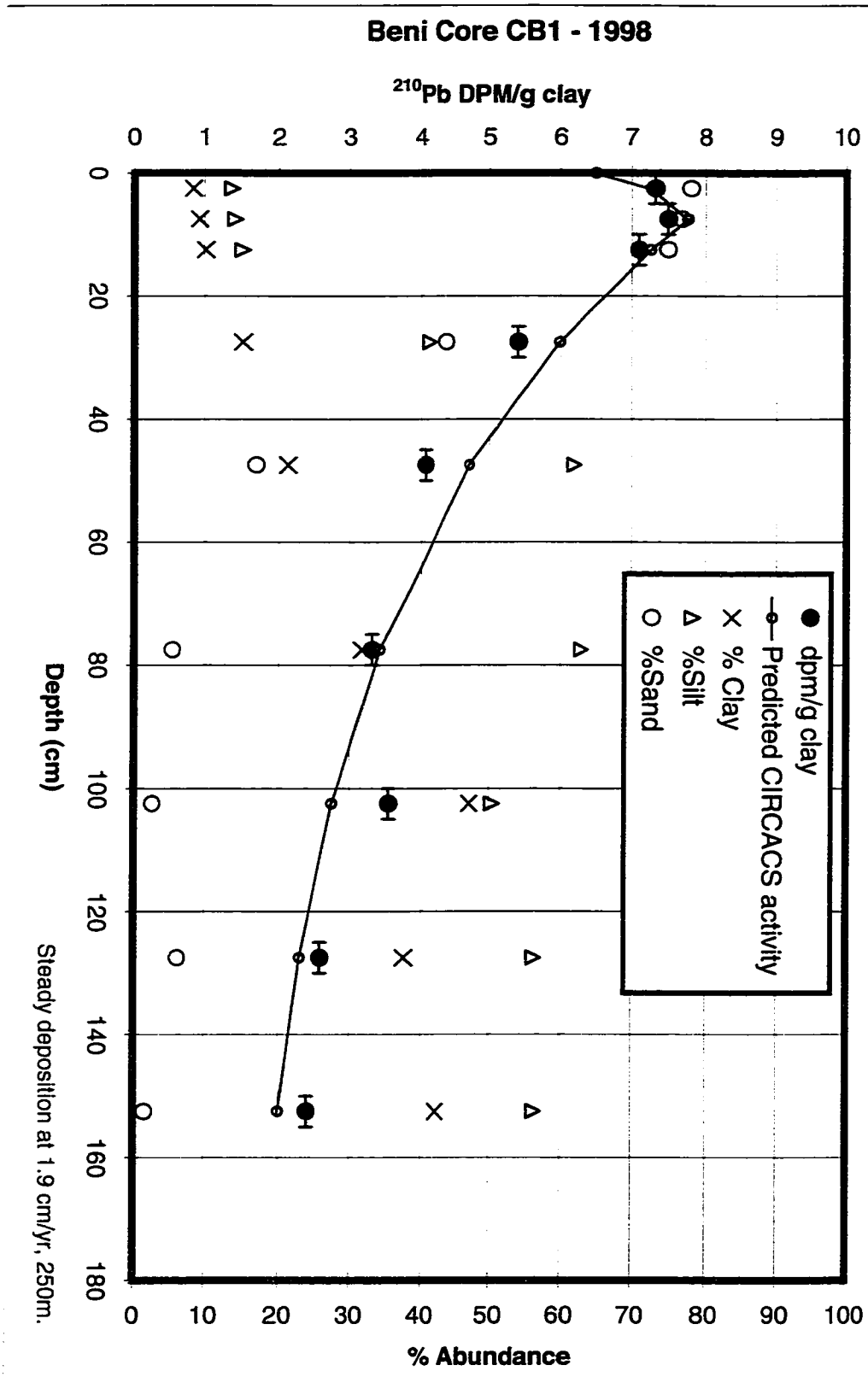
Beni Core CB1 - 1998
210Pb DPM/g clay
0 1 2 3 4 5 6 7 8 9 10
0 20 40 60 80 100 120 140 160 180
Depth (cm)
0 10 20 30 40 50 60 70 80 90 100
% Abundance
dpm/g clay
Predicted CIRCACS activity
% Clay
%Silt
%Sand
Steady deposition at 1.9 cm/yr, 250m.

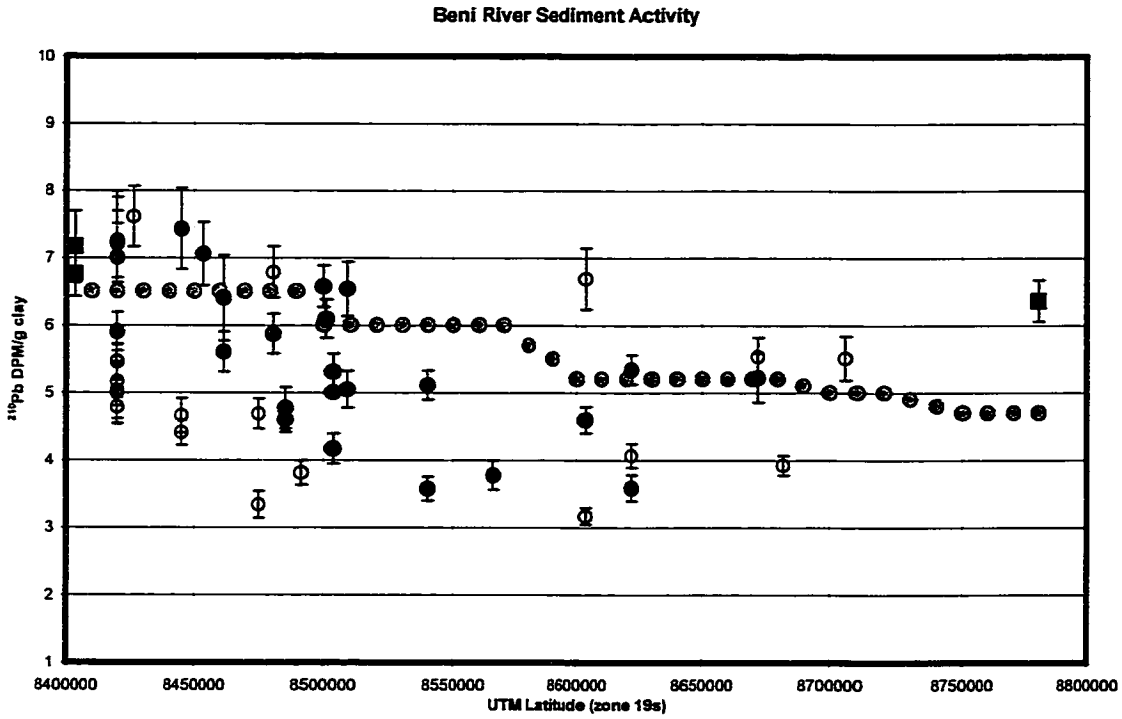

Figure 4.8. ^{210}Pb activity of clay in fresh Beni River sediment, plotted versus UTM latitude. Red circles are for grab samples taken from topographically high locations on the point bars. Open circles represent grab samples taken at topographically lower locations on the bar or from the top of the channel cut bank. Blue squares represent the activity of sediment filtered from the river water collected during a moderate stage event, February 2001. Gray circles represent activities determined from fresh floodplain deposits (cores) and date-matching using the empirical CIRCA technique.

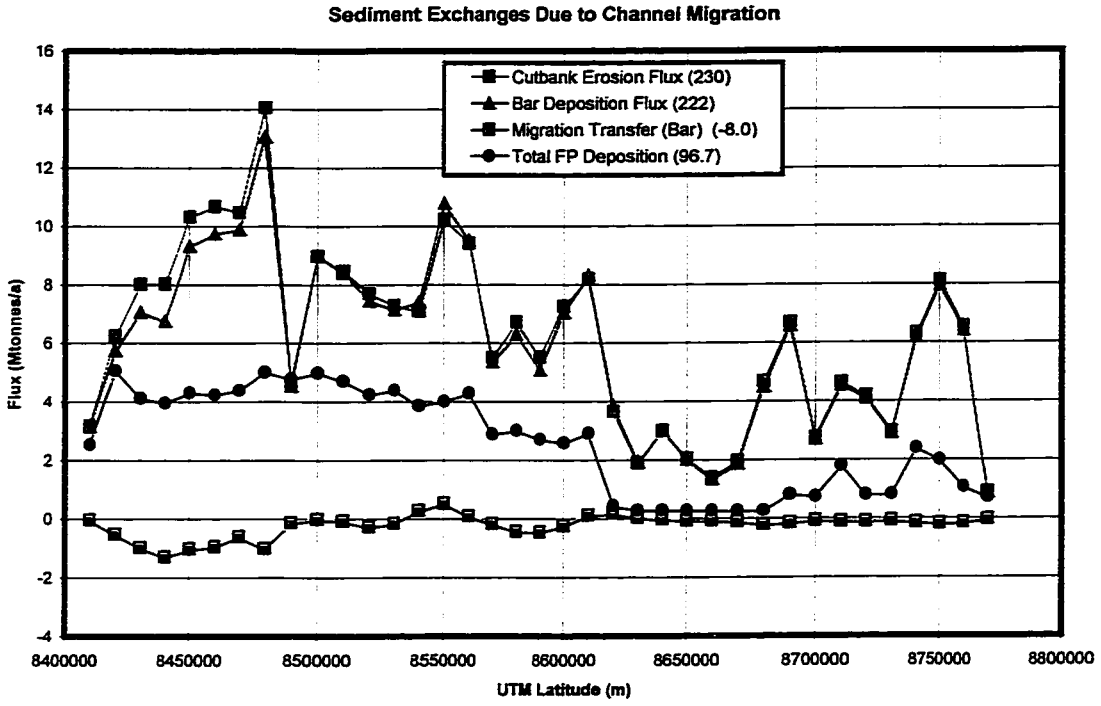

Figure 4.9. Sediment exchanges due to channel migration, plotted for 10 km UTML increments (from Chapter 2). Bar deposition flux is the mass of sediment deposited due to channel migration, up to the vegetation on the point bar. Cutbank erosion flux is the mass eroded into the channel due to migration, a loss of floodplain material to the channel. However, here it is inverted and plotted as positive value to facilitate comparison with the bar flux. The net change in the floodplain storage of sediment due to channel migration, "migration transfer," is also depicted – here, a negative value indicates a loss of floodplain sediment to the channel. Also portrayed is the total floodplain deposition for each reach, the sum of sedimentation across all the different floodplain regions as discussed in Chapter 2.

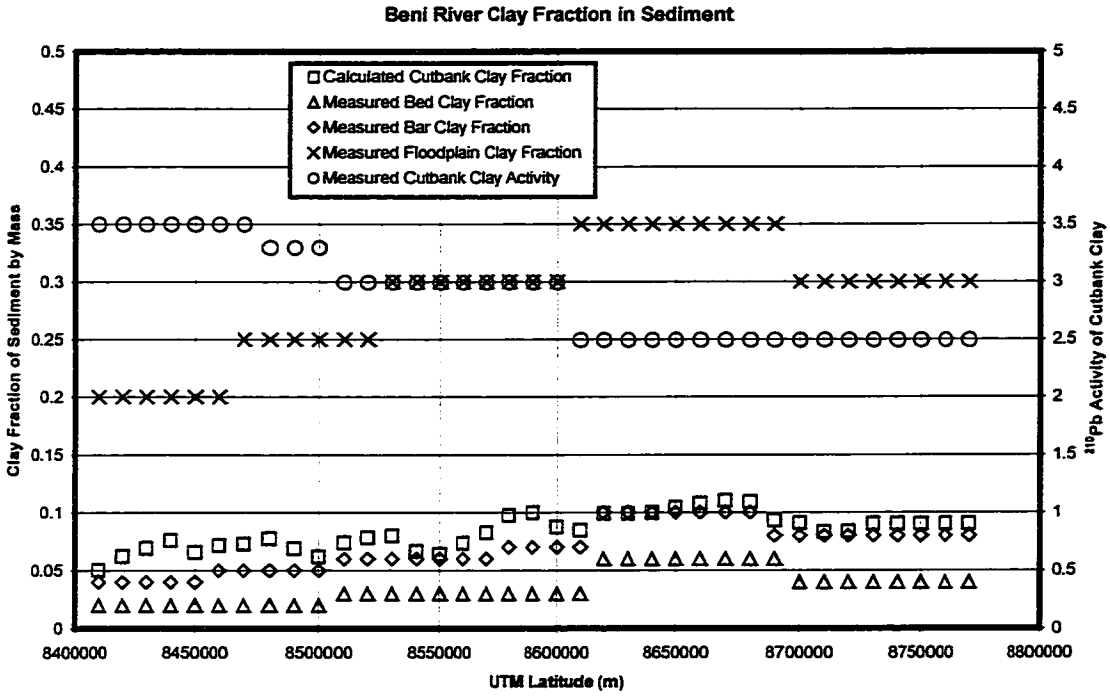

Figure 4.10. Average clay fraction in sediment and cutbank ^{210}Pb activities, as entered into the numerical CIRCA model. All measured values represent smoothed average estimates of the values recorded in hundreds of grab samples across the river channel and onto the floodplain (Chapter 2, Appendix B), including numerous samples taken as vertical profiles at cutbank locations that provide measurements of ^{210}Pb activity and granulometry deep into the floodplain. The floodplain clay values are derived from more than a thousand discrete measurements from the floodplain cores (Appendix C). Average cutbank clay fraction is calculated by depth-averaging the measured clay fraction of each sedimentary unit within the total cutbank section (e.g., the sandy bar unit and the silty floodplain unit, accounting for the total channel aggradation since bar deposition).

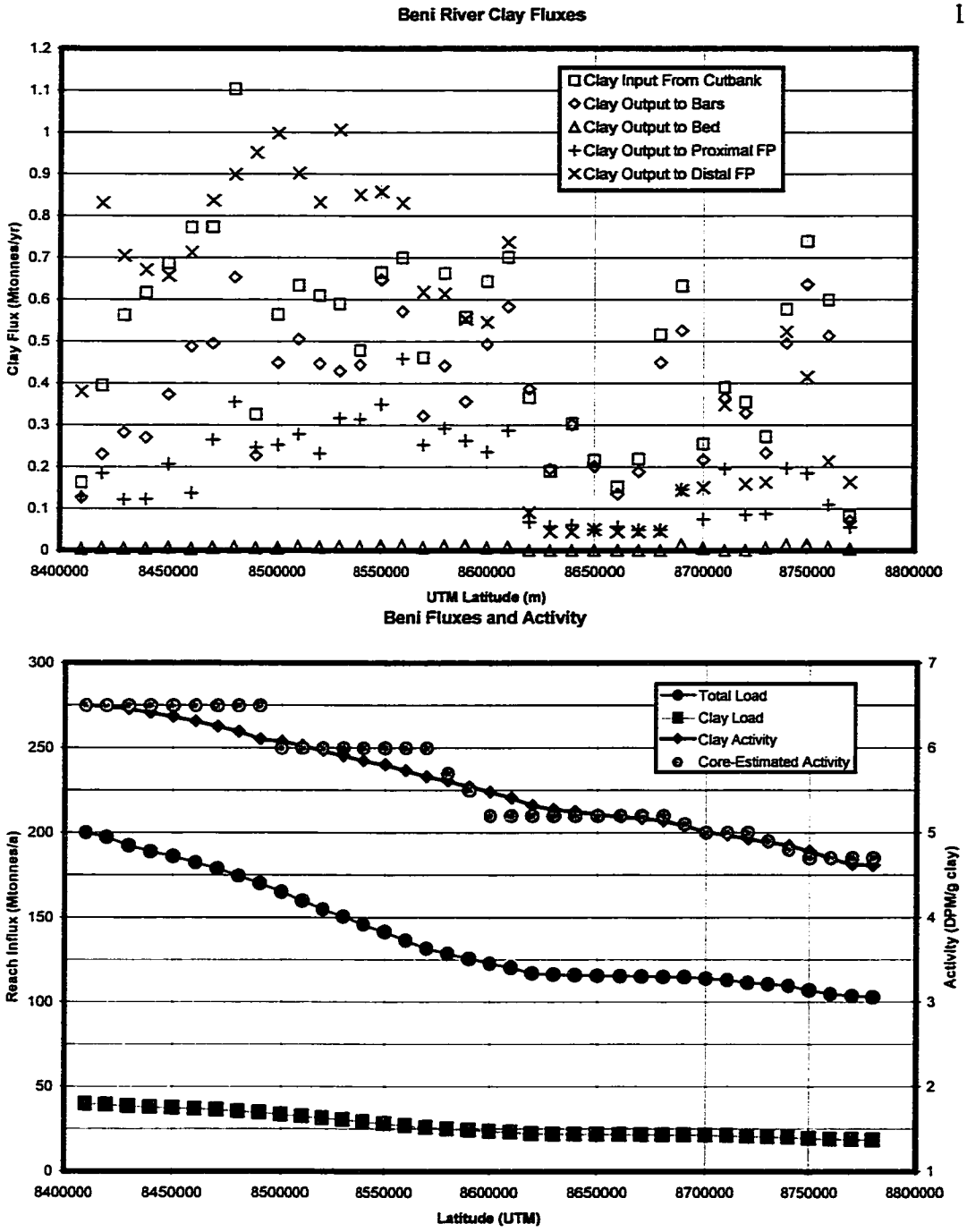

Figure 4.11. (a) Calculated clay fluxes plotted by 10 km UTML reach. Proximal floodplain is defined as < 300 m from the river channel, and distal floodplain as > 300 m from the channel. (b) Total sediment and clay fluxes across the Beni Foreland. The modeled ^{210}Pb activity of clay in river sediment is depicted, along with values from the empirical CIRCA technique, as determined from floodplain cores. Clay input at Rurrenabaque is determined from long-term gauging records and water samples.

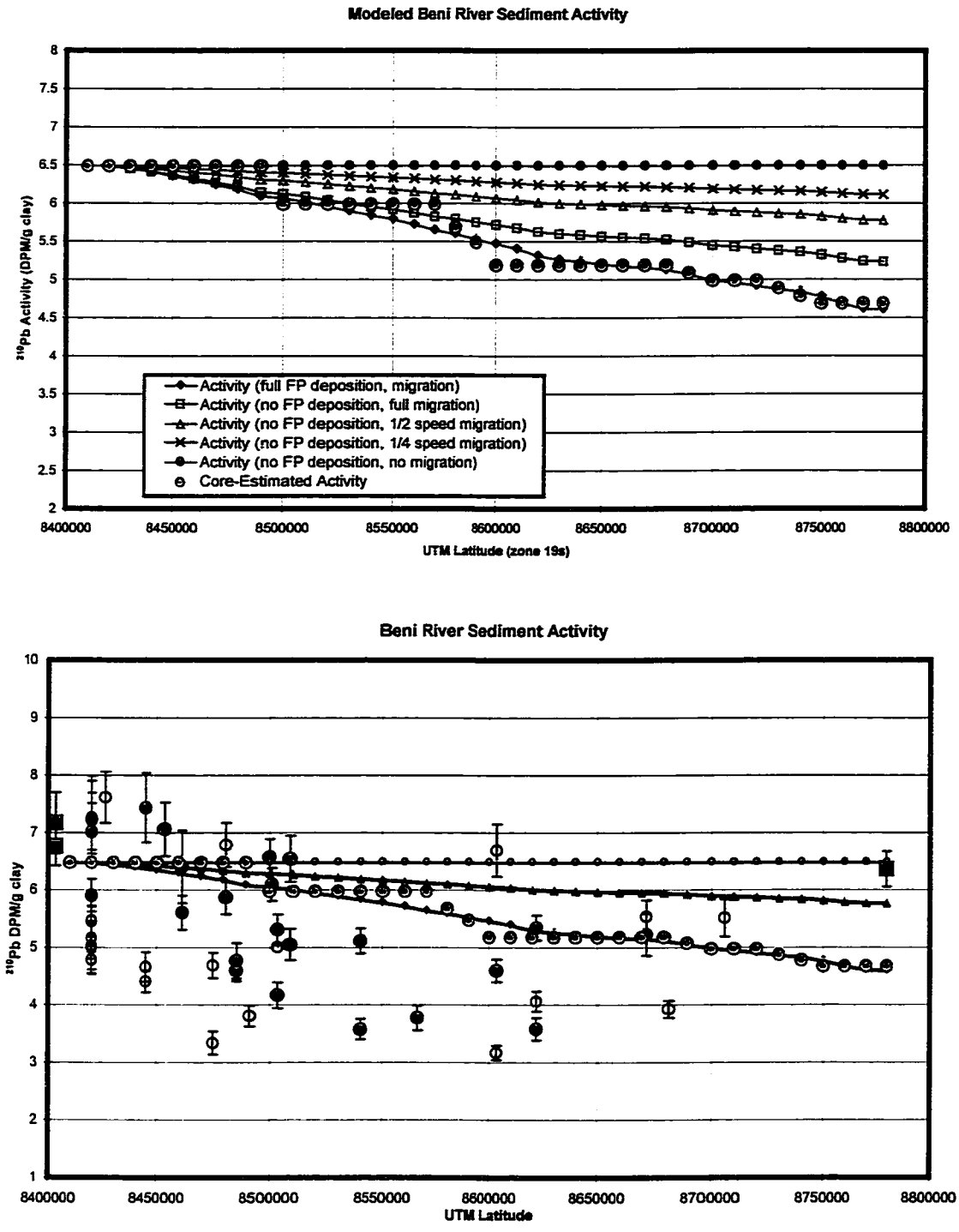

Figure 4.12. (a) The ^{210}Pb activity of clay modeled at decreasing rates of river migration and floodplain deposition. (b) Selected results from Figure 4.12a plotted for comparison against the data in Figure 4.8.

Figure 4.13. Floodplain core from Beni River site LVB-6, located along a small tributary 2.5 km from the main river.

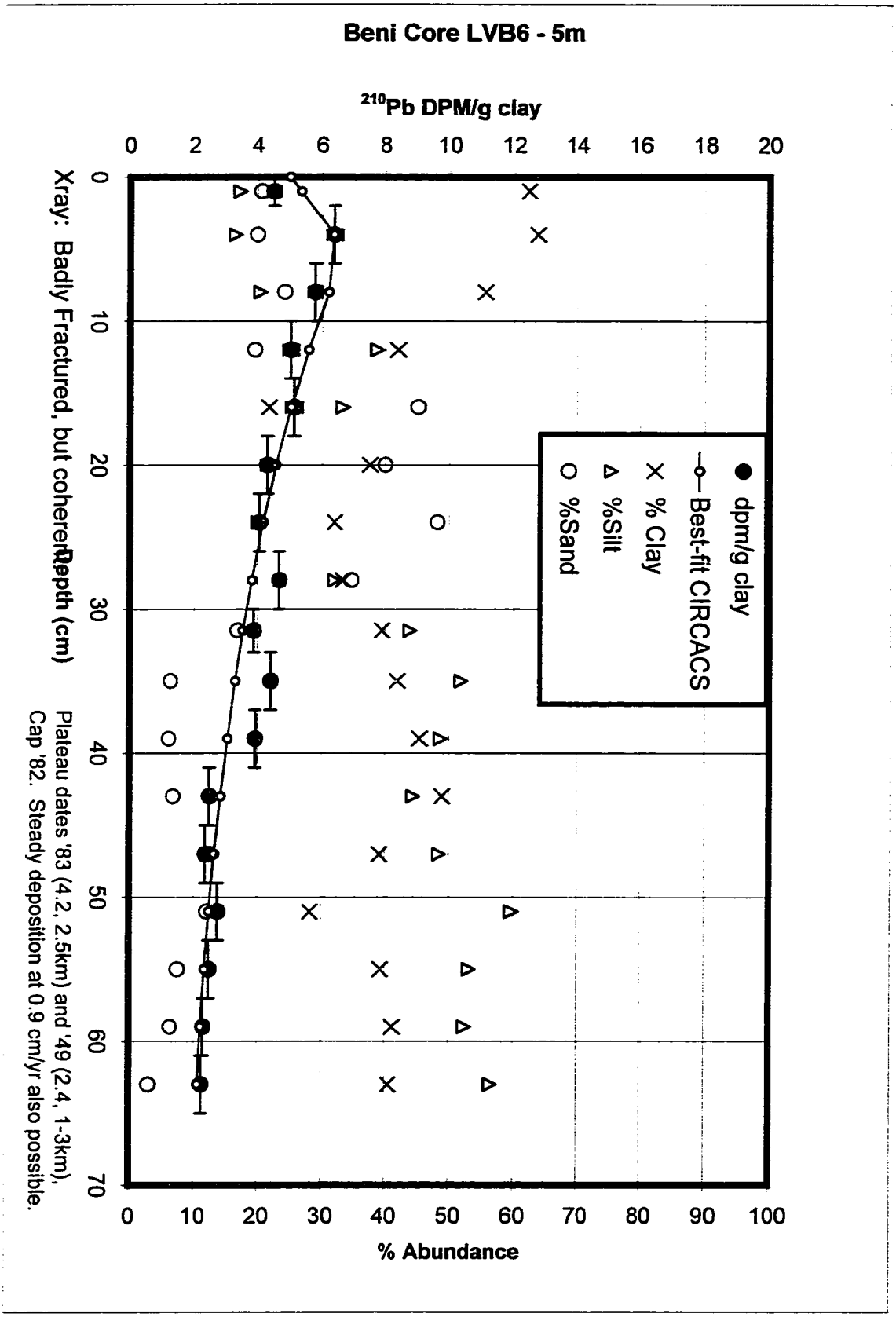
Beni Core LVB6 - 5m
^{210}Pb DPM/g clay
0 2 4 6 8 10 12 14 16 18 20
0 10 20 30 40 50 60 70
Depth (cm)
0 10 20 30 40 50 60 70 80 90 100
% Abundance
dpm/g clay
Best-fit CIRCACS
% Clay
%Silt
%Sand
Xray: Badly Fractured, but coherent
Plateau dates '83 (4.2, 2.5km) and '49 (2.4, 1-3km),
Cap '82. Steady deposition at 0.9 cm/yr also possible.

Figure 4.14. (a) Example of a terrace core, site 34 (proximal to floodplain site 41), located ~ 15 m above the low-stage water surface. Clay-normalized activity quickly declines to a supported level of 1.4 DPM/g clay over about 10cm. Total unsupported activity near the core top indicates (from a depth-density-clay-fraction integration over the top 20 cm) an average meteoric ^{210}Pb fallout of 42 DPM/cm^2.

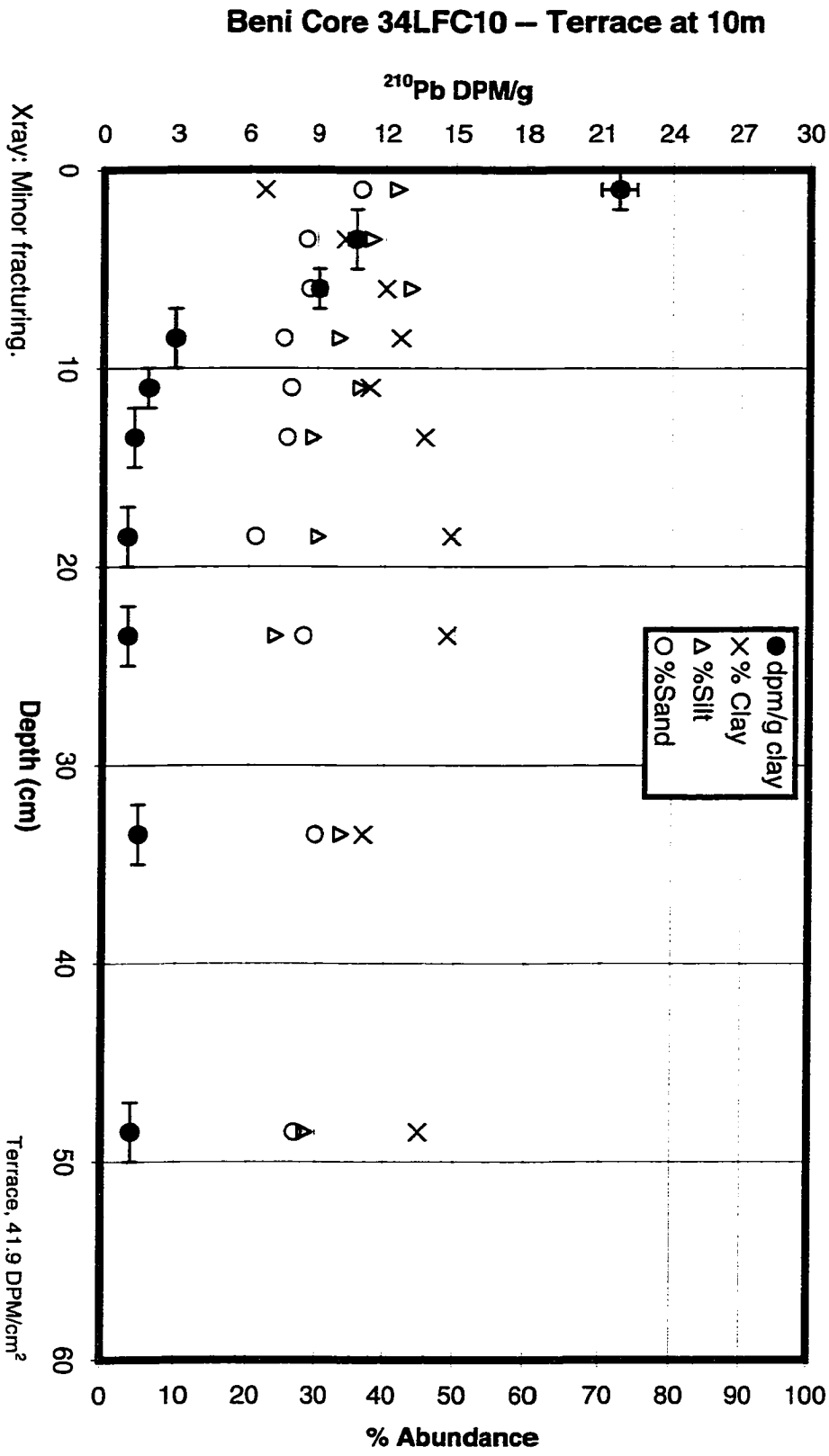
Beni Core 34LFC10 -- Terrace at 10m
^{210}Pb DPM/g
0 3 6 9 12 15 18 21 24 27 30
Xray: Minor fracturing.
Depth (cm)
0 10 20 30 40 50 60
Terrace, 41.9 DPM/cm^2
dpm/g clay
% Clay
%Silt
%Sand
0 10 20 30 40 50 60 70 80 90 100
% Abundance

Figure 4.14. (b) Companion core, taken 6 m away, exhibiting similar characteristics.

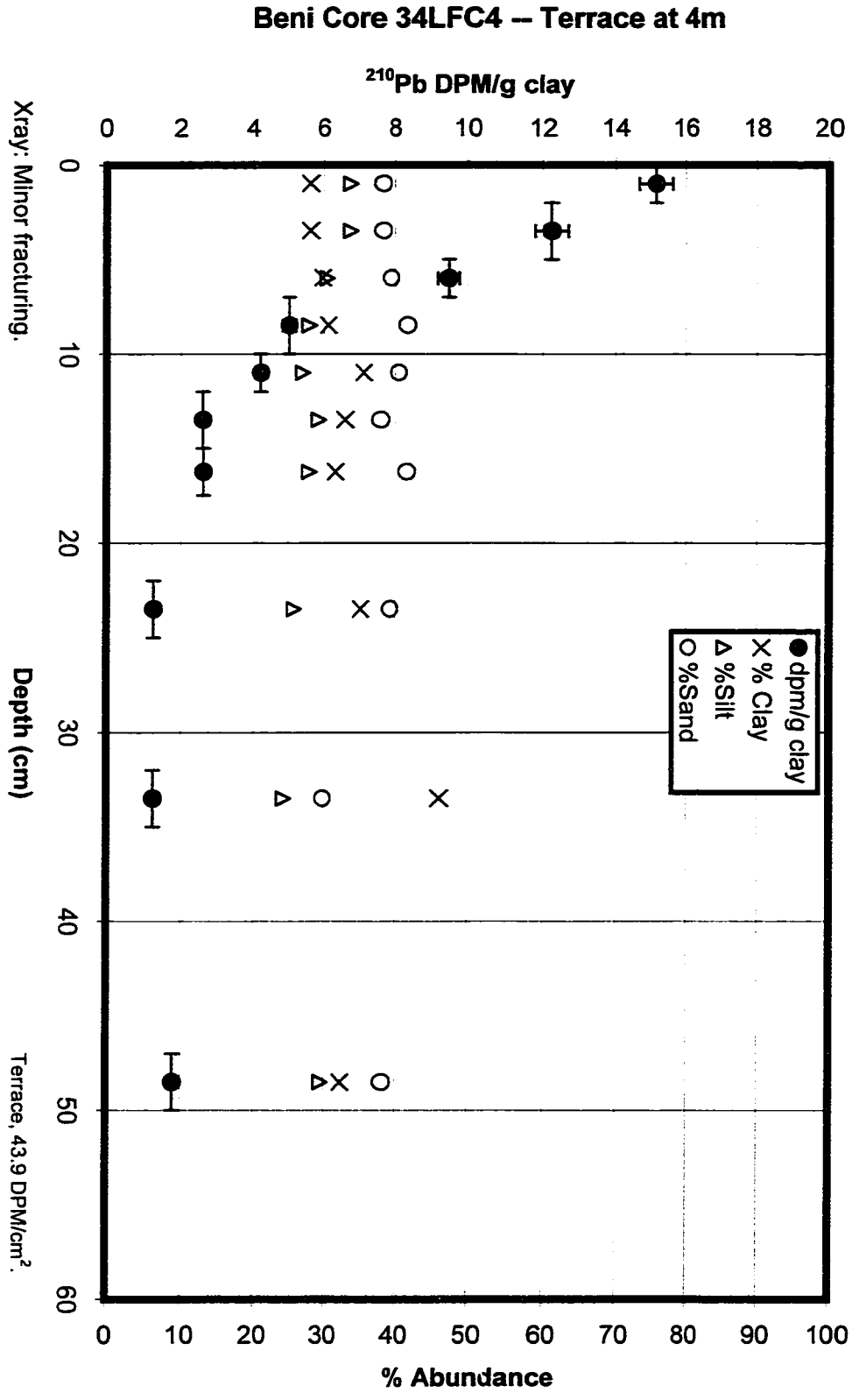
Beni Core 34LFC4 -- Terrace at 4m
^{210}Pb DPM/g clay
0 2 4 6 8 10 12 14 16 18 20
Xray: Minor fracturing.
Depth (cm)
0 10 20 30 40 50 60
dpm/g clay
% Clay
%Silt
%Sand
0 10 20 30 40 50 60 70 80 90 100
% Abundance
Terrace, 43.9 DPM/cm^2.

Figure 4.15. An example core from the Mamore river system, located 500 km SE of the Beni Foredeep, illustrating that the CIRCAUS approach of identifying sediment plateaus and meteoric caps is transportable to other dynamic river systems. For this reach of the Mamore, the CIRCA value is ~ 6.0, the meteoric fallout of ^{210}Pb is 65 DPM/g clay, and the supported ^{210}Pb activity is 1.4. The 59-year-old event depicted here is also resolved in nearby cores along the same transect. Since that time, there has been no significant floodplain accumulation of sediment.

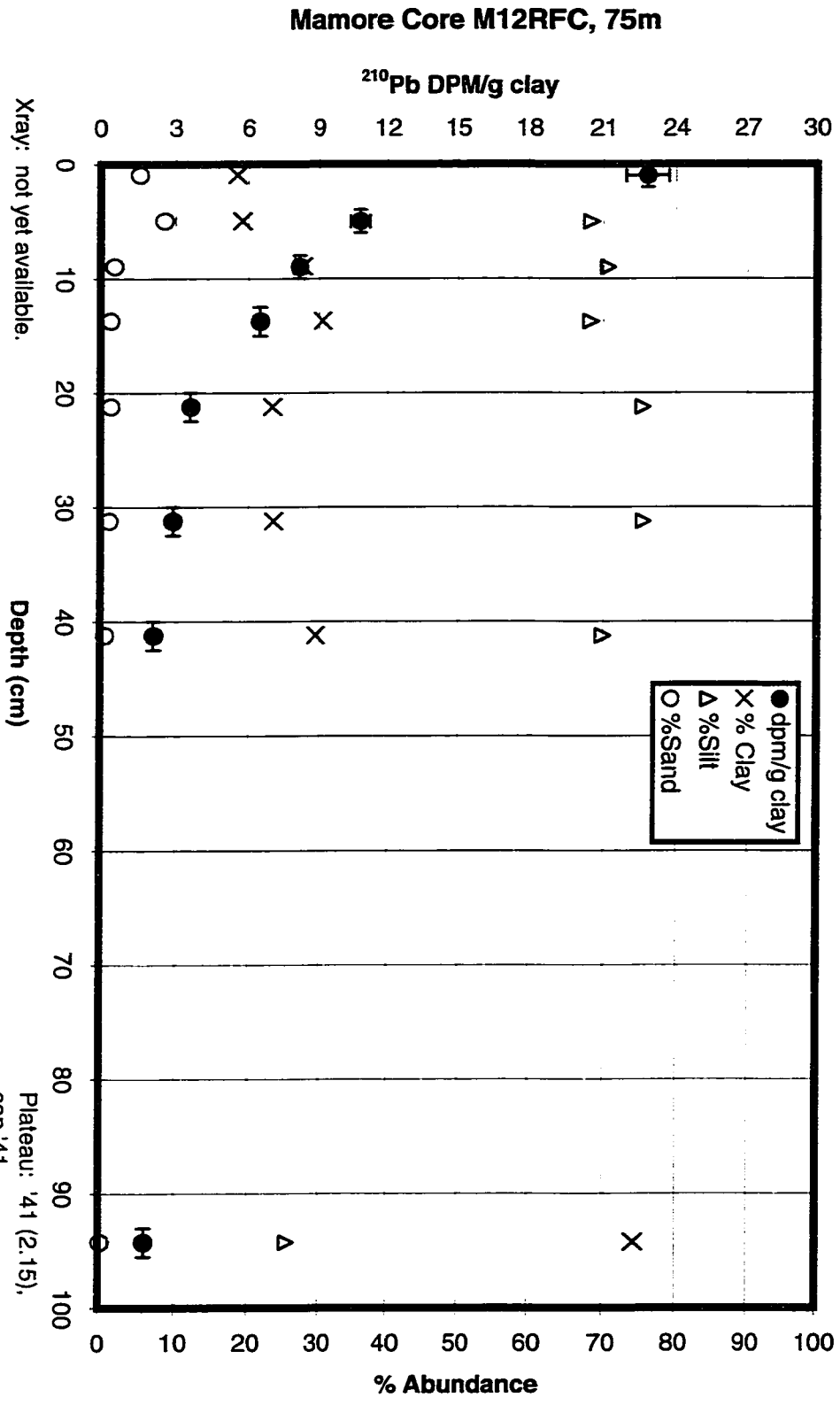
Mamore Core M12RFC, 75m
^{210}Pb DPM/g clay
0 3 6 9 12 15 18 21 24 27 30
Xray: not yet available.
Depth (cm)
0 10 20 30 40 50 60 70 80 90 100
dpm/g clay
% Clay
%Silt
%Sand
Plateau: '41 (2.15), cap '41.
0 10 20 30 40 50 60 70 80 90 100
% Abundance

Chapter 5

Sedimentation processes on the Beni River floodplain: the relationship of episodic floodplain deposition to ENSO

Abstract

Decadal-scale floodplain-channel interactions within large, sand-bedded rivers are a topic of considerable global significance. The Beni River, which drains 68,000 km^2 of the northern Bolivian Andes into the Amazon Basin, offers an opportunity to study a pristine river which interacts dynamically with its forested floodplain, depositing ~ 100 Mtonnes of sediment annually as it traverses a large foreland basin. This study investigates system-wide floodplain accumulation rates measured with a modified methodology for ^{210}Pb geochronology on floodplains. The sampling strategy is devised to quantify rates of floodplain accumulation within 3 km of the channel, as a function of both channel geometry and distance. These field data are interpreted within the spatial and temporal context provide by a GIS analysis of five decades of channel migration derived from Landsat and aerial imagery. Accumulation rates are determined as a function of the effective site distance from the channel, using floodplain transects of sediment cores, keyed to the GIS analysis.

Locations proximal to the channel (< 300 m) average at least 5 cm of annual accumulation, with rates monotonically declining to 1 cm/yr at distances farther than 3 km. Integrated over total floodplain area, the data suggest that the majority of the net system sediment accumulation is distributed throughout the distal floodplain (> 300 m), while channel-proximal accumulation plays a secondary role. This predominantly distal floodplain accumulation occurs in remarkable 20- to 120-cm thick episodic pulses with recurrence intervals of about a decade, linked to major floods. Because of the timing, distribution, thickness, and stratigraphy of these features, I interpret them as crevasse splay deposits.

A comparison of the temporal distribution of these deposition events to water and sediment discharge records and Pacific Sea Surface Temperature Anomaly suggests that these events are probably associated with the largest "La Niña" flood events (ENSO cold phase). Surprisingly, despite annual flooding, even floodplain sites proximal to the channel rarely show geochronological evidence for quasi-annual accumulation; the thick tropical rainforest and natural levees may impede the overbank transport of sediment during all but the most extreme ENSO flooding events capable of breaching the levees. Combining these floodplain accumulation transects with observations of floodplain morphology and stratigraphy, I suggest that most of the Beni floodplain is aggrading at approximately 2 - 5 cm per year. Because the Beni is the principal sediment supplier to the Madeira River (and analogous to other sediment-laden rivers immediately to the NW and SE), which in turn is the principal sediment source for the mainstem Amazon, these ENSO-driven processes may modulate sediment delivery to the the mainstem Amazon, estuary, and shelf environs.

Introduction

Large rivers construct lowland floodplains by the processes of channel-proximal point-bar formation and distal-floodplain deposition of sediment conveyed overbank by turbid waters during flooding. To determine the average annual accumulation of riverborne material across such floodplains, sedimentation processes must be investigated for a wide expanse of floodplain locations and quantified on at least a decade-to-century temporal scale, so as to resolve annual variations in the spatial distribution and quantity of sediment conveyance from the channel to the floodplain. Ideally, rates of floodplain accumulation must be quantified at a variety of distances from the channel, preferably on a reach-by-reach basis so as to account for down-valley variation in the rates of these processes.

Most previous studies of floodplain accumulation have either described the spatial extent and depth of deposits from flooding events (e.g., Kesel et al., 1992),

estimated floodplain deposition using numerical models (e.g., Howard, 1992; James, 1985; Pizzuto, 1987), or used flood routing schemes to calculate the overbank advection of turbid water (e.g., Dunne et al., 1998). At best, such studies provide no more than limited field data to support the modeled floodplain accumulation rates, and therefore their ability to predict spatial and temporal patterns of sedimentation on natural floodplains has not been demonstrated.

Only a few studies have measured floodplain accumulation using geochronology sufficient to resolve these rates on a decade-to-century scale. Nicholas and Walling (1997) combined numerical modeling of overbank sedimentation on a floodplain with radiocaesium measurements, supplementing the work of He and Walling (1996), who measured accumulation rates using ^{210}Pb at the same site, along the River Culm, a small river of width ~ 12 m, U.K. Goodbred and Kuehl (1998) and Allison et al. (1998) measured and estimated accumulation rates across a large floodplain/delta complex in the Bengal Basin using ^{137}Cs and ^{210}Pb geochronology. With their 60 sample cores, they were able to distinguish variations in sedimentation rate for the fluvial braidbelt, the distal floodplain, and the low-lying bils (bottomland basins). Because these previous studies have used a CICCS (constant initial concentration, constant sedimentation) model for ^{210}Pb geochronology, most core samples have been homogenized to measure bulk-averaged ^{210}Pb activity, assuming quasi-continuous sedimentation and precluding any recognition of large single deposition events spanning much of the core (Chapter 4). Consequently, it has not been determined if the CICCS model is indeed appropriate for most such homogenized cores, and therefore the reported rates of sediment accumulation are often of unknown veracity. Additionally, the majority of these studies use ^{137}Cs radioisotope geochronology, which provides only ~35 years of medium-term records, in contrast to the ~100 years of record allowed by the ^{210}Pb nuclide. These prior studies of sedimentation processes on river floodplains have each made significant contributions towards developing a new framework for the application of radioisotope geochronology,

but further work is needed to document the spatial and temporal distribution of floodplain sedimentation along a range of rivers types and sizes.

Building upon this previous research, in this chapter I present results from a study of floodplain sedimentation along an 800-km sinuous section of the Beni River as it traverses 450 km across a large foreland basin. In particular, there are three major procedural enhancements over previous work. First, I use a newly-developed procedure for ^{210}Pb geochronology of floodplains, which resolves and dates individual deposition events, accounts for basin-wide variation in the activity of riverborne sediment, and relies only upon a few testable assumptions (Chapter 4). Second, I collected hundreds of core samples throughout the floodplain, for a wide variety of channel-floodplain geometries, distances from the channel, and locations across the Beni foreland basin. Such spatial resolution allows me to 1) resolve discrete deposition events along transects traversing hundreds of meters of floodplain, with cores typically spaced every 50 m, and 2) measure sedimentation along hundreds of kilometers of a major river traversing an important foreland basin. Third, in a coordinated study (Chapter 2), I have measured decadal-scale rates of channel migration and the associated bank erosion and bar deposition, thereby developing a model for the rates of sediment transport, exchange, and accumulation for 10-km reaches across this dynamic foreland basin. Moreover, there are long-term gauging records of sediment supply into and efflux from the Beni foreland, extensive topographic and granulometric data for the channel, and a detailed GIS (geographical information system) analysis of channel locations dating back to 1960. As such, it is possible to evaluate the floodplain accumulation results presented here within the larger context of sediment transport and exchange across the entire channel-floodplain system. Together, these various procedures provide the first detailed insight into the processes of floodplain accumulation (and sediment transport) along a major sand-bedded river spanning a foreland basin.

Study Area

The Bolivian Llanos (Figure 5.1) is an excellent locale to study active river-floodplain systems and floodplain sedimentation within foreland basins. The water and sediment fluxes, channel-floodplain interchanges, and net sediment sinks are all enormous and well recorded for many stations throughout the basin (Guyot, 1993; Maurice-Bourgoin, 2001), facilitating geomorphic interpretation, flux measurement, and calculation of differences in mass flux. The tectonic setting is relatively simple and well understood (Jordan, 1995) – the type example of a large, overfilled retroarc foreland basin with substantial basement depression (2–7 km), consisting of a continuous system of wedge-top, foredeep, forebulge, and back-bulge depozones (Horton and DeCelles, 1997). The Beni basin is essentially pristine, without artificial levees, dams, roads, significant deforestation or cultivation, or other anthropogenic complications detracting from the study of natural floodplain and fluvial processes. The Bolivian Llanos, traversed by the Beni and Mamore Rivers, are significant in many globally important ways: the Beni River is the principal sediment supplier to the Madiera River (Guyot, 1993), which emerges from the far side of the basin and accounts for half of the sediment flux input into the mainstem Amazon River (Dunne et al., 1998); and the basin is representative of the vast expanse of Andean-Amazonian foreland basins to the north.

The study focuses on the reach of river between Rurrenabaque and Riberalta (Figure 5.1, pocket material), which traverses the entire foredeep, forebulge, and secondary back-bulge basin. At Rurrenabaque, the Beni has a drainage area of 68,000 km^2 and a mean annual discharge of 2,200 m^3/s (Guyot, 1993), with recorded flood discharges of > 20,000 m^3/s and regularly in excess of 15,000 m^3/s (Maurice-Bourgoin, 2001). From an elevation of 190 m (above mean sea level) at Rurrenabaque, the Beni flows along ~ 800 km of channel as it crosses its foreland basin and descends to about 120 m elevation at Riberalta, where it has a total basin area of 119,000 km^2. This reach is remarkable in that there is only one major tributary, the Madidi River, along its entire

course. Thus, the many observed changes in river and floodplain morphology and mechanics are primarily due to transport mechanics and neotectonics, not major tributary effects (e.g., sudden increases in water and/or sediment discharge – rather, the Beni gradually increases its water discharge from the cumulative effects of dozens of minor "blackwater" floodplain tributaries).

I established numerous survey transects into the Beni floodplain, collecting core samples and topographic measurements approximately every 50 m. I combined these data with system-wide surveys of topography and granulometry (Chapter 2), and an extensive GIS analysis of channel migration over the past four decades (Chapters 2 and 3). Together, these data help quantify rates of sediment exchange between the channel and floodplain, and net sediment deposition within the Beni foreland. This paper presents a brief summary of the study methods and focuses primarily on the mechanisms of sediment accumulation across the Beni floodplain. This investigation of the timing and rates of floodplain accumulation provides an important context for parallel studies of all major sediment fluxes within the Beni Foreland (Chapter 2), and the meso-scale geomorphic controls on channel morphology (Chapter 3).

Field and laboratory methods

The principal sampling excursion occurred during August and September of 1999, during the dry season when the river and floodplain are the most accessible and the river stage is relatively constant. Sampling was conducted both in the river and on the floodplain, and is discussed further in Chapter 2.

I chose 25 transect locations (Table 5.1) for their representative position in the foreland basin or for other morphometric reasons, such as to sample a variety of channel-floodplain geometries. Figure 5.2, for example, depicts a series of transects at a point bar. Extended channel transects were surveyed onto the floodplain, including samples collected 50–1200 m from the river. I would systematically sample the point bar, cut bank, and at regular intervals along a transect across the forested floodplain (Figure 5.3),

including topographic surveys, granulometric "grab" samples on the bar and cutbank, and sediment cores extracted 65–160-cm deep into the vegetated floodplain. Water-surface elevations, bar and floodplain locations, and boat locations on cross-channel transects were all recorded with a Trimble Pathfinder ProXRS DGPS system, differentially corrected with the RACAL satellite DGPS service for South America. To complement the DGPS system, cutbank, bar, and terrace heights, channel widths, and sometimes floodplain topography were also measured with a survey-grade laser rangefinder (Laser Technology IMPULSE 200LR), and water depth was measured with a hand-held sonar. In some cases, stadia rod and eye-level surveys were conducted with a survey tape to independently measure floodplain, bank, and bar topography.

Cores and sediment grab samples were collected across the channel and onto the floodplain in standardized locations (Figure 5.3). For the core samples, dry loose leaf litter on the forest floor was brushed aside, revealing the floodplain sediment surface (the abundant termites and ants apparently consume all the dead plant material, preventing the formation of an organic soil horizon). A 65-cm long sampling probe was inserted, collecting a 2.5-cm-diameter soil core within an internal clear polyethylene tube (slightly oversized such as to allow easy entry of the cut soil core). Once the probe was extracted, the plastic tube was removed and capped, and then trimmed to the sample length and securely taped for transport. In some cases, a hole was augered to a 65 cm depth adjacent to the first sample, cleaned, and then a second 65 cm core was taken from 65 - 130 cm depth for a combined total core depth of 130 cm. At a few additional locations, samples were collected to 160 - 200 cm depth using a soil auger and extension rods. For some cases of large grab and auger samples, several hundred grams of sample were collected into taped, double-bagged, 6-mil Ziploc freezer bags. All sample material was sealed, securely packed into wood crates, and flown back to the University of Washington laboratory, where it was stored at 5° C until ready for analysis. Further details, including the collection and analysis of the sediment grab samples are discussed in Chapter 2.

Prior to cutting for analysis, all cores were photographed at two angles (orthogonal) with an X-ray machine (Faxitron Cabinet X-ray Model 43855C) to evaluate the sedimentary structures and potential disturbance within each of the floodplain cores. After imaging, the cores were cut at discrete depth intervals, dried in aluminum sample pans at 80° C for 24 hours, weighed, and then two ~ 5 gram samples (dry weight) from each depth interval were separated for further analysis. One of these resulting samples was analyzed for sediment granulometry, using a combination of wet-sieving at 63 microns (to determine sand fraction) and detailed analysis of the silt and clay (particles < 4 microns diameter) distributions using a Micromeretics Sedigraph 5100 particle analyzer calibrated for river sediment. To determine the ^{210}Pb activity, the second 5 g sample was spiked with ^{209}Po and put through a series of sequential acid leachings (nitric and hydrochloric) over a hot plate. Ionic polonium was then autodeposited onto a silver planchet suspended in the leachate for ~ 24 hrs. Resulting samples are counted in an alpha spectrometer (EG&G Ortec) for 48–100+ hours (as long as is needed to record at least 1000 decays of ^{210}Po). Supported levels of ^{210}Pb were determined by measuring the down-core asymptote of clay-normalized ^{210}Pb activity in numerous floodplain and terrace cores. Further discussion and details of these laboratory procedures are presented in Chapter 4.

Calibration of the CIRCAUS methodology for the Beni River

^{210}Pb is a member of the ^{238}U natural radioactive series, and its presence in the atmosphere is due to the release of ^{222}Rn (daughter of ^{226}Rn) from the lithosphere into the atmosphere and its subsequent decay. ^{210}Pb is removed from the atmosphere by precipitation and dry fallout, and quickly adsorbs to fine sediments (primarily clays), where it is chemically immobile and undergoes beta decay to ^{210}Bi with a half-life of 22.3 years. While the background production rate of ^{210}Pb has remained essentially uniform, there may be regional-scale differences in these rates, and therefore the general rate of direct atmospheric fallout should be determined from a reference inventory core

for each general study region. For a floodplain sample, ^{210}Pb is derived from three sources: in-situ production from ^{222}Rn decay, local atmospheric fallout, and catchment-derived input from deposited sediment. It is the latter dominant source that facilitates measurement of rates of floodplain deposition.

^{210}Pb radioisotope geochronology is commonly applied to lacustrine and marine environments, which often meet the crude assumptions of homogeneity and steady-state flux underpinning common aquatic models (e.g., constant rate of supply, constant flux and constant sedimentation rate, or constant initial concentration). As previously discussed, the ^{210}Pb method has only been recently extended via the proposed CICCS model (Goodbred and Kuehl, 1998; He and Walling, 1996b) to river floodplains, which are far more heterogeneous and difficult to interpret with simplistic assumptions. However, in Chapter 4, I have presented evidence that neither the assumption for constant input concentration nor for constant sedimentation rate is viable for dating floodplain sedimentation processes along the Beni River. Therefore, the CICCS procedure of depth-homogenizing cores would yield results that are not only likely to be incorrect, but also difficult to evaluate regarding the appropriateness of the model assumptions. Hence, for the analysis here I employ a new methodology for ^{210}Pb radionuclide geochronology developed in Chapter 4.

The CIRCAUS method (constant initial reach clay activity, unknown sedimentation) requires three basic calibrations. First, the average annual meteoric fallout must be established across the study area. I accomplished this by coring high terraces elevated 15 – 30 m above the low-stage river surface, distributed throughout the basin (Figure 5.4a), establishing a meteoric ^{210}Pb fallout of ~ 44 DPM/cm^2 for the Beni Foredeep and ~ 51 DPM/cm^2 for the forebulge. The terrace cores were all very similar, depicting only a minor (< 5%) variation in measured meteoric input and a close agreement between duplicate cores taken meters apart (Appendix C). These cores were taken from soils composed of aged river floodplain deposits, which have similar mineralogy to modern river deposits. Hence, I can also employ these terrace cores

(Figure 5.4a) to determine the second calibration, a typical level of supported ^{210}Pb activity observed across the entire foreland is 1.4 DPG/g clay. There is one distal floodplain core in the forebulge which has apparently not accumulated any sediment in more than a century, exhibiting fallout and supported ^{210}Pb activities which concur with my terrace measurements. Furthermore, these calibration values produce consistent results within cores when comparing the age of the meteoric cap (the time needed to grow in a cap of elevated activity from meteoric fallout) to the age of the underlying sediment deposit (the time needed to decay ^{210}Pb from the initial river reach clay activity to the observed core activity) as determined with the CIRCAUS method.

The third necessary calibration is to determine the initial clay-normalized ^{210}Pb activity for each reach of the Beni River as it crosses the entire foreland basin. Entering the foreland basin at Rurrenabaque, the clay suspended in river water has been eroded from thousands of hillslopes, banks, and mobilized from temporary channel deposits throughout the 68,000 km^2 drainage basin, which together integrate to provide a roughly constant activity during high flood stage. My measurements of clay activity in flood waters and fresh floodplain deposits near Rurrenabaque place this activity at ~ 6.5 DPM/g clay (Chapter 4). Clay activity then diminishes monotonically across the Beni Foreland as a result of (1) the deposition of higher-activity river sediment into point bar and channel bed deposits and onto the floodplain, and (2) the excavation of lower-activity (radiometrically older) floodplain sediment from the cut banks due to channel migration. Because I have determined sediment exchanges and deposition (Chapter 2) and the associated clay fraction and ^{210}Pb activity throughout the Beni Foreland (Chapter 4), it is possible to construct a numerical mixing model for the activity in fresh river sediment as a function of UTM latitude (Figure 5.4b). It is also possible to use an independent empirical means to determine this downstream activity profile (Chapter 4). Because 1998-1999 was a major flood year on the Beni River, I have a number of fresh floodplain deposits across the foreland that can be used to constrain the maximum value for constant initial reach clay activity (CIRCA), as well as a scattered distribution of

activities determined from bar grab samples (these are often deposited at a lower, falling stage when banks are collapsing, so are of limited value). Furthermore, within a narrow range of possibilities, some values provide sediment dates that best match the independently determined ages of the associated overlying meteoric cap. Thus, considering information from cores (Appendix C) and, to a lesser degree, grab samples, my measured input concentration at Rurrenabaque, and following the rule that activity must decrease monotonically downstream, it is possible to construct an empirical estimation of CIRCA versus UTM latitude (gray circles in Figure 5.4b, which are utilized for CIRCAUS geochronology). Because both approaches are in close agreement, the modeling and interpretation have likely provided an accurate estimate for the initial clay-normalized ^{210}Pb activity on a reach-by-reach basis across the Beni Foreland.

Discussion of results from the ^{210}Pb geochronology

Given the foregoing calibrations for the CIRCAUS method, I can proceed with the interpretation of results for all 78 floodplain cores processed to date (Appendix C, with locations in listed Table 1, Appendixes A, and the pocket material). Figures 5.5(a-b) depict two examples of floodplain sites located ~ 1,200 m from the river channel when a pulse of sediment was deposited around 1954. These figures illustrate the common and anticipated situation that nearby floodplain cores exhibit similar deposition histories. It is particularly compelling that the independently determined ages of the meteoric caps and the dated sediment agree closely for both cores. Figures 5.5(c-e) show results from a large meander which was selected for detailed analysis (Figure 5.2). All three cores record a major sedimentation event around 1973, as do the majority of cores from this active meander (Appendix C). Figure 5.5d illustrates a "two-layer" core, with sediment of two radiometrically different ages, events which are also portrayed in nearby cores (Figure 5.5e and the intervening core, 60RFC-200m, Appendix C). Figure 5.5f portrays a single recent 50 cm deposition event located atop a high clay cutbank, a thick

lacustrine deposit with a radiometric age of ~ 1885 (determined from grab samples taken down the river cutbank 50 meters away). An extraordinary flood occurred for the Beni River in March of 1999, which is recorded in fresh deposits at this and some other sites. Finally, Figure 5.5g depicts the rare case of quasi-steady-state accumulation, occurring at approximately 1.9 cm/yr. Only 2–4% of cores exhibit such behavior, with most depicting one or sometimes two sedimentation events. Note that in this example, as in the case of all other "steady-state" cores, the supported ^{210}Pb activity of 1.4 DPM/g clay is not reached, so the CICCS model would significantly underestimate the sediment accumulation rate here. Combining the discussed results from these figures with all other cores, Table 5.2 depicts all results for dated Beni Floodplain core sediment currently available. These cores are predominately from the higher floodplain on the cut-bank side of the river (Figure 5.3 and Chapter 2), not the lower and younger floodplain corresponding to the recently deposited and vegetated point-bar. Therefore, all subsequent results and discussion primarily apply to this high, mature floodplain.

In Table 5.2, all total depths of dated sediment are reported. In the vast majority of cases, floodplain sediment arrives as discrete packages of uniform age across an observed depth range. Inspection of these dates, core granulometry (Appendix C), and core X-radiographs (examples in Figure 5.6) suggests that this sediment is typically silt sized and is deposited as a coherent package in a moderate-to-low energy environment Core lithology generally exhibits fine horizontal laminations and other micro-structures at a sub-millimeter scale, suggesting that the floodplain sediment has not been significantly disturbed since deposition and that bioturbation is negligible at most locations (discussed further in Chapter 4). Cross-bedding and similar evidence for higher-energy deposition environments is rare on the cutbank side of the floodplain, and is mainly found in point bar deposits close to the edge of the vegetation. Adjacent coring sites along floodplain transects (or even groups of transects, such as in sites 60 – 64) usually record similar events, suggesting that such sediment packages typically blanket regions hundreds to thousands of meters in width. Total average depth of sedimentation

is difficult to ascertain rigorously with shallow cores, but there are numerous examples of discrete sedimentation events of 40–80 cm in total thickness, and limited evidence (from 3–6-m vertical cutbank sample transects collected proximal to about a dozen floodplain cores) that maximum deposit thickness does not exceed 2 m. Furthermore, the radioisotope geochronology not only shows no evidence for annual floodplain aggradation between these episodic sedimentation events, but the sediment at the floodplain surface (ignoring the meteoric cap) is often decades old, not blanketed by fresh sediment from the more recent sedimentation events depicted in a subset of locations across the Beni Foredeep. For example, although it is clear that many floodplain coring locations received sediment in 1998, 1988, or 1983, there are nonetheless numerous other locations which depict a surface sediment age of 1973 or 1955. Beni floodplain sediment arrives as discrete pulses, but any particular floodplain location receives sediment infrequently, not in every major pulse (Figure 5.8). These observations for the timing of sedimentation, core stratigraphy, and granulometry provide evidence that episodic sedimentation is the predominant mechanism for floodplain accumulation across the Beni Foredeep. Despite the irregular nature of this process, from the depths and dates determined with ^{210}Pb radioisotope geochronology, it is possible to quantify minimum estimates for these floodplain accumulation rates as a function of spatial location.

All unbounded dated depth intervals in floodplain cores can be interpreted as minimum depths of sedimentation, and hence can be divided by deposit age (in years before 2000, the water year of the next major flood following the 1999 field campaign) to determine an associated minimum average deposition rate in centimeters per year. Some deposits have a defined lower bound, in which case the actual average rate is well-defined. In a few cases, it is possible to approximate the radioisotope signature with a CICCS-type steady accumulation model. Such cores are all close (< 300 m) to the channel and have a zone of low, swampy floodplain not far behind them. However, none of these cores with constant accumulation reach supported background ^{210}Pb activity, so

CICCS would always fail – I use a more flexible CS model for constant accumulation as developed in Chapter 4. Combining these results in Table 5.2, I also record the approximate distance from each floodplain core site to the river channel at the specific year of the sedimentation event (determined from the GIS analysis of four decades of channel migration, as discussed in Chapters 2 and 3 and depicted in Appendixes A and the pocket material). As such, is it possible to tabulate the average sediment accumulation rate as a function of floodplain distance from the active river channel (Table 5.2 and Figure 5.7). Here, minimum accumulation rates are highest proximal to the channel (5.3 cm/yr from 0–100 m and 4.7 cm/yr from 100–300 m), drop significantly to 1 km (2.2 cm/yr from 300–1000 m), and decline gradually outwards from there into the distal floodplain (1.4 cm/yr from 1–2 km, and 1.3 cm/yr from 2–3 km). The farthest floodplain sample was 2.9 km from the Beni River at the time of deposition.

Previous workers have developed numerical models of lateral sediment diffusion onto floodplains that suggest the rate of floodplain sedimentation declines following an exponential relationship with distance from the channel (Bridge and Leeder, 1979; Howard, 1992; James, 1985; Pizzuto, 1987). In Figure 5.7, an exponential decay function significantly underestimates the decline in sedimentation within 2 km of the river and overestimates the decline at 2 – 3 km from the channel. This poor fit is not surprising, because common mechanisms for episodic floodplain deposition (such as crevasse splays) are catastrophic, vigorous, advective phenomena which do not obviously mimic the processes of lateral diffusion. The documented fact that, despite regular flooding, little if any sediment is transported from the river into most of the floodplain (no regular sedimentation is observed in the cores) suggests that conventional concepts of sediment transport by lateral diffusion are not appropriate for the Beni River and its floodplain. I propose that this condition is due to a combination of natural levees (Chapter 2) and dense rainforest vegetation, which act in concert to minimize and retard both diffusive and advective transport of sediment-laden water from the flooded river channel into the distal floodplain. According to this interpretation, the zone of high

accumulation rates observed within 300 m of the river is indicative of the process that builds natural levees: overbank decanting of modest amounts of sediment during regular flooding and deposition of this material within the densely vegetated floodplain near to the river. Such regular sedimentation is not observed farther than 300 m from the channel, where accumulation rates are substantially lower and decline only slightly with increasing distance from the channel. Sediment accumulates only infrequently at any particular floodplain location distal from the channel, where it arrives as discrete packages of considerable thickness. This indicates an episodic, vigorous mechanism for sediment accumulation on the distal floodplain, which is clearly different from the more gradual process which forms the levees proximal to the river channel.

At the bottom of Table 5.2, I present average minimum and bounded deposition rates for a number of spatial subsets. For the Beni Foredeep, the average floodplain sedimentation rate (all rates) is 3.3 +/- 0.6 cm/yr, declining to 2.0 +/- 0.9 cm/yr across the forebulge, where the dataset is limited to 8 samples. The upper foredeep (upstream of 8,520 km UTM latitude) exhibits a considerably higher sedimentation rate, 3.6 +/- 0.8, than measured for the lower foredeep, 2.2 +/- 0.4. These values follow the conceptual foreland model (Horton et al., 2001) of highest sediment accumulation in the deep foredeep, proximal to the range front, lower rates in the distal foredeep, which exhibits much less basement depression, and lowest rates across the forebulge, which should accumulate very little sediment. Because the dataset is composed primarily of estimates for minimum accumulation rate, the actual accumulation rates may be higher. Vertical ^{210}Pb transects at a handful of cutbank locations suggest that deposit thickness does not exceed ~ 2 m. Of the 20 deposition events with a resolved lower bound (Table 5.2), the average thickness is 38 cm, with most of the values between 30 and 40 cm. However, this dataset is biased towards thinner events, because it is not possible to resolve bounded events thicker than 50–55 cm in a typical 65-cm core. The remaining 44 unbounded depositional events provide only the insight that most sedimentation events are thicker than the 50–65 cm typically resolved by floodplain cores. Discarding the two

most extreme events, the depth of unbounded sediment packages ranges from 25 to 118 cm, with an average of 55 cm. Data from deeper cores would better constrain these values.

Finally, I plot the occurrence frequency of all sedimentation events in Table 5.2 versus the year of deposition (Figure 5.8). As previously discussed, floodplain sedimentation across the foreland clearly occurs in distinct pulses, separated temporally by many years characterized by no recorded deposition. Over the past six decades, floodplain accumulation events have occurred on average every seven years. This is a separate phenomenon from my prior observation that many decades may pass between sedimentation events at a single floodplain location. Previously, I have presented evidence that any **specific** floodplain location does not receive sediment during most decades, even during major flooding of the river channel. Here, I have presented geochronological records from locations spanning the entire Beni Foreland which suggest that the flooding conditions needed to facilitate sedimentation **at numerous places on the floodplain** (such that I would have sampled a few of them) occur approximately every seven years. Because younger sedimentation events bury older ones and most of the cores are only 65-cm long, this record is necessarily biased toward the last few decades. Furthermore, some river reaches were heavily sampled (e.g., Sites 60 – 64), so representation of their events is correspondingly strong. Therefore, only the dates of the peaks in Figure 5.8 should be considered important, not the relative heights of the peaks.

Variation in water and sediment discharge at Rurrenabaque

To examine potential causes of the distribution of floodplain sedimentation events depicted in Figure 5.8, I investigated the records of water and sediment discharge at Rurrenabaque. The daily records (Figure 5.9a) exhibit a considerable range of values, with water fluxes increasing 70-fold during large floods and the corresponding sediment fluxes escalating by a factor of 12,500. During a single day of the highest recorded flood

discharge in March of 1999, the Beni River could account for about 4% and 28% of its average annual water and sediment discharge at Rurrenabaque (as recorded from 1995 – 2001). These records emphasize the significance of extreme floods in supplying enormous quantities of water and sediment to the Beni Foreland.

Monthly hydrological records are available for Rurrenabaque dating back to 1967 (Figure 5.9b). The maximum monthly average recorded for each water year provides the best-available proxy for major flooding events. For example, here there is good representation for the large 1998 (March 1999 is part of the 1998 water year) flooding event portrayed in the daily discharge records in Figure 5.9a. Over the past 34 years, this average monthly discharge record depicts ~ 6 major flooding events (defined as years with a maximum mean monthly discharge average of greater than 7,000 CMS). A comparison of these flood years to the temporal distribution of floodplain sedimentation shown in Figure 5.8 shows a very good correlation. Unfortunately, the gauging records over the mid-to-late 1980s are probably not reliable, so it is not possible to evaluate the discharge corresponding to the notable 1988 floodplain sedimentation event. I will next consider these flood years according to their corresponding regional climate, a function of the prevailing ENSO status.

Relation of flooding and floodplain sedimentation to ENSO

It has long been recognized that eastern Bolivia suffers droughts during strong warm phase ENSO events (El Niño), and receives abnormally high amounts of rainfall during cold phase events (La Niña). The Beni River follows this trend, flooding during strong La Niña conditions and exhibiting low-to-normal discharge during El Niños (Figure 5.9b). To further investigate this relationship, I obtained a standard proxy for ENSO strength, the Japanese Meteorological Agency record for sea-surface-temperature anomaly (JMA SSTA), a monthly average of water temperature deviations in the equatorial Pacific (Figure 5.10a) recorded since 1949 and reconstructed back until 1868 (Meyers et al., 1999). For the last century of record relevant to the ^{210}Pb geochronology,

I devised an index pertinent to the Beni River, the average JMA SSTA for the months of November through February (Figure 5.10b). The major rains typically begin in late November to early December, building to a maximum in February. If I define major cold-phase ENSO years as those for which NDJF JMA SSTA falls more than one degree below normal, there are 10 such years over the last century (Figure 5.10b). Comparing this ENSO index to the discharge record at Rurrenabaque (Figure 5.10c), it appears that most large floods correspond to major cold-phase ENSO years. I further observe that two of the exceptions, 1983 and 1998, are for minor cold-phase ENSO years that immediately follow exceptionally large warm-phase ENSO years. For the Beni River, I observe that flooding correlates to cold phase years which show a substantial negative differential over the preceding warm phase year – this might explain why relatively minor flooding occurred in 1975 and 1999. The only exception to this rule is 1977, which exhibits some flooding despite being a warm phase ENSO year with only a relatively minor cooling over the preceding year.

Pursuing this hypothesis, I next compare the dated floodplain accumulation events to the NDJF JMA SSTA record (Figure 5.11, Table 5.3). With the notable exception of 1977, there is a strong association of floodplain sedimentation to cold phase ENSO years which show a substantial negative differential over the preceding warm phase year. In short, these results present compelling evidence that significant flooding of the Beni River and episodic sediment accumulation across the Beni Foreland is orchestrated by La Niñas, particularly those immediately following large El Niños.

Crevasse splay deposits?

Any mechanism proposed to account for the described floodplain sedimentation events must meet a number of specific criteria. It must be episodic in several precise ways: 1) across the entire foreland and in the distal floodplain, events must only correspond to very large floods; 2) there is generally a lack of temporal correlation between distant transect locations, even for these largest floods; and 3) at any specific

distal floodplain location, sediment will accumulate only during some of these events, with several decades typically separating sediment pulses. The event mechanism must also account for single deposits that are 20–120 cm in thickness and hundreds to thousands of meters in width, as recorded across floodplain transects and sets of transects (e.g., transects 60–64 record events blanketing several km of floodplain). The environment of deposition must be moderate-to-low energy, as indicated by the sub-millimeter-scale laminations seen in most floodplain X-radiographs and the scarceness of sand in these deposits. The dominance of silt and clay indicate that the source material must be derived from high in the river column of water, where the fraction of sand is minimal (Chapter 2). There are not channel-associated deposits.

This list of criteria constrains the list of viable mechanisms for episodic sediment accumulation across the distal floodplain. Channelized flow or channel cutoff features have much coarser granulometry and are not obviously associated with the largest floods. My investigation of oxbow lakes on the Beni floodplain indicates that they do indeed receive fine sediment, but these lakes are much lower than the surrounding floodplain and infill only slowly over hundreds of years (Chapter 2). Regular inundation of all of the floodplain by sediment-laden water during large floods would result in chronic sediment accumulation, not the episodic deposition recorded here. It is also hard to envision how limited amounts of water decanting over the tops of the natural levees, the mechanism I have proposed to construct these levees near the channel, could account for deposits of such thickness and extent across the distal floodplain. Topographic steering and ponding of such decanted floodwaters on the floodplain could focus sedimentation at some locations, but this mechanism is not likely for two reasons: 1) it would result in regular deposition during most large floods, which is not observed; and 2) topographic features such as scroll bars and floodplain drainage channels are unusually scarce on the Beni River floodplain. A more vigorous and infrequent mechanism is indicated.

I propose that these episodic deposits are formed by crevasse splay deposition during large floods. The natural levees that I have documented (Chapter 2) are

composed of porous, unconsolidated, silty deposits. Despite the luxuriant vegetation, there are not many fine roots or grasses stabilizing the loamy soil – this is particularly evident in forests more than a few decades old, where the understory is shaded by the high canopy. Such levees would be susceptible to scour and incision of splay channels during significant overtopping events. Once a splay channel starts to form, it will incise rapidly and large volumes of silt-laden water would debouch into the distal floodplain at that location. Although the levee break itself is a high-energy channel, the water would immediately diverge into the densely-vegetated floodplain on the far side of the break, depositing its load in a low-energy environment. Because this water is decanted through the levee break from high in the suspended sediment profile of the main river channel (Chapter 2), it would primarily carry a suspended load of silt and clay. Such deposits are stratigraphically similar to general literature descriptions of crevasse splay deposits, including several recent studies which describe ancestral foredeep crevasse splay deposits preserved in the high Andes (Horton and DeCelles, 2001; Horton et al., 2001).

Once the splay deposit is formed, aggrading the local floodplain relative to the river, the levee break fills in, restoring the high natural levees and preventing floodplain sedimentation until the next large levee break. Channels are probably more likely to break their natural levees when the surrounding floodplains are relatively low, because the higher local energy slope into the floodplain would tend to promote scour and the excavation of a levee breach. Conversely, a floodplain that has recently aggraded as a result of crevasse splay deposition would be much closer in elevation to the crest of the natural levee, making it significantly less likely to experience another splay deposit in the immediate future. As time progresses, the channel bed and adjacent natural levees would continue to aggrade as the channel migrates across the Beni foredeep, gradually raising the levees with respect to the surrounding floodplains, and ultimately building a sufficiently high energy gradient to again breach the levee and debouch another crevasse splay deposit to blanket the previous one.

My interpretation of the data in Figure 5.7 is that the proximal floodplain (0–300 m) frequently receives sediment during major floods, rapidly building the natural levees, but the thick vegetation and emergent levees prevent this sediment from being transported more than a few hundred meters. Because of very rapid channel migration, the majority of the dated cores were located more than 300 m from the river at the time of the most recent deposition, in spite of the fact that only one transect extended farther than 300 m from the Beni River channel when sampled in 1999. According to the crevasse splay hypothesis, only when a natural levee fails can significant quantifies of sediment be transported into the distal floodplain. This concept does not apply to the recently deposited point bar side of the river, for which I have limited granulometric, topographic, and geochronologic data. Such point bar locations would probably receive sediment during moderate flooding, because they are both topographically lower and are characteristically surrounded by and close to the river channel; inundation of vegetated point bar surfaces with sediment-laden river water would likely be both a regular and measured (non-catastrophic) process.

Discharge at Rurrenabaque (Figure 5.9a) exceeds 28,000 m^3/s during ENSO year 1998, coinciding with the only recorded floodplain deposition during the six years of available daily records. This is twice the typical maximum annual discharge of ~ 14,000 m^3/s, substantially exceeding the capacity of the river channel, which generally adjusts to convey a two-year flood. I propose that Beni River floods of this approximate size are needed to breach portions of the natural levee system, debouching crevasse splays across the adjoining floodplain. If this hypothesis is substantiated with further field data and discharge records, a new model should be developed to account for the repeated accumulation of crevasse splays across the distal floodplain, as integrated over a timescale of centuries.

Summary

This study describes and quantifies floodplain accumulation across a large

foreland basin. It employs the CIRCAUS method of ^{210}Pb radioisotope geochronology for river floodplains (Chapter 4), yielding a number of significant results:

(1) River sediment is deposited across the floodplain only during extraordinary floods. Any particular floodplain locale receives sediment only rarely, exhibiting no discernible accumulation during most of large floods. This unexpected result means that much of the floodplain surface is many decades old. Consequently, for the Beni Foreland, conventional floodplain sedimentation models that call for regular advective or diffusive conveyance of river sediment onto floodplains during flooding do not seem appropriate. There is no evidence for such chronic accumulation.

(2) The floodplain cores and cutbank transects illustrate that floodplain sediment arrives as discrete pulses 20- to 120-cm thick and hundreds of meters to kilometers in width. Core granulometry and X-ray images depict a low-to-moderate energy depositional environment characteristic of the distal regions of crevasse splay deposits such as might form in a densely-vegetated rainforest floodplain. This and other evidence suggests that crevasse splay deposits might account for the vast majority of floodplain accumulation across the Beni Foreland, analogous to similar deposits preserved in exposures of ancestral foreland basin lithology in the Andes. While further field data and theoretical development are needed to fully verify and model this proposed mechanism, it is evident that the standard geomorphic schemes for advecting or diffusing excess sediment onto the floodplain are not appropriate for rivers that frequently debouch crevasse splays across their surrounding floodplains.

(3) These episodic floodplain deposits occur in temporal association with major Beni River flooding events, as determined at the long-term gauging station at Rurrenabaque. Besides providing the necessary water discharge to break

natural levees to form splays, such infrequent floods also convey an extraordinary quantity of sediment into (and across) the Beni Foredeep.

(4) Major Beni River floods are closely correlated with La Niñas, particularly those immediately following large El Niños. As such, sediment transport by the Beni River and splay deposition across the floodplain are dominated by major floods orchestrated by extreme ENSO events. Because the Beni is the principal sediment supplier to the Madeira River (and analogous to other sediment-laden rivers immediately to the NW and SE), which is turn are the principal sediment source for the mainstem Amazon, these ENSO-driven processes may modulate sediment delivery to the the mainstem Amazon, estuary, and shelf environs.

(5) It is possible to convert the dated deposit thicknesses into estimates of minimum accumulation rate. Binning these rates by spatial location, I construct a plot of mean floodplain accumulation as a function of distance from the active channel (Figure 5.7). The core sedimentation data set can also be subdivided to quantify minimum average accumulation rates across the Beni Foredeep and Forebulge. Rates decline monotonically both away from the channel and down-basin with increasing distance from the range front. However, unlike popular theoretical models for floodplain sedimentation as a function of channel distance, the accumulation rates do not exhibit a compelling exponential decline away from the Beni River. This is probably because crevasse splays do not mimic the processes and exponential distribution of floodplain accumulation associated with conventional diffusive or advective models.

(6) The plot of mean floodplain accumulation rate versus river distance (Figure 5.7) can also be interpreted as an approximate aggradation rate for the floodplain. As such, it is evident that within 300 m of the channel, the floodplain aggrades at least 5 cm/yr, probably reflecting the rapid growth of

channel-proximal natural levees. In comparison, the distal floodplain aggrades at least 1.5 – 2 cm/yr, probably reflecting the overall average infilling rate of the foredeep basin. Therefore, the active channel-floodplain system spanning the Beni Foreland may aggrade at 2–5 cm/yr relative to the cratonic basement.

Table 5.1. List of all floodplain sampling locations for the Beni River, including the 25 survey transect locations where samples were collected and topography was measured over long distances (usually on both sides of the river, spanning the point bar and the channel). A sample GIS location map is presented in Figure 5.2, and in Appendixes A, E, F, and G.

			Water	Floodplain Survey Length		
Transect #	East (UTM 19s)	North (UTM 19s)	Elevation (m)	Cutbank (m)	Bar (m)	Description
1	672533	8503591	163	50	50	short transect
2	678338	8508874	159	100	50	short transect
3	675573	8519691	155	1250	50	very long transect on fp
4	690003	8539939	155	50	50	short transect
6	713201	8554524		5	5	banks of blackwater tributary
7	712524	8565731	150	50	50	short transect
8	722828	8584404		300	none	single core on high terrace
9	722010	8586316	148	50	50	short transect
10	719996	8599633	144	100	50	transect
11	722743	8603551	142	300	50	longer transect
14	723343	8622025	138	150	50	transect
18	729247	8672095	138	300	50	longer transect
25	651369	8373045	217	50	none	single core on floodplain
27	658467	8383200	211	50	none	single core on floodplain
34	656742	8411877	185	10	none	two cores on high terrace
41	656200	8414890	182	600	none	meander neck transect
48	678224	8499947		1000	none	core from oxbow lake limb
49	674889	8494758	163	5	none	vertical transect
50	677119	8491756	164	50	100	transect
51	669443	8485943	164	300	50	longer transect
52	667855	8481240	165	700	none	survey around oxbow cutoff
54	659492	8475573	168	50	5	transect
55	660703	8461648	174	50	5	transect
56	661496	8453645	173	50	50	transect, very large sand bar
57	662197	8444955	173	50	50	transect
59	660427	8426380	177	50	50	transect
60	664551	8420047	178	300	100	longer transect
61	664551	8420047		200	50	transect
62	664551	8420047		200	50	transect
63	664551	8420047		200	50	transect
64	664551	8420047		200	50	transect

Table 5.2. Summary of results from all dated cores, including sample depths, associated dates, and corresponding GIS channel distances. Survey transect locations are listed in a downstream direction, with sites 14 and 18 located in the forebulge, all of the other sites in the Beni Foredeep. Minimum accumulation rates are determined by dividing the representative thickness of the deepest sample by its age (years before 2000). Bounded accumulation rates are from sedimentation events with resolved bottoms. Any cores that might possibly be interpreted with a "constant sedimentation" model are also analyzed with the CIRCACS model (credible fits are highlighted in red). Average rates are reported for various distances from the channel and locations within the foreland. All plateau dates ("49" means 1949, etc.) are standardized to ENSO water year (Oct. – Sept.). The expected dating error depends primarily on 1) the confidence interval for the clay-normalized activity of the plateau, 2) the typical reach variability in CIRCA during flooding, and 3) the age of the sediment (Chapter 4). For the Beni River, this error is typically 1–2 years.

Site	Site Name	deepest sample (cm)	partial depth (when not entire core) (cm)	CIRCAUS Date of Deposition	Corresponding GIS Channel Distance (m)	CS rate (cm/a)	Accumulation Rate (cm/ yr, minimum, all)	Bounded Accumulation Rate (cm/yr)
41	41RFC200	115		49	200		2.25	
	41RFC300	43		70	500		1.43	
	41RFC450	49		76	350		2.04	
	41RFC523	50		70	250		1.67	
60	60LFB5	52		98	5		26.00	
	60RFC5	56		98	150		28.00	
	60RFC50	25		88	700		2.08	
	60RFC100	48		88	750		4.00	
	60RFC150	50		72	2000		1.79	
a	60RFC200		15	74	2000		0.58	0.58
b	60RFC200	25		47	2800		0.19	
a	60RFC250		80	74	2000		3.08	3.08
b	60RFC250	120		49	2900		0.78	
	60RFC300		40	82	1300		2.22	2.22
61a	61RFC100		30	89	620		2.73	2.73
b	61RFC100	52		50	2400		0.44	
	61RFC200	53		77	1650		2.30	
62a	62RFC5		30	87	160		2.31	2.31
b	62RFC5	49		83	325		1.12	
	62RFC50	43		83	210		2.53	
	62RFC100	53		73	900		1.96	
	62RFC150	48		50	1500		0.96	
a	62RFC200		40	75	1000		1.60	1.60
b	62RFC200	59		50	1600		0.38	
63	63RFC5	53		77	1700		2.30	
	63RFC100	62		70	1800		2.07	
a	63RFC200		35	97	300		11.67	11.67
b	63RFC200	53		88	675		1.50	
64	64RFC5	33		90	260		3.30	
	64RFC50	43		73	480		1.59	
	64RFC100		37	82	575		2.06	2.06
	64RFC150	42		72	550		0.18	
	64RFC200	43		77	480		1.87	
59	59RFC50	48		55	50		1.07	
cb2	CB2 - 1998	156		87	300		12.00	
57	57RFC50	43		73	150		1.59	

Table 5.2. (continued)

cb1	CB1 - 1998	165			250	1.9	1.90	1.90
56	56RFC50	43		74	2500		1.65	
55	55LTC50	63		98	50		31.50	
54	54LFC50	53		97	225		17.67	
51	51RFC50	43		88	50		3.58	
a	51LFC5		40	84	5		2.50	2.50
a	51LFC50		44	84	50		2.75	2.75
b	51LFC50	53		74	50		0.35	
	51LFC100	53		73	100		1.96	
a	51LFC200		30	56	200		0.68	0.68
b	51LFC200	46		17	200		0.19	
a	51LFC300		25	55	300		0.56	0.56
b	51LFC300	53		43	300		0.49	
50	50RFC5	35		76	925		1.46	
	50RFC50	118			250	1.15	1.15	1.15
	50RFC50	118		49	800		2.31	
1	1LFC50	52		83	750		3.06	
2	2RFC50	53		74	225		2.04	
3	3A-1200M	50		54	1200		1.09	
	3B-1150M	43		55	1150		0.96	
a	3D-900M		23	49	900		0.45	0.45
b	3D-900M	43		14	1000		0.23	
	3E-20M	30		48	20		0.58	
6a	6LVB5		40	83	2500		2.35	2.35
6b	6LVB5	65		49	2000		0.49	
	6RVC5	54		82	2500		3.00	
7	7RFC50	58		88	400		4.83	
8	8RFC400	50		49	400		0.98	
9	9RFC50	53		75	400		2.12	
a	10LFC50		35	88	550		2.92	2.92
b	10LFC50	53		48	1000		0.35	
11	11LFC50	27		56	2000		0.61	
a	11LFC100		50	83	750		2.94	2.94
b	11LFC100	57		48	2000		0.13	
	11LFC150	63		88	675		5.25	
	11LFC200	53		88	725		4.42	
	11LFC250	53		87	775		4.08	
a	11LFC300		53	89	825		4.82	4.82
b	11LFC300	60		54	2200		0.15	
14	14RFB5	53		71	55		1.83	
a	14RFB50		35	71	100		1.21	1.21
b	14RFB50	43		44	100		0.14	
	14RFB100	50		74	150		1.92	
a	14RFB150		43	71	200		1.48	1.48
b	14RFB150	53		56	200		0.23	
18a	18RFC5		30	97	5		10.00	10.00
18b	18RFC5	53		56	100		0.52	
	18RFC50	117		42	150		2.02	
	18RFC100	51		42	200		0.88	

Average Distance From Channel (m)	Measured Minimum Rate (cm/yr)
50	5.3
200	4.7
650	2.2
1500	1.4
2500	1.3

	CS rate (cm/yr)	Sed. Rate (min., all, cm/yr)	Bounded Sed. Rate (cm/yr)
All samples	1.5	3.2	2.8
Foredeep		3.4	2.6
Foredeep to #3		3.6	2.4
Foredeep from #6		2.5	3.3
Straight Foredeep (51, 3)		0.7	0.6
Forebulge		2.0	4.2

Table 5.3. List of all dated floodplain sedimentation years, with summary of relation to gauged discharge and ENSO records. Deposition occurs during large floods, which generally correspond to larger ENSO cold phase events, especially those which follow significant warm phase events. The NDJF JMA SSTA value, a measure of the Pacific Ocean surface temperature anomaly, is discussed in the text.

ENSO Year	# of Sed. Events	Max. Monthly Discharge (CMS)	NDJF JMA SSTA (deg)	d [NDJF JMA SSTA] (deg)
1998	6	7828	-0.8	-3.8
1988	14	data bad	-1.2	-2.0
1983	10	8010	-0.2	-2.9
1977	6	7080	0.3	-0.6
1973	12	7200	-1.4	-3.0
1970	7	8250	-1.4	-2.1
1955	9	na	-1.2	-0.4
1949	13	na	-1.2	-1.2
1942	4	na	-1.4	-1.8
1916	2	na	-1.9	-1.4

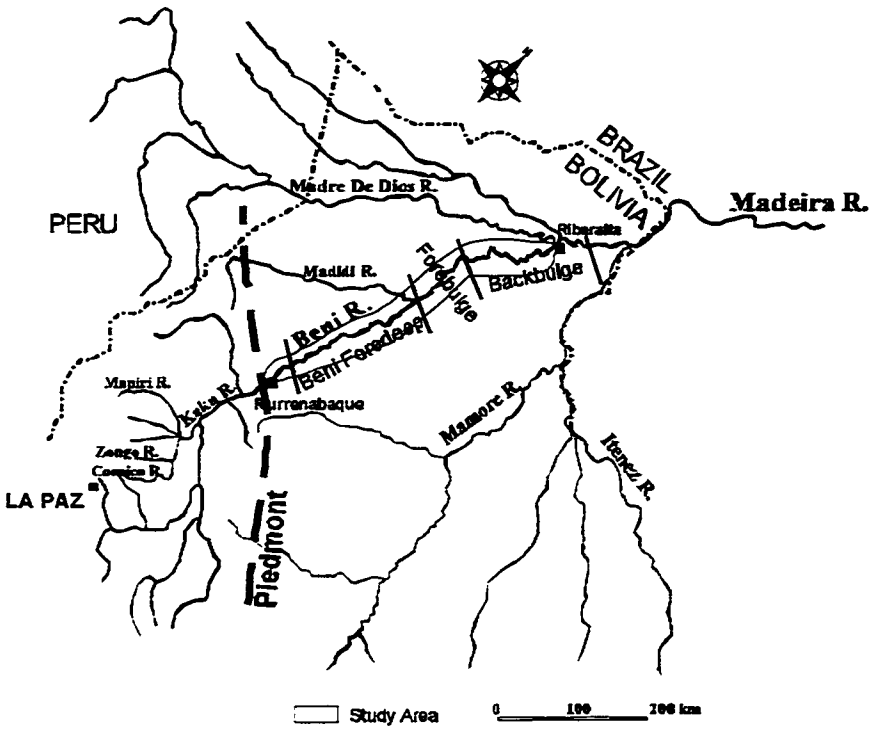

Figure 5.1. Hydrological map of major Madeira River tributaries, depicting the Beni River, the study focus area for floodplain sampling, and principal long-term river gauging stations at Rurrenabaque and Riveralta. Approximate location of the foredeep, forebulge, and backbulge secondary basin are depicted, as determined by DGPS surveys of longitudinal river gradient.

Figure 5.2. Example of a GIS detail map for a Beni floodplain survey site. This site was chosen to measure sedimentation rates along a series of five transects spaced along an active meander: 60, 61, 62, 63, and 64. In the image, bare sand or earth (band 5) is red, vegetation (band 4) is green, and water (band 3) is blue. Additional GIS detail maps are presented in Appendix A, and the GIS procedure is discussed in Chapter 2.

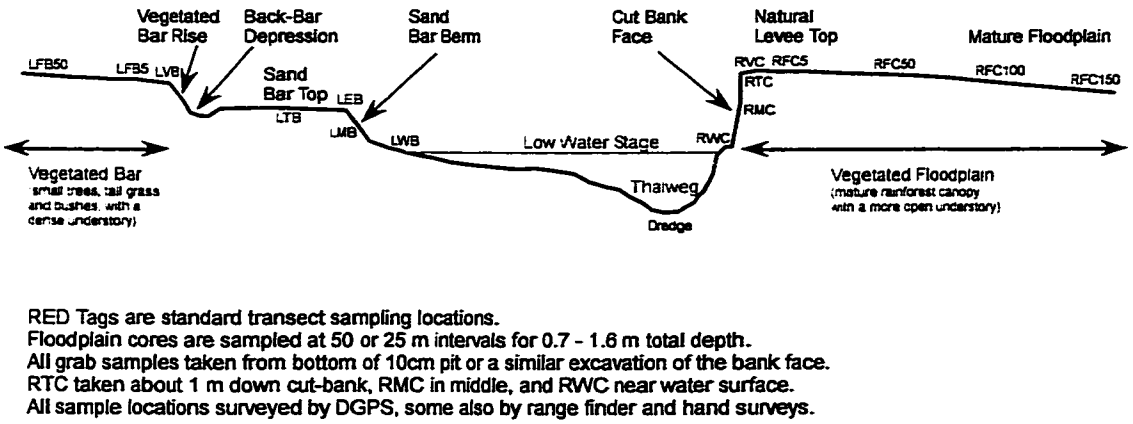

Figure 5.3. Sketch of a typical survey transect across a Beni River meander apex. All grab samples taken from the bottom of a 10 cm pit or a similar excavation of the bank face. Floodplain cores were sampled at 50- or 25-m intervals for 65–130 cm total depth. All sample locations surveyed by DGPS, and many also by laser or hand level surveys, as discussed in Chapter 2.

Figure 5.4. (a) Example of a terrace core, site 34 (proximal to floodplain site 41), located ~ 15 m above the low-stage water surface. Clay-normalized activity quickly declines to a supported level of 1.4 DPM/g clay. Total unsupported activity near the core top indicates (from a depth-density-clay-fraction integration over the top 20 cm) an average meteoric input of 44 DPM/cm^2.

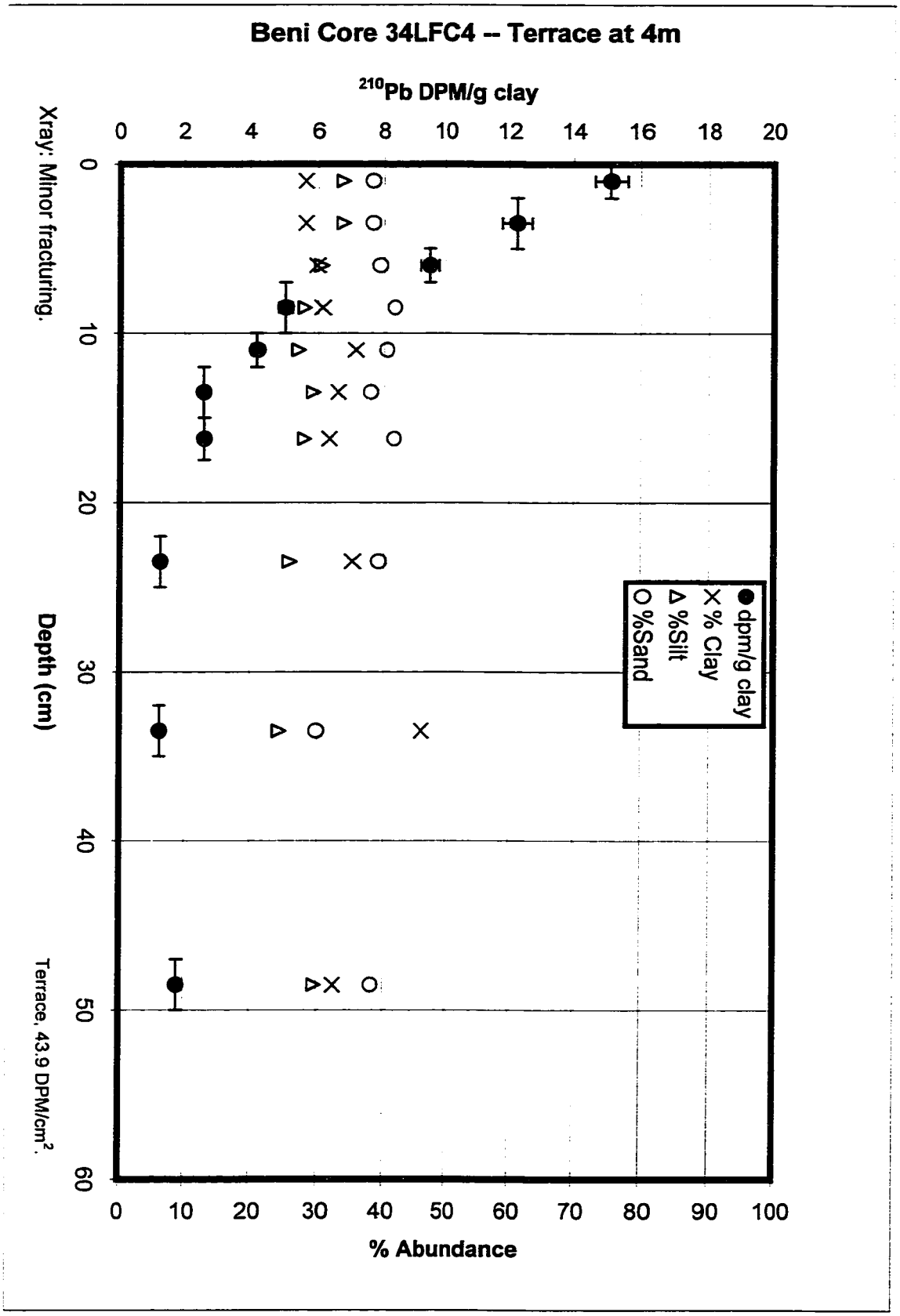
Beni Core 34LFC4 -- Terrace at 4m
^{210}Pb DPM/g clay
0 2 4 6 8 10 12 14 16 18 20
Xray: Minor fracturing.
Depth (cm)
0 10 20 30 40 50 60
dpm/g clay
% Clay
%Silt
%Sand
0 10 20 30 40 50 60 70 80 90 100
% Abundance
Terrace, 43.9 DPM/cm^2.

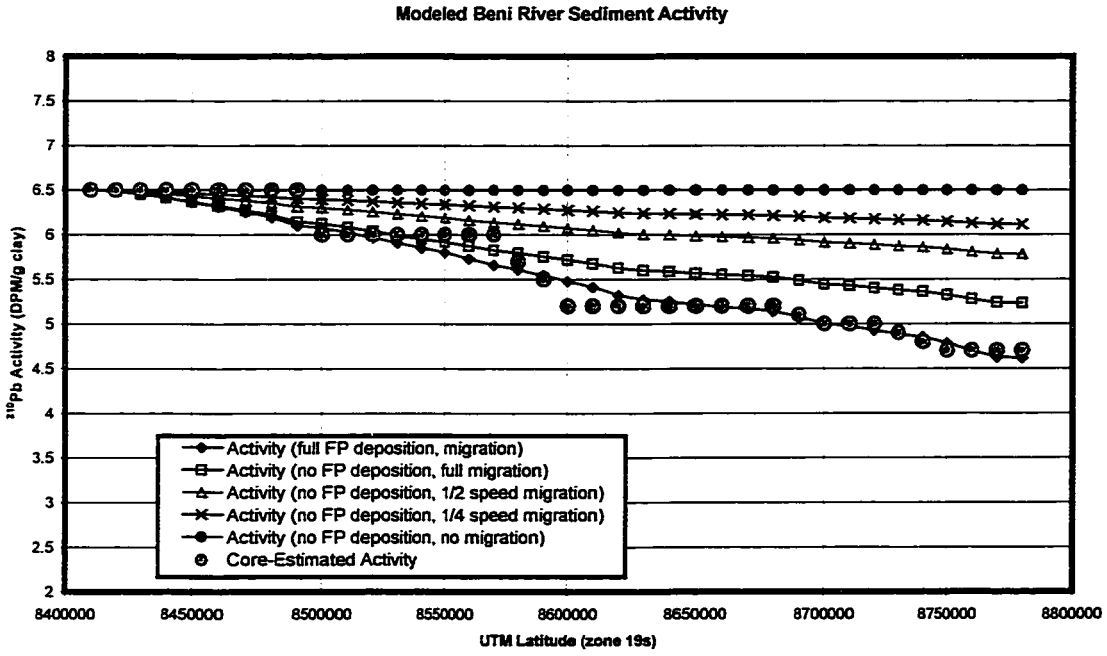

Figure 5.4. (b) Modeled clay-normalized ^{210}Pb activity in river sediment plotted versus UTML, based on the exchanges of clay associated with the mass fluxes presented in Chapter 2. Red line represents full flood conditions, with all exchange and depositional processes occurring at their mean annual rates. Gray circles depict measured sediment activity from channel-proximal floodplain samples. The full description of the procedure and analysis results are presented in Chapter 4.

Figure 5.5. Floodplain cores depicting clay-normalized activity, grain size, summary of the X-radiograph, and results from the CIRCAUS geochronology: any date(s) of activity plateau(s) and the date of the meteoric cap (if any). (a) Site 3-A, located 1200 m from the channel when the sediment was deposited in 1954.

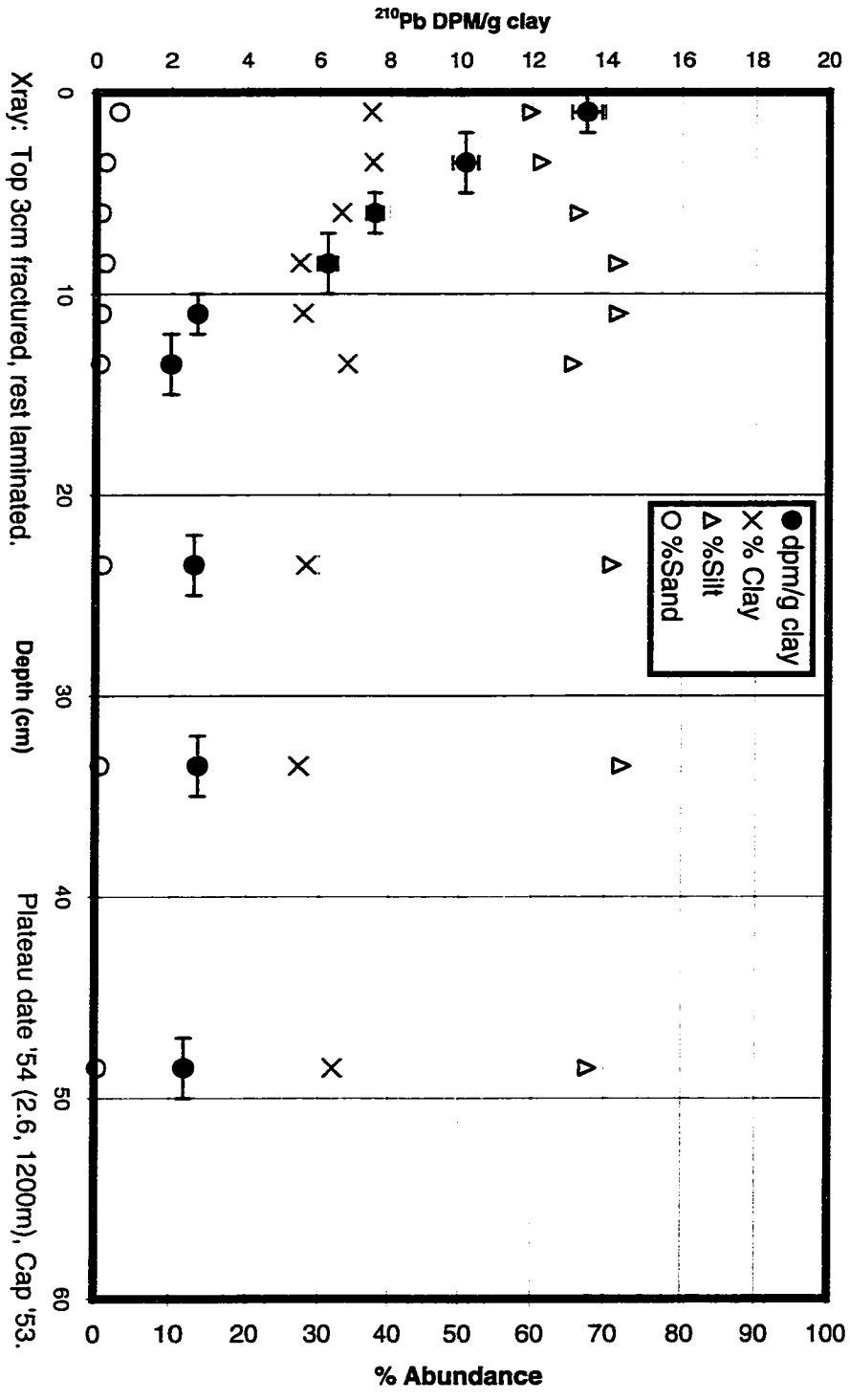
Beni Core 3A - >1km from River
^{210}Pb DPM/g clay
0 2 4 6 8 10 12 14 16 18 20
Xray: Top 3cm fractured, rest laminated.
Depth (cm)
0 10 20 30 40 50 60
dpm/g clay
% Clay
%Silt
%Sand
Plateau date '54 (2.6, 1200m), Cap '53.
0 10 20 30 40 50 60 70 80 90 100
% Abundance

Figure 5.5. (b) Site 3-B.

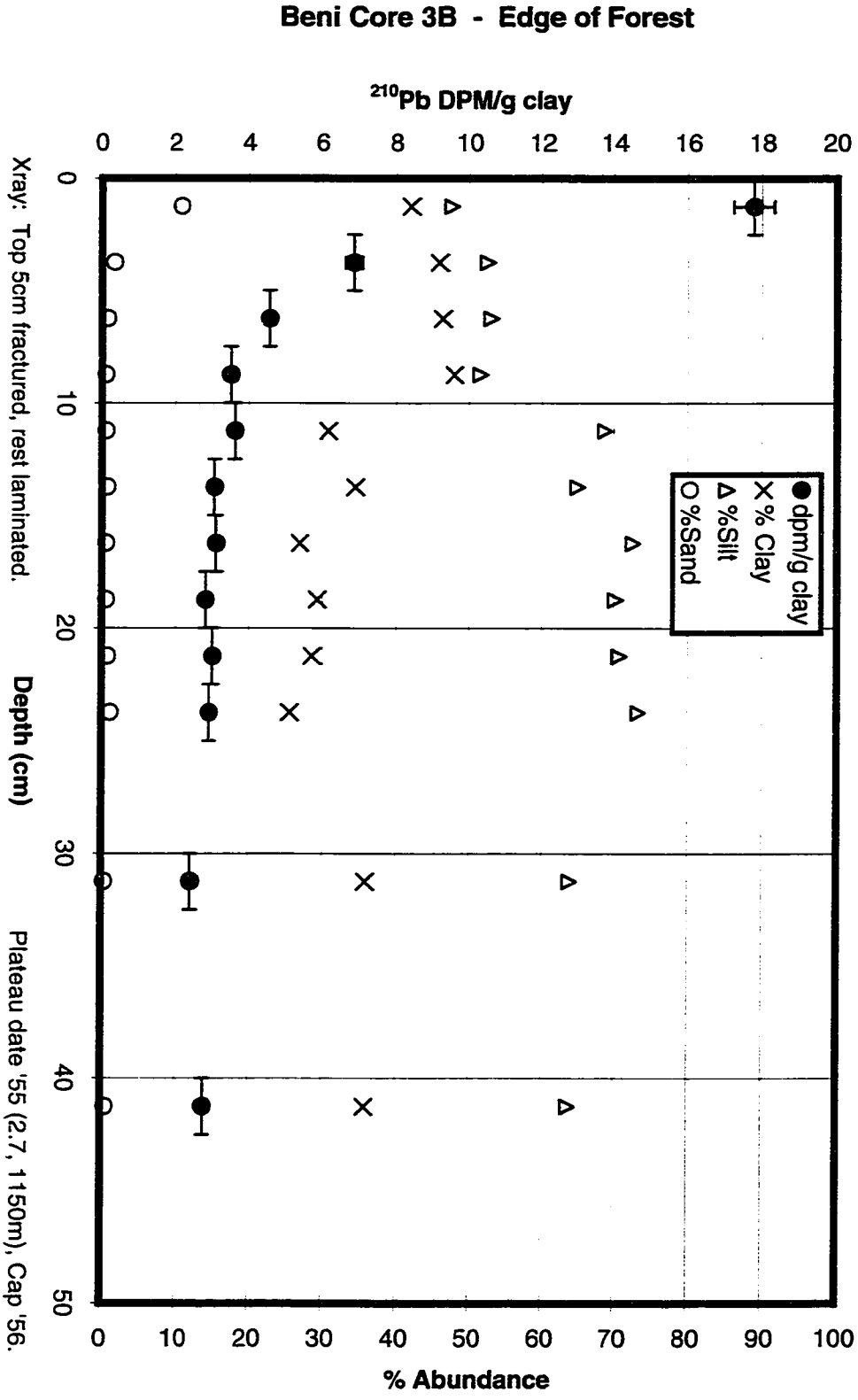
Beni Core 3B - Edge of Forest
^{210}Pb DPM/g clay
0 2 4 6 8 10 12 14 16 18 20
Xray: Top 5cm fractured, rest laminated.
Depth (cm)
0 10 20 30 40 50
dpm/g clay
% Clay
%Silt
%Sand
0 10 20 30 40 50 60 70 80 90 100
% Abundance
Plateau date '55 (2.7, 1150m), Cap '56.

Figure 5.5. (c) Site 62 RFC-100m, located 900 m from channel when the sediment was deposited in 1973.

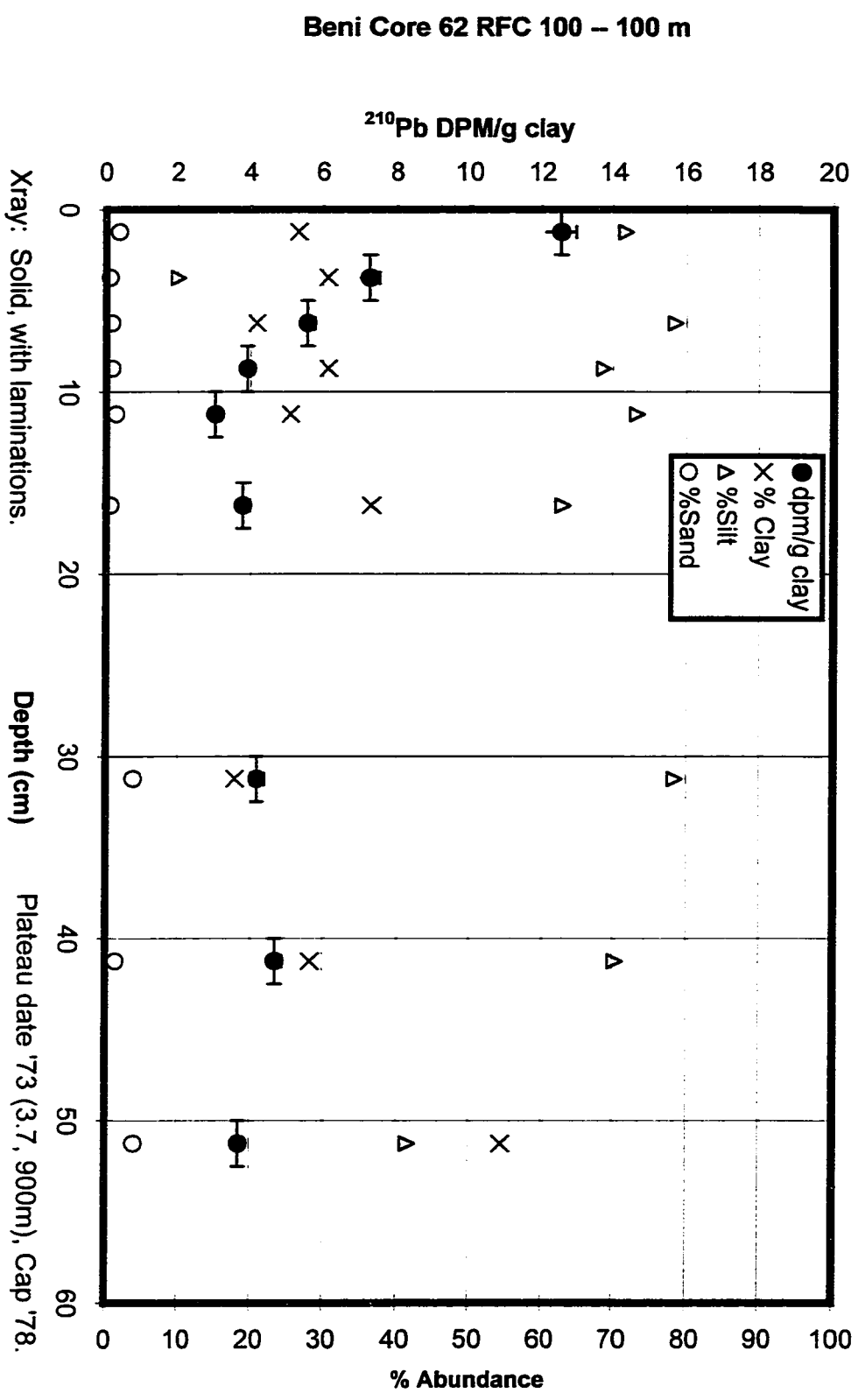
Beni Core 62 RFC 100 -- 100 m
^{210}Pb DPM/g clay
0 2 4 6 8 10 12 14 16 18 20
Xray: Solid, with laminations.
Depth (cm)
Plateau date '73 (3.7, 900m), Cap '78.
0 10 20 30 40 50 60
0 10 20 30 40 50 60 70 80 90 100
% Abundance
dpm/g clay
% Clay
%Silt
%Sand

Figure 5.5. (d) Site 60RFC-250m, depicting two depositional events in 1974 and 1949. The transition between the two lies at ~ 80 cm.

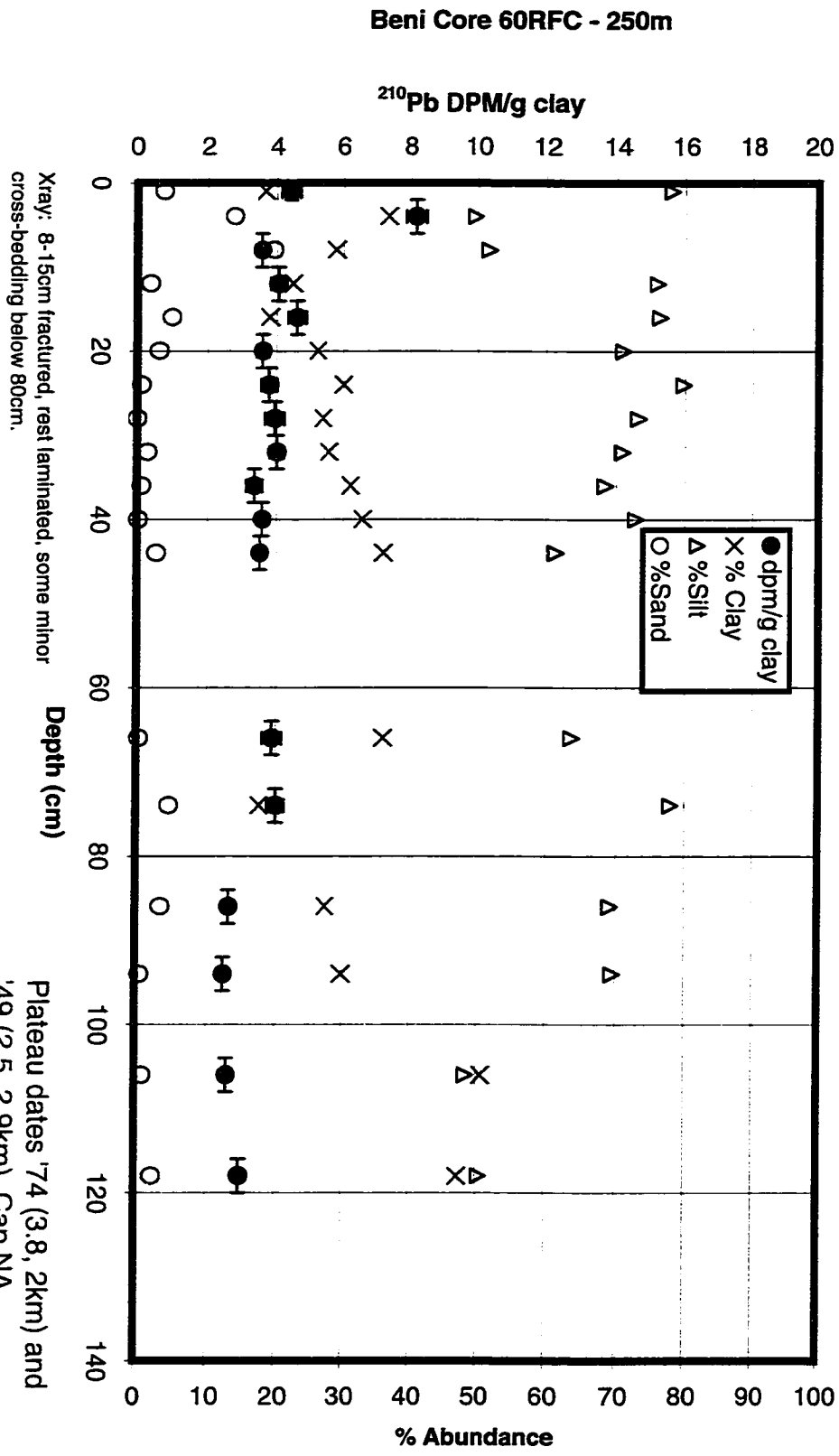
Beni Core 60RFC - 250m
^{210}Pb DPM/g clay
0 2 4 6 8 10 12 14 16 18 20
0 20 40 60 80 100 120 140
Depth (cm)
dpm/g clay
% Clay
%Silt
%Sand
0 10 20 30 40 50 60 70 80 90 100
% Abundance
Xray: 8-15cm fractured, rest laminated, some minor cross-bedding below 80cm.
Plateau dates '74 (3.8, 2km) and '49 (2.5, 2.9km), Cap NA.

Figure 5.5. (e) Site 60RFC-150m.

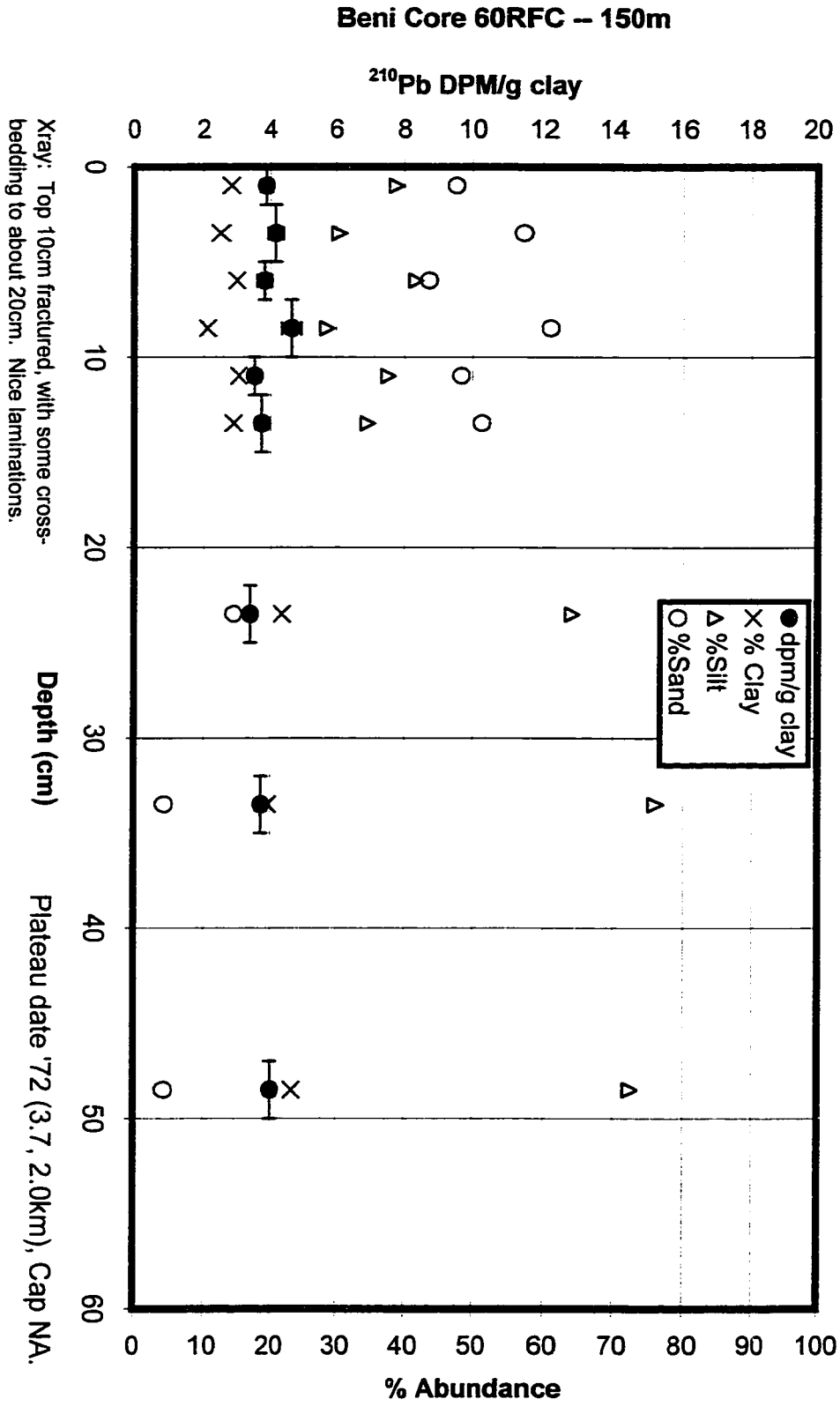
Beni Core 60RFC -- 150m
^{210}Pb DPM/g clay
0 2 4 6 8 10 12 14 16 18 20
Xray: Top 10cm fractured, with some cross-bedding to about 20cm. Nice laminations.
Depth (cm)
0 10 20 30 40 50 60
dpm/g clay
% Clay
%Silt
%Sand
0 10 20 30 40 50 60 70 80 90 100
% Abundance
Plateau date '72 (3.7, 2.0km), Cap NA.

Figure 5.5. (f) Site 54LFC-50m, depicting only recent deposition in 1997. At > 1 m depth, the sediment lays atop a thick lacustrine clay deposit radiometrically older than 110 years.

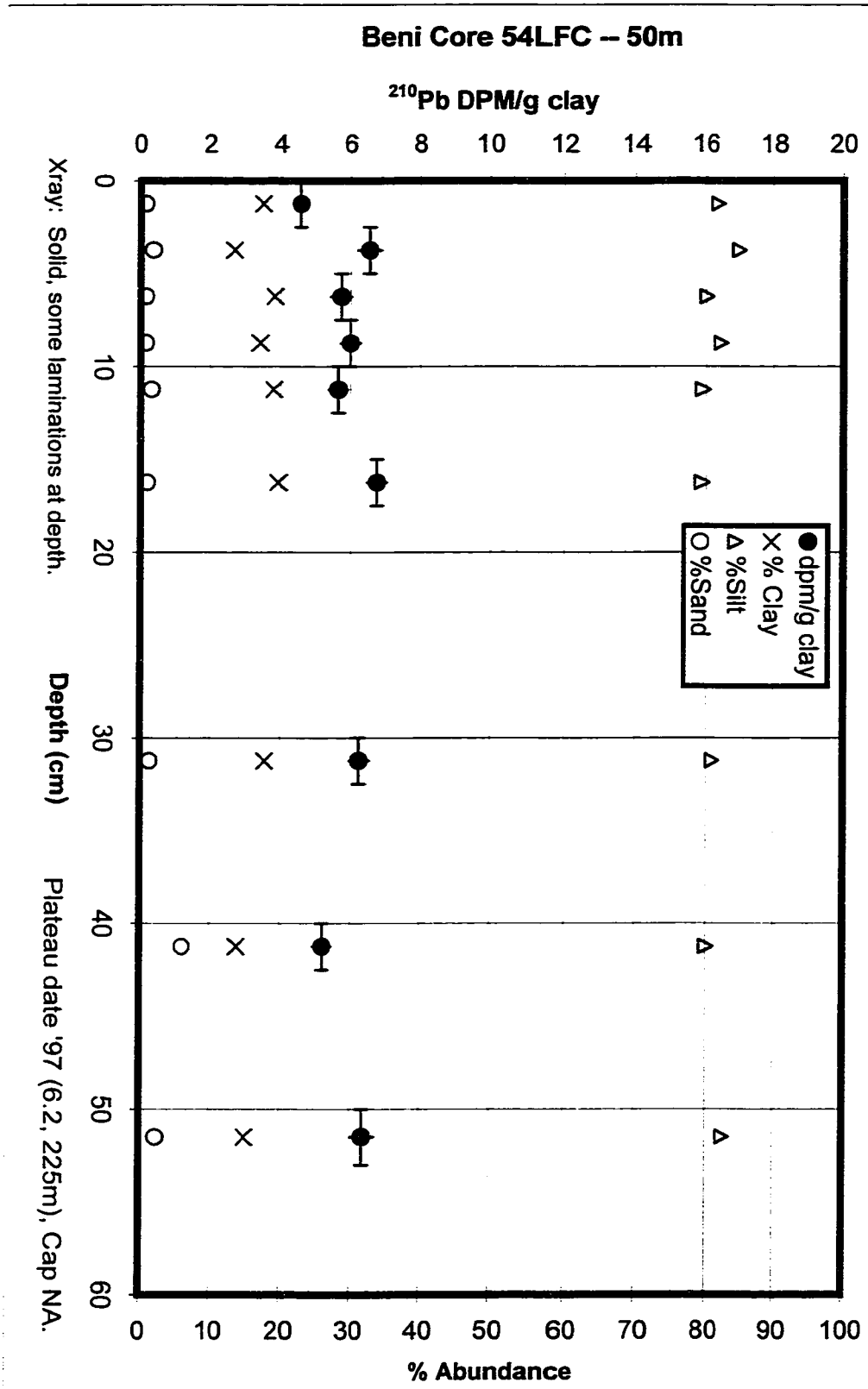
Beni Core 54LFC -- 50m
^{210}Pb DPM/g clay
0 2 4 6 8 10 12 14 16 18 20
Depth (cm)
0 10 20 30 40 50 60
% Abundance
0 10 20 30 40 50 60 70 80 90 100
dpm/g clay
% Clay
%Silt
%Sand
Xray: Solid, some laminations at depth.
Plateau date '97 (6.2, 225m), Cap NA.

Figure 5.5. (g) Site CB-1, depicting evidence for constant accumulation over ~ 80 years. Because the supported ^{210}Pb activity of 1.4 DPM/g clay is not reached in this core, the CICCS model would underestimate the sediment accumulation rate.

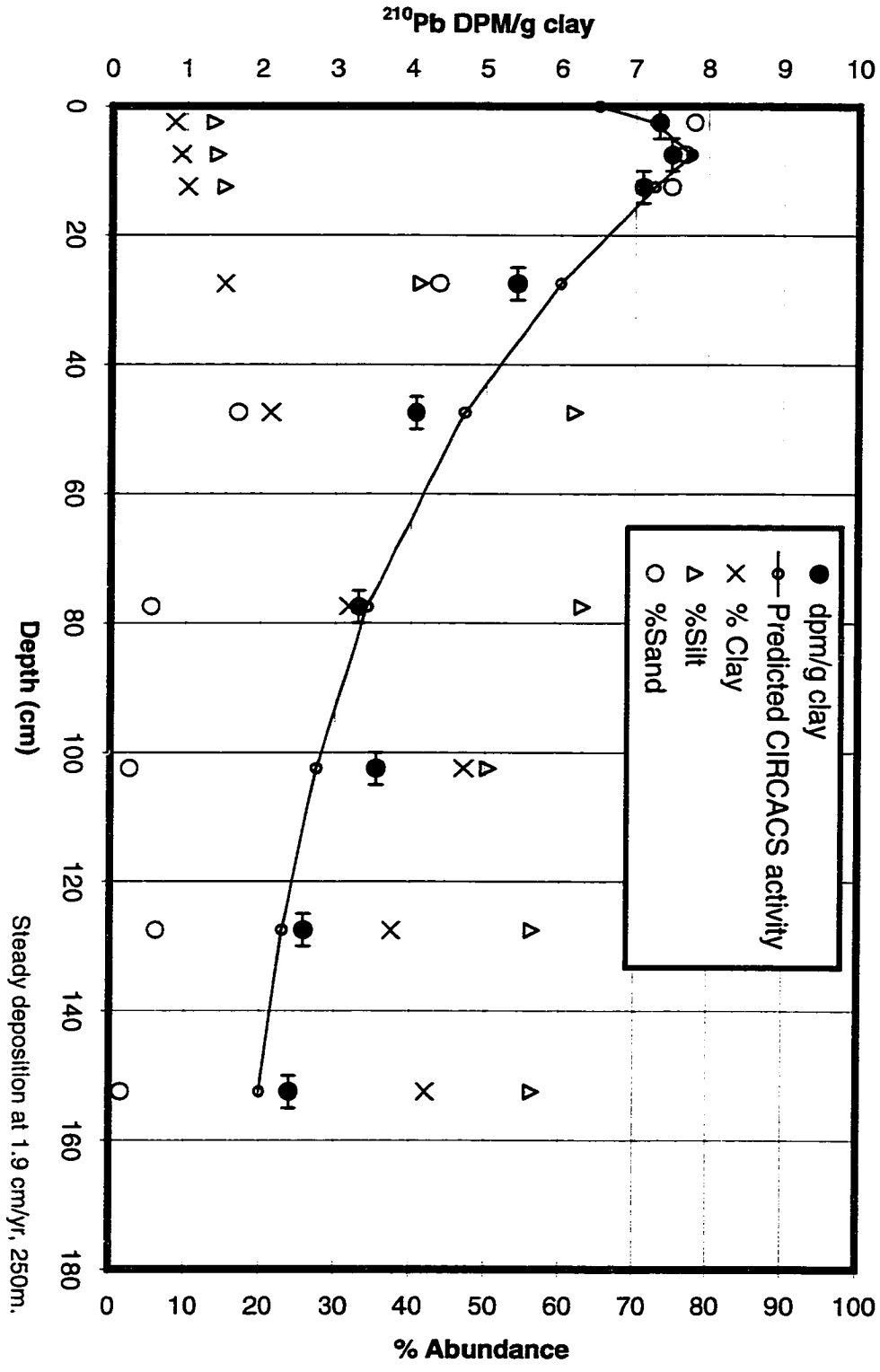
Beni Core CB1 - 1998
210Pb DPM/g clay
0 1 2 3 4 5 6 7 8 9 10
0 20 40 60 80 100 120 140 160 180
Depth (cm)
0 10 20 30 40 50 60 70 80 90 100
% Abundance
dpm/g clay
Predicted CIRCACS activity
% Clay
%Silt
%Sand
Steady deposition at 1.9 cm/yr, 250m.

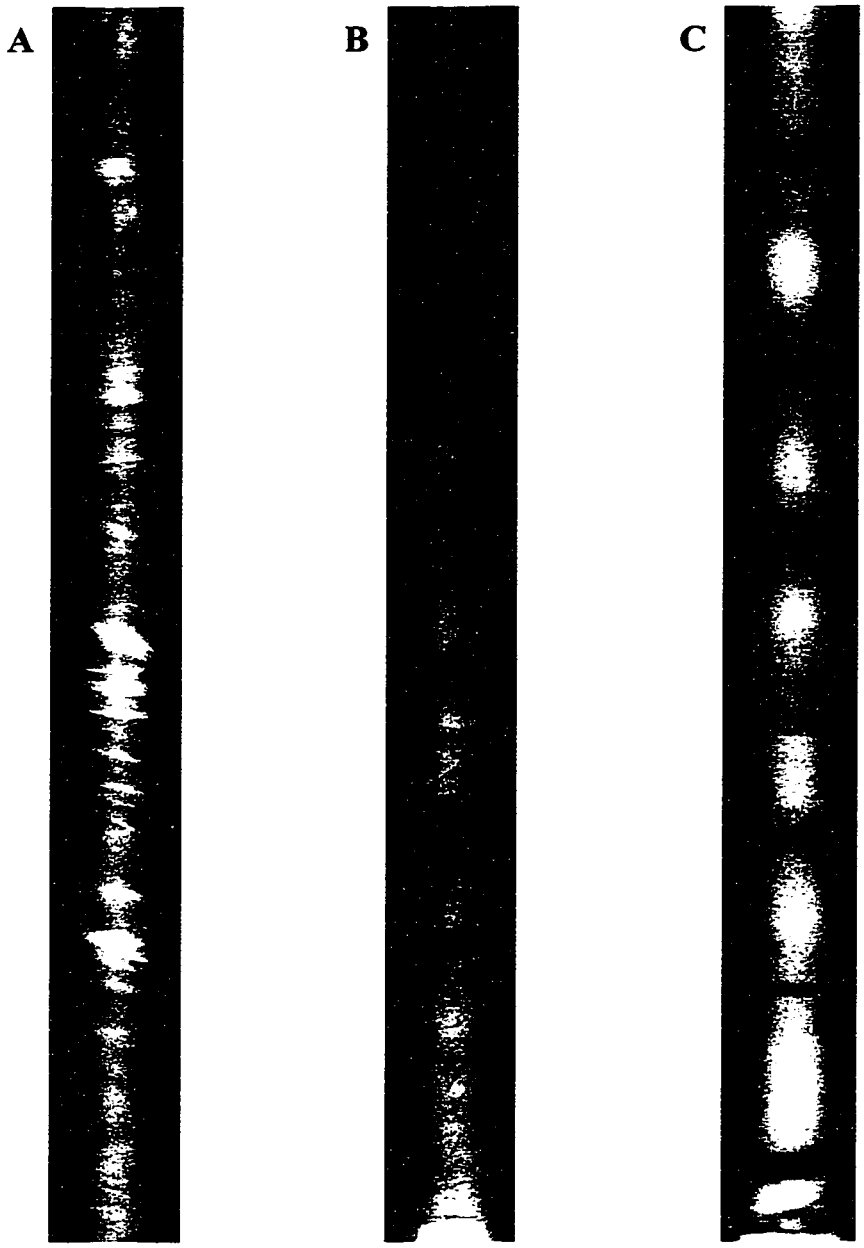

Figure 5.6. (a) X-ray image of a core located 5 m from the edge of the vegetation on a point bar deposit, site 49. Note the well-defined cross-bedding, which reflects the energetic depositional environment. (b) X-ray image of a core located on the forested floodplain 3 km from the river at the time of deposition, site 60. Fine horizontal lamina and massive silty deposits suggest a medium-to-low-energy depositional environment. (c) X-ray image of a core located on the forested floodplain 50 m from the river at the time of deposition, site 51, depicting massive banding and fine horizontal lamina. Images are approximately half of life size.

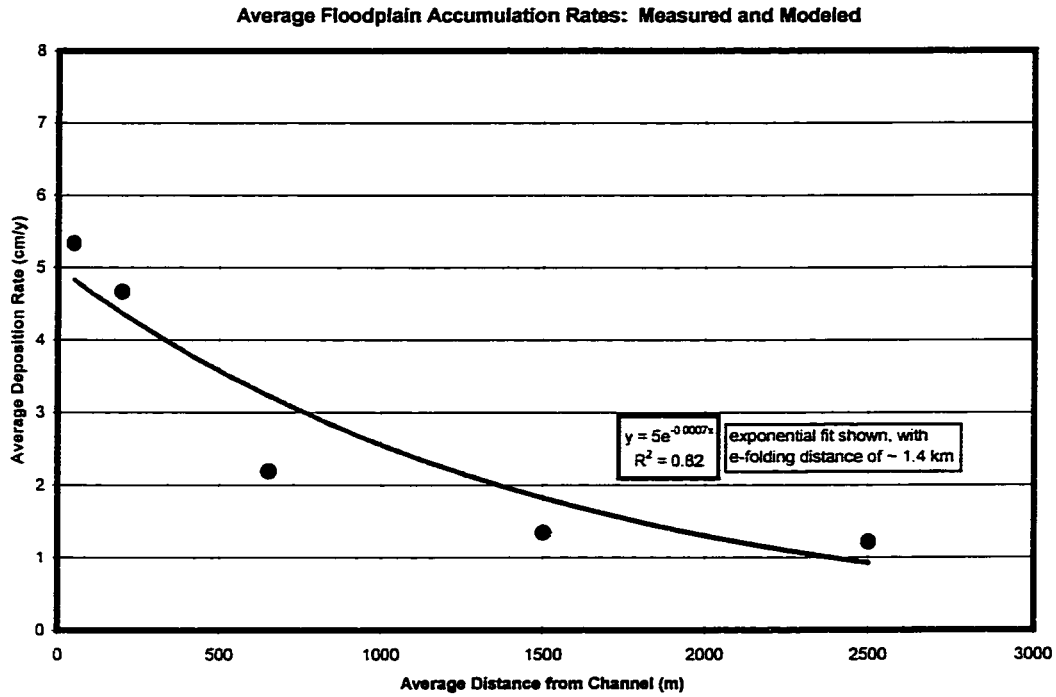

Figure 5.7. Average minimum floodplain accumulation rates as a function of distance from the channel. The red circles indicate the average measured minimum accumulation rates, and the brown line is a best-fit exponential relationship. River distances were determined at the recorded date of each sedimentation event, as presented in Table 5.2. The yellow circles depict the floodplain deposition rates assumed for the total Beni Foreland flux analysis in Chapter 2, including the distance intervals (black horizontal bars) over which these rates are assumed.

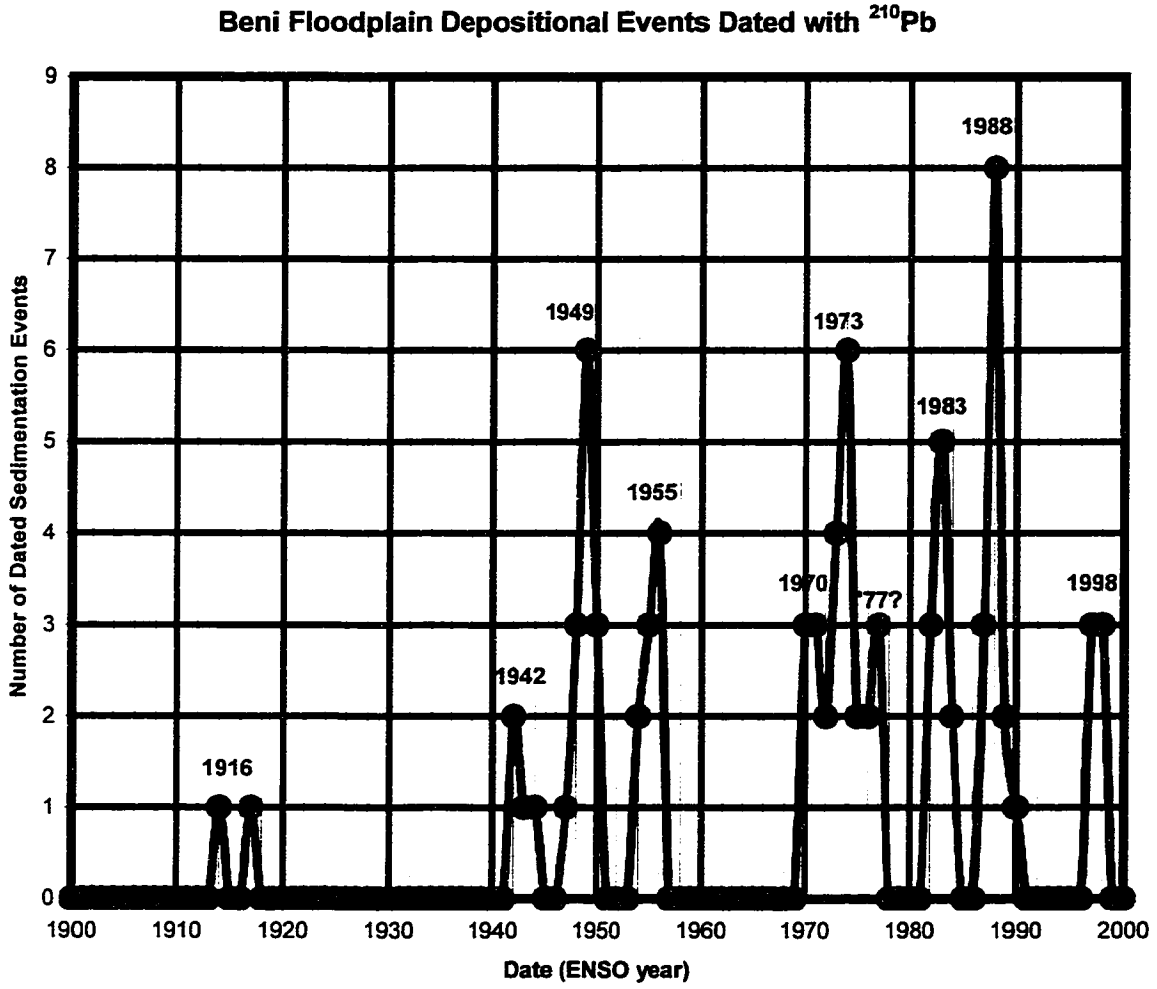

Figure 5.8. All dated floodplain sedimentation events plotted according to year of occurrence. The date of the corresponding cold phase ENSO event (Figure 5.10b) is denoted in red, with other flooding dates marked in black.

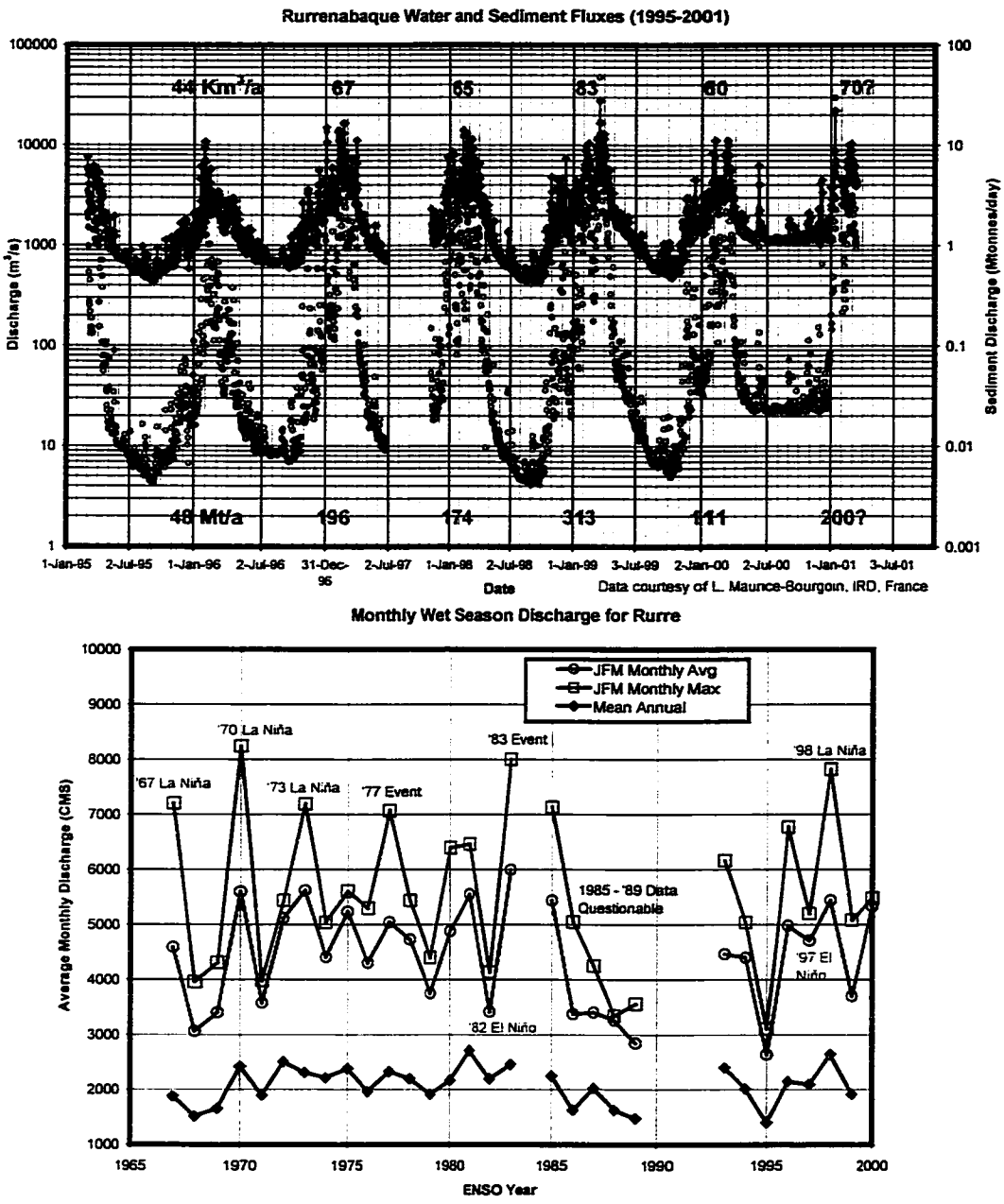

Figure 5.9. (a) Daily record of water and sediment discharge at Rurrenabaque from 1995 – 2001, data and sediment flux calculations by Maurice-Bourgoin, 2001. Total annual water (blue) and sediment (red) discharge have reported for the last six water years. Data from the last part of 2001 are not yet available, so the approximate fluxes have been estimated. Further discussion in Chapter 2. (b) Average and maximum monthly wet-season (Jan. – Mar.) discharge and average annual discharge recorded at Rurrenabaque. ENSO cold phase events are depicted in red, warm phase events in green (Figure 5.10b). Other major flood dates are marked in black. Water and ENSO years run from Oct. to Sept.

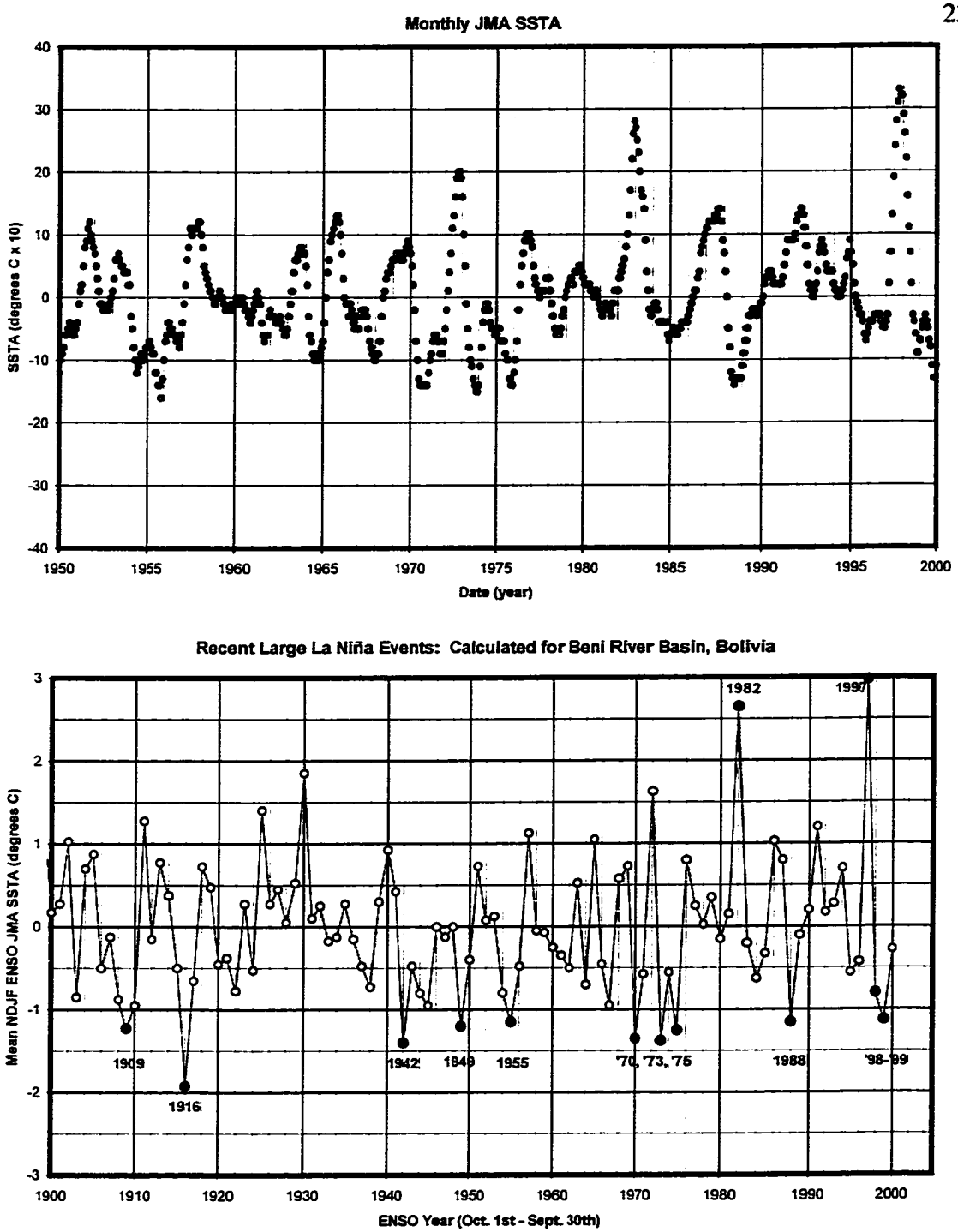

Figure 5.10. (a) JMA sea surface temperature anomaly plotted monthly over the past five decades. (b) JMA SSTA average for the months of November – February, plotted annually over the past century. For this study, years colder than 1 degree below normal are considered major cold phase events and are marked in red.

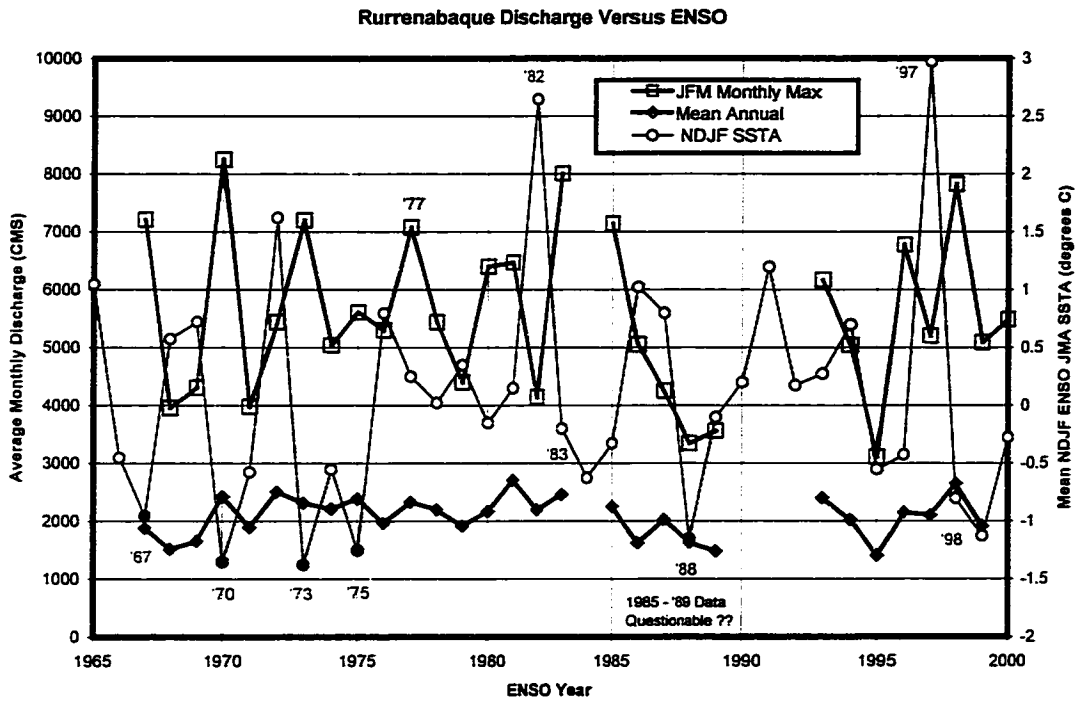

Figure 5.10. (c) Comparison of maximum monthly discharge at Rurrenabaque to NDJF JMA SSTA.

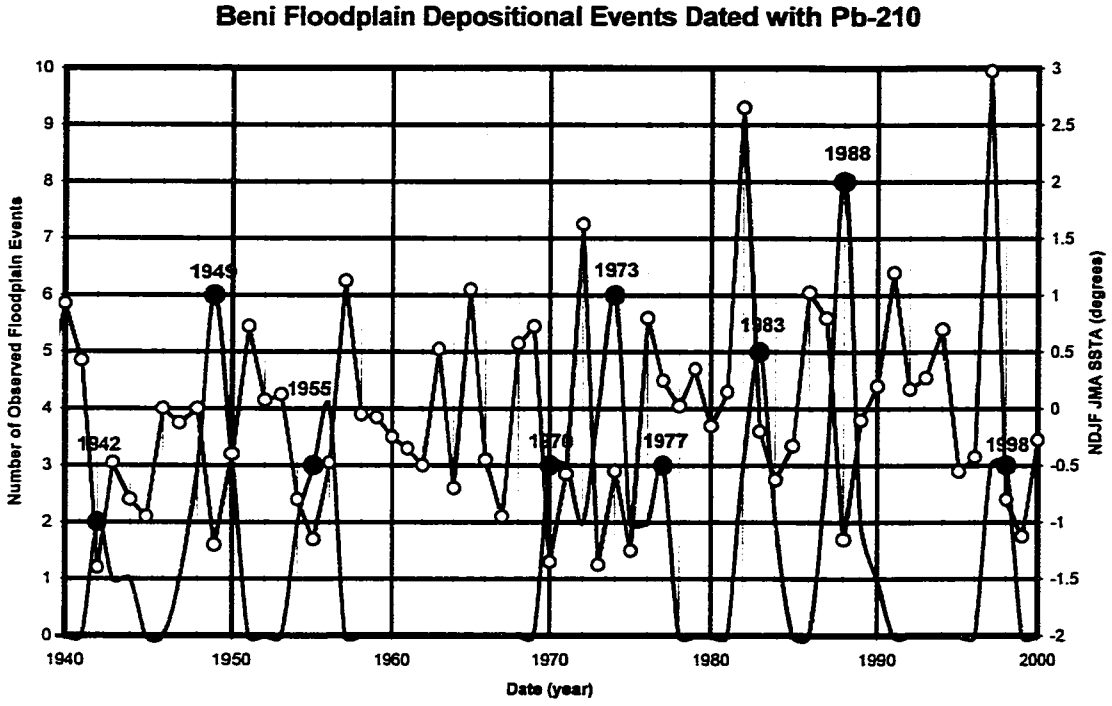

Figure 5.11. Comparison of dated floodplain sedimentation events to NDJF JMA SSTA.

Bibliography

Aalto, R., 1995, Discordance between suspended sediment diffusion theory and observed sediment concentration profiles in rivers [M.S. thesis]: University of Washington, 98 p.

Aalto, R., and Dunne, T., 1996, Geomorphic controls of Andean denudation rates: EOS AGU Transactions, v. 77, no. 46, p. 245.

Aalto, R., Dunne, T., and Guyot, J. L., 1999, Geomorphic controls on Andean denudation rates, *in* Hydrological and Geochemical Processes in Large Scale River Basins, Manaus, Brazil.

Ackers, P., and White, W. R., 1973, Sediment transport: new approach and analysis: Journal of the Hydraulic Division, American Society of Civil Engineers, v. 99, no. HY11, p. 2041-2060.

Adams, J., 1980, Active tilting of the United States midcontinent: geodetic and geomorphic evidence: Geology, v. 8, p. 442-446.

Ahnert, F., 1970, Functional relationships between denudation, relief, and uplift in large mid-latitude drainage basins: American Journal of Science, v. 268, p. 243-263.

Allison, M. A., Kuehl, S. A., Martin, T. C., and Hassan, A., 1998, Importance of flood-plain sedimentation for river sediment budgets and terrigenous input to the oceans: Insights from the Brahmaputra-Jamuna River: Geology, v. 26, no. 2, p. 175-178.

Anderson, R. S., 1994, Evolution of the Santa Cruz mountains, California, through tectonic growth and geomorphic decay: Journal of Geophysical Research, v. 99, p. 20161-20179.

Appleby, G., and Oldfield, F., 1978, The calculation of lead-210 dates assuming a constant rate of supply of unsupported Pb-210 to the sediment: Catena, v. 5, p. 1-8.

-, 1983, The assessment of Pb-210 data from sites with varying sediment accumulation rates: Hydrobiologia, v. 103, p. 29-35.

Bagnold, R. A., 1966, An approach to the sediment transport problem from general physics: USGS Professional Paper, 422-J.

-, 1980, An empirical correlation of bedload transport rates in flumes and natural rivers: Proceedings of the Royal Society, Series A, v. 372, p. 453-473.

Beck, S., Zandt, G., Myers, S. C., Wallace, T. C., Silver, P. G., and Drake, L., 1996, Crustal-thickness variations in the central Andes: Geology, v. 24, p. 407-410.

Benniger, L. K., Aller, R. C., Cochran, J. K., and Turekian, K. K., 1979, Effects of biological sediment mixing on the Pb-210 chronology and trace metal distribution in a Long Island Sound sediment core: Earth and Planetary Science Letters, v. 43, p. 241-259.

Bliss, N., and Olsen, L., 1996, 30-arc-second Digital Elevation Model (DEM) for South America, United States Geologic Survey, EROS Data Center.

Bray, D. I., 1982, Regime equations for gravel-bed rivers, *in* Hey, R. D., Bathhurst, J. C., and Thorne, C. R., eds., Gravel-Bed Rivers: Fluvial processes, Engineering and Management: Chichester, U.K., Wiley, p. 517-542.

Bridge, J. S., and Leeder, M. R., 1979, A simulation model of alluvial stratigraphy: Sedimentology, v. 26, p. 617-644.

Burbank, D. W., Leland, J., Fielding, E., Anderson, R. S., Brozovic, N., Reid, M. R., and Duncan, C., 1996, Bedrock incision, rock uplift and threshold hillslopes in the northwestern Himalayas: Nature, v. 379, p. 505-510.

Burnett, A. W., and Schumm, S. A., 1983, Active tectonics and river response in Lousiana and Mississippi: Science, v. 222, p. 49-50.

Chang, H. H., 1992, Fluvial Processes in River Engineering, Krieger Publishing Company.

Chase, C. G., 1992, Fluvial landsculpting and the fractal dimension of topography: Geomorphology, v. 5, p. 39-57.

Chow, V. T., 1959, Open Channel Hydraulics: New York, McGraw-Hill.

Collins, B., and Dunne, T., 1989, Gravel transport, gravel harvesting, and channel-bed degradation in rivers draining the Southern Olympic Mountains, Washington, USA: Environmental Geology and Water Sciences, v. 13, p. 213-224.

Comans, N. N. J., Haller, M., and De Preter, P., 1991, Sorption of cesium on illite: Non-equilibrium behaviour and reversibility: Geochimica et Cosmochimica Acta, v. 55, p. 433-440.

Cremers, A., Elsen, A., De Preter, P., and Maes, A., 1988, Quantitative analysis of radiocaesium retention in soils: Nature, v. 335, p. 247-249.

Cutshall, N. H., Ingvar, L. L., and Curtis, R. O., 1983, Direct analysis of Pb-210 in sediment samples: self-absorption corrections: Nuclear Instruments and Methods, v. 206, p. 309-312.

Dietrich, W. E., 1982, Flow, boundary shear stress, and sediment transport in a river meander [Ph.D. thesis]: University of Washington, 261 p.

Dietrich, W. E., Day, G., and Parker, G., 1999, The Fly River, Papua New Guinea: inferences about river dynamics, floodplain sedimentation and fate of sediment, *in* Miller, A. J., and Gupta, A., eds., Varieties of Fluvial Form, John Wiley & Sons Ltd., p. 345-376.

Dietrich, W. E., and Smith, J. D., 1983, Influence of the point bar on flow through curved channels: Water Resources Research, v. 19, no. 5, p. 1173-1192.

DMA, 1995, Rio Beni, Bolivia: Mapas de Ruta Fluvial, Instituto Geografico Militar de Bolivia, La Paz, 103 p.

Dunne, T., 2001, Personal communication.

Dunne, T., Mertes, L. A. K., Meade, R. H., Richey, J. E., and Forsberg, B. R., 1998, Exchanges of sediment between the floodplain and channel of the Amazon River in Brazil: Geological Society of America Bulletin, v. 110, no. 4, p. 450-467.

Einstein, H. A., 1950, The bedload function for sediment transportation in open channel flows: USDA Soil Conservation Service Technical Bulletin, 1026.

Einstein, H. A., and Chien, M., 1954, Second approximation to the solution of suspended-load theory: Institute of Engineering Research, University of California, 3.

Engelund, F., and Hansen, E., 1972, A monograph on sediment transport in alluvial streams: Teknisk Forlag.

Flemings, P. B., and Jordan, T. E., 1989, A synthetic stratigraphic model of foreland basin development: Journal of Geophysical Research, v. 94, p. 3851-3866.

Fournier, F., 1960, Climat et erosion; la relation entre l'erosion du sol par l'eau et les precipitations atmospheriques: Paris, Univ. France Press.

Francis, C. W., and Brinkley, F. S., 1976, Preferential adsorption of Cs-137 to micaceous minerals in contaminated freshwater sediment: Nature, v. 260, p. 511-513.

Gibbs, R. J., 1967, The geochemistry of the Amazon River system: Part I. The factors that control the salinity and the composition and concentration of the suspended solids: Geological Society of America Bulletin, v. 78, p. 1203-1232.

Goodbred, S. L., Jr., and Kuehl, S. A., 1998, Floodplain processes in the Bengal Basin and the storage of Ganges-Brahmaputra river sediment: an accretion study using Cs-137 and Pb-210 geochronology: Sedimentary Geology, v. 121, p. 239-258.

Granger, D. E., Kirchner, J. W., and Finkel, R., 1996, Spatially averaged long-term erosion rates measured from in-situ-produced cosmogenic nuclides: Journal of Geology, v. 104, p. 249-257.

Gubbels, T. L., Isacks, B. L., and Farrar, E., 1993, High-level surfaces, plateau uplift, and foreland development, Bolivian Central Andes: Geology, v. 21, p. 695-698.

Guyot, J. L., 1993, Hydrogéochimie Des Fleuves De L'Amazonie Bolivienne [Thèse de Docteur en Sciences Naturelles thesis], 261 p.

Guyot, J. L., Bourges, J., Calle, H., Cortes, J., Hoorelbecke, R., and Roche, M. A., 1989a, Transport of suspended sediments to the Amazon by an Andean river: the river Mamore, Bolivia, *in* Proceedings of the Fourth International Symposium on River Sedimentation, Beijing, China, p. 106-113.

Guyot, J. L., Calle, H., Cortes, J., Pereira, M., and Rodriguez, H., 1989b, Erosion, Balance de Sedimentos y Materias Disueltas en la Cuenca Alta del Rio Paraguay (Rios Pilcomayo y Bermejo, Bolivia), *in* Simposio sobre la Preservación del Medio Ambiente, La Paz, Bolivia.

Guyot, J. L., Calle, H., Cortes, J., and Periera, M., 1990, Transport de matières dissoutes et particulairies des Andes vers le Rio de La Plata par les tributaires boliiviens (rios Pilcomayo et Bermejo) du Rio Paraguay: Hydrological Sciences Journal, v. 35, p. 653-665.

Guyot, J. L., Jouanneau, J. M., and Wasson, J. G., 1999, Characterisation of river bed and suspended sediments in the Rio Madeira drainage basin (Bolivian Amazonia): Journal of South American Earth Sciences, v. 12, p. 401-410.

Hallet, B., Hunter, L., and Bogen, J., 1996, Rates of erosion and sediment evacuation by glaciers: a review of field data and their implications: Global and Planetary Change, v. 12, p. 213-235.

He, Q., and Walling, D. E., 1996a, Interpreting particle size effects in the adsorption of Cs-137 and unsupported Pb-210 by mineral soils and sediments: Journal of Environmental Radioactivity, v. 30, no. 2, p. 117-137.

-, 1996b, Use of fallout Pb-210 measurements to investigate longer-term rates and patterns of overbank sediment deposition on the floodplains of lowland rivers: Earth Surface Processes and Landforms, v. 21, p. 141-154.

Heller, P. L., and Paola, C., 1992, The large-scale dynamics of grain-size variation in alluvial basins, 2: Applications to syntectonic conglomerate: Basin Research, v. 4, p. 91-102.

Hicks, D. M., Hill, J., and Shankar, U., 1996, Variation of suspended sediment yields around New Zealand; the relative importance of rainfall and geology, p. 149-156.

Horton, B. K., 1999, Erosional control on the geometry and kinematics of thrust belt development in the central Andes: Tectonics, v. 18, p. 1292-1304.

Horton, B. K., and DeCelles, P. G., 1997, The modern foreland basin system adjacent to the Central Andes: Geology, v. 25, no. 10, p. 895-898.

-, 2001, Modern and ancient fluvial megafans in the foreland basin system of the central Andes, southern Bolivia: implications for drainage network evolution in fold-thrust belts: Basin Research, v. 13, p. 4-63.

Horton, B. K., Hampton, B. A., and Waanders, G. L., 2001, Paleogene synorogenic sedimentation in the Altiplano plateau and implications for initial mountain building in the central Andes: Geological Society of America Bulletin, v. 113, no. 11, p. 1387-1400.

Hovius, N., 1998, Controls on sediment supply by large rivers, *in* Shanley, K. W., and McCabe, P. J., eds., Relative Role of Eustasy, Climate and Tectonics in Continental Rocks, Soc. Econ. Paleont. Mineral. Spec. Publ., p. 3-16.

Howard, A. D., 1992, Modeling channel migration and floodplain sedimentation in meandering streams, *in* Carling, P. A., and Petts, G. E., eds., Lowland Floodplain Rivers: Geomorphological Perspectives, John Wiley and Sons, Ltd., p. 1-41.

-, 1994, A detachment-limited model of drainage basin evolution: Water Resources Research, v. 30, p. 2261-2285.

James, C. S., 1985, Sediment transfer to overbank sections: Journal of Hydraulic Research, v. 23, p. 435-452.

Jordan, T. E., 1995, Retroarc foreland and related basins, *in* Busby, C. J., and Ingersoll, R. V., eds., Tectonics of Sedimentary Basins: Cambridge, MA, Blackwell Science, p. 331-362.

Kesel, R. H., Yodis, E. G., and McCraw, D. J., 1992, An approximation of the sediment budget of the lower Mississippi River prior to major human modification: Earth Surface Processes and Landforms, v. 17, p. 711-722.

Kirkby, M. J., 1987, Modeling some influences of soil erosion, landslides and valley gradient on drainage density and hollow development: Catena Suppl., v. 10, p. 1-14.

Lane, E. W., 1955, The importance of fluvial geomorphology in hydraulic engineering: Proceeding of the American Society of Civil Engineers, v. 81, no. 745, p. 1-17.

Langbein, W. B., and Schumm, S. A., 1958, Yield of sediment in relation to mean annual precipitation: AGU Transactions, v. 39, p. 1076-1084.

Leopold, L. B., 1973, River channel change with time: an example: Geological Society of America Bulletin, v. 84, p. 1845-1860.

Leopold, L. B., and Maddock, T., Jr., 1953, The hydraulic geometry of stream channels and some physiographic implications: US Geological Survey Professional Paper, 252.

Leopold, L. B., and Wolman, M. G., 1960, River meanders: Geological Society of America Bulletin, v. 71, p. 769-794.

Ludwig, W., and Probst, J. L., 1998, River sediment discharge to the oceans: present-day controls and global budgets: American Journal of Science, v. 298, p. 265-295.

Mackin, J. H., 1948, Concept of a graded river: Geological Society of America Bulletin, v. 59, p. 463-512.

Masek, J. G., Isacks, B. L., Gubbels, T. L., and Fielding, E. J., 1994, Erosion and tectonics at the margins of continental plateaus: Journal of Geophysical Research, v. 99, no. B7, p. 13,941-13,956.

Maurice-Bourgoin, L., 2001, unpublished, Water and sediment flux records for Rurrenabaque and Riberalta.

Meade, R. H., Dunne, T., Richey, J. E., Santos, U. d. M., and Salati, E., 1985, Storage and remobilization of suspended sediment in the lower Amazon River of Brazil: Science, v. 228, p. 488-490.

Mertes, L. A. K., 1997, Description and significance of the perirheic zone on inundated floodplains: Water Resources Research, v. 33, p. 1749-1762.

Mertes, L. A. K., Dunne, T., and Martinelli, L. A., 1996, Channel-floodplain geomorphology along the Solimoes-Amazon River, Brazil: Geological Society of America Bulletin, v. 108, no. 9, p. 1089-1107.

Mertes, L. A. K., Smith, M. O., and Adams, J. B., 1993, Estimating suspended sediment concentrations in surface waters of the Amazon River wetlands from Landsat images: Remote Sensing of Environment, v. 43, p. 281-301.

Meybeck, M., 1987, Global chemical weathering of surficial rocks estimated from river dissolved loads: American Journal of Science, v. 287, p. 401-428.

Meyer-Peter, E., and Muller, R., 1948, Formula for bed-load transport, *in* International association for hydraulic research, 2nd meeting, Stockholm.

Meyers, S. D., Thelin, E., and O'Brien, J. J., 1999, Reconstruction of monthly SST in the tropical Pacific Ocean during 1868-1993 using adaptive climate basis functions: Monthly Weather Reviews, v. 127, p. 1599-1612.

Milliman, J. D., and Meade, R. H., 1983, World-wide delivery of river sediment to the oceans: Journal of Geology, v. 91, no. 1, p. 1-21.

Milliman, J. D., Qin, Y. S., Ren, M. E., and Saito, Y., 1987, Man's influence on the erosion and transport of sediment by Asian rivers: Journal of Geology, v. 95, p. 751-762.

Milliman, J. D., and Syvitski, J. P. M., 1992, Geomorphic/tectonic control of sediment discharge to the ocean: the importance of small mountainous rivers: Journal of Geology, v. 100, p. 525-544.

Montgomery, D. R., and Aalto, R., 2001, Comparison of the SRTM DEM for the Olympic Mountains to existing DEMs of varying resolutions: results and general implications for application of SRTM data to models of hillslope and fluvial processes in mountainous regions: EOS AGU Transactions, v. 82, no. 47, p. G22B-22.

Montgomery, D. R., Balco, G., and Willet, S. D., 2001, Climate, tectonics, and the morphology of the Andes: Geology, v. 29, p. 579-582.

Nanson, G. C., and Hickin, E. J., 1983, Channel migration and incision on the Beatton River: Journal of Hydraulic Engineering, American Society of Civil Engineers, v. 109, p. 327-337.

Naval, 1960, Air photo series of Bolivian Llanos: Servicio Nacional de Hidrografia Naval, La Paz, Bolivia.

Nicholas, A. P., and Walling, D. E., 1997a, Investigating spatial patterns of medium-term overbank sedimentation on floodplains: a combined numerical modeling and radiocaesium-based approach: Geomorphology, v. 19, p. 133-150.

-, 1997b, Modeling flood hydraulics and overbank deposition on river floodplains: Earth Surface Processes and Landforms, v. 22, p. 59-77.

Nittrouer, C. A., Kuehl, S. A., Sternberg, R. W. F., A. G., Jr., and Faria, L. E. C., 1995, An introduction to the geological significance of sediment transport and accumulation on the Amazon continental shelf: Marine Geology, v. 125, p. 177-192.

Nittrouer, C. A., Sternberg, R. W., Carpenter, R., and Bennett, J. T., 1979, The use of Pb-210 geochronology as a sedimentological tool: application to the Washington continental shelf: Marine Geology, v. 31, p. 297-316.

Norabuena, E., Leffler-Griffin, L., Mao, A., Dixon, T., Stein, S., Sacks, I. S., Ocola, L., and Ellis, M., 1998, Space geodetic observations of Nazca-South America convergence across the central Andes: Science, v. 279, p. 358-362.

Oldfield, F., and Appleby, G., 1984, Empirical testing of Pb-210 dating models for lake sediments, *in* Haworth, E. Y., and Lund, J. W. G., eds., Lake Sediments and Environmental History: Leicester, Leicester University Press, p. 93-114.

Paola, C., 1989, A simple basin-filling model for coarse-grained alluvial systems, *in* Cross, T. A., ed., Quantitative Dynamic Stratigraphy, Prentice Hall, p. 363-374.

Pareja, J. L., and Ballón, A. R., 1978, Mapa Geológico de Bolivia: Servicio Geológico de Bolivia.

Parker, G., 1990, Surface-based bedload transport relationship for gravel rivers: Journal of Hydraulic Research, v. 28, no. 4, p. 417-436.

Parker, G., Kingeman, P. C., and McLean, D. G., 1982, Bedload and size distribution in paved gravel-bed streams: Journal of the Hydraulic Division, American Society of Civil Engineers, v. 108, no. HY4, p. 544-571.

Pinet, P., and Souriau, M., 1988, Continental erosion and large-scale relief: Tectonics, v. 7, p. 563-582.

Pizzuto, J. E., 1987, Sediment diffusion during overbank flows: Sedimentology, v. 34, p. 301-317.

Polidori, L., Chorowicz, J., and Guillande, R., 1991, Description of terrain as a fractal surface and application to digital elevation model quality assessment: Photogrammetric Engineering & Remote Sensing, v. 57, p. 1329-1332.

Potter, P. E., 1978, Significance and origin of big rivers: Journal of Geology, v. 86, p. 13-33.

Preston, D., 1998, Livelihood strategies improving the environment? A heretical view, *in* XXI International Congress of the Latin American Studies Association, Chicago.

Probst, J. L., 1990, Géochimie et hydrologie de l'érosion continentale. Mécanismes, bilan global actuel et fluctuations au cours des 500 derniers millions d'années [Thèse de Docteur es Sciences Naturelles thesis], 185 p.

Rasanen, M. E., Salo, J. S., and Kalliola, R. J., 1987, Fluvial perturbance in the western Amazon basin: Regulation by long-term sub-Andean tectonics: Science, v. 238, p. 1398-1401.

Reid, L. M., and Dunne, T., 1996, Rapid Evaluation of Sediment Budgets, Geo-Ecology Texts: Reiskirchen, Germany, Catena Verlag, 164 p.

Riebe, C. S., Kirchner, J. W., Granger, D. E., and Finkel, R. C., 2001, Minimal climatic control on erosion rates in the Sierra Nevada, California: Geology, v. 29, p. 447-450.

Robinson, R. A. J., and Slingerland, R.L., 1998, Origin of fluvial grain-size trends in a foreland basin: the Pocono formation of the central Appalachian basin: Journal of Sedimentary Research, v. 68, no. 3, p. 473-486.

Safran, E. B., 1998, Channel network incision and patterns of mountain geomorphology [Ph.D. Dissertation thesis]: University of California, 326 p.

Sanford, M. W., Kuehl, S. A., and Nittrouer, C. A., 1990, Modern sedimentary processes in the Wilmington Canyon area, US East coast: Marine Geology, v. 92, p. 205-226.

Schmidt, K. M., and Montgomery, D. R., 1995, Limits to relief: Science, v. 270, p. 617-620.

Schumm, S. A., 1986, Alluvial river response to active tectonics, Active tectonics studies in geophysics: Washington, D.C., National Academy Press, p. 80-94.

Schumm, S. A., and Khan, H. R., 1972, Experimental study of channel patterns: Geological Society of America Bulletin, v. 83, p. 1755-1770.

Seidl, M. A., and Dietrich, W. E., 1992, The problem of channel erosion into bedrock: Catena Suppl., v. 23, p. 101-124.

Semena, 1969, Depth survey of the Beni River: Servicio al Mejoramiento de la Navegacion Amazonica, La Paz, Bolivia.

Smith, J. D., and McLean, S. R., 1977, Spatially averaged flow over a wavy surface: Journal of Geophysical Research, v. 82, p. 1735-1746.

Smith, J. N., Ellis, K. M., and Nelson, D. M., 1987, Time-dependent modeling of fallout radionuclide transport in a drainage basin: significance of 'slow' erosional and 'fast' hydrological components: Chemical Geology, v. 63, p. 157-180.

Summerfield, M. A., and Hulton, N. J., 1994, Natural controls of fluvial denudation rates in major world drainage basins: Journal of Geophysical Research, v. 99, p. 13871-13883.

Trimble, S. W., 1976, Unsteady state denudation: Science, v. 191, p. 871.

-, 1977, The fallacy of stream equilibrium in contemporary denudation studies: American Journal of Science, v. 277, p. 876-887.

Tucker, G. E., and Slingerland, R. L., 1994, Erosional dynamics, flexural isotasy, and long-lived escarpments: A numerical modeling study: Journal of Geophysical Research, v. 99, p. 12229-12243.

Walling, D. E., and He, Q., 1997, Use of fallout Cs-137 in investigations of overbank sediment deposition on river floodplains: Catena, v. 29, p. 263-282.

Walling, D. E., Quine, T. A., and He, Q., 1992, Investigating contemporary rates of floodplain sedimentation, *in* Carling, P. A., and Petts, G. E., eds., Lowland Floodplain Rivers: Geomorphological Perspectives: Chichester, John Wiley & Sons, p. 165-184.

Walling, D. E., and Webb, B. W., 1981, The reliability of suspended sediment load data, Erosion and Sediment Transport Measurement, IAHS, p. 177-194.

-, 1983, Patterns of sediment yield, *in* Gregory, K. J., ed., Background to Paleohydrology: Chichester, UK, John Wiley, p. 69-100.

Wolman, M. G., 1955, The natural channel of Brandywine Creek, Pennsylvania: US Geological Survey Professional Paper 271.

Yang, C. T., 1972, Unit stream power and sediment transport: Journal of the Hydraulic Division, American Society of Civil Engineers, v. 98, no. HY10 9295, p. 1805-1826.

-, 1996, Sediment Transport, McGraw-Hill.

Appendix A

Common caption for all figures in Appendix A

This appendix contains a series of GIS detail maps for most of the Beni River survey transects. Each figure key lists the specific sites portrayed within the image, with the site number written in yellow letters at the actual location of each transect or survey location. Small red crosses on the images indicate the location of sediment samples (grab samples or floodplain cores) taken along each transect (Table 2.1 lists standard sample locations), or the location of water depth measurements (if the crosses are superimposed above water). All figures use the 1999 Landsat ETM+ images for their base map, with the prior river locations superimposed as lines colored according to the figure key. Geographic locations are referenced to UTM Zone 19 South, north is up, and the listed map scale may be incorrect due to a possible reduction in figure size during copying. Table 2.2 and Table 2.3 contain further descriptions of each survey transect, with grab sample granulometry presented in Appendix B and floodplain core granulometry and ^{210}Pb geochronology presented in Appendix C. The base maps for the entire Beni foreland basin are located in the Pocket Material.

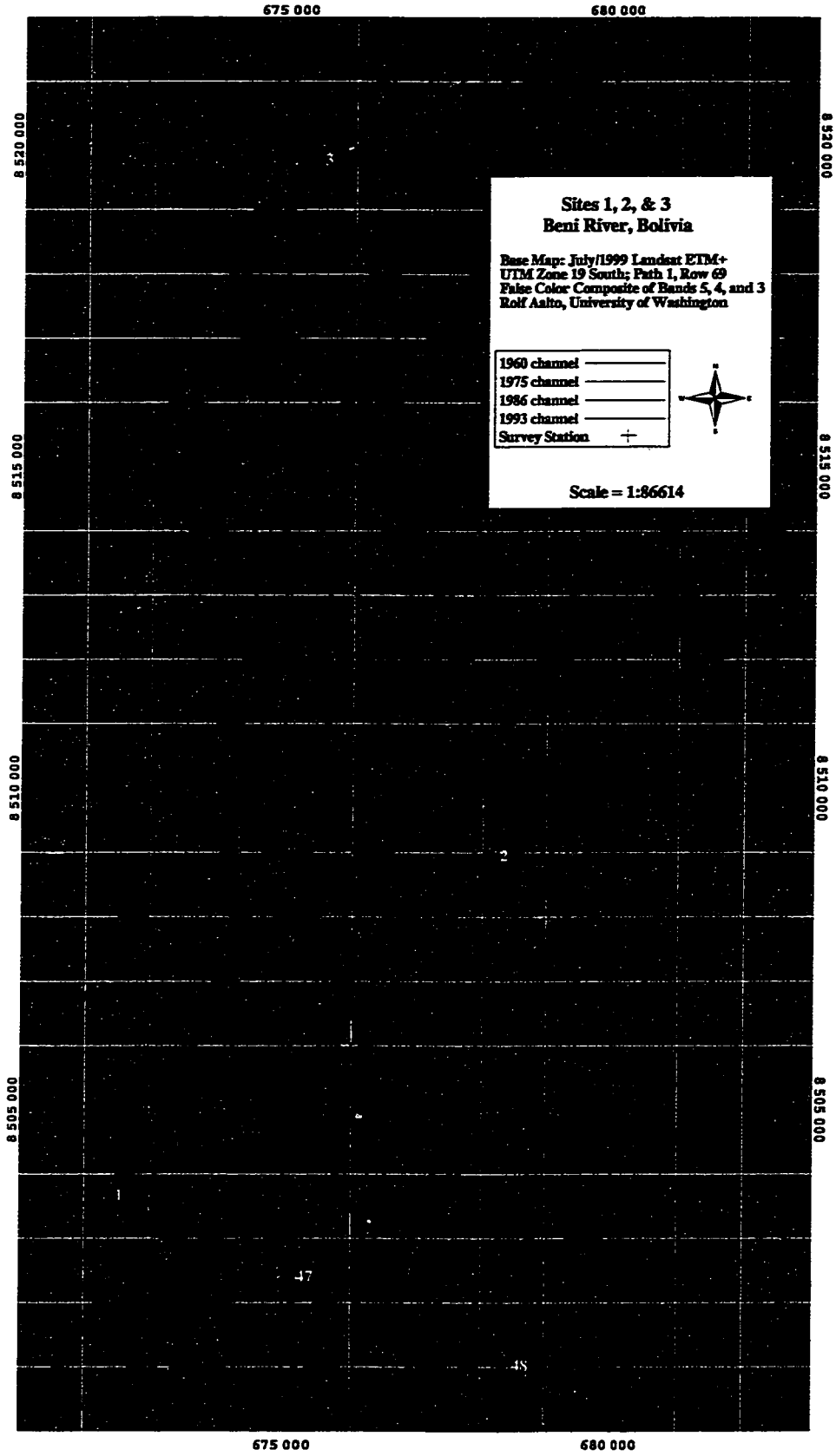
675 000
680 000
8 520 000
8 515 000
8 510 000
8 505 000
Sites 1, 2, & 3
Beni River, Bolivia
Base Map: July/1999 Landsat ETM+
UTM Zone 19 South; Path 1, Row 69
False Color Composite of Bands 5, 4, and 3
Rolf Aalto, University of Washington
1960 channel
1975 channel
1986 channel
1993 channel
Survey Station
Scale = 1:86614
3
2
1
47
48

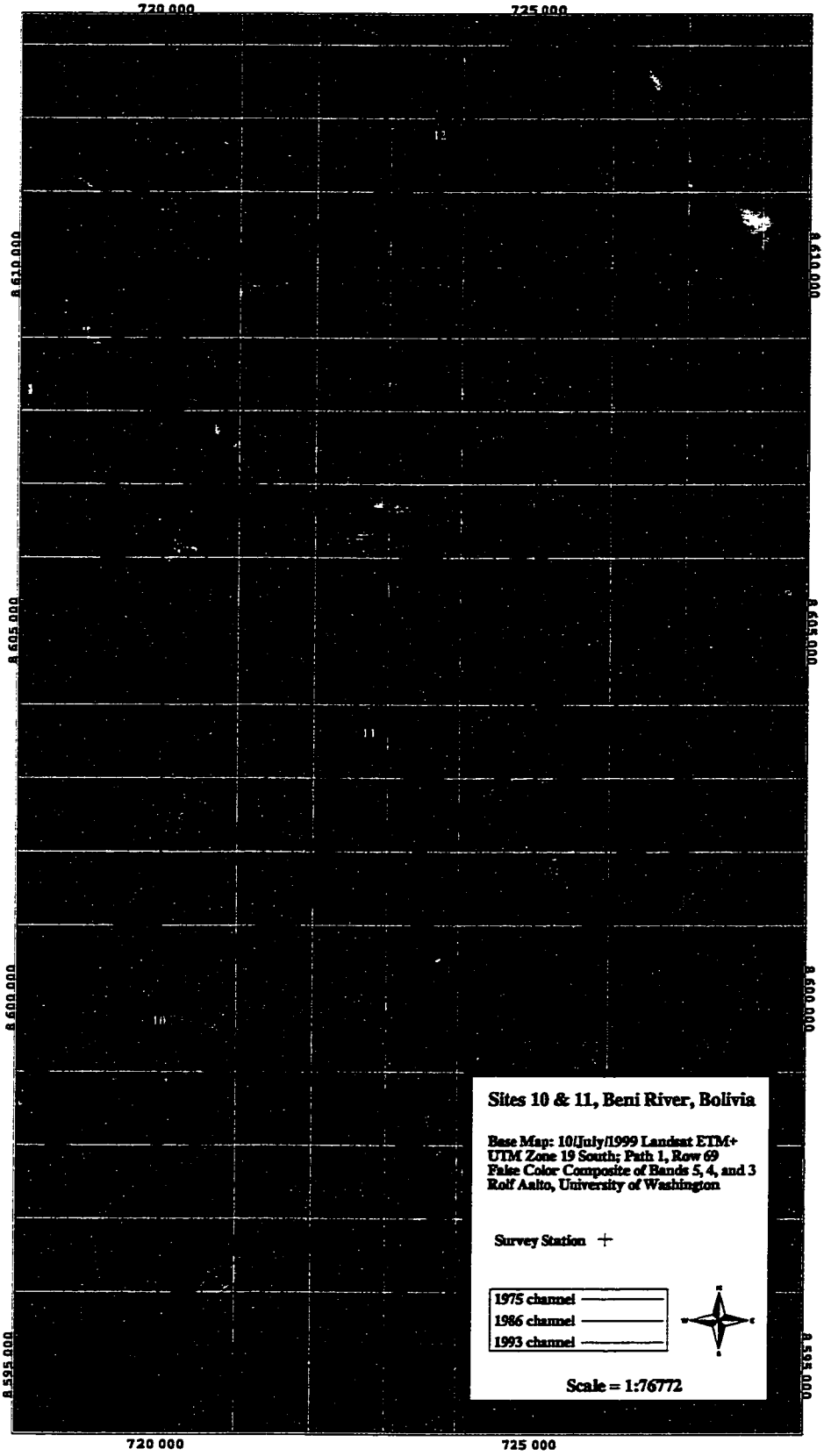
720 000
725 000
8 610 000
8 605 000
8 600 000
8 595 000
12
11
10
Sites 10 & 11, Beni River, Bolivia
Base Map: 10/July/1999 Landsat ETM+
UTM Zone 19 South; Path 1, Row 69
False Color Composite of Bands 5, 4, and 3
Rolf Aalto, University of Washington
Survey Station
1975 channel
1986 channel
1993 channel
Scale = 1:76772

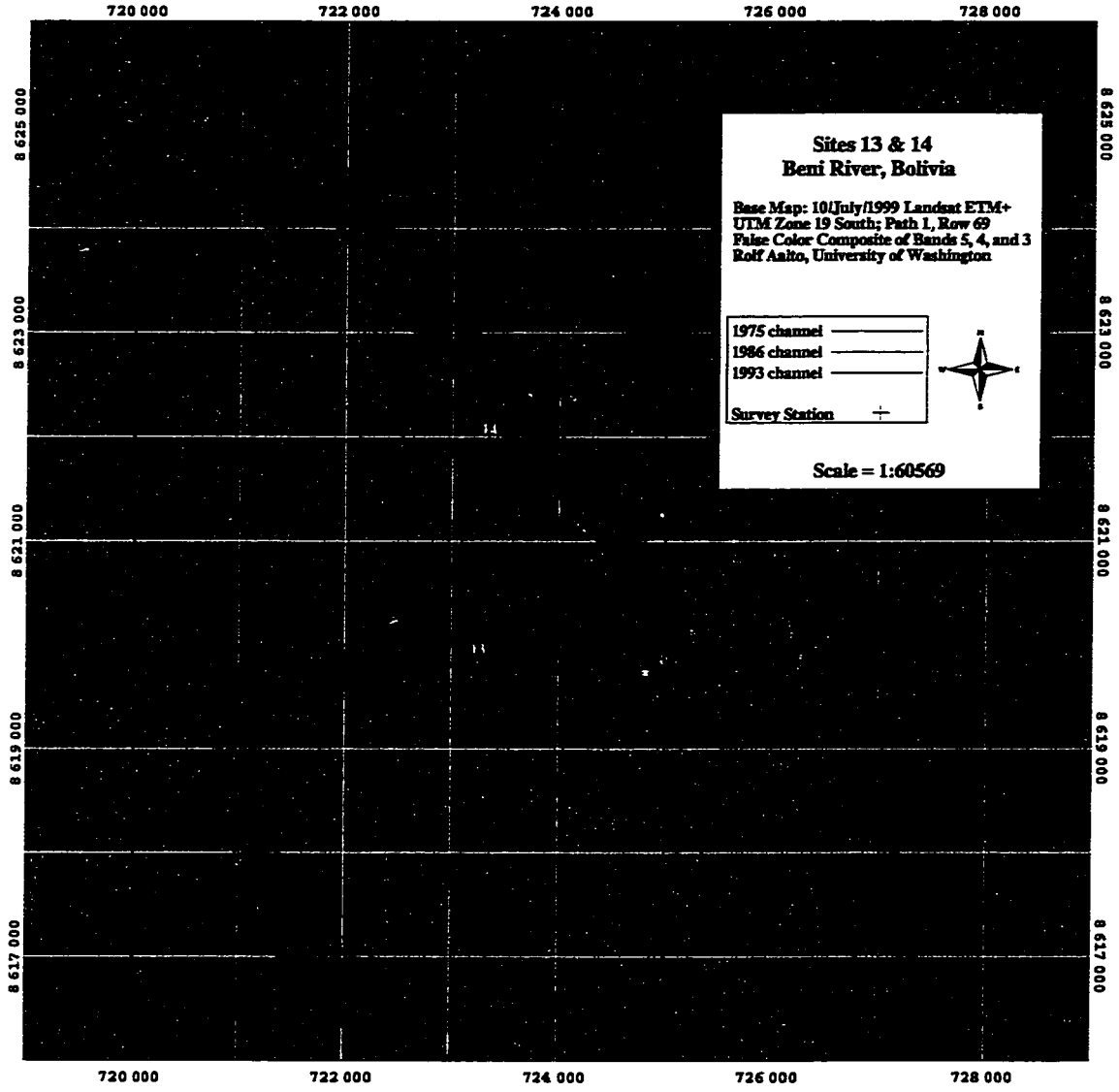
720 000
722 000
724 000
726 000
728 000
8 625 000
8 623 000
8 621 000
8 619 000
8 617 000
Sites 13 & 14
Beni River, Bolivia
Base Map: 10/July/1999 Landsat ETM+
UTM Zone 19 South; Path 1, Row 69
False Color Composite of Bands 5, 4, and 3
Rolf Aalto, University of Washington
1975 channel
1986 channel
1993 channel
Survey Station
Scale = 1:60569
14
13

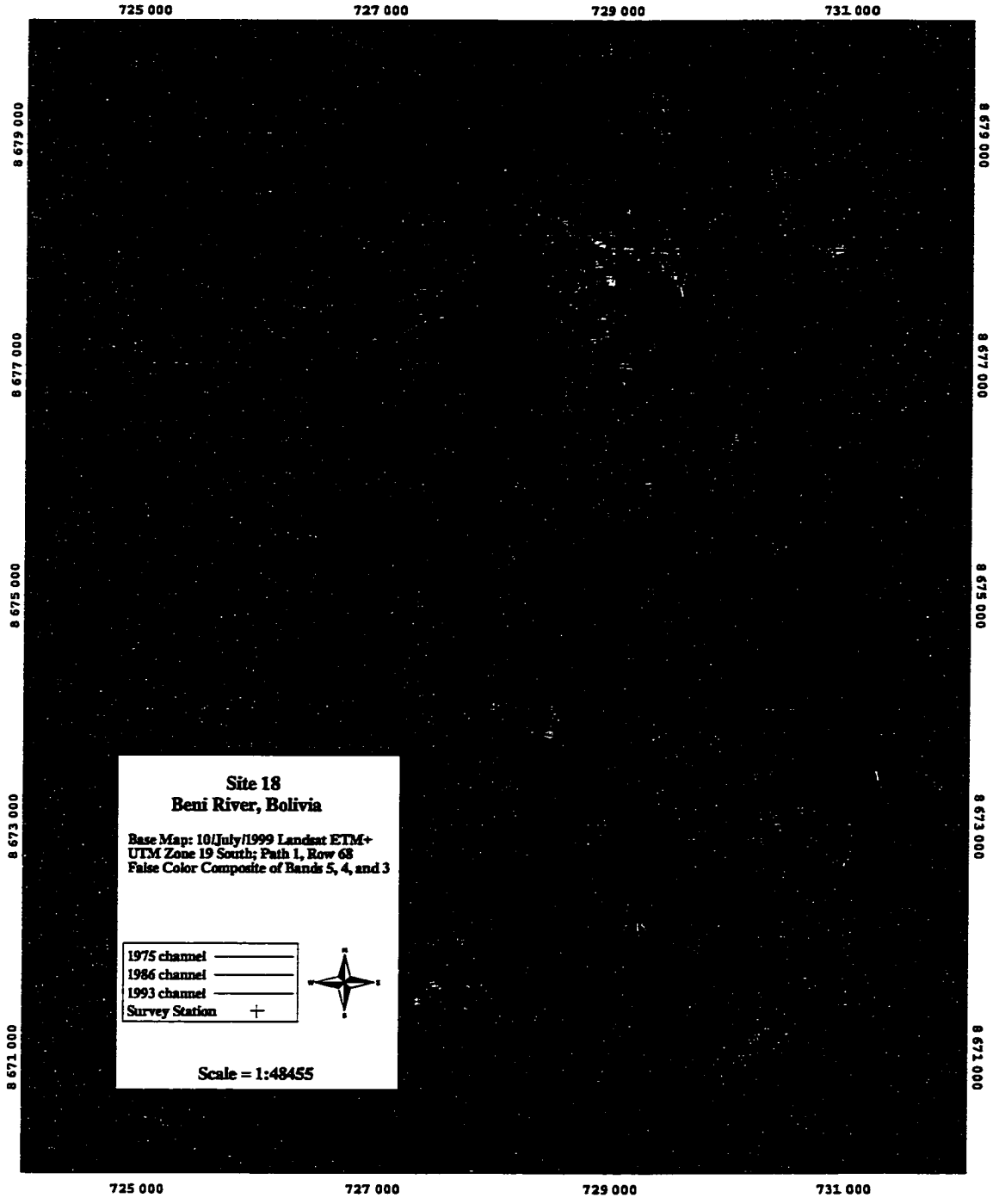
725 000
727 000
729 000
731 000
8 679 000
8 677 000
8 675 000
8 673 000
8 671 000
Site 18
Beni River, Bolivia
Base Map: 10/July/1999 Landsat ETM+
UTM Zone 19 South; Path 1, Row 68
False Color Composite of Bands 5, 4, and 3
1975 channel
1986 channel
1993 channel
Survey Station
Scale = 1:48455

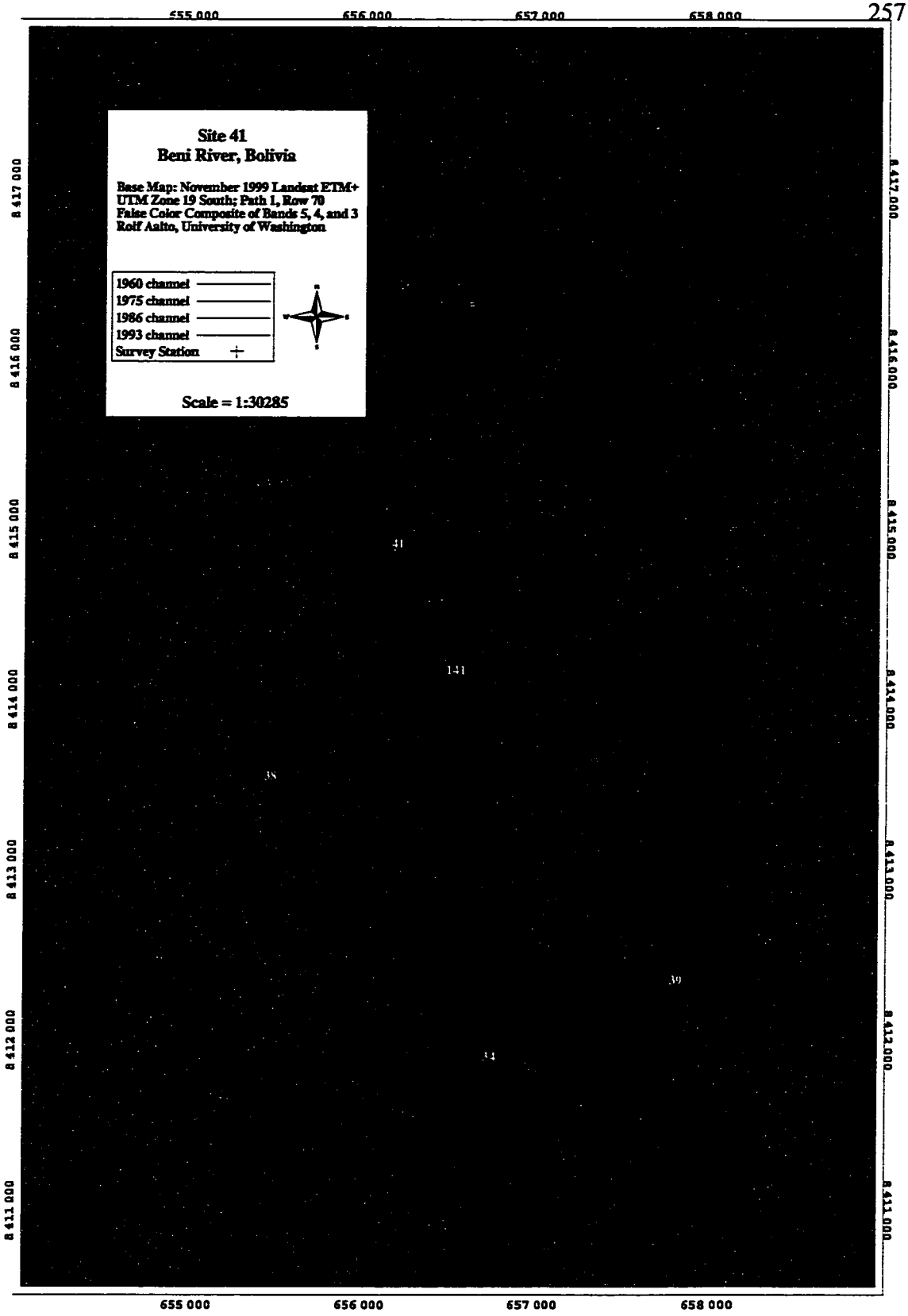
655 000
656 000
657 000
658 000
8 417 000
8 416 000
8 415 000
8 414 000
8 413 000
8 412 000
8 411 000
Site 41
Beni River, Bolivia
Base Map: November 1999 Landsat ETM+
UTM Zone 19 South; Path 1, Row 70
False Color Composite of Bands 5, 4, and 3
Rolf Aalto, University of Washington
1960 channel
1975 channel
1986 channel
1993 channel
Survey Station
Scale = 1:30285
41
141
38
39
34

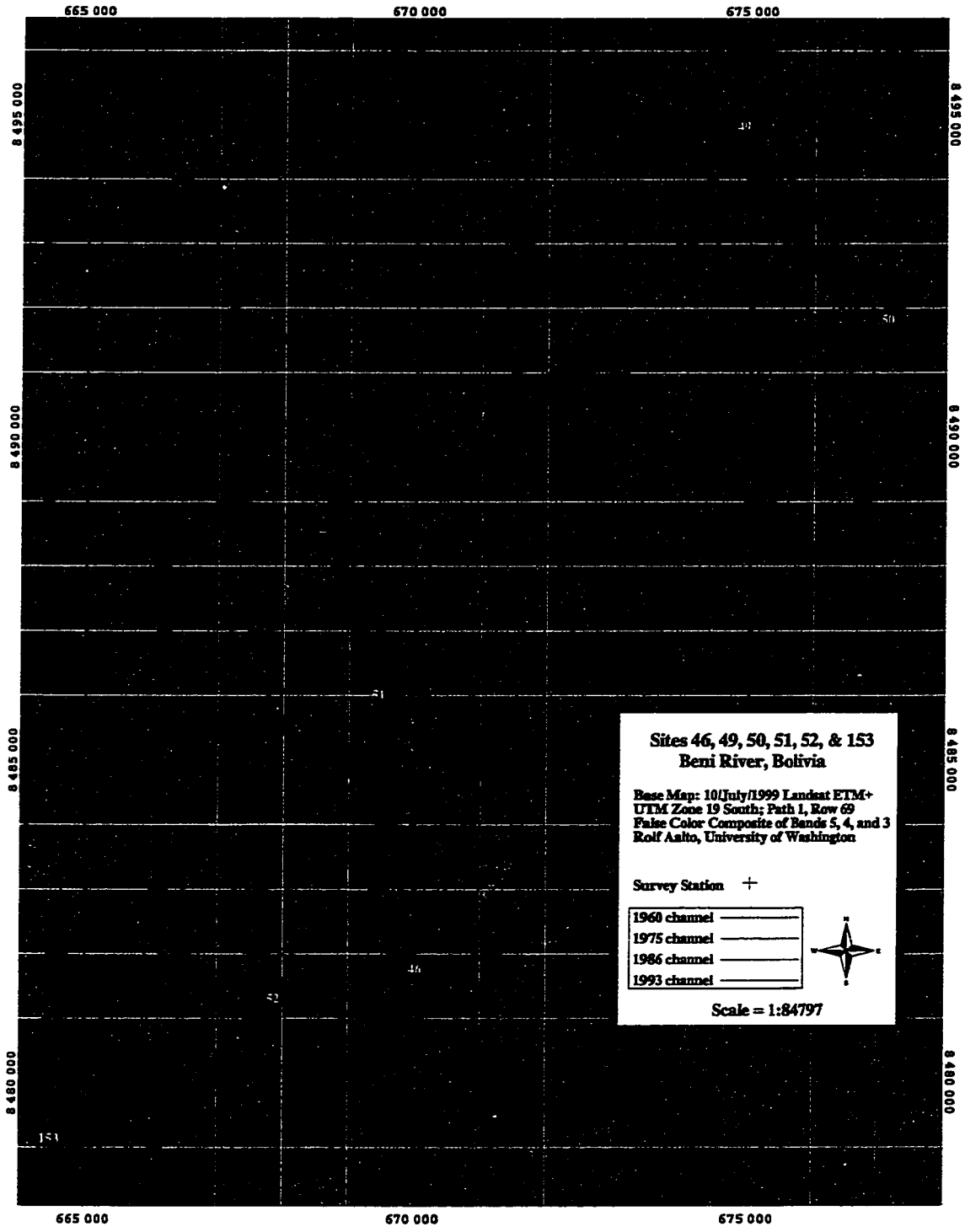
665 000
670 000
675 000
8 495 000
8 490 000
8 485 000
8 480 000
49
50
51
46
52
153
Sites 46, 49, 50, 51, 52, & 153
Beni River, Bolivia
Base Map: 10/July/1999 Landsat ETM+
UTM Zone 19 South; Path 1, Row 69
False Color Composite of Bands 5, 4, and 3
Rolf Aalto, University of Washington
Survey Station
1960 channel
1975 channel
1986 channel
1993 channel
N
W
E
S
Scale = 1:84797

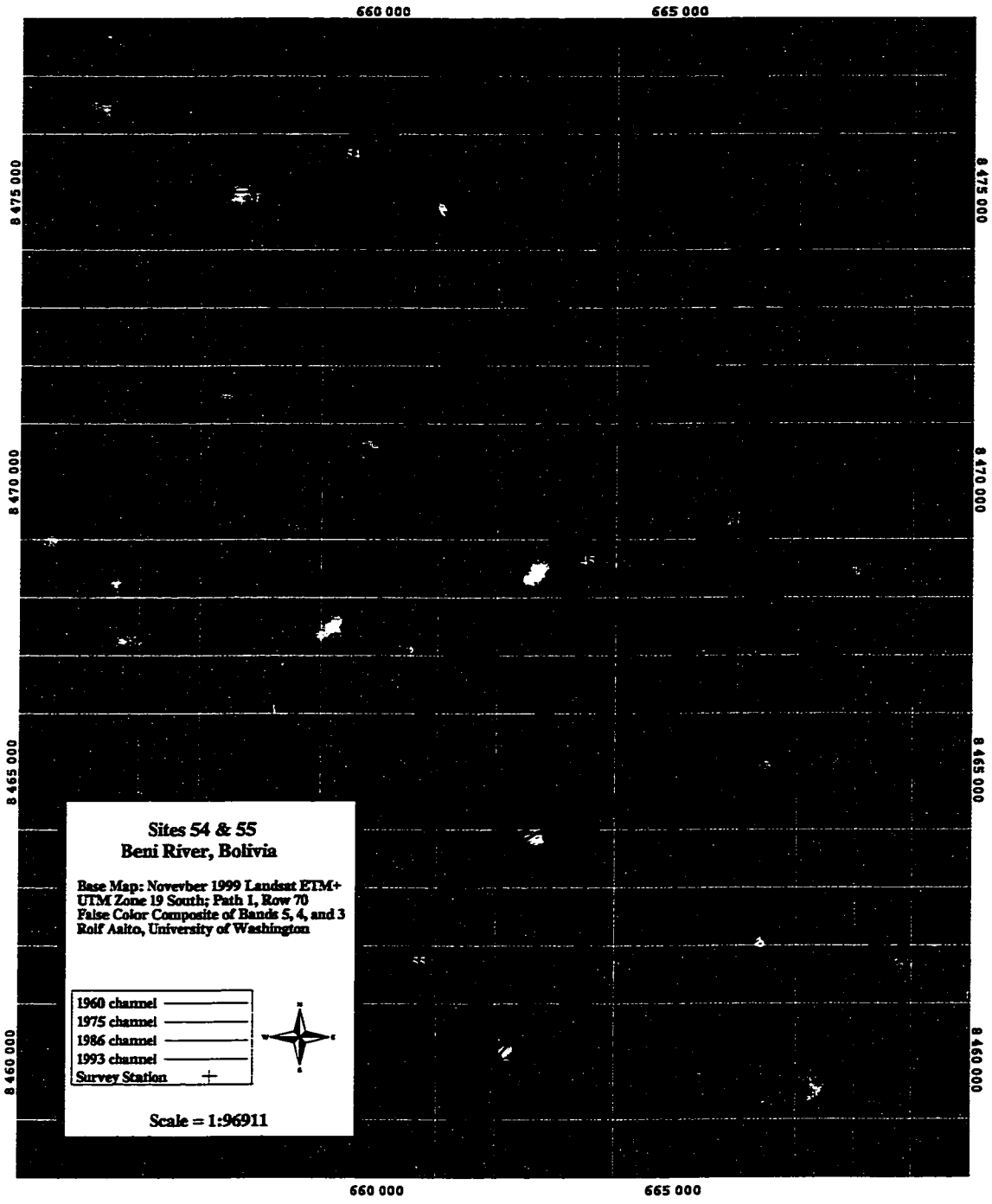
660 000
665 000
8 475 000
8 470 000
8 465 000
8 460 000
Sites 54 & 55
Beni River, Bolivia
Base Map: Novevber 1999 Landsat ETM+
UTM Zone 19 South; Path 1, Row 70
False Color Composite of Bands 5, 4, and 3
Rolf Aalto, University of Washington
1960 channel
1975 channel
1986 channel
1993 channel
Survey Station
Scale = 1:96911

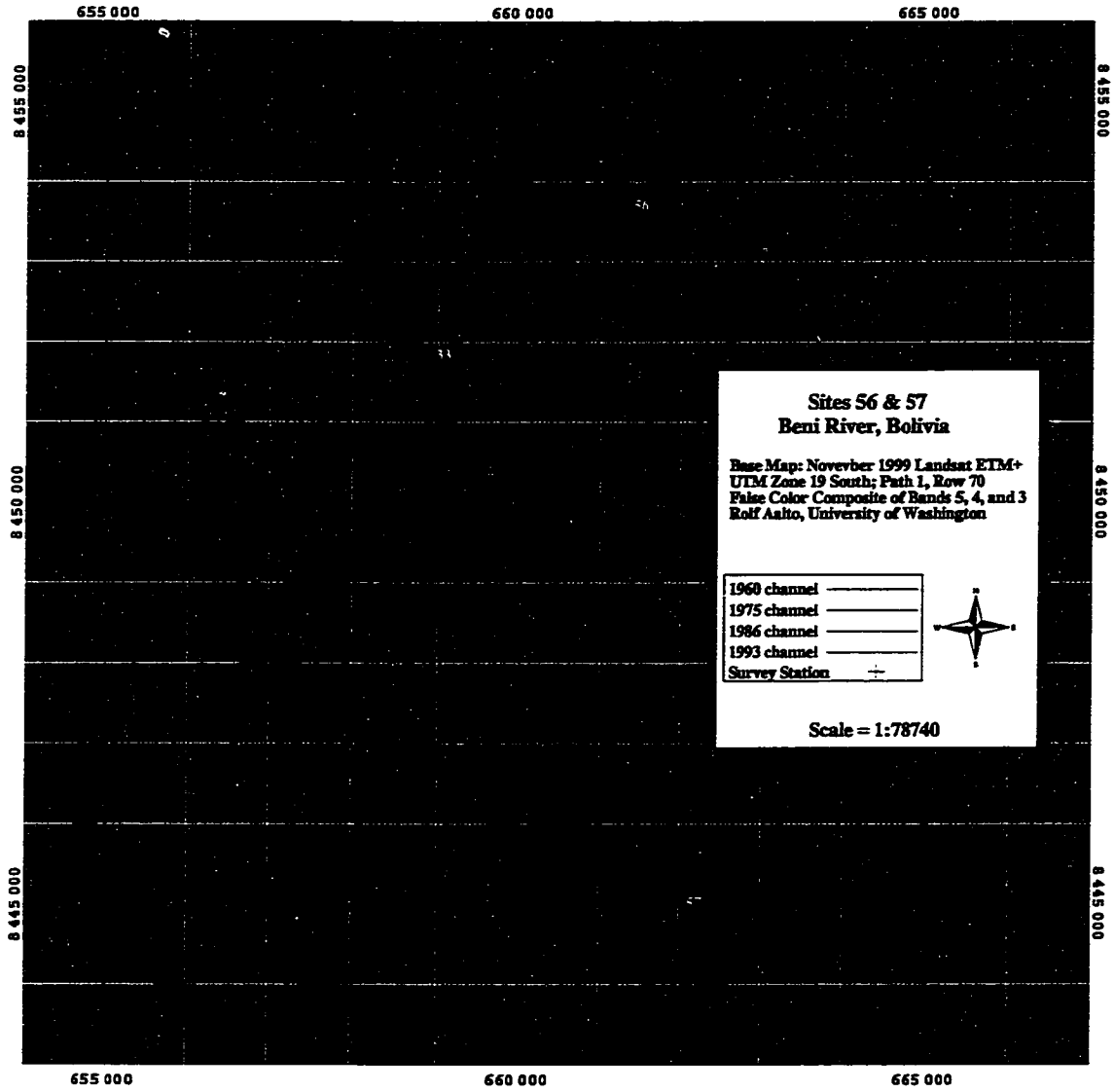
655 000
660 000
665 000
8 455 000
8 450 000
8 445 000
Sites 56 & 57
Beni River, Bolivia
Base Map: Novevber 1999 Landsat ETM+
UTM Zone 19 South; Path 1, Row 70
False Color Composite of Bands 5, 4, and 3
Rolf Aalto, University of Washington
1960 channel
1975 channel
1986 channel
1993 channel
Survey Station
Scale = 1:78740

Beni River, Bolivia, Row 1 Path 70, Site 60

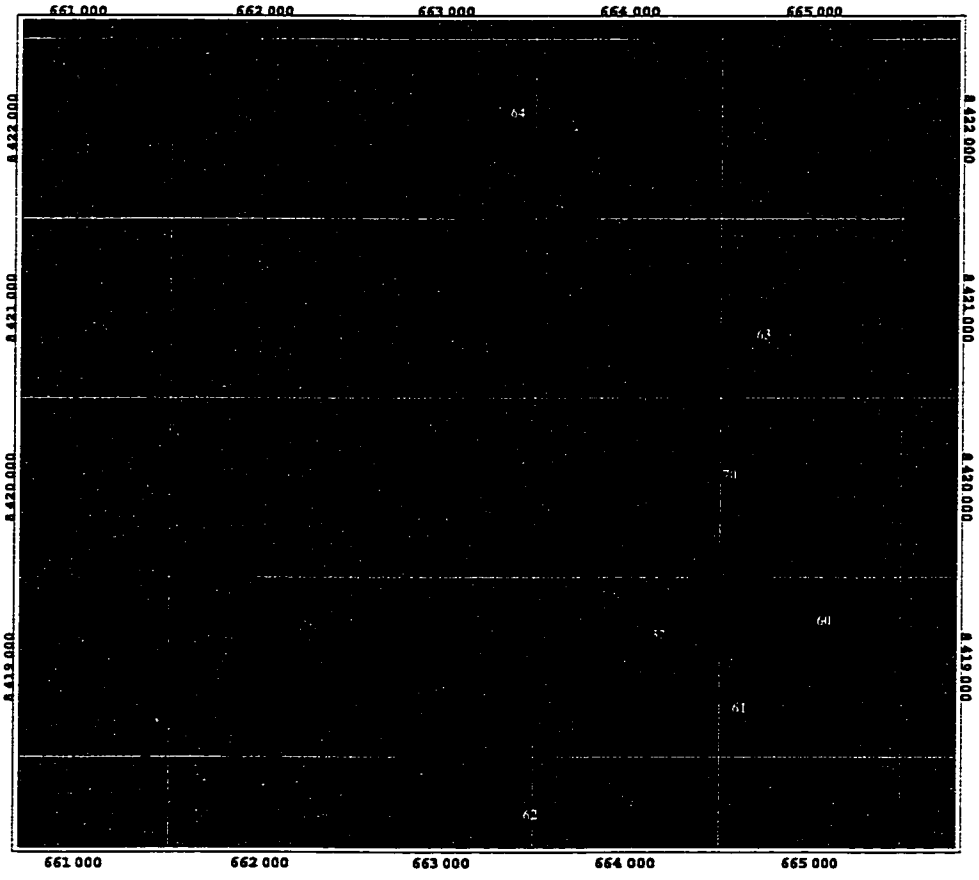

Scale = 1:32465

1960 channel
1975 channel
1986 channel
1993 channel

Nov/1999 Landsat ETM+ Path 1, Row 70
UTM Zone 19 South
Composite of Bands 5, 4, and 3

Appendix B

Common caption for all figures in Appendix B

This appendix contains a series of plots of local elevation (relative to the water surface) versus sediment D_{50} for survey transects across meander bend apexes and other floodplain locations. All figures list the corresponding site number. Text for cut bank locations is colored red, river thalweg location is black, and point bar locations are in blue. Table 2.1 lists the codes used here, which correspond to standard sediment sample locations for survey transects across meander apexes. Table 2.2 and Table 2.3 contain further descriptions of each survey transect, with GIS detail maps for most of the survey transects presented in Appendix A and floodplain core granulometry and ^{210}Pb geochronology presented in Appendix C. The base maps for the entire Beni foreland basin are located in the Pocket Material.

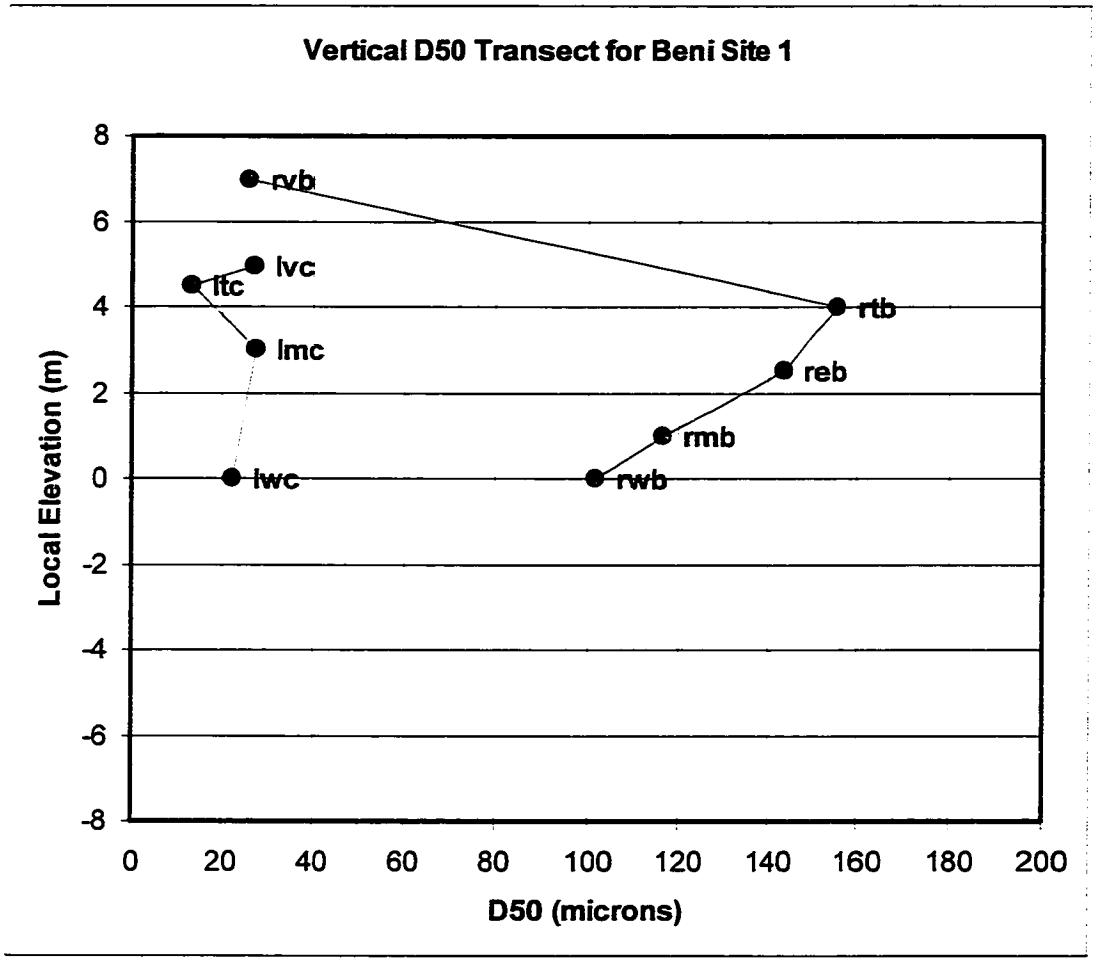
Vertical D50 Transect for Beni Site 1
Local Elevation (m)
8
6
4
2
0
-2
-4
-6
-8
0
20
40
60
80
100
120
140
160
180
200
D50 (microns)
rvb
lvc
ltc
lmc
lwc
rtb
reb
rmb
rwb

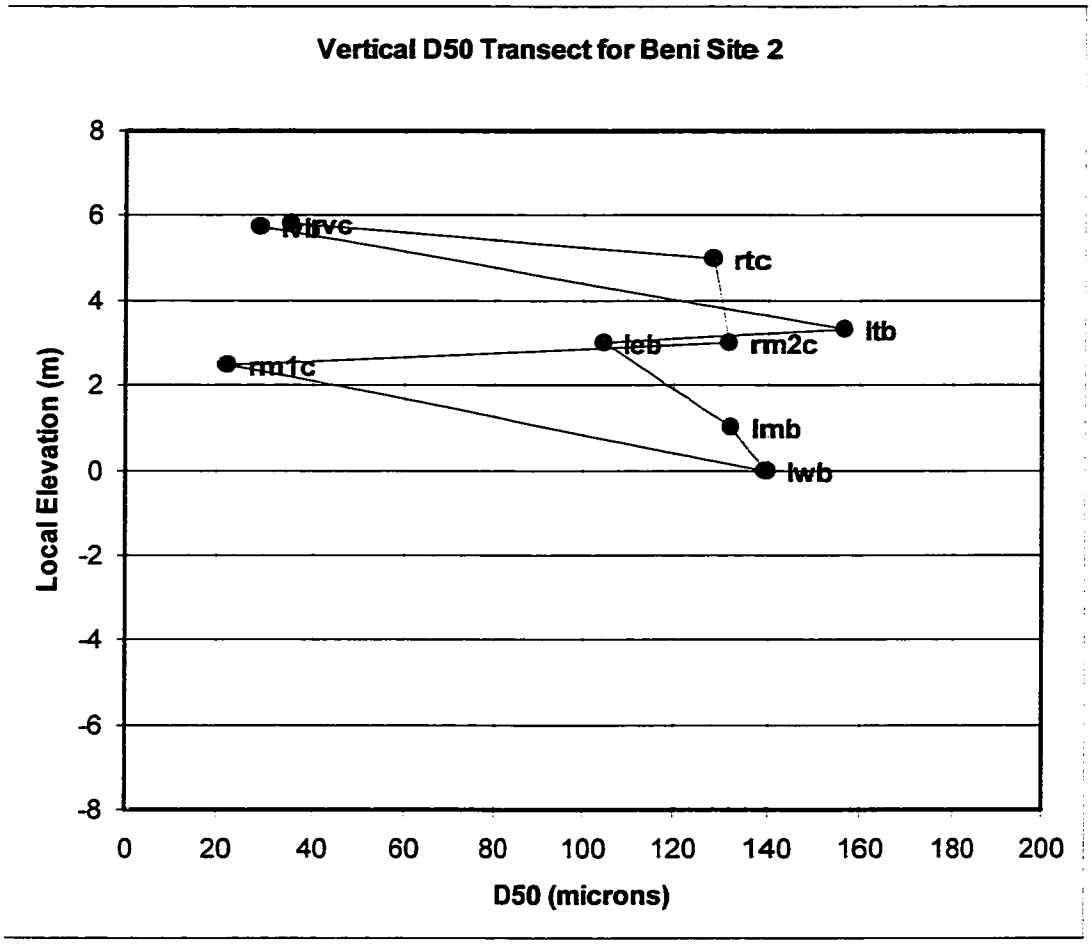
Vertical D50 Transect for Beni Site 2
Local Elevation (m)
8
6
4
2
0
-2
-4
-6
-8
0
20
40
60
80
100
120
140
160
180
200
D50 (microns)
rtc
ltb
rm2c
lmb
lwb

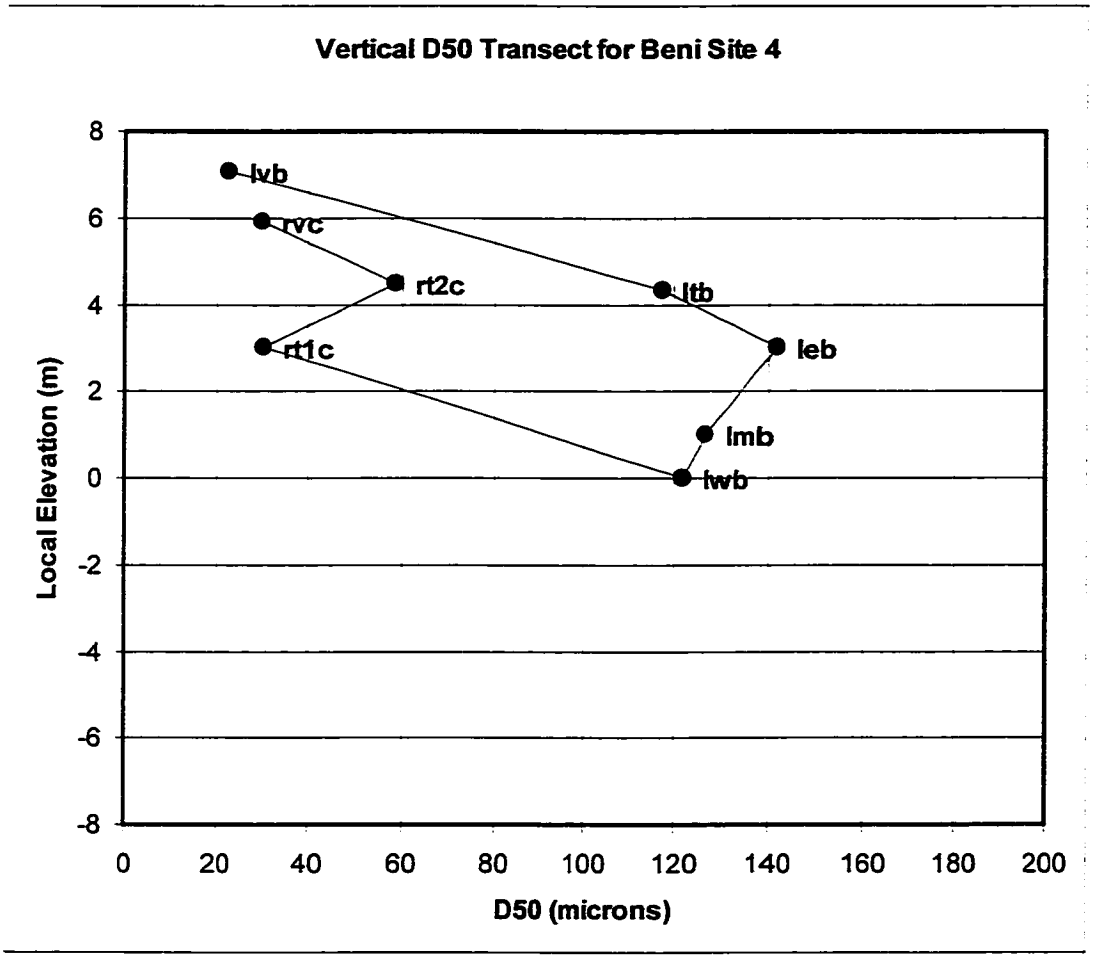
Vertical D50 Transect for Beni Site 4
Local Elevation (m)
8
6
4
2
0
-2
-4
-6
-8
0
20
40
60
80
100
120
140
160
180
200
D50 (microns)
lvb
rvc
rt2c
rt1c
ltb
leb
lmb
lwb

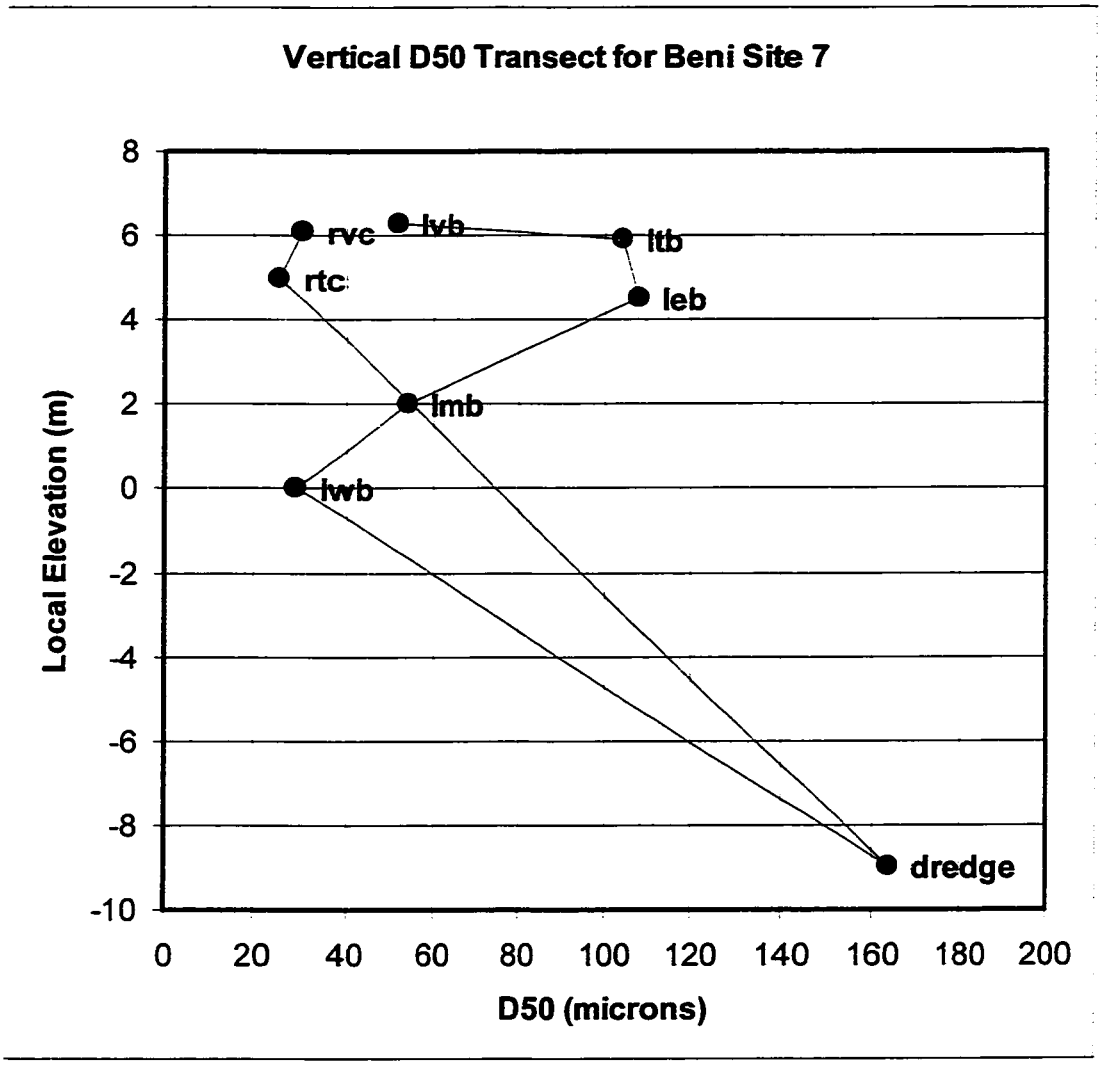
Vertical D50 Transect for Beni Site 7
Local Elevation (m)
8
6
4
2
0
-2
-4
-6
-8
-10
0
20
40
60
80
100
120
140
160
180
200
D50 (microns)
rvc
lvb
ltb
rtc
leb
lmb
lwb
dredge

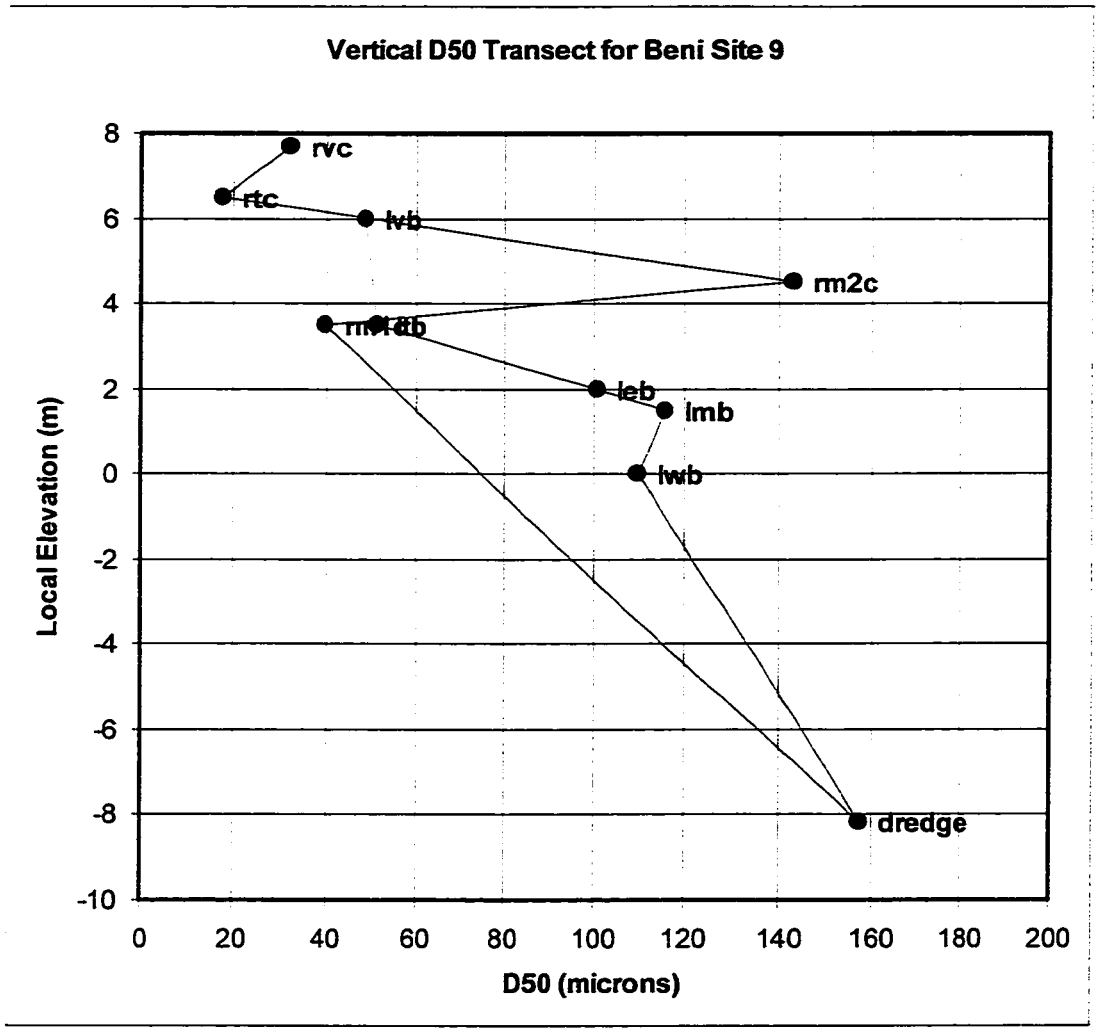
Vertical D50 Transect for Beni Site 9
Local Elevation (m)
D50 (microns)
8
6
4
2
0
-2
-4
-6
-8
-10
0
20
40
60
80
100
120
140
160
180
200
rvc
rtc
lwb
rm2c
leb
lmb
lwb
dredge

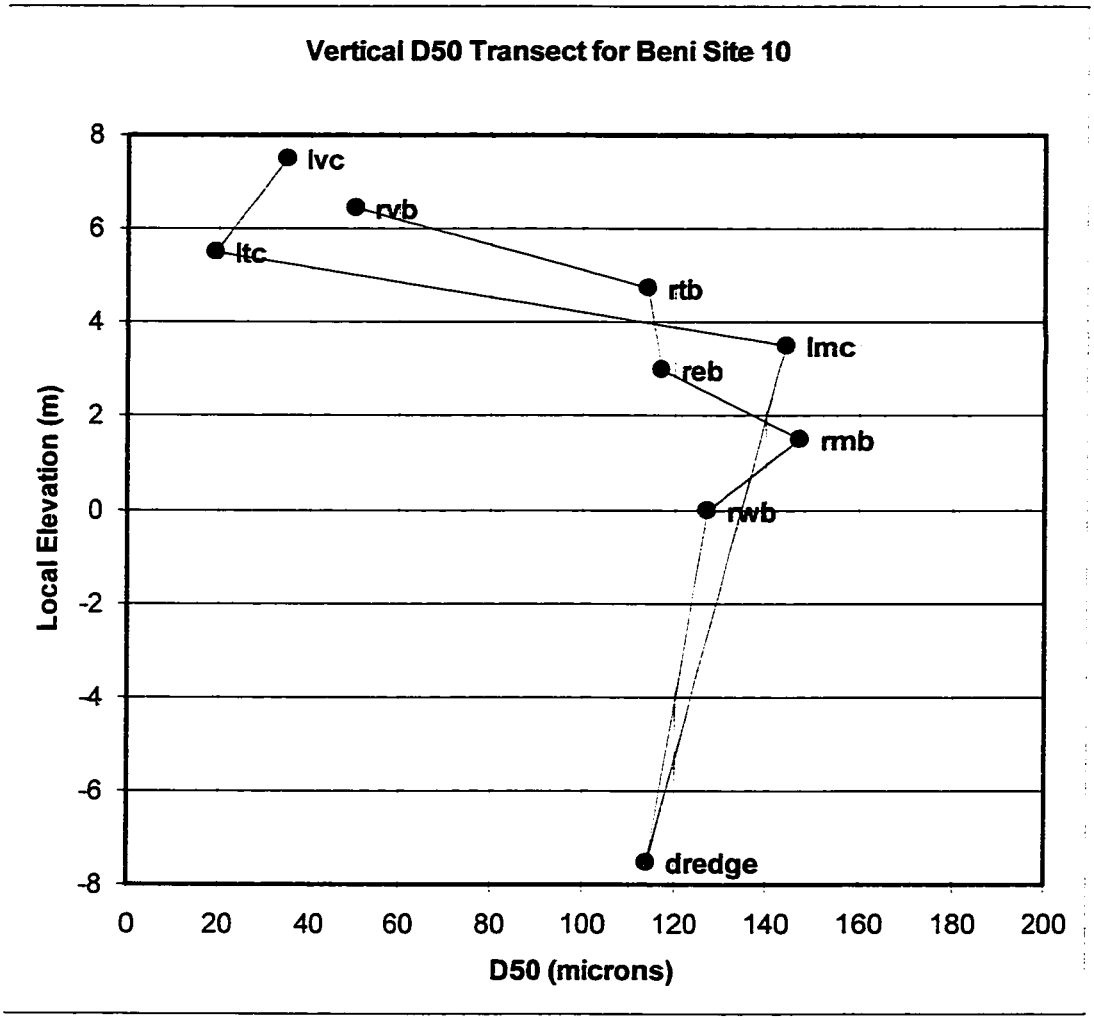
Vertical D50 Transect for Beni Site 10
Local Elevation (m)
8
6
4
2
0
-2
-4
-6
-8
0
20
40
60
80
100
120
140
160
180
200
D50 (microns)
lvc
rvb
ltc
rtb
lmc
reb
rmb
rwb
dredge

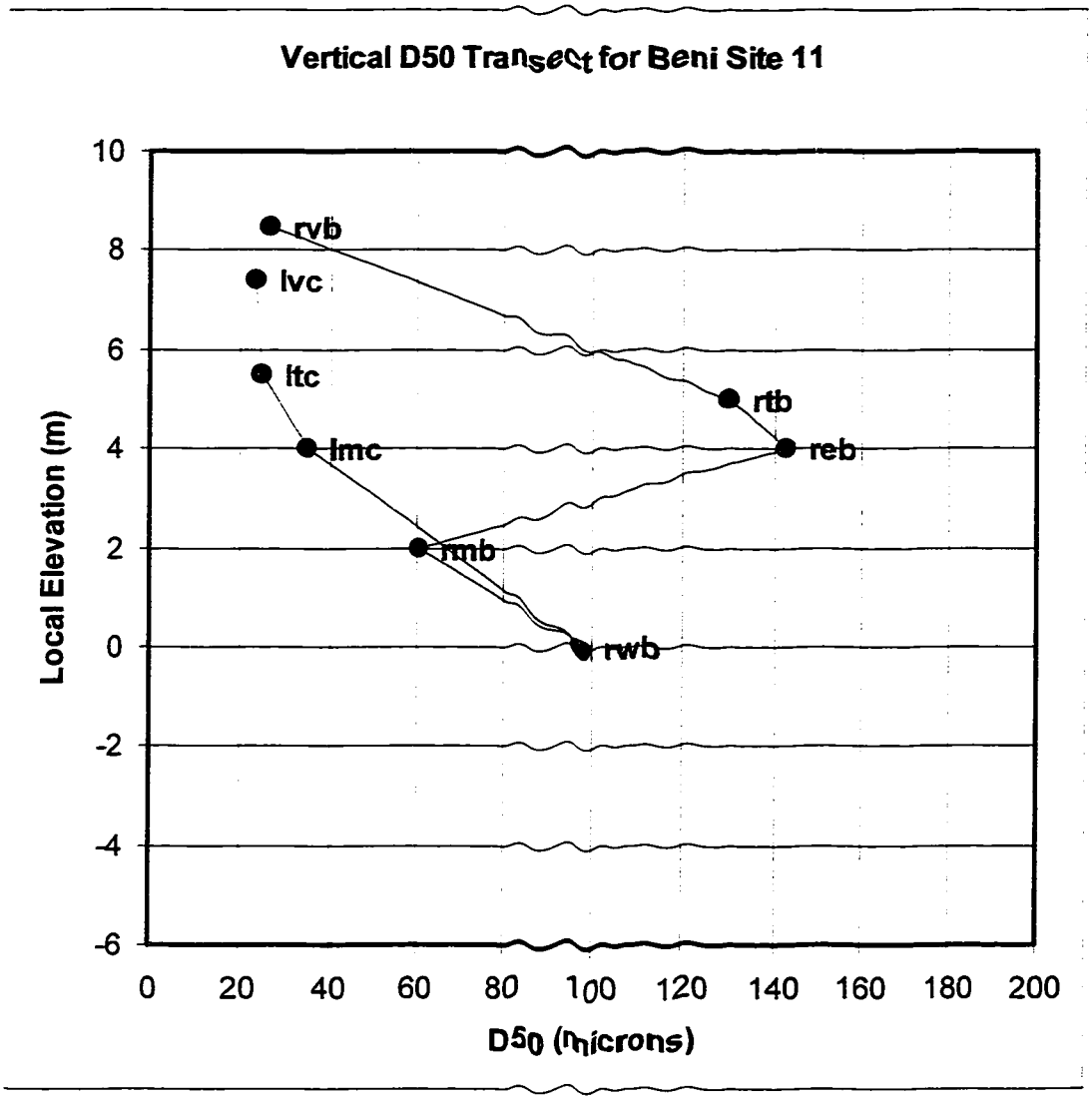
Vertical D50 Transect for Beni Site 11
Local Elevation (m)
10
8
6
4
2
0
-2
-4
-6
0
20
40
60
80
100
120
140
160
180
200
D50 (microns)
rvb
lvc
ltc
lmc
rtb
reb
rmb
rwb

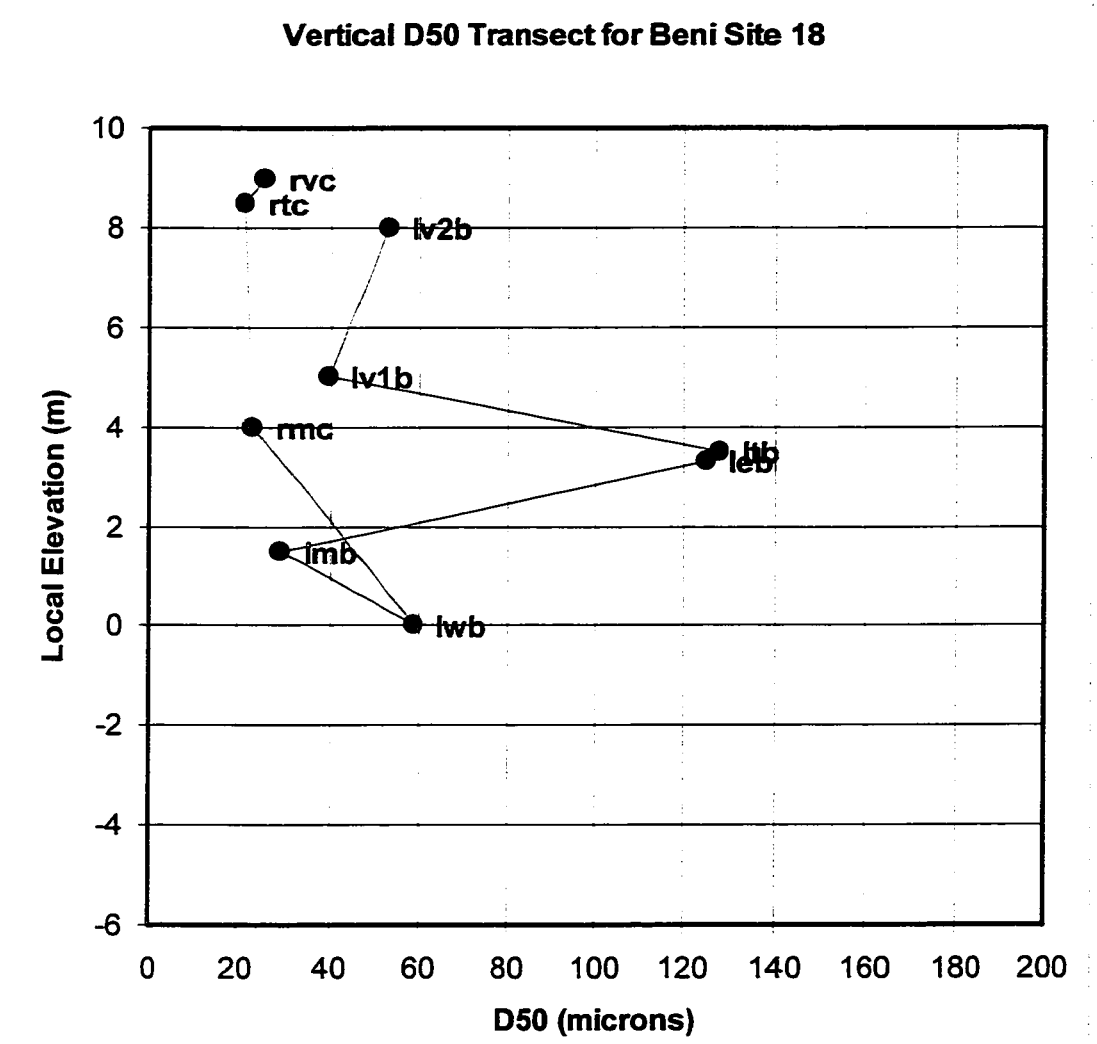
Vertical D50 Transect for Beni Site 18
Local Elevation (m)
10
8
6
4
2
0
-2
-4
-6
0
20
40
60
80
100
120
140
160
180
200
D50 (microns)
rvc
rtc
lv2b
lv1b
rmc
ltb
leb
lmb
lwb

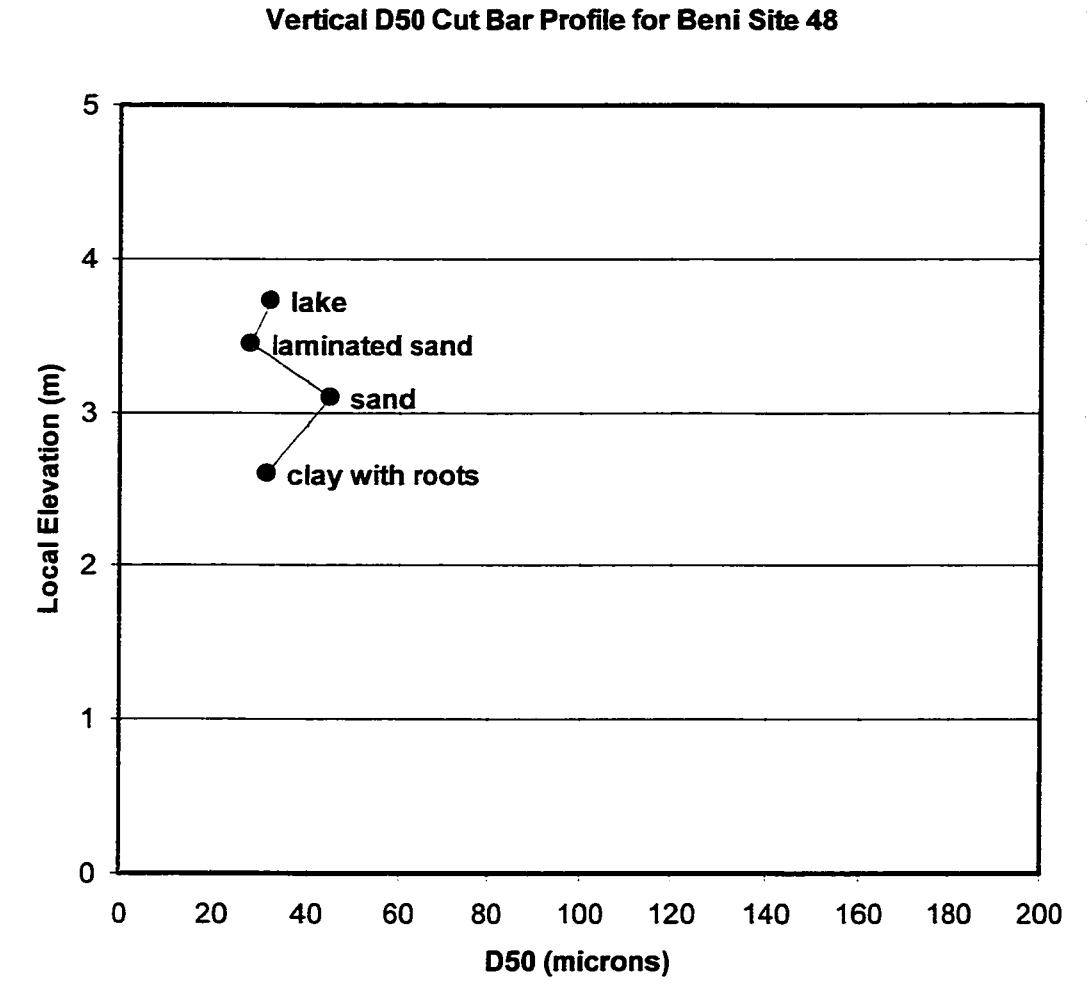
Vertical D50 Cut Bar Profile for Beni Site 48
Local Elevation (m)
5
4
3
2
1
0
lake
laminated sand
sand
clay with roots
0
20
40
60
80
100
120
140
160
180
200
D50 (microns)

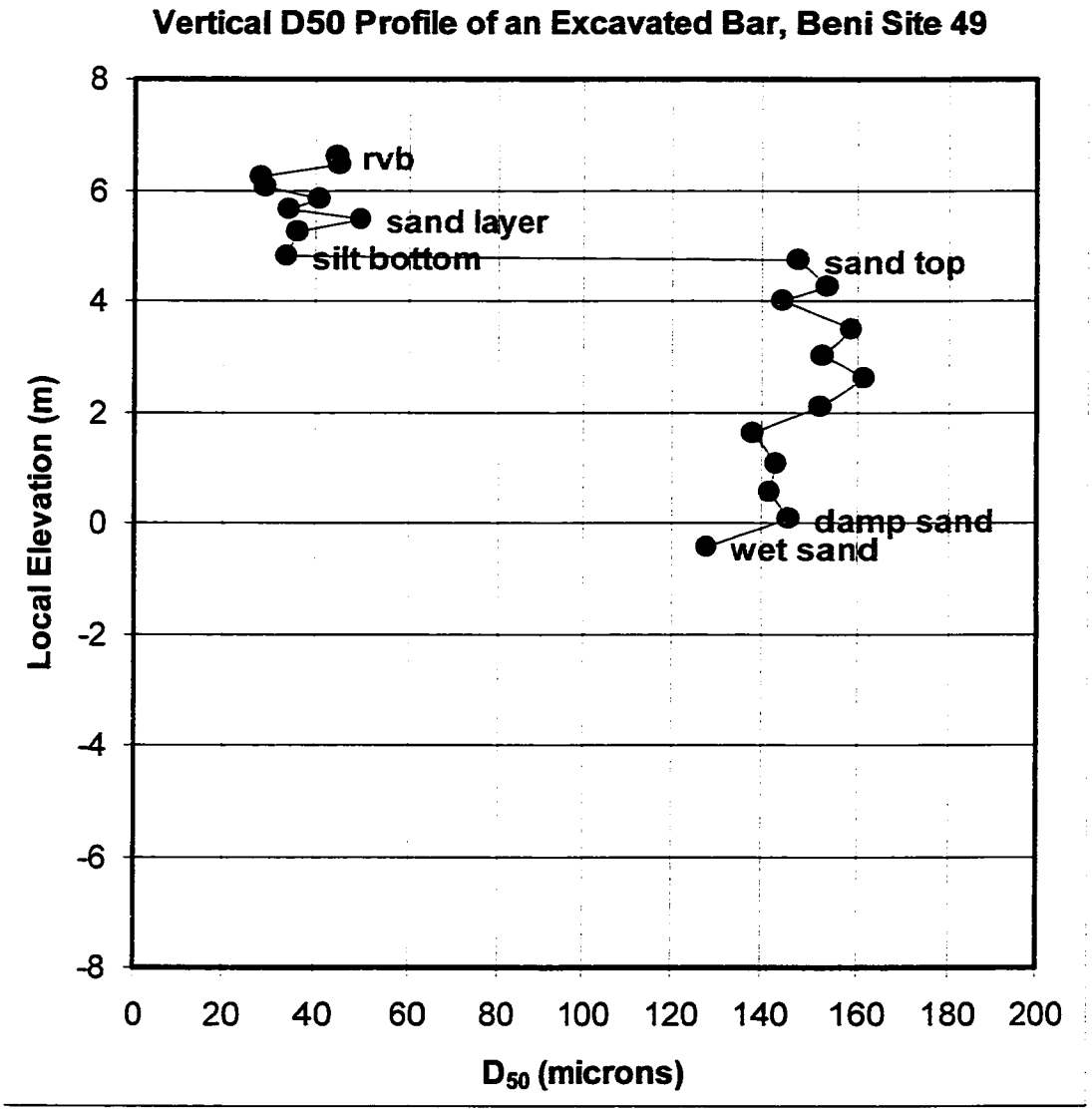
Vertical D50 Profile of an Excavated Bar, Beni Site 49
Local Elevation (m)
8
6
4
2
0
-2
-4
-6
-8
0
20
40
60
80
100
120
140
160
180
200
D50 (microns)
rvb
sand layer
silt bottom
sand top
damp sand
wet sand

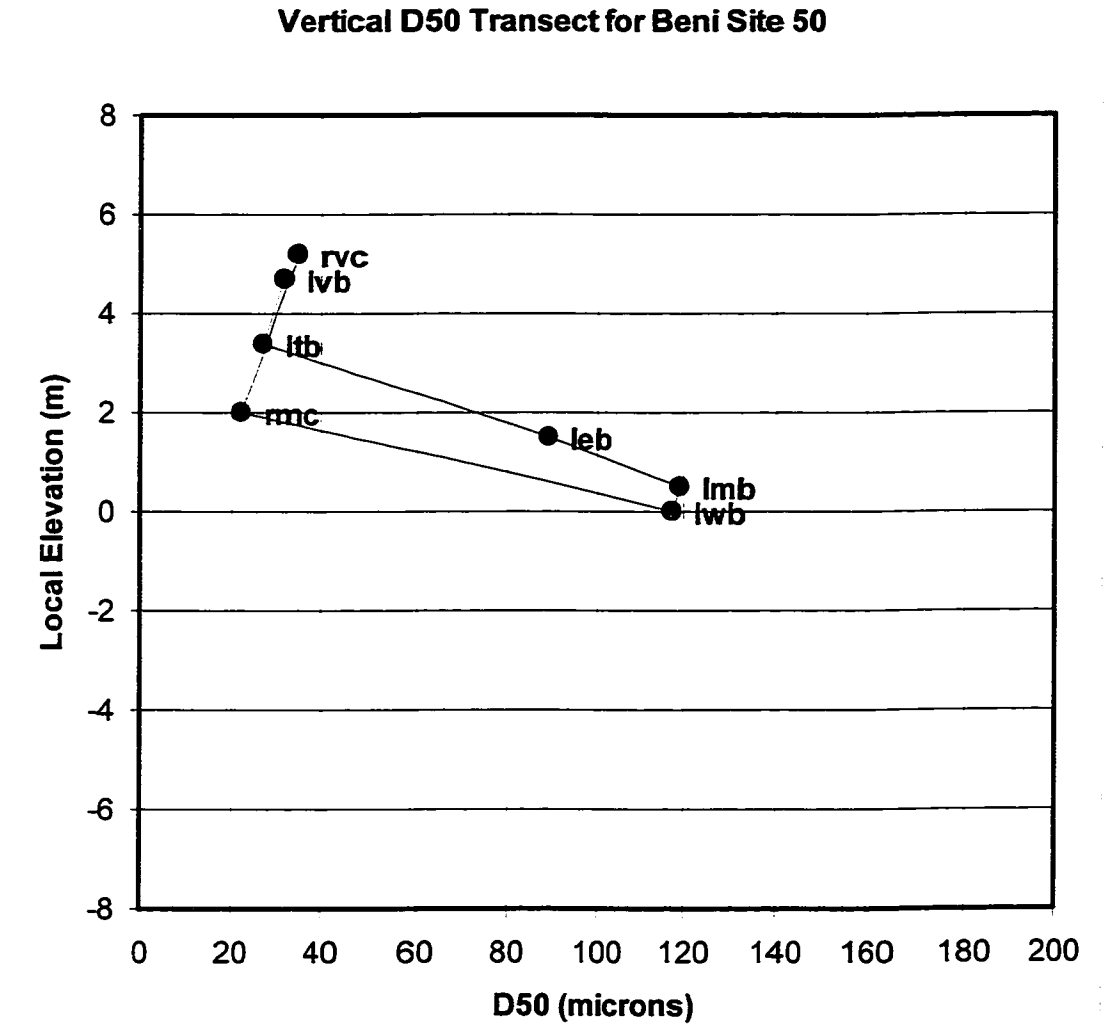
Vertical D50 Transect for Beni Site 50
Local Elevation (m)
8
6
4
2
0
-2
-4
-6
-8
0
20
40
60
80
100
120
140
160
180
200
D50 (microns)
rvc
lvb
ltb
rmc
leb
lmb
lwb

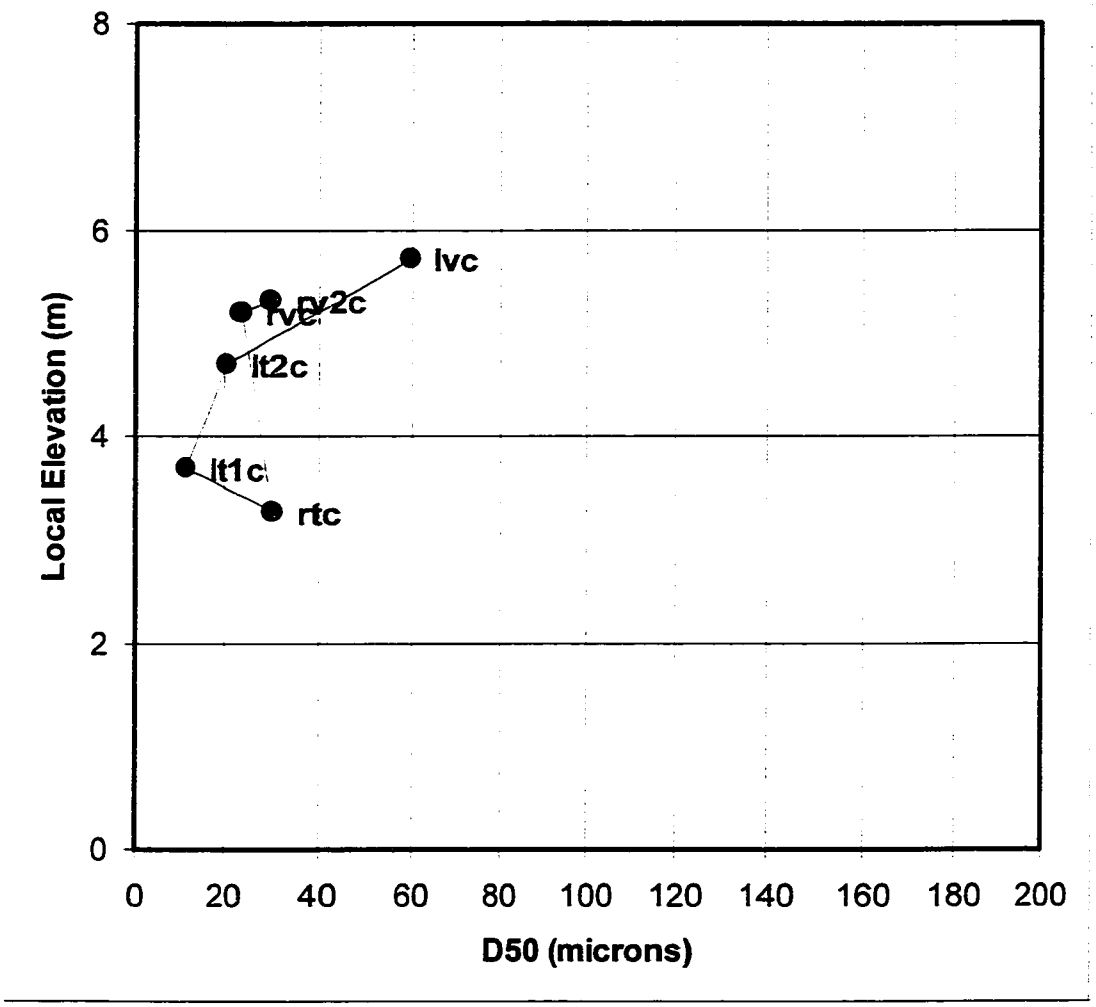
Vertical D50 Transect for Beni Site 51
Local Elevation (m)
8
6
4
2
0
0
20
40
60
80
100
120
140
160
180
200
D50 (microns)
lvc
rvc
rv2c
lt2c
lt1c
rtc

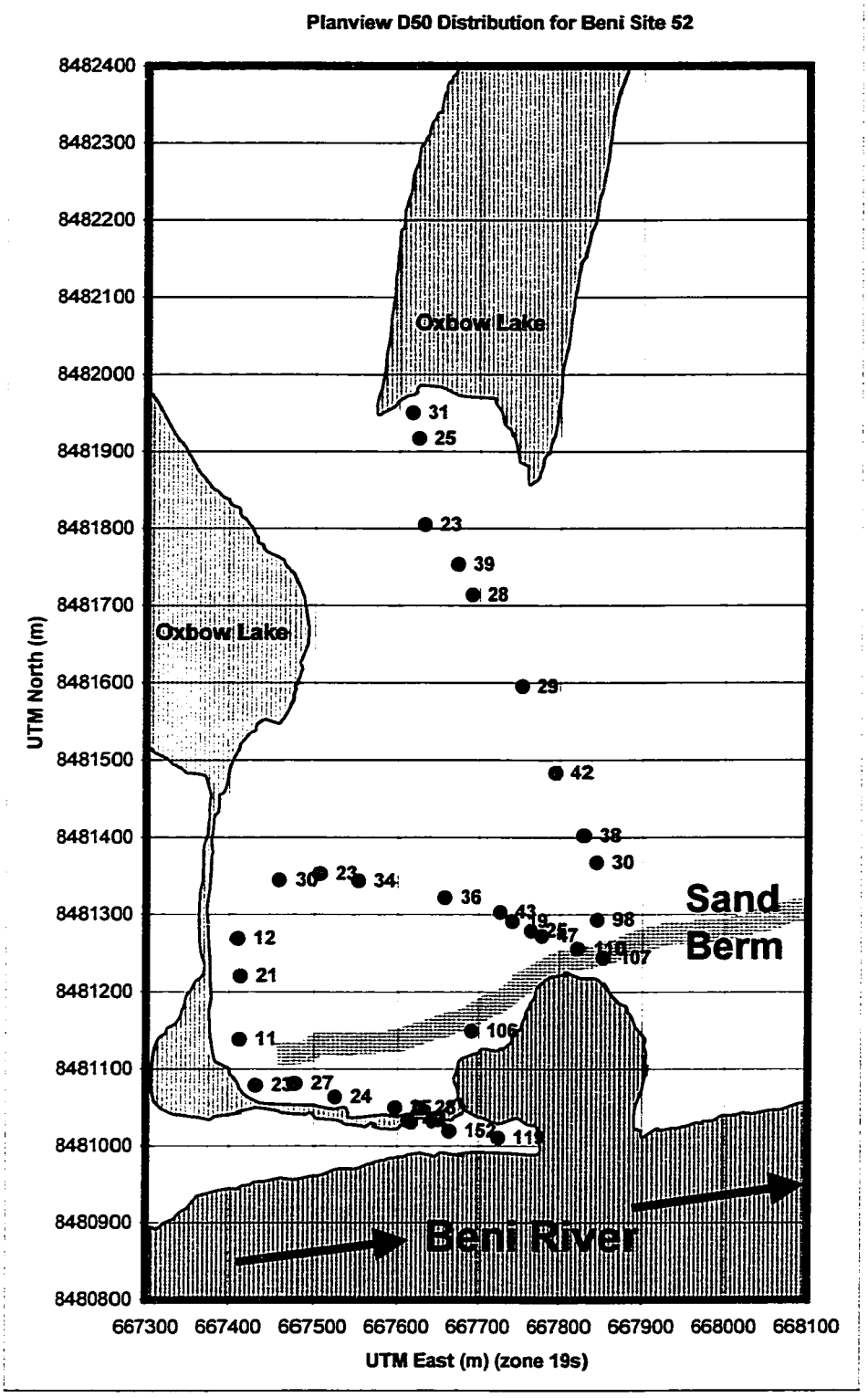
Planview D50 Distribution for Beni Site 52
8482400
8482300
8482200
8482100
8482000
8481900
8481800
8481700
8481600
8481500
8481400
8481300
8481200
8481100
8481000
8480900
8480800
UTM North (m)
667300
667400
667500
667600
667700
667800
667900
668000
668100
UTM East (m) (zone 19s)
Oxbow Lake
Oxbow Lake
Sand
Berm
Beni River
31
25
23
39
28
29
42
38
30
12
21
11
106
107
98
27
24
152

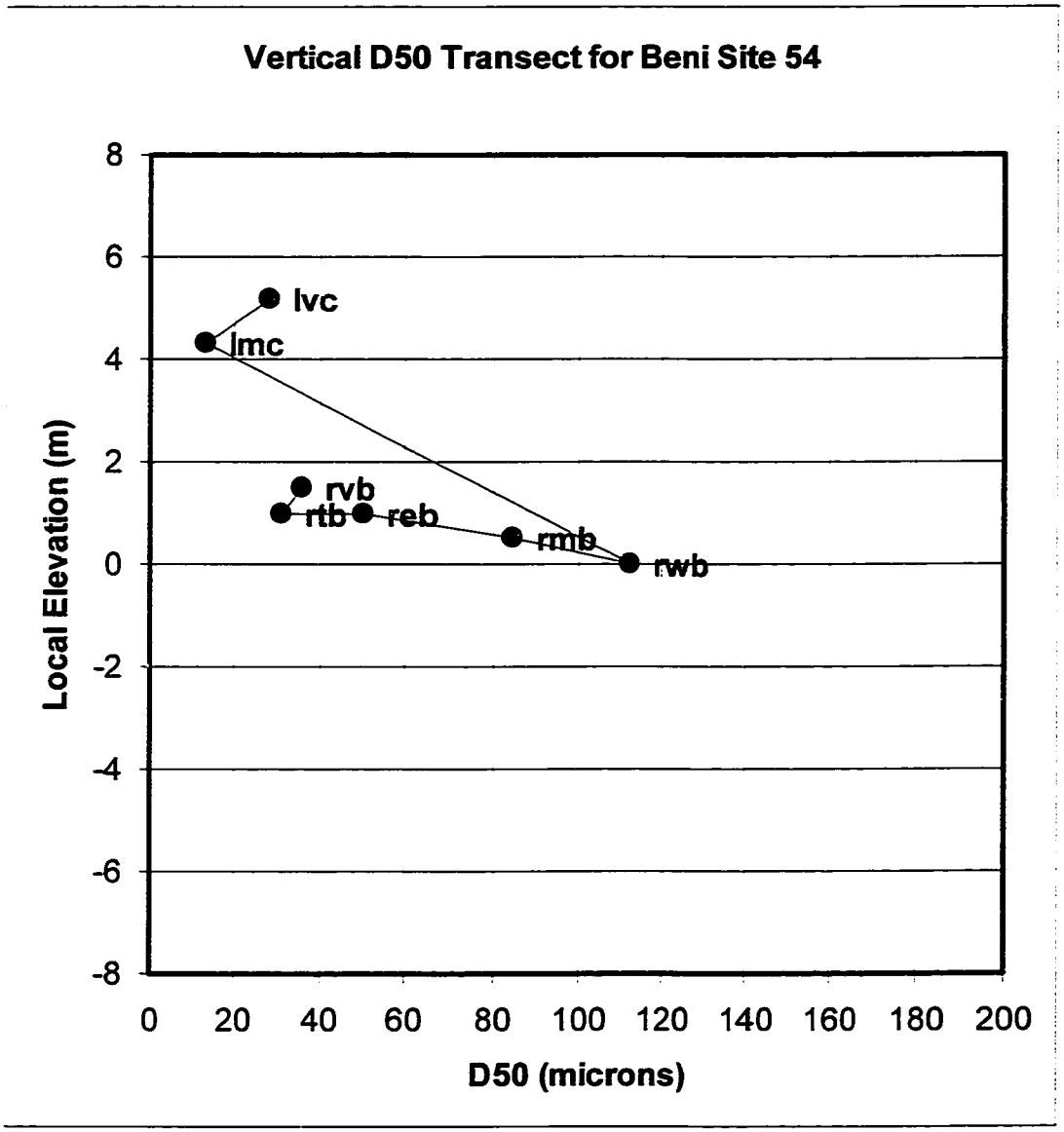
Vertical D50 Transect for Beni Site 54
Local Elevation (m)
8
6
4
2
0
-2
-4
-6
-8
0
20
40
60
80
100
120
140
160
180
200
D50 (microns)
lvc
lmc
rvb
rtb
reb
rmb
rwb

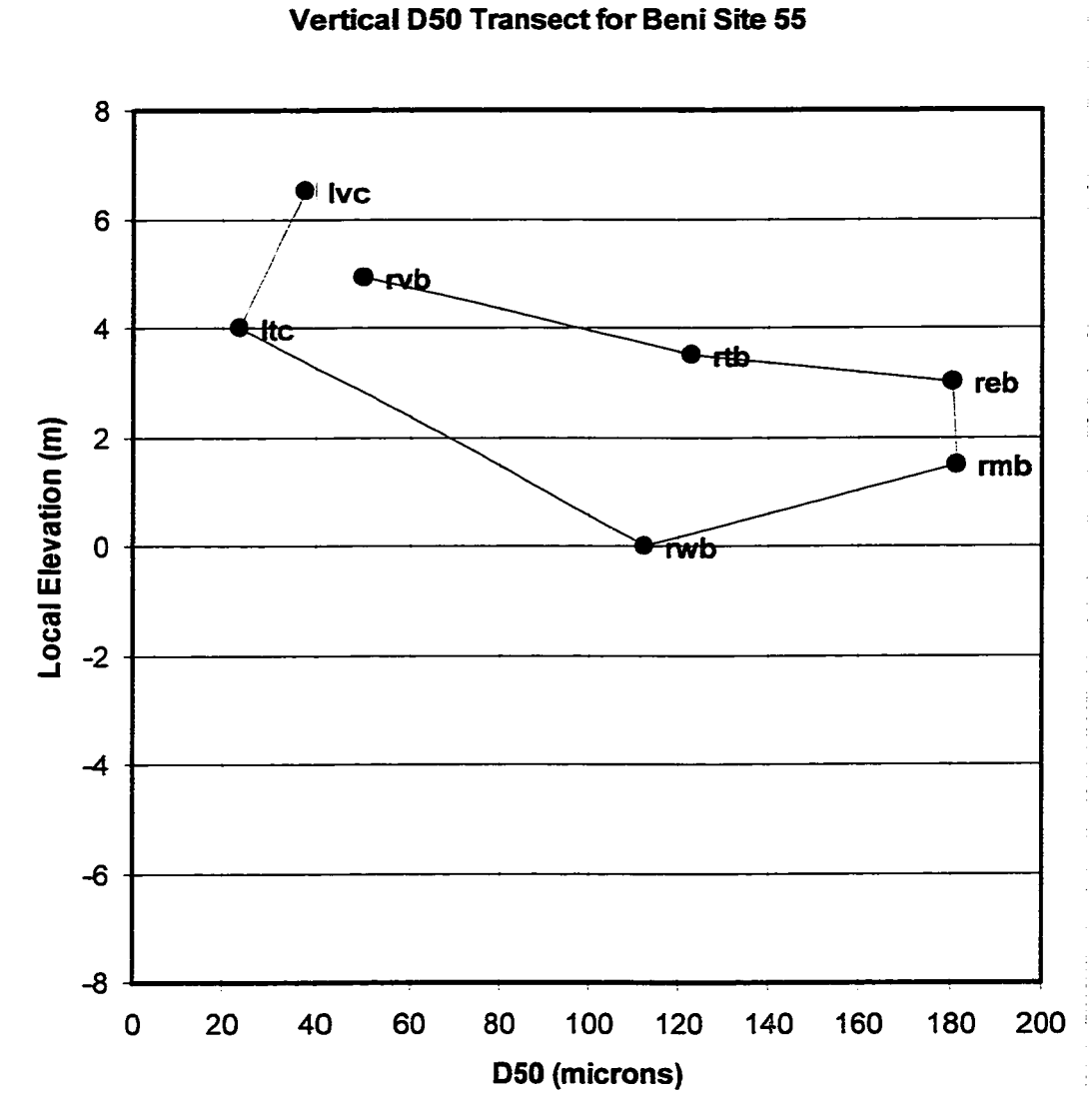
Vertical D50 Transect for Beni Site 55
Local Elevation (m)
8
6
4
2
0
-2
-4
-6
-8
0
20
40
60
80
100
120
140
160
180
200
D50 (microns)
lvc
rvb
ltc
rtb
reb
rmb
rwb

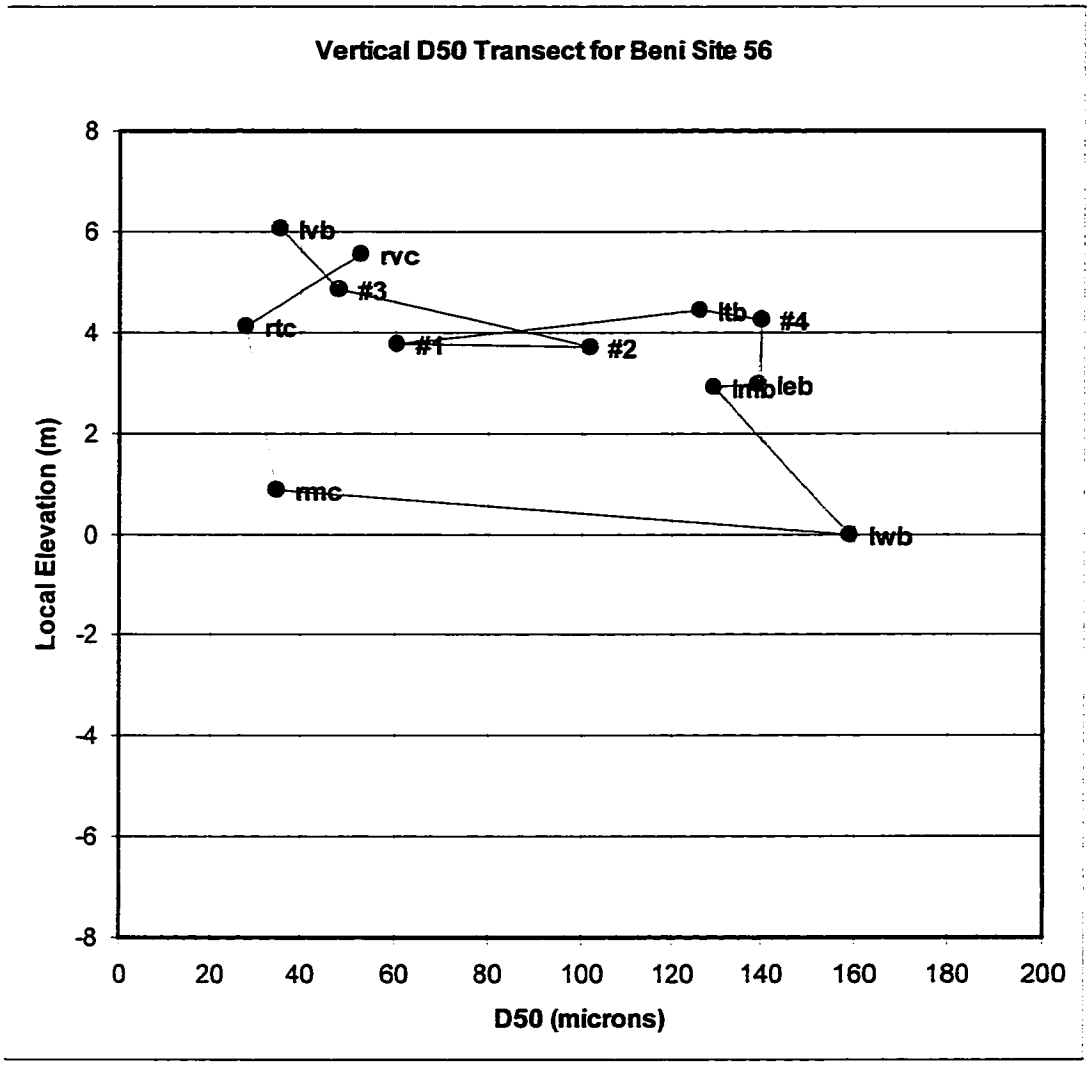
Vertical D50 Transect for Beni Site 56
Local Elevation (m)
8
6
4
2
0
-2
-4
-6
-8
0
20
40
60
80
100
120
140
160
180
200
D50 (microns)
lvb
rvc
#3
rtc
#1
#2
ltb
#4
lmbleb
rmc
lwb

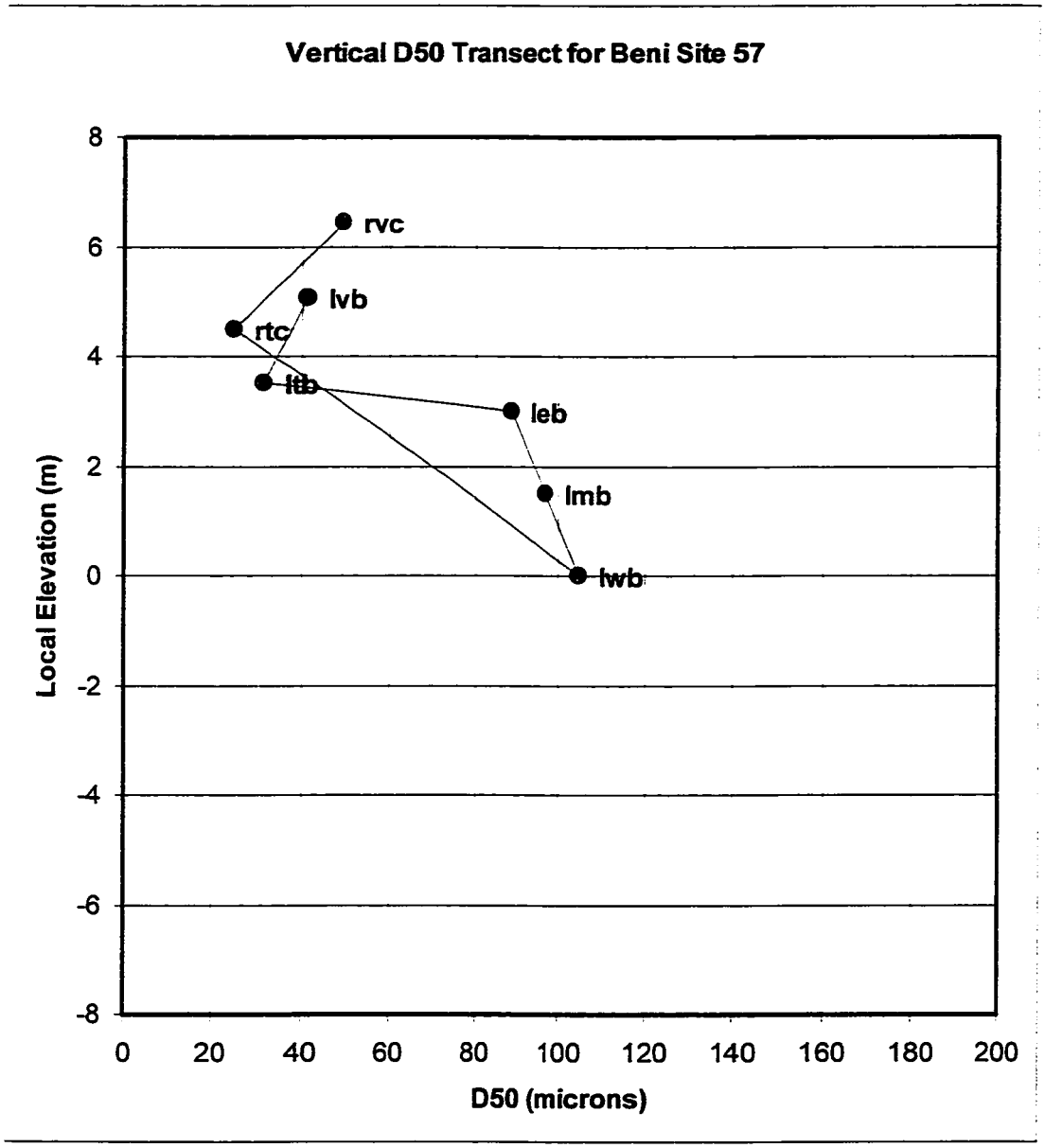
Vertical D50 Transect for Beni Site 57
Local Elevation (m)
8
6
4
2
0
-2
-4
-6
-8
0
20
40
60
80
100
120
140
160
180
200
D50 (microns)
rvc
lvb
rtc
ltb
leb
lmb
lwb

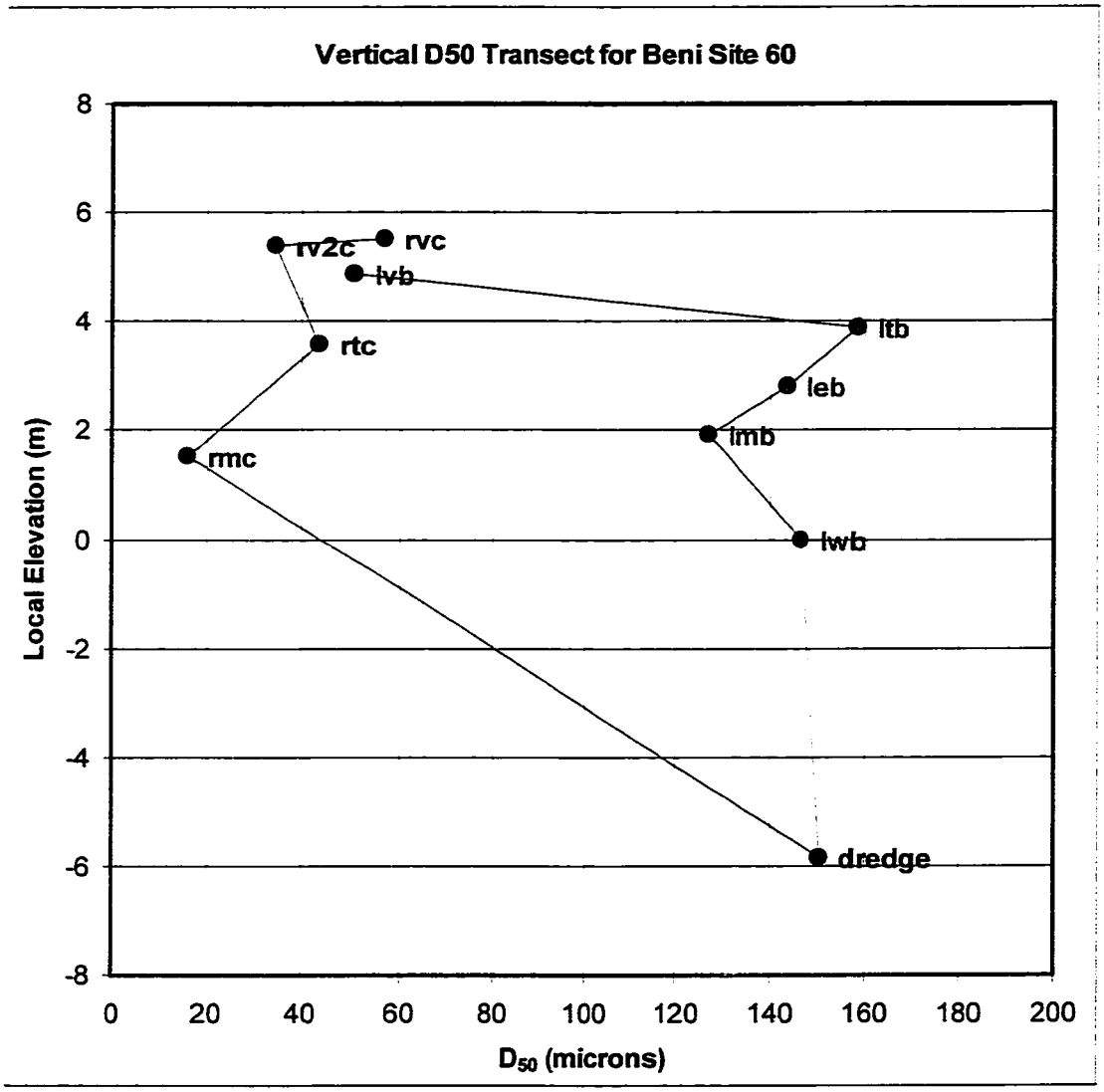
Vertical D50 Transect for Beni Site 60
Local Elevation (m)
8
6
4
2
0
-2
-4
-6
-8
0
20
40
60
80
100
120
140
160
180
200
D50 (microns)
rv2c
rvc
lvb
ltb
rtc
leb
lmb
rmc
lwb
dredge

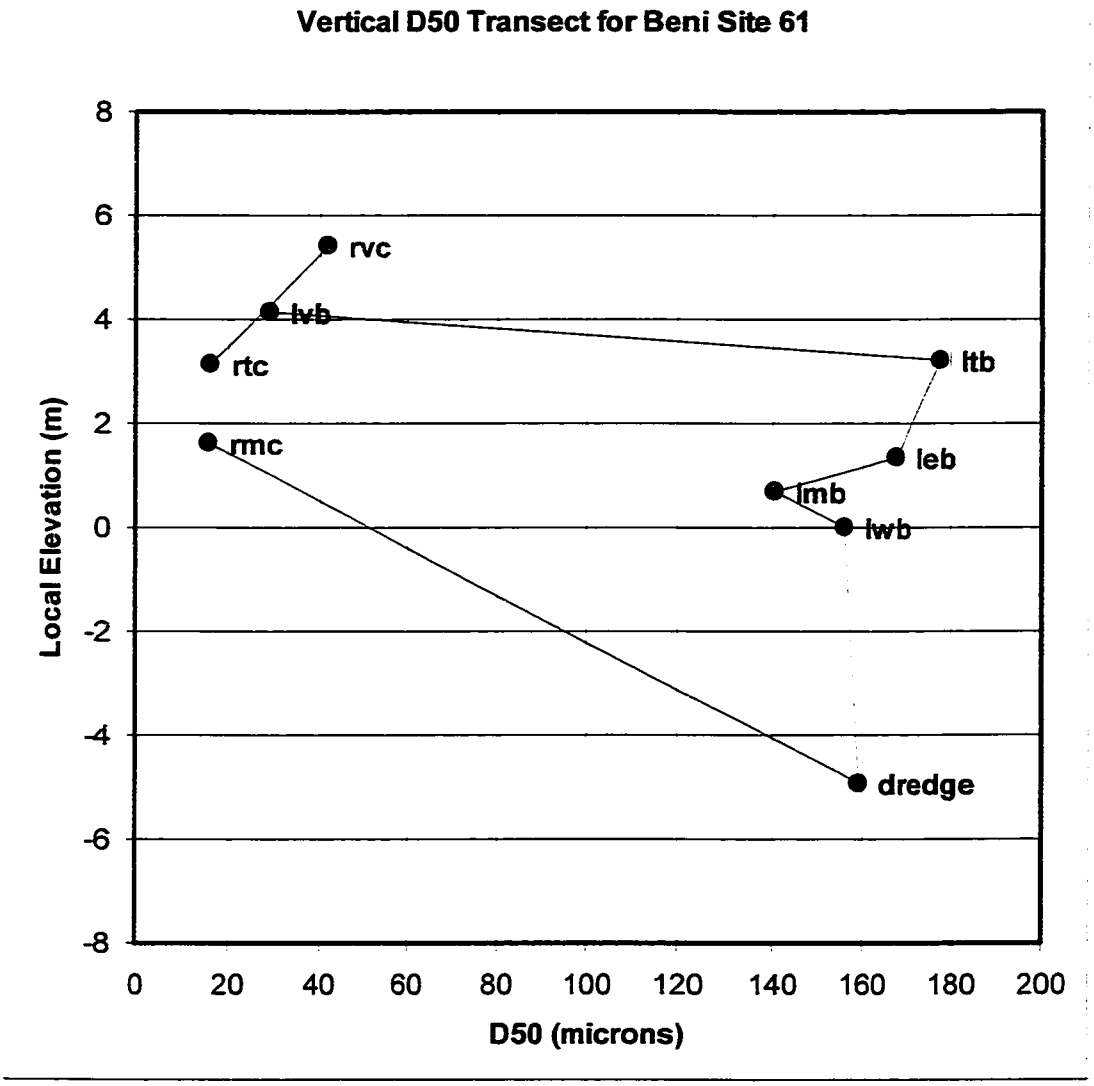
Vertical D50 Transect for Beni Site 61
Local Elevation (m)
8
6
4
2
0
-2
-4
-6
-8
0
20
40
60
80
100
120
140
160
180
200
D50 (microns)
rvc
lvb
rtc
ltb
rmc
leb
lmb
lwb
dredge

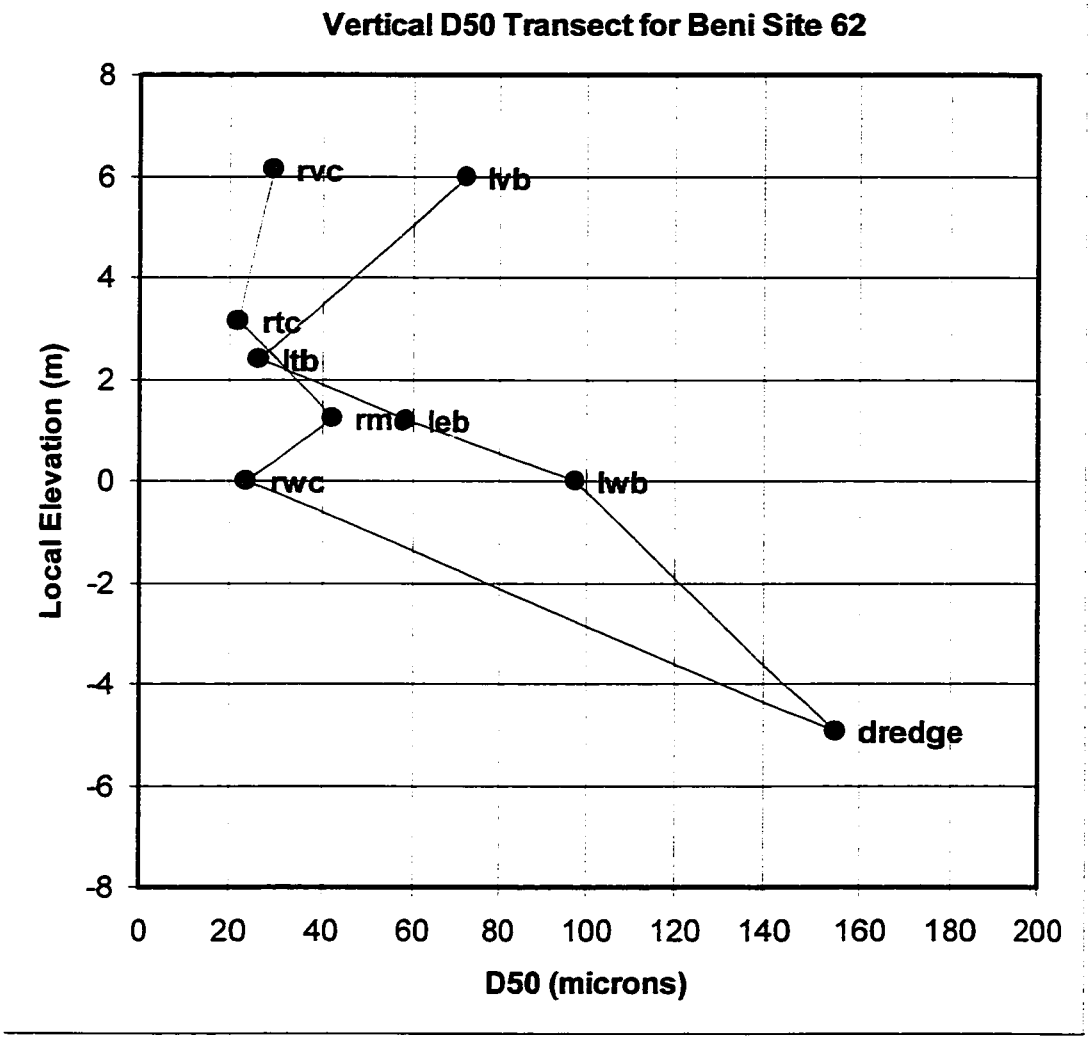
Vertical D50 Transect for Beni Site 62
Local Elevation (m)
8
6
4
2
0
-2
-4
-6
-8
0
20
40
60
80
100
120
140
160
180
200
D50 (microns)
rvc
lvb
rtc
ltb
rm
leb
rwc
lwb
dredge

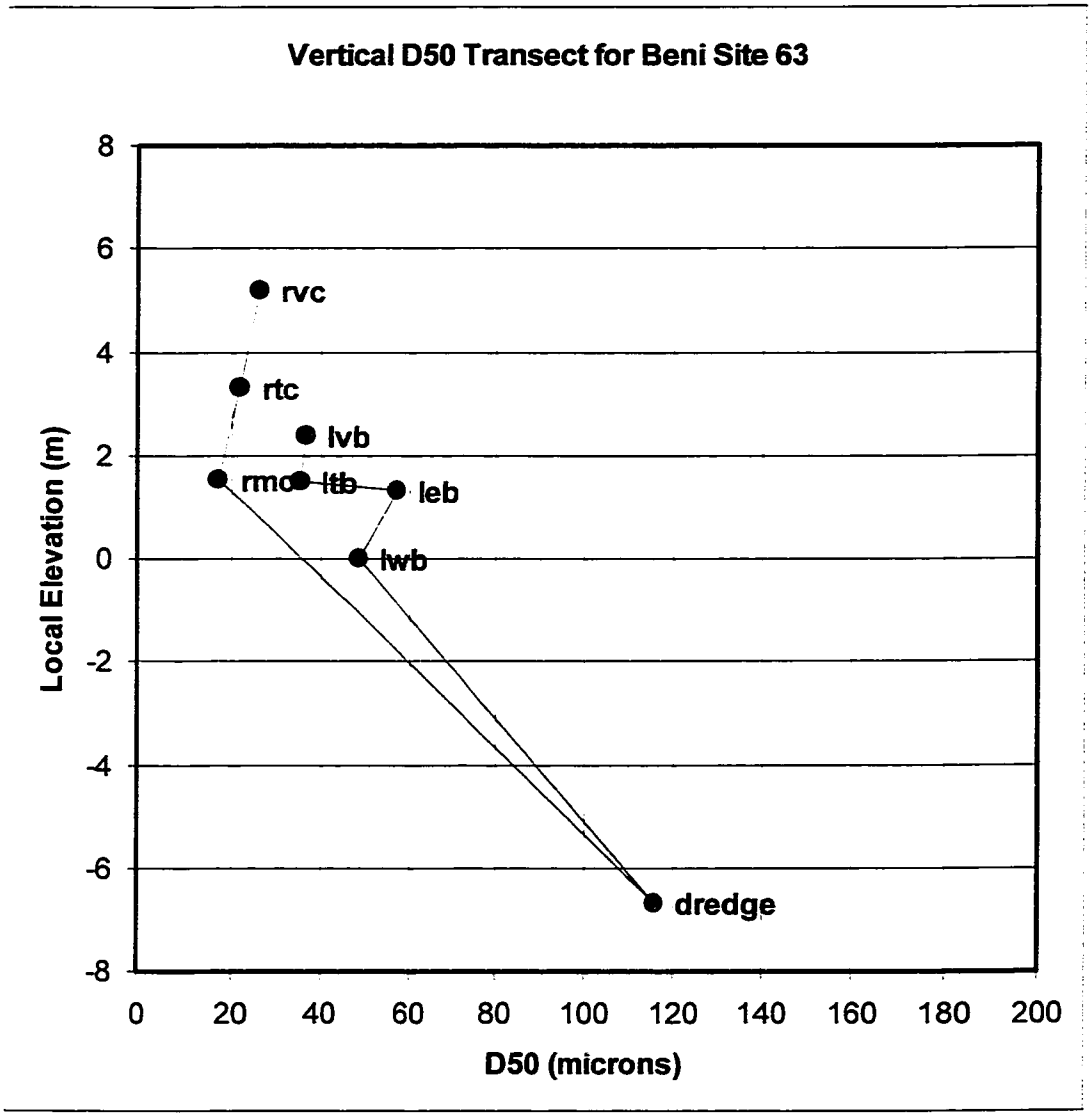
Vertical D50 Transect for Beni Site 63
Local Elevation (m)
8
6
4
2
0
-2
-4
-6
-8
rvc
rtc
lvb
rmc
ltb
leb
lwb
dredge
0
20
40
60
80
100
120
140
160
180
200
D50 (microns)

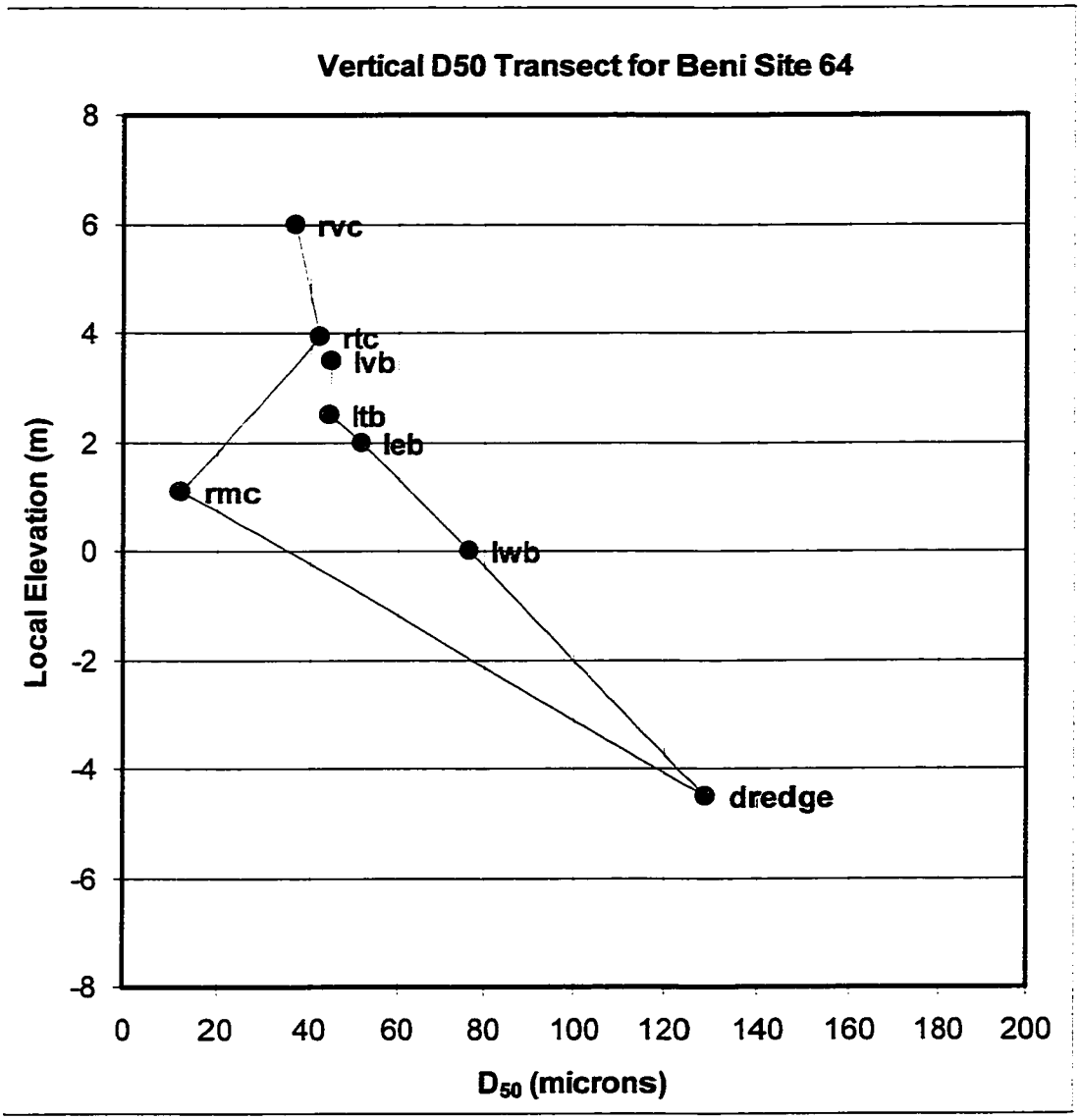
Vertical D50 Transect for Beni Site 64
Local Elevation (m)
8
6
4
2
0
-2
-4
-6
-8
0
20
40
60
80
100
120
140
160
180
200
D50 (microns)
rvc
rtc
lvb
ltb
leb
rmc
lwb
dredge

Appendix C

Common caption for all figures in Appendix C

This appendix contains all processed core profiles from the Beni River survey transects. Cores were primarily sampled from and processed for the forested floodplains on the cutbank side of the river, but also include some forested floodplain locations on the bar side of the channel. The figures depict the percentage of clay, silt, and sand at each discrete sample depth, along with clay-normalized ^{210}Pb activity plotted versus sample depth. Each figure includes a concise summary (in black text) of the corresponding X-radiograph for that core. Following the CIRCAUS methodology (Chapter 4), a brief interpretation of the ^{210}Pb geochronology is presented (in red text), including year of sediment deposition and the corresponding site distance from the river channel at that date (determined from the GIS maps in Appendix A and in the Pocket Material). To test for the possibility of constant sediment accumulation, a plot of the best-fit activity profile for the constant sedimentation hypothesis (CIRCACS, discussed in Chapter 4) is also included for cores that depict a downwards-decreasing clay-normalized ^{210}Pb activity that could possibly be interpreted as "steady" accumulation.

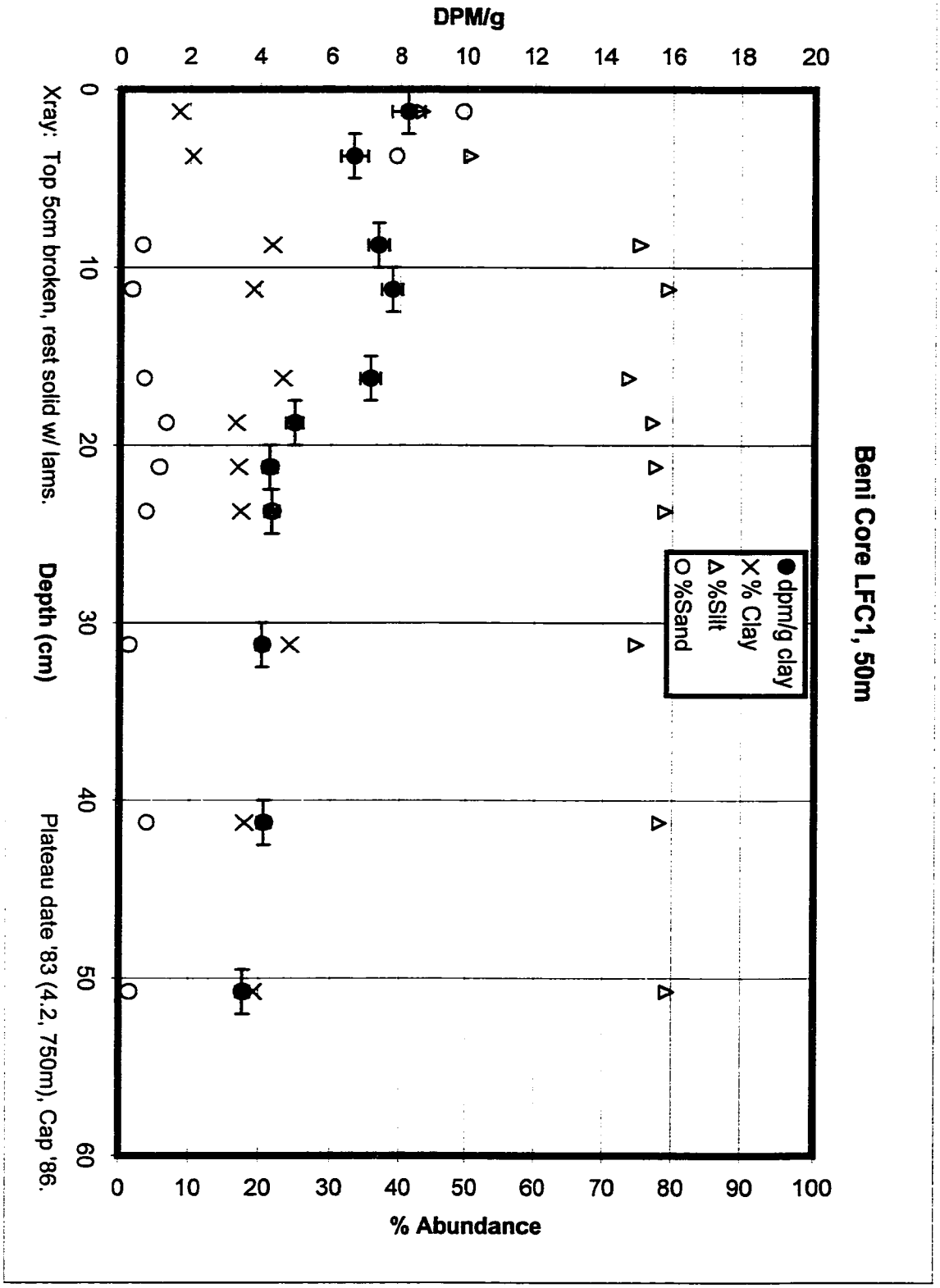
DPM/g
0 2 4 6 8 10 12 14 16 18 20
0 10 20 30 40 50 60
Depth (cm)
0 10 20 30 40 50 60 70 80 90 100
% Abundance
Beni Core LFC1, 50m
dpm/g clay
% Clay
%Silt
%Sand
Xray: Top 5cm broken, rest solid w/ lams.
Plateau date '83 (4.2, 750m), Cap '86.

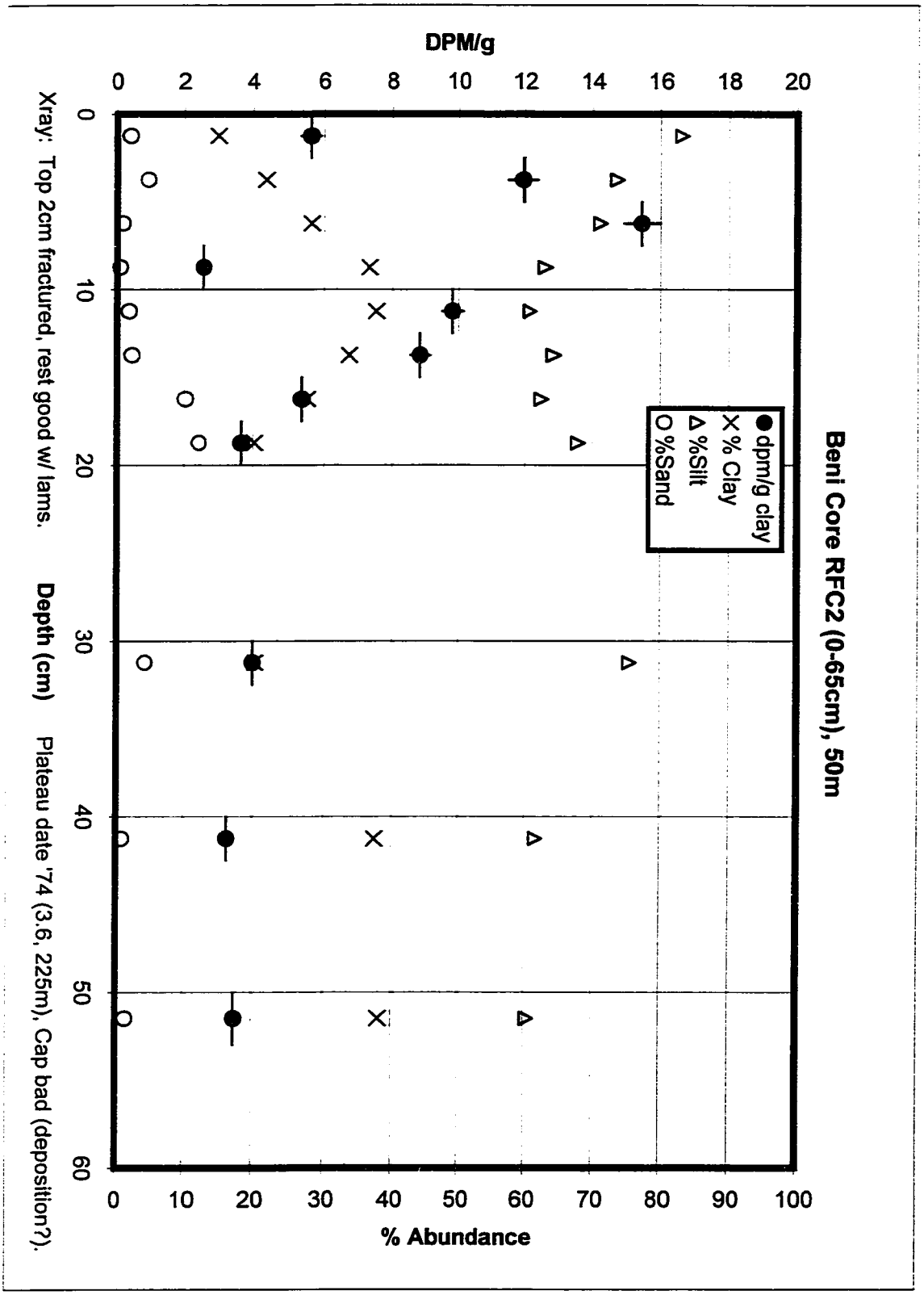
DPM/g
0 2 4 6 8 10 12 14 16 18 20
Beni Core RFC2 (0-65cm), 50m
dpm/g clay
% Clay
%Silt
%Sand
0 10 20 30 40 50 60
Depth (cm)
0 10 20 30 40 50 60 70 80 90 100
% Abundance
Xray: Top 2cm fractured, rest good w/ lams.
Plateau date '74 (3.6, 225m), Cap bad (deposition?).

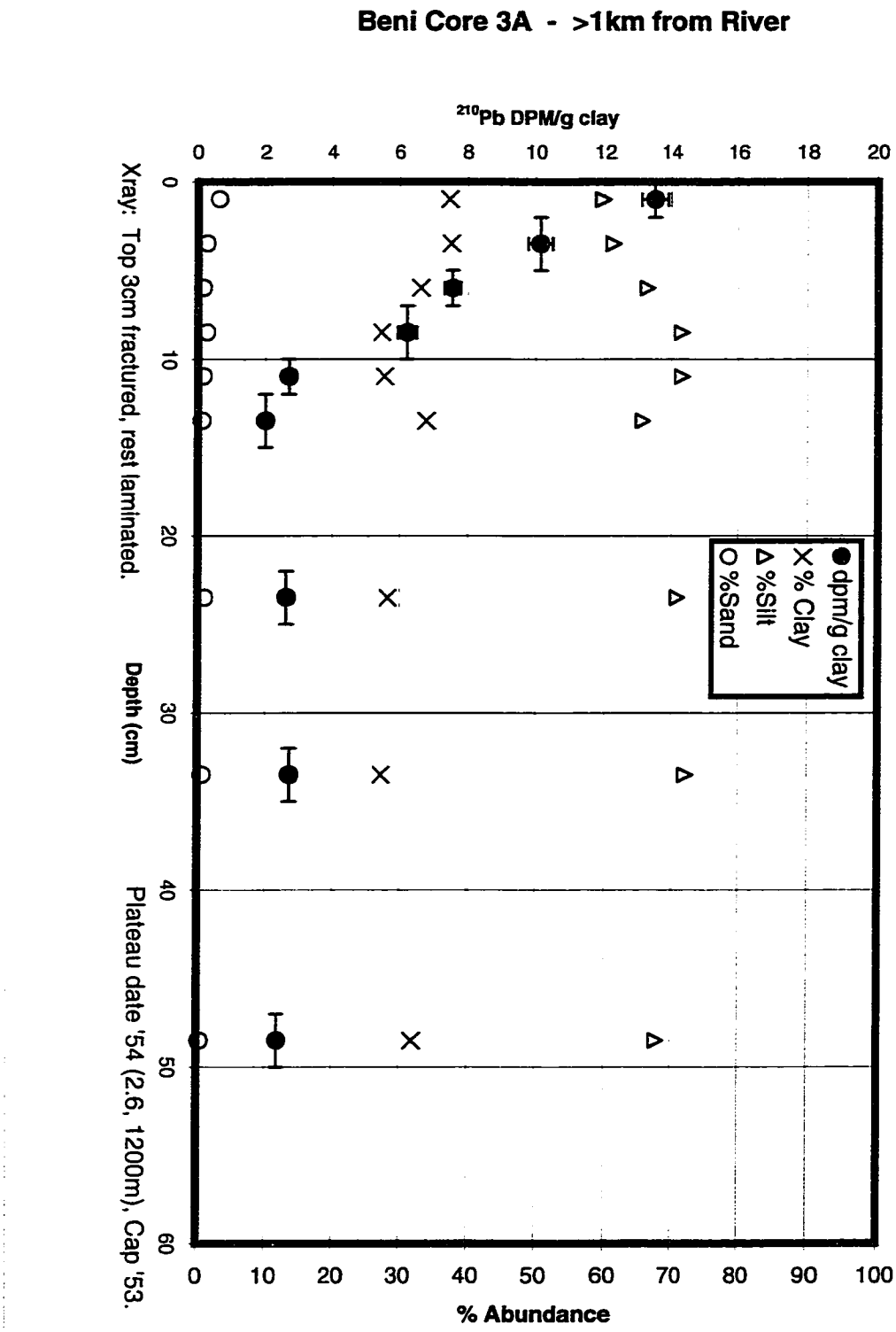
Beni Core 3A - >1km from River
^{210}Pb DPM/g clay
0 2 4 6 8 10 12 14 16 18 20
Xray: Top 3cm fractured, rest laminated.
Depth (cm)
Plateau date '54 (2.6, 1200m), Cap '53.
0 10 20 30 40 50 60
0 10 20 30 40 50 60 70 80 90 100
% Abundance
dpm/g clay
% Clay
%Silt
%Sand

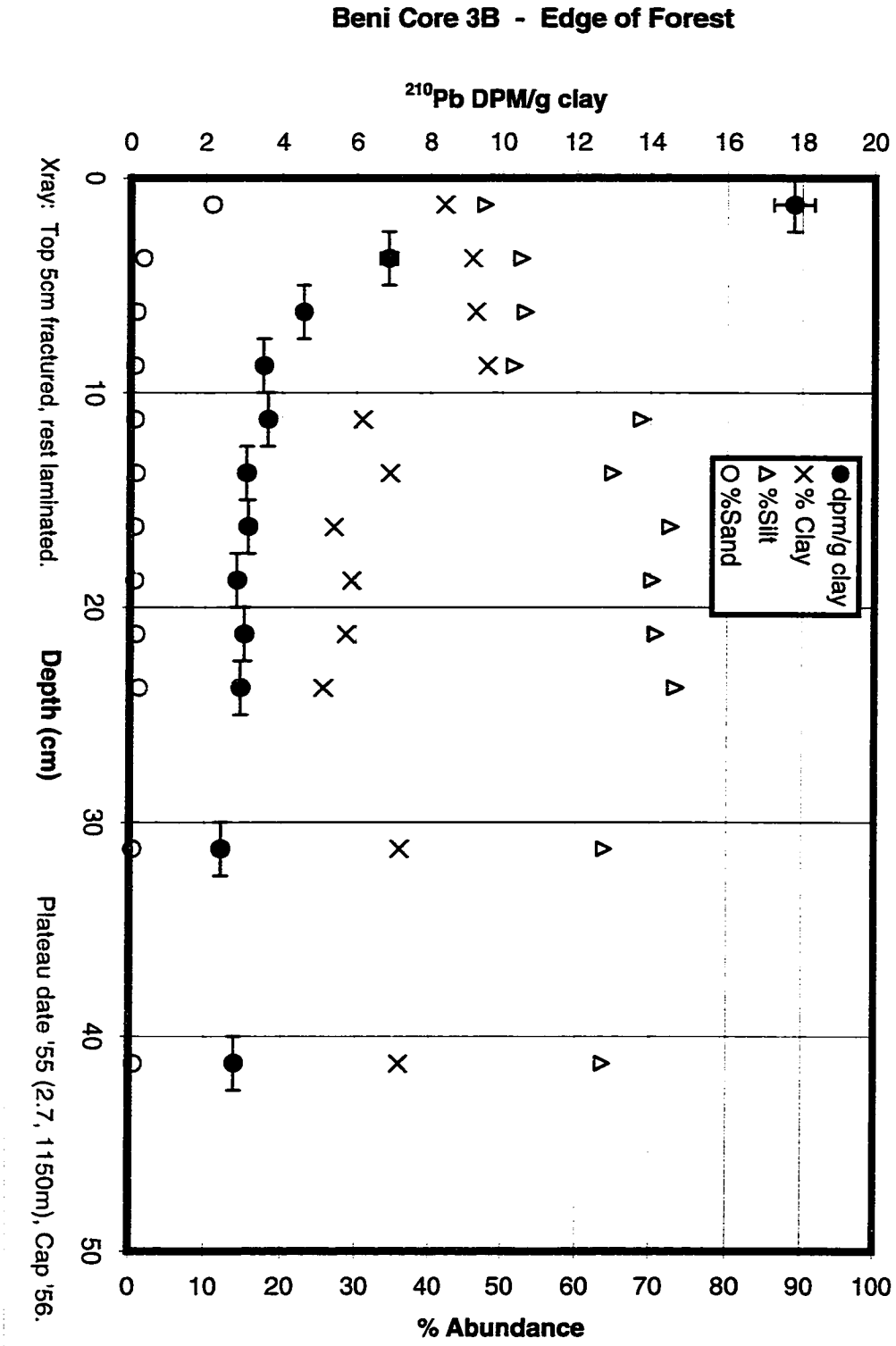
Beni Core 3B - Edge of Forest
210Pb DPM/g clay
0 2 4 6 8 10 12 14 16 18 20
Xray: Top 5cm fractured, rest laminated.
Depth (cm)
0 10 20 30 40 50
Plateau date '55 (2.7, 1150m), Cap '56.
dpm/g clay
% Clay
%Silt
%Sand
0 10 20 30 40 50 60 70 80 90 100
% Abundance

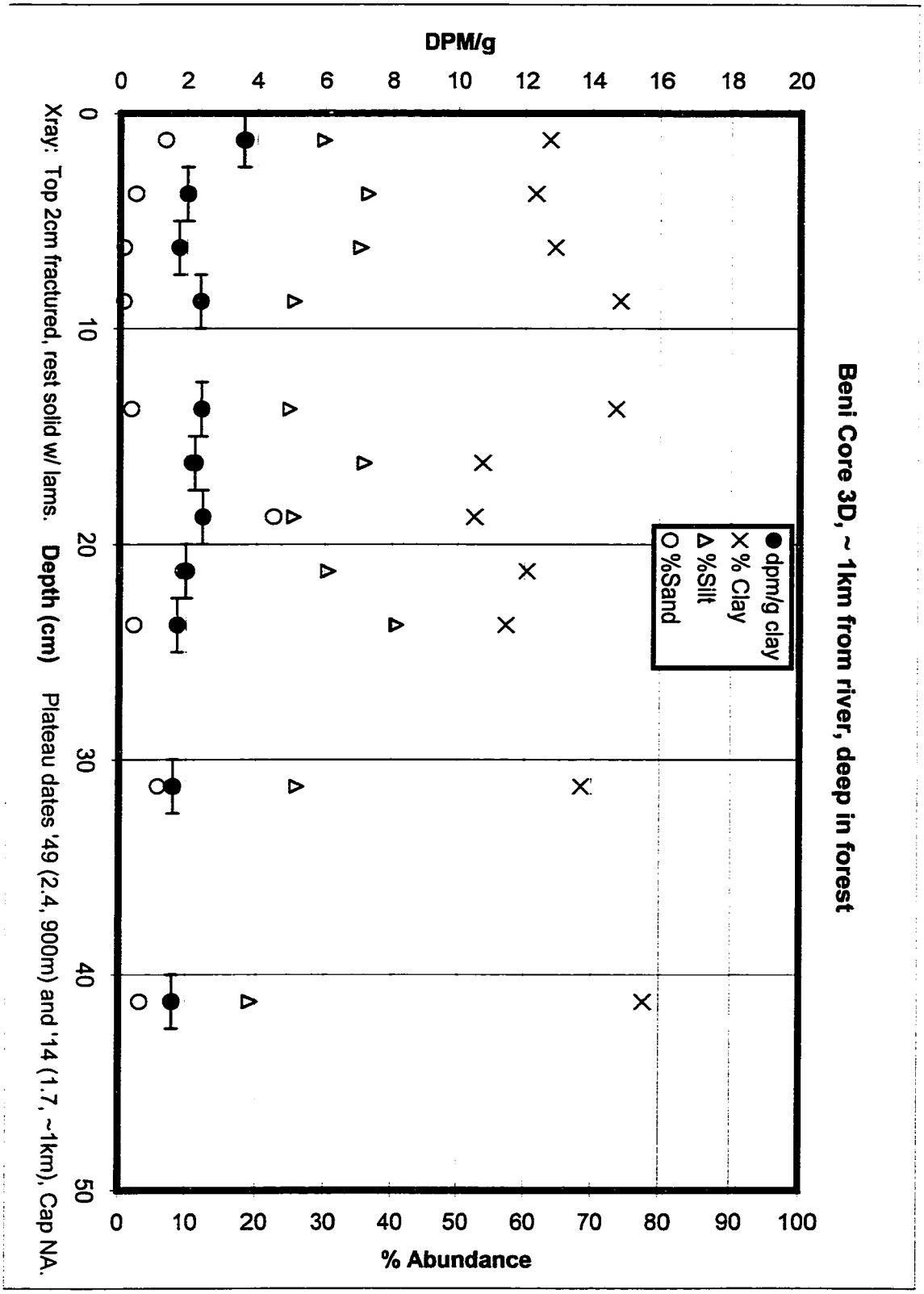
Beni Core 3D, ~ 1km from river, deep in forest
DPM/g
0 2 4 6 8 10 12 14 16 18 20
% Abundance
0 10 20 30 40 50 60 70 80 90 100
Depth (cm)
0 10 20 30 40 50
dpm/g clay
% Clay
%Silt
%Sand
Xray: Top 2cm fractured, rest solid w/ lams. Plateau dates '49 (2.4, 900m) and '14 (1.7, ~1km), Cap NA.

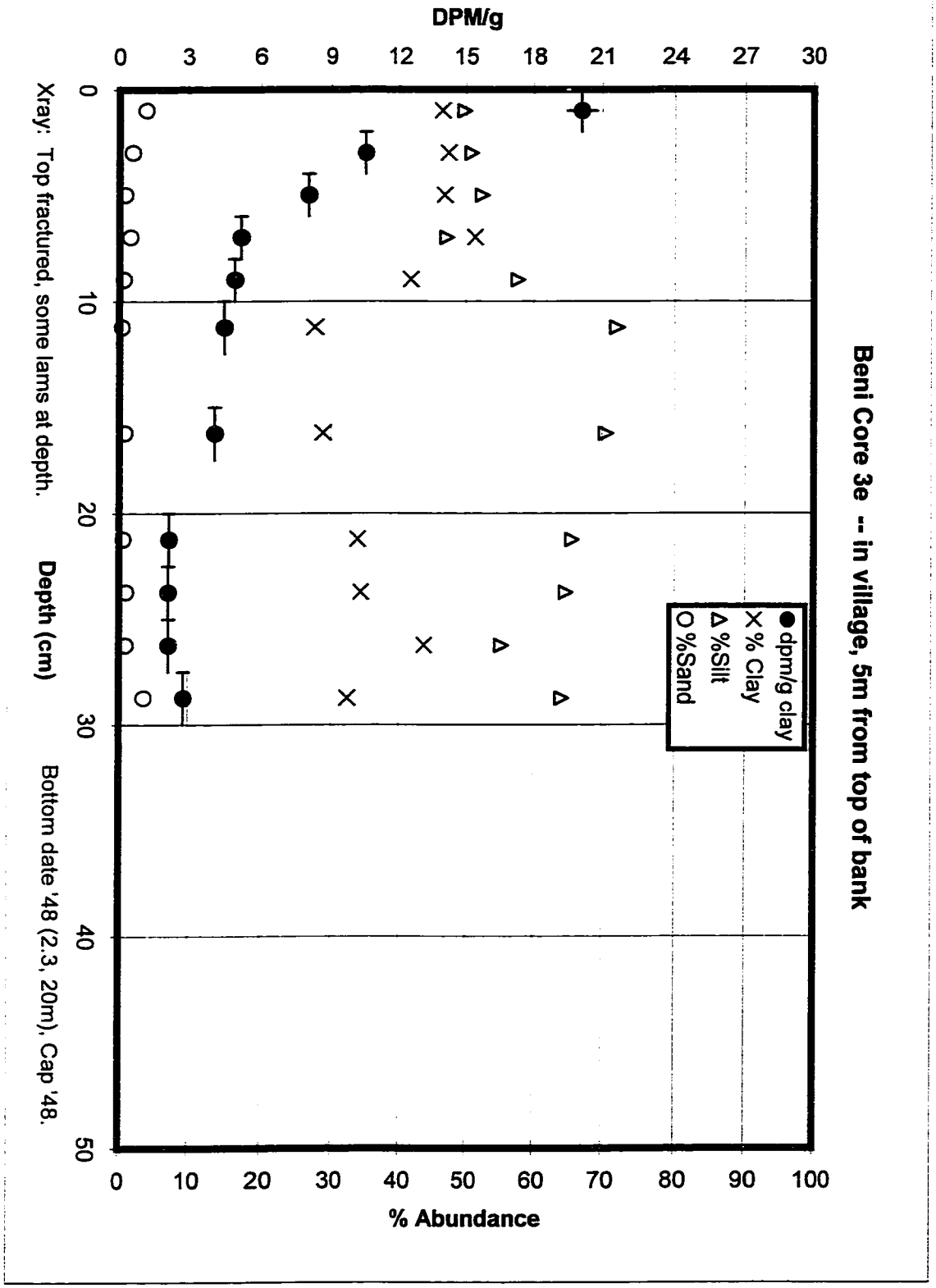
Beni Core 3e -- in village, 5m from top of bank
DPM/g
0 3 6 9 12 15 18 21 24 27 30
% Abundance
0 10 20 30 40 50 60 70 80 90 100
Depth (cm)
0 10 20 30 40 50
dpm/g clay
% Clay
%Silt
%Sand
Xray: Top fractured, some lams at depth.
Bottom date '48 (2.3, 20m), Cap '48.

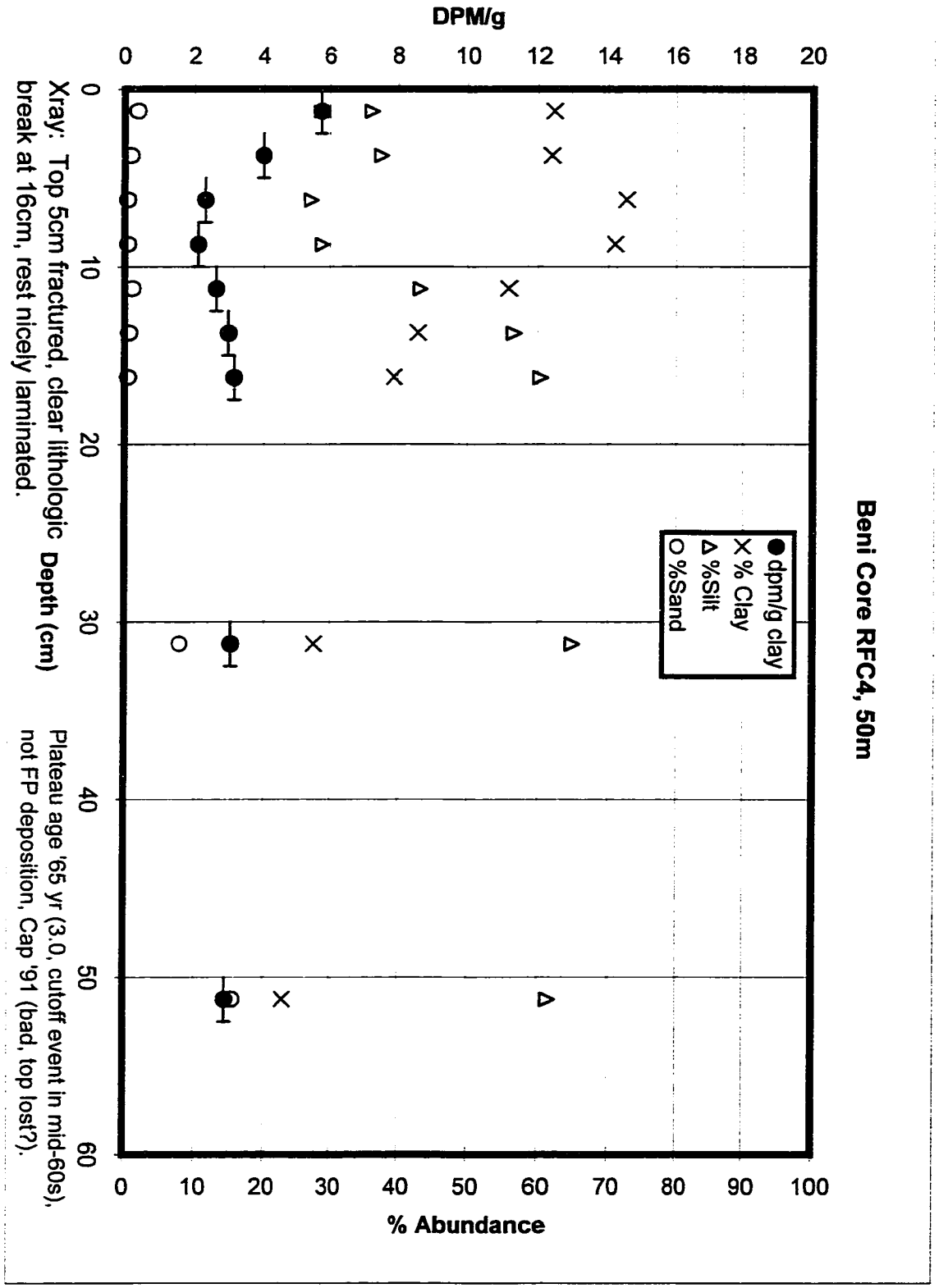
Beni Core RFC4, 50m
DPM/g
0 2 4 6 8 10 12 14 16 18 20
% Abundance
0 10 20 30 40 50 60 70 80 90 100
Depth (cm)
0 10 20 30 40 50 60
dpm/g clay
% Clay
%Silt
%Sand
Xray: Top 5cm fractured, clear lithologic break at 16cm, rest nicely laminated.
Plateau age '65 yr (3.0, cutoff event in mid-60s), not FP deposition, Cap '91 (bad, top lost?).

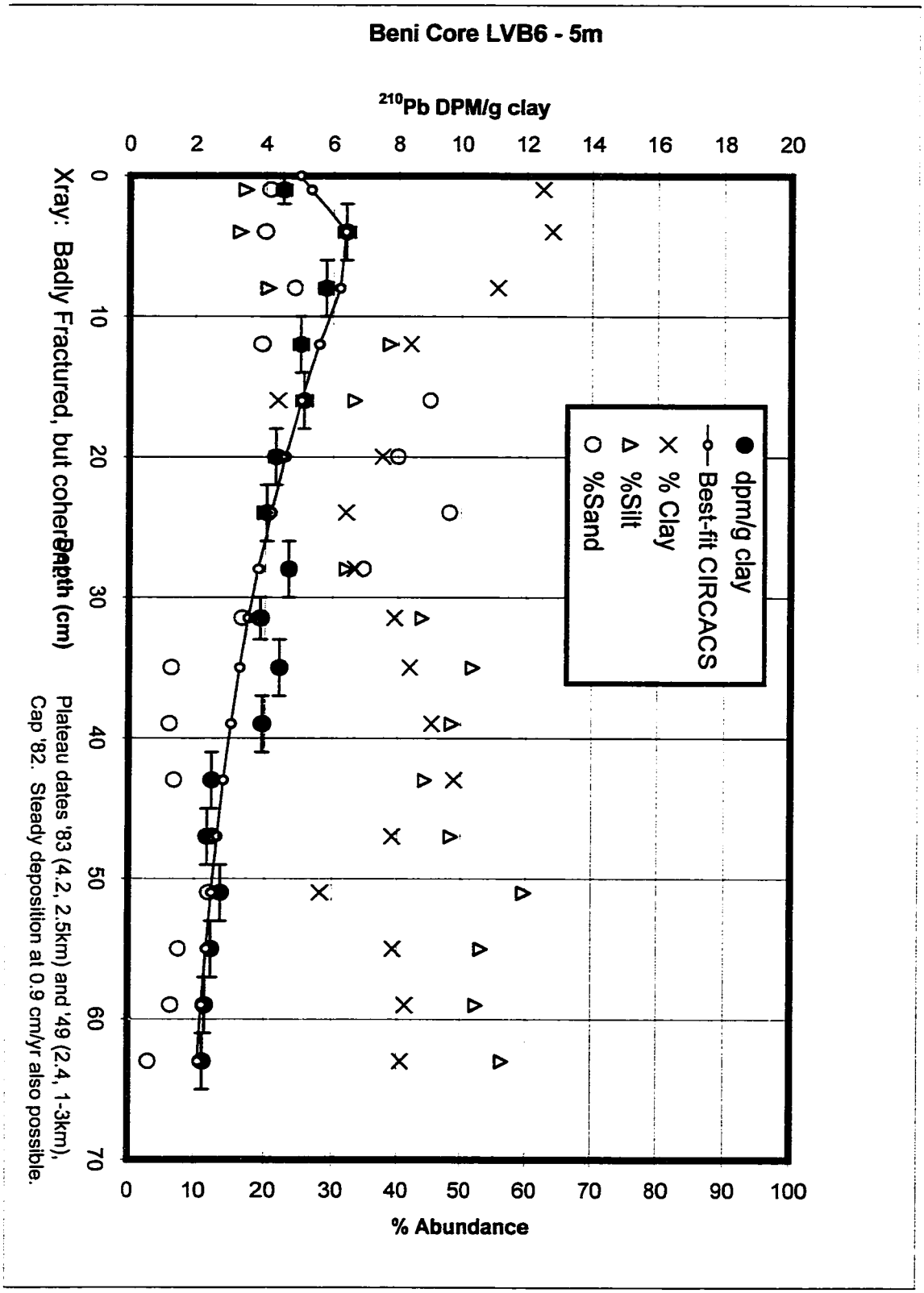
Beni Core LVB6 - 5m
210Pb DPM/g clay
0 2 4 6 8 10 12 14 16 18 20
0 10 20 30 40 50 60 70
Depth (cm)
0 10 20 30 40 50 60 70 80 90 100
% Abundance
dpm/g clay
Best-fit CIRCACS
% Clay
%Silt
%Sand
Xray: Badly Fractured, but coherent.
Plateau dates '83 (4.2, 2.5km) and '49 (2.4, 1-3km), Cap '82. Steady deposition at 0.9 cm/yr also possible.

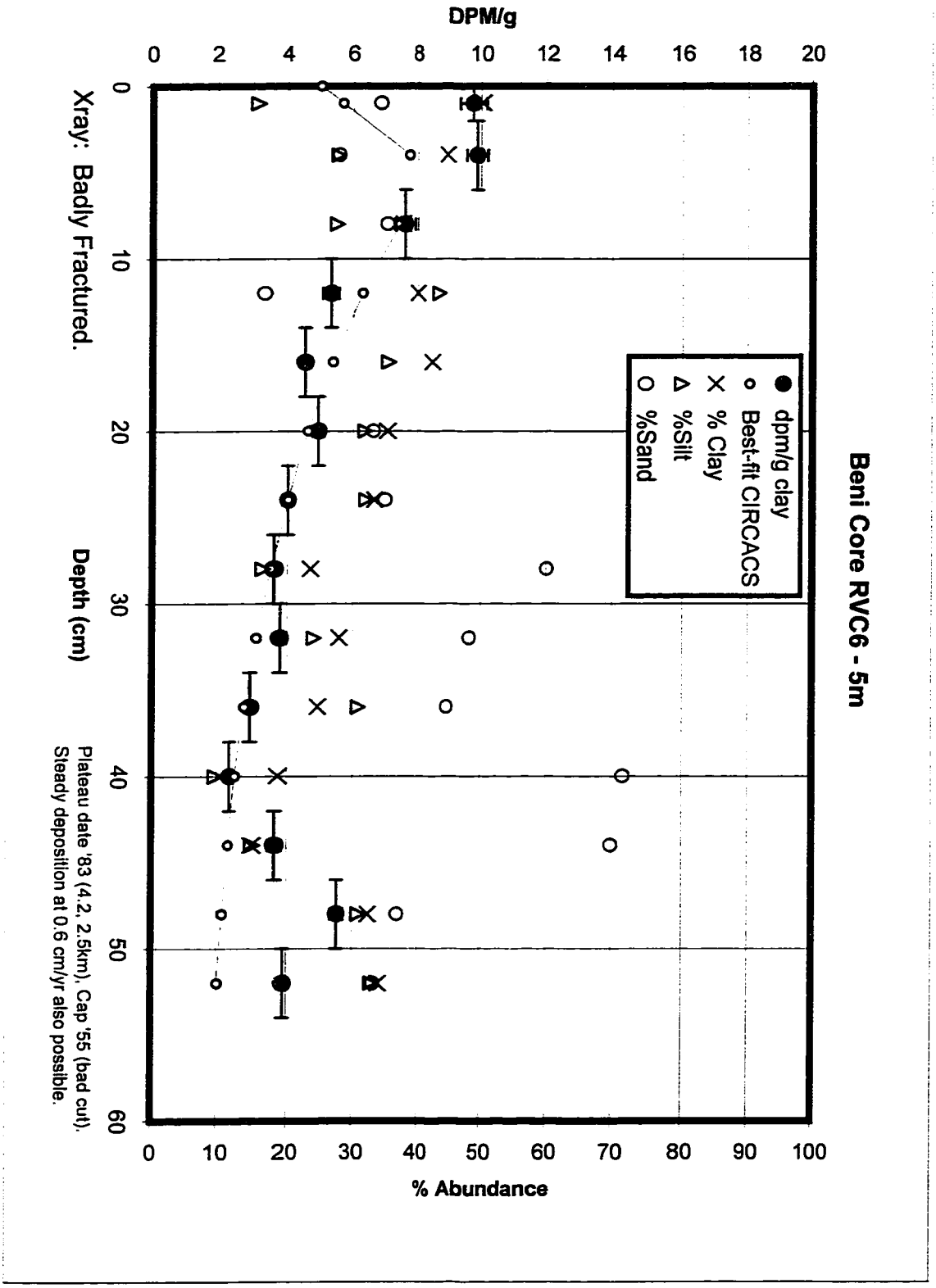
DPM/g
0 2 4 6 8 10 12 14 16 18 20
Xray: Badly Fractured.
Depth (cm)
0 10 20 30 40 50 60
dpm/g clay
Best-fit CIRCACS
% Clay
%Silt
%Sand
0 10 20 30 40 50 60 70 80 90 100
% Abundance
Beni Core RVC6 - 5m
Plateau date '83 (4.2, 2.5km), Cap '55 (bad cut).
Steady deposition at 0.6 cm/yr also possible.

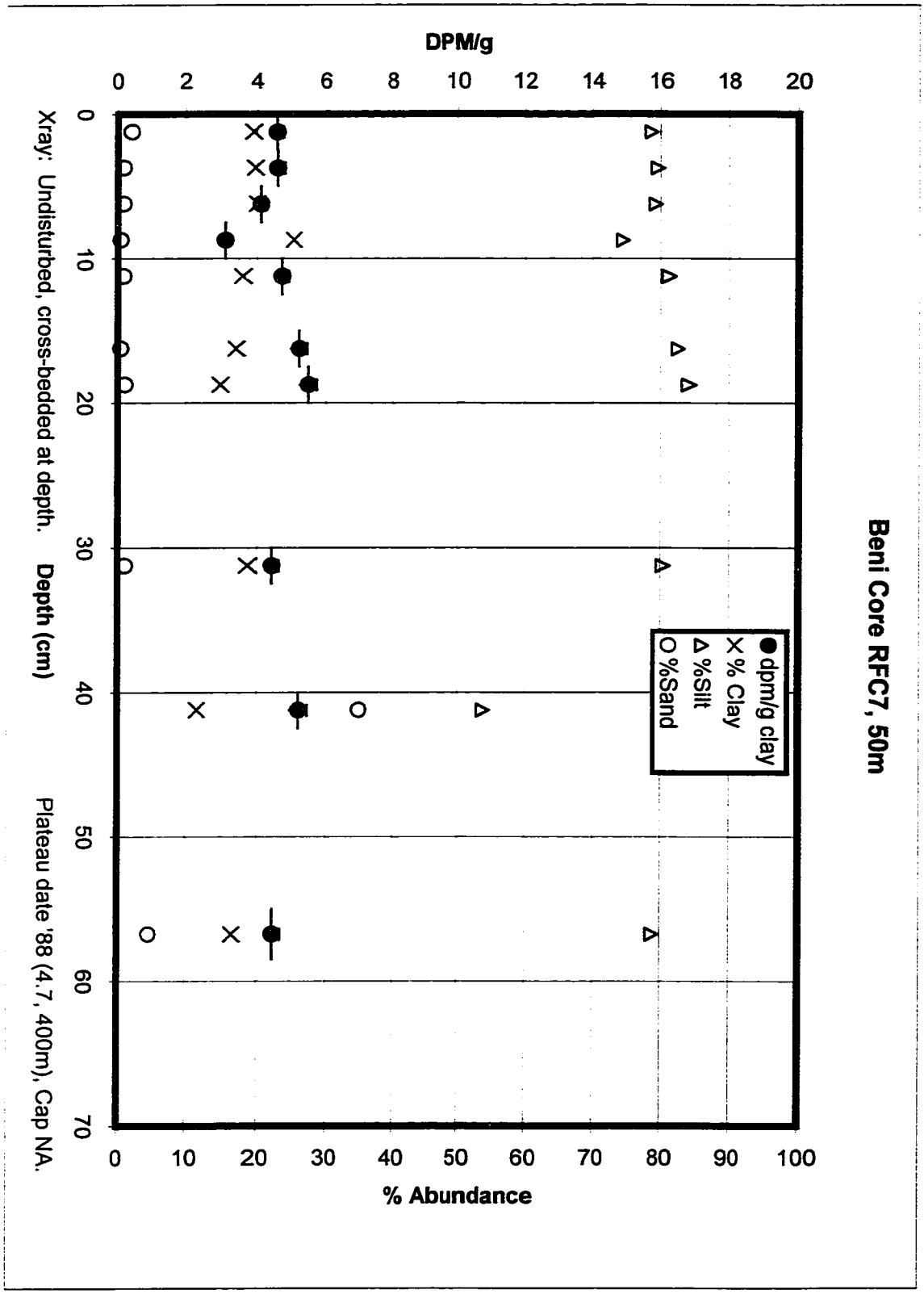
Beni Core RFC7, 50m
DPM/g
0 2 4 6 8 10 12 14 16 18 20
% Abundance
0 10 20 30 40 50 60 70 80 90 100
Depth (cm)
0 10 20 30 40 50 60 70
● dpm/g clay
× % Clay
Δ %Silt
○ %Sand
Xray: Undisturbed, cross-bedded at depth.
Plateau date '88 (4.7, 400m), Cap NA.

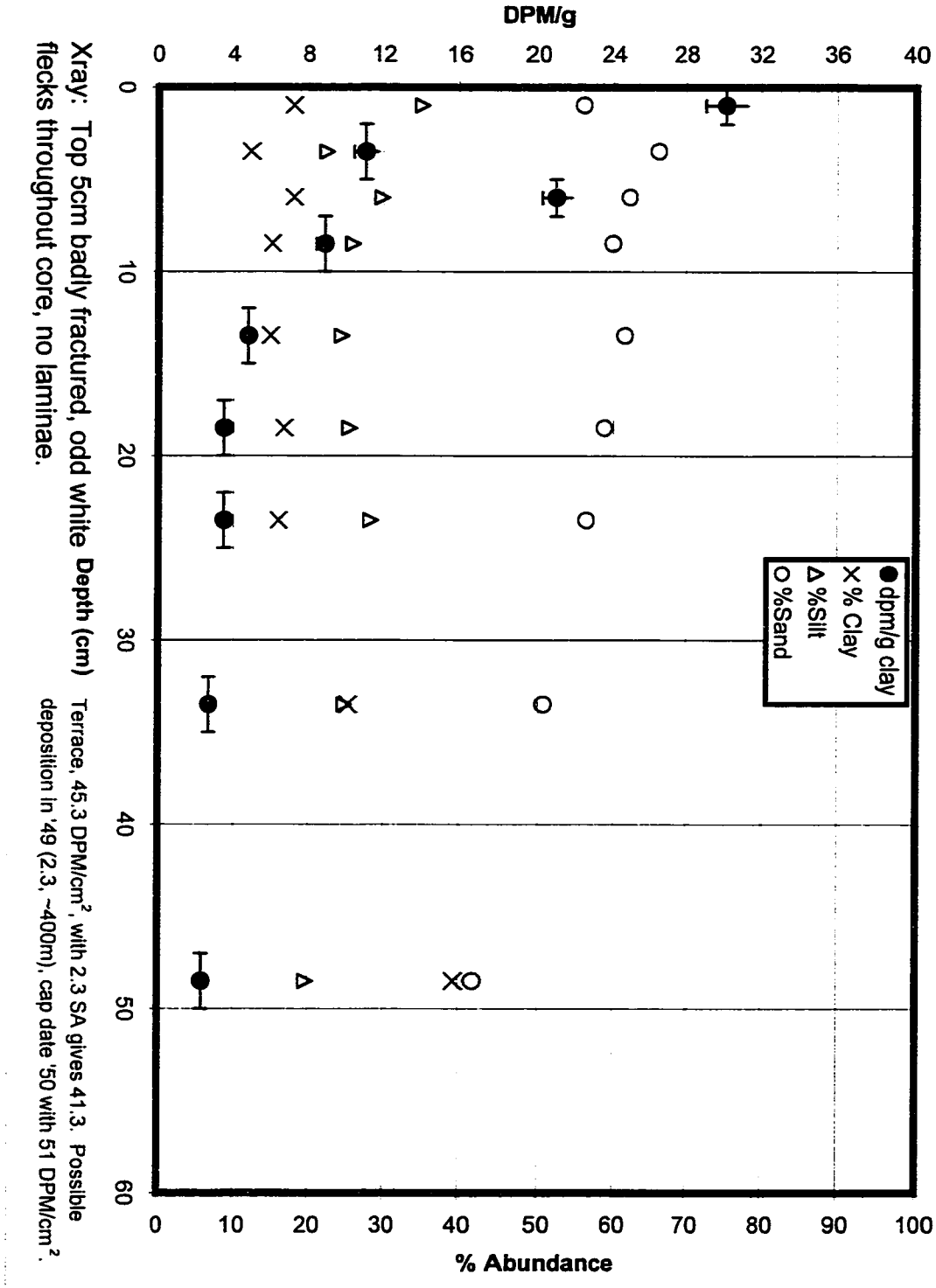

Xray: Top 5cm badly fractured, odd white flecks throughout core, no laminae.

Terrace, 45.3 DPM/cm^2, with 2.3 SA gives 41.3. Possible deposition in '49 (2.3, ~400m), cap date '50 with 51 DPM/cm^2.

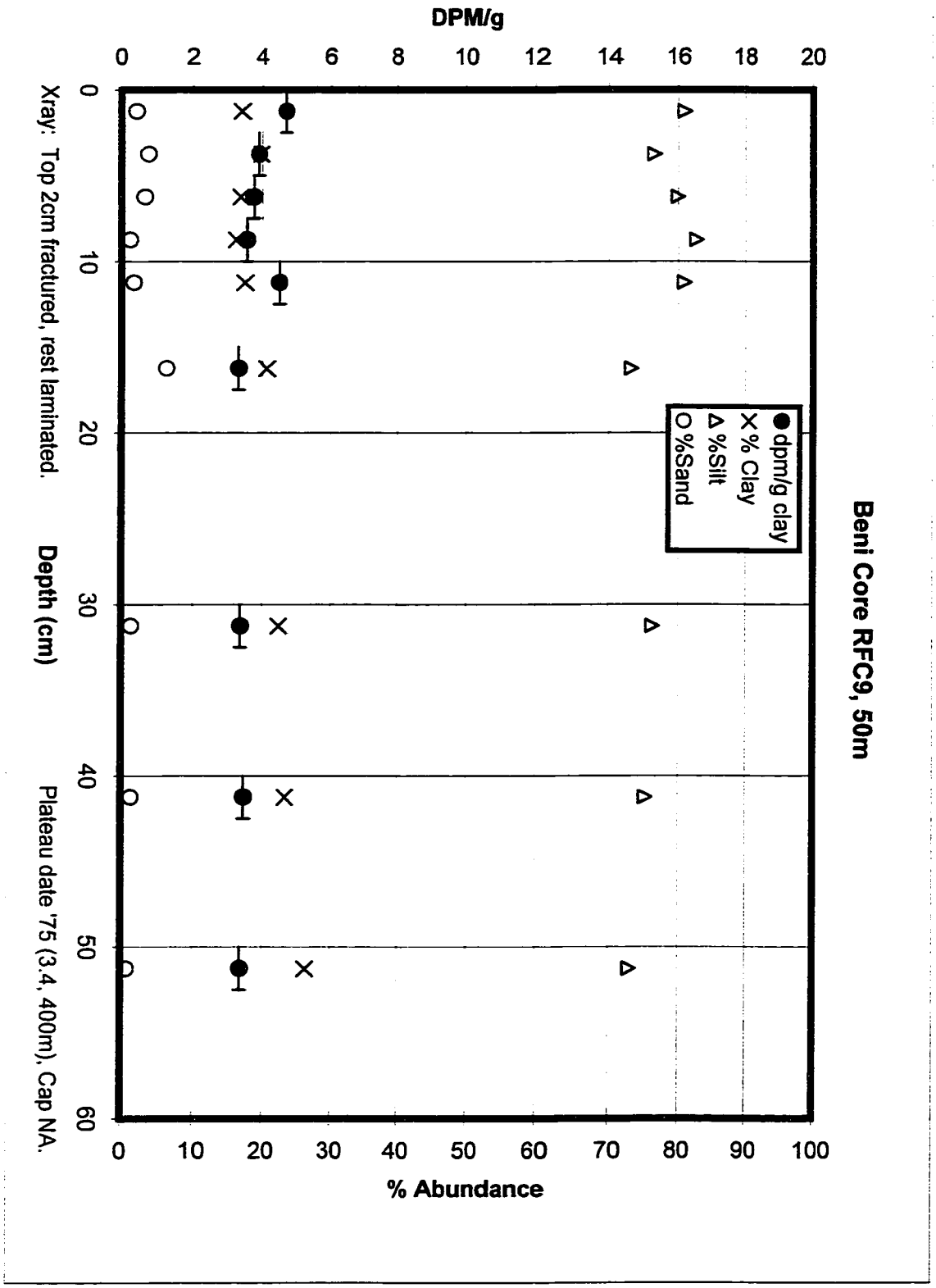
DPM/g
0 2 4 6 8 10 12 14 16 18 20
Depth (cm)
0 10 20 30 40 50 60
% Abundance
0 10 20 30 40 50 60 70 80 90 100
dpm/g clay
% Clay
%Silt
%Sand
Beni Core RFC9, 50m
Xray: Top 2cm fractured, rest laminated.
Plateau date '75 (3.4, 400m). Cap NA.

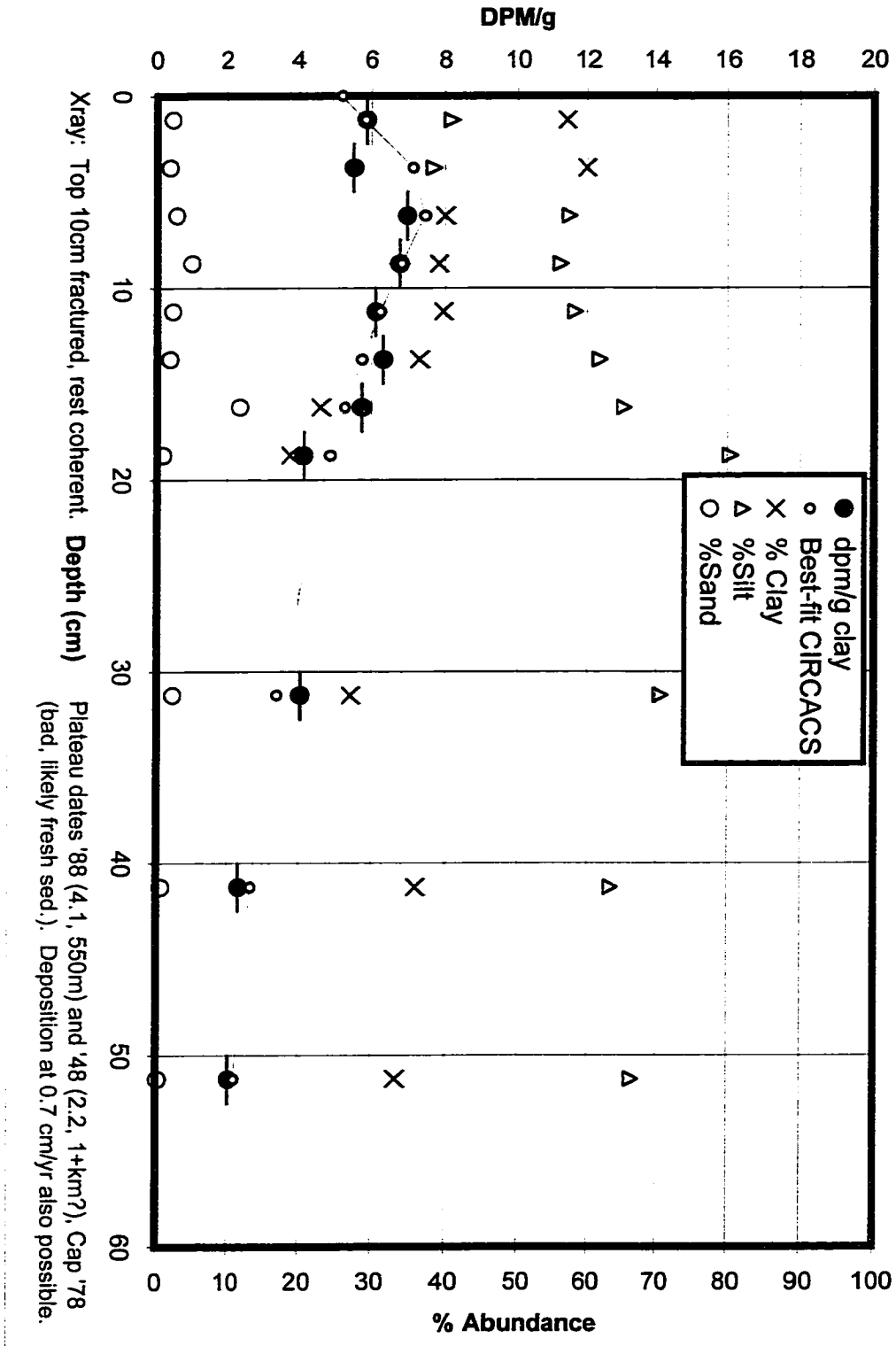

Xray: Top 10cm fractured, rest coherent. **Depth (cm)**

Plateau dates '88 (4.1, 550m) and '48 (2.2, 1+km?), Cap '78 (bad, likely fresh sed.). Deposition at 0.7 cm/yr also possible.

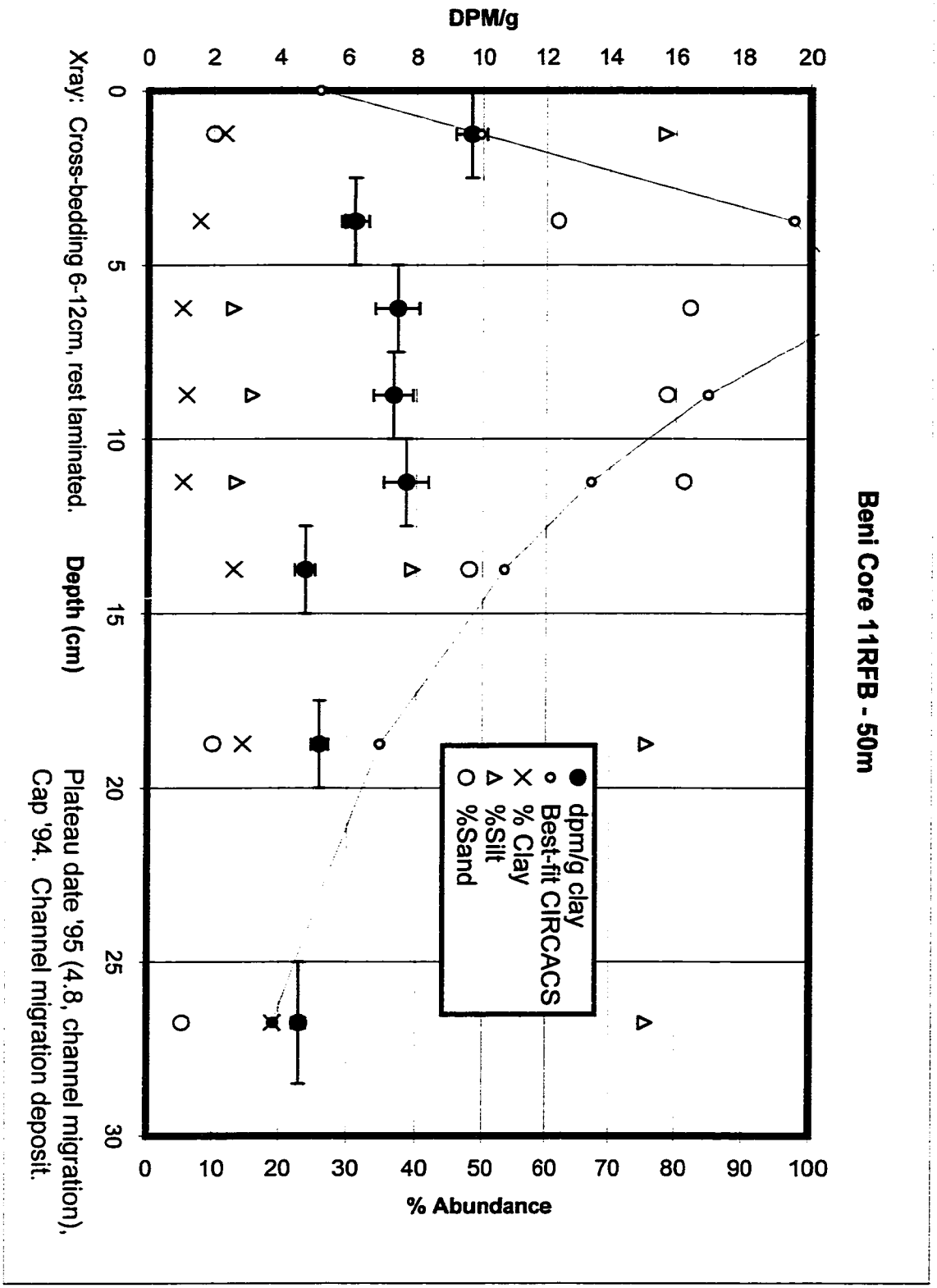
Beni Core 11RFB - 50m
DPM/g
0 2 4 6 8 10 12 14 16 18 20
% Abundance
0 10 20 30 40 50 60 70 80 90 100
Depth (cm)
0 5 10 15 20 25 30
dpm/g clay
Best-fit CIRCACS
% Clay
%Silt
%Sand
Xray: Cross-bedding 6-12cm, rest laminated.
Plateau date '95 (4.8, channel migration),
Cap '94. Channel migration deposit.

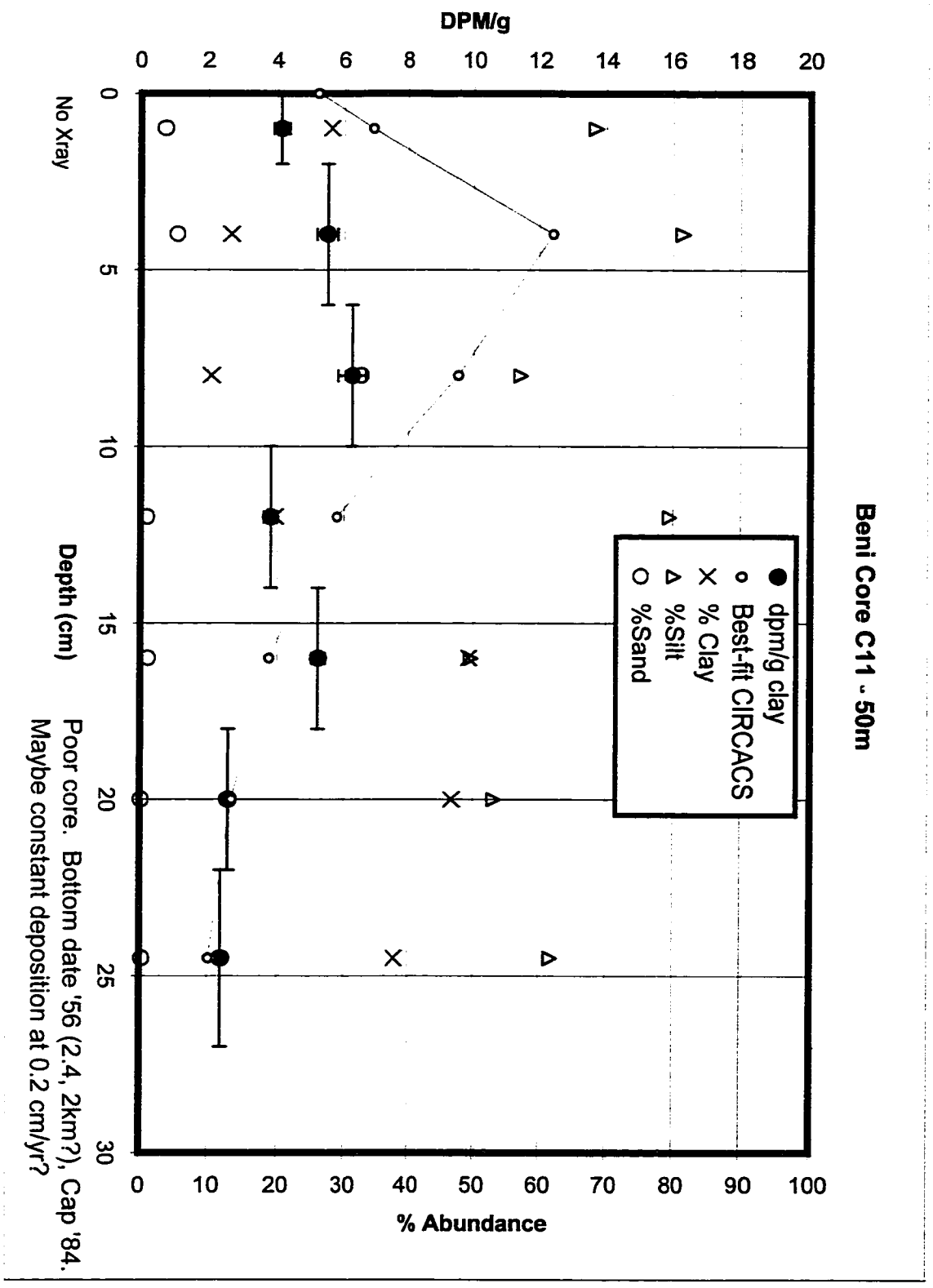
DPM/g
0 2 4 6 8 10 12 14 16 18 20
No Xray
Depth (cm)
0 5 10 15 20 25 30
0 10 20 30 40 50 60 70 80 90 100
% Abundance
dpm/g clay
Best-fit CIRCACS
% Clay
%Silt
%Sand
Beni Core C11 - 50m
Poor core. Bottom date '56 (2.4, 2km?), Cap '84.
Maybe constant deposition at 0.2 cm/yr?

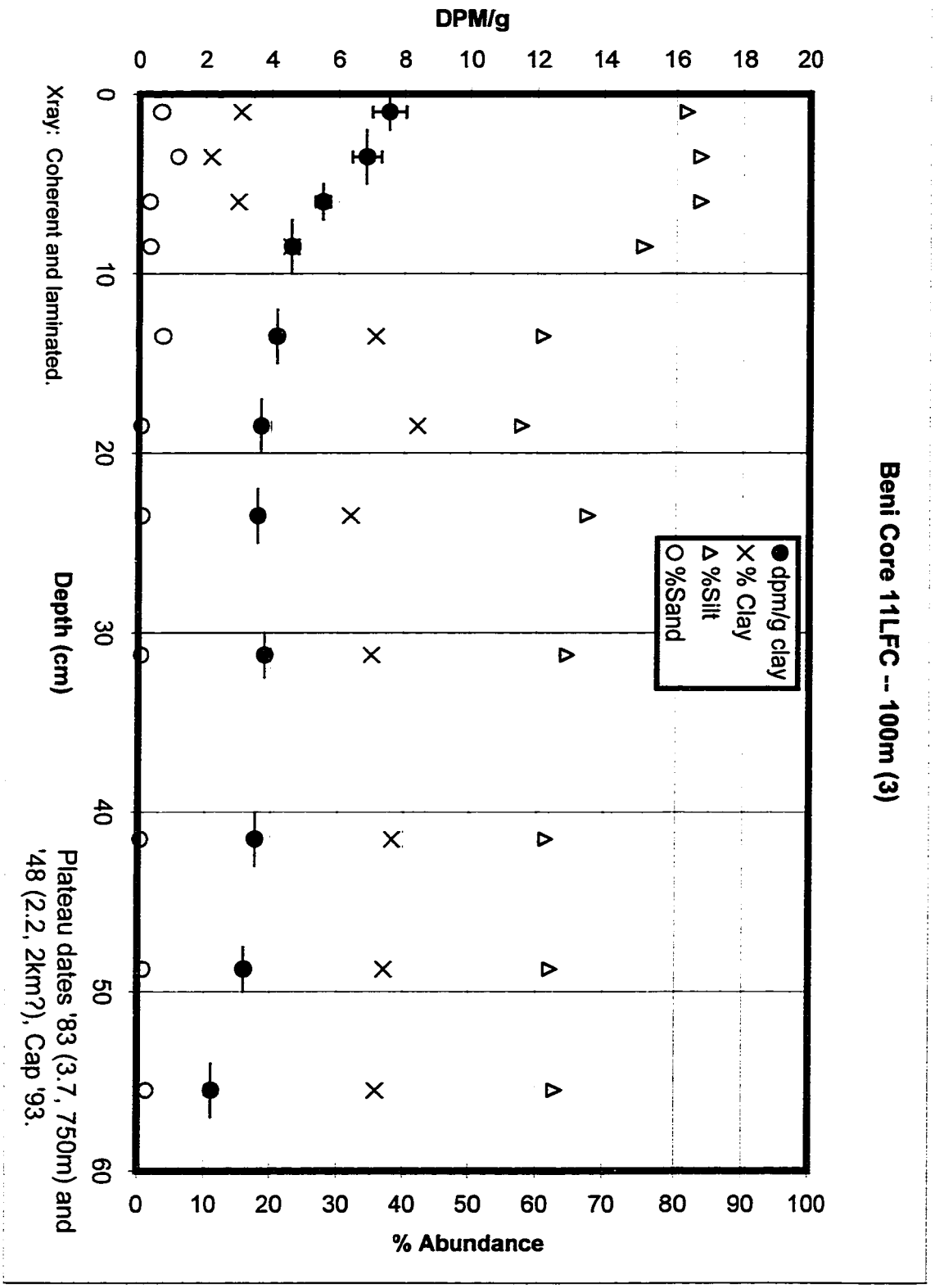
Beni Core 11LFC -- 100m (3)
DPM/g
0 2 4 6 8 10 12 14 16 18 20
% Abundance
0 10 20 30 40 50 60 70 80 90 100
Depth (cm)
0 10 20 30 40 50 60
dpm/g clay
% Clay
%Silt
%Sand
Xray: Coherent and laminated.
Plateau dates '83 (3.7, 750m) and '48 (2.2, 2km?), Cap '93.

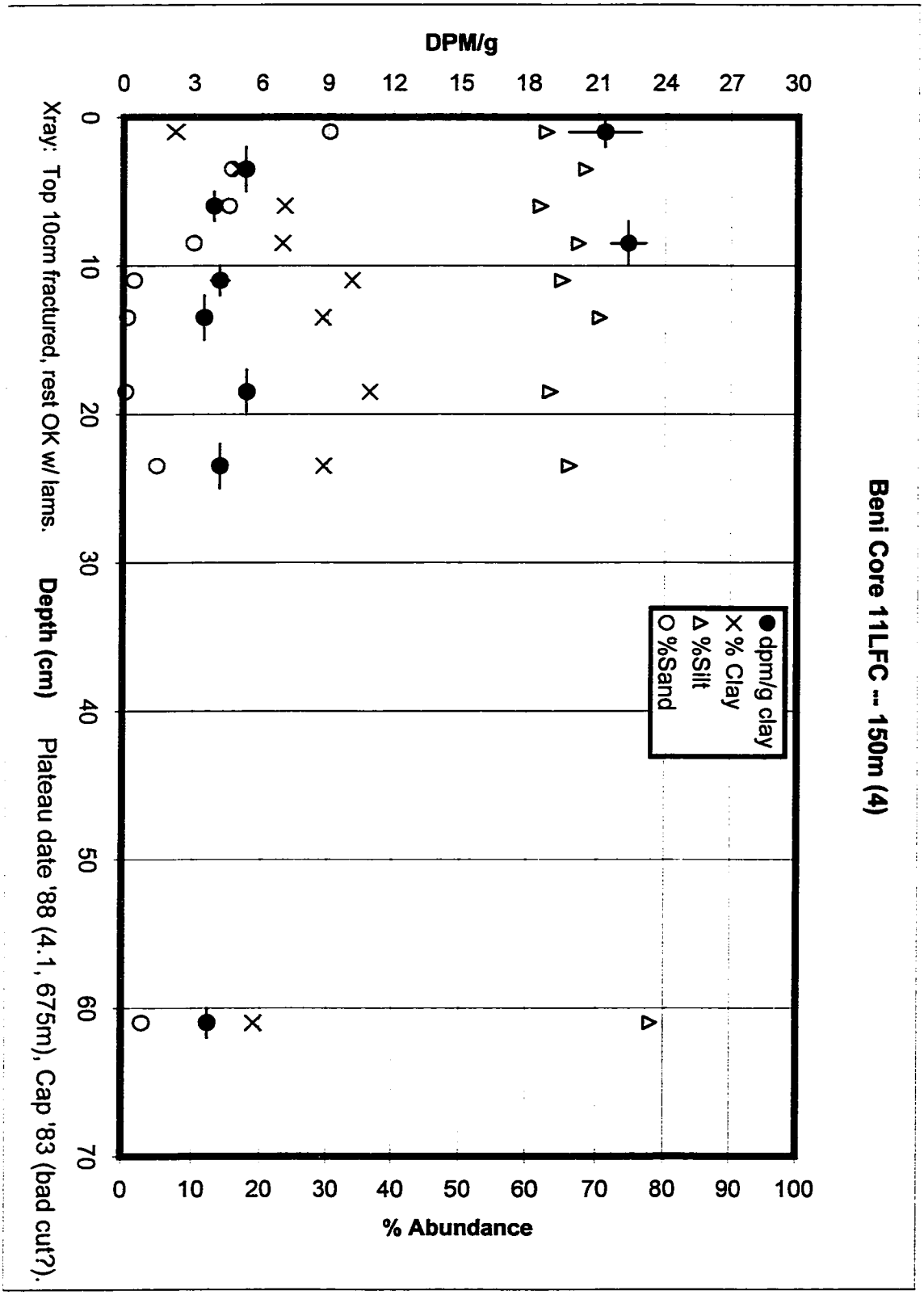
Beni Core 11LFC -- 150m (4)
DPM/g
0 3 6 9 12 15 18 21 24 27 30
% Abundance
0 10 20 30 40 50 60 70 80 90 100
Depth (cm)
0 10 20 30 40 50 60 70
dpm/g clay
% Clay
%Silt
%Sand
Xray: Top 10cm fractured, rest OK w/ lams.
Plateau date '88 (4.1, 675m), Cap '83 (bad cut?).

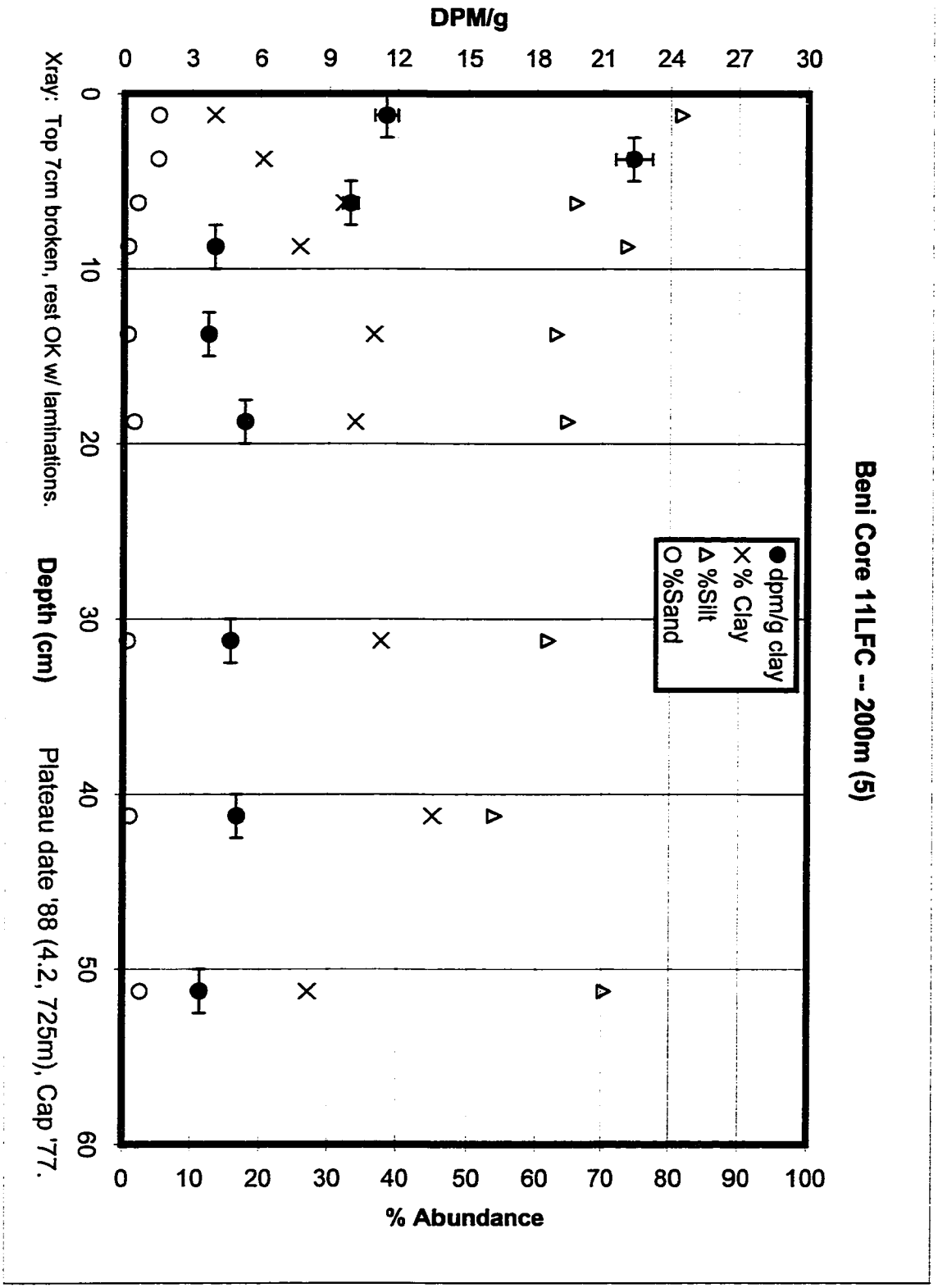
Beni Core 11LFC -- 200m (5)
DPM/g
0 3 6 9 12 15 18 21 24 27 30
% Abundance
0 10 20 30 40 50 60 70 80 90 100
Depth (cm)
0 10 20 30 40 50 60
dpm/g clay
% Clay
%Silt
%Sand
Xray: Top 7cm broken, rest OK w/ laminations.
Plateau date '88 (4.2, 725m), Cap '77.

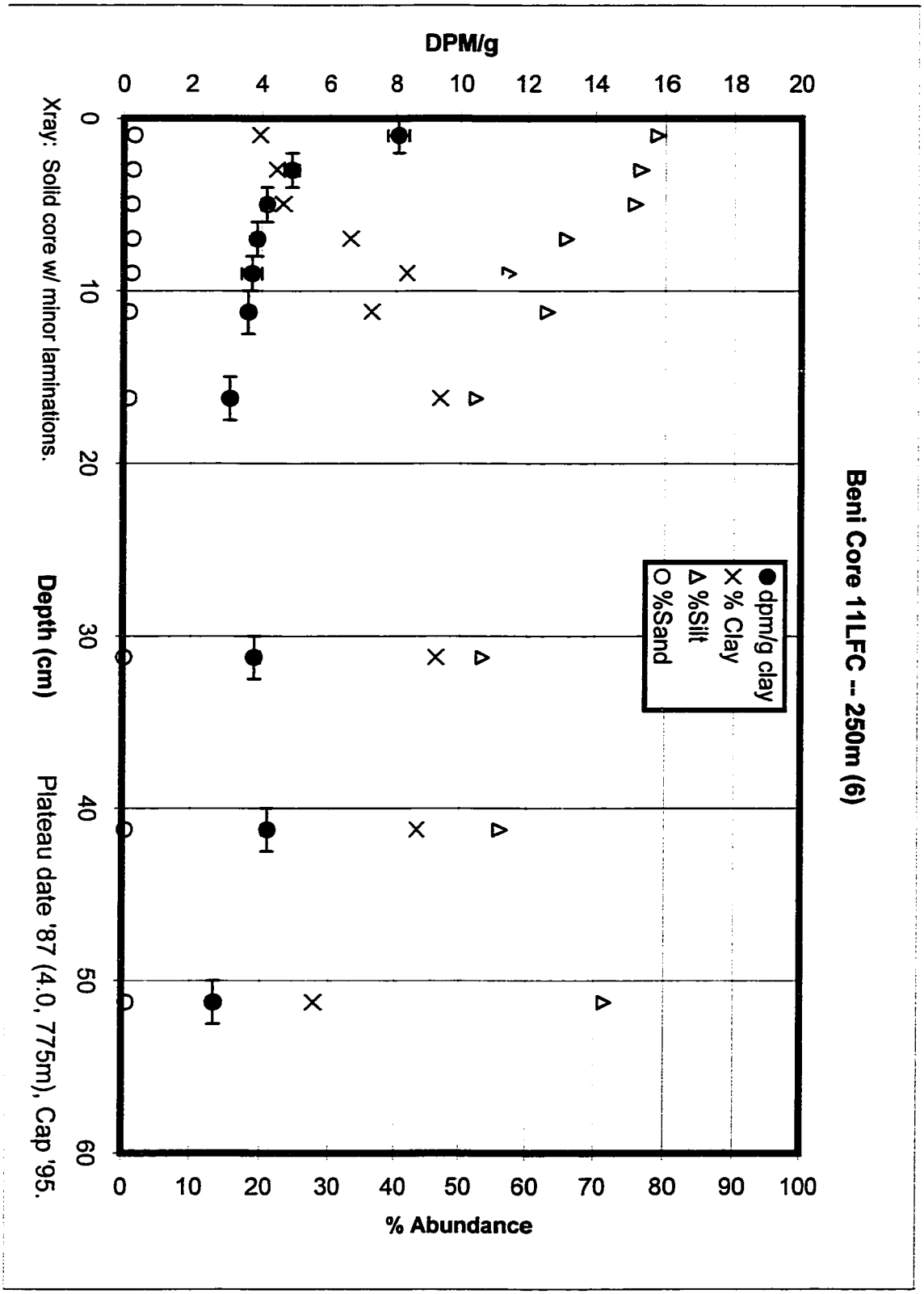
Beni Core 11LFC -- 250m (6)
DPM/g
0 2 4 6 8 10 12 14 16 18 20
% Abundance
0 10 20 30 40 50 60 70 80 90 100
Depth (cm)
0 10 20 30 40 50 60
dpm/g clay
% Clay
%Silt
%Sand
Xray: Solid core w/ minor laminations.
Plateau date '87 (4.0, 775m), Cap '95.

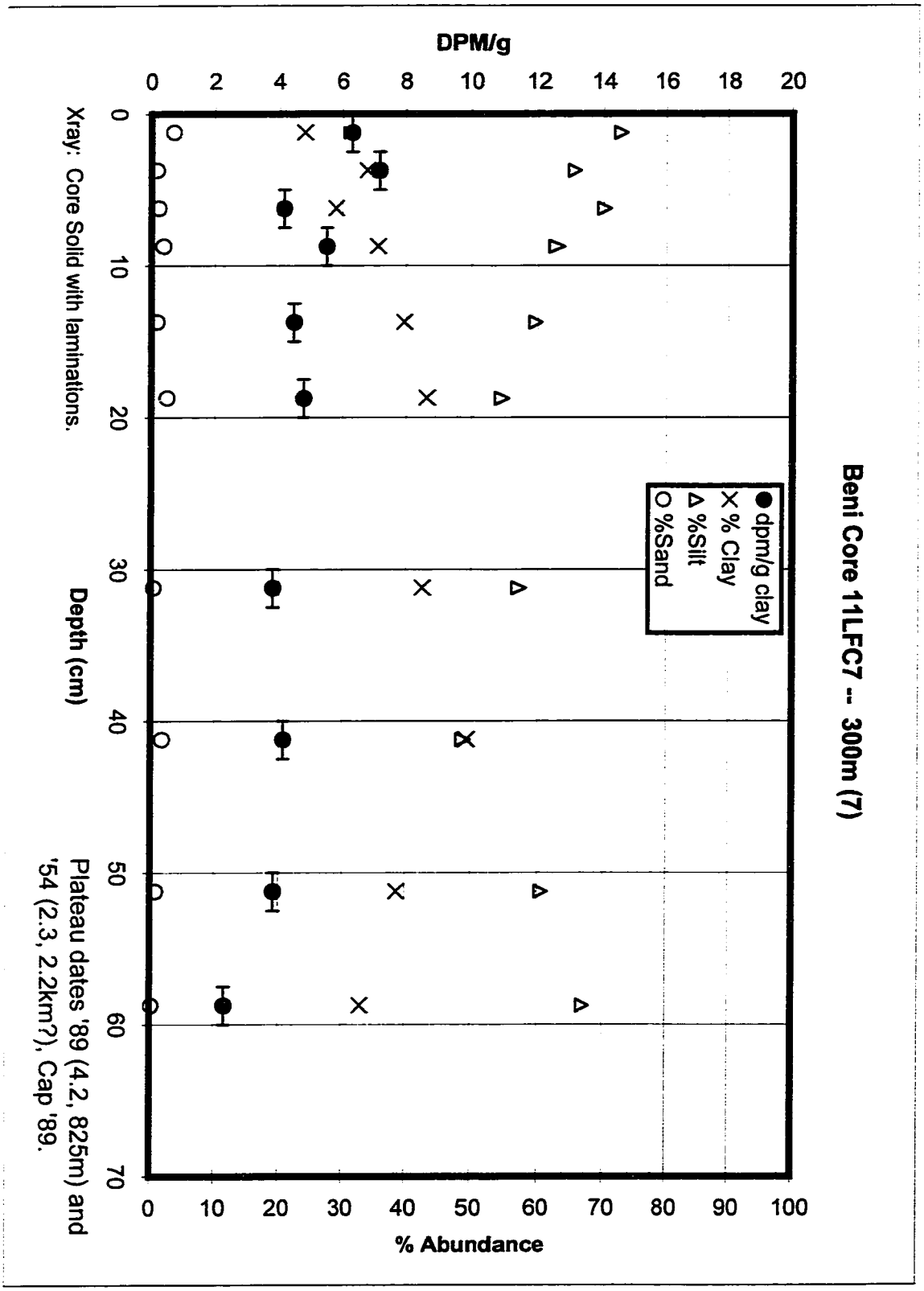
Beni Core 11LFC7 -- 300m (7)
DPM/g
0 2 4 6 8 10 12 14 16 18 20
0 10 20 30 40 50 60 70
Depth (cm)
0 10 20 30 40 50 60 70 80 90 100
% Abundance
dpm/g clay
% Clay
%Silt
%Sand
Xray: Core Solid with laminations.
Plateau dates '89 (4.2, 825m) and '54 (2.3, 2.2km?), Cap '89.

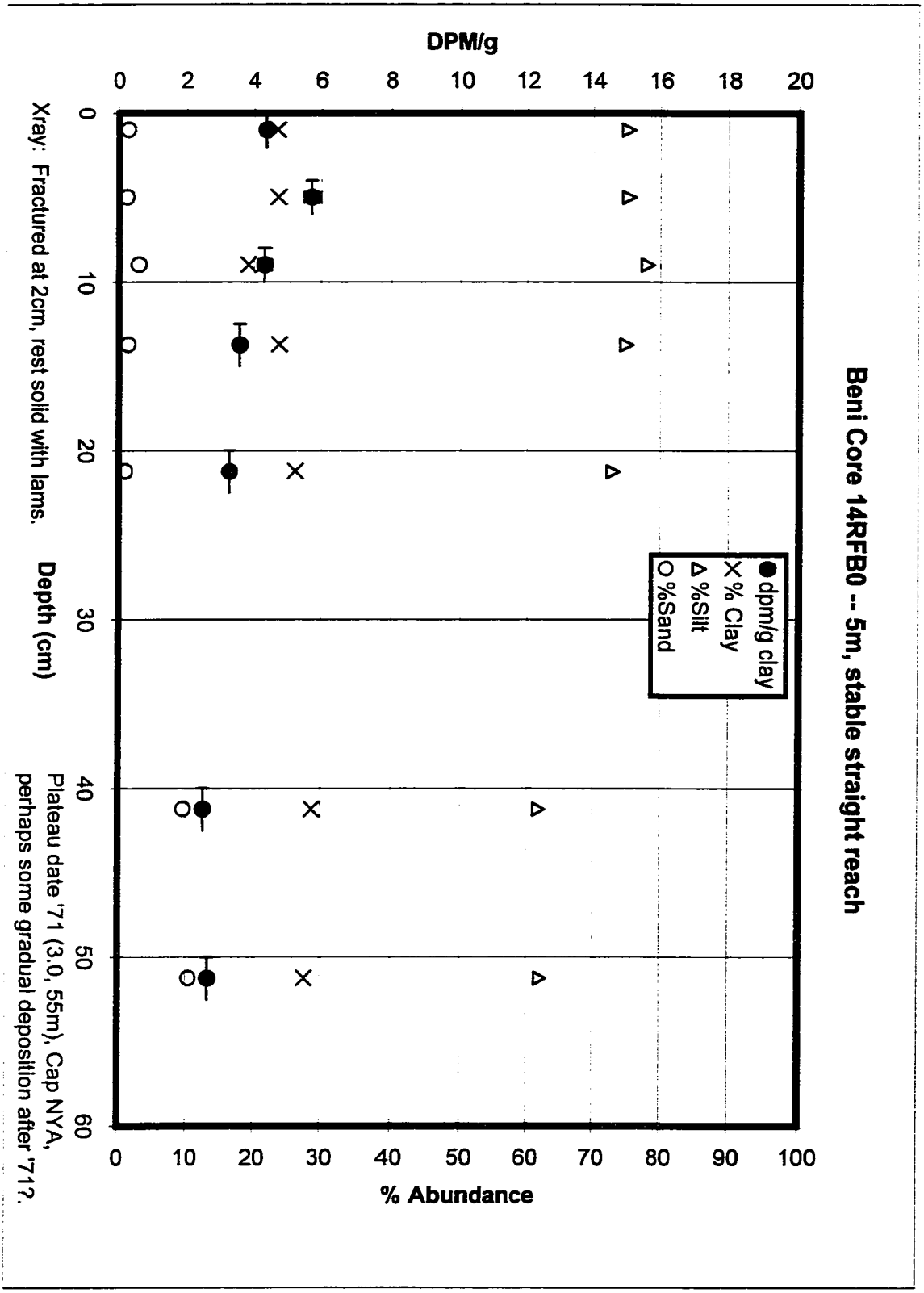
Beni Core 14RFB0 -- 5m, stable straight reach
DPM/g
0 2 4 6 8 10 12 14 16 18 20
% Abundance
0 10 20 30 40 50 60 70 80 90 100
Depth (cm)
0 10 20 30 40 50 60
dpm/g clay
% Clay
%Silt
%Sand
Xray: Fractured at 2cm, rest solid with lams.
Plateau date '71 (3.0, 55m), Cap NYA,
perhaps some gradual deposition after '71?.

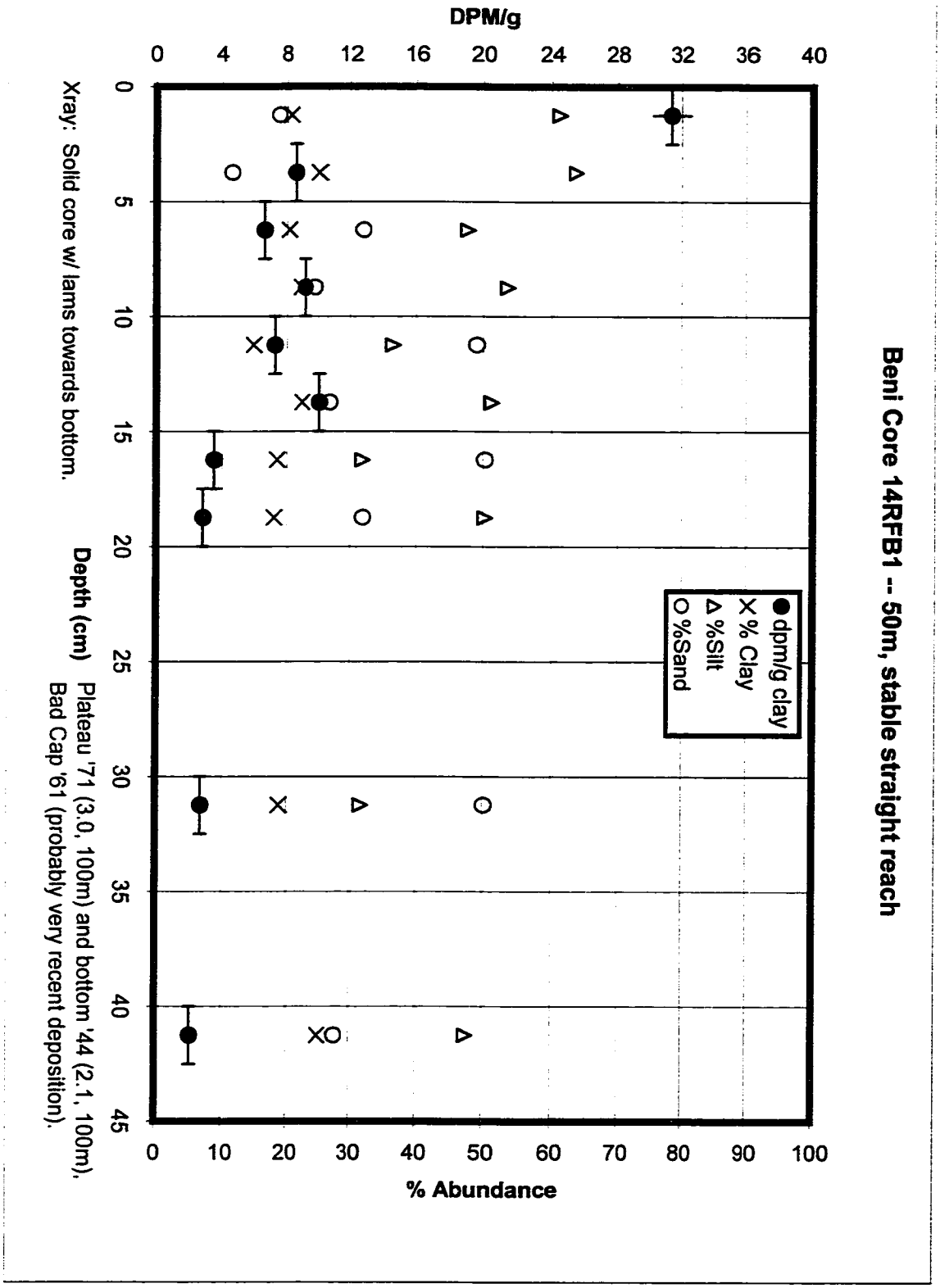
Beni Core 14RFB1 -- 50m, stable straight reach
DPM/g
0 4 8 12 16 20 24 28 32 36 40
0 5 10 15 20 25 30 35 40 45
Depth (cm)
0 10 20 30 40 50 60 70 80 90 100
% Abundance
dpm/g clay
% Clay
%Silt
%Sand
Xray: Solid core w/ lams towards bottom.
Plateau '71 (3.0, 100m) and bottom '44 (2.1, 100m), Bad Cap '61 (probably very recent deposition).

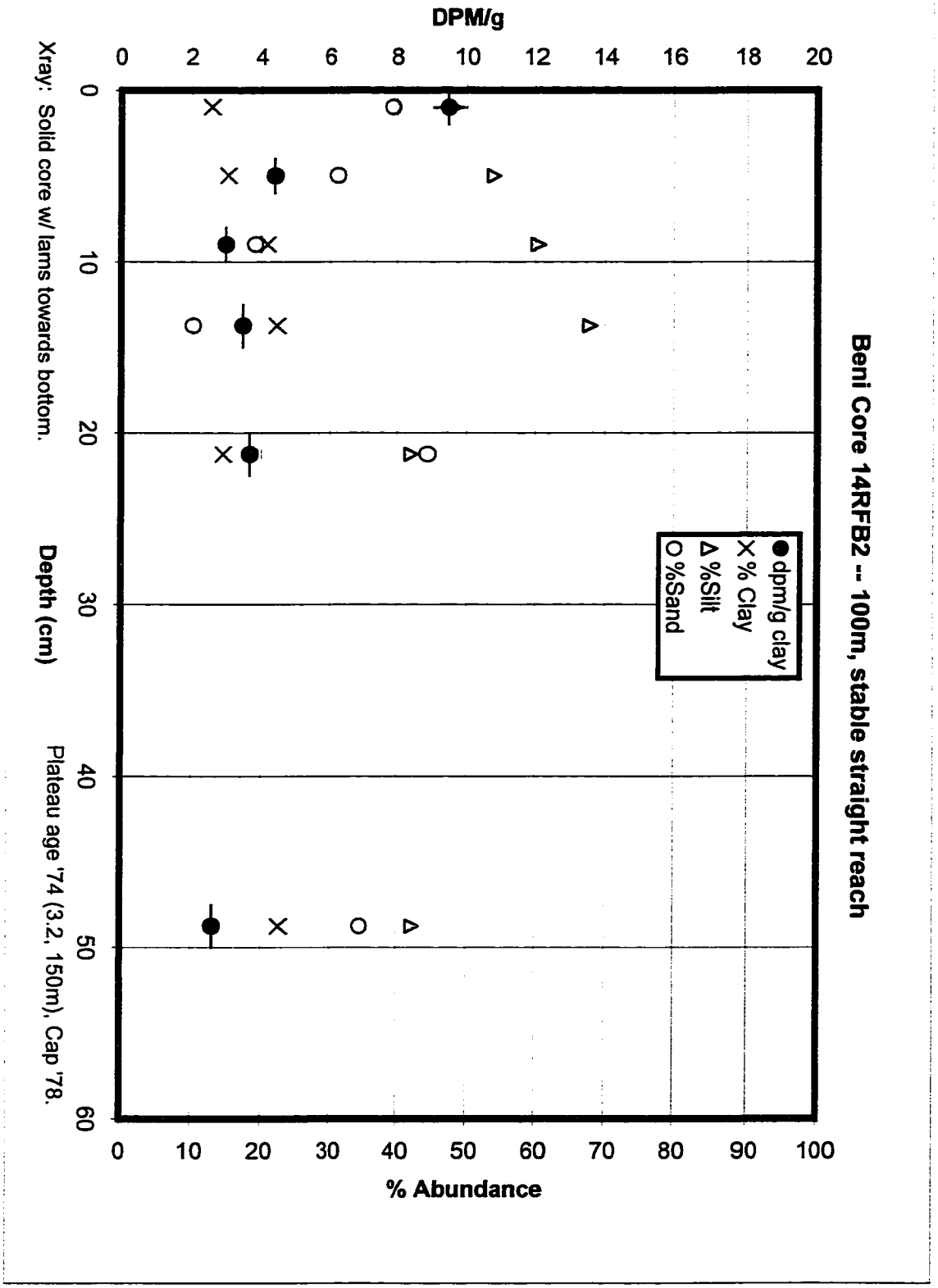
Beni Core 14RFB2 -- 100m, stable straight reach
DPM/g
0 2 4 6 8 10 12 14 16 18 20
Depth (cm)
0 10 20 30 40 50 60
% Abundance
0 10 20 30 40 50 60 70 80 90 100
dpm/g clay
% Clay
%Silt
%Sand
Xray: Solid core w/ lams towards bottom.
Plateau age '74 (3.2, 150m), Cap '78.

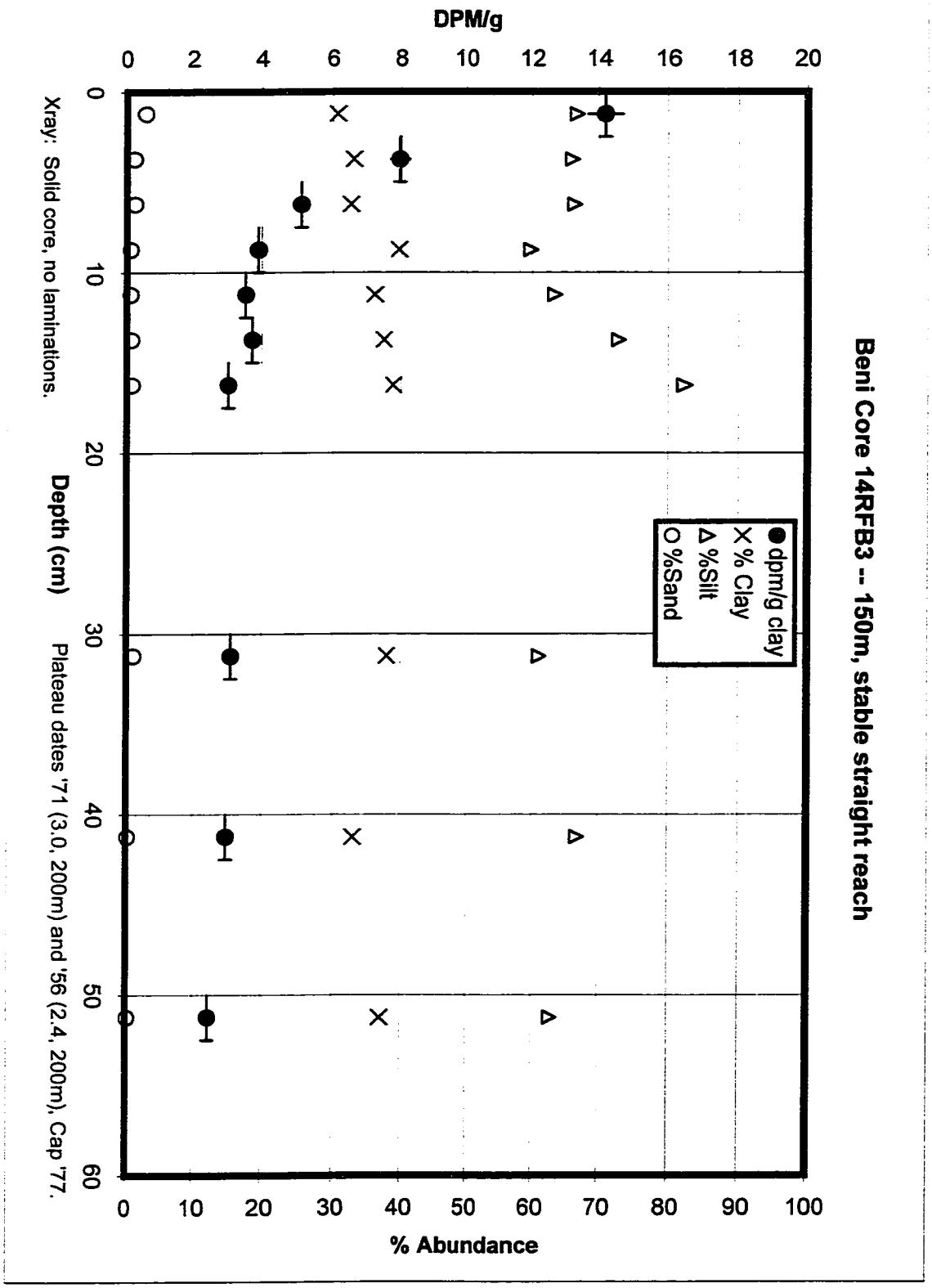
Beni Core 14RFB3 -- 150m, stable straight reach
DPM/g
0 2 4 6 8 10 12 14 16 18 20
Depth (cm)
0 10 20 30 40 50 60
% Abundance
0 10 20 30 40 50 60 70 80 90 100
dpm/g clay
% Clay
%Silt
%Sand
Xray: Solid core, no laminations.
Plateau dates '71 (3.0, 200m) and '56 (2.4, 200m), Cap '77.

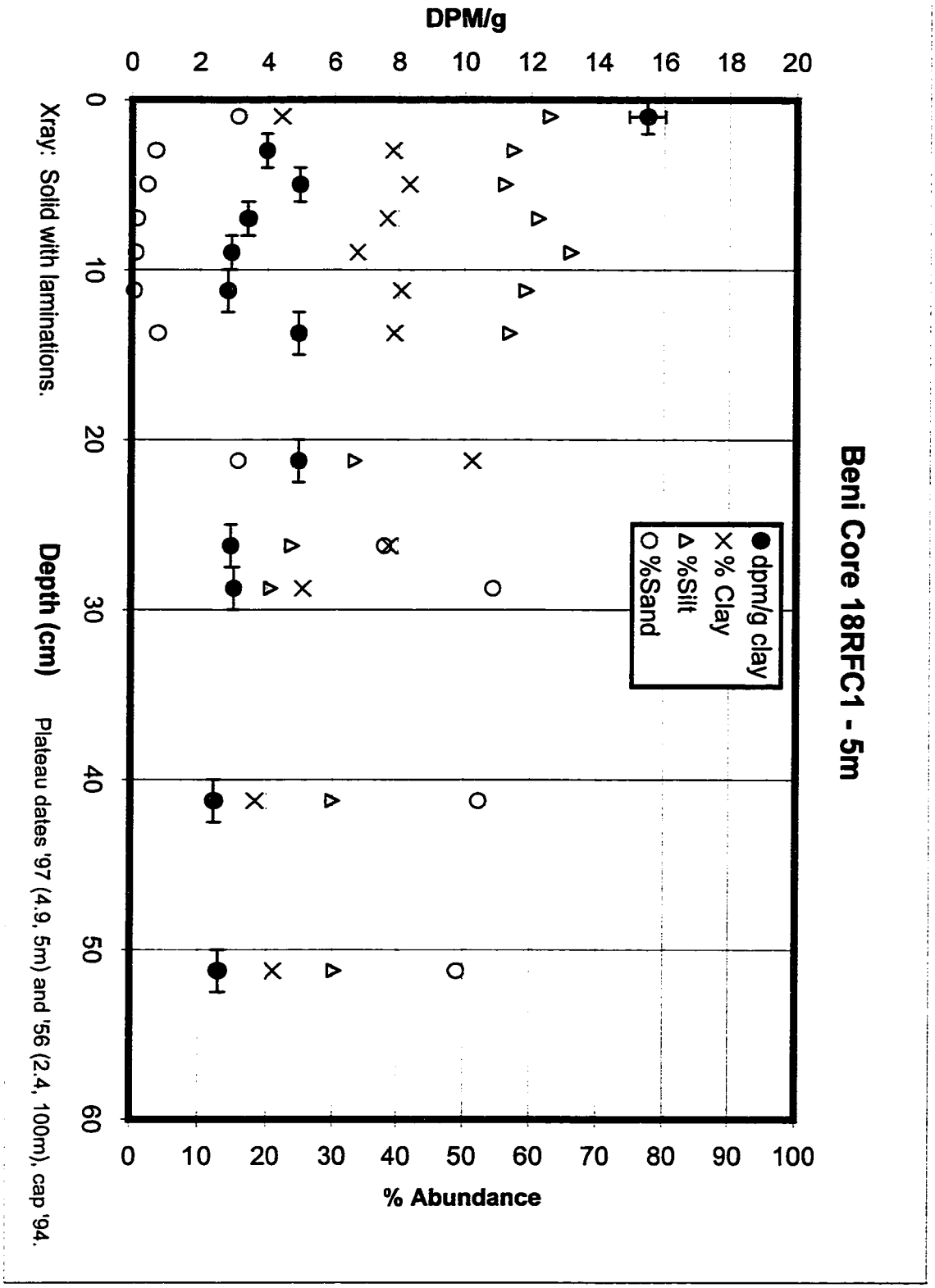
Beni Core 18RFC1 - 5m
DPM/g
0 2 4 6 8 10 12 14 16 18 20
0 10 20 30 40 50 60
Depth (cm)
0 10 20 30 40 50 60 70 80 90 100
% Abundance
● dpm/g clay
× % Clay
Δ %Silt
○ %Sand
Xray: Solid with laminations.
Plateau dates '97 (4.9, 5m) and '56 (2.4, 100m), cap '94.

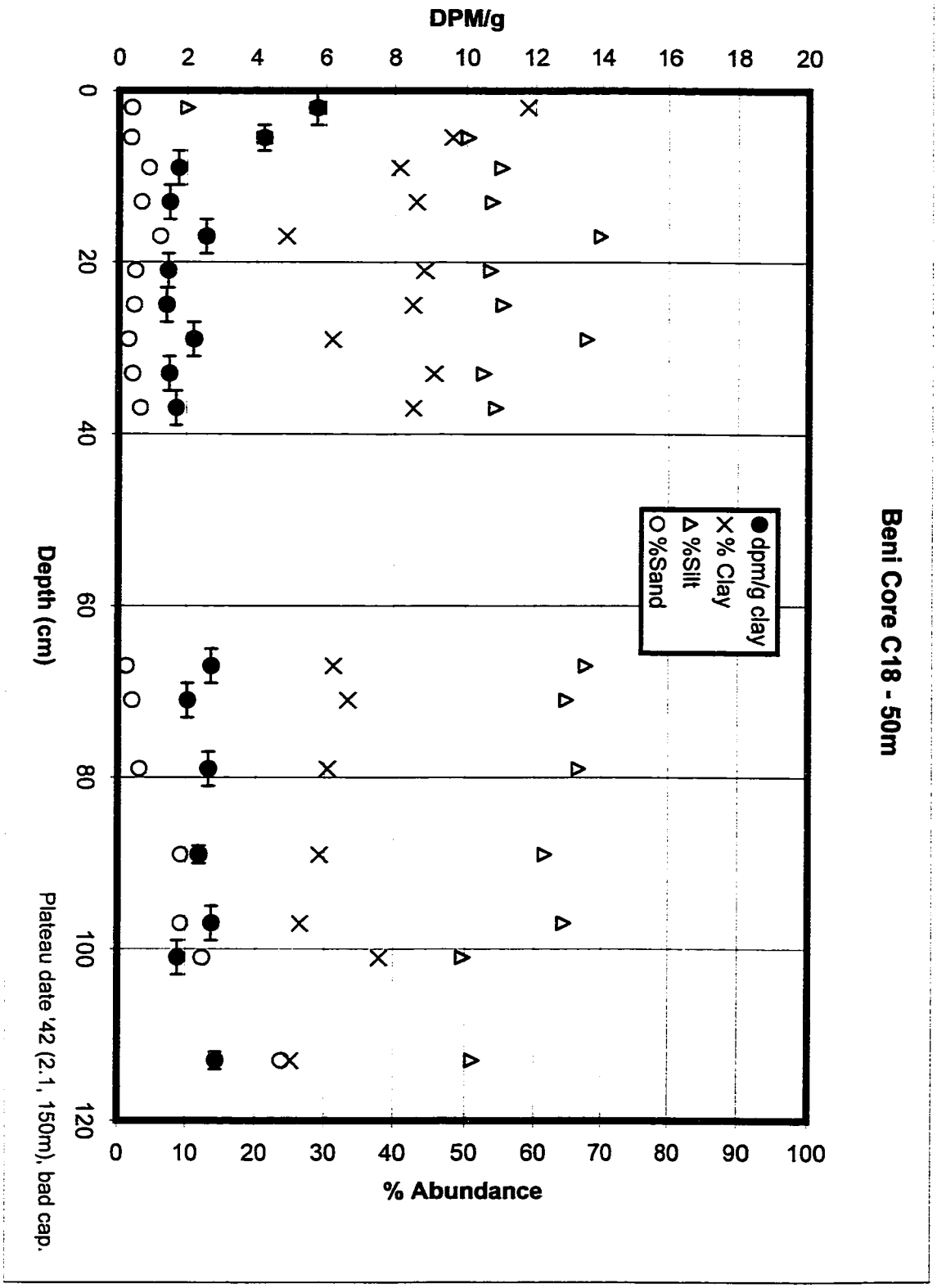
DPM/g
0
2
4
6
8
10
12
14
16
18
20
Depth (cm)
0
20
40
60
80
100
120
% Abundance
0
10
20
30
40
50
60
70
80
90
100
dpm/g clay
% Clay
%Silt
%Sand
Beni Core C18 - 50m
Plateau date '42 (2.1, 150m), bad cap.

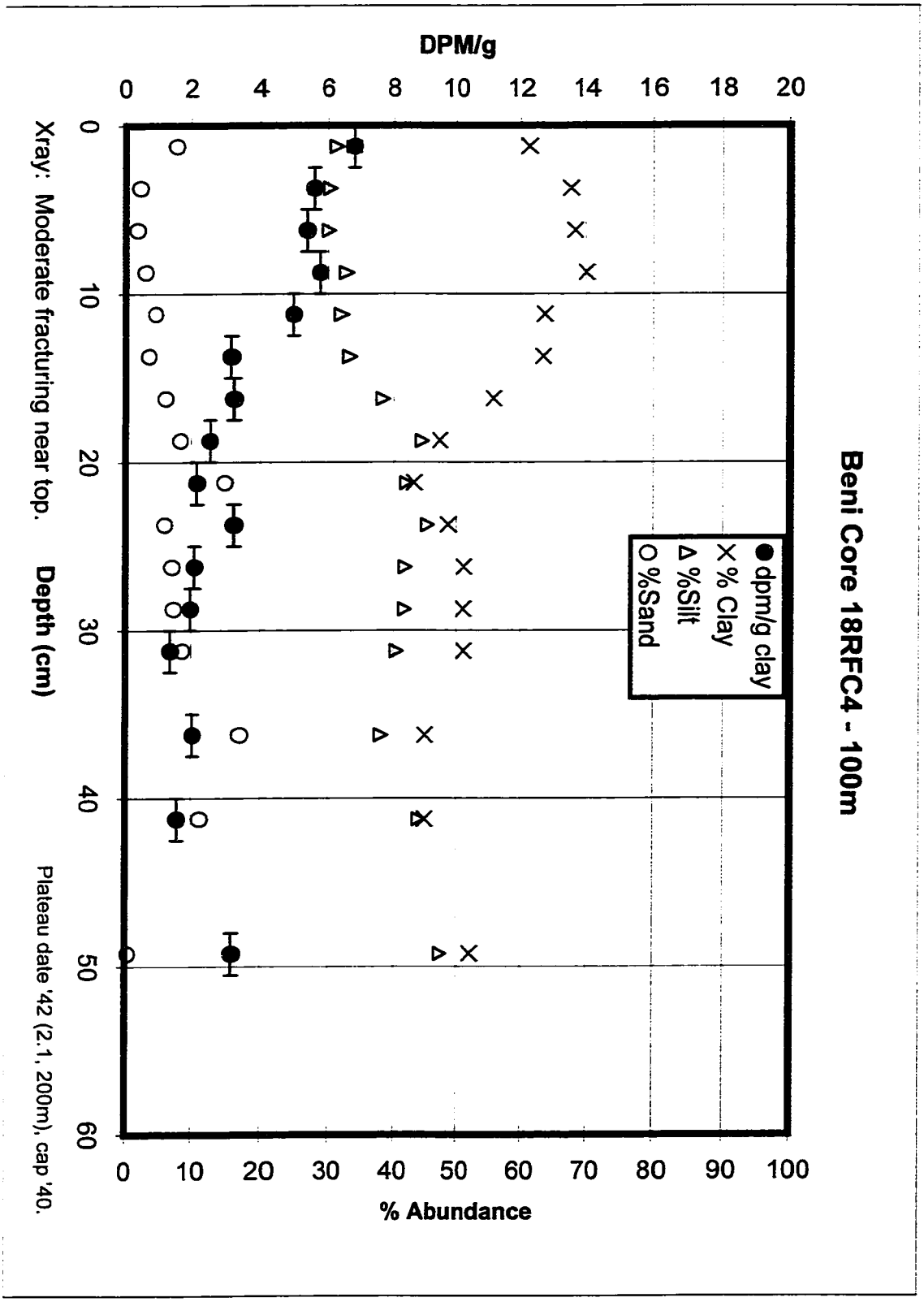
Beni Core 18RFC4 - 100m
DPM/g
0 2 4 6 8 10 12 14 16 18 20
0 10 20 30 40 50 60
Depth (cm)
0 10 20 30 40 50 60 70 80 90 100
% Abundance
● dpm/g clay
× % Clay
Δ %Silt
○ %Sand
Xray: Moderate fracturing near top.
Plateau date '42 (2.1, 200m), cap '40.

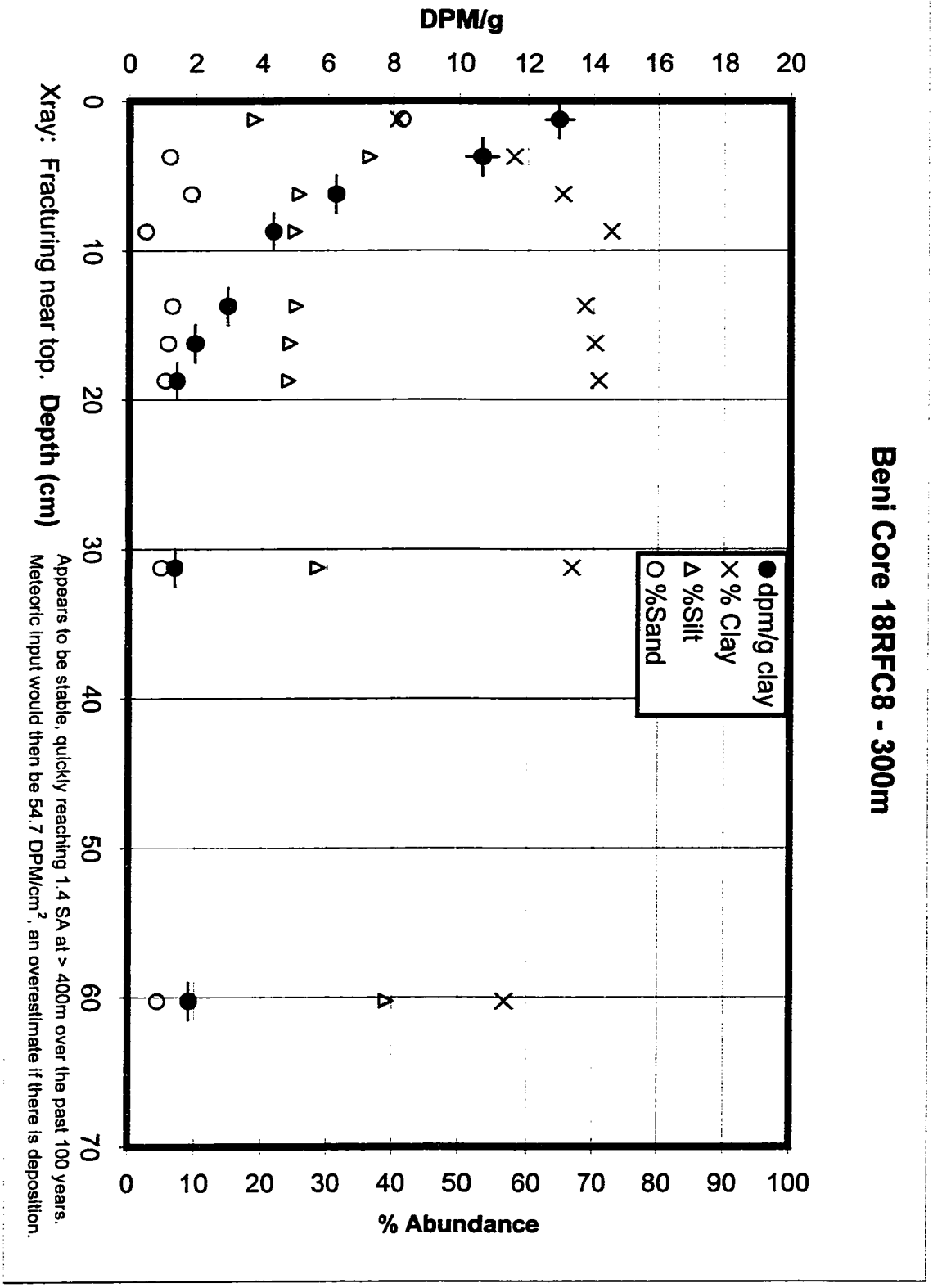
Beni Core 18RFC8 - 300m
DPM/g
0 2 4 6 8 10 12 14 16 18 20
0 10 20 30 40 50 60 70
Depth (cm)
0 10 20 30 40 50 60 70 80 90 100
% Abundance
● dpm/g clay
× % Clay
Δ %Silt
○ %Sand
Xray: Fracturing near top.
Appears to be stable, quickly reaching 1.4 SA at > 400m over the past 100 years.
Meteoric input would then be 54.7 DPM/cm^2, an overestimate if there is deposition.

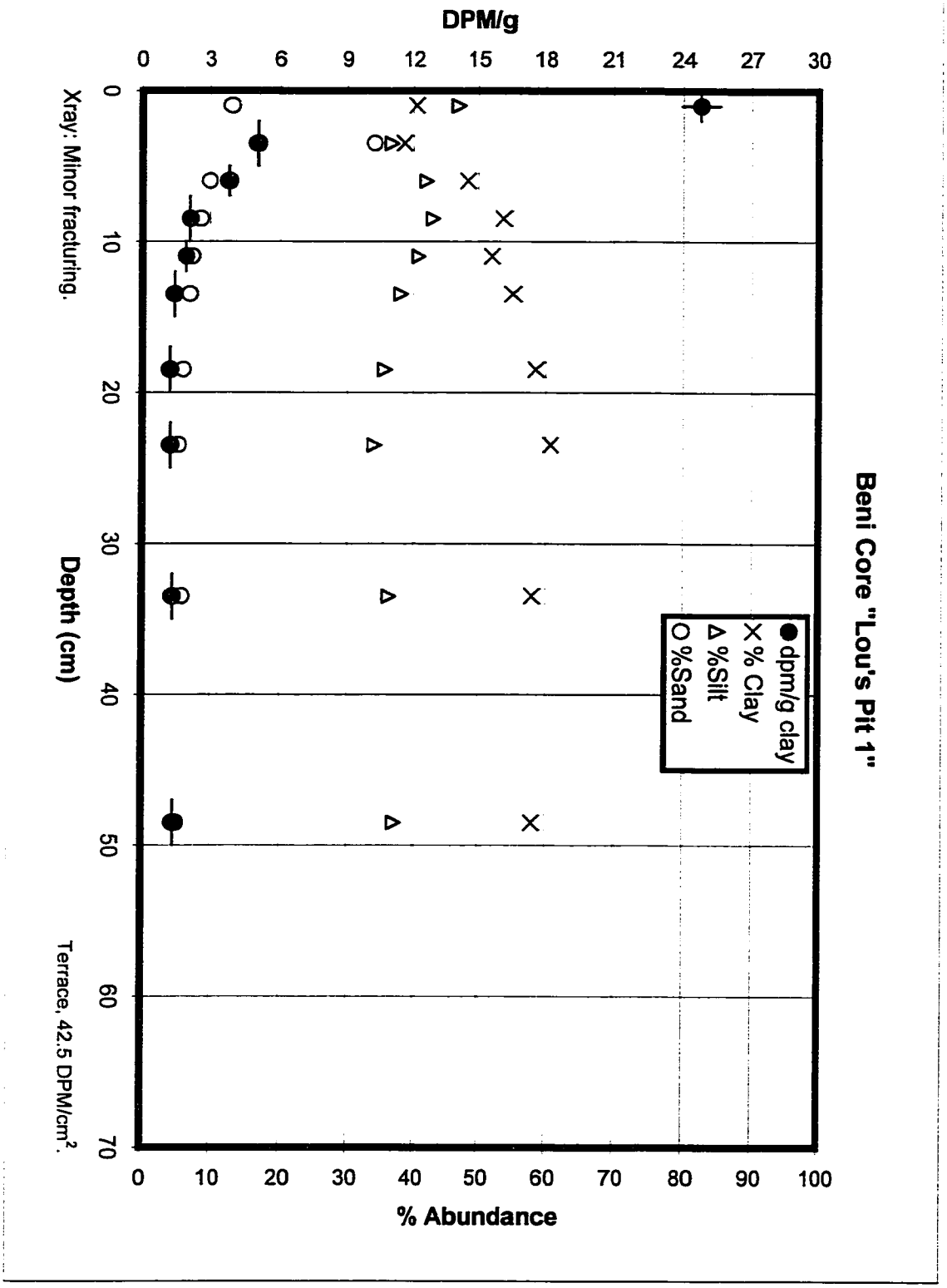
DPM/g
0 3 6 9 12 15 18 21 24 27 30
Depth (cm)
0 10 20 30 40 50 60 70
% Abundance
0 10 20 30 40 50 60 70 80 90 100
Beni Core "Lou's Pit 1"
● dpm/g clay
X % Clay
Δ %Silt
O %Sand
Xray: Minor fracturing.
Terrace, 42.5 DPM/cm².

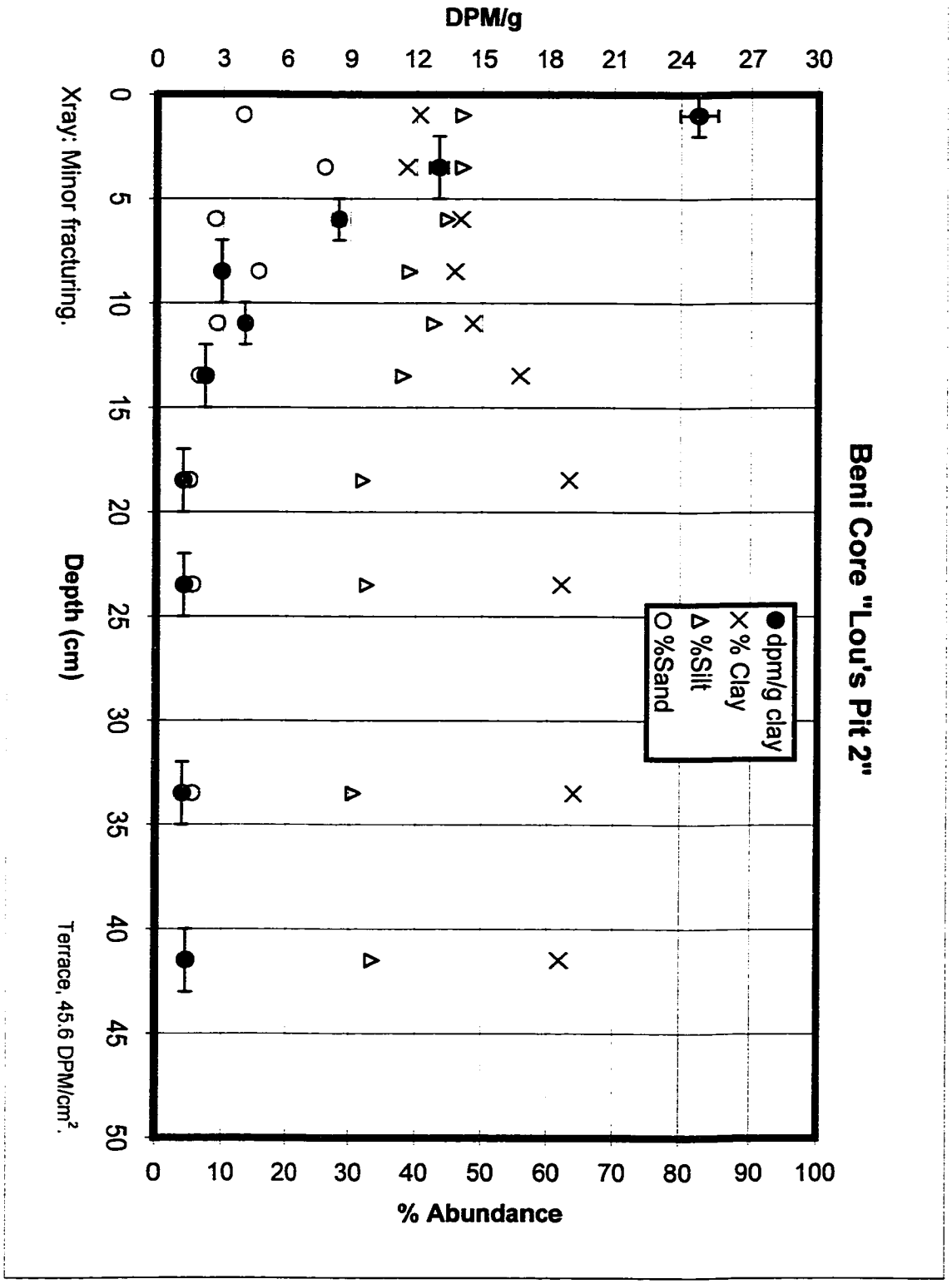
DPM/g
0 3 6 9 12 15 18 21 24 27 30
Xray: Minor fracturing.
Depth (cm)
0 5 10 15 20 25 30 35 40 45 50
Terrace, 45.6 DPM/cm².
dpm/g clay
% Clay
%Silt
%Sand
Beni Core "Lou's Pit 2"
0 10 20 30 40 50 60 70 80 90 100
% Abundance

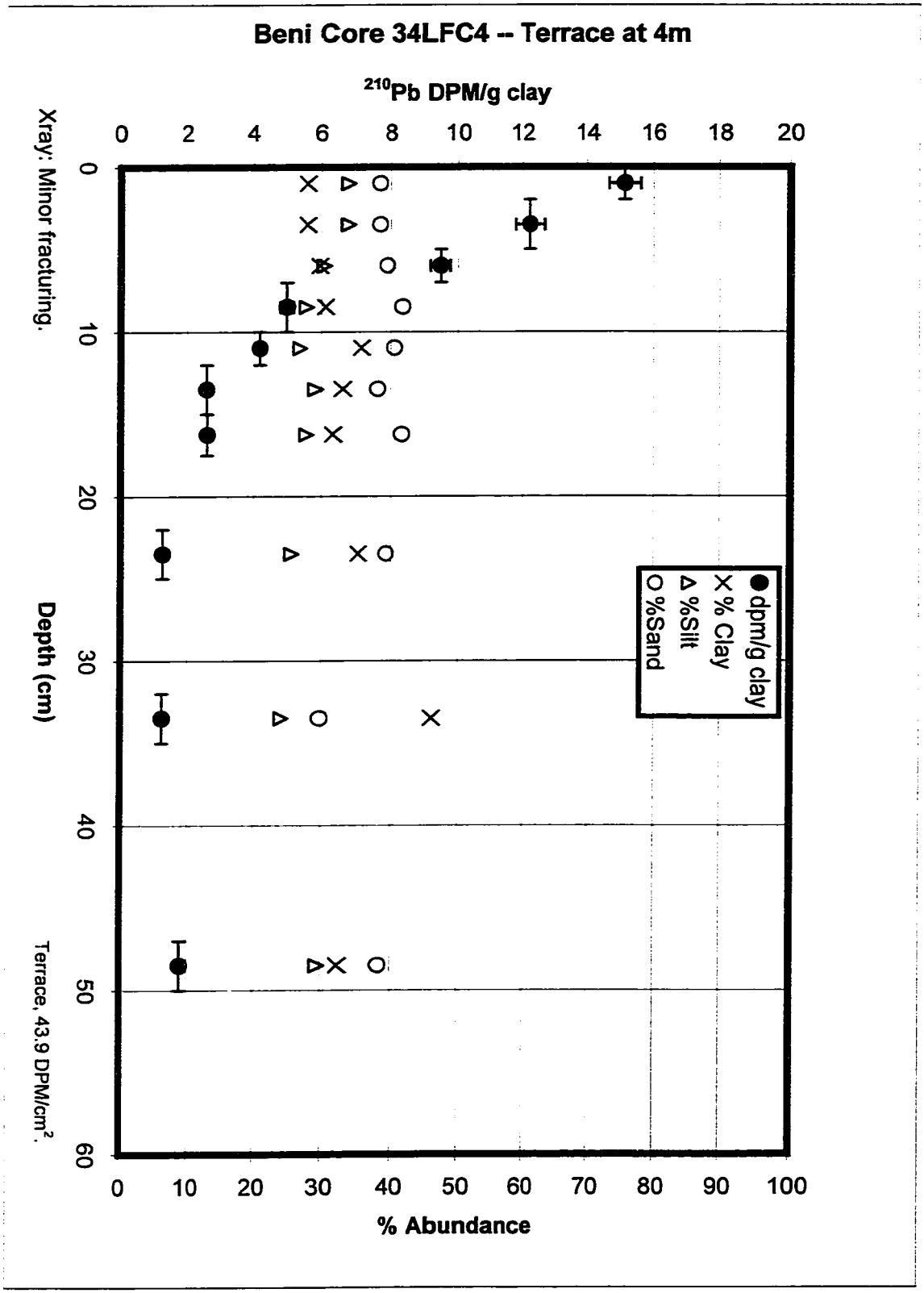
Beni Core 34LFC4 -- Terrace at 4m
210Pb DPM/g clay
0 2 4 6 8 10 12 14 16 18 20
Xray: Minor fracturing.
Depth (cm)
0 10 20 30 40 50 60
Terrace, 43.9 DPM/cm2.
dpm/g clay
% Clay
%Silt
%Sand
0 10 20 30 40 50 60 70 80 90 100
% Abundance

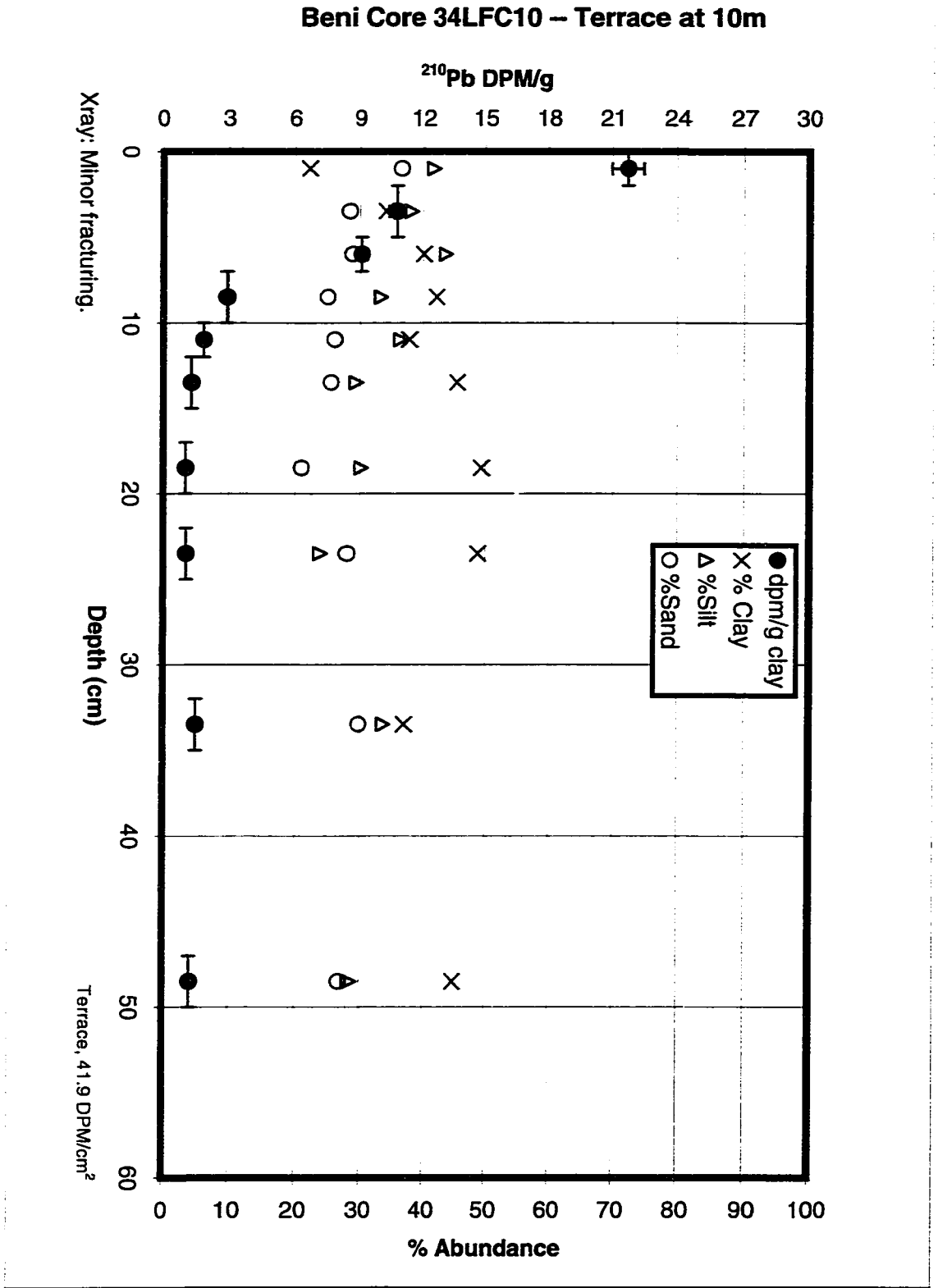
Beni Core 34LFC10 -- Terrace at 10m
^{210}Pb DPM/g
0 3 6 9 12 15 18 21 24 27 30
Xray: Minor fracturing.
Depth (cm)
0 10 20 30 40 50 60
Terrace, 41.9 DPM/cm^2
● dpm/g clay
X % Clay
Δ %Silt
○ %Sand
0 10 20 30 40 50 60 70 80 90 100
% Abundance

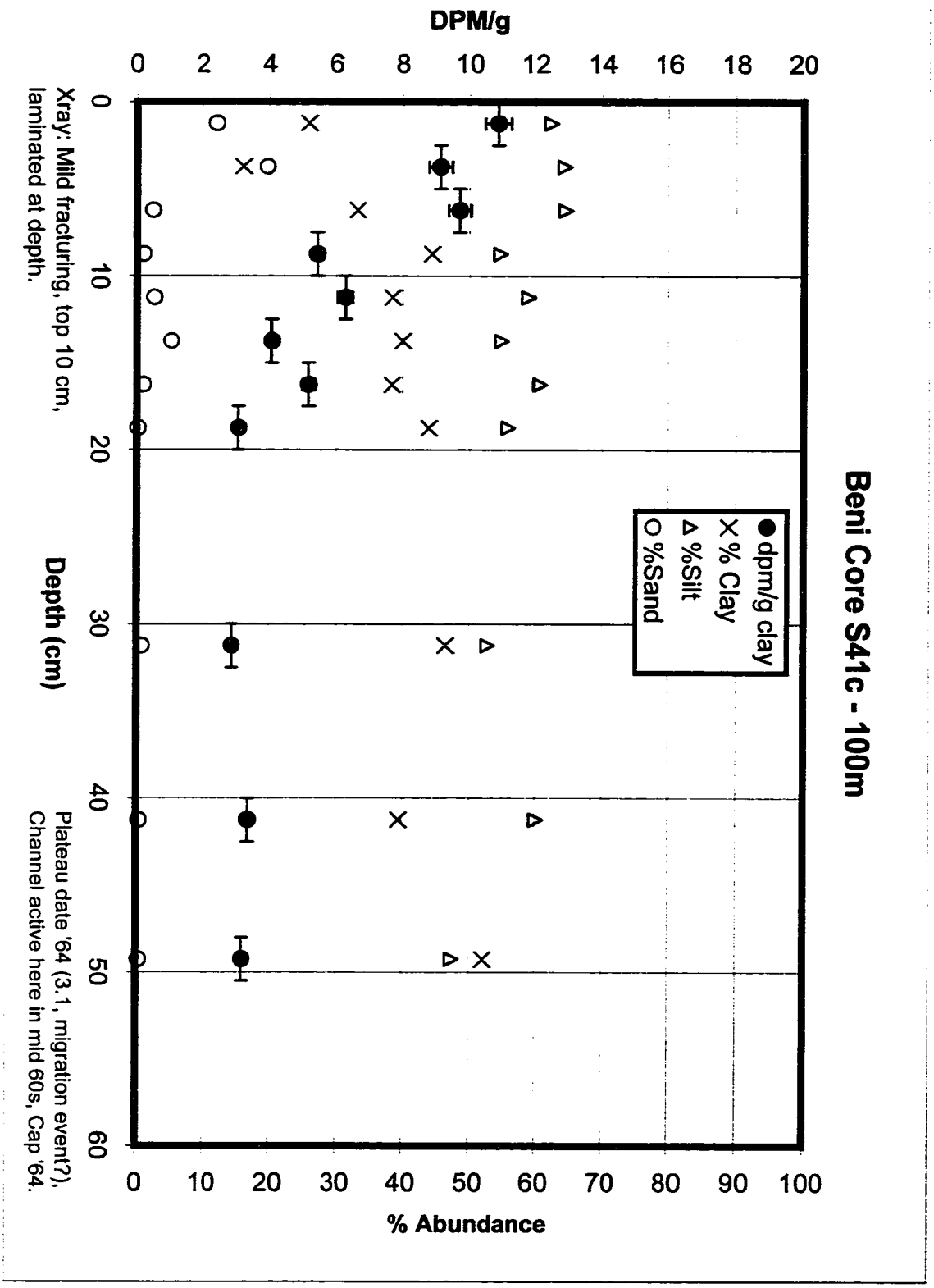
Beni Core S41c - 100m
DPM/g
0 2 4 6 8 10 12 14 16 18 20
Depth (cm)
0 10 20 30 40 50 60
% Abundance
0 10 20 30 40 50 60 70 80 90 100
dpm/g clay
% Clay
%Silt
%Sand
Xray: Mild fracturing, top 10 cm, laminated at depth.
Plateau date '64 (3.1, migration event?), Channel active here in mid 60s, Cap '64.

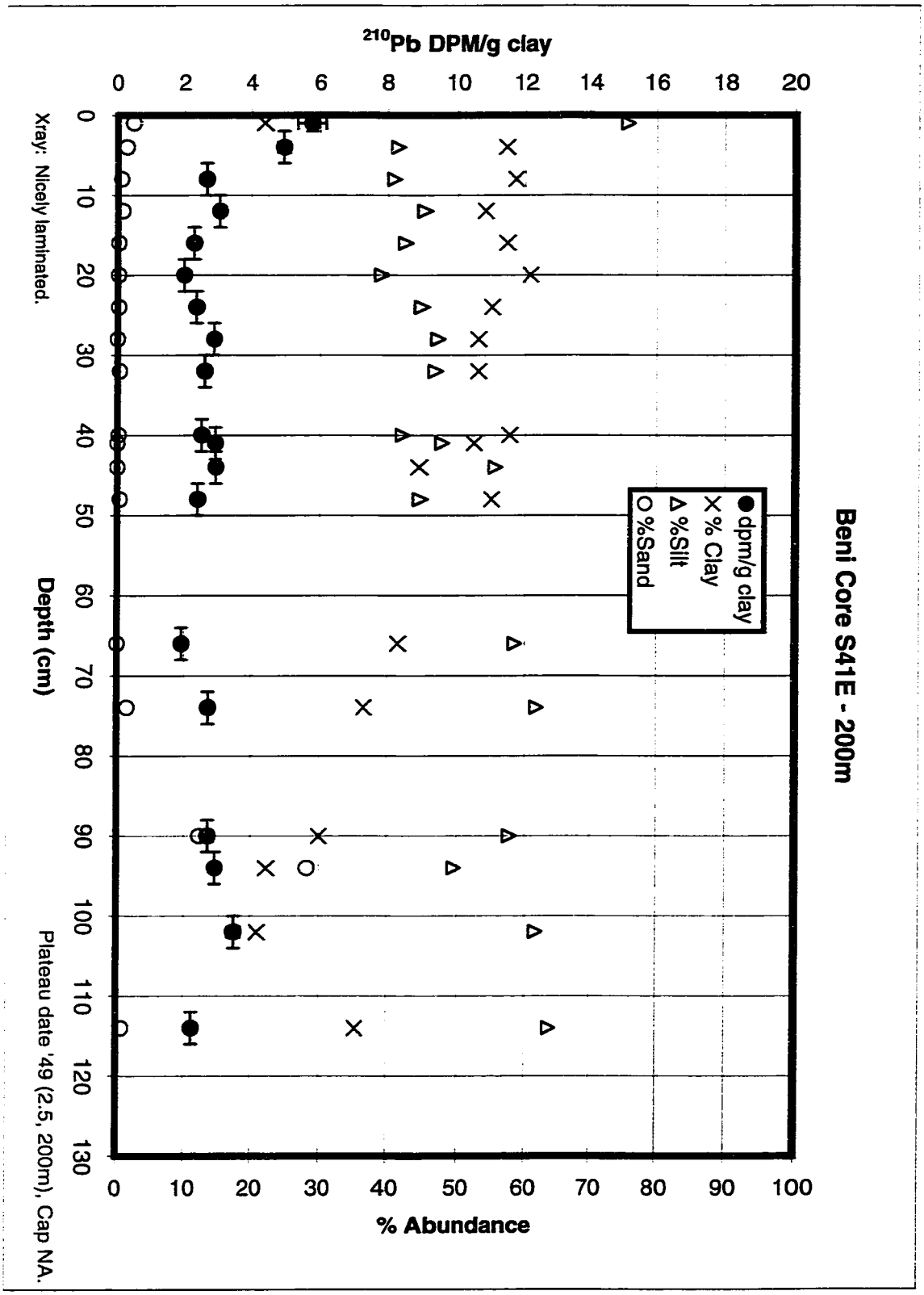
210Pb DPM/g clay
0 2 4 6 8 10 12 14 16 18 20
Depth (cm)
0 10 20 30 40 50 60 70 80 90 100 110 120 130
% Abundance
0 10 20 30 40 50 60 70 80 90 100
dpm/g clay
% Clay
%Silt
%Sand
Beni Core S41E - 200m
Xray: Nicely laminated.
Plateau date '49 (2.5, 200m), Cap NA.

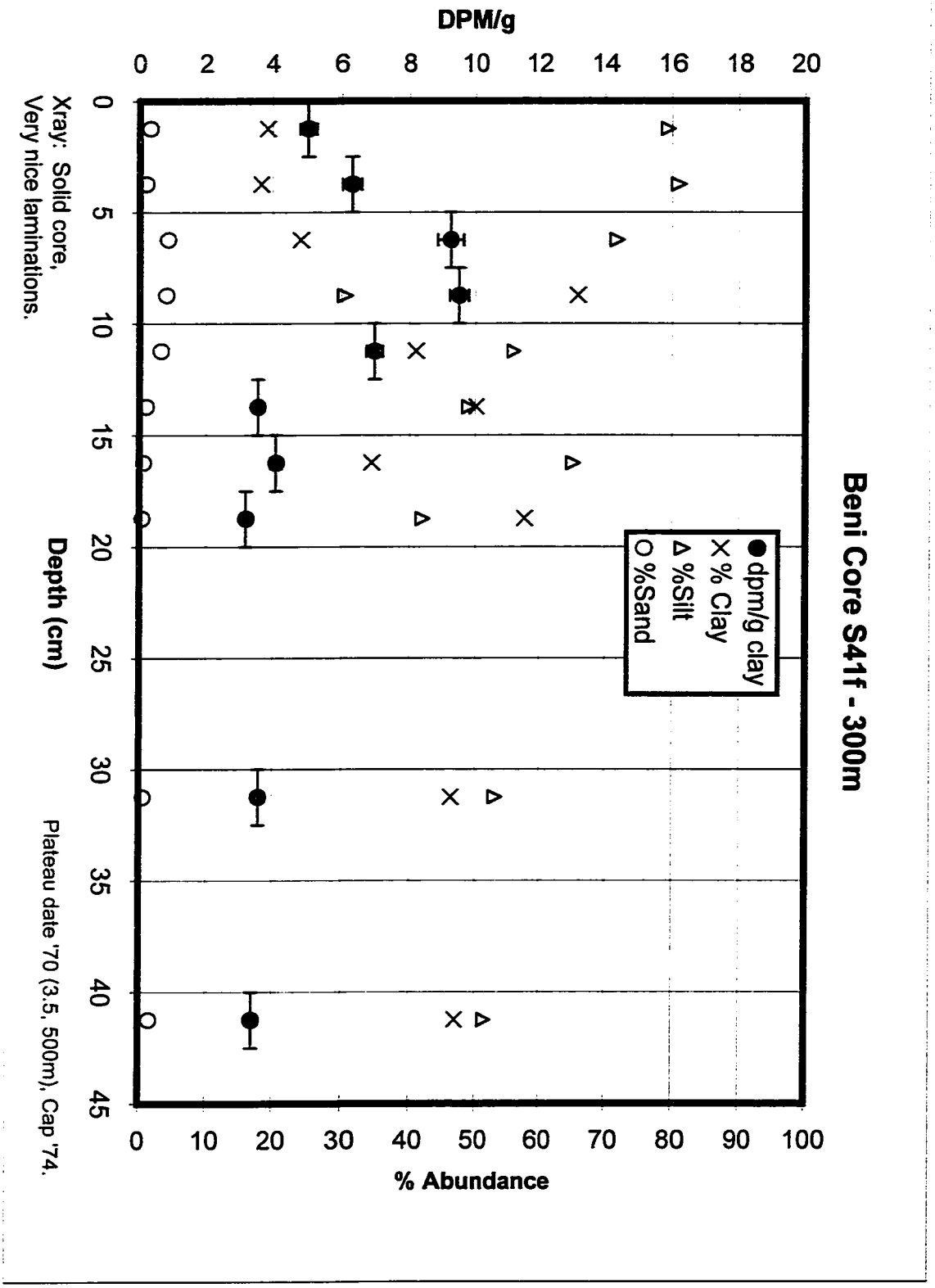
Beni Core S41f - 300m
DPM/g
0 2 4 6 8 10 12 14 16 18 20
Depth (cm)
0 5 10 15 20 25 30 35 40 45
% Abundance
0 10 20 30 40 50 60 70 80 90 100
● dpm/g clay
× % Clay
Δ %Silt
○ %Sand
Xray: Solid core,
Very nice laminations.
Plateau date '70 (3.5, 500m), Cap '74.

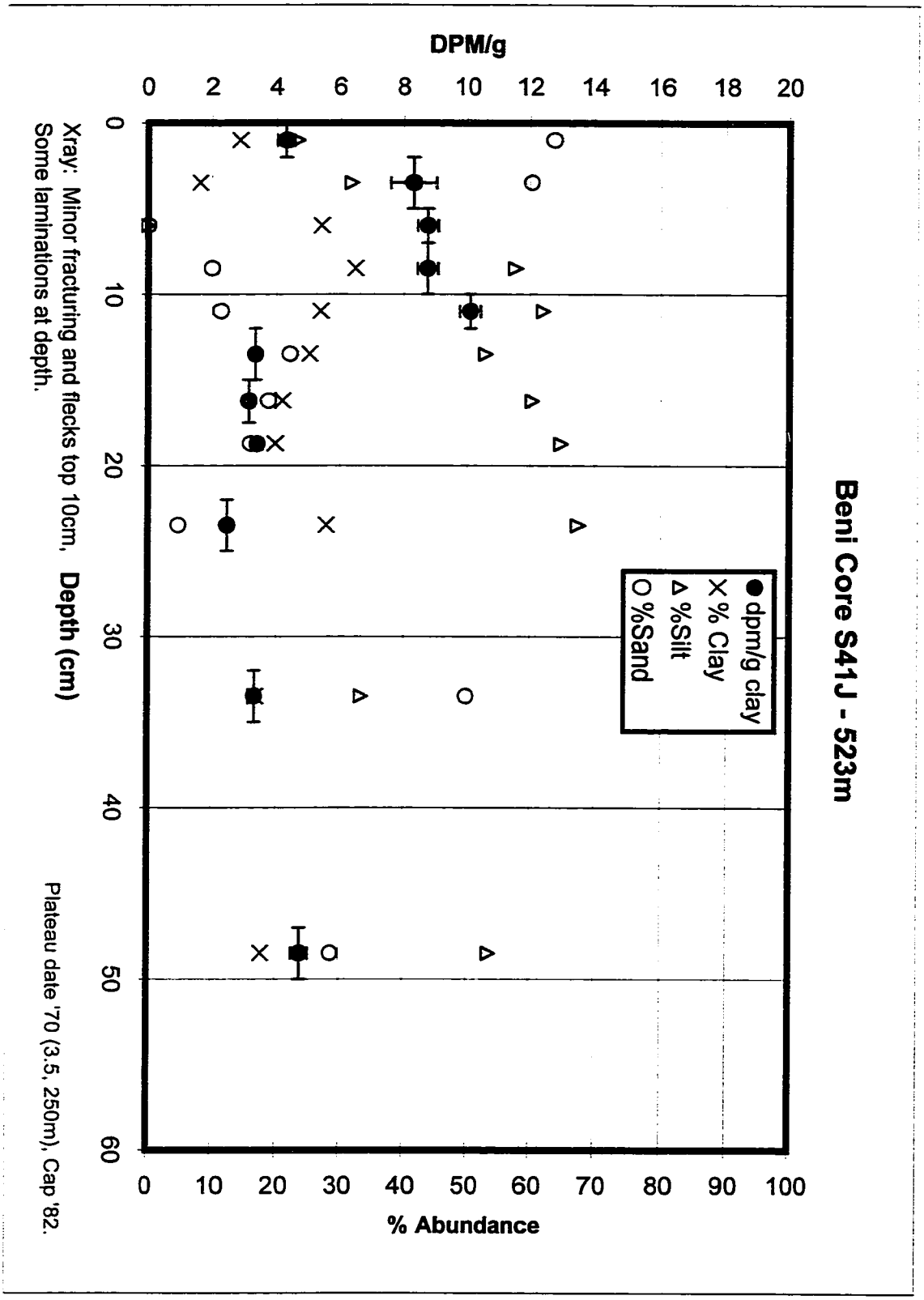
Beni Core S41J - 523m
DPM/g
0 2 4 6 8 10 12 14 16 18 20
Depth (cm)
0 10 20 30 40 50 60
% Abundance
0 10 20 30 40 50 60 70 80 90 100
dpm/g clay
% Clay
%Silt
%Sand
Xray: Minor fracturing and flecks top 10cm, Some laminations at depth.
Plateau date '70 (3.5, 250m), Cap '82.

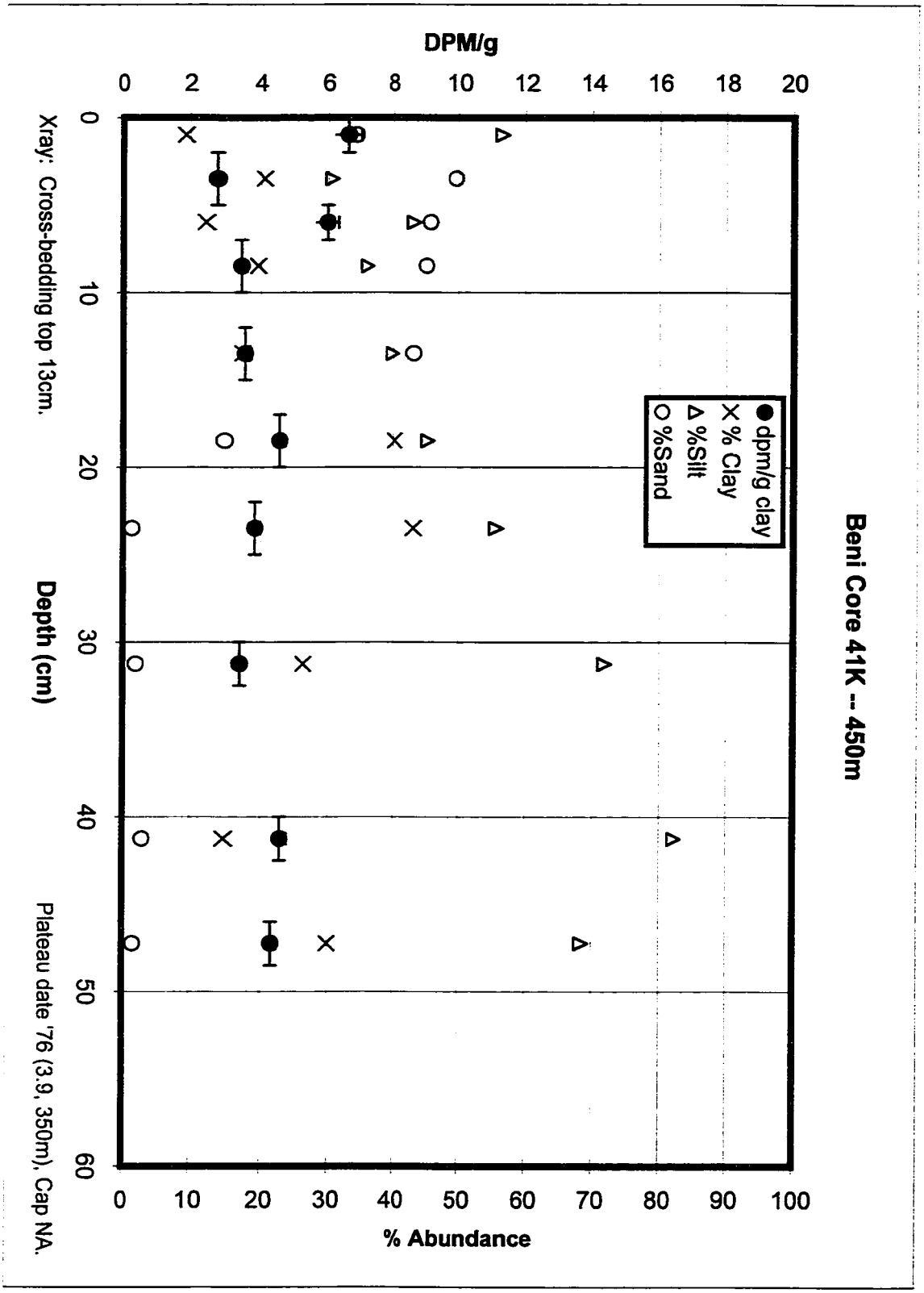
DPM/g
0 2 4 6 8 10 12 14 16 18 20
Depth (cm)
0 10 20 30 40 50 60
dpm/g clay
% Clay
%Silt
%Sand
0 10 20 30 40 50 60 70 80 90 100
% Abundance
Beni Core 41K -- 450m
Xray: Cross-bedding top 13cm.
Plateau date '76 (3.9, 350m). Cap NA.

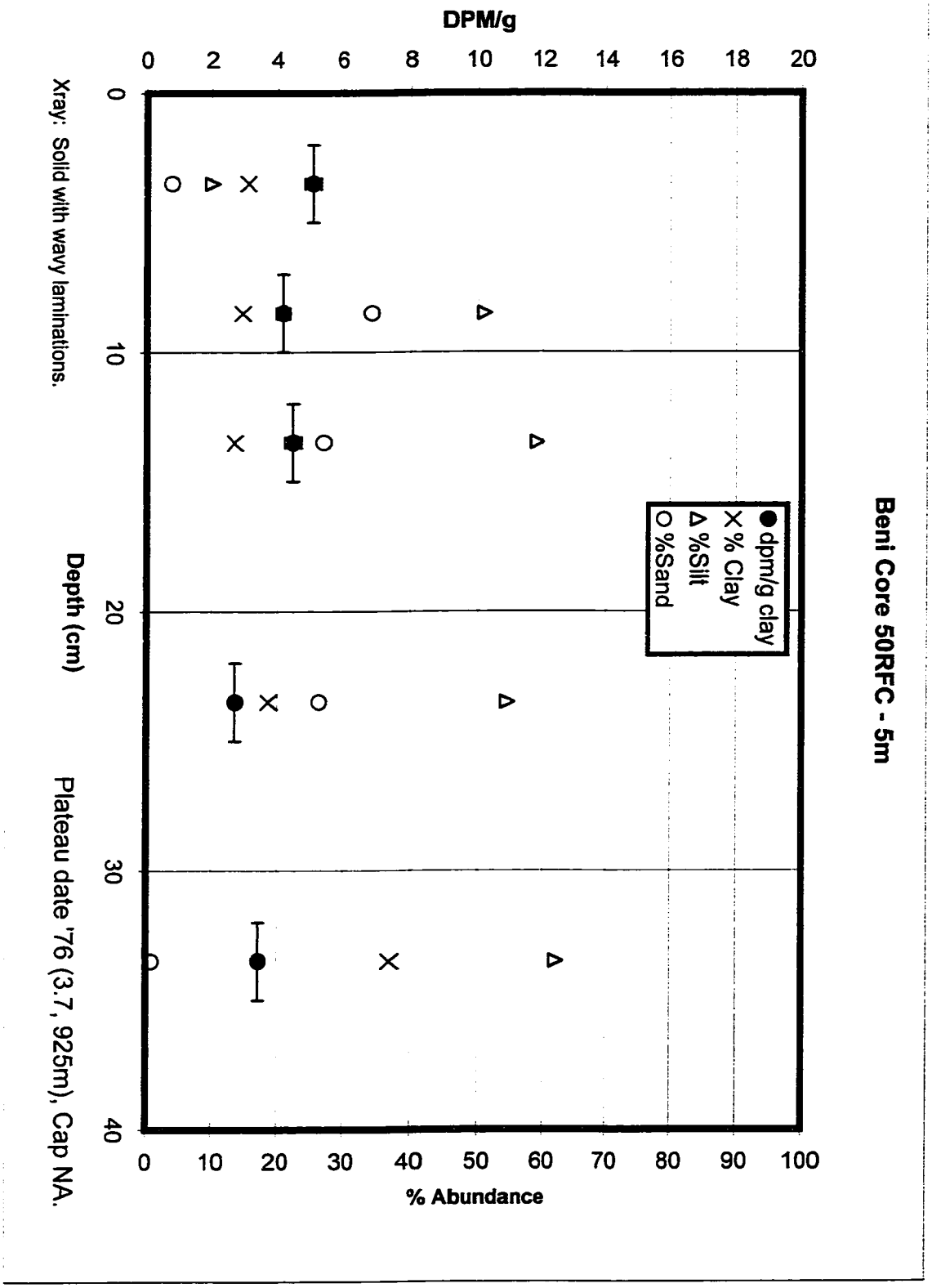
Beni Core 50RFC - 5m
DPM/g
0 2 4 6 8 10 12 14 16 18 20
0 10 20 30 40
Depth (cm)
0 10 20 30 40 50 60 70 80 90 100
% Abundance
● dpm/g clay
× % Clay
Δ %Silt
○ %Sand
Xray: Solid with wavy laminations.
Plateau date '76 (3.7, 925m), Cap NA.

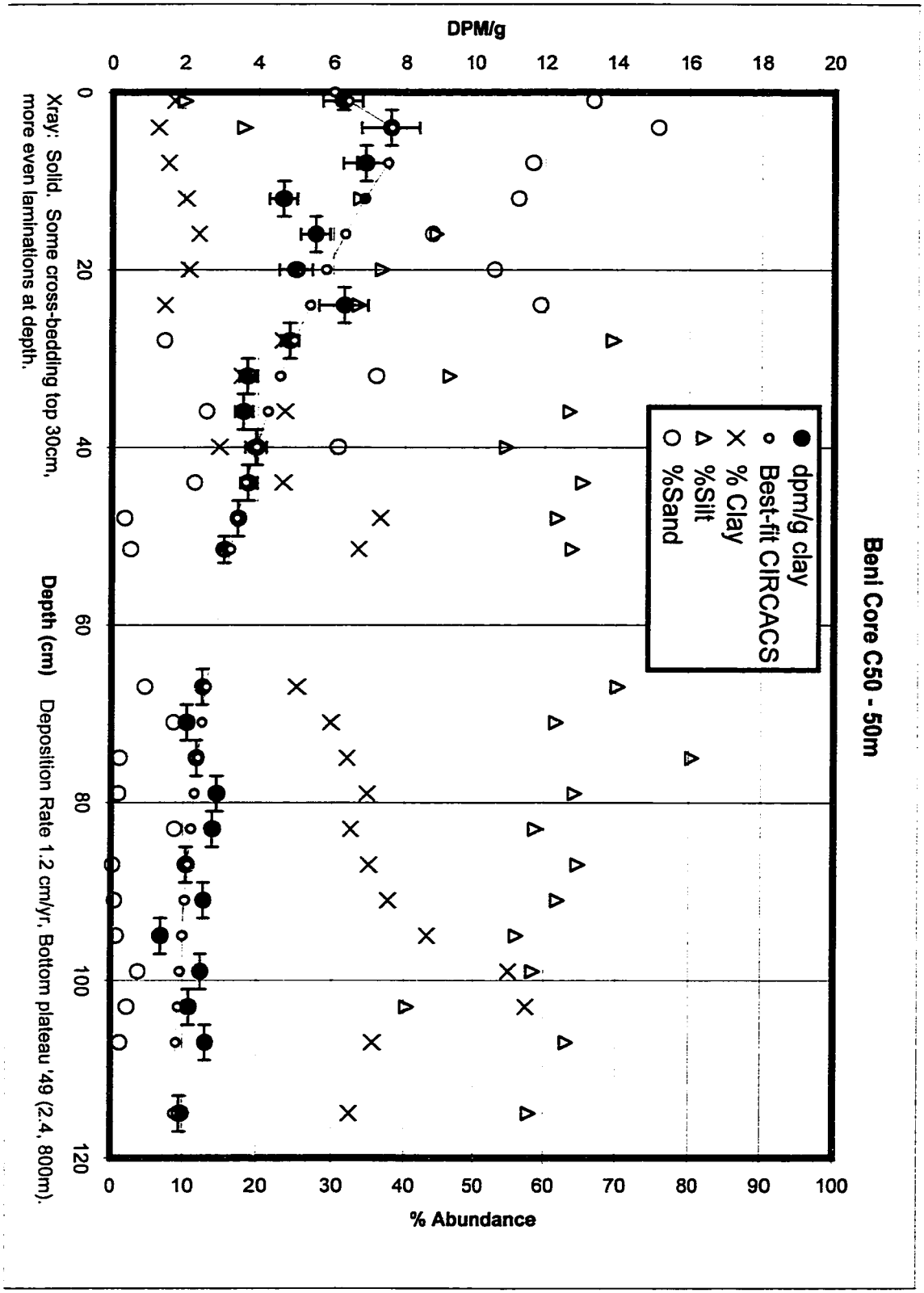
DPM/g
0 2 4 6 8 10 12 14 16 18 20
Beni Core C50 - 50m
dpm/g clay
Best-fit CIRCACS
% Clay
%Silt
%Sand
Depth (cm)
0 20 40 60 80 100 120
0 10 20 30 40 50 60 70 80 90 100
% Abundance
Xray: Solid. Some cross-bedding top 30cm, more even laminations at depth.
Deposition Rate 1.2 cm/yr, Bottom plateau '49 (2.4, 800m).

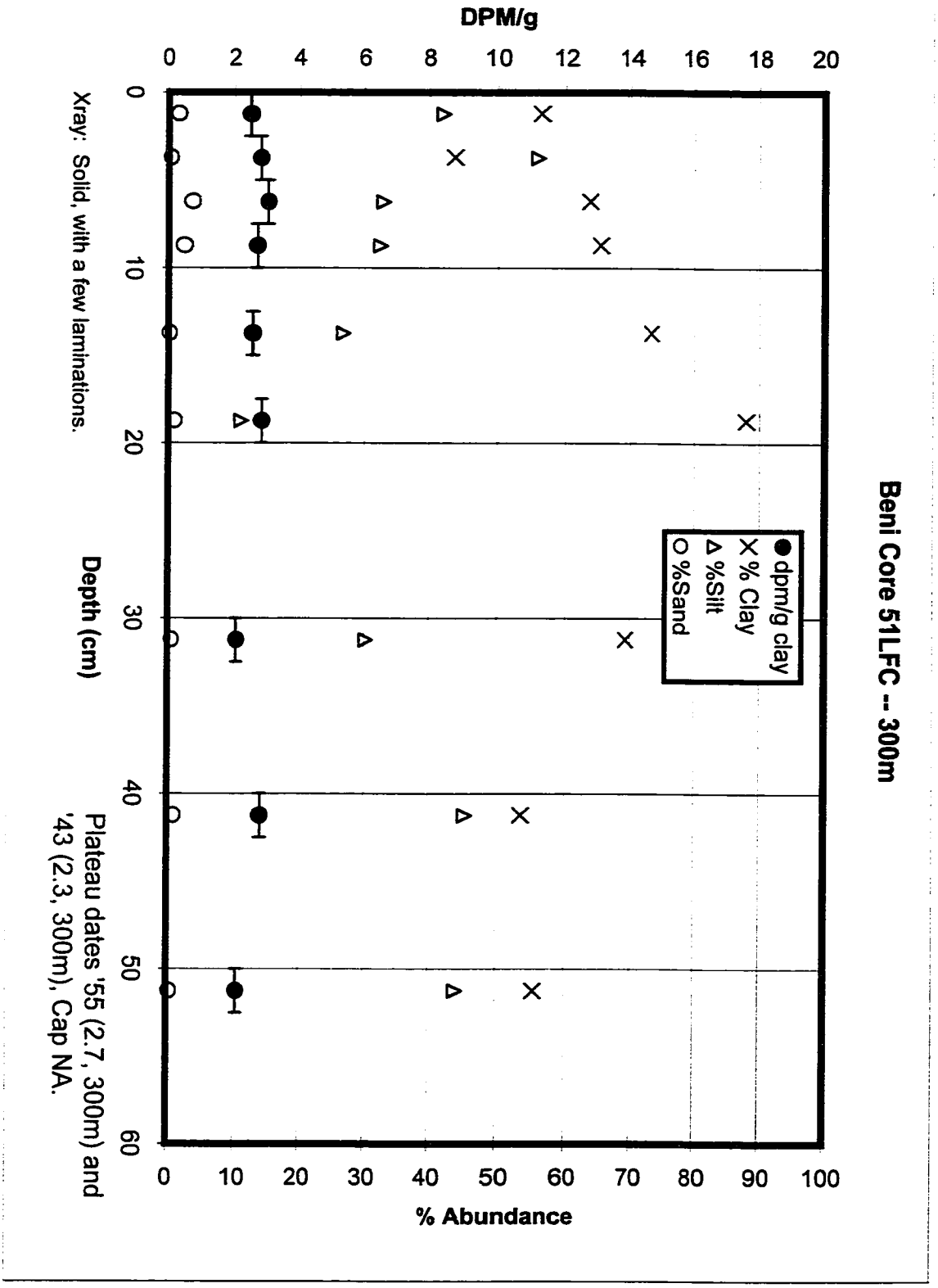
Beni Core 51LFC -- 300m
DPM/g
0 2 4 6 8 10 12 14 16 18 20
0 10 20 30 40 50 60
Depth (cm)
0 10 20 30 40 50 60 70 80 90 100
% Abundance
● dpm/g clay
X % Clay
Δ %Silt
○ %Sand
Xray: Solid, with a few laminations.
Plateau dates '55 (2.7, 300m) and '43 (2.3, 300m), Cap NA.

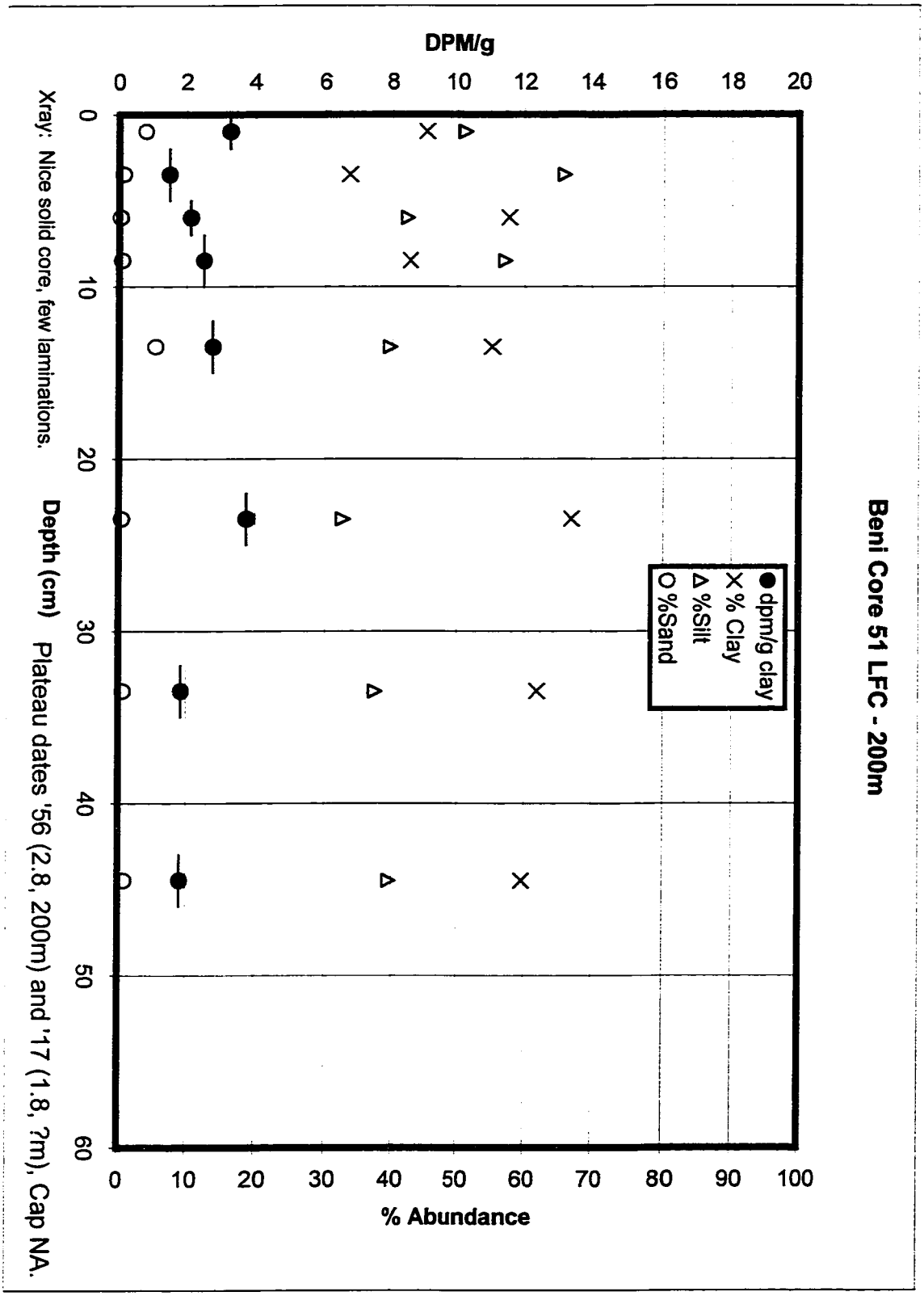
Beni Core 51 LFC - 200m
DPM/g
0 2 4 6 8 10 12 14 16 18 20
% Abundance
0 10 20 30 40 50 60 70 80 90 100
Depth (cm)
0 10 20 30 40 50 60
dpm/g clay
% Clay
%Silt
%Sand
Xray: Nice solid core, few laminations.
Plateau dates '56 (2.8, 200m) and '17 (1.8, ?m), Cap NA.

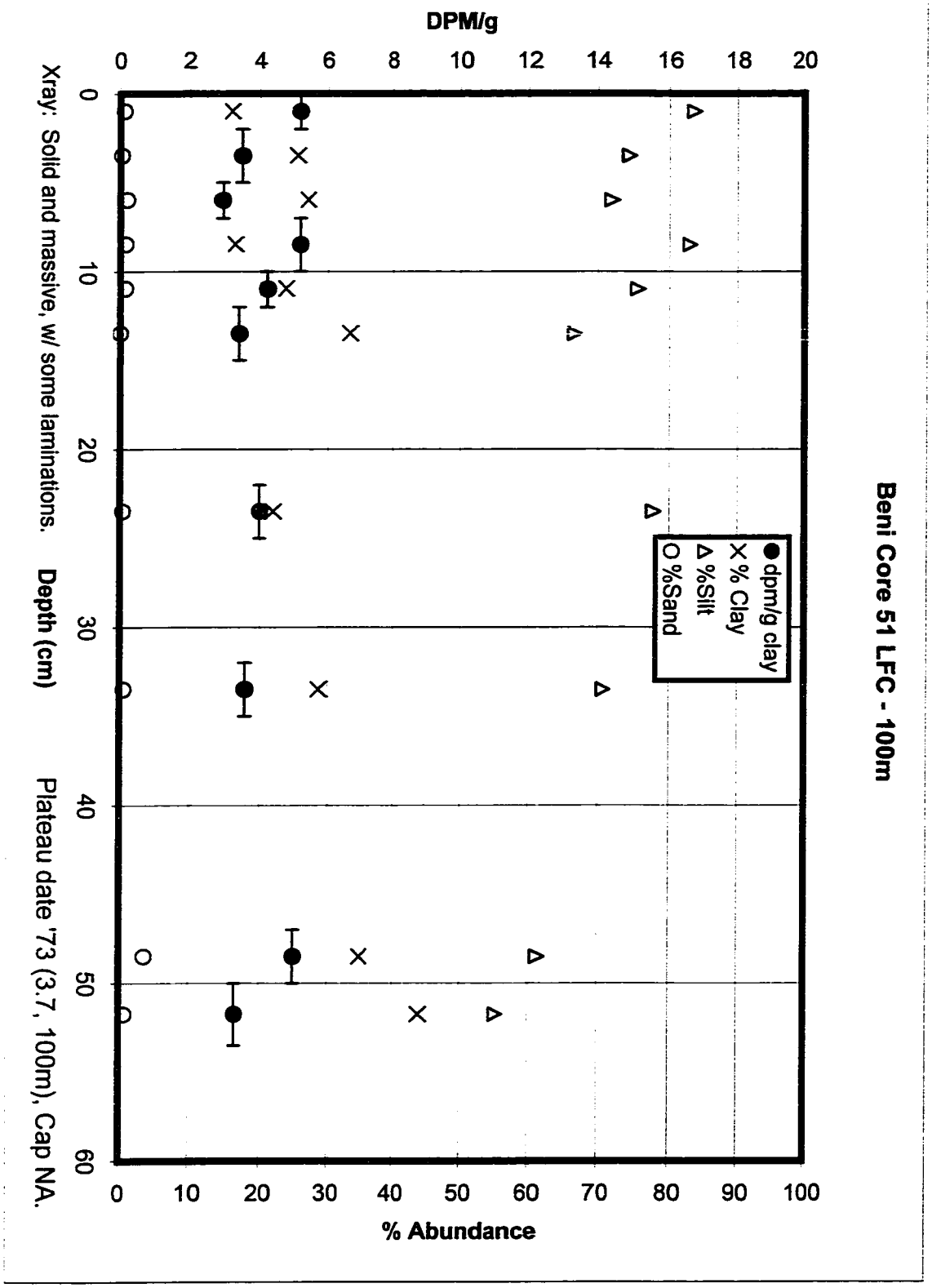
Beni Core 51 LFC - 100m
DPM/g
0 2 4 6 8 10 12 14 16 18 20
% Abundance
0 10 20 30 40 50 60 70 80 90 100
Depth (cm)
0 10 20 30 40 50 60
dpm/g clay
% Clay
%Silt
%Sand
Xray: Solid and massive, w/ some laminations.
Plateau date '73 (3.7, 100m), Cap NA.

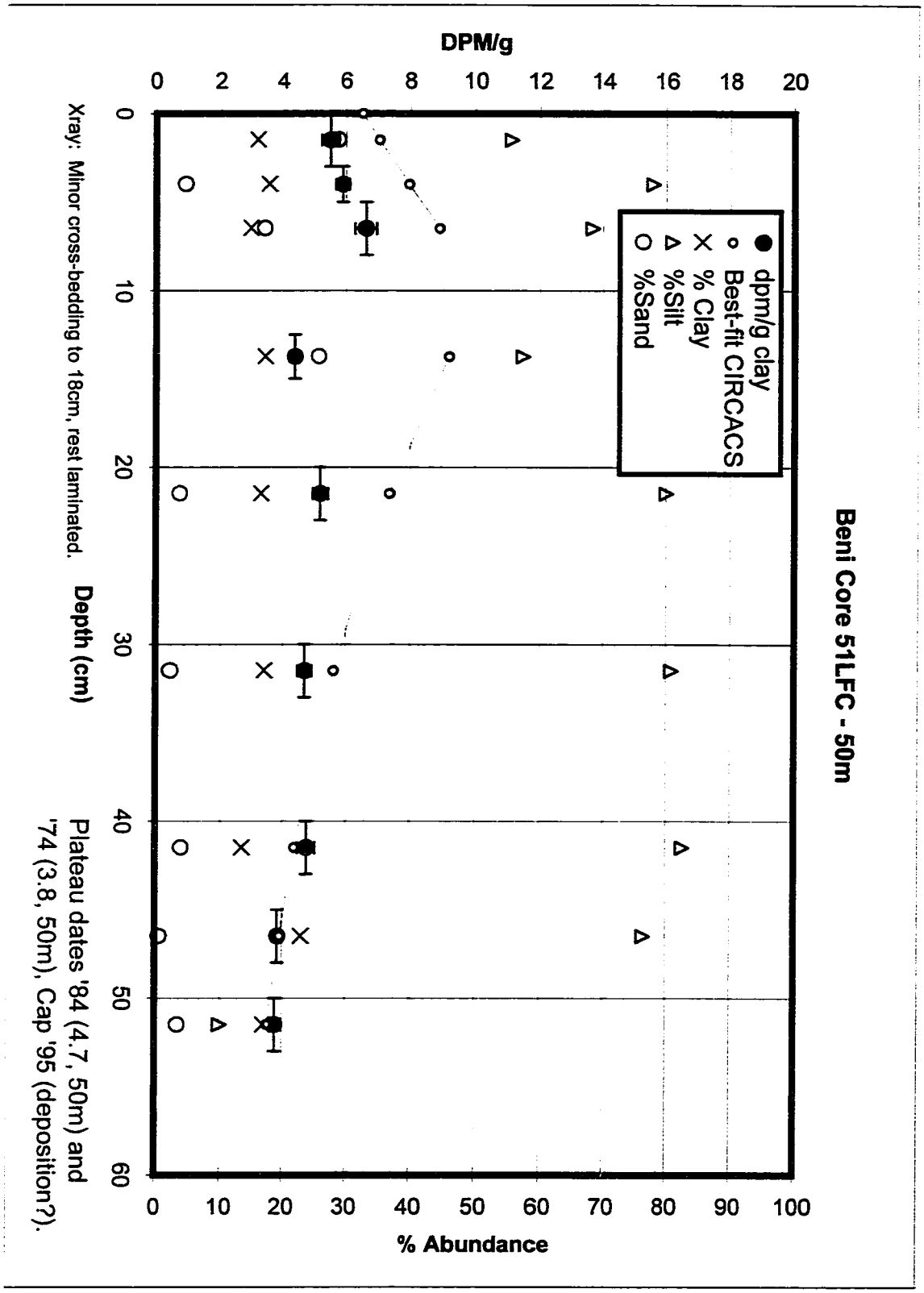
Beni Core 51LFC - 50m
DPM/g
0 2 4 6 8 10 12 14 16 18 20
0 10 20 30 40 50 60
Depth (cm)
0 10 20 30 40 50 60 70 80 90 100
% Abundance
dpm/g clay
Best-fit CIRCACS
% Clay
%Silt
%Sand
Xray: Minor cross-bedding to 18cm, rest laminated.
Plateau dates '84 (4.7, 50m) and '74 (3.8, 50m), Cap '95 (deposition?).

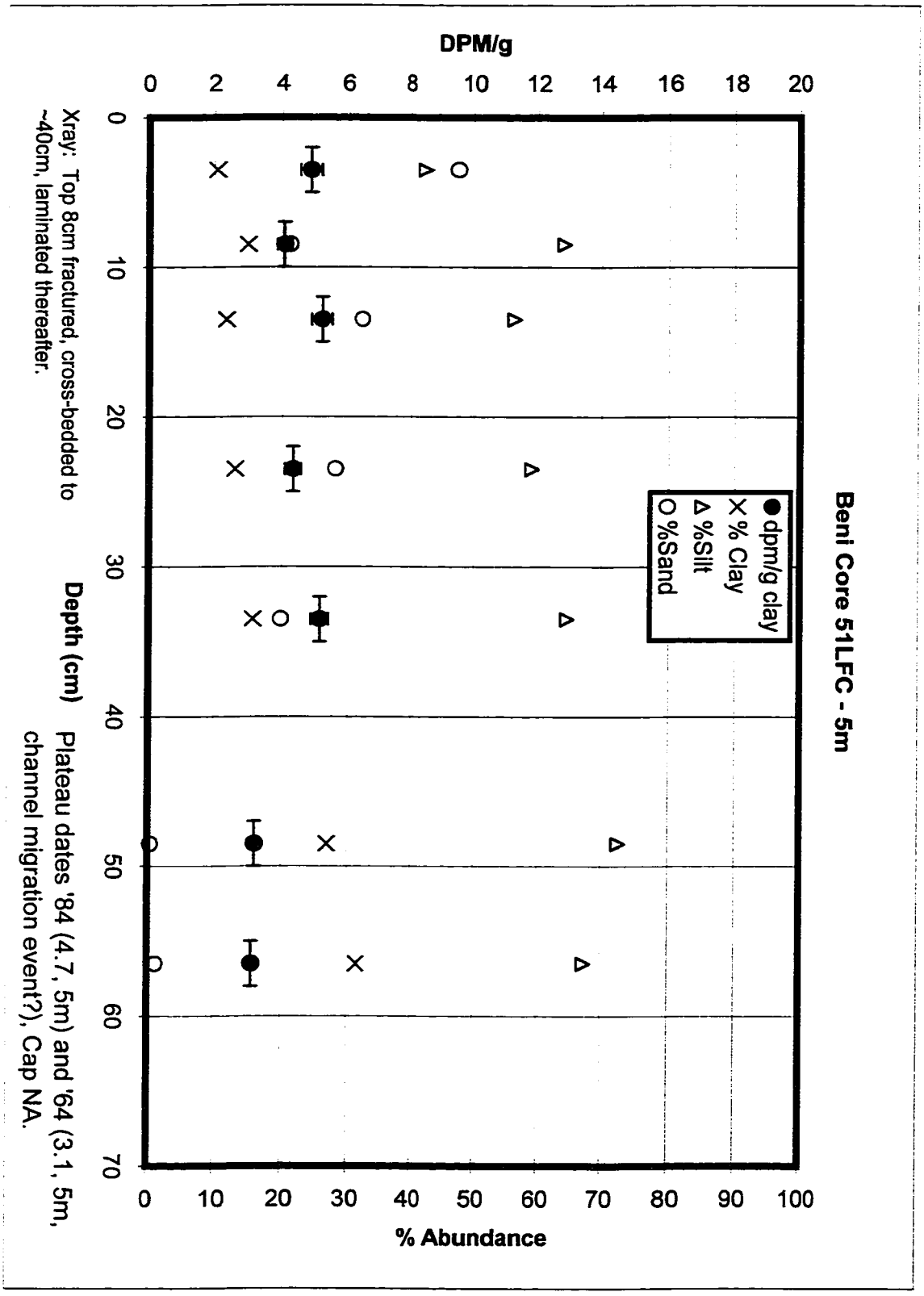
DPM/g
0 2 4 6 8 10 12 14 16 18 20
0 10 20 30 40 50 60 70
Depth (cm)
0 10 20 30 40 50 60 70 80 90 100
% Abundance
● dpm/g clay
× % Clay
Δ %Silt
○ %Sand
Beni Core 51LFC - 5m
Xray: Top 8cm fractured, cross-bedded to ~40cm, laminated thereafter.
Plateau dates '84 (4.7, 5m) and '64 (3.1, 5m, channel migration event?), Cap NA.

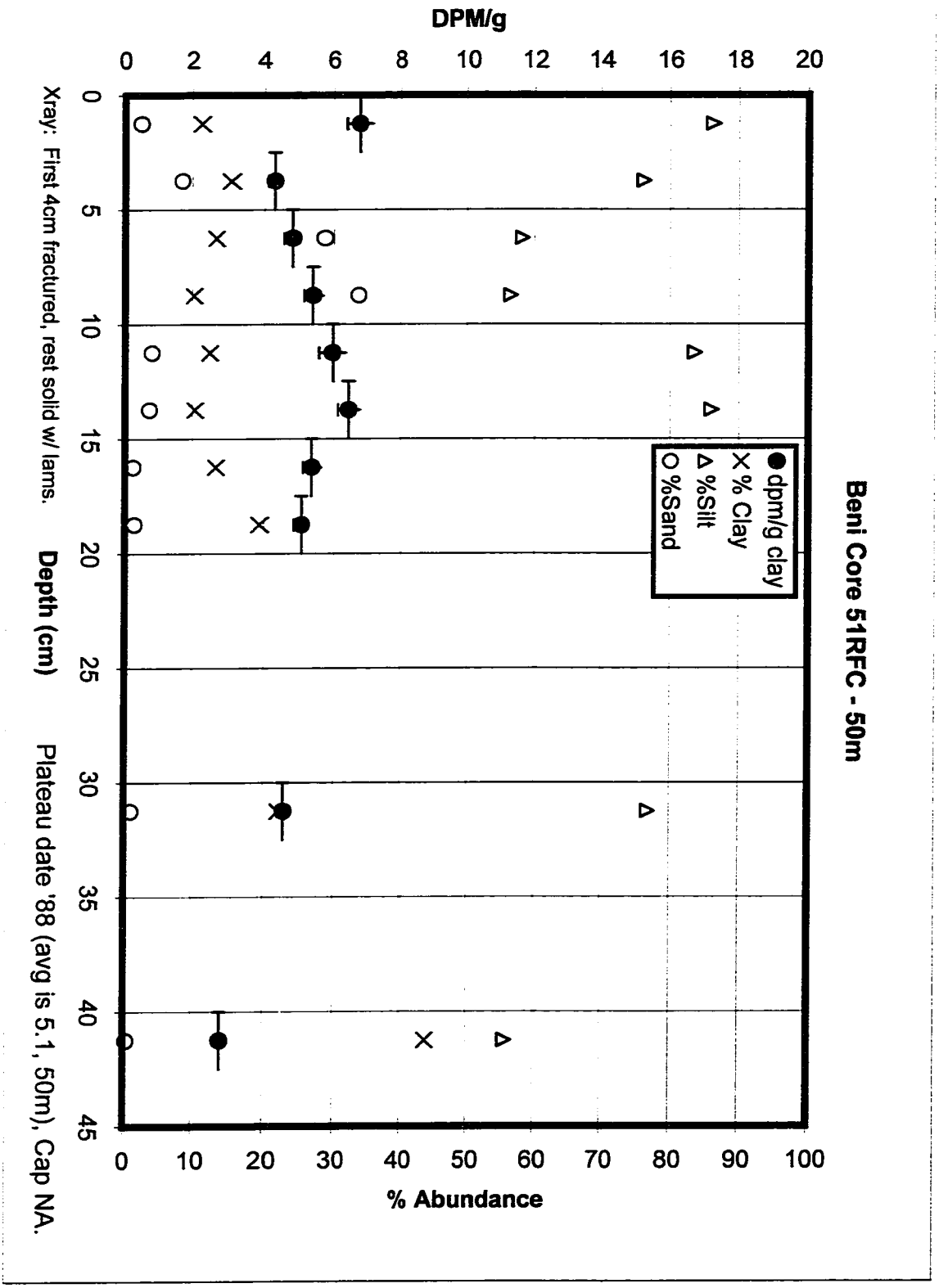
DPM/g
0 2 4 6 8 10 12 14 16 18 20
0 5 10 15 20 25 30 35 40 45
Depth (cm)
0 10 20 30 40 50 60 70 80 90 100
% Abundance
dpm/g clay
% Clay
%Silt
%Sand
Beni Core 51RFC - 50m
Xray: First 4cm fractured, rest solid w/ lams.
Plateau date '88 (avg is 5.1, 50m), Cap NA.

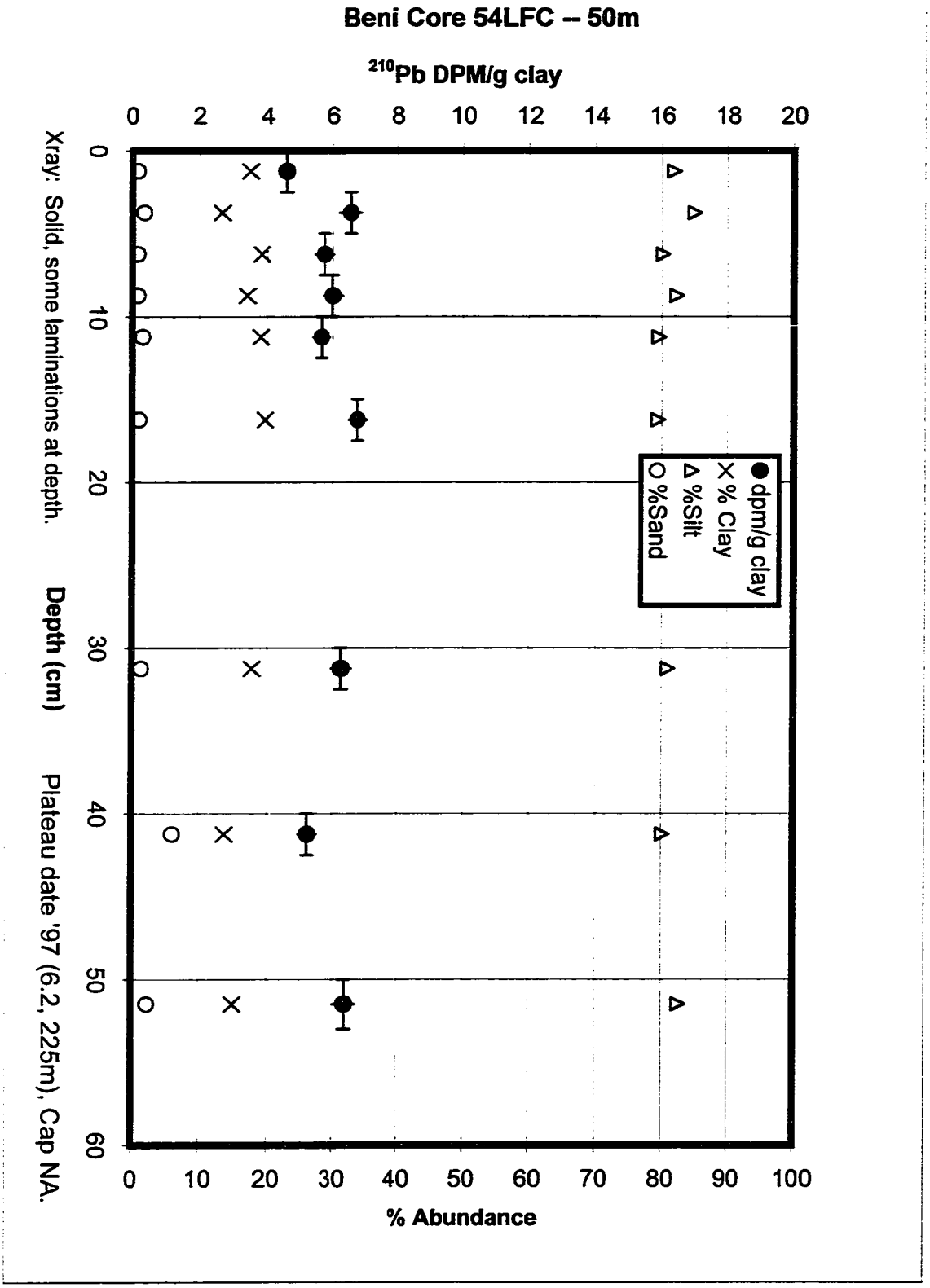
Beni Core 54LFC -- 50m
^{210}Pb DPM/g clay
0 2 4 6 8 10 12 14 16 18 20
Depth (cm)
0 10 20 30 40 50 60
% Abundance
0 10 20 30 40 50 60 70 80 90 100
dpm/g clay
% Clay
%Silt
%Sand
Xray: Solid, some laminations at depth.
Plateau date '97 (6.2, 225m), Cap NA.

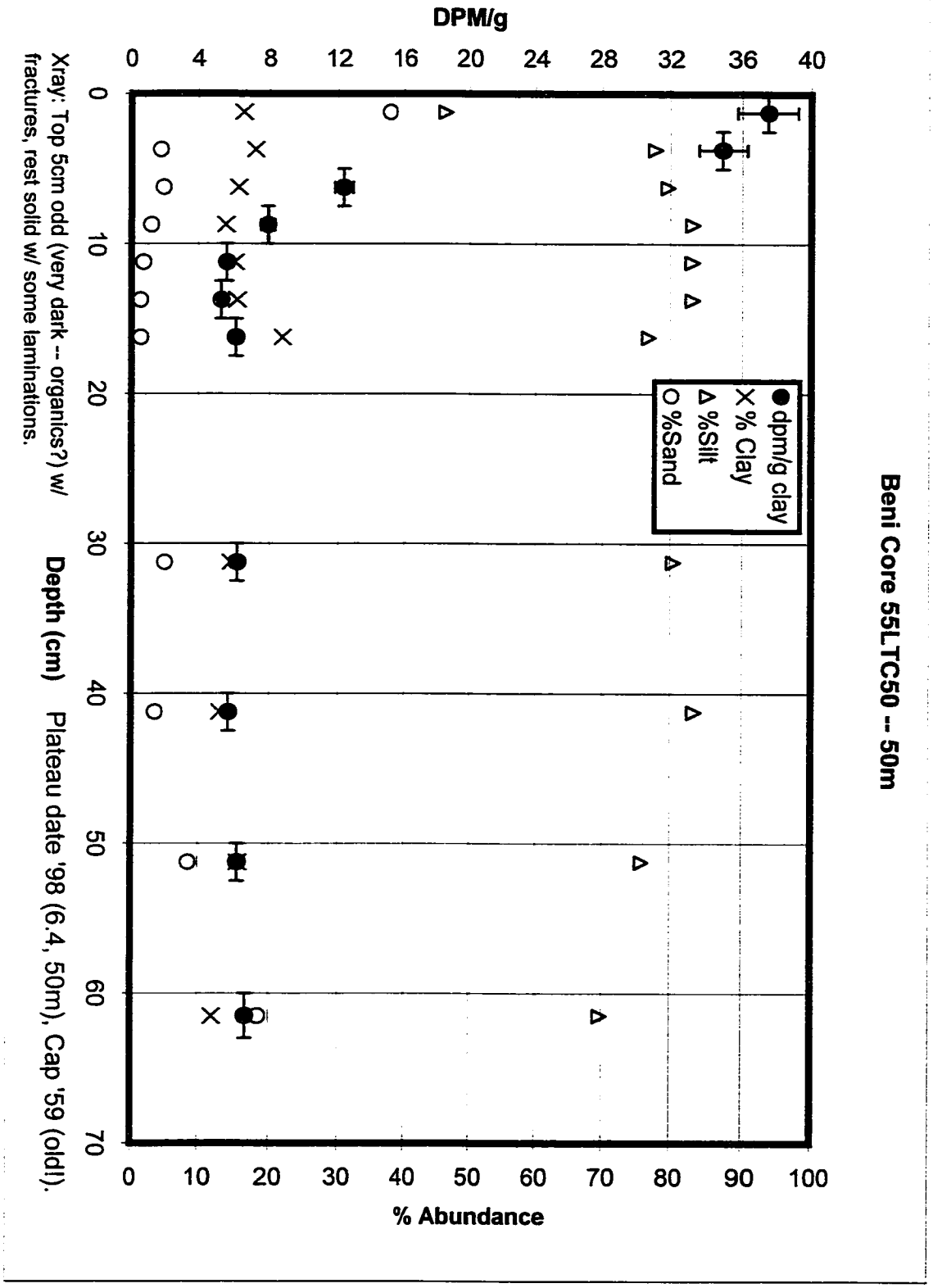
Beni Core 55LTC50 -- 50m
DPM/g
0
4
8
12
16
20
24
28
32
36
40
dpm/g clay
% Clay
%Silt
%Sand
0
10
20
30
40
50
60
70
Depth (cm)
0
10
20
30
40
50
60
70
80
90
100
% Abundance
Xray: Top 5cm odd (very dark -- organics?) w/ fractures, rest solid w/ some laminations.
Plateau date '98 (6.4, 50m), Cap '59 (old!).

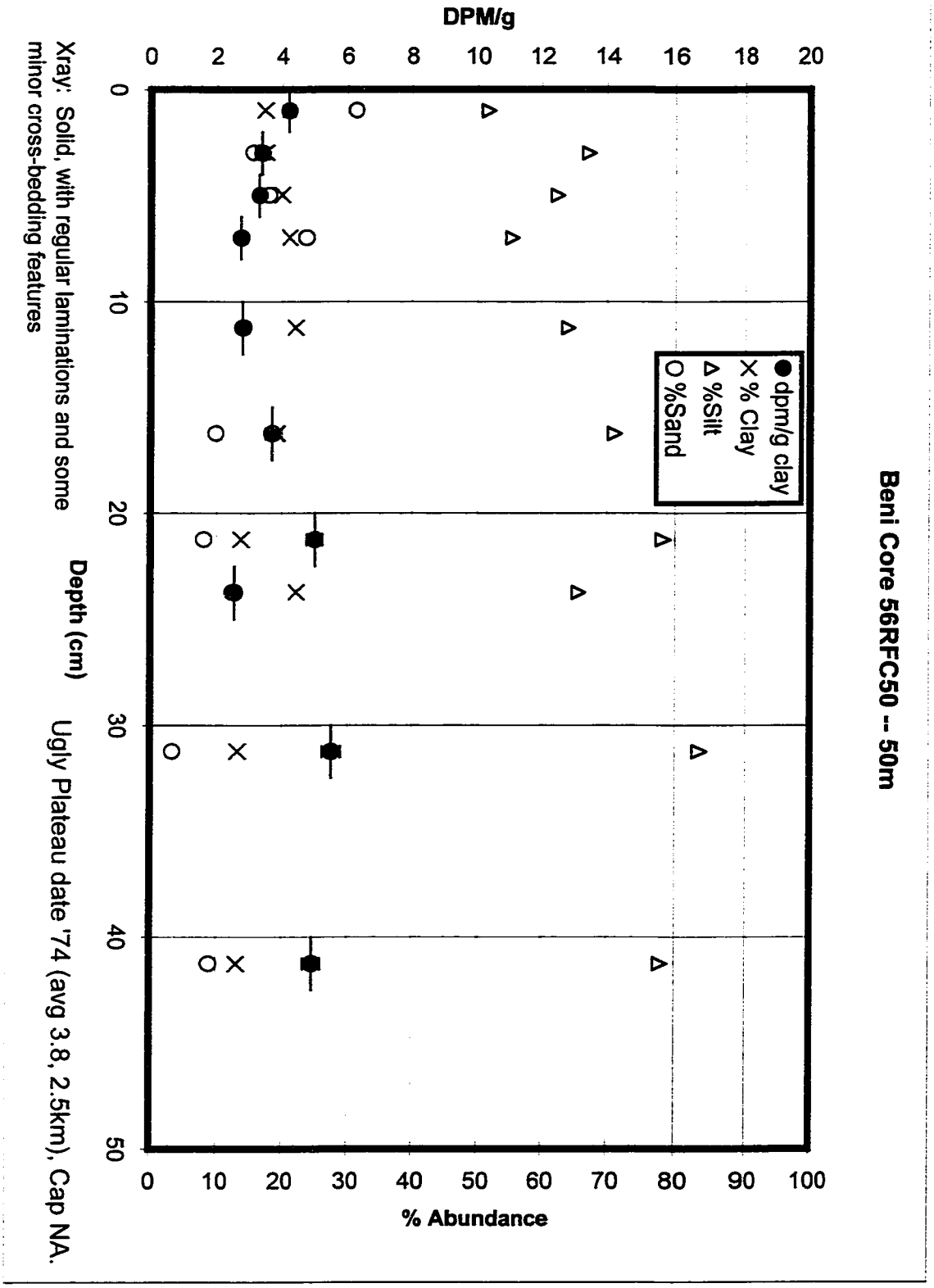
Beni Core 56RFC50 -- 50m
DPM/g
0 2 4 6 8 10 12 14 16 18 20
0 10 20 30 40 50
Depth (cm)
0 10 20 30 40 50 60 70 80 90 100
% Abundance
dpm/g clay
% Clay
%Silt
%Sand
Xray: Solid, with regular laminations and some minor cross-bedding features
Ugly Plateau date '74 (avg 3.8, 2.5km), Cap NA.

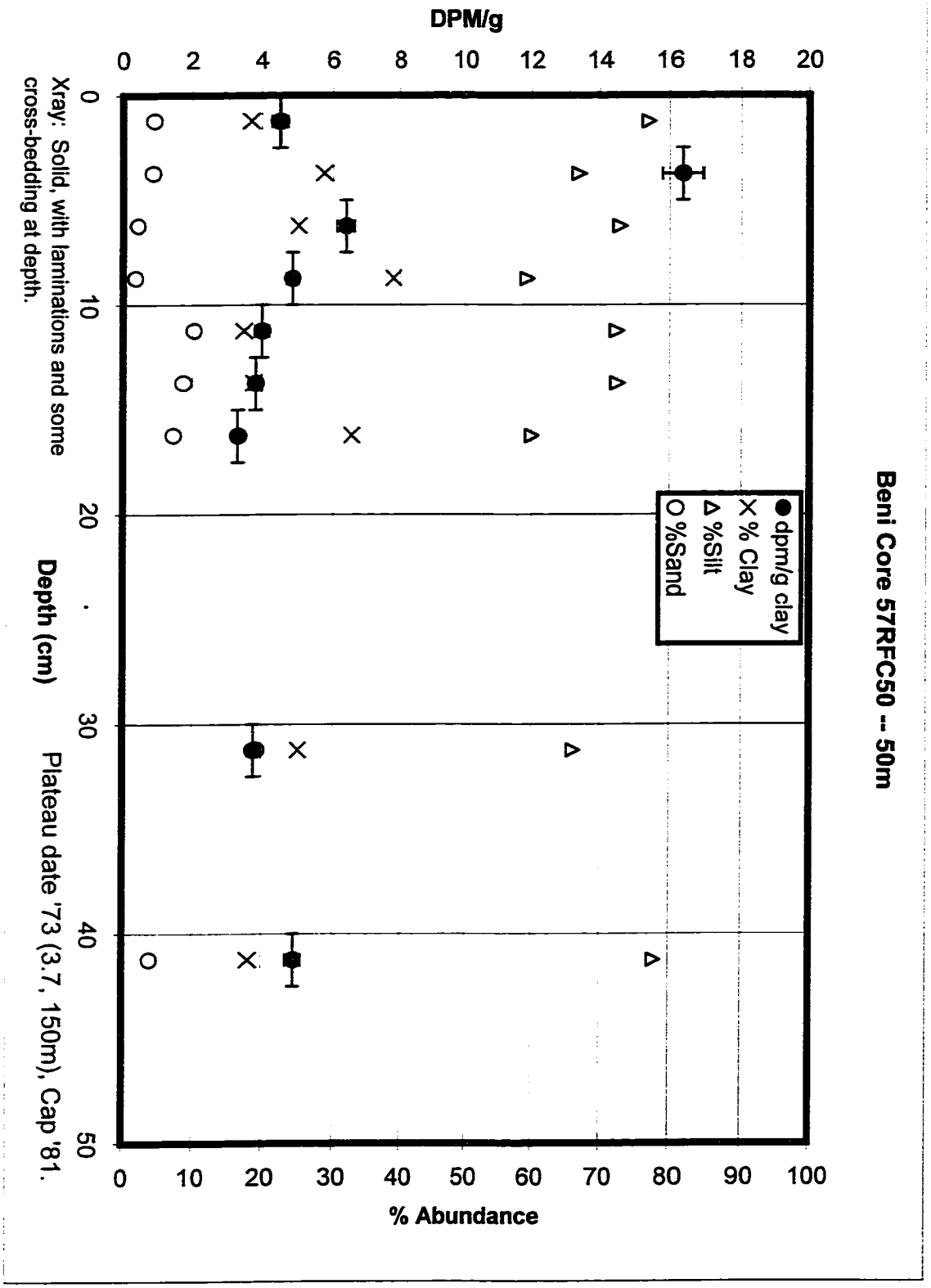
Beni Core 57RFC50 -- 50m
DPM/g
0 2 4 6 8 10 12 14 16 18 20
% Abundance
0 10 20 30 40 50 60 70 80 90 100
Depth (cm)
0 10 20 30 40 50
● dpm/g clay
× % Clay
Δ %Silt
○ %Sand
Xray: Solid, with laminations and some cross-bedding at depth.
Plateau date '73 (3.7, 150m), Cap '81.

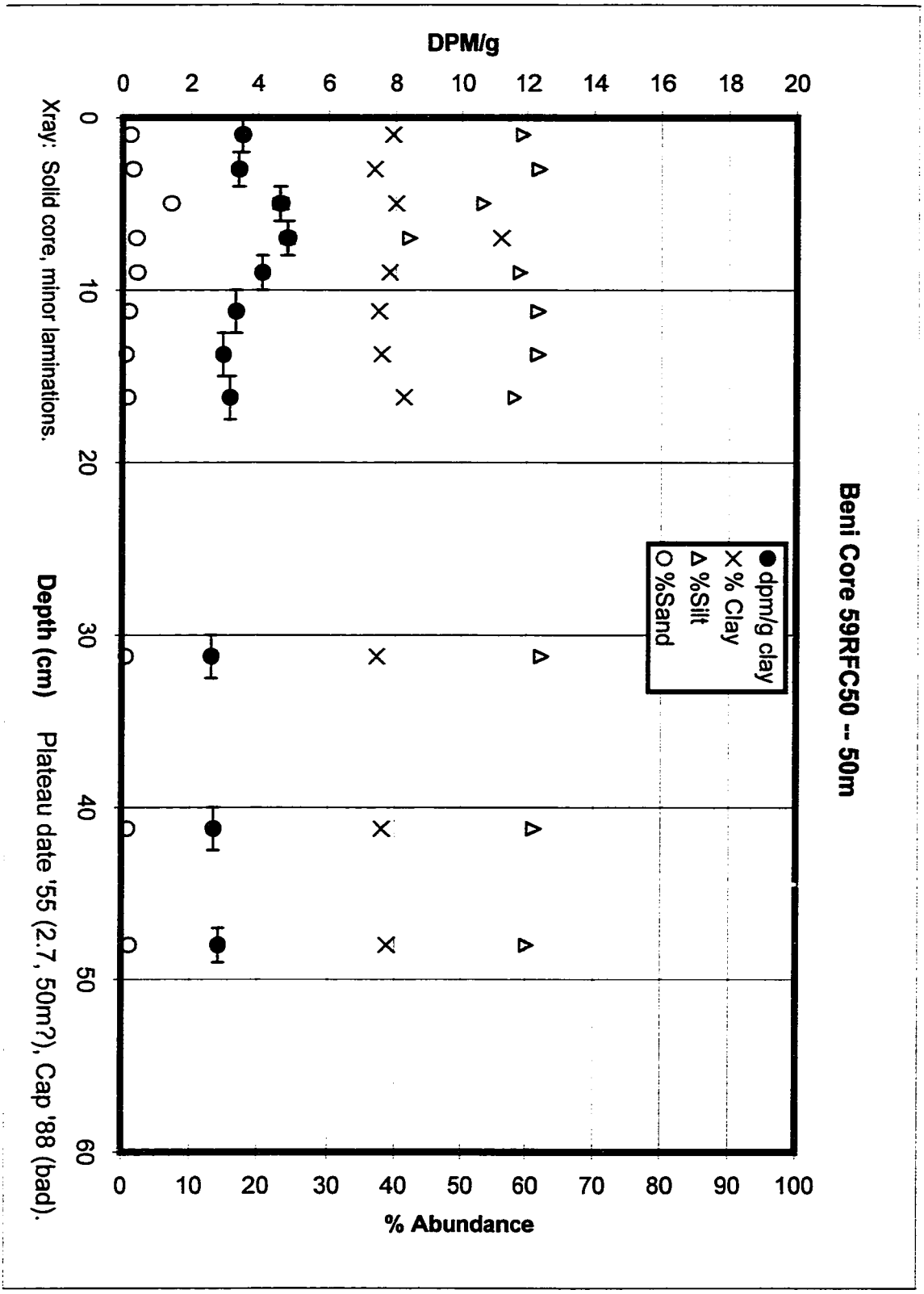
Beni Core 59RFC50 -- 50m
DPM/g
0 2 4 6 8 10 12 14 16 18 20
% Abundance
0 10 20 30 40 50 60 70 80 90 100
Depth (cm)
0 10 20 30 40 50 60
dpm/g clay
% Clay
%Silt
%Sand
Xray: Solid core, minor laminations.
Plateau date '55 (2.7, 50m?), Cap '88 (bad).

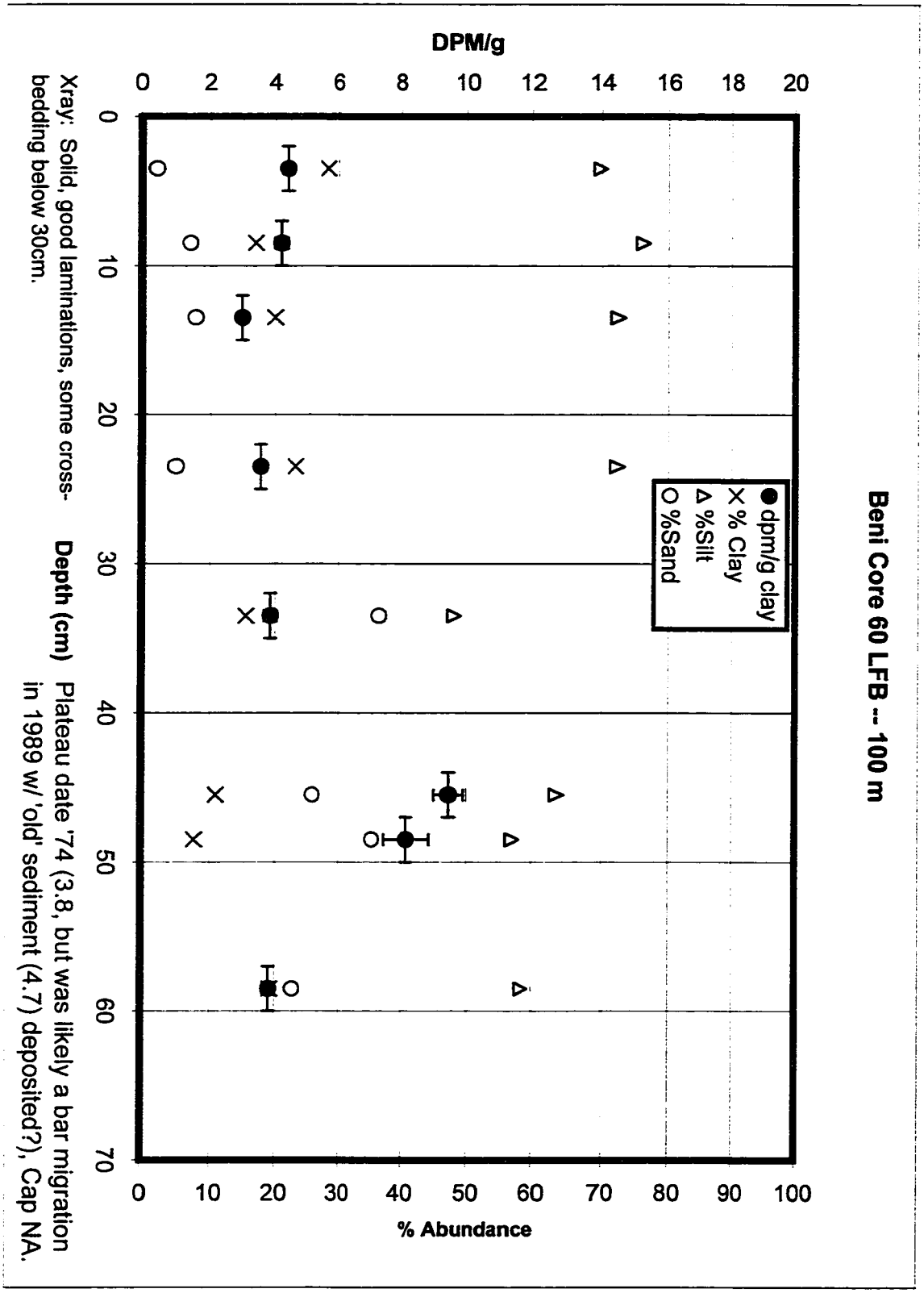

Xray: Solid, good laminations, some cross-bedding below 30cm.

Plateau date '74 (3.8, but was likely a bar migration in 1989 w/ 'old' sediment (4.7) deposited?), Cap NA.

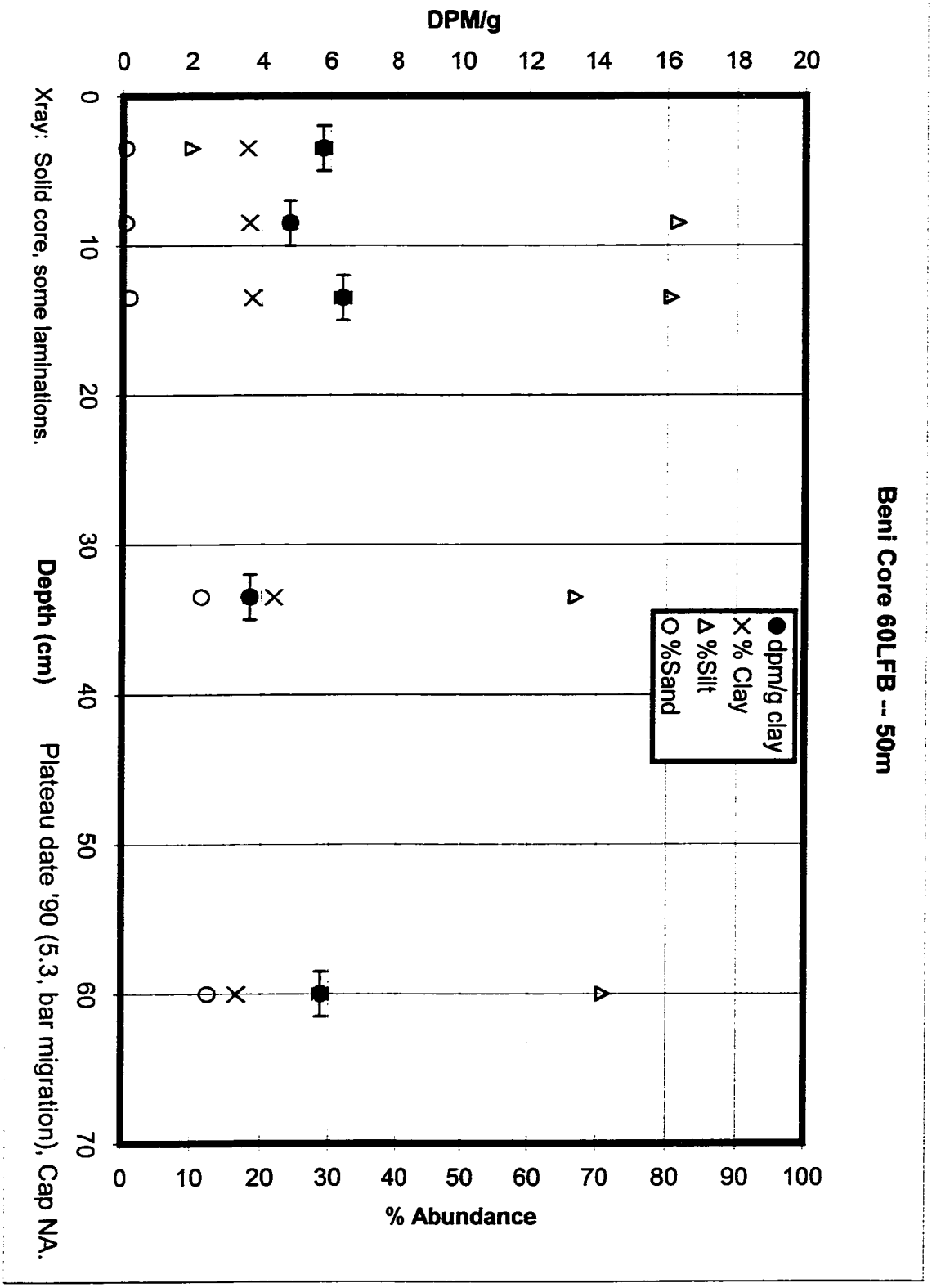
DPM/g
0 2 4 6 8 10 12 14 16 18 20
0 10 20 30 40 50 60 70
Depth (cm)
0 10 20 30 40 50 60 70 80 90 100
% Abundance
dpm/g clay
% Clay
%Silt
%Sand
Beni Core 60LFB -- 50m
Xray: Solid core, some laminations.
Plateau date '90 (5.3, bar migration), Cap NA.

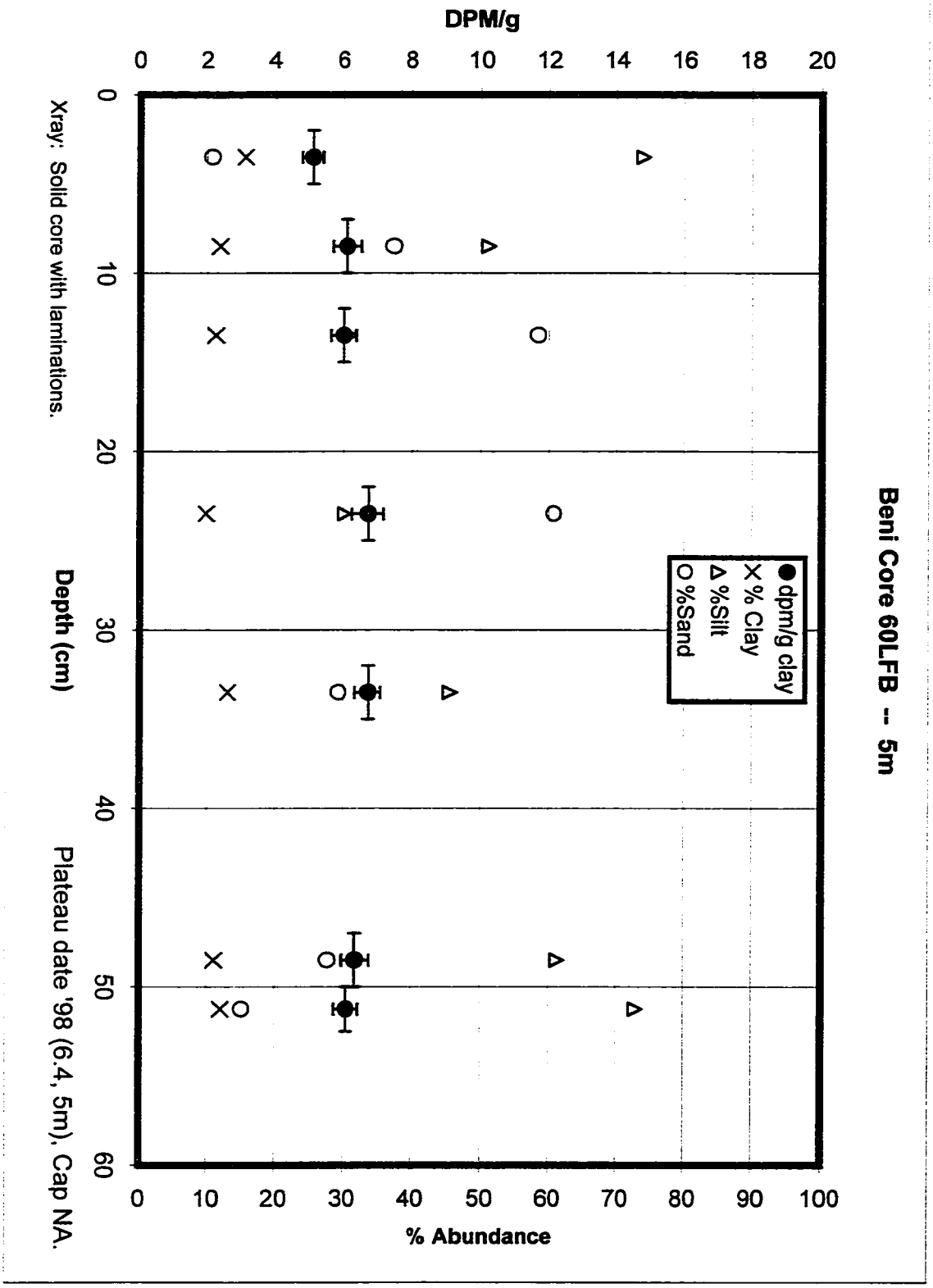
Beni Core 60LFB -- 5m
DPM/g
0 2 4 6 8 10 12 14 16 18 20
Depth (cm)
0 10 20 30 40 50 60
% Abundance
0 10 20 30 40 50 60 70 80 90 100
dpm/g clay
% Clay
%Silt
%Sand
Xray: Solid core with laminations.
Plateau date '98 (6.4, 5m), Cap NA.

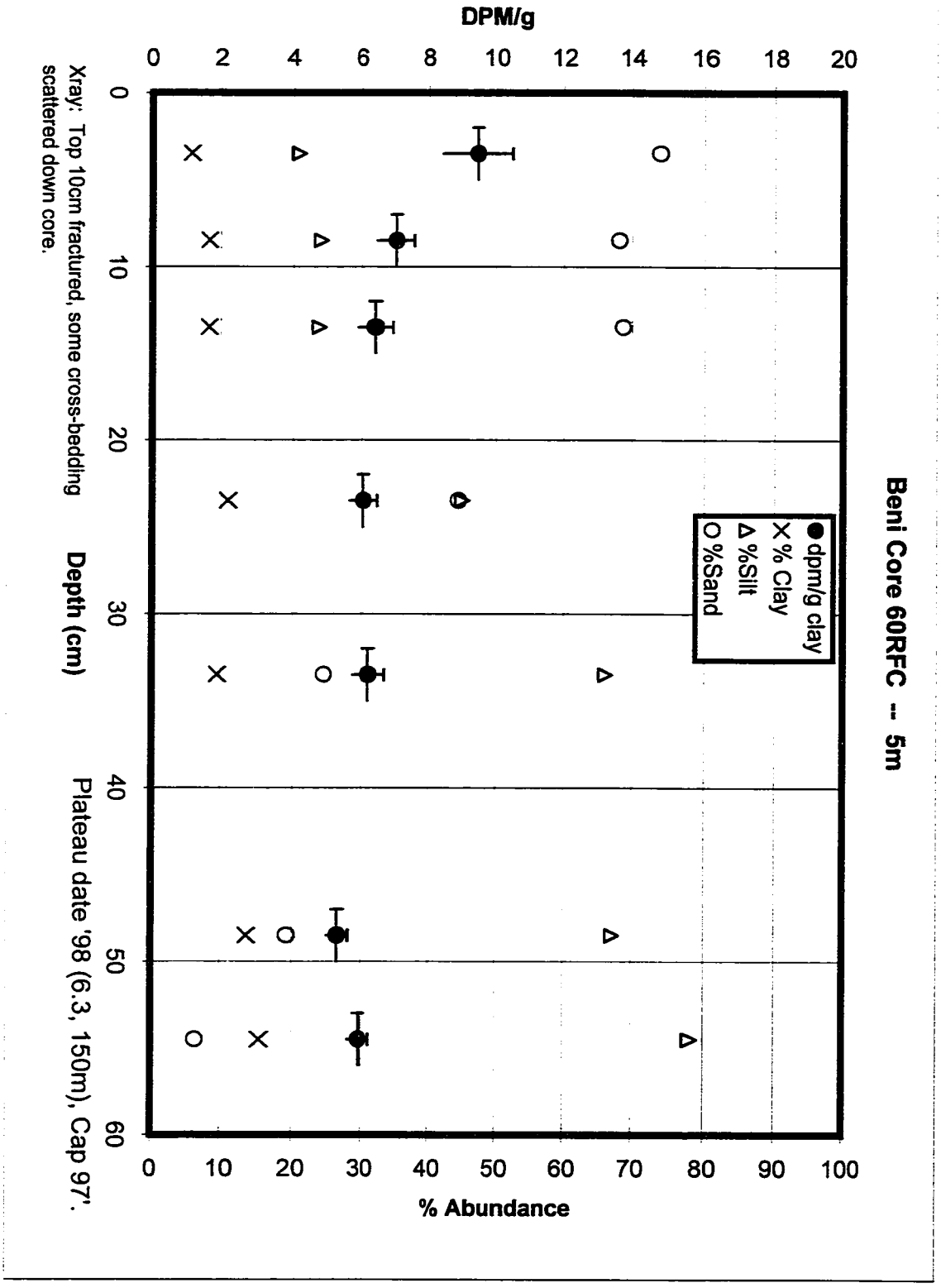
Beni Core 60RFC -- 5m
DPM/g
0 2 4 6 8 10 12 14 16 18 20
0 10 20 30 40 50 60
Depth (cm)
0 10 20 30 40 50 60 70 80 90 100
% Abundance
● dpm/g clay
× % Clay
Δ %Silt
○ %Sand
Xray: Top 10cm fractured, some cross-bedding scattered down core.
Plateau date '98 (6.3, 150m), Cap 97'.

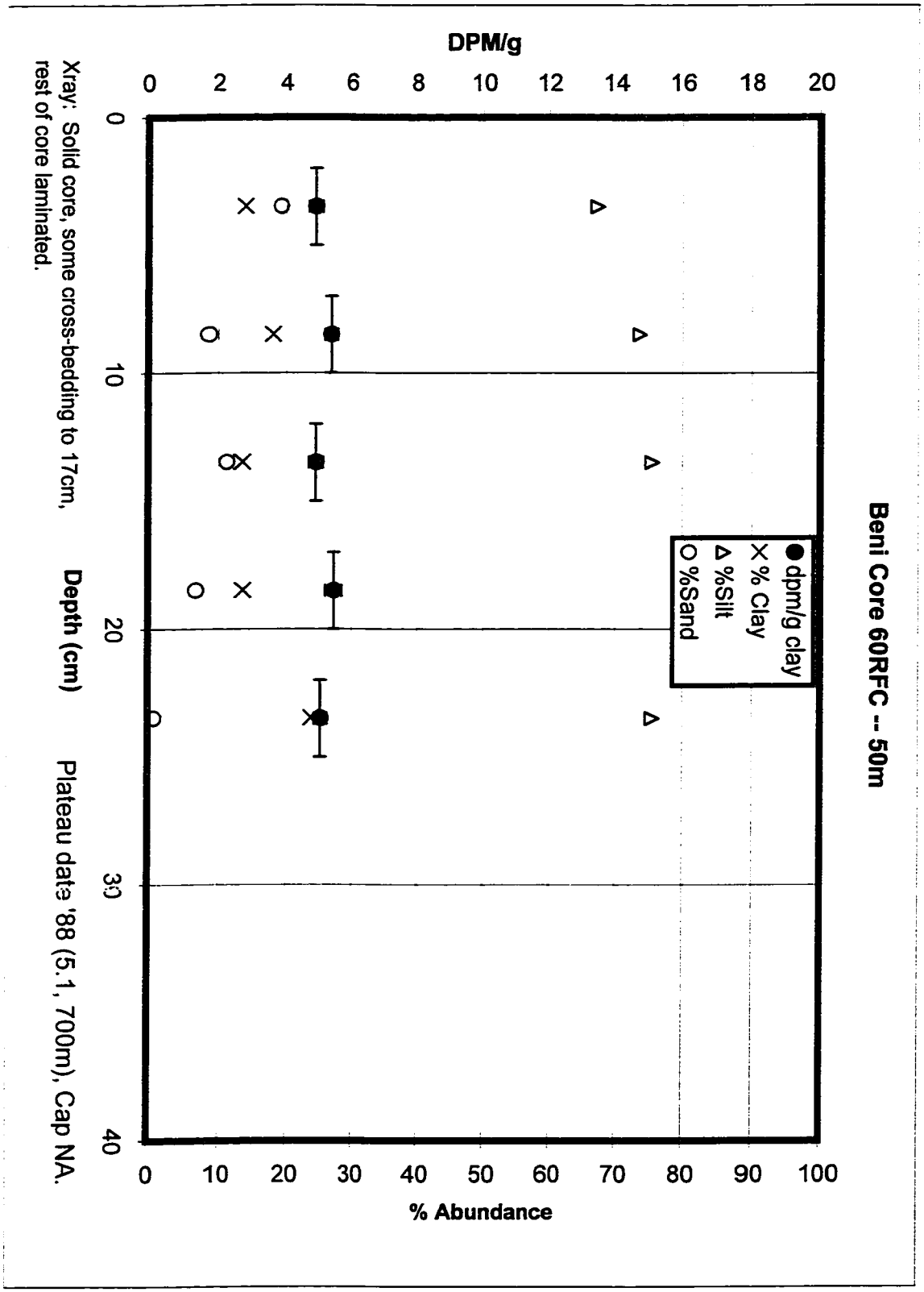
Beni Core 60RFC -- 50m
DPM/g
0 2 4 6 8 10 12 14 16 18 20
0 10 20 30 40
Depth (cm)
0 10 20 30 40 50 60 70 80 90 100
% Abundance
● dpm/g clay
× % Clay
Δ %Silt
○ %Sand
Xray: Solid core, some cross-bedding to 17cm, rest of core laminated.
Plateau date '88 (5.1, 700m), Cap NA.

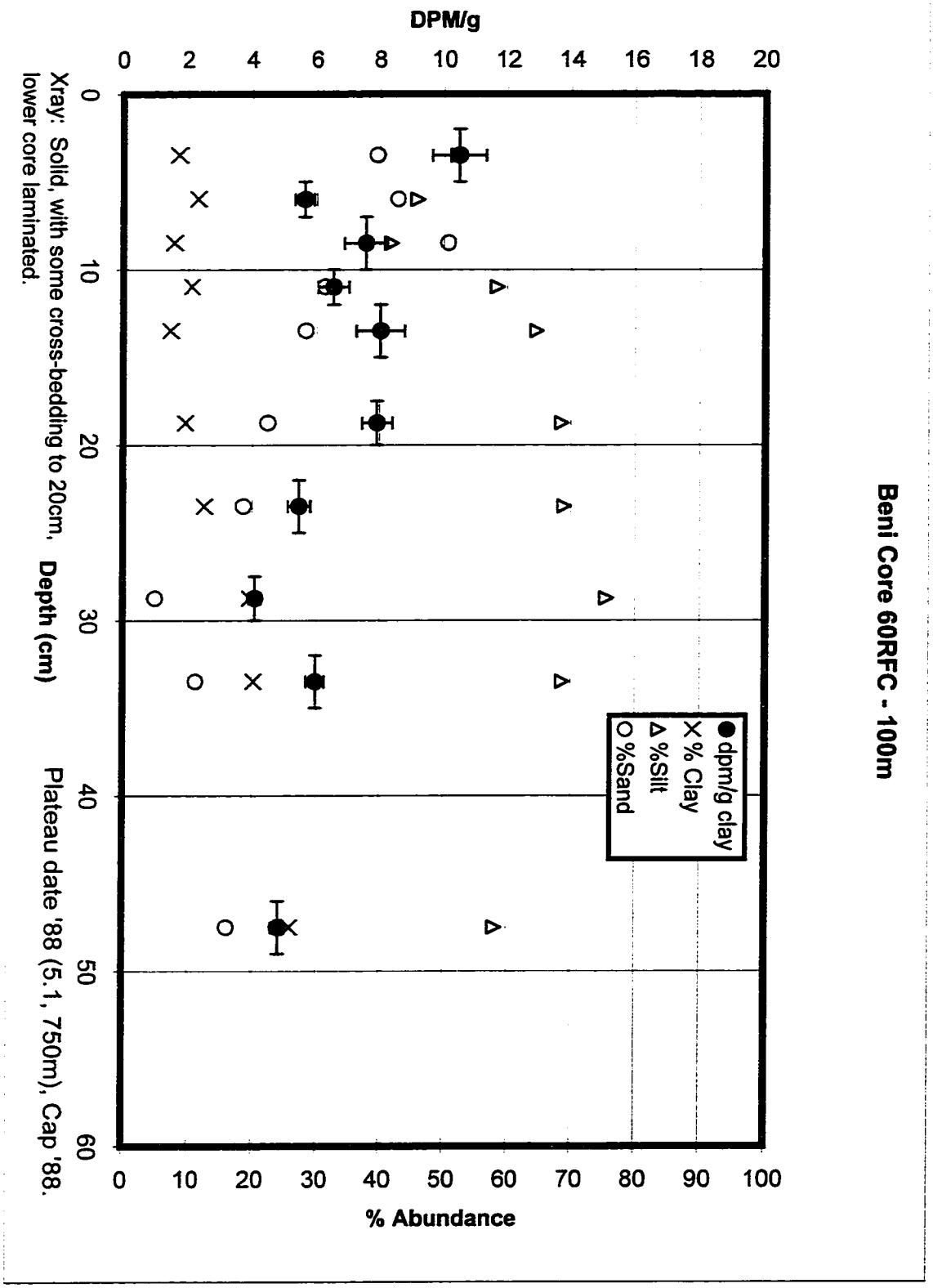
Beni Core 60RFC - 100m
DPM/g
0 2 4 6 8 10 12 14 16 18 20
Depth (cm)
0 10 20 30 40 50 60
% Abundance
0 10 20 30 40 50 60 70 80 90 100
● dpm/g clay
× % Clay
Δ %Silt
○ %Sand
Xray: Solid, with some cross-bedding to 20cm, lower core laminated.
Plateau date '88 (5.1, 750m), Cap '88.

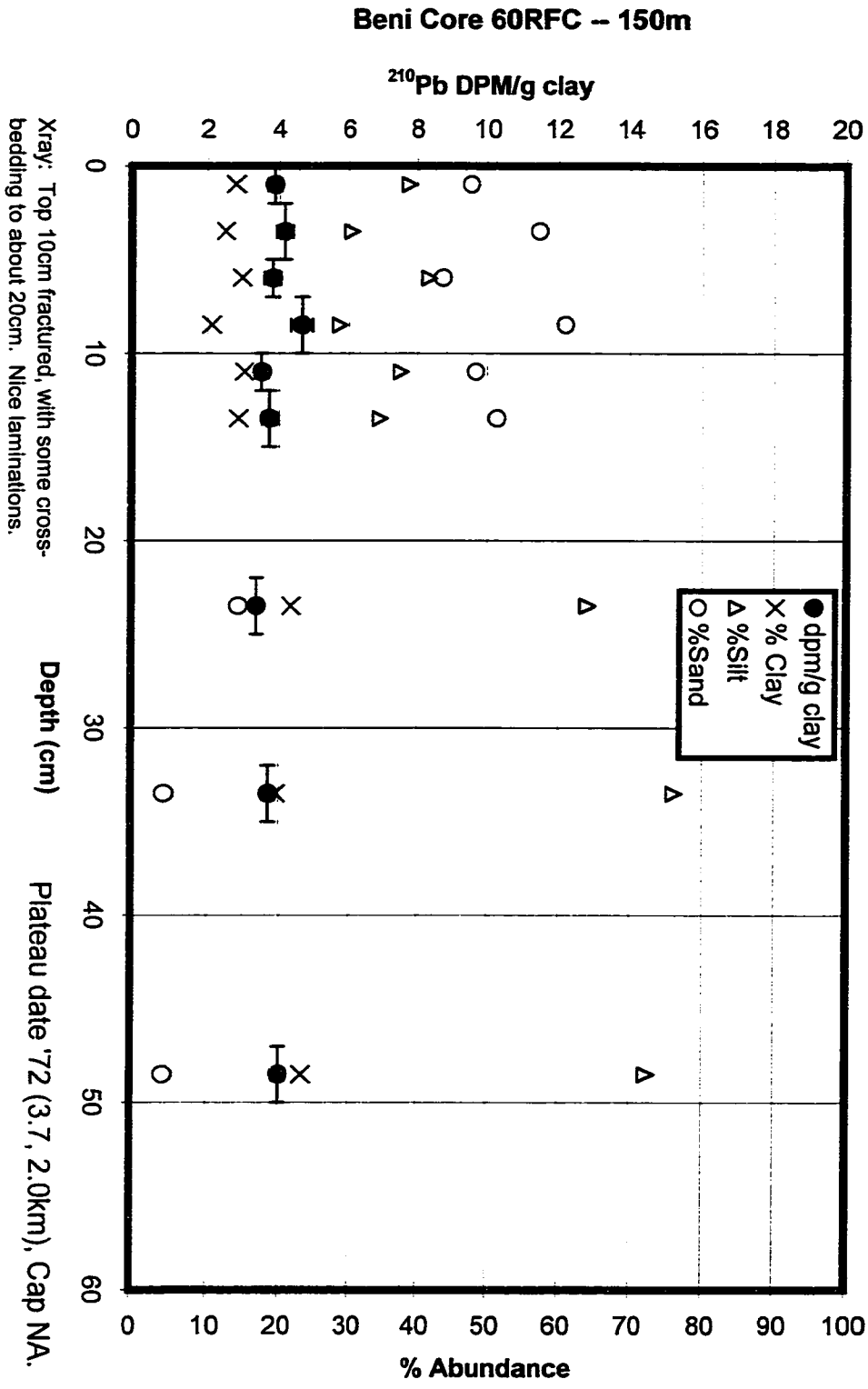
Beni Core 60RFC -- 150m
^{210}Pb DPM/g clay
0 2 4 6 8 10 12 14 16 18 20
Xray: Top 10cm fractured, with some cross-bedding to about 20cm. Nice laminations.
Depth (cm)
0 10 20 30 40 50 60
dpm/g clay
% Clay
%Silt
%Sand
0 10 20 30 40 50 60 70 80 90 100
% Abundance
Plateau date '72 (3.7, 2.0km), Cap NA.

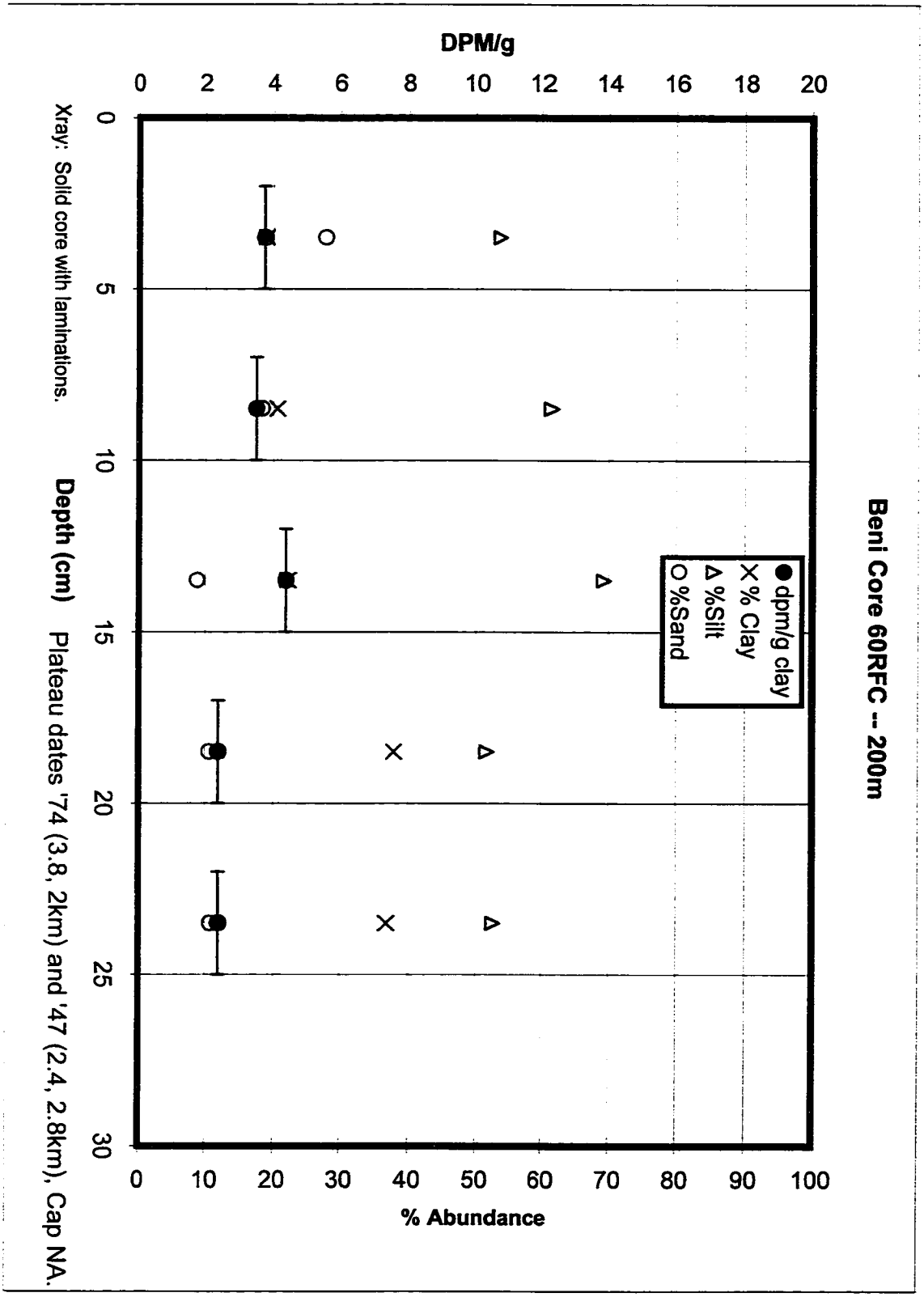
Beni Core 60RFC -- 200m
DPM/g
0 2 4 6 8 10 12 14 16 18 20
0 5 10 15 20 25 30
Depth (cm)
0 10 20 30 40 50 60 70 80 90 100
% Abundance
● dpm/g clay
× % Clay
Δ %Silt
○ %Sand
Xray: Solid core with laminations.
Plateau dates '74 (3.8, 2km) and '47 (2.4, 2.8km), Cap NA.

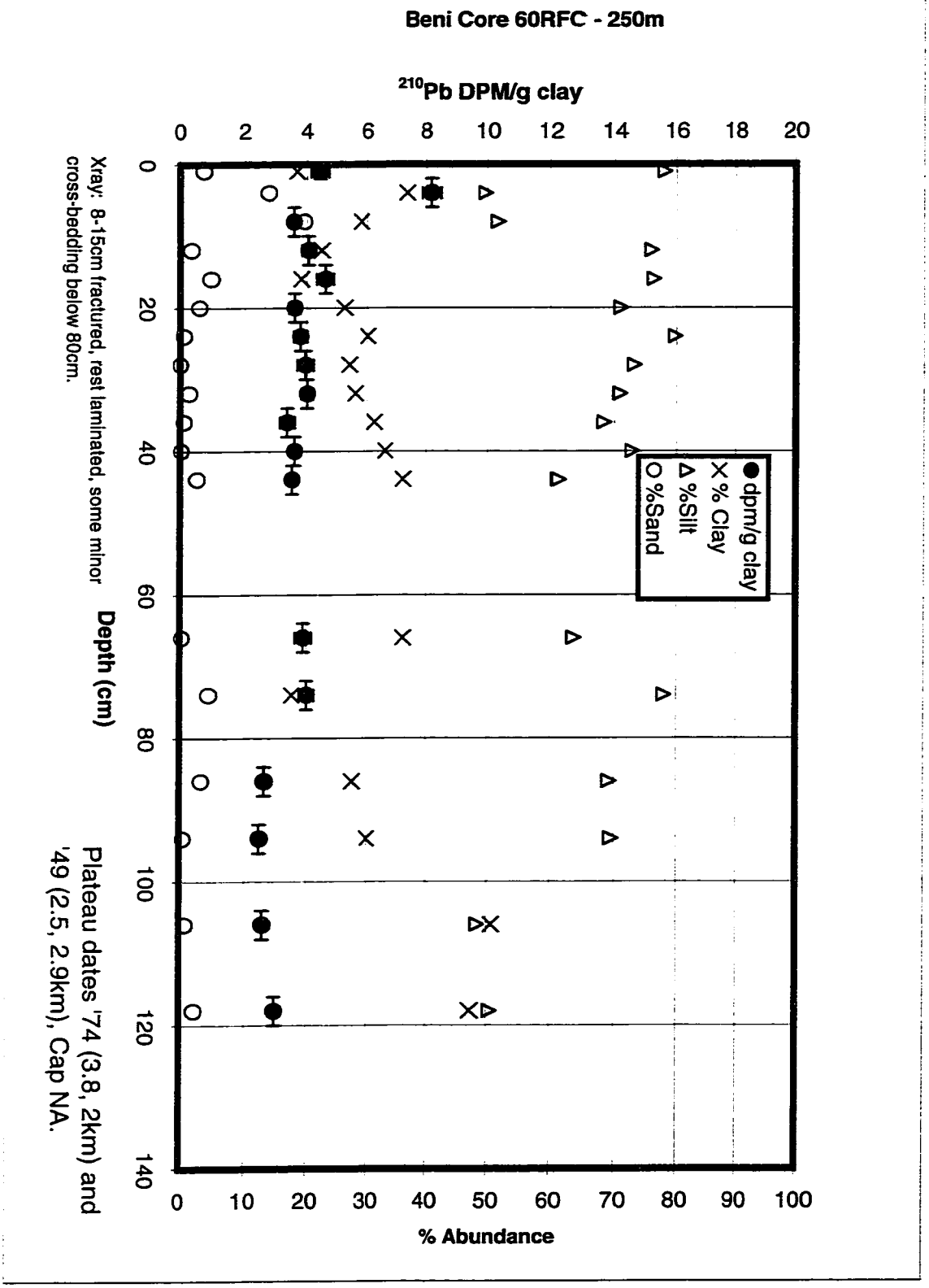
Beni Core 60RFC - 250m
^{210}Pb DPM/g clay
0 2 4 6 8 10 12 14 16 18 20
0 20 40 60 80 100 120 140
Depth (cm)
0 10 20 30 40 50 60 70 80 90 100
% Abundance
dpm/g clay
% Clay
%Silt
%Sand
Xray: 8-15cm fractured, rest laminated, some minor cross-bedding below 80cm.
Plateau dates '74 (3.8, 2km) and '49 (2.5, 2.9km), Cap NA.

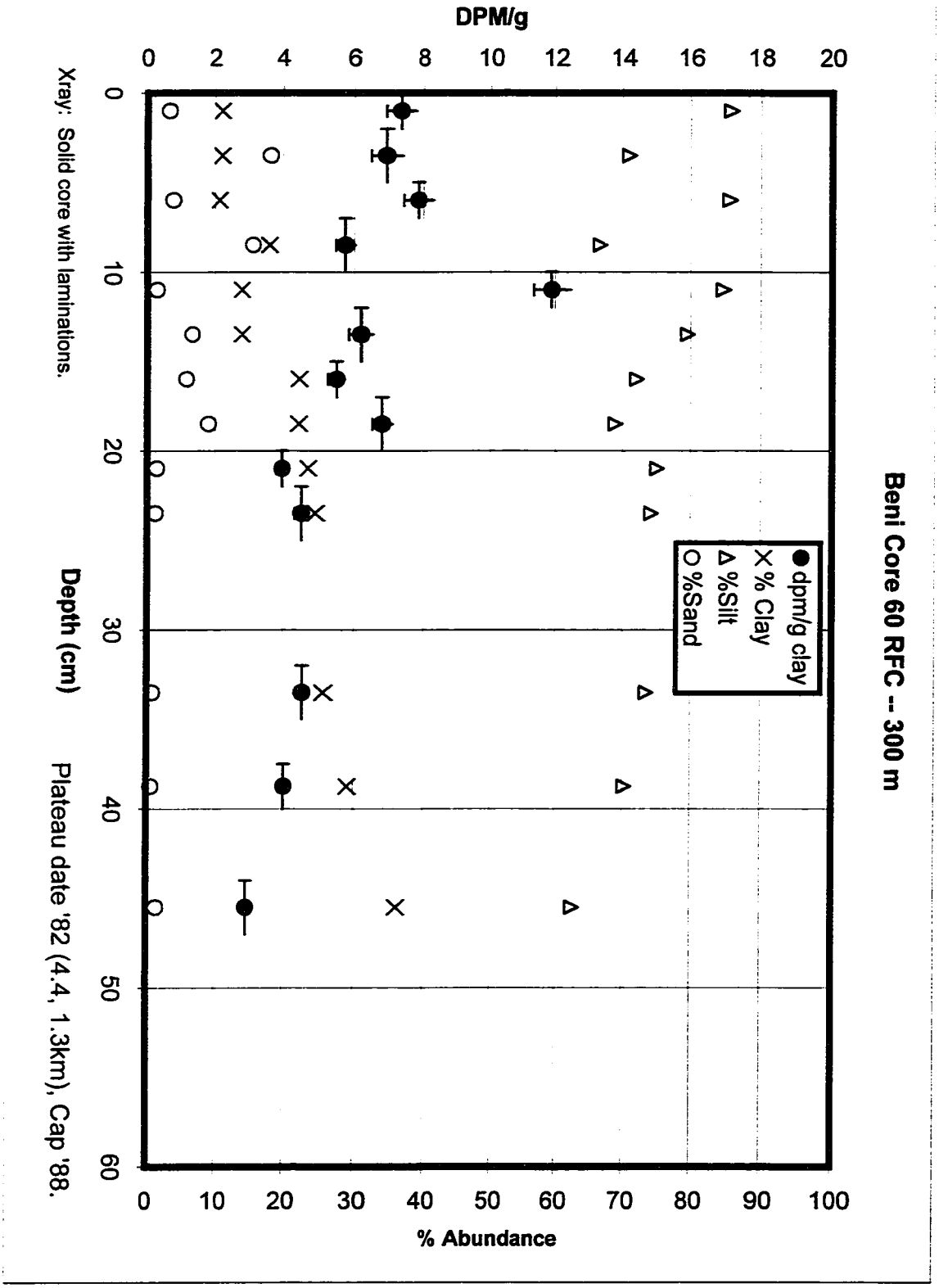
Beni Core 60 RFC -- 300 m
DPM/g
0 2 4 6 8 10 12 14 16 18 20
% Abundance
0 10 20 30 40 50 60 70 80 90 100
Depth (cm)
0 10 20 30 40 50 60
dpm/g clay
% Clay
%Silt
%Sand
Xray: Solid core with laminations.
Plateau date '82 (4.4, 1.3km), Cap '88.

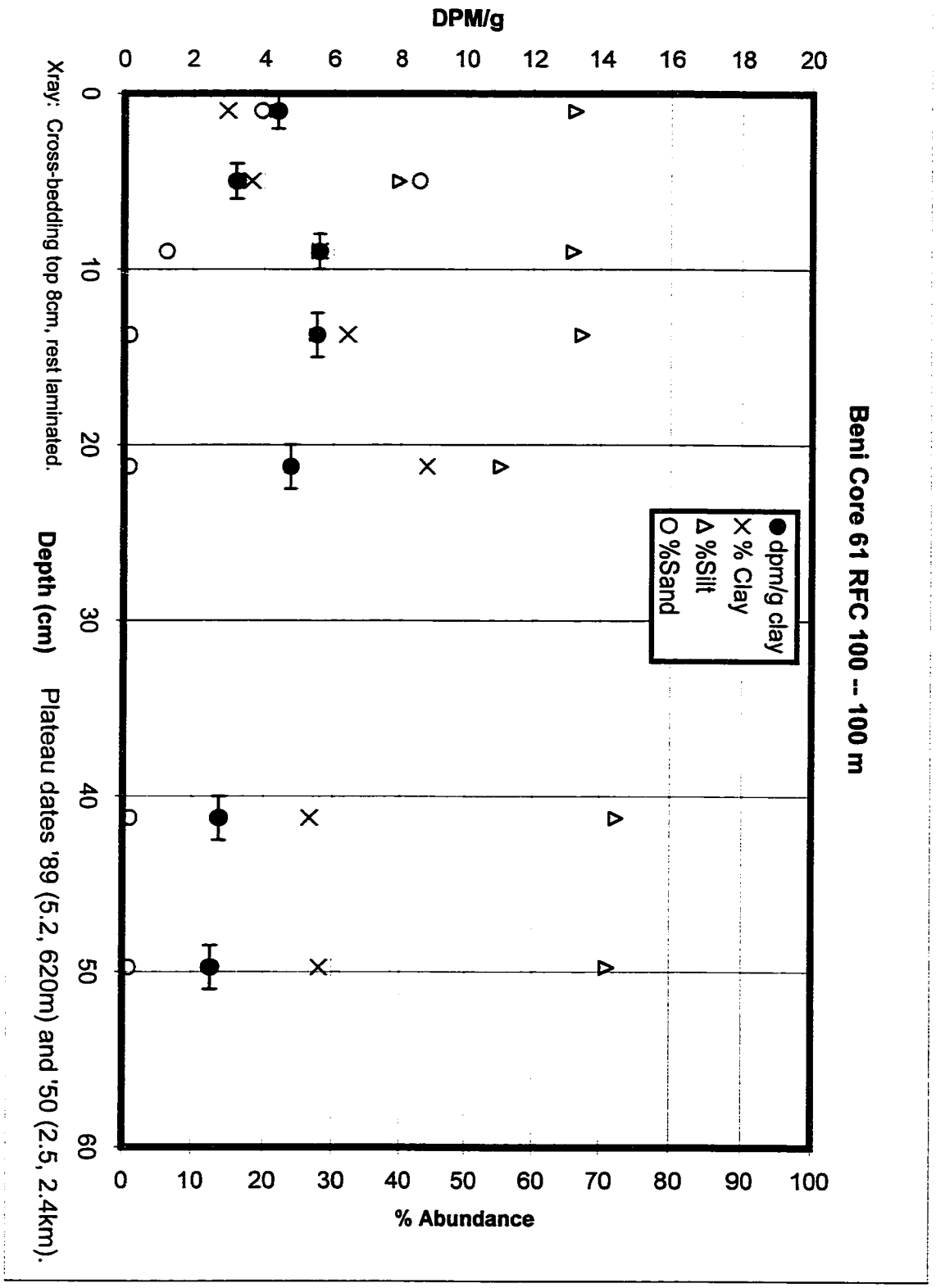
Beni Core 61 RFC 100 -- 100 m
DPM/g
0 2 4 6 8 10 12 14 16 18 20
% Abundance
0 10 20 30 40 50 60 70 80 90 100
Depth (cm)
0 10 20 30 40 50 60
● dpm/g clay
× % Clay
Δ %Silt
○ %Sand
Xray: Cross-bedding top 8cm, rest laminated.
Plateau dates '89 (5.2, 620m) and '50 (2.5, 2.4km).

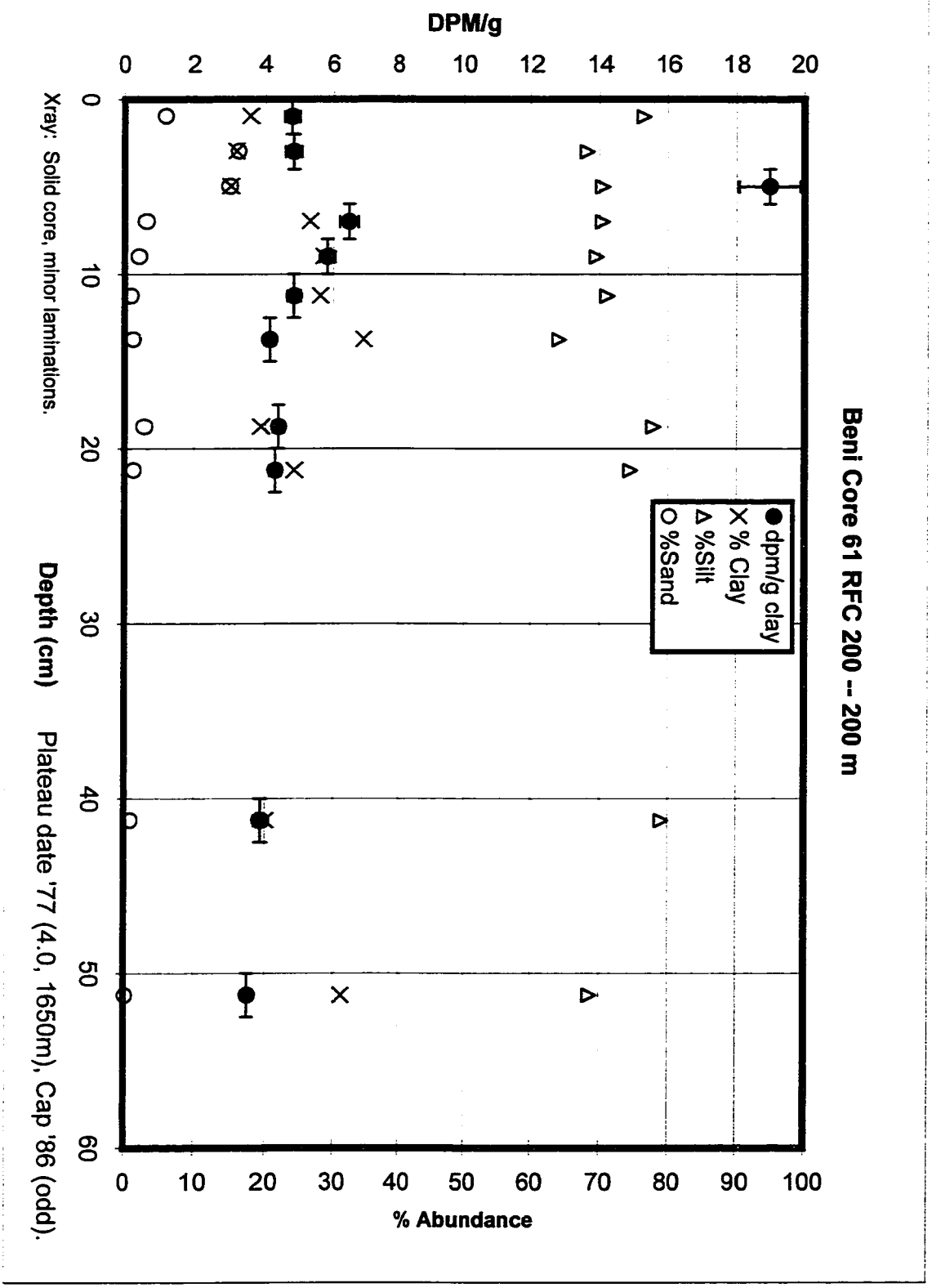
Beni Core 61 RFC 200 -- 200 m
DPM/g
0 2 4 6 8 10 12 14 16 18 20
% Abundance
0 10 20 30 40 50 60 70 80 90 100
Depth (cm)
0 10 20 30 40 50 60
dpm/g clay
% Clay
%Silt
%Sand
Xray: Solid core, minor laminations.
Plateau date '77 (4.0, 1650m), Cap '86 (odd).

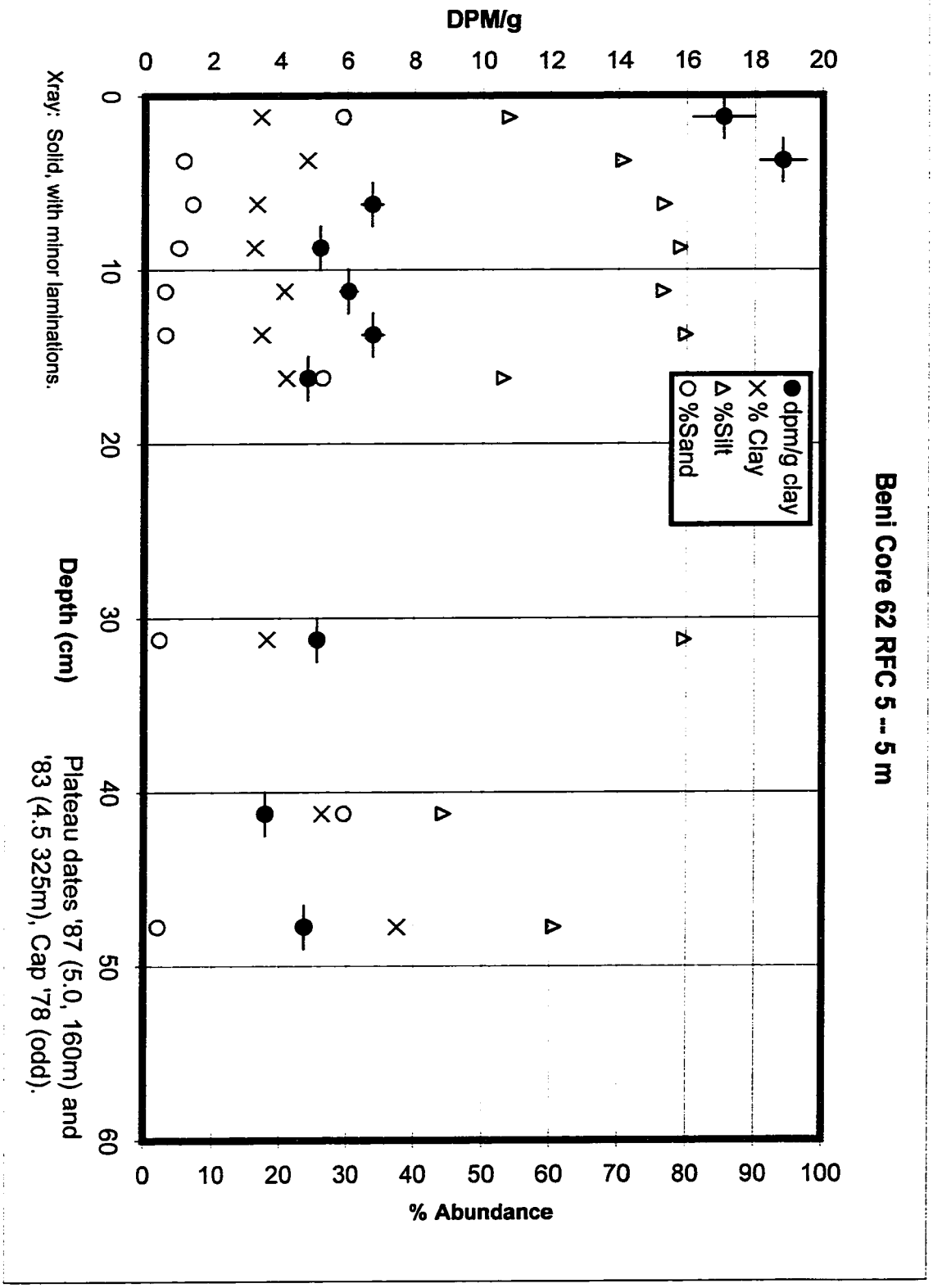
Beni Core 62 RFC 5 -- 5 m
DPM/g
0 2 4 6 8 10 12 14 16 18 20
Depth (cm)
0 10 20 30 40 50 60
% Abundance
0 10 20 30 40 50 60 70 80 90 100
dpm/g clay
% Clay
%Silt
%Sand
Xray: Solid, with minor laminations.
Plateau dates '87 (5.0, 160m) and '83 (4.5 325m), Cap '78 (odd).

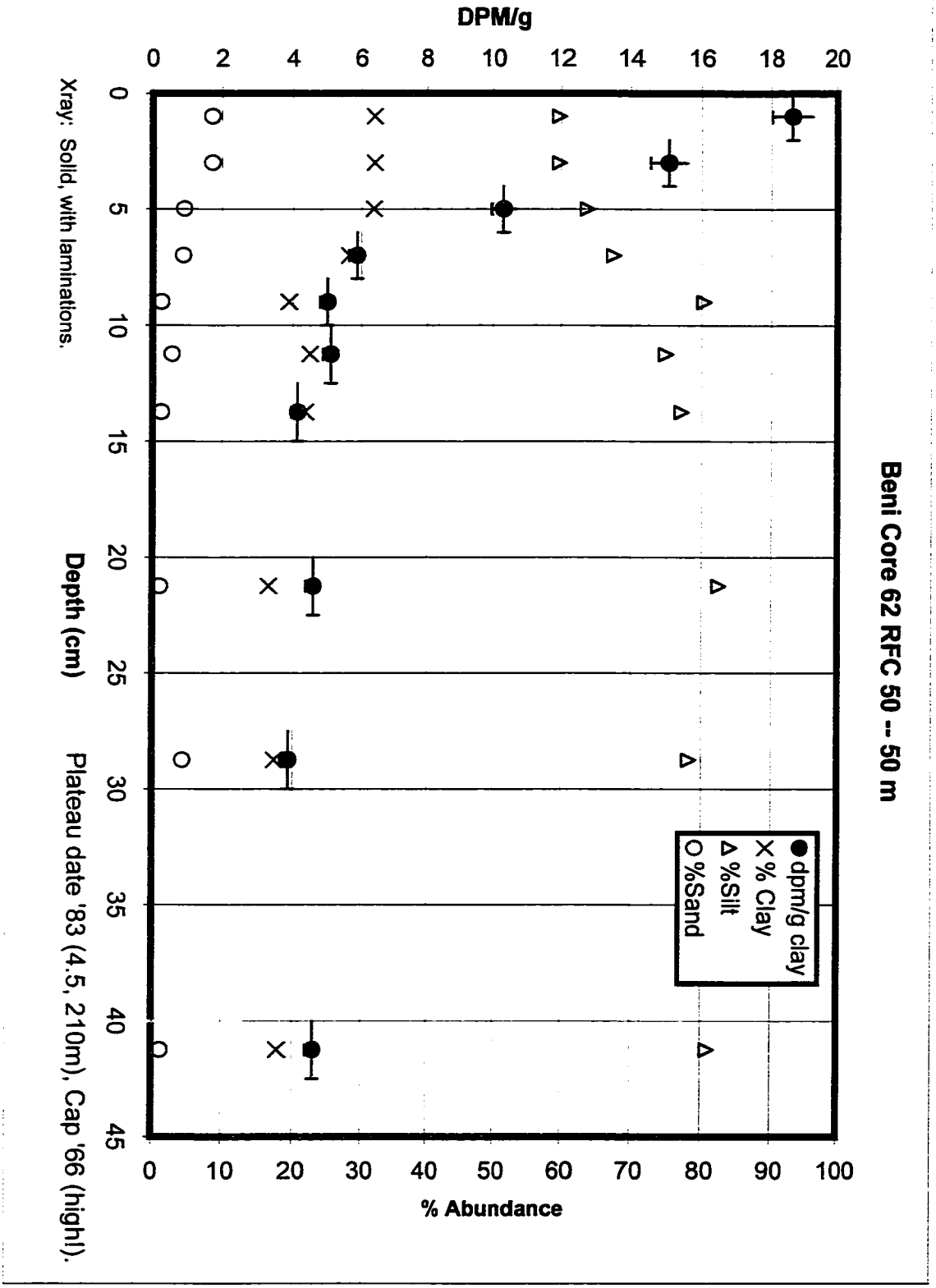
Beni Core 62 RFC 50 -- 50 m
DPM/g
0 2 4 6 8 10 12 14 16 18 20
Depth (cm)
0 5 10 15 20 25 30 35 40 45
% Abundance
0 10 20 30 40 50 60 70 80 90 100
● dpm/g clay
X % Clay
Δ %Silt
O %Sand
Xray: Solid, with laminations.
Plateau date '83 (4.5, 210m), Cap '66 (highl).

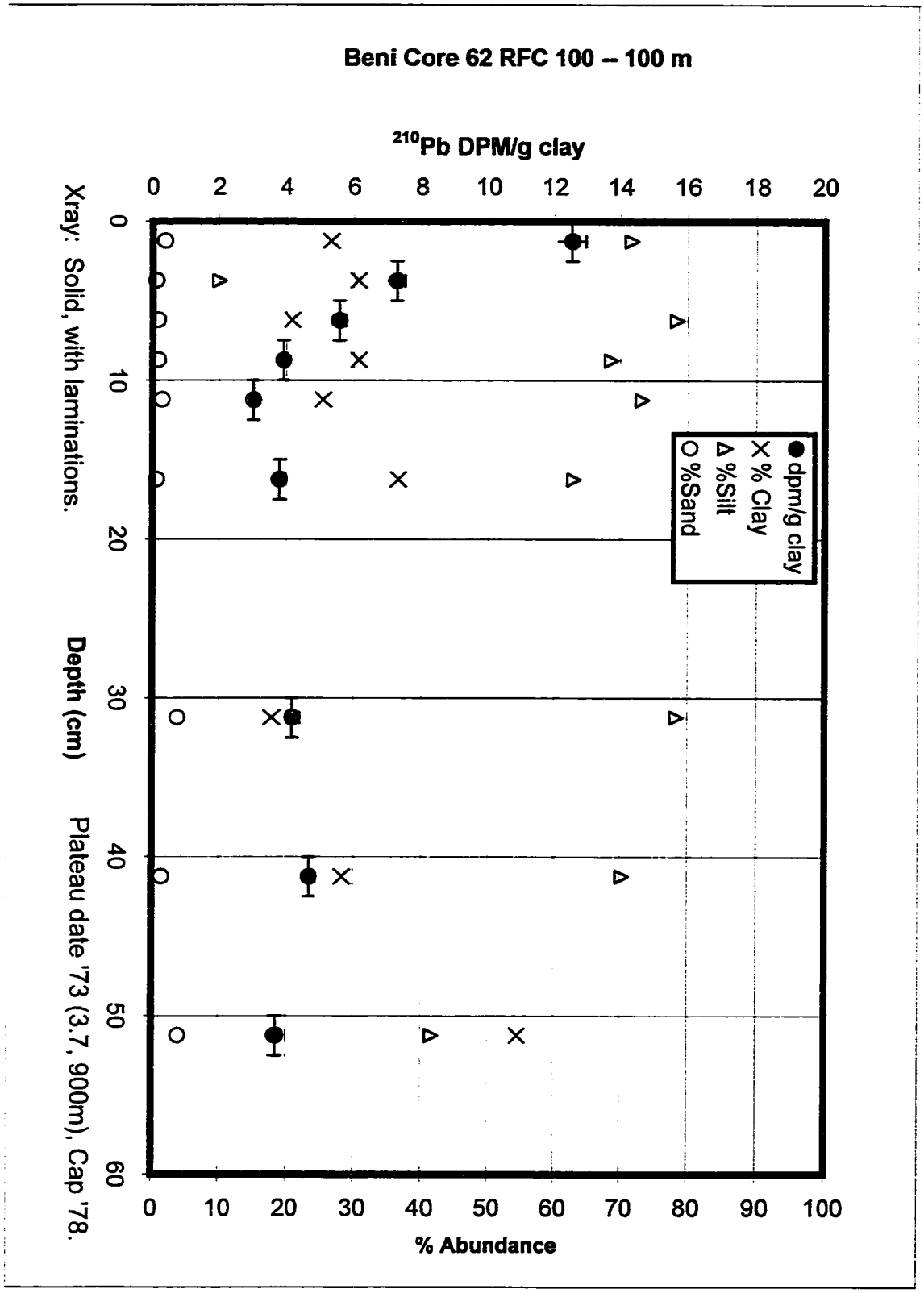
Beni Core 62 RFC 100 -- 100 m
^{210}Pb DPM/g clay
0 2 4 6 8 10 12 14 16 18 20
Depth (cm)
0 10 20 30 40 50 60
% Abundance
0 10 20 30 40 50 60 70 80 90 100
dpm/g clay
% Clay
%Silt
%Sand
Xray: Solid, with laminations.
Plateau date '73 (3.7, 900m), Cap '78.

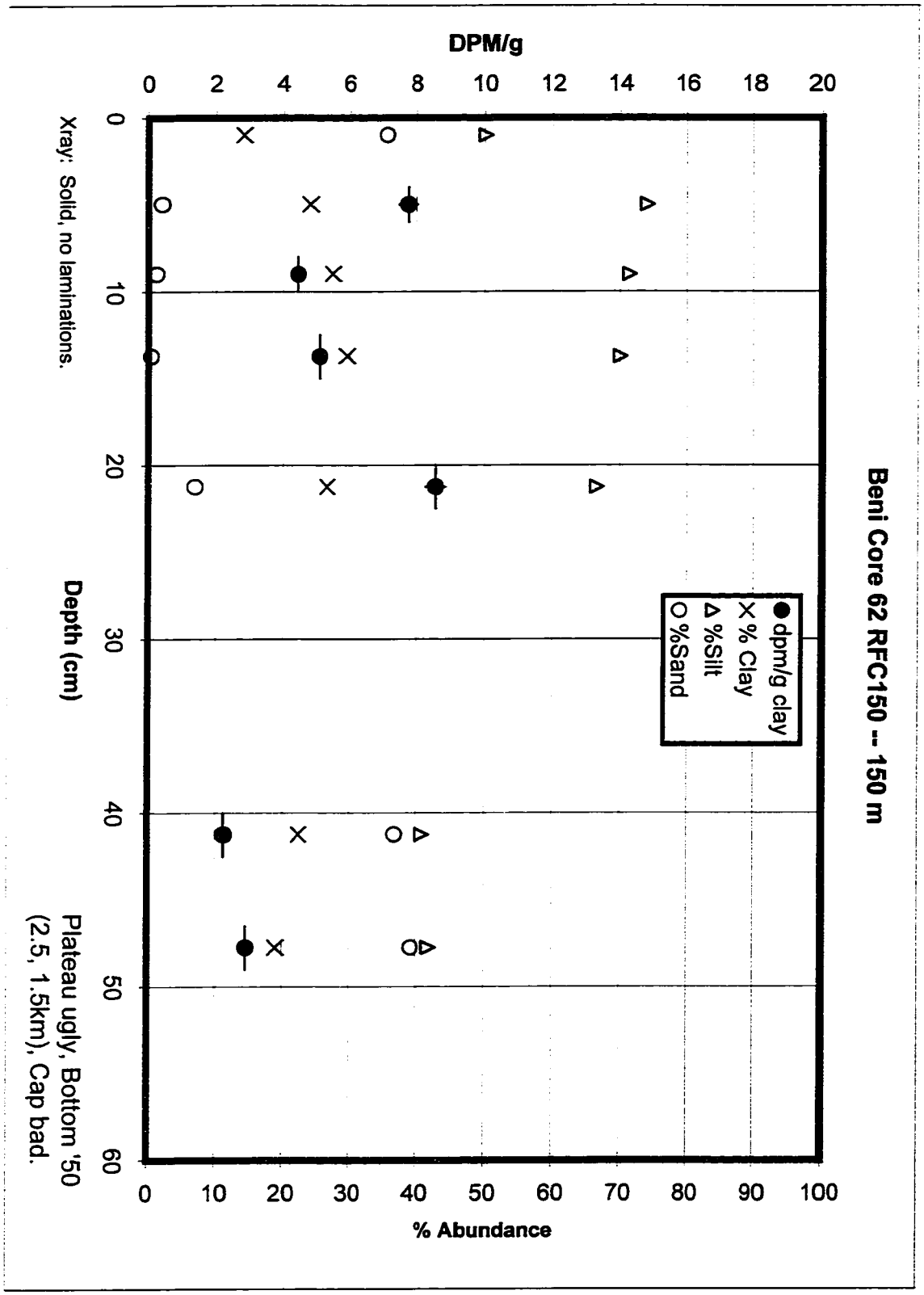
DPM/g
0 2 4 6 8 10 12 14 16 18 20
Depth (cm)
0 10 20 30 40 50 60
% Abundance
0 10 20 30 40 50 60 70 80 90 100
● dpm/g clay
× % Clay
Δ %Silt
○ %Sand
Beni Core 62 RFC150 -- 150 m
Xray: Solid, no laminations.
Plateau ugly, Bottom '50
(2.5, 1.5km), Cap bad.

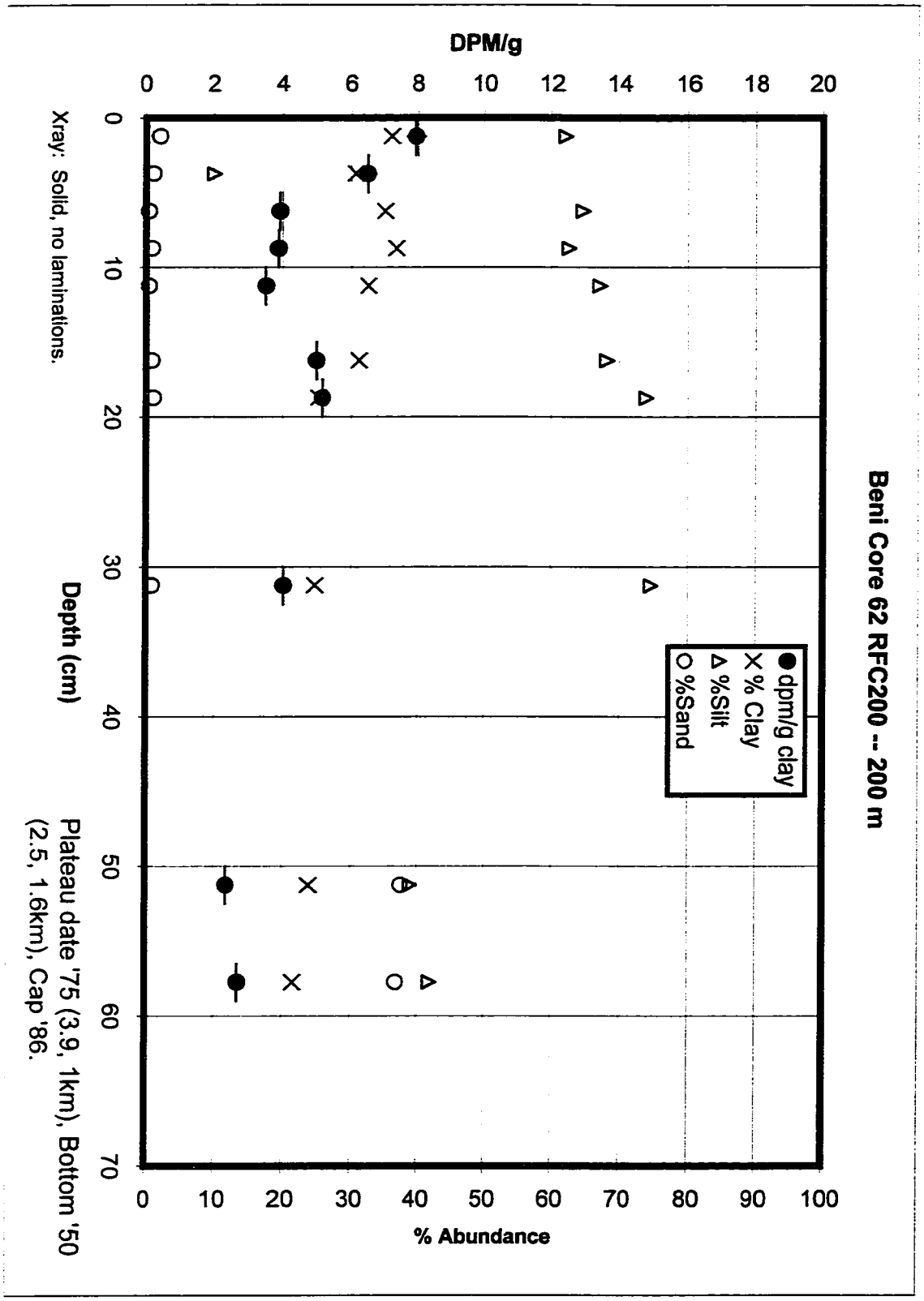
Beni Core 62 RFC200 -- 200 m
DPM/g
0 2 4 6 8 10 12 14 16 18 20
Depth (cm)
0 10 20 30 40 50 60 70
% Abundance
0 10 20 30 40 50 60 70 80 90 100
● dpm/g clay
× % Clay
Δ %Silt
○ %Sand
Xray: Solid, no laminations.
Plateau date '75 (3.9, 1km), Bottom '50 (2.5, 1.6km), Cap '86.

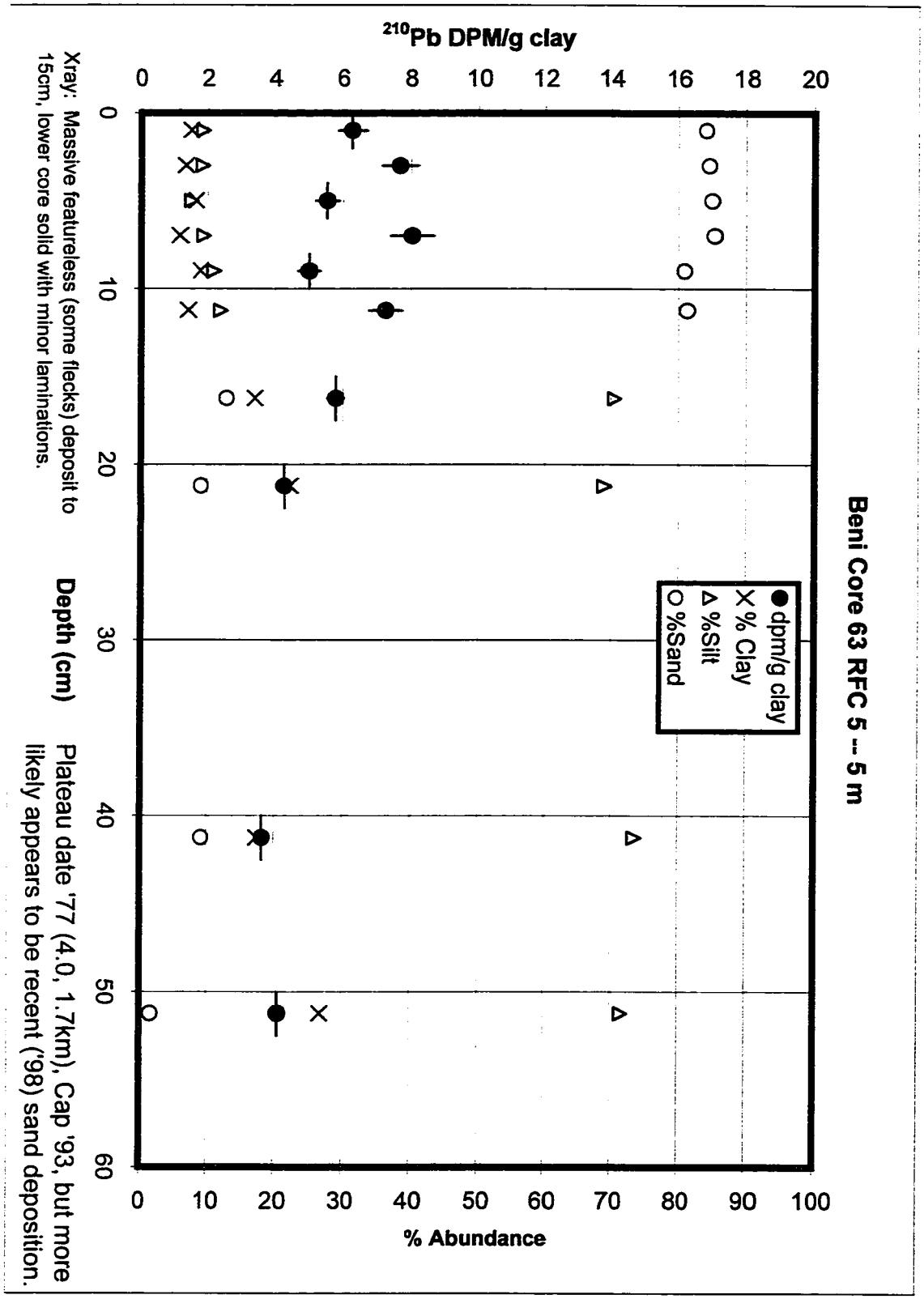

Xray: Massive featureless (some flecks) deposit to 15cm, lower core solid with minor laminations.

Plateau date '77 (4.0, 1.7km), Cap '93, but more likely appears to be recent ('98) sand deposition.

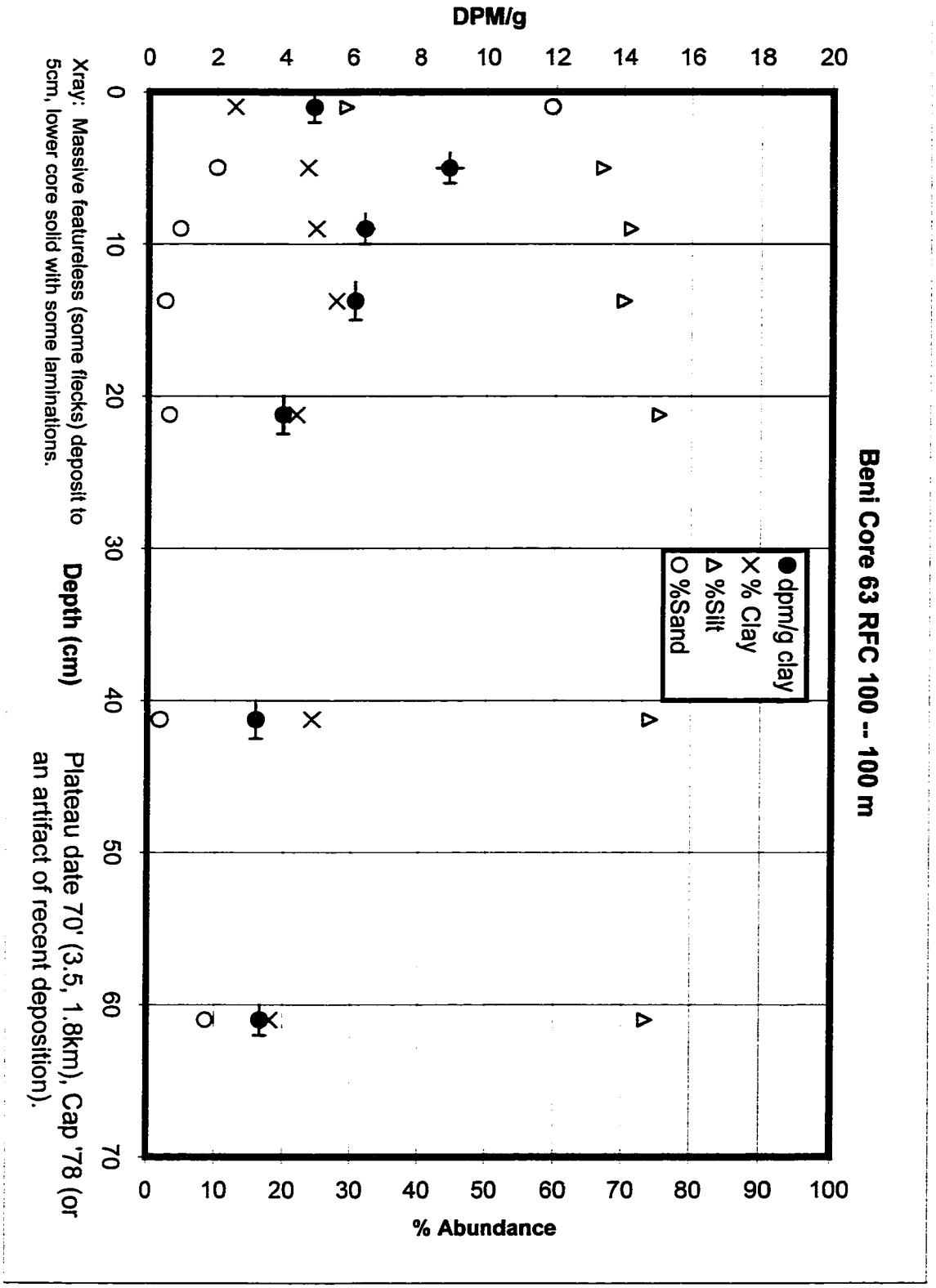
Beni Core 63 RFC 100 -- 100 m
DPM/g
0 2 4 6 8 10 12 14 16 18 20
0 10 20 30 40 50 60 70
Depth (cm)
0 10 20 30 40 50 60 70 80 90 100
% Abundance
dpm/g clay
% Clay
%Silt
%Sand
Xray: Massive featureless (some flecks) deposit to 5cm, lower core solid with some laminations.
Plateau date 70' (3.5, 1.8km), Cap '78 (or an artifact of recent deposition).

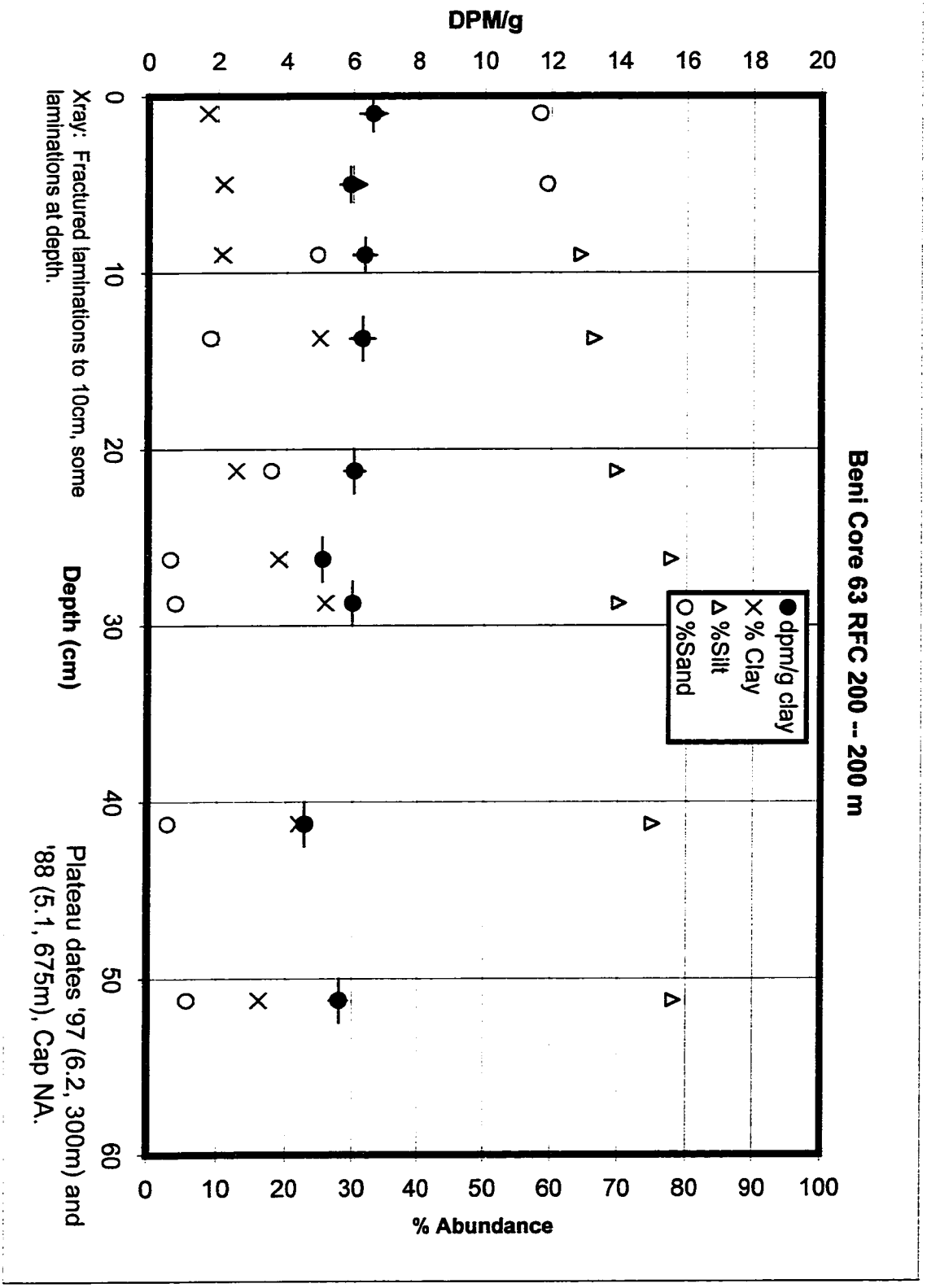
Beni Core 63 RFC 200 -- 200 m
DPM/g
0 2 4 6 8 10 12 14 16 18 20
% Abundance
0 10 20 30 40 50 60 70 80 90 100
Depth (cm)
0 10 20 30 40 50 60
dpm/g clay
% Clay
%Silt
%Sand
Xray: Fractured laminations to 10cm, some laminations at depth.
Plateau dates '97 (6.2, 300m) and '88 (5.1, 675m), Cap NA.

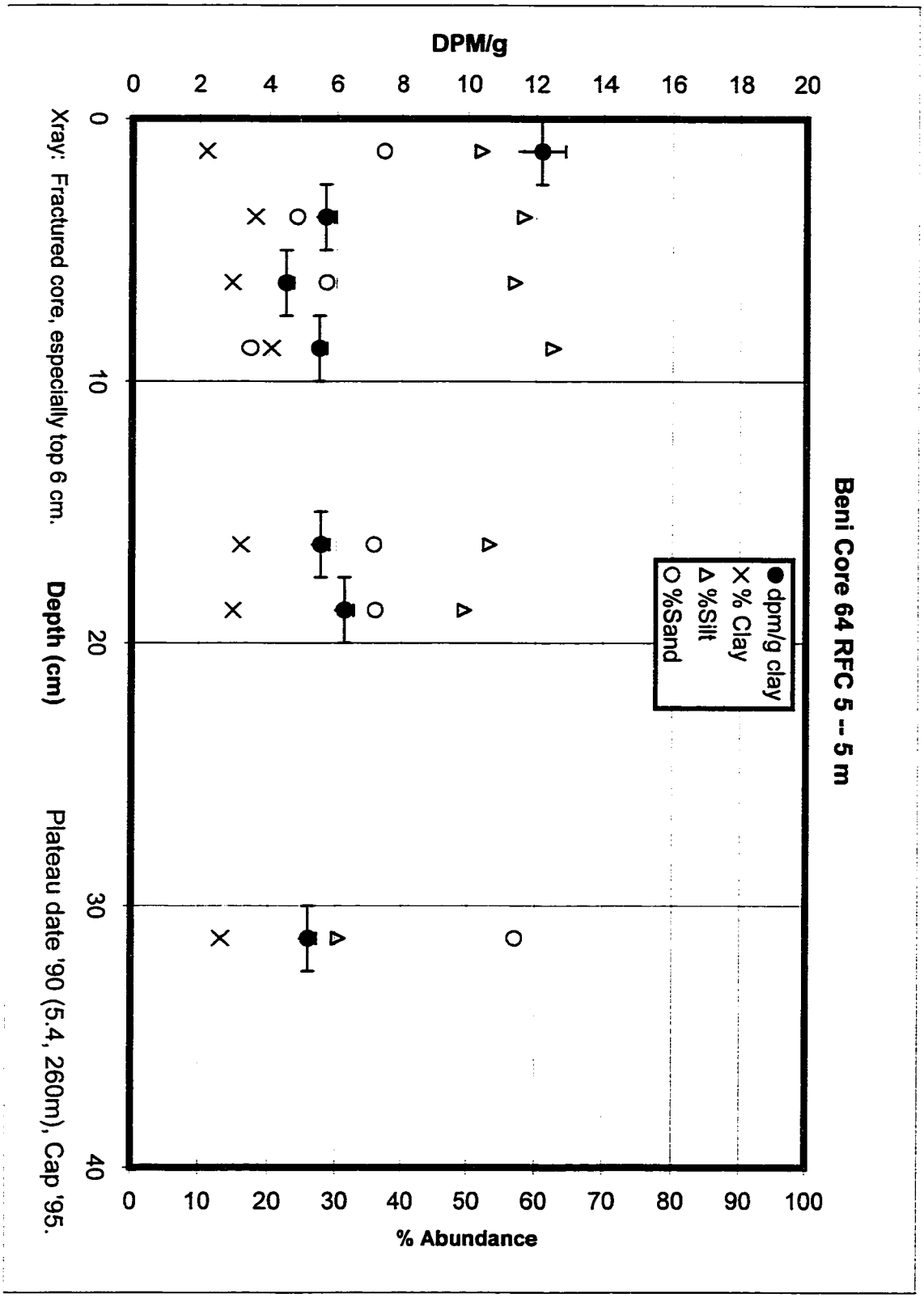
DPM/g
0 2 4 6 8 10 12 14 16 18 20
0 10 20 30 40
Depth (cm)
0 10 20 30 40 50 60 70 80 90 100
% Abundance
● dpm/g clay
× % Clay
Δ %Silt
○ %Sand
Beni Core 64 RFC 5 -- 5 m
Xray: Fractured core, especially top 6 cm.
Plateau date '90 (5.4, 260m), Cap '95.

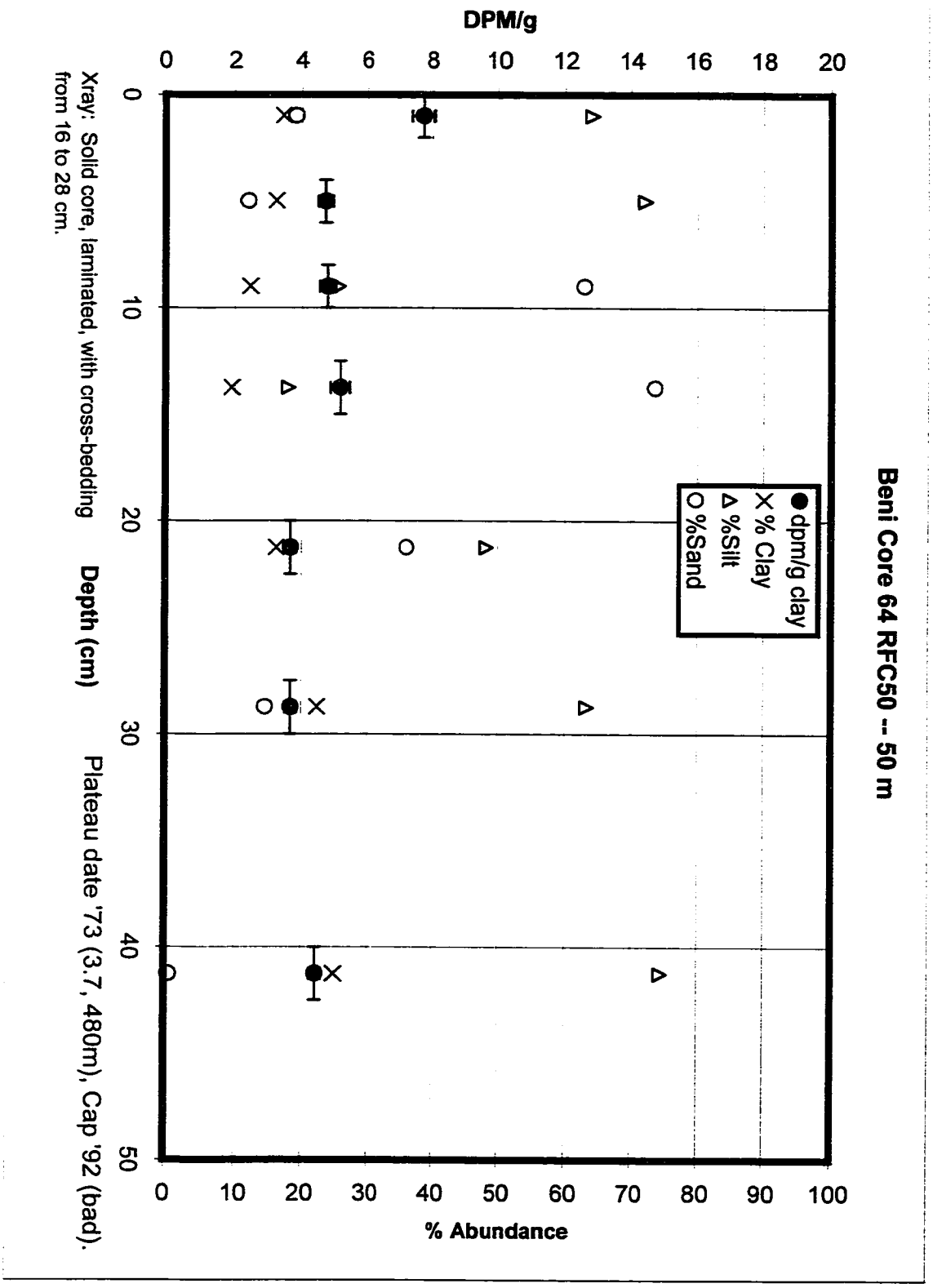
Beni Core 64 RFC50 -- 50 m
DPM/g
0 2 4 6 8 10 12 14 16 18 20
% Abundance
0 10 20 30 40 50 60 70 80 90 100
Depth (cm)
0 10 20 30 40 50
● dpm/g clay
X % Clay
Δ %Silt
○ %Sand
Xray: Solid core, laminated, with cross-bedding from 16 to 28 cm.
Plateau date '73 (3.7, 480m), Cap '92 (bad).

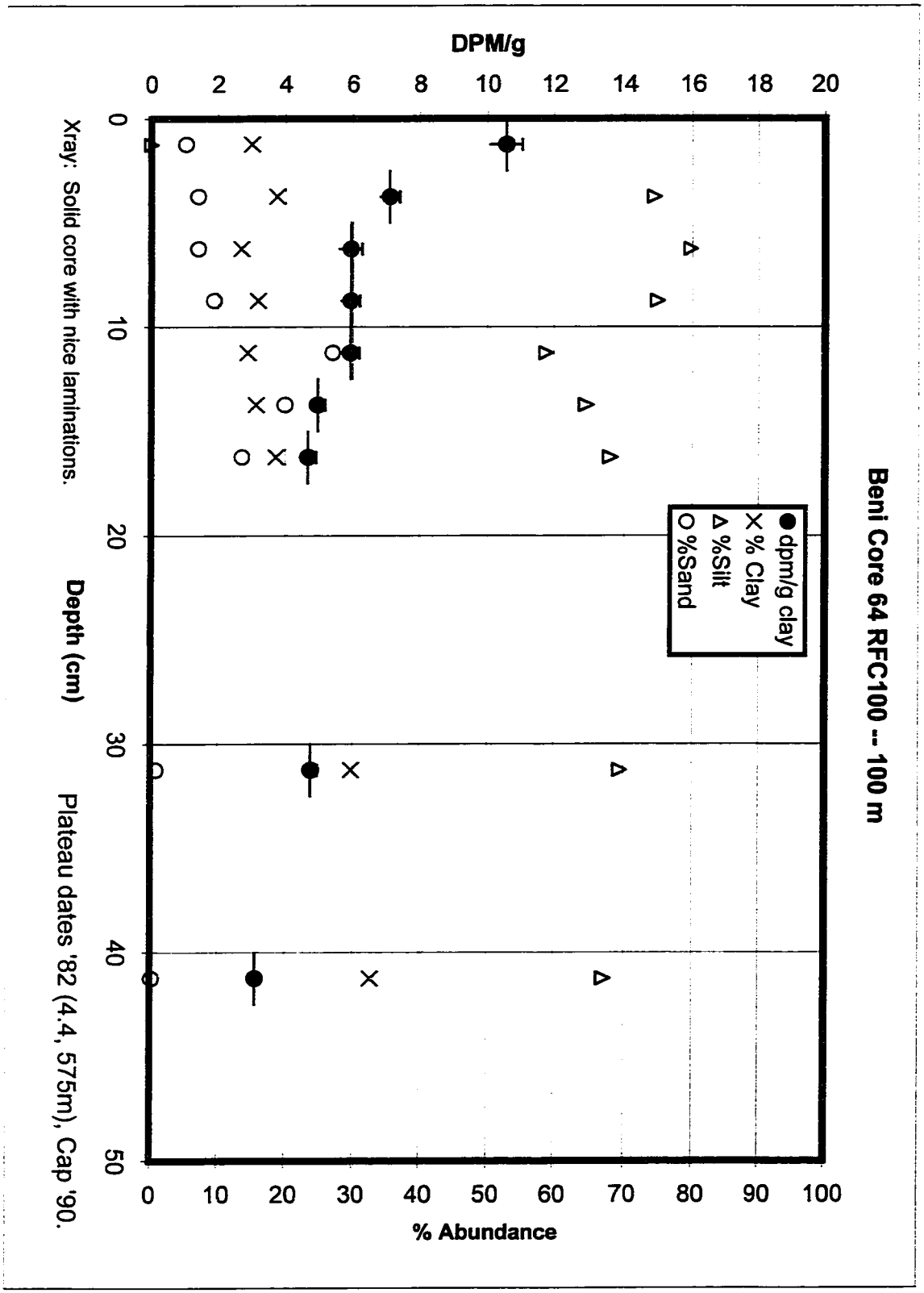
Beni Core 64 RFC100 -- 100 m
DPM/g
0 2 4 6 8 10 12 14 16 18 20
0 10 20 30 40 50
Depth (cm)
0 10 20 30 40 50 60 70 80 90 100
% Abundance
● dpm/g clay
X % Clay
Δ %Silt
O %Sand
Xray: Solid core with nice laminations.
Plateau dates '82 (4.4, 575m), Cap '90.

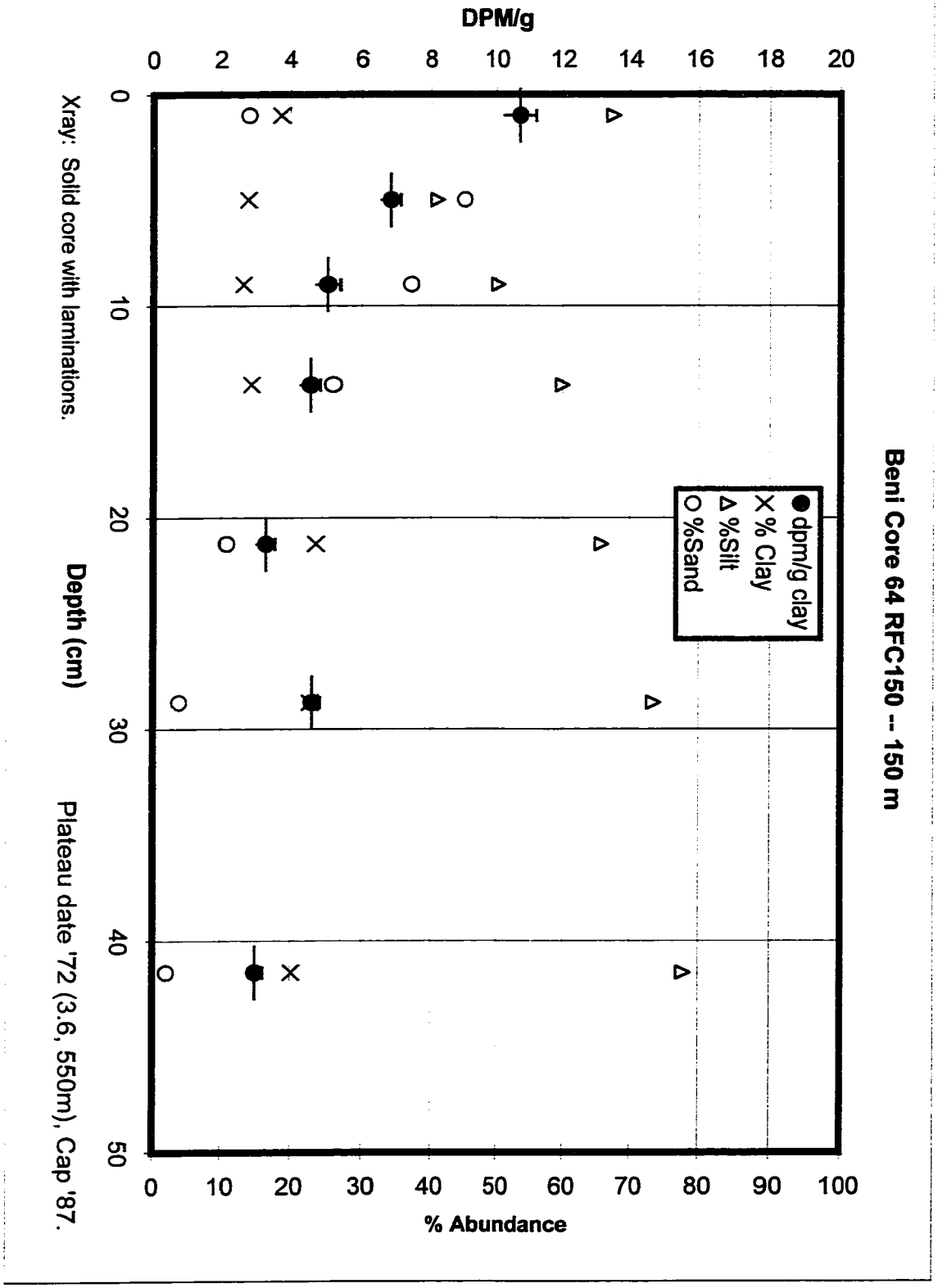
DPM/g
0 2 4 6 8 10 12 14 16 18 20
0 10 20 30 40 50
Depth (cm)
0 10 20 30 40 50 60 70 80 90 100
% Abundance
dpm/g clay
% Clay
%Silt
%Sand
Beni Core 64 RFC150 -- 150 m
Xray: Solid core with laminations.
Plateau date '72 (3.6, 550m), Cap '87.

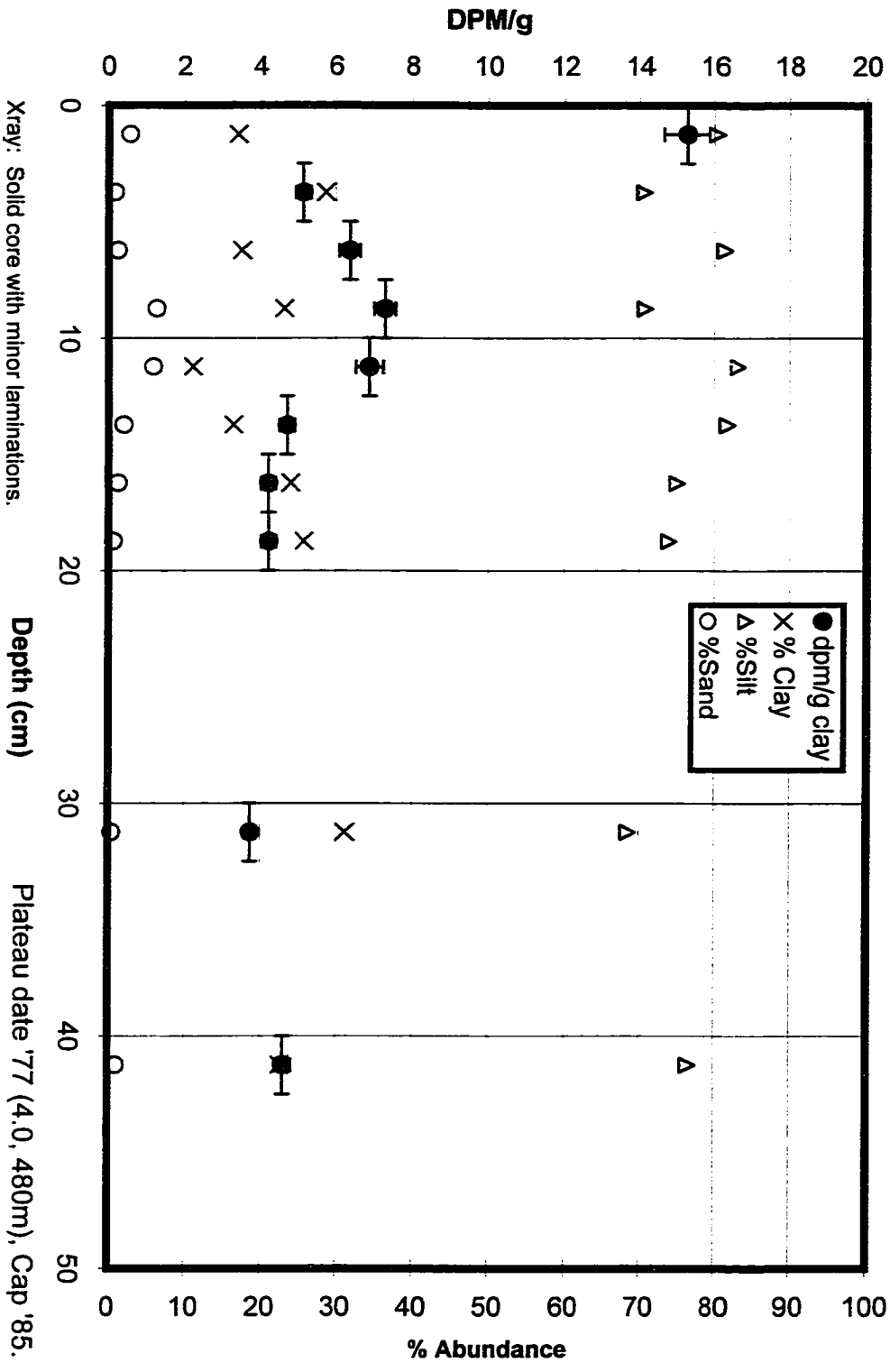
Beni Core 64 RFC 200 -- 200m
DPM/g
0 2 4 6 8 10 12 14 16 18 20
0 10 20 30 40 50
Depth (cm)
0 10 20 30 40 50 60 70 80 90 100
% Abundance
dpm/g clay
% Clay
%Silt
%Sand
Xray: Solid core with minor laminations.
Plateau date '77 (4.0, 480m), Cap '85.

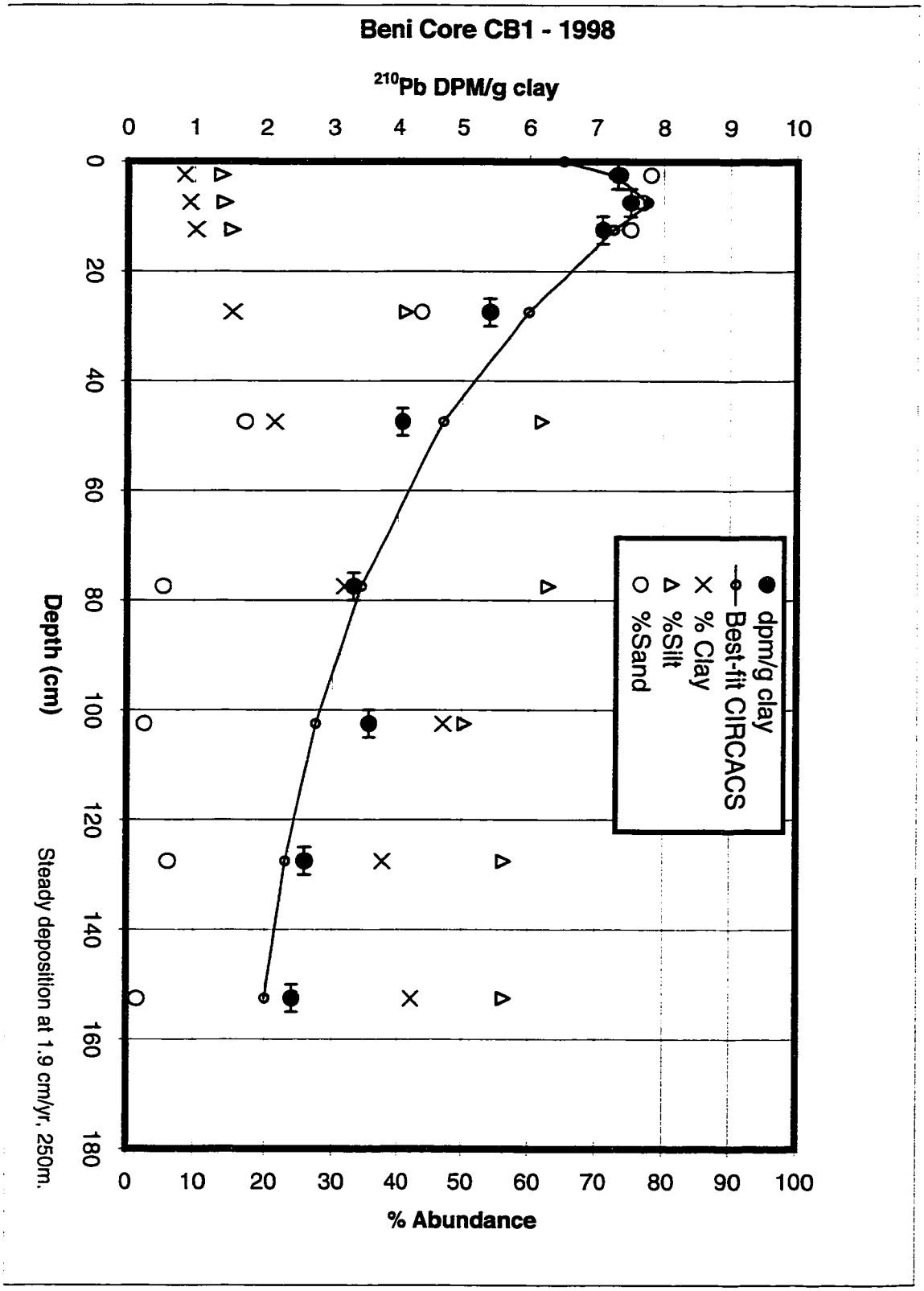
Beni Core CB1 - 1998
210Pb DPM/g clay
0 1 2 3 4 5 6 7 8 9 10
0 20 40 60 80 100 120 140 160 180
Depth (cm)
Steady deposition at 1.9 cm/yr, 250m.
0 10 20 30 40 50 60 70 80 90 100
% Abundance
dpm/g clay
Best-fit CIRCACS
% Clay
%Silt
%Sand

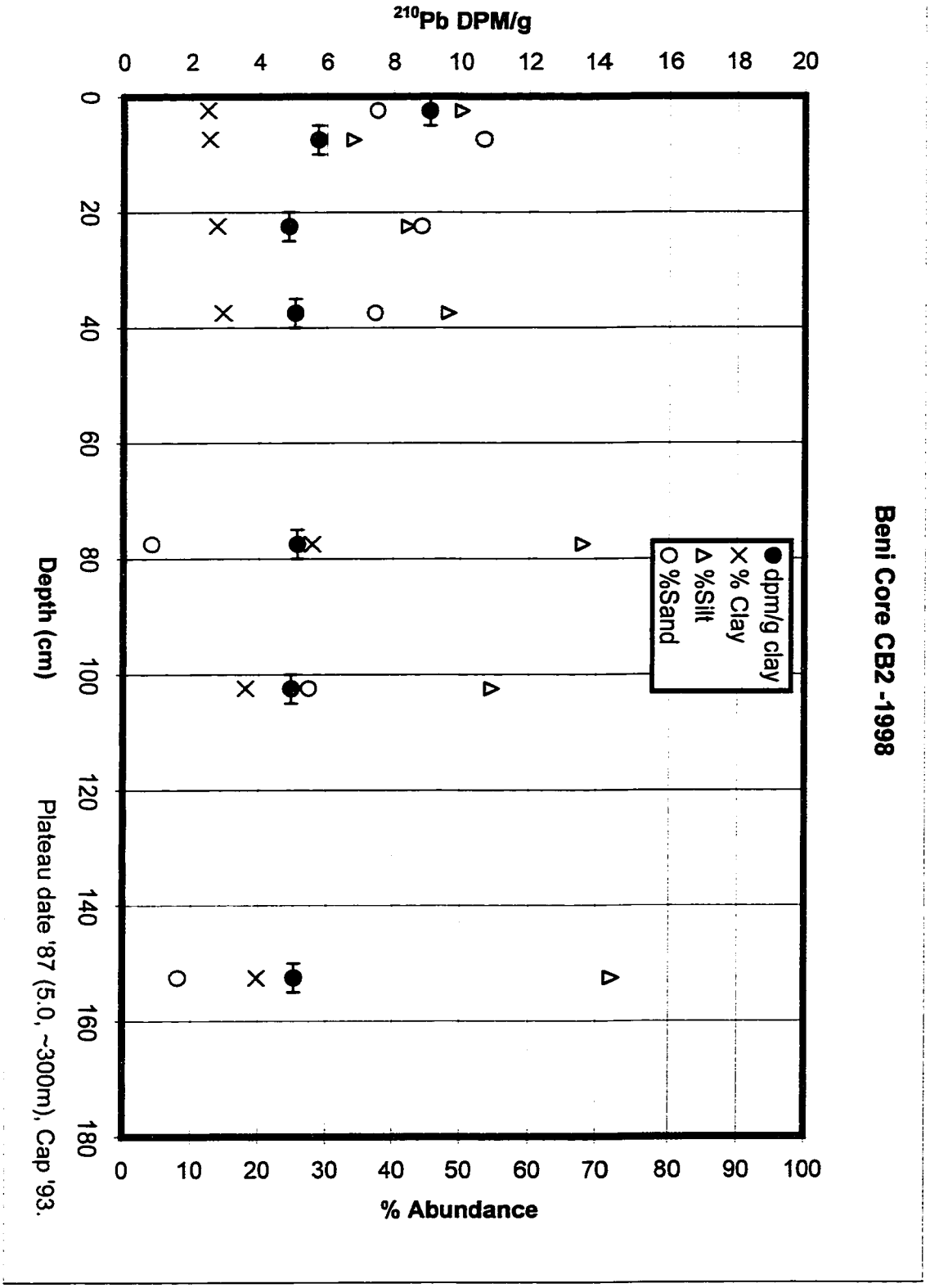
^{210}Pb DPM/g
0 2 4 6 8 10 12 14 16 18 20
0 20 40 60 80 100 120 140 160 180
Depth (cm)
0 10 20 30 40 50 60 70 80 90 100
% Abundance
dpm/g clay
% Clay
%Silt
%Sand
Beni Core CB2 -1998
Plateau date '87 (5.0, ~300m), Cap '93.

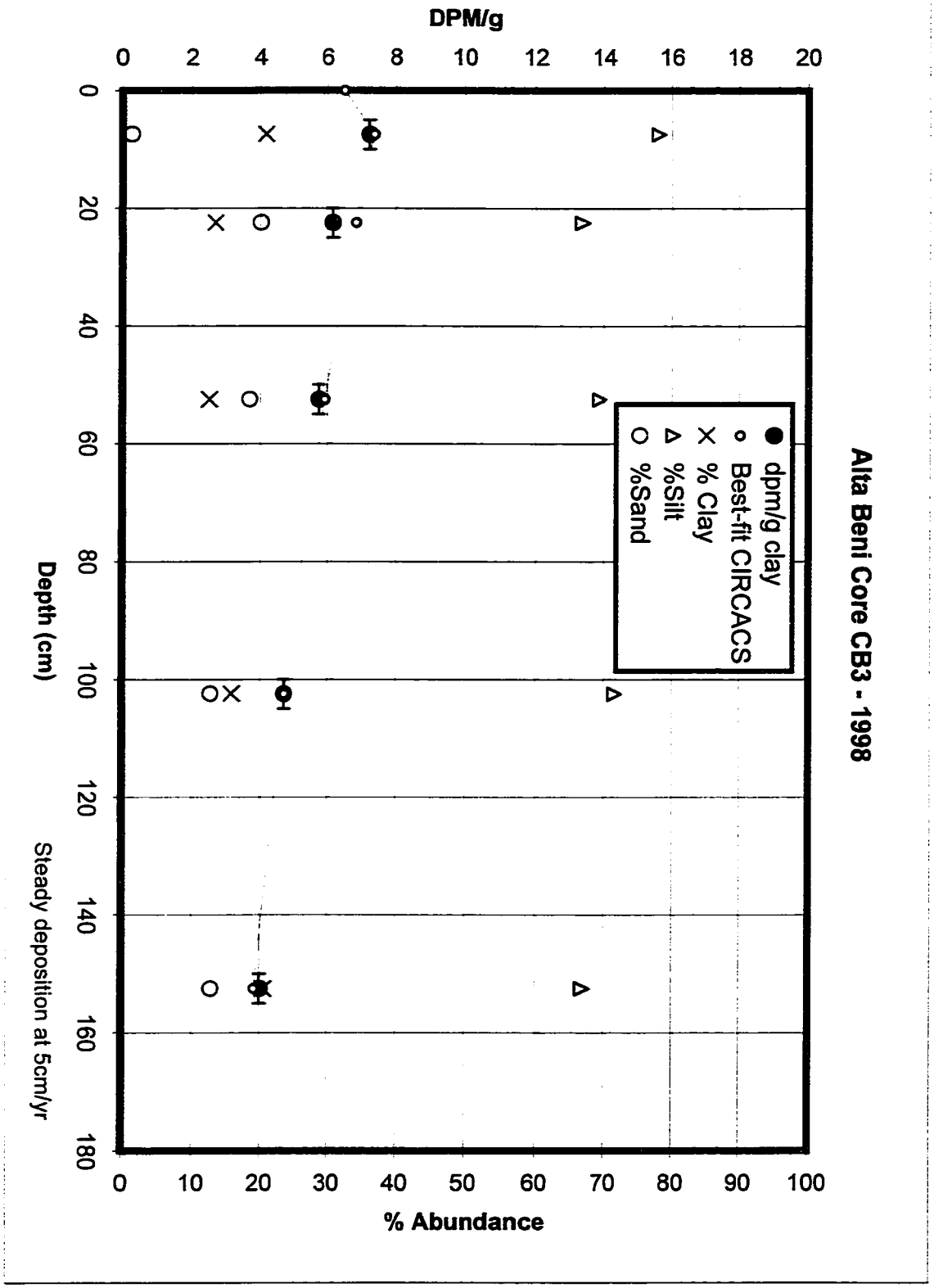
DPM/g
0
2
4
6
8
10
12
14
16
18
20
Depth (cm)
0
20
40
60
80
100
120
140
160
180
% Abundance
0
10
20
30
40
50
60
70
80
90
100
dpm/g clay
Best-fit CIRCACS
% Clay
%Silt
%Sand
Steady deposition at 5cm/yr
Alta Beni Core CB3 - 1998

Vita

Rolf Erhart Aalto

Education

2002	**Ph.D., Geological Sciences,** University of Washington, Seattle. 4.0 GPA. Dissertation: Geomorphic Form and Process of Sediment Flux within an Active Orogen: Denudation of the Bolivian Andes and Sediment Conveyance across the Beni Foreland. Committee: Thomas Dunne (chair), David Montgomery (co-chair), Charles Nittrouer, and Alan Gillespie.
1995	**M.S., Geological Sciences,** University of Washington, Seattle. 4.0 GPA. Thesis: Discordance between suspended sediment diffusion theory and observed sediment concentration profiles in rivers. Committee: Thomas Dunne (chair) and David Montgomery.
1993	**B.A., Geology and Applied Mathematics (Double Major),** University of California, Berkeley. 3.8 GPA in Geology. Honors Thesis: Mechanics of river meandering in a low-density medium. Advisor: William Dietrich.
1987	**High School,** The Loomis Chaffee School, Windsor, CT. 4.0 GPA. Overall top scholar and top science student.

Research Awards

2001 – 2003	**NASA SRTM.** $199,960 awarded. Title: Modeling continental-scale erosion in mountainous regions. Conceived and written by Aalto. Co-submitted with Montgomery, Gillespie, and Hallet.
1999 – 2002	**NSF Geology and Paleontology** (EAR-9903157). $299,976 awarded. Title: Quantitative meso-scale routing of sediment across foreland basins. Conceived and written by Aalto. Co-submitted with Dunne, Montgomery, and Nittrouer.
1996 – 1999	**NASA Earth Systems Science Graduate Fellowship.** $66,000 awarded. Title: Quantitative meso-scale geomorphology of the Amazon basin.
1993 – 1996	**Research Assistantship,** University of Washington.

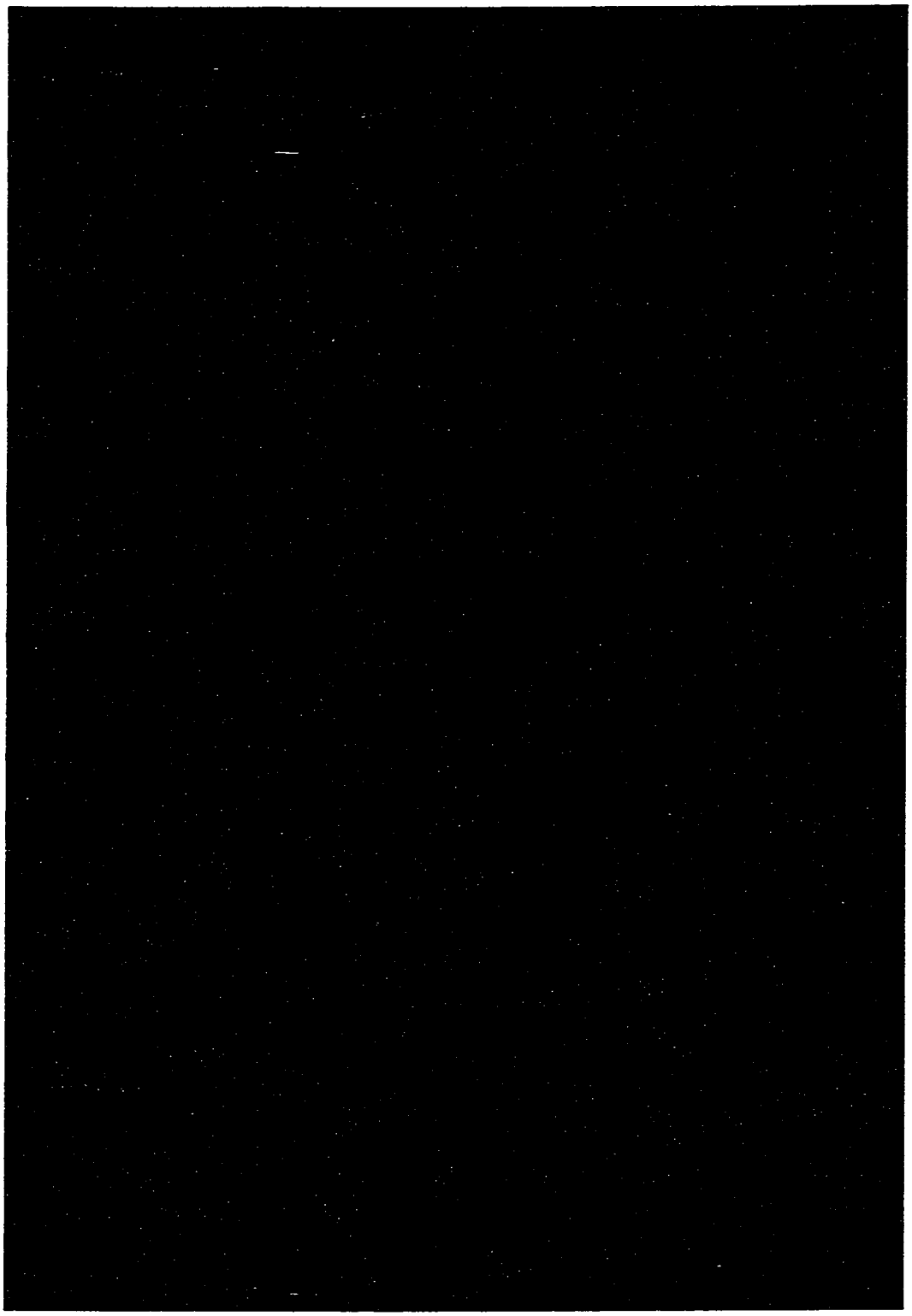

Mainst

67+2
67+1
67+0
-10+9
-11+0
-11+1
700 000
710 000
720 000
8 790 000
8 780 000
8 770 000

stream Channel Locatio

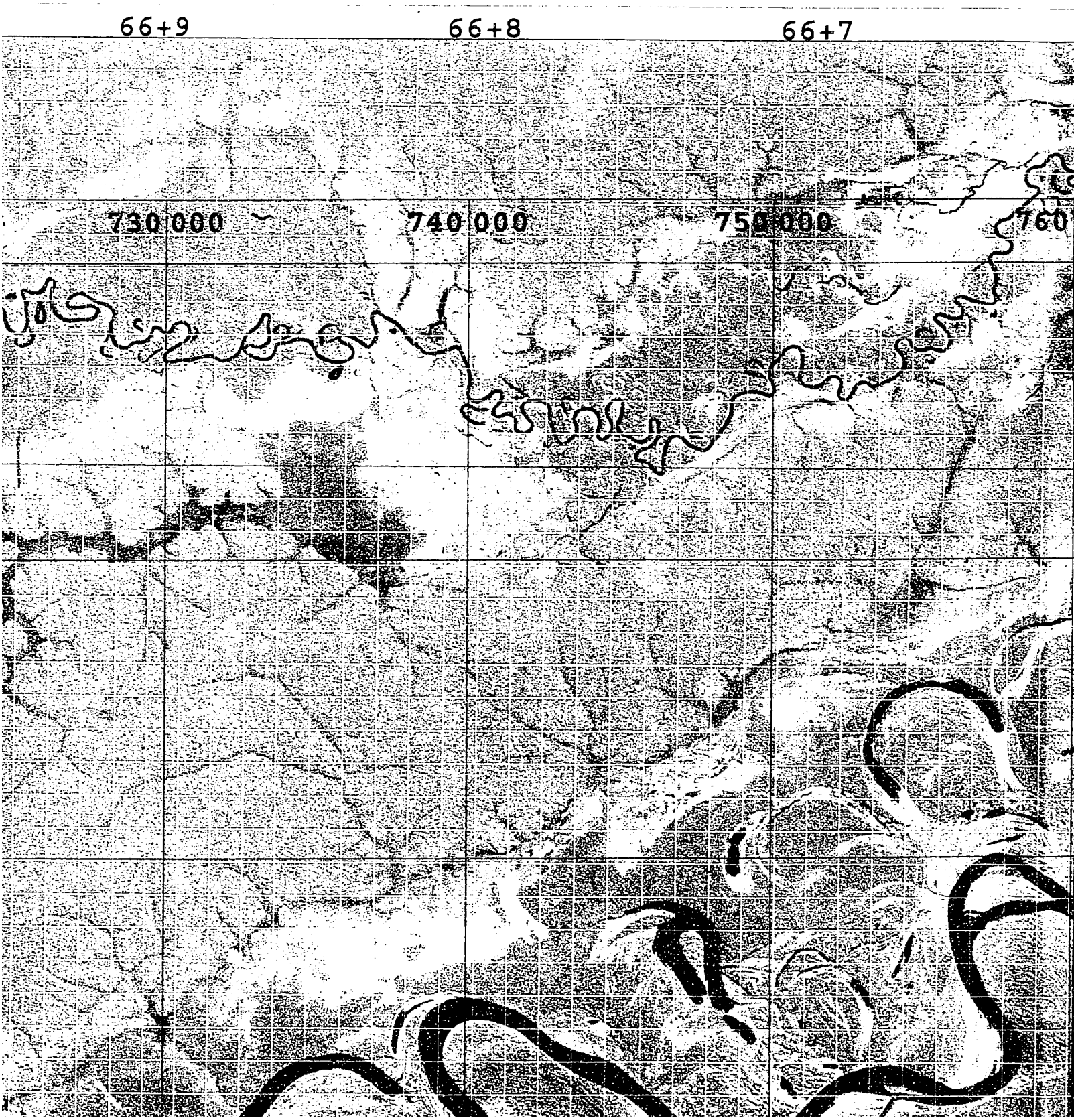

on Map for Beni River, B

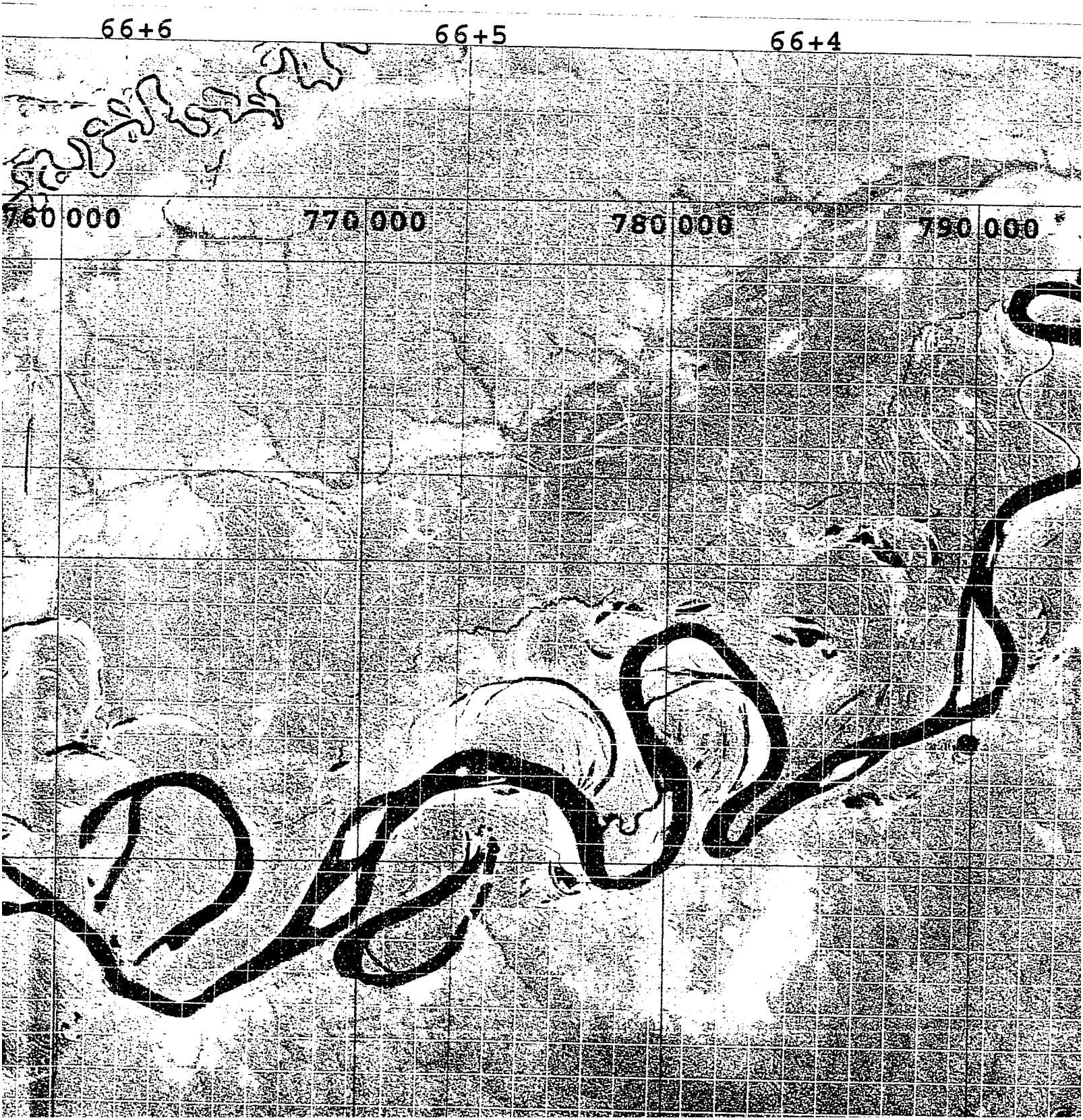

Bolivia


66+3
66+2
66+1
-10+9
-11+0
-11+1
800 000
810 000
8 790 000
8 780 000
8 770 000

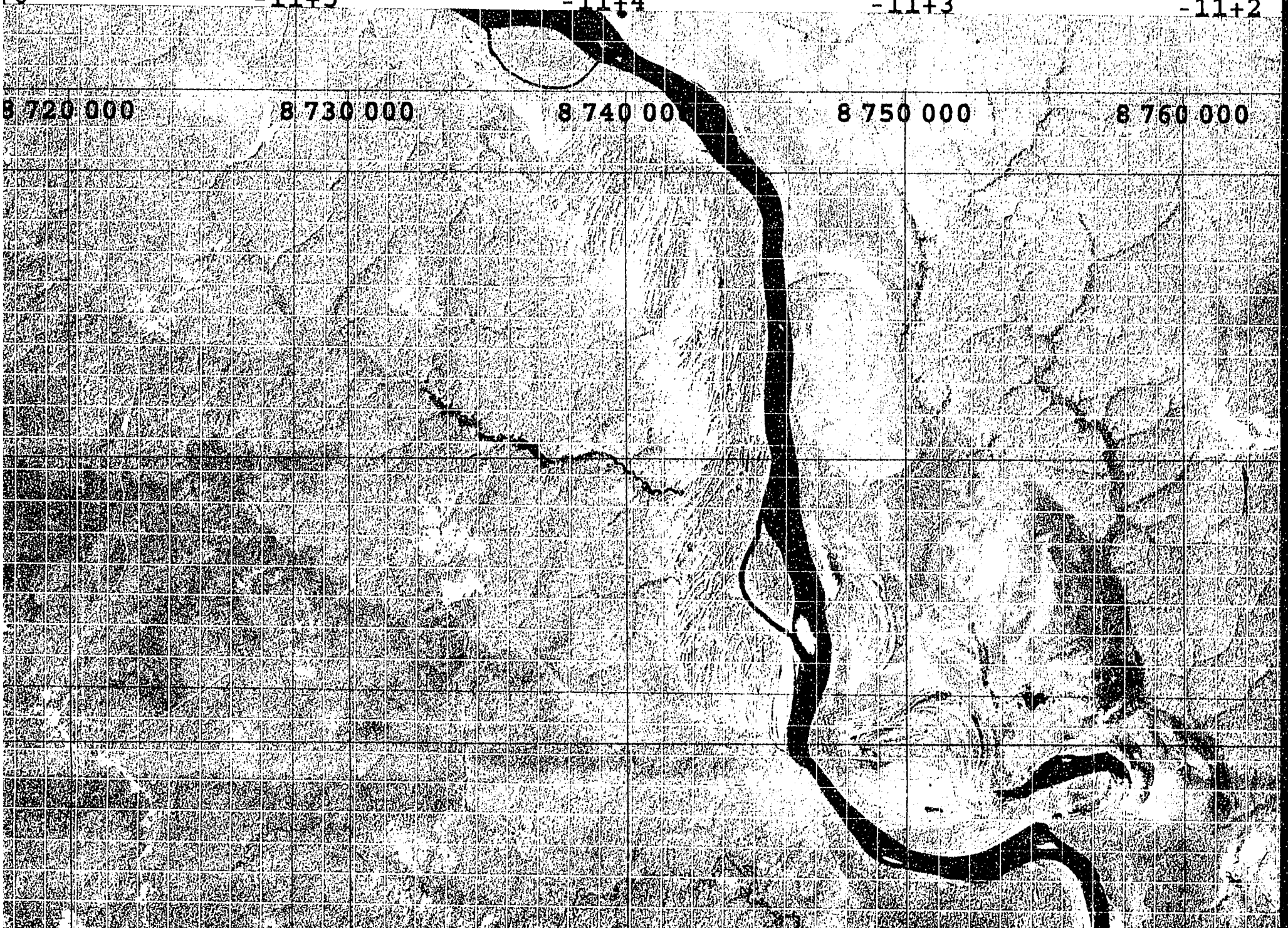
-11+6
-11+5
-11+4
-11+3
-11+2
8 720 000
8 730 000
8 740 000
8 750 000
8 760 000

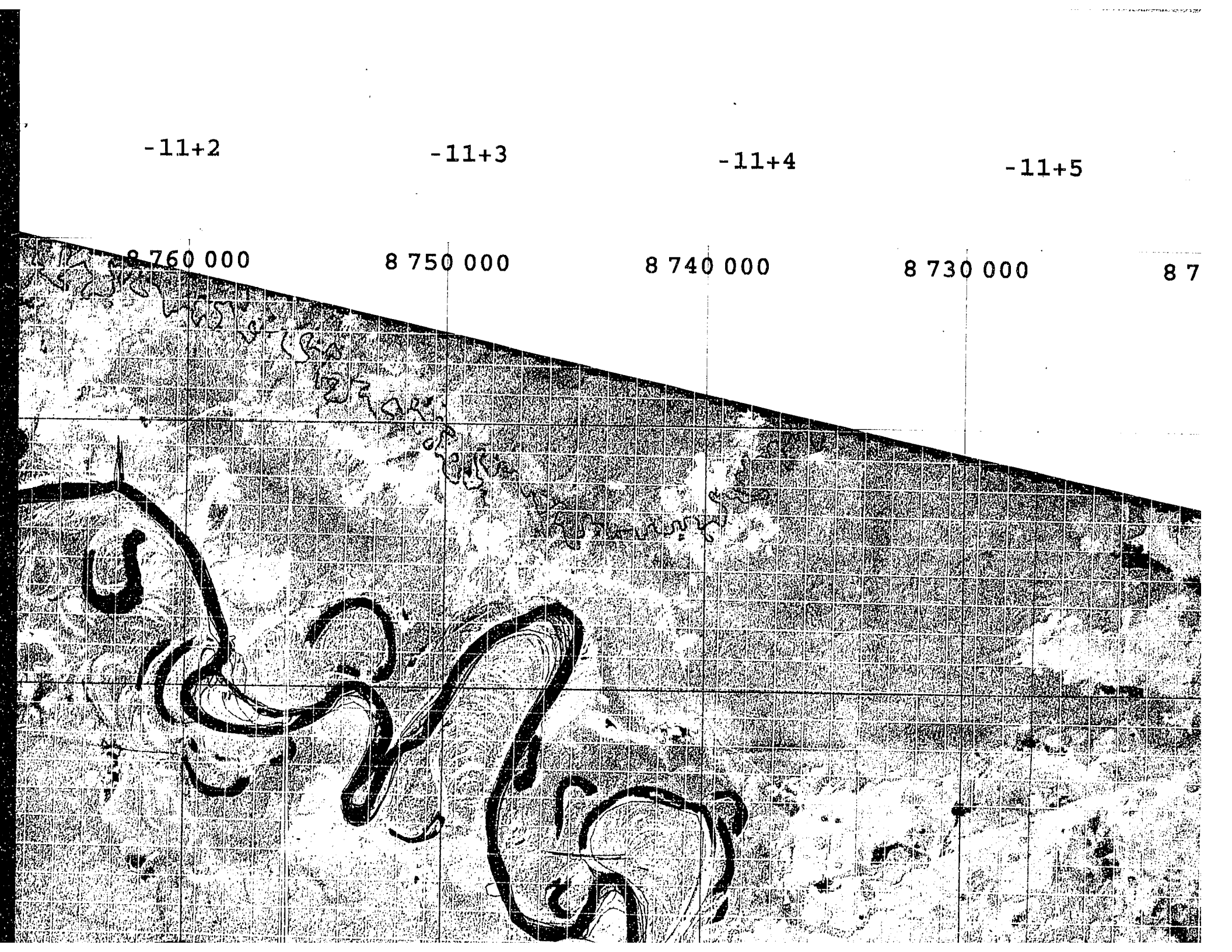
-11+2
-11+3
-11+4
-11+5
8 760 000
8 750 000
8 740 000
8 730 000
8 7

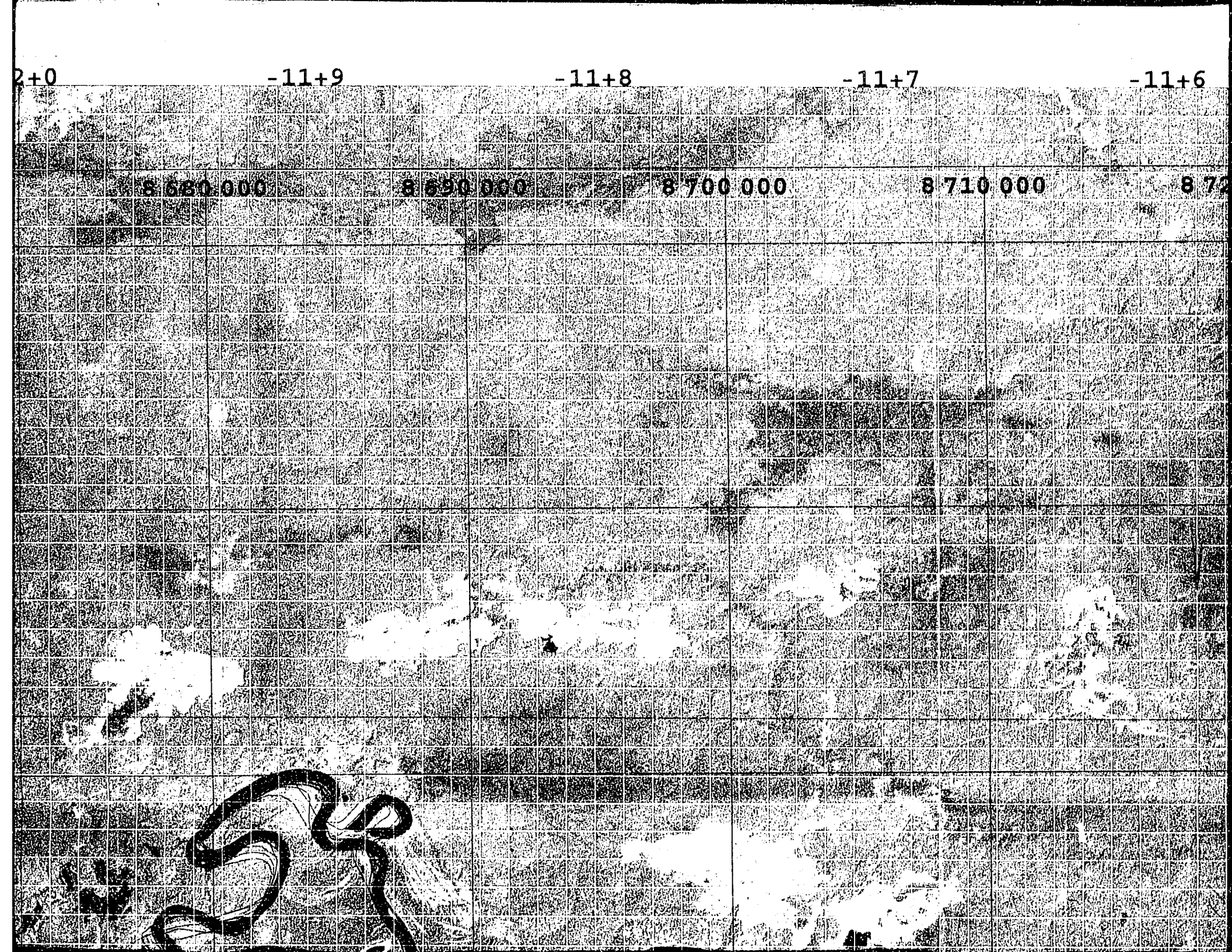
2+0
-11+9
-11+8
-11+7
-11+6
8 680 000
8 690 000
8 700 000
8 710 000
8 72

-11+6 -11+7 -11+8 -11+9

000 8 710 000 8 700 000 8 690 000 8 680 000

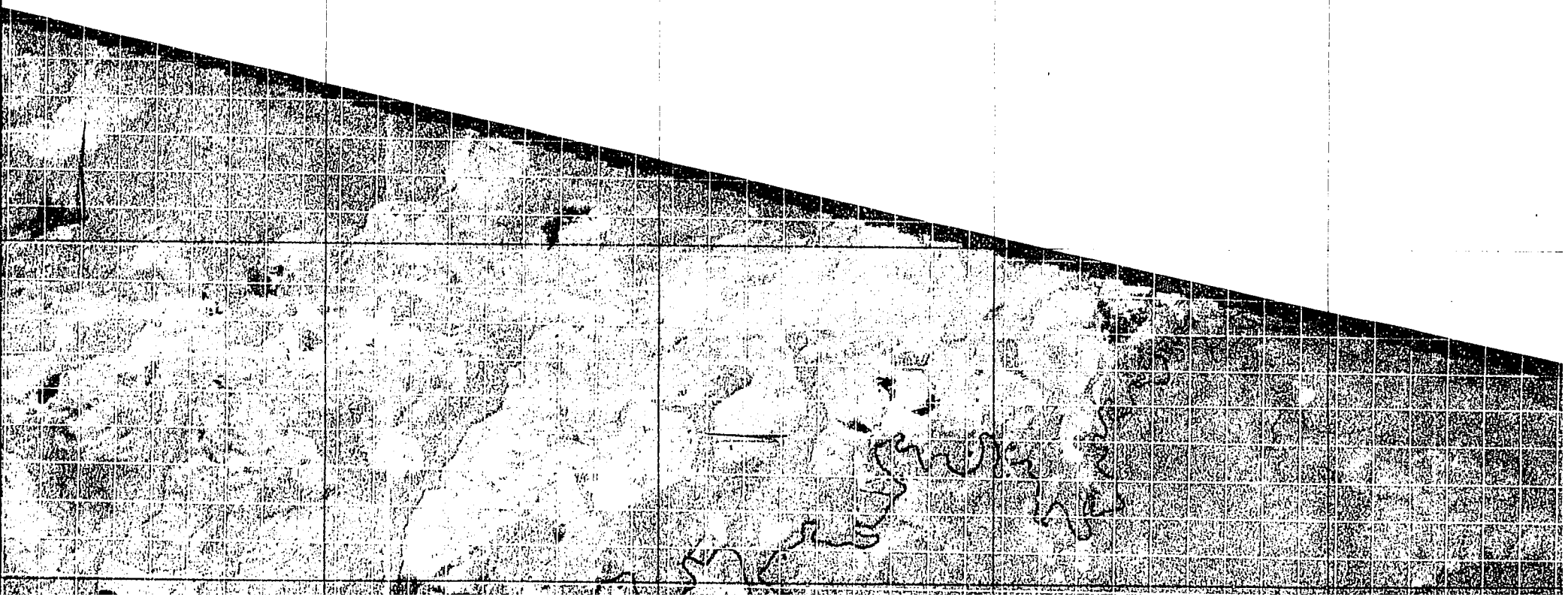

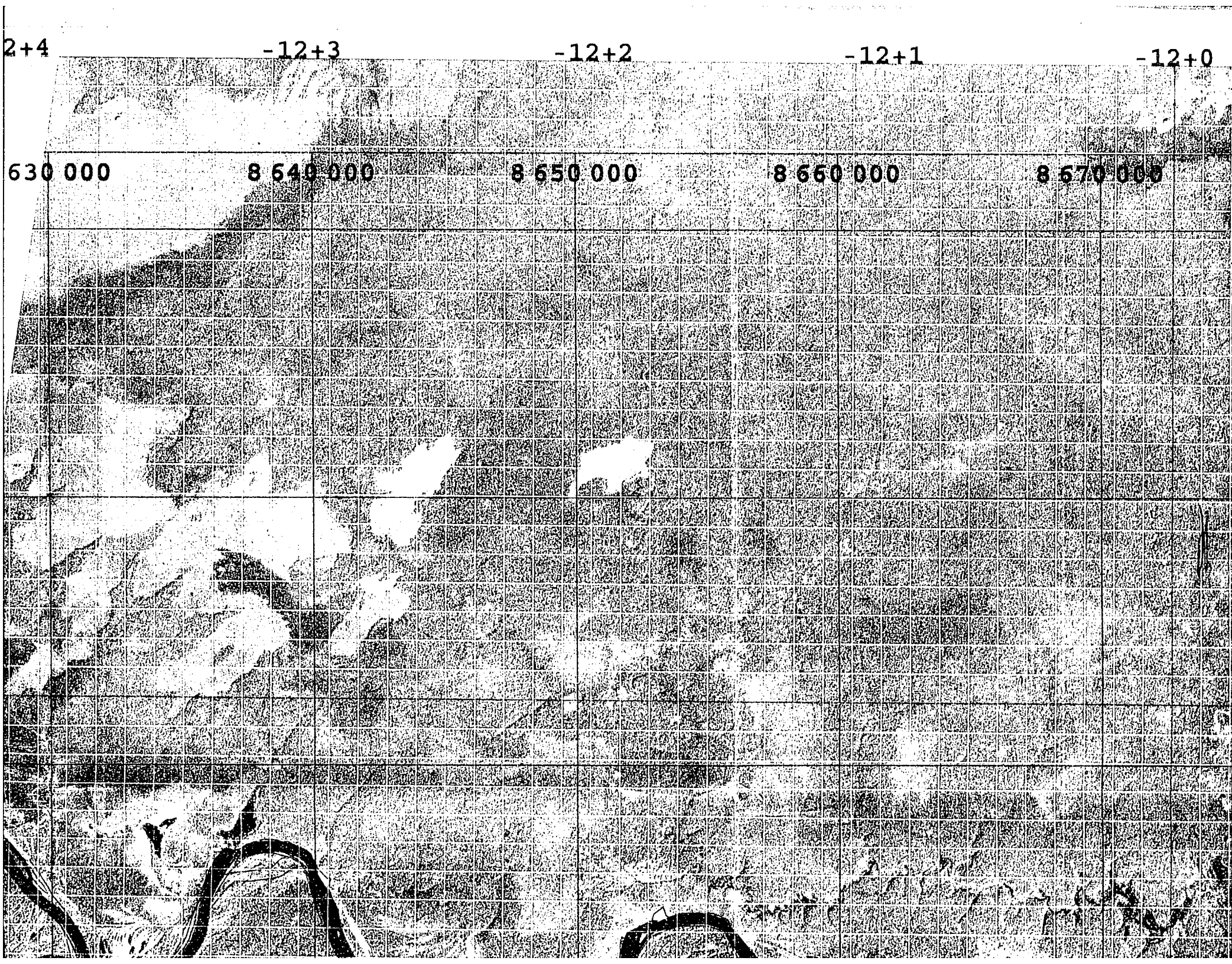
2+4
-12+3
-12+2
-12+1
-12+0
630 000
8 640 000
8 650 000
8 660 000
8 670 000

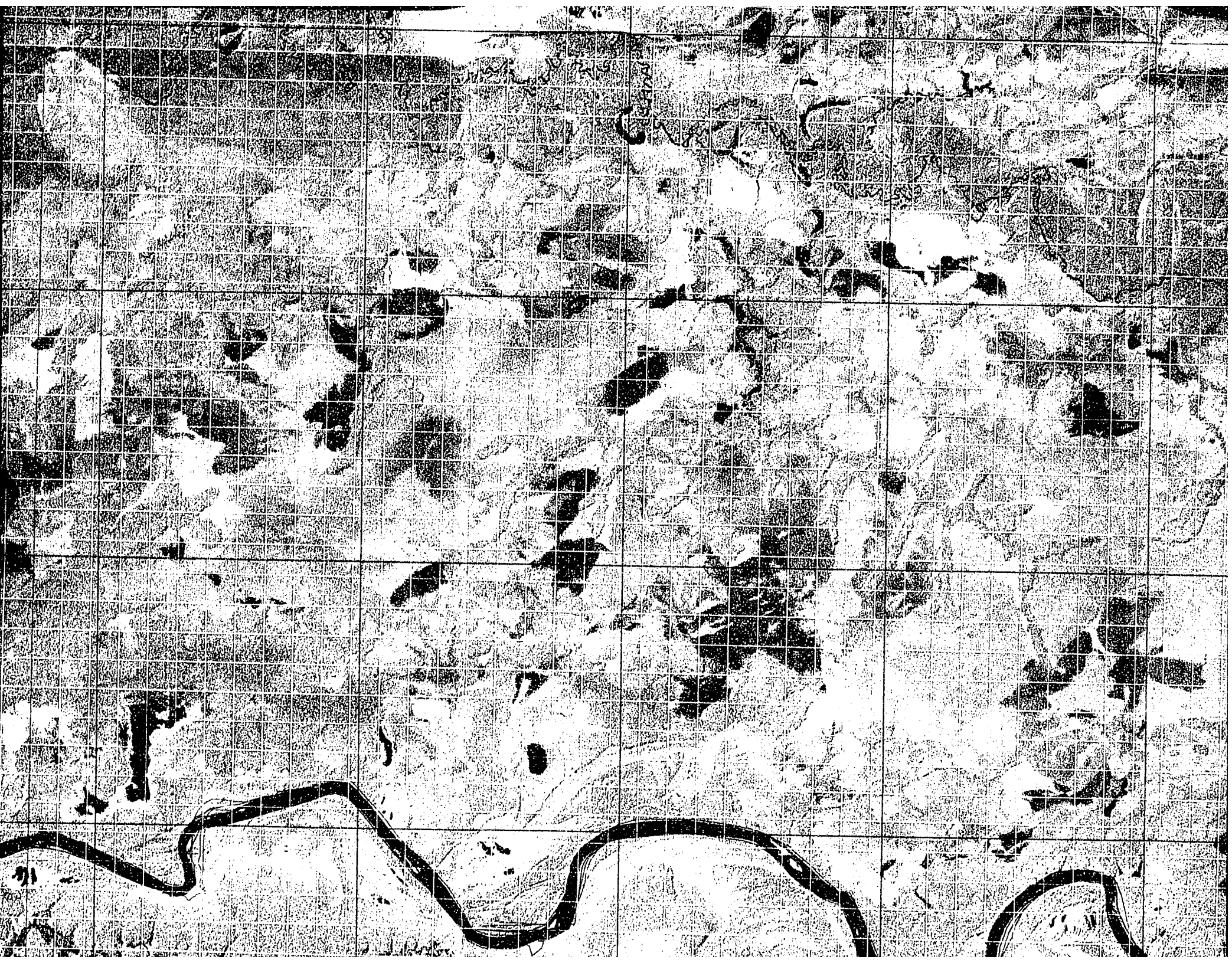

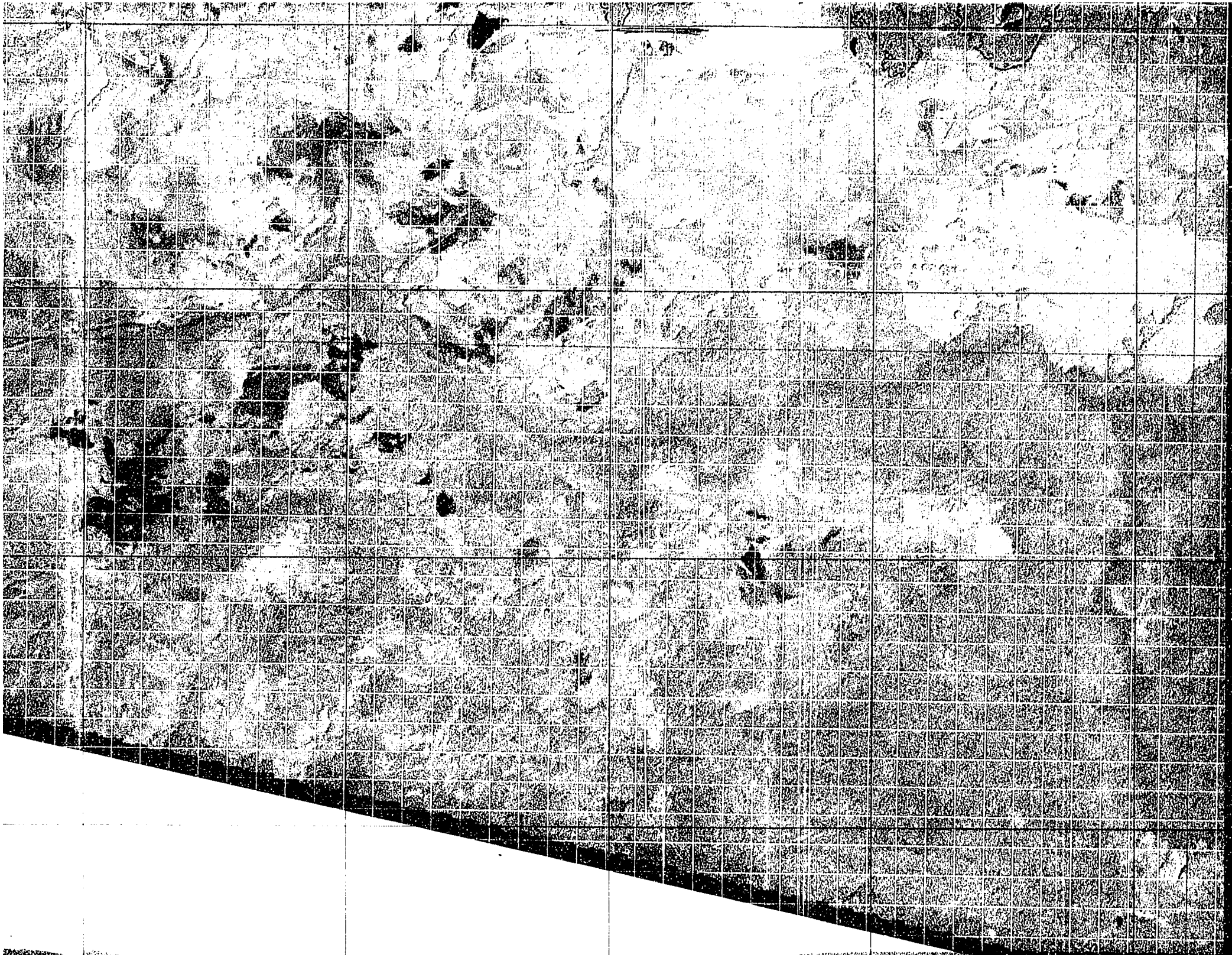

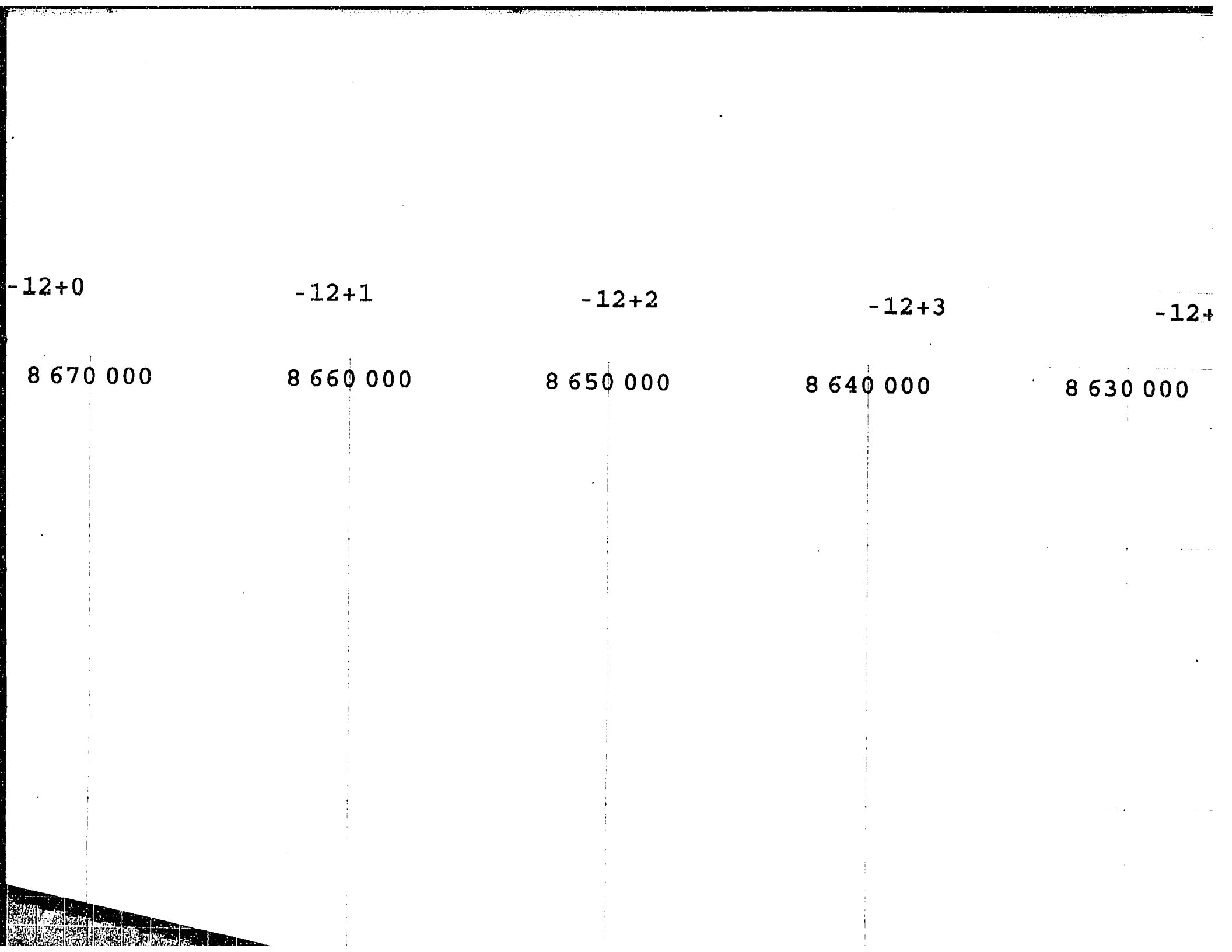
-12+0
-12+1
-12+2
-12+3
-12+
8 670 000
8 660 000
8 650 000
8 640 000
8 630 000

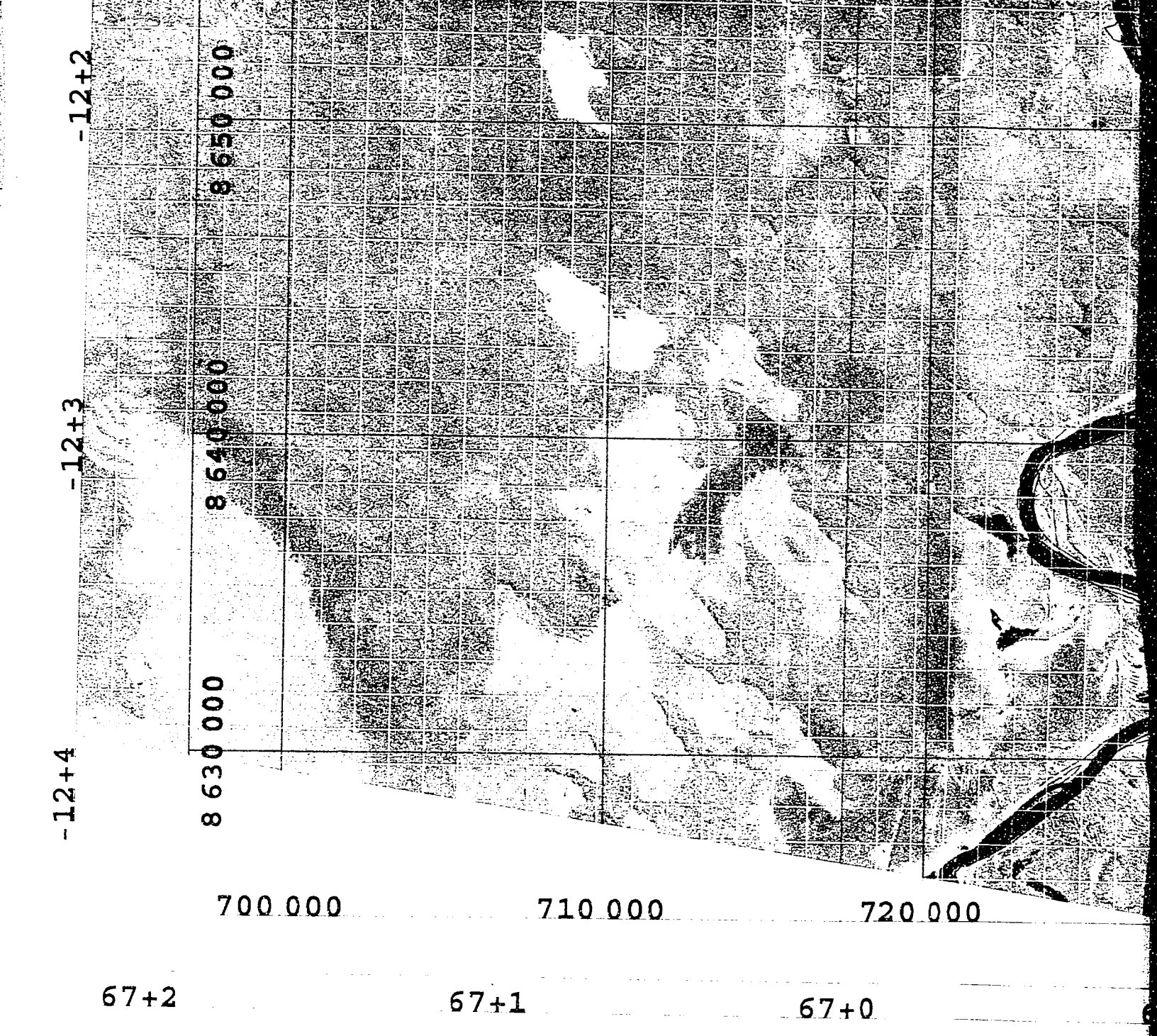

1975 channel

1986 channel

1993 channel

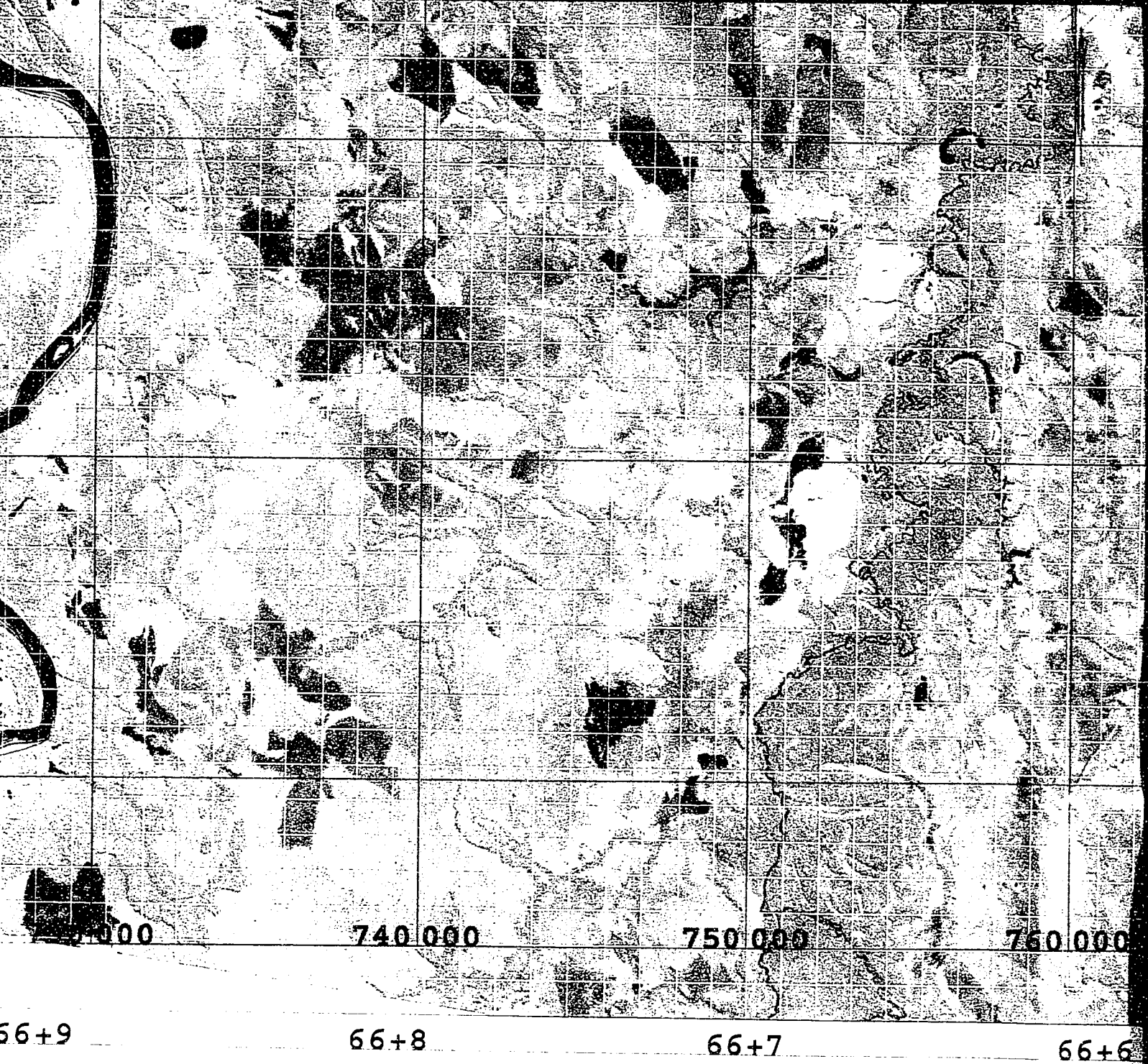

Base Map: 10/July/1999 Landsa
UTM Zone 19 South
False Color Composite of Bands

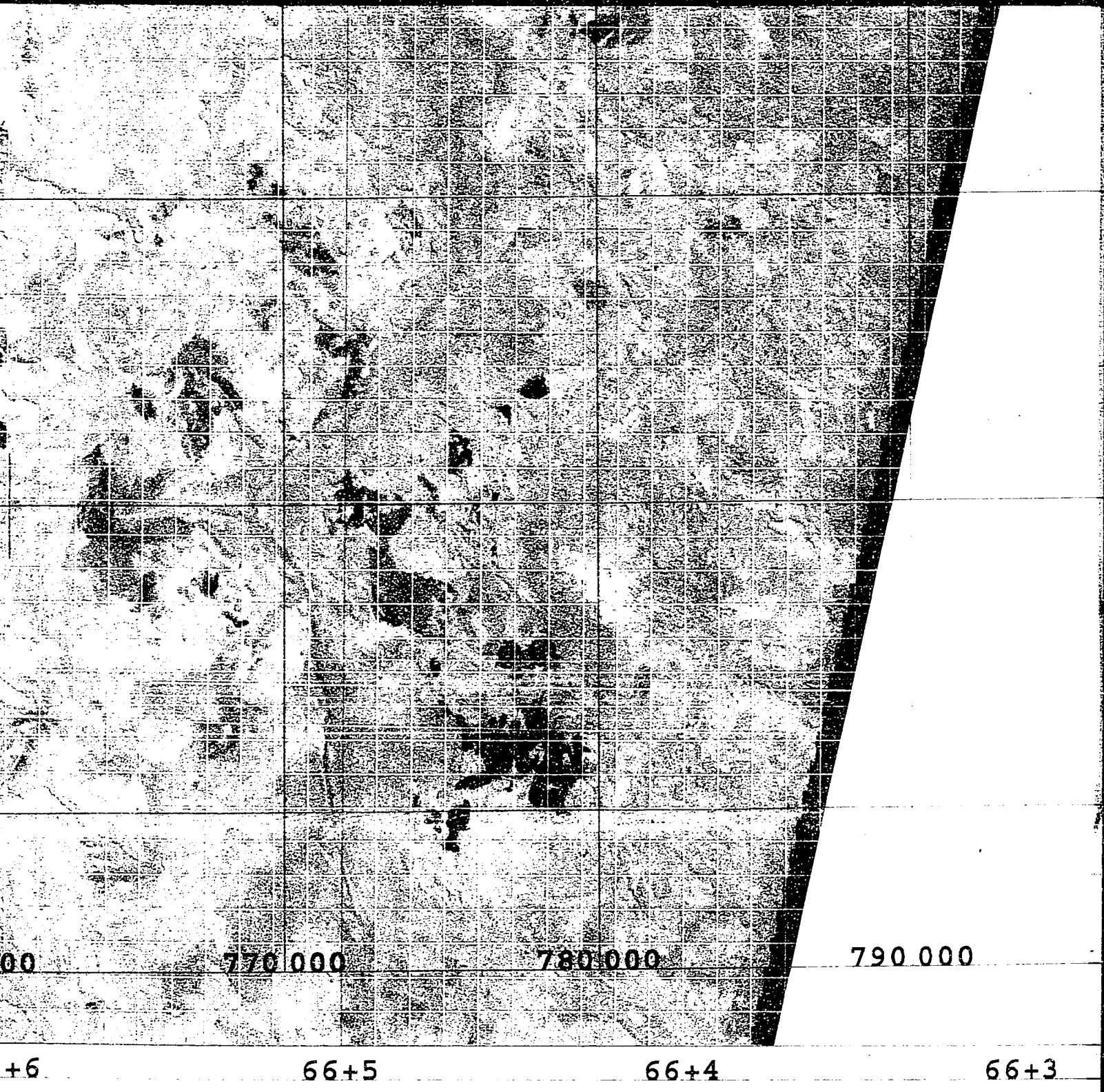

dsat ETM+ Path 1, Row 68

nds 5, 4, and 3

8 650 000

8 640 000

8 630 000

-12+2

-12+3

-12+4

800 000

810 000

66+3

66+2

66+1

Mainstream

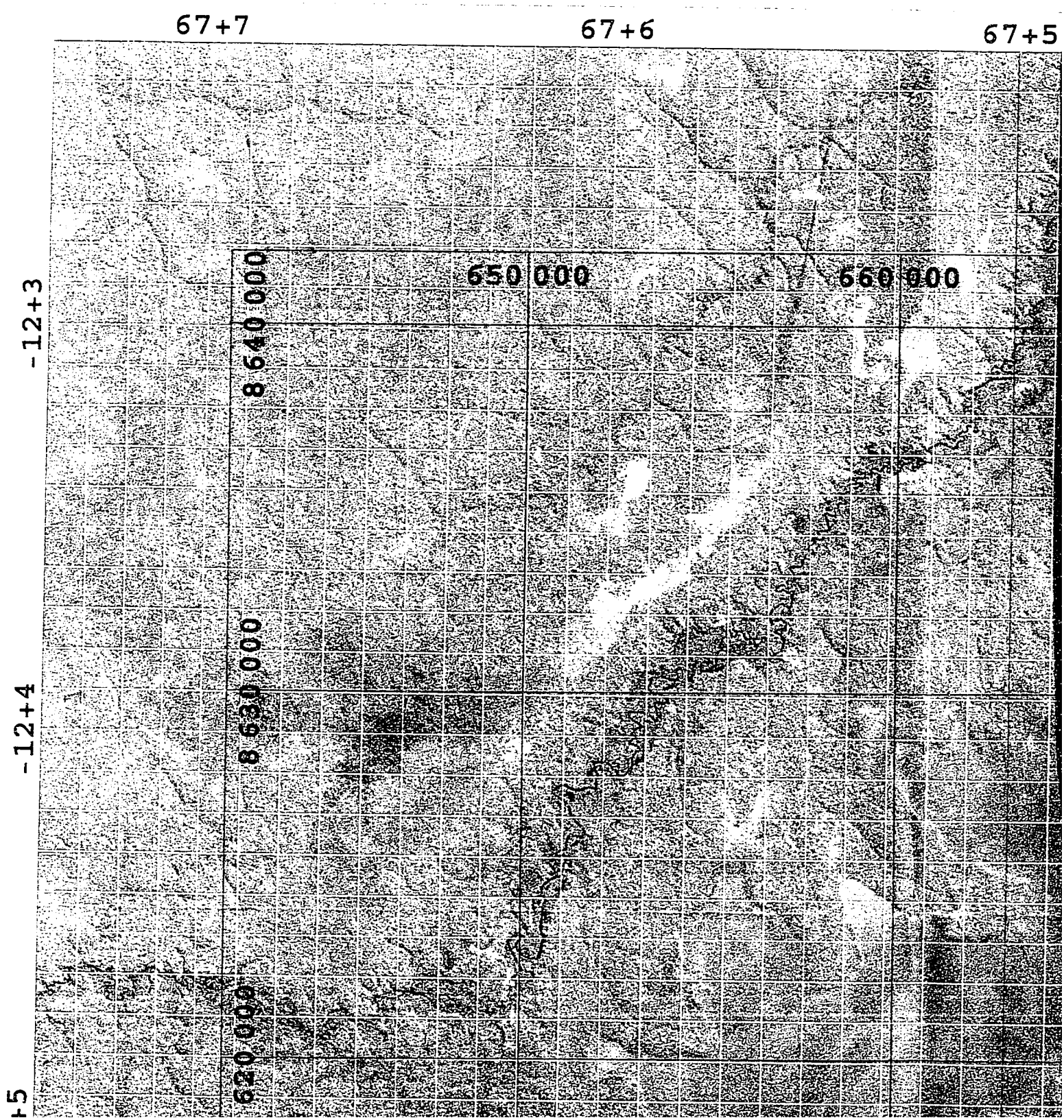

n Channel Location

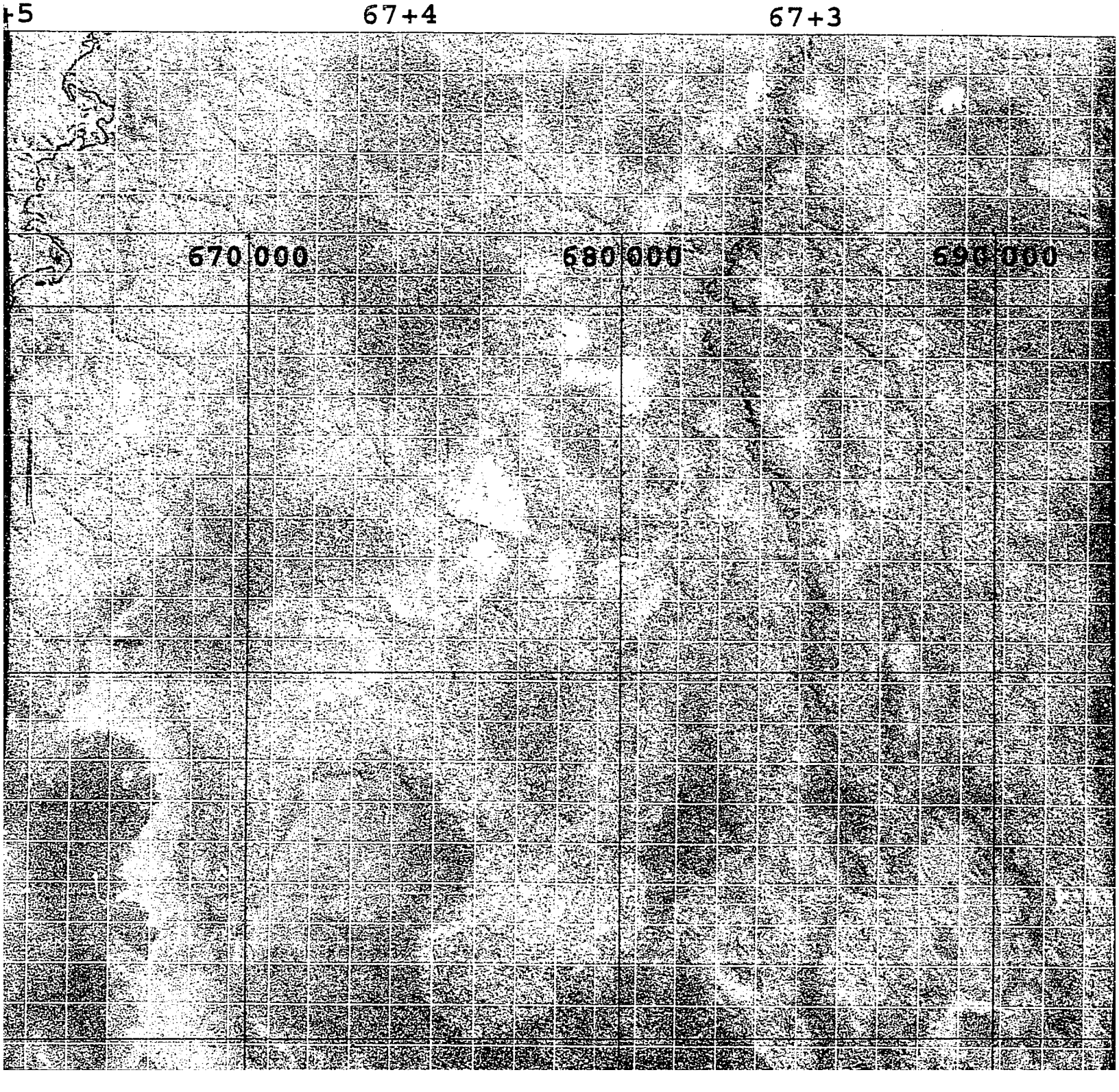

n Map for Beni Rive

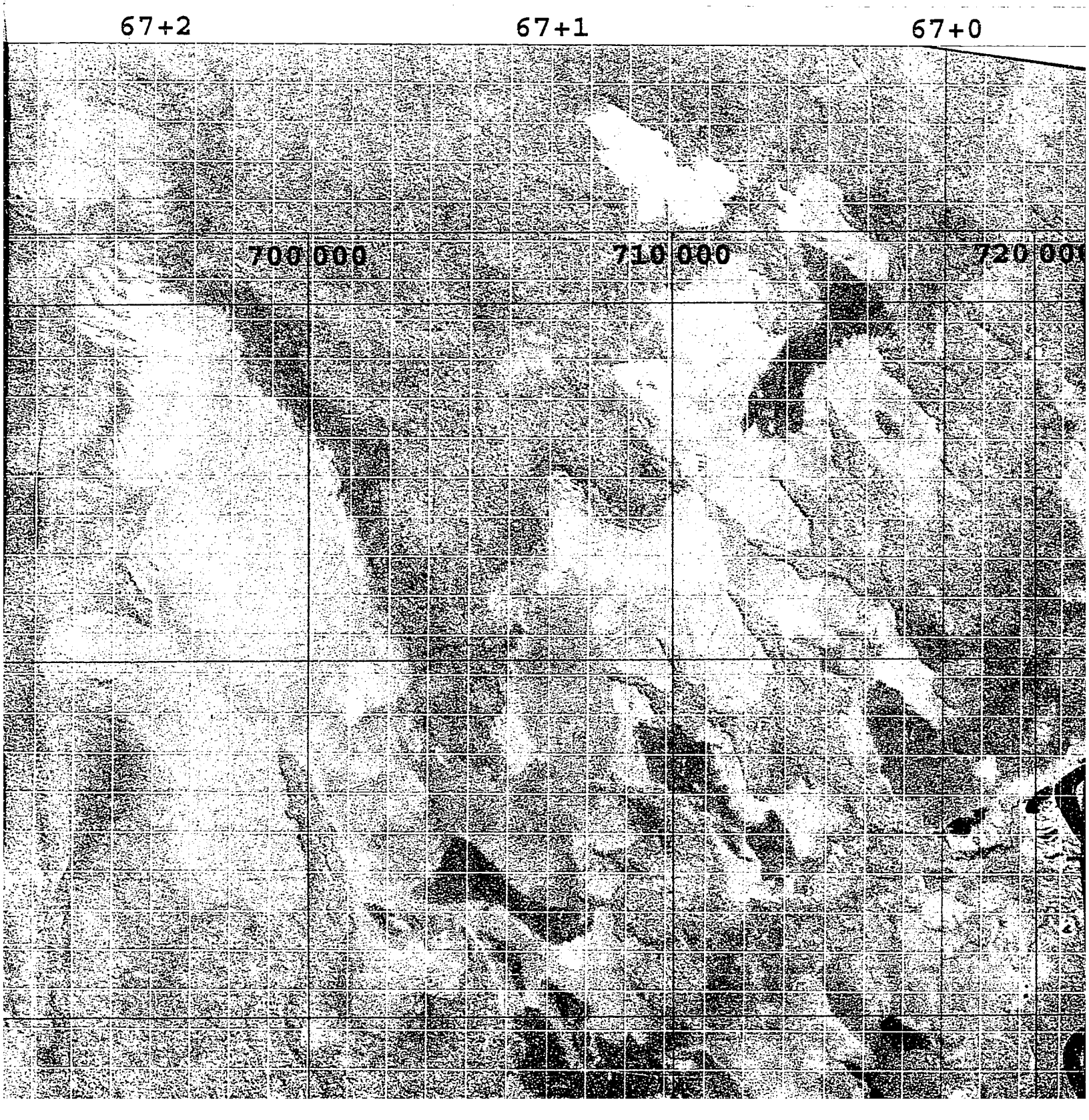

er, Bolivia

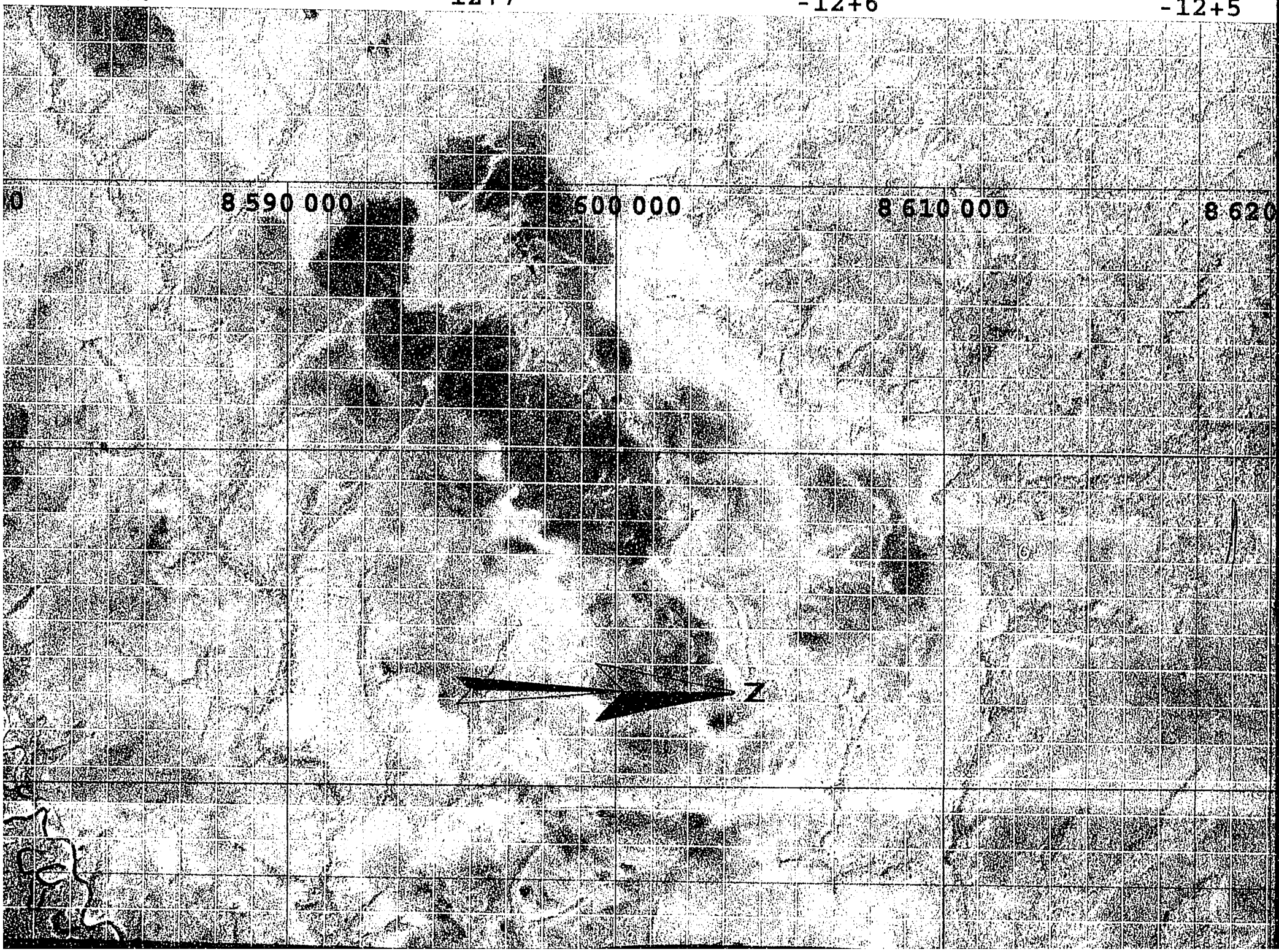
-12+8
-12+7
-12+6
-12+5
0
8 590 000
600 000
8 610 000
8 620
Z

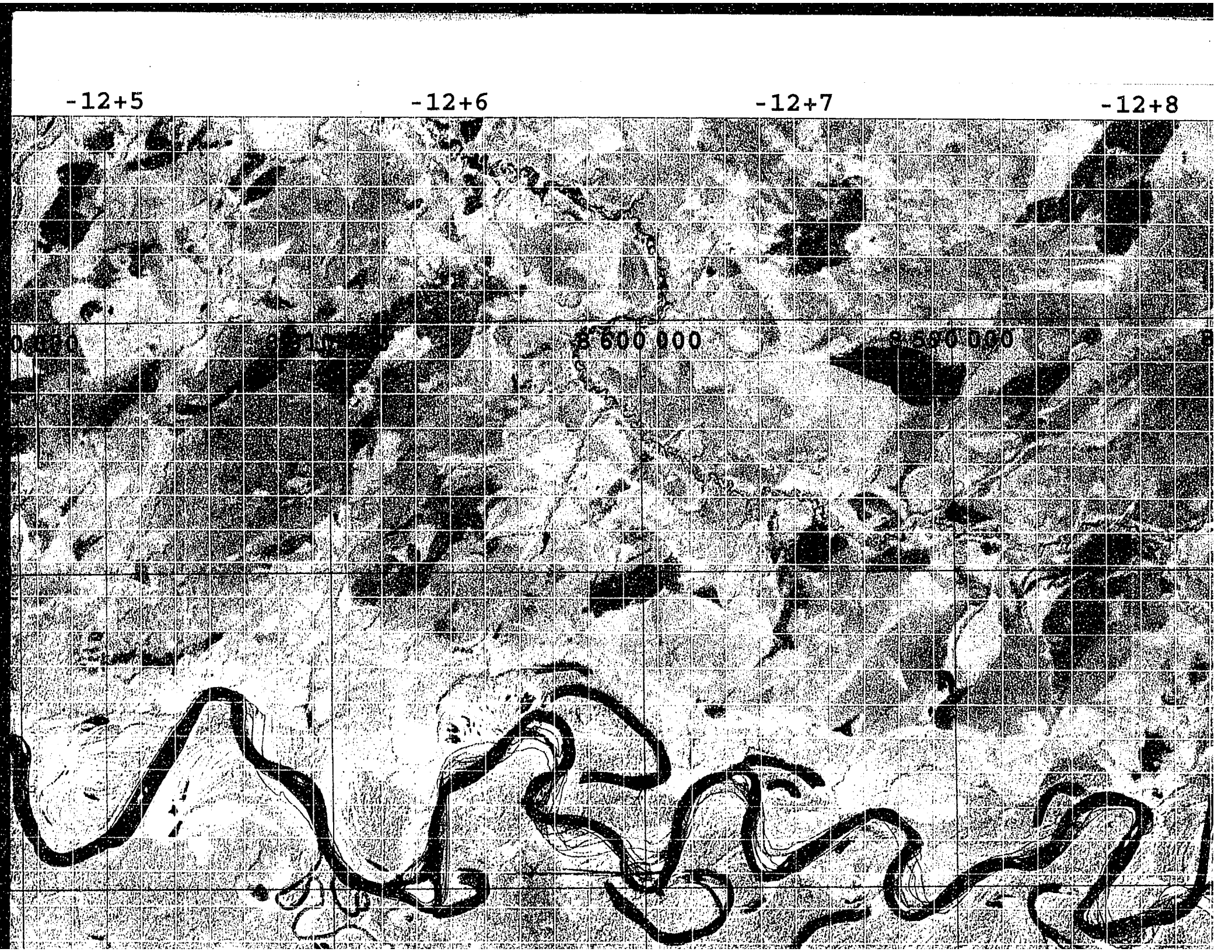
-12+5
-12+6
-12+7
-12+8
8 600 000
8 580 000

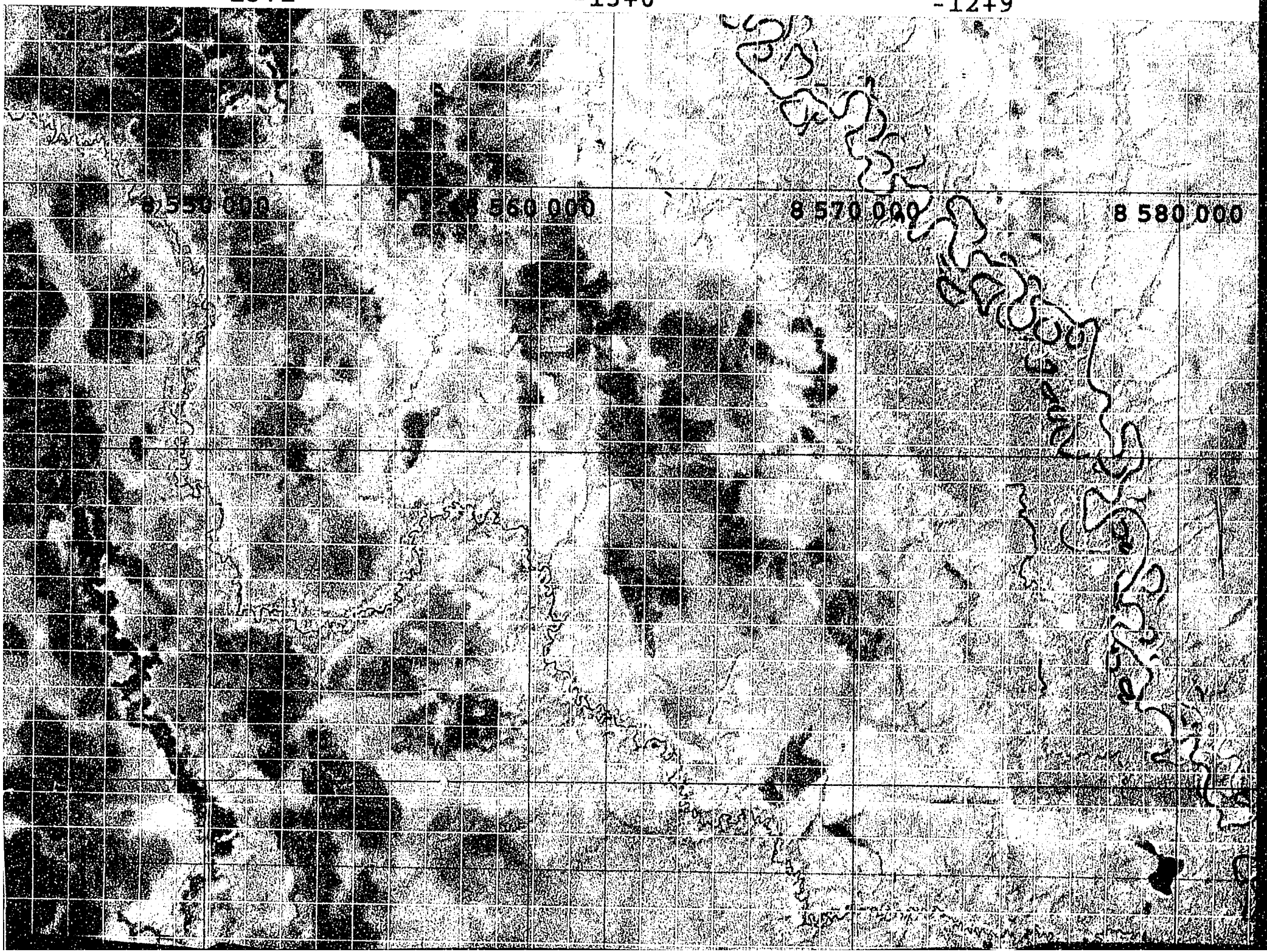
-13+1
-13+0
-12+9
8 560 000
8 570 000
8 580 000

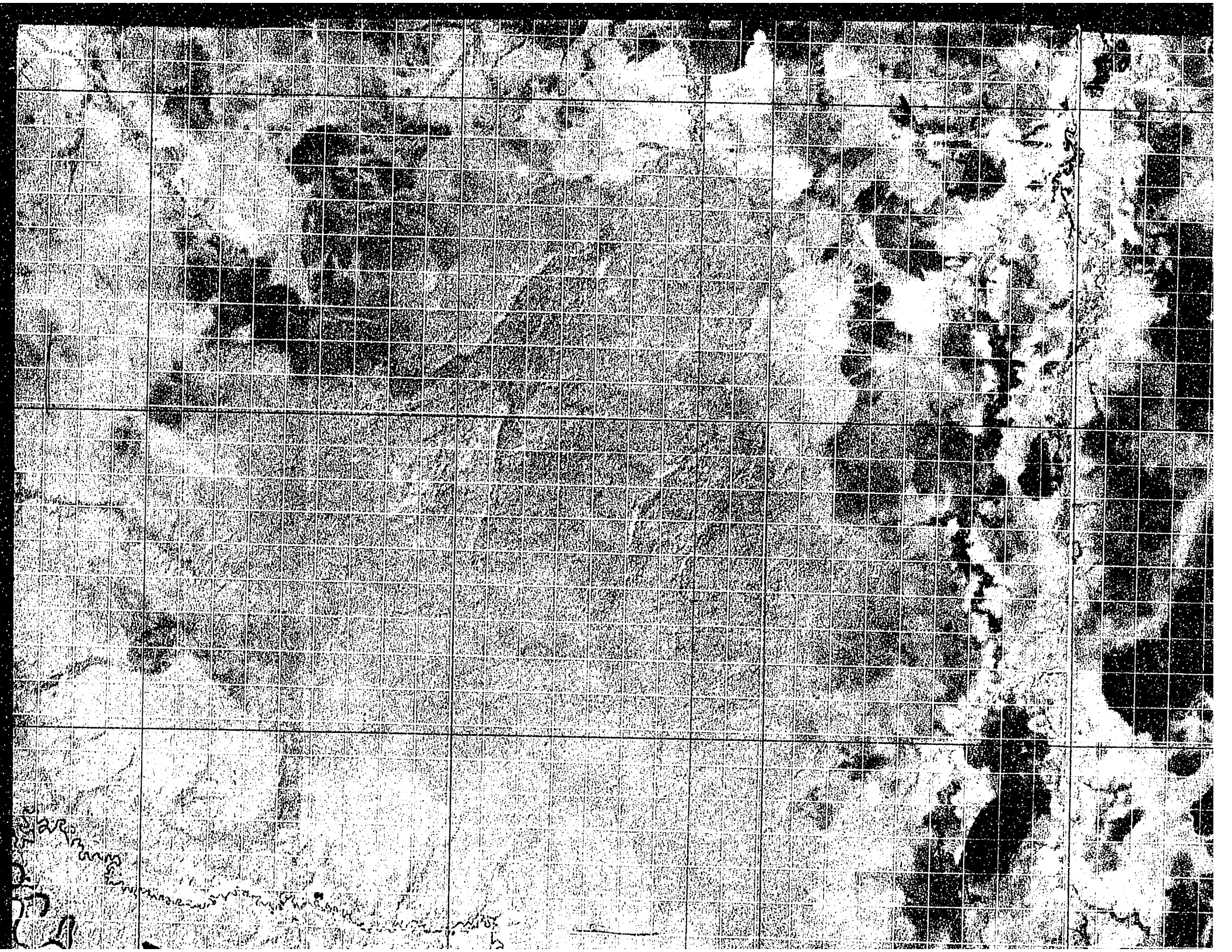

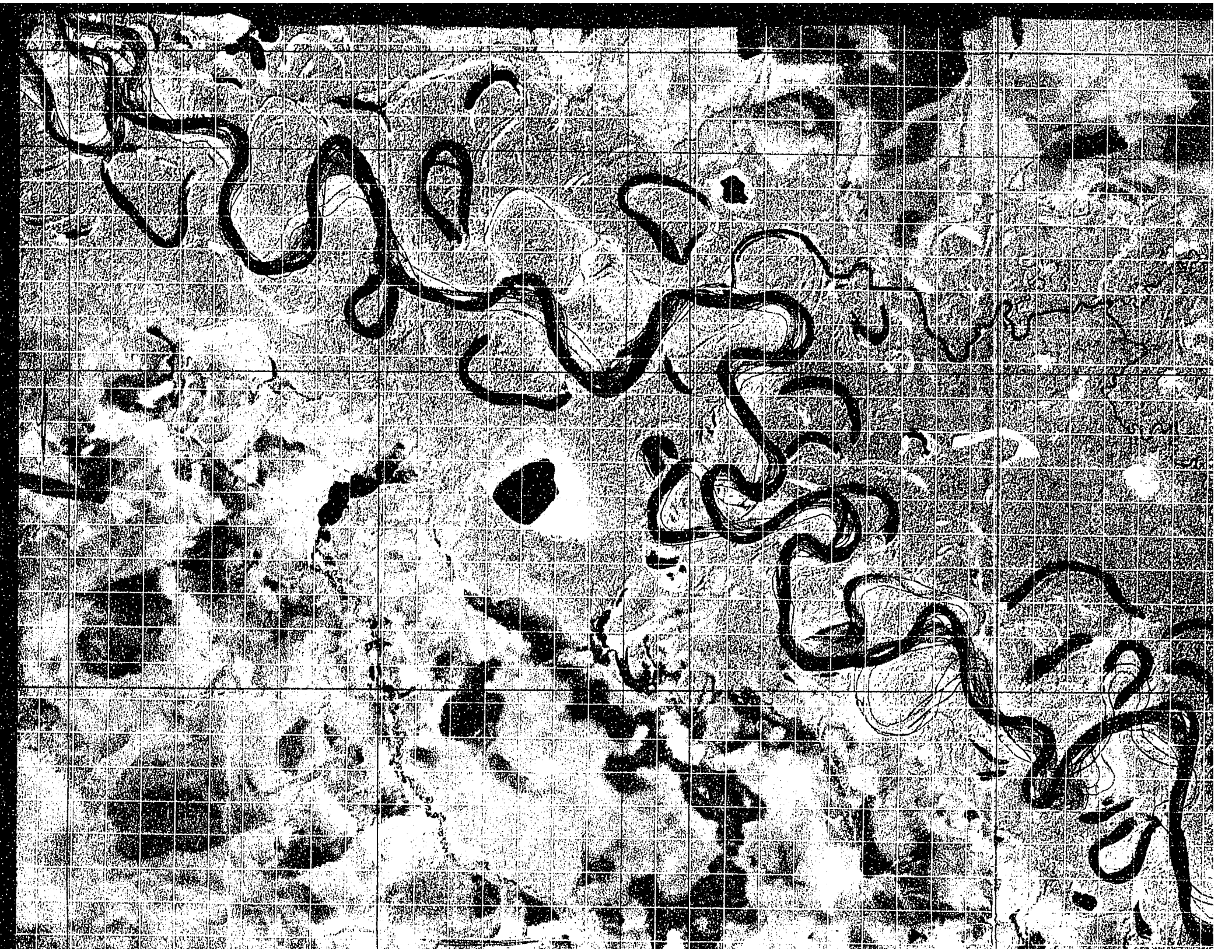

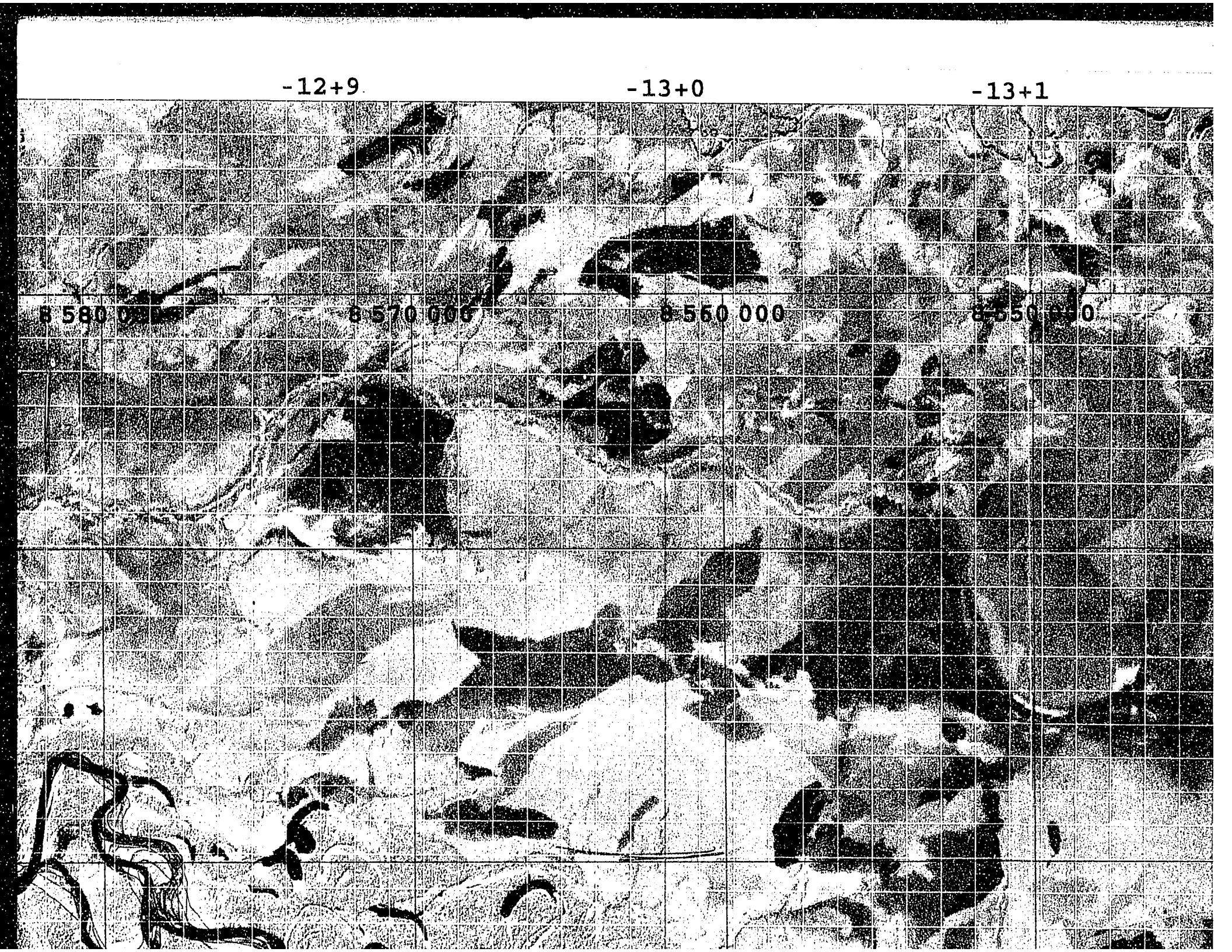
-12+9
-13+0
-13+1
8 580 000
8 570 000
8 560 000
8 550 000

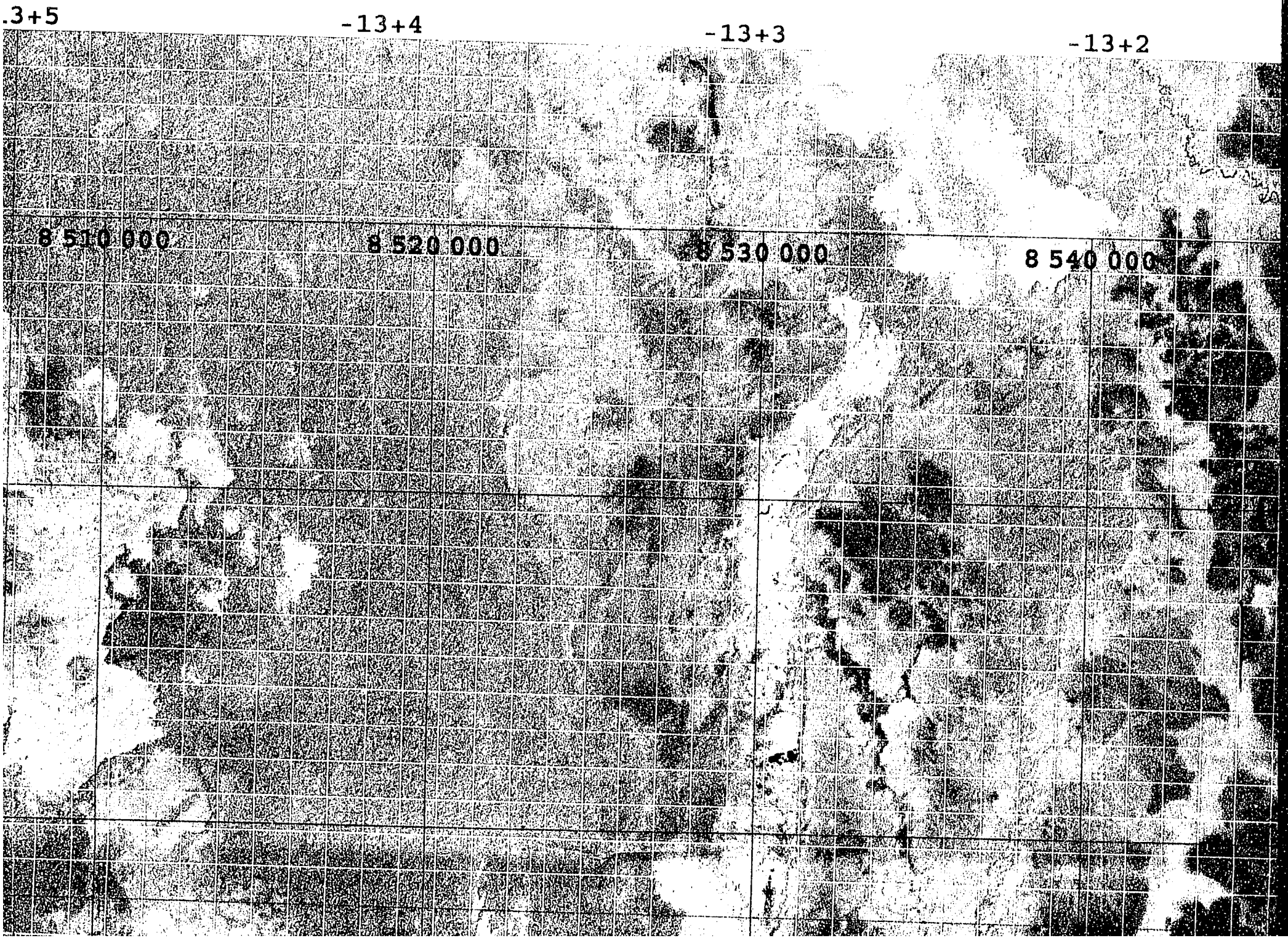
.3+5
-13+4
-13+3
-13+2
8 510 000
8 520 000
8 530 000
8 540 000

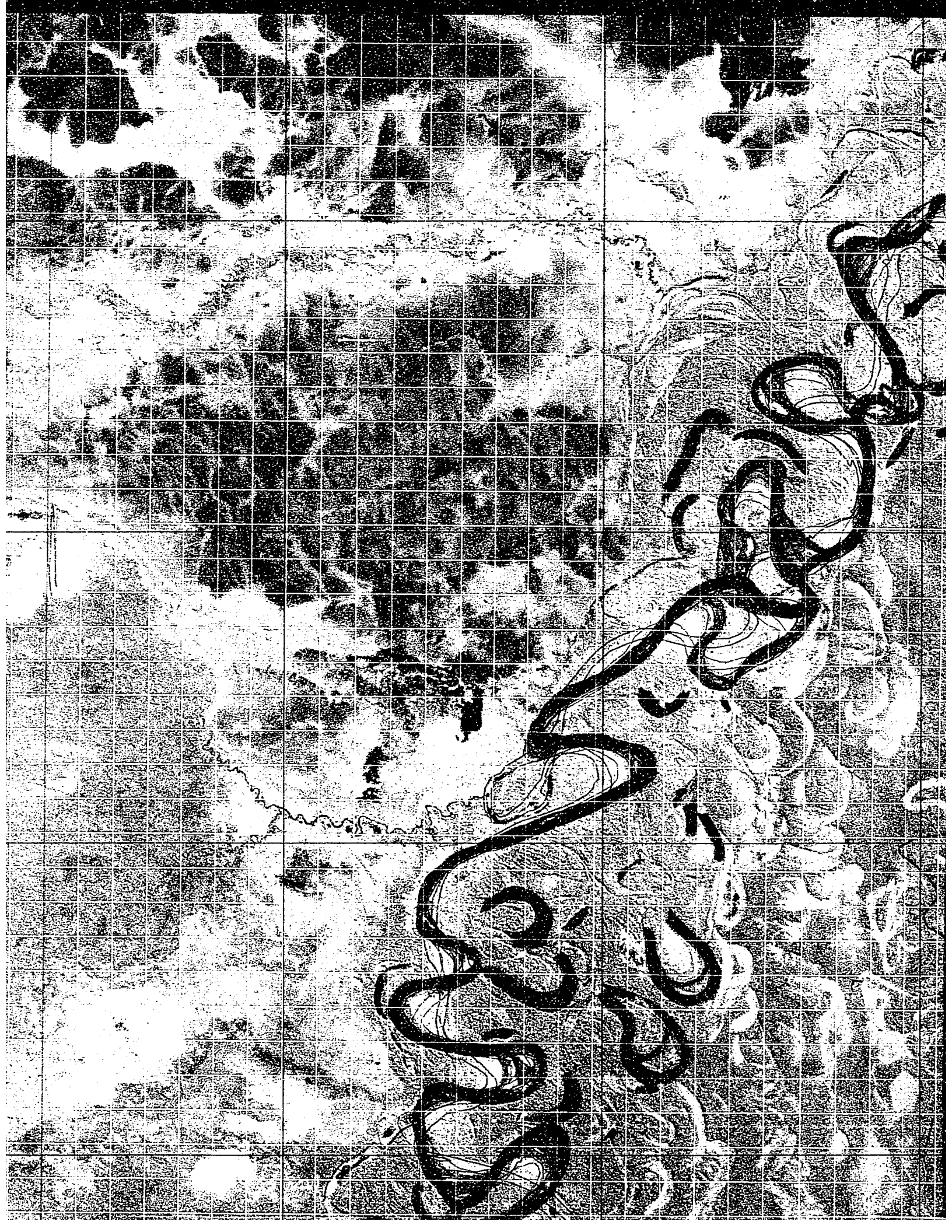

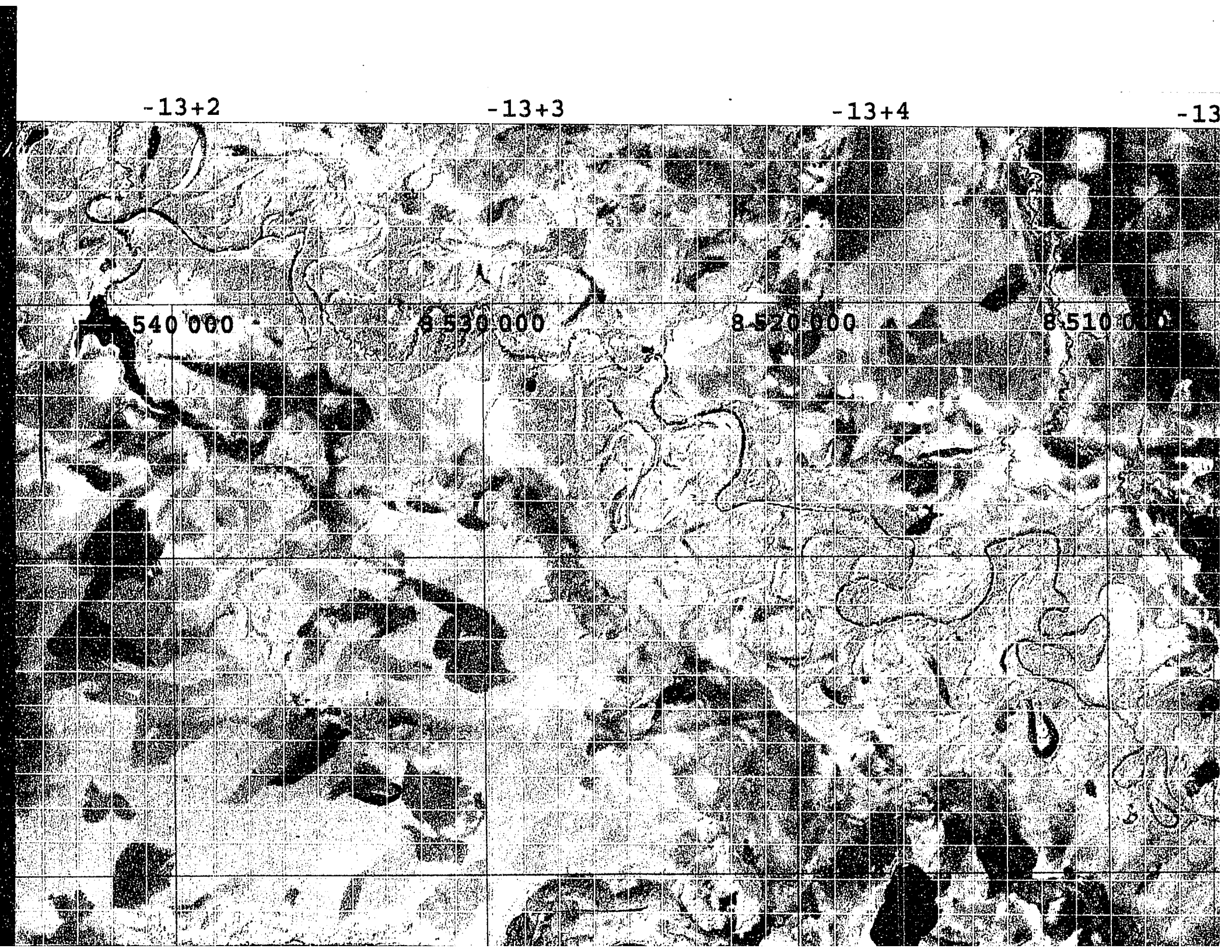
-13+2
-13+3
-13+4
-13
540 000
8 530 000
8 520 000
8 510 0

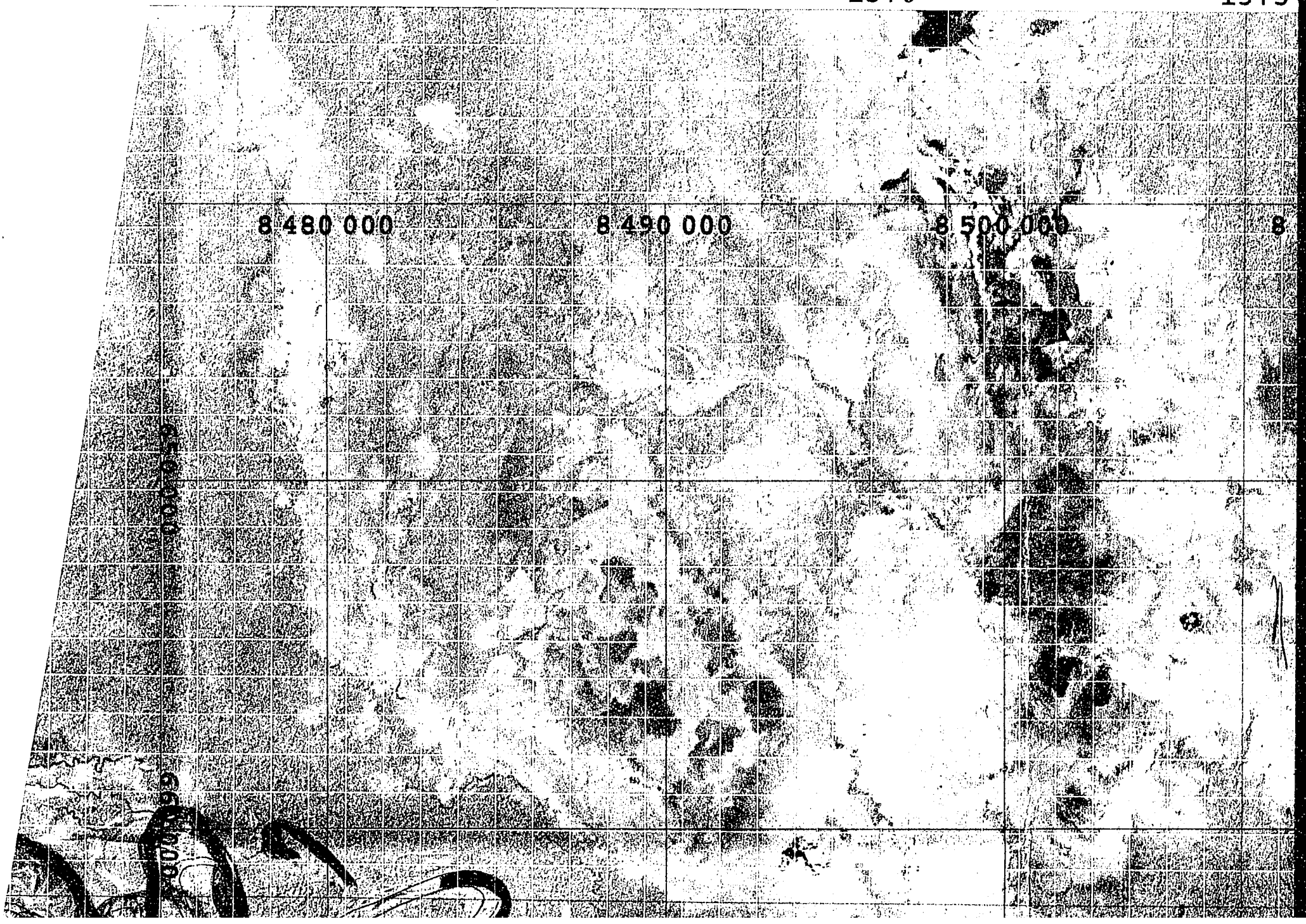
-13+8
-13+7
-13+6
-13+5
8 480 000
8 490 000
8 500 000
8

670 000
680 000
690 000

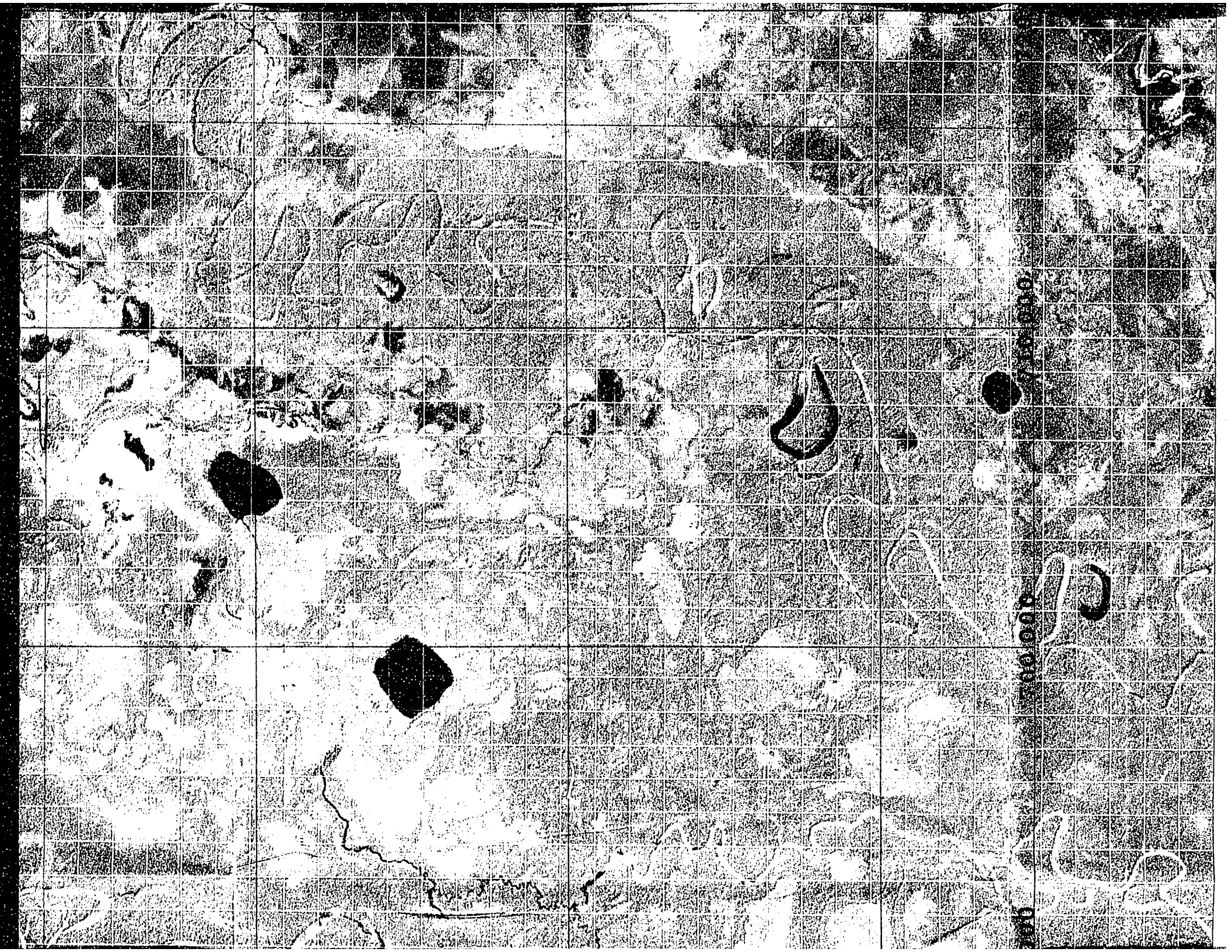

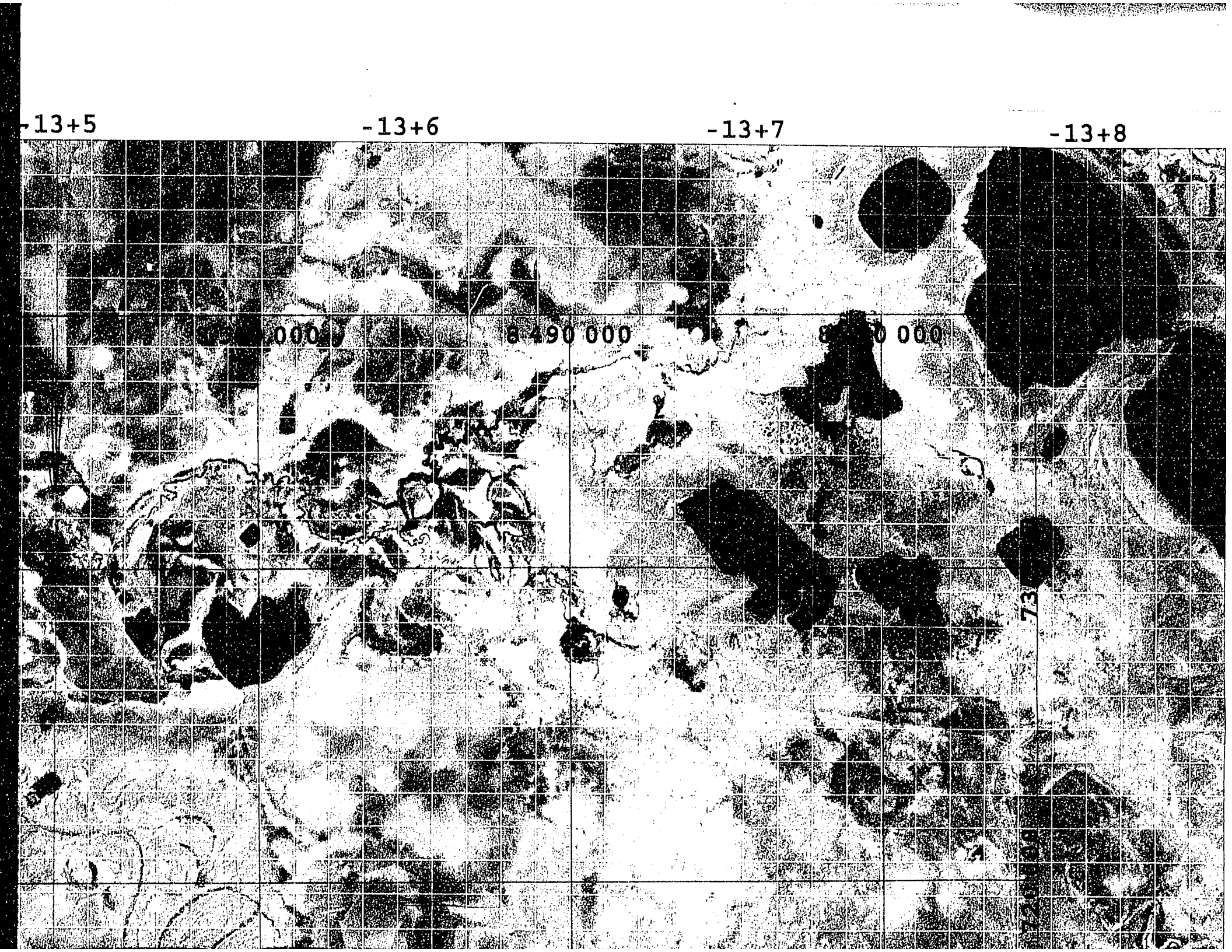
-13+5
-13+6
-13+7
-13+8
8 490 000

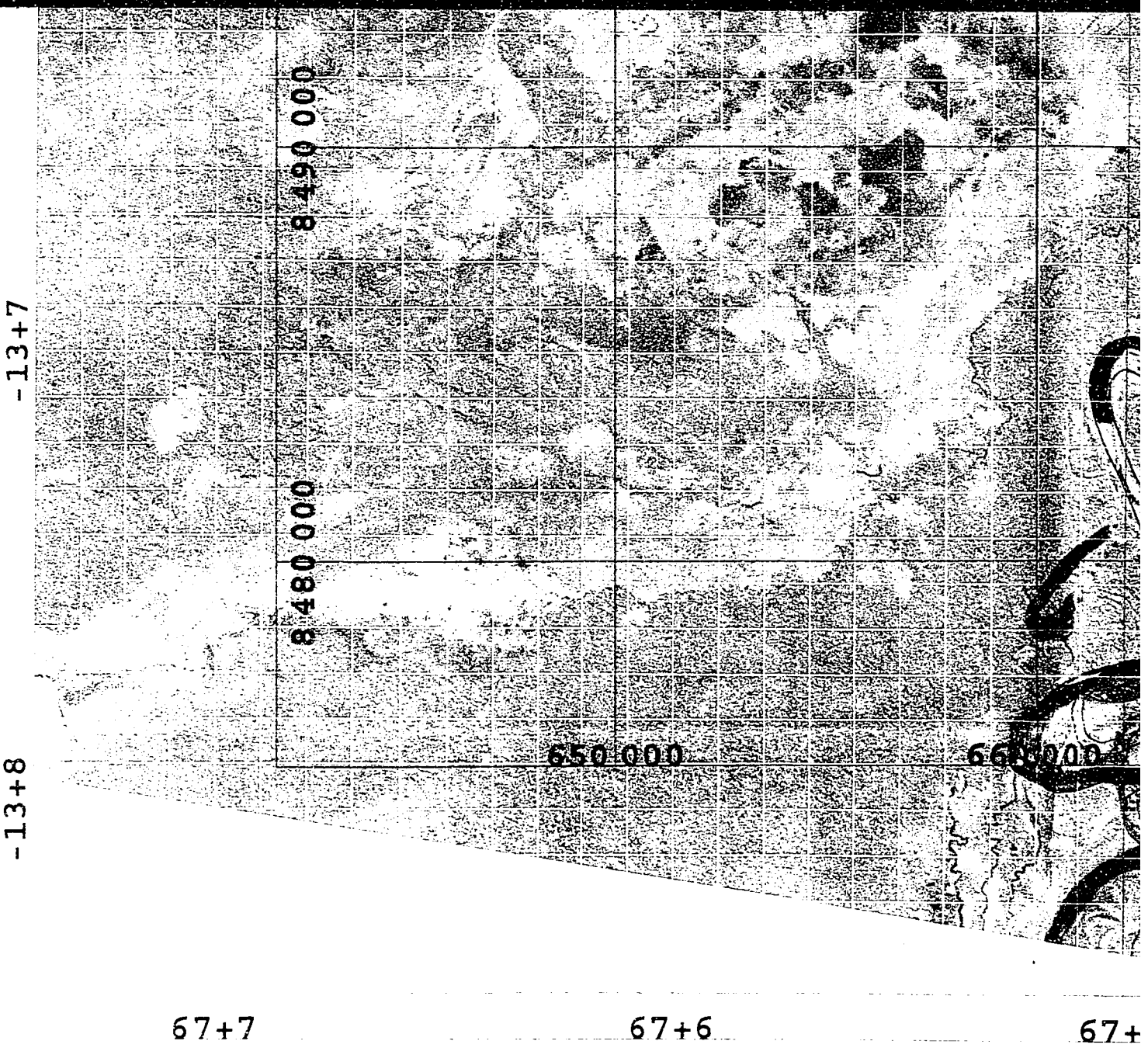

1960 channel

1975 channel

1986 channel

1993 channel

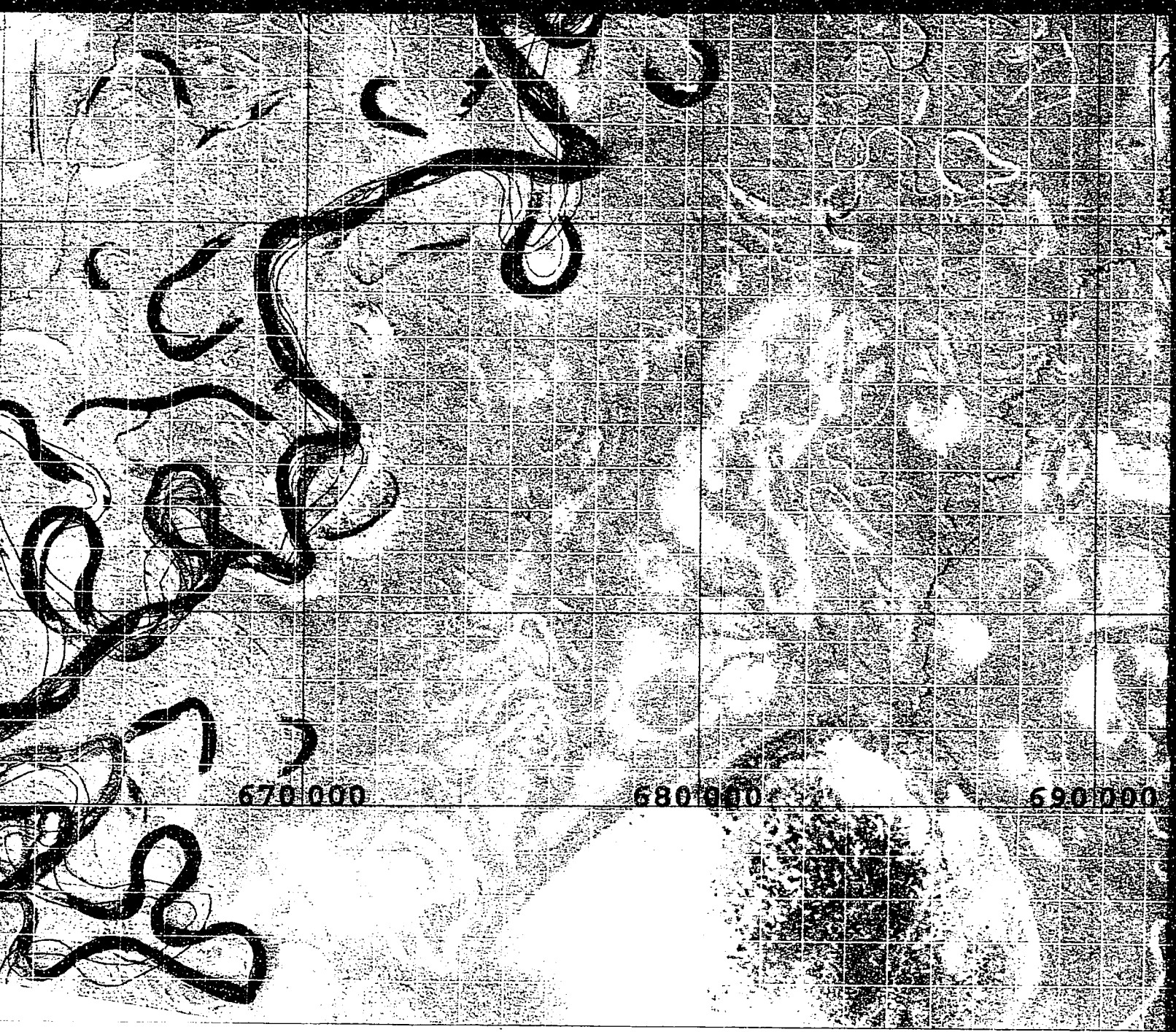

Base Map: 10/July/1999 Landsat ETM+ Path 1
UTM Zone 19 South
False Color Composite of Bands 5, 4, and 3

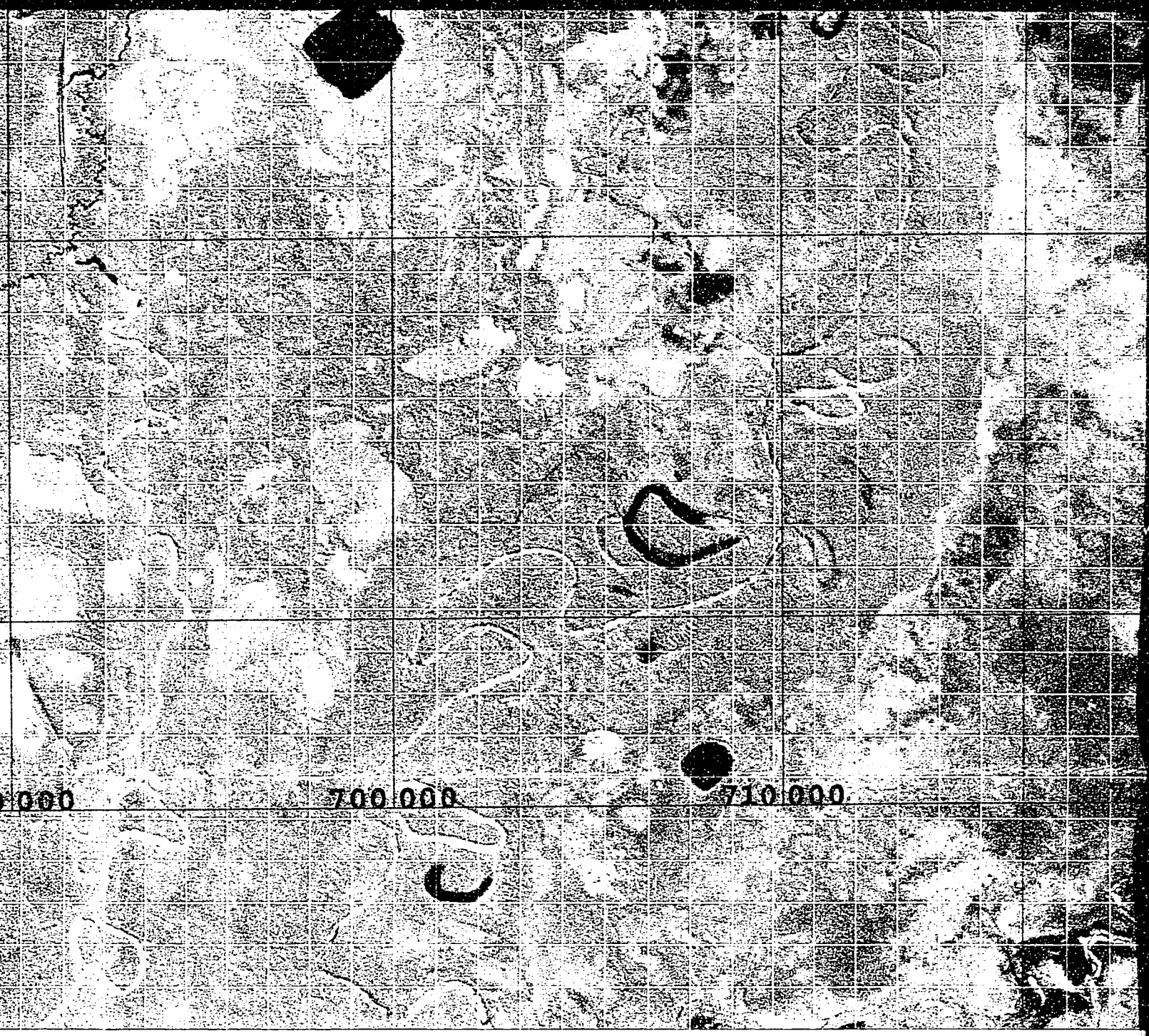

Path 1, Row 69

3

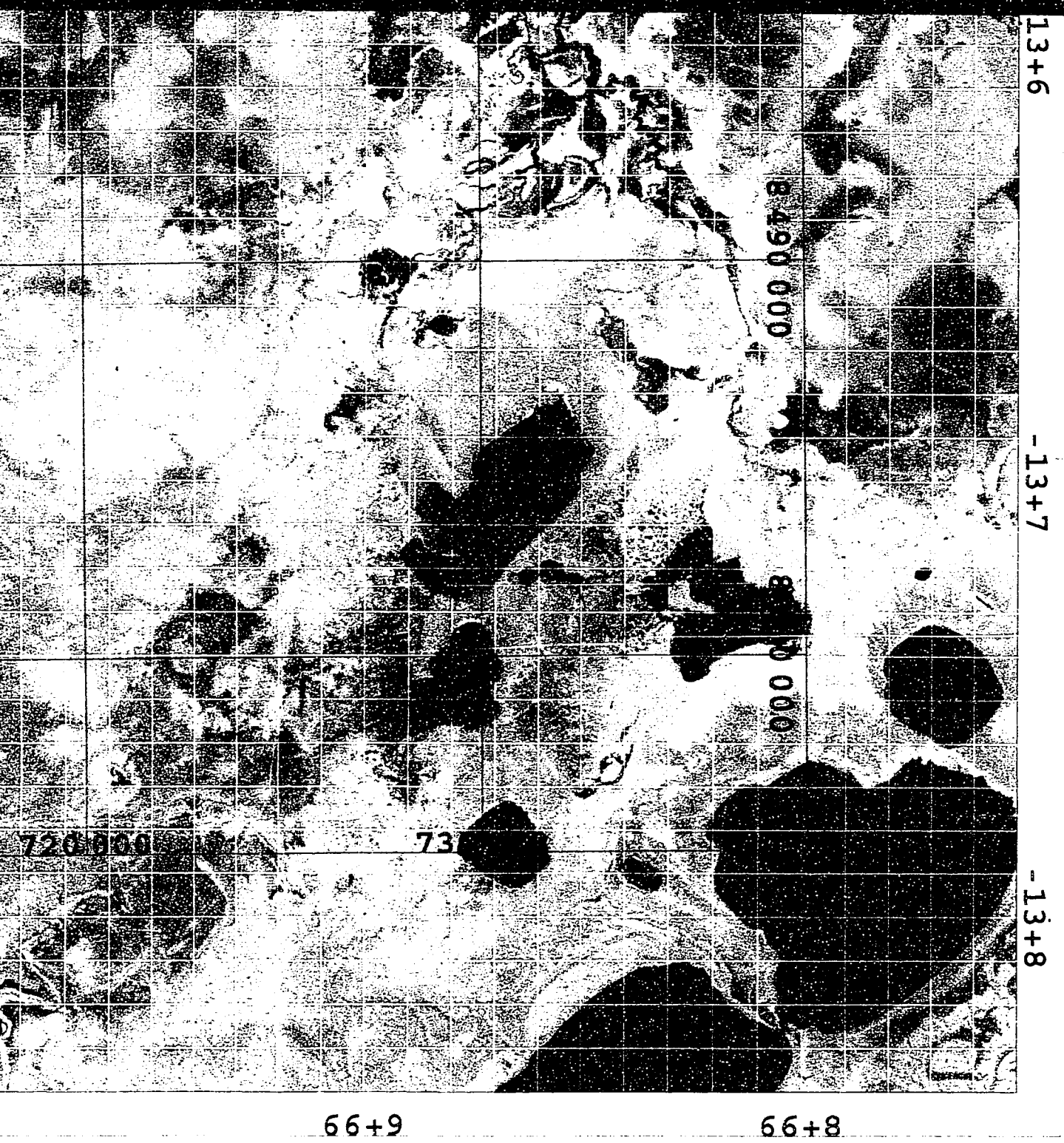

Mainstream

67+7

-13+7

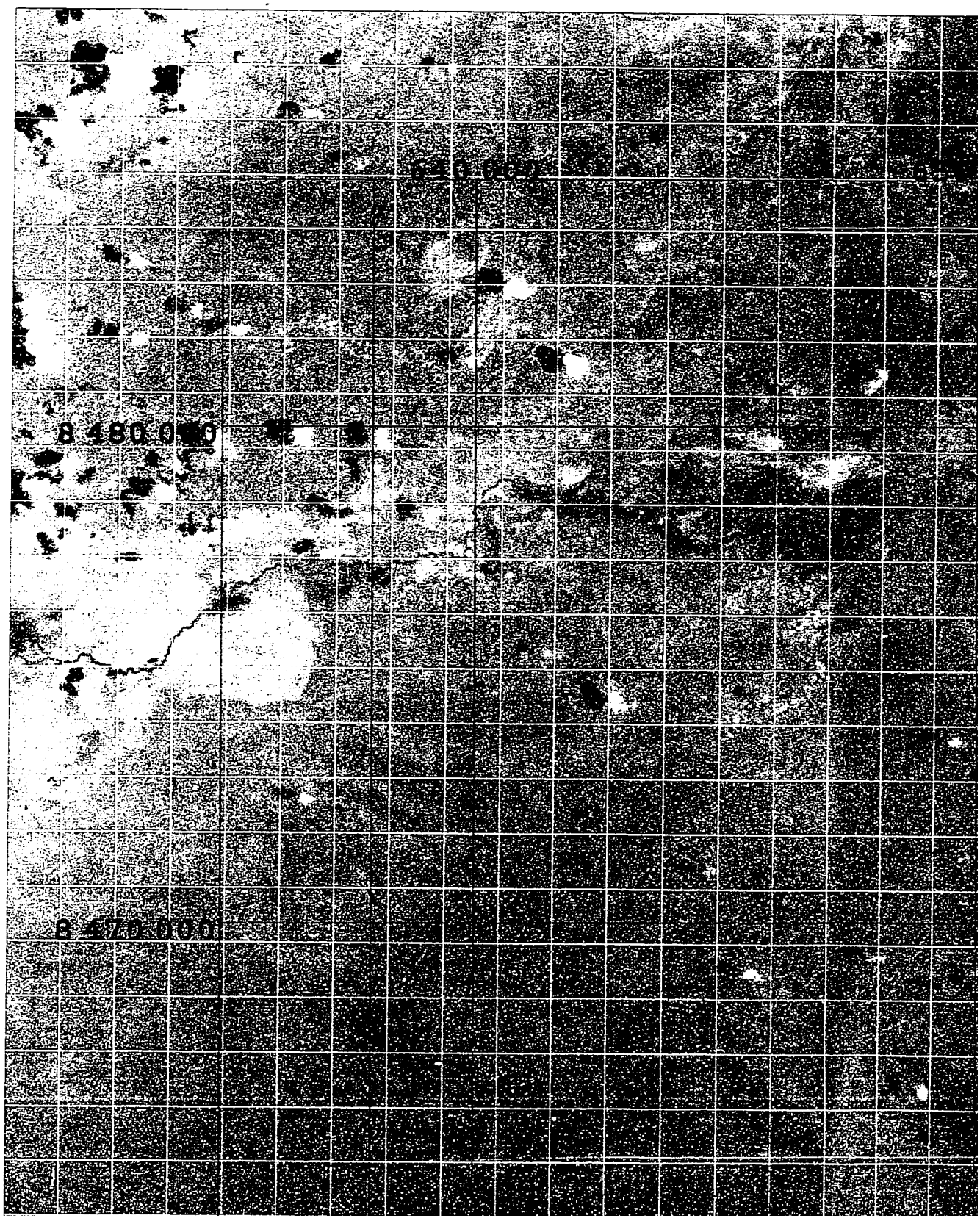

-13+8

n Channel Location

67+6 67+5 6'

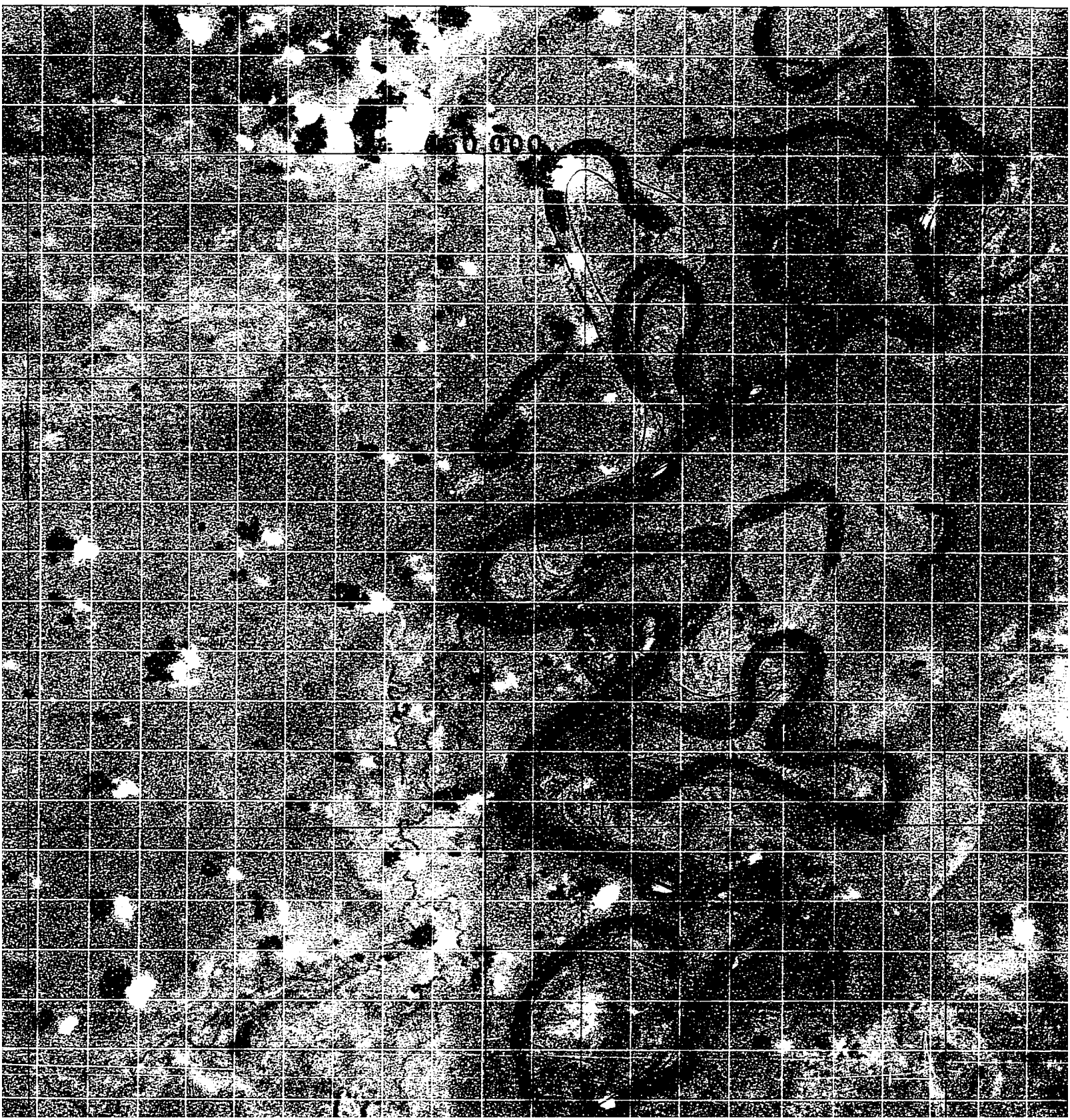

n Map for Beni Riv

67+4 67+3 6

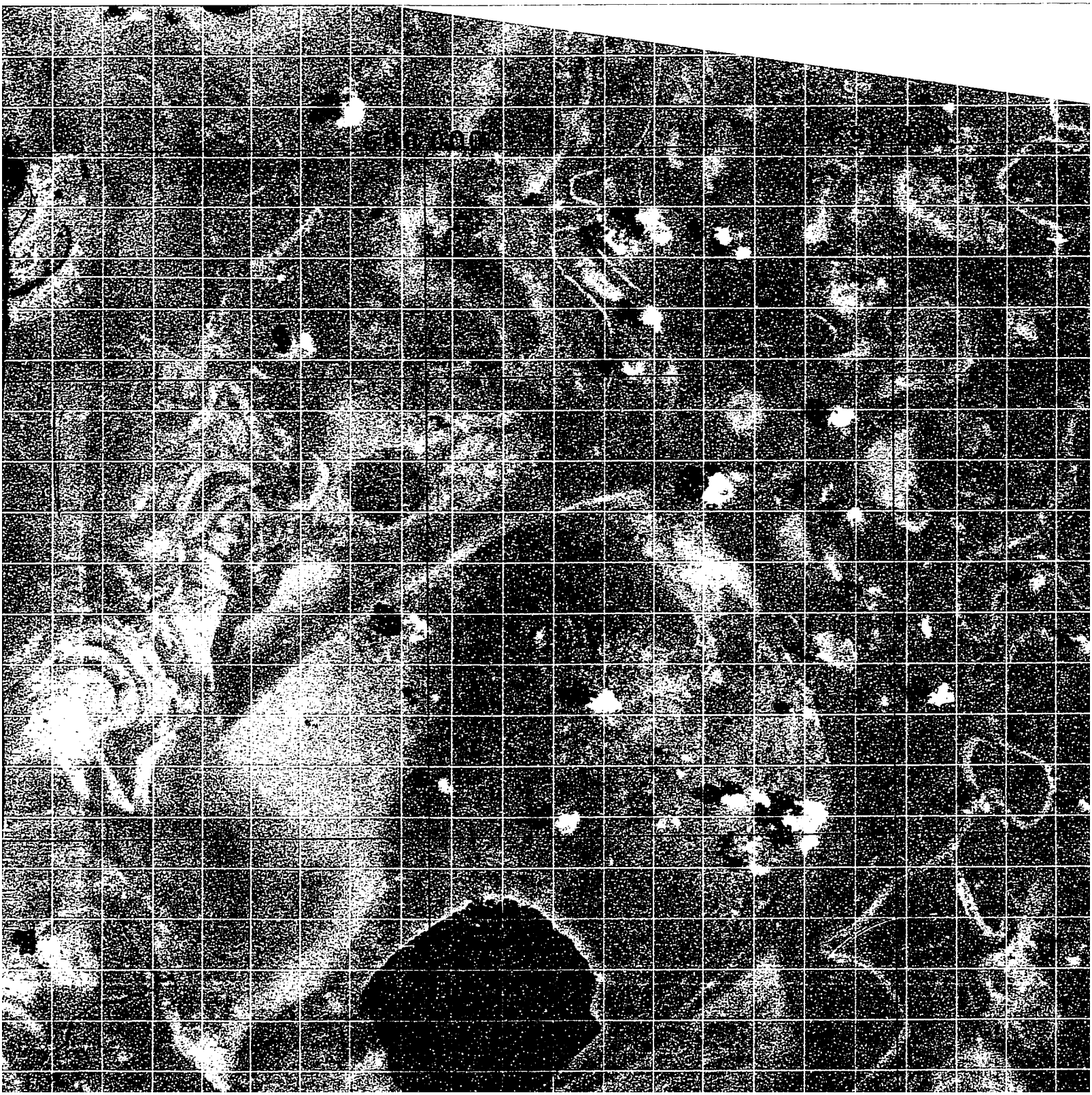

er, Bolivia

67+2

67+1

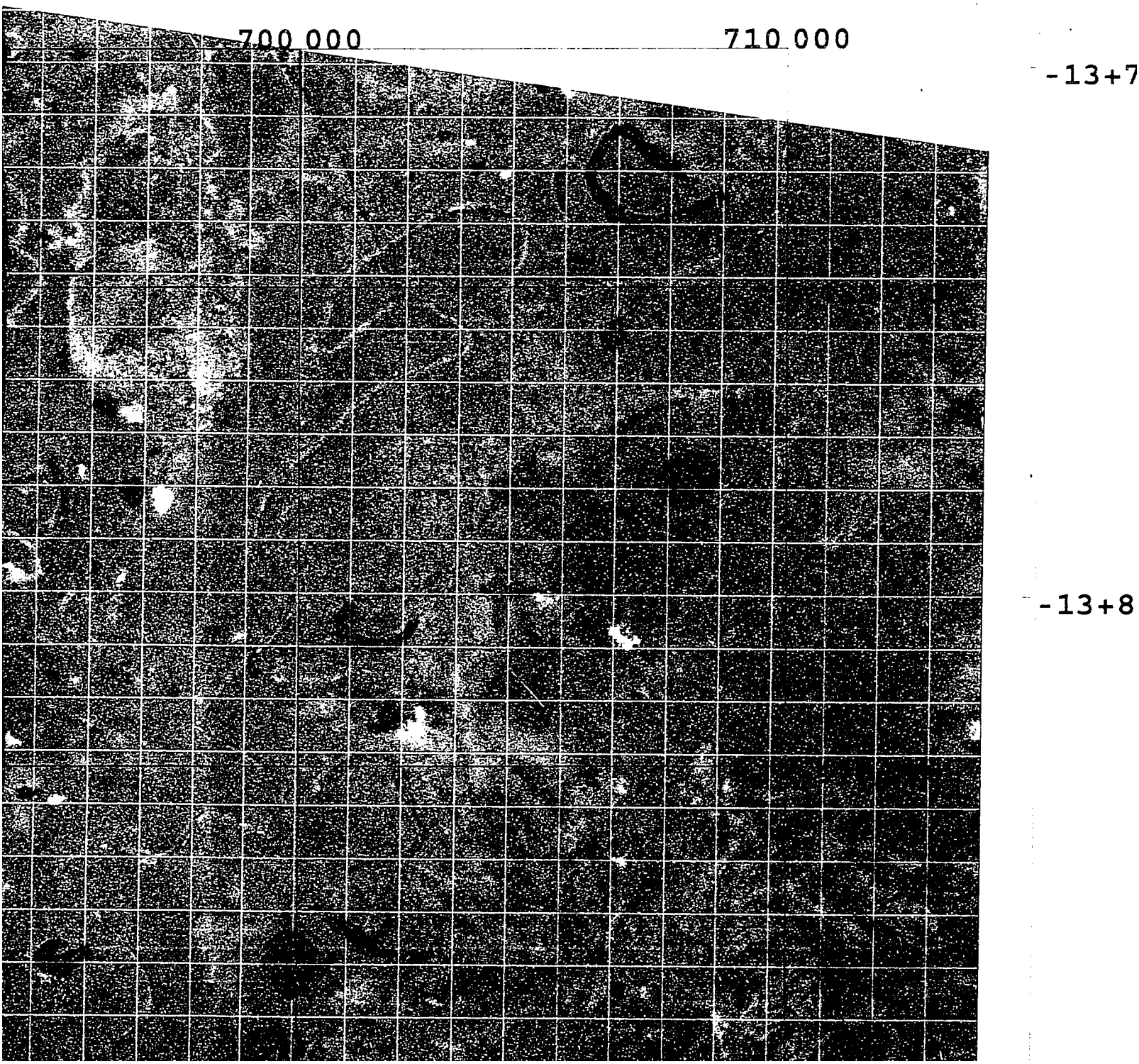

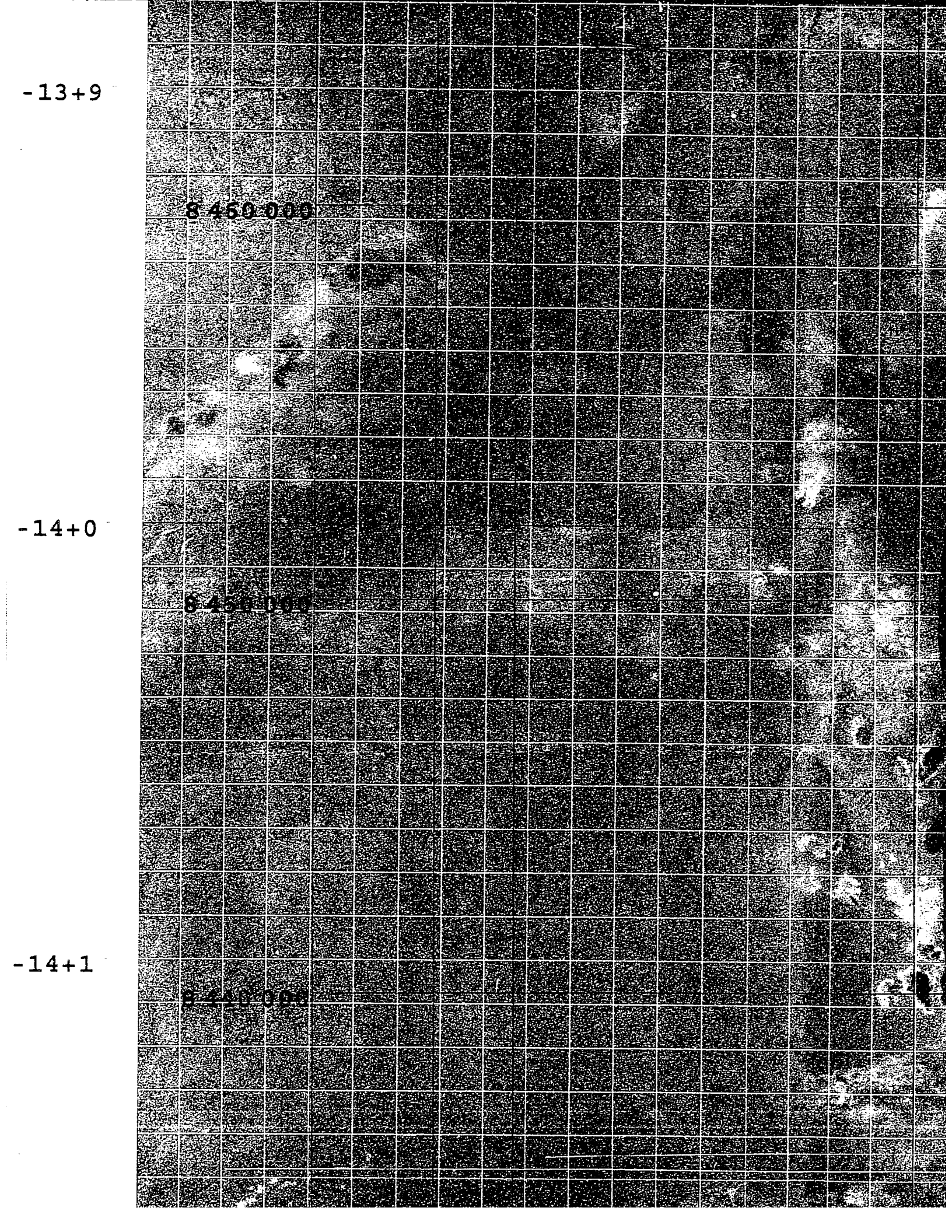
-13+9
8 460 000
-14+0
8 450 000
-14+1
8 440 000

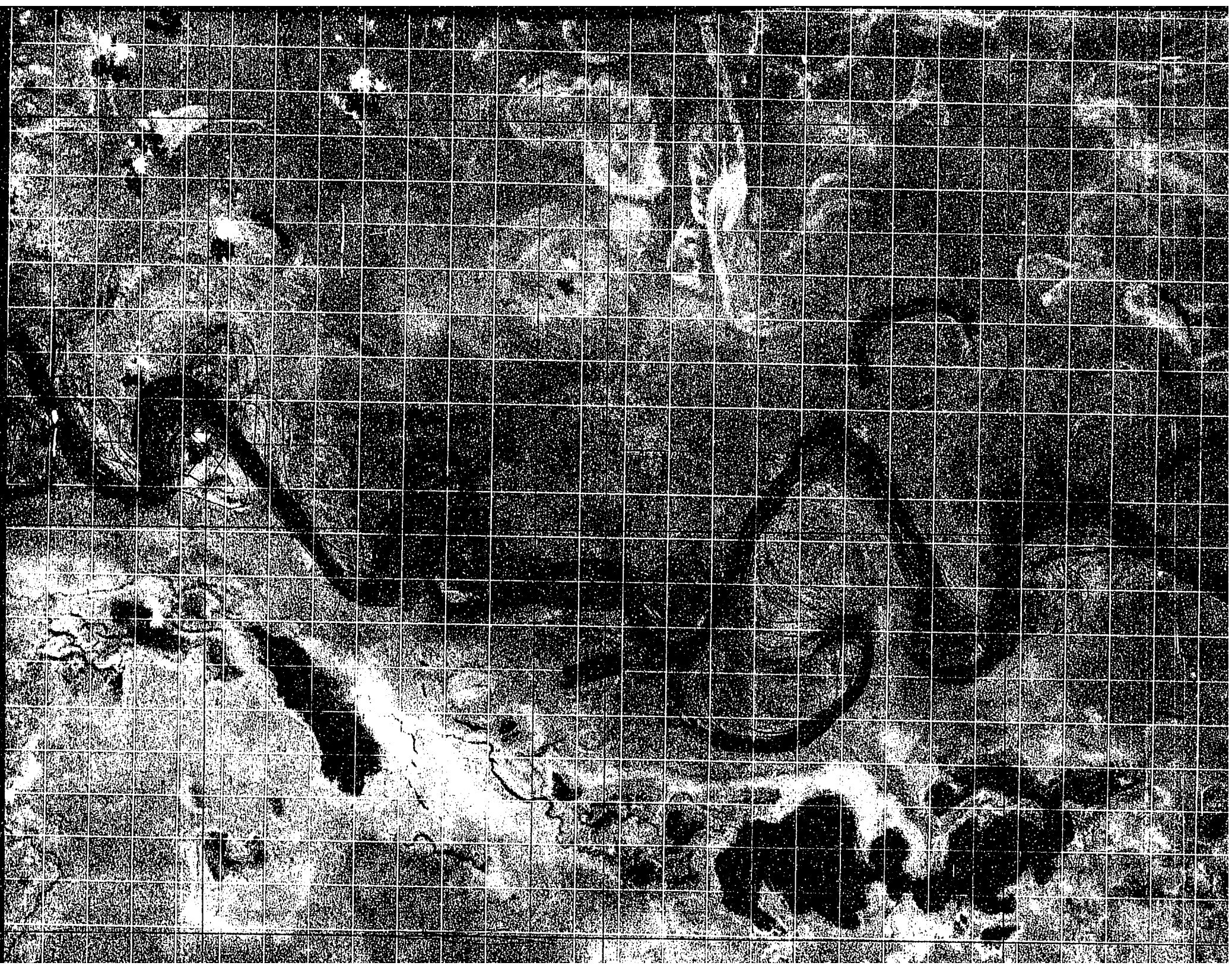

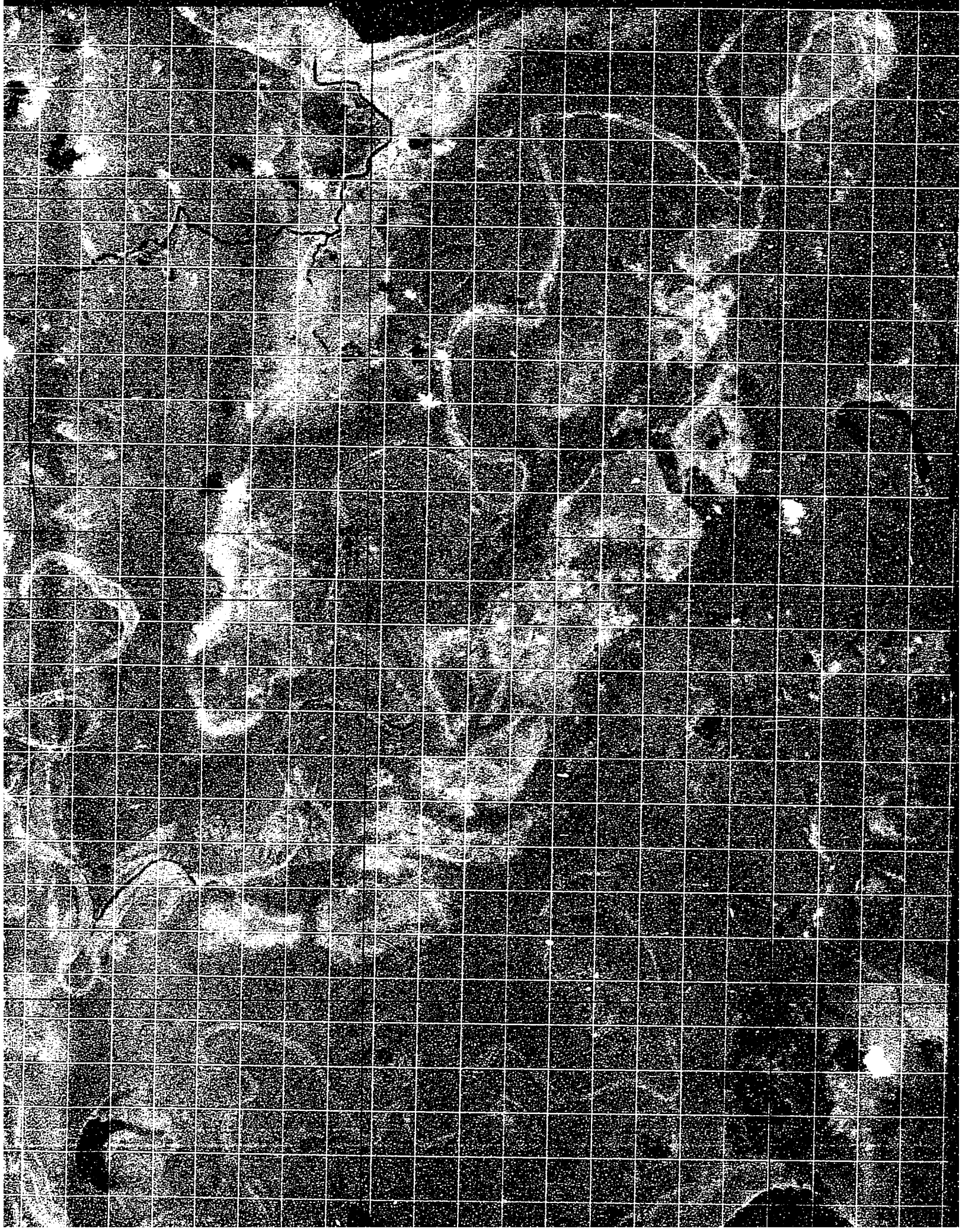

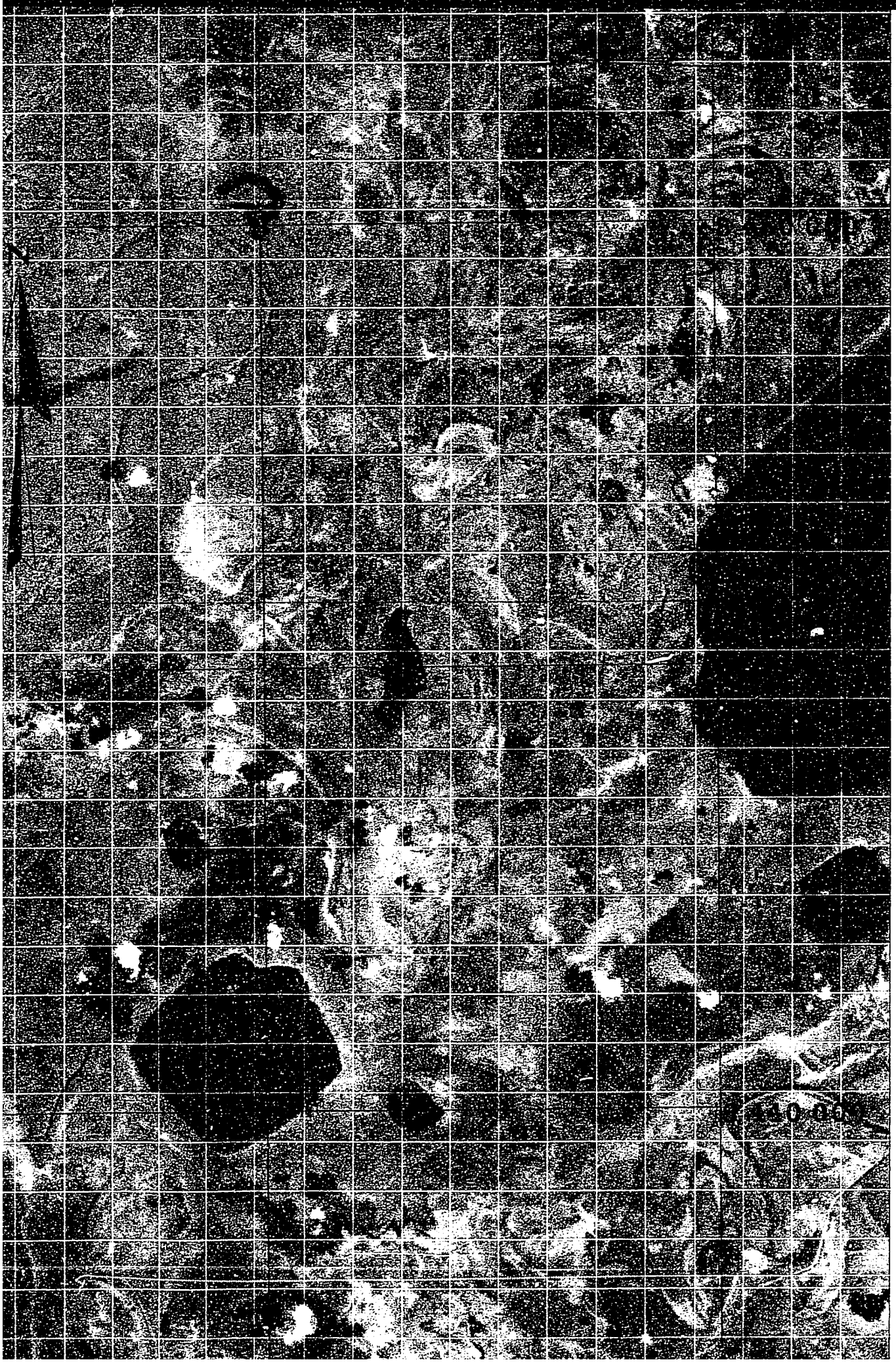
-13+9
-14+0
-14+1

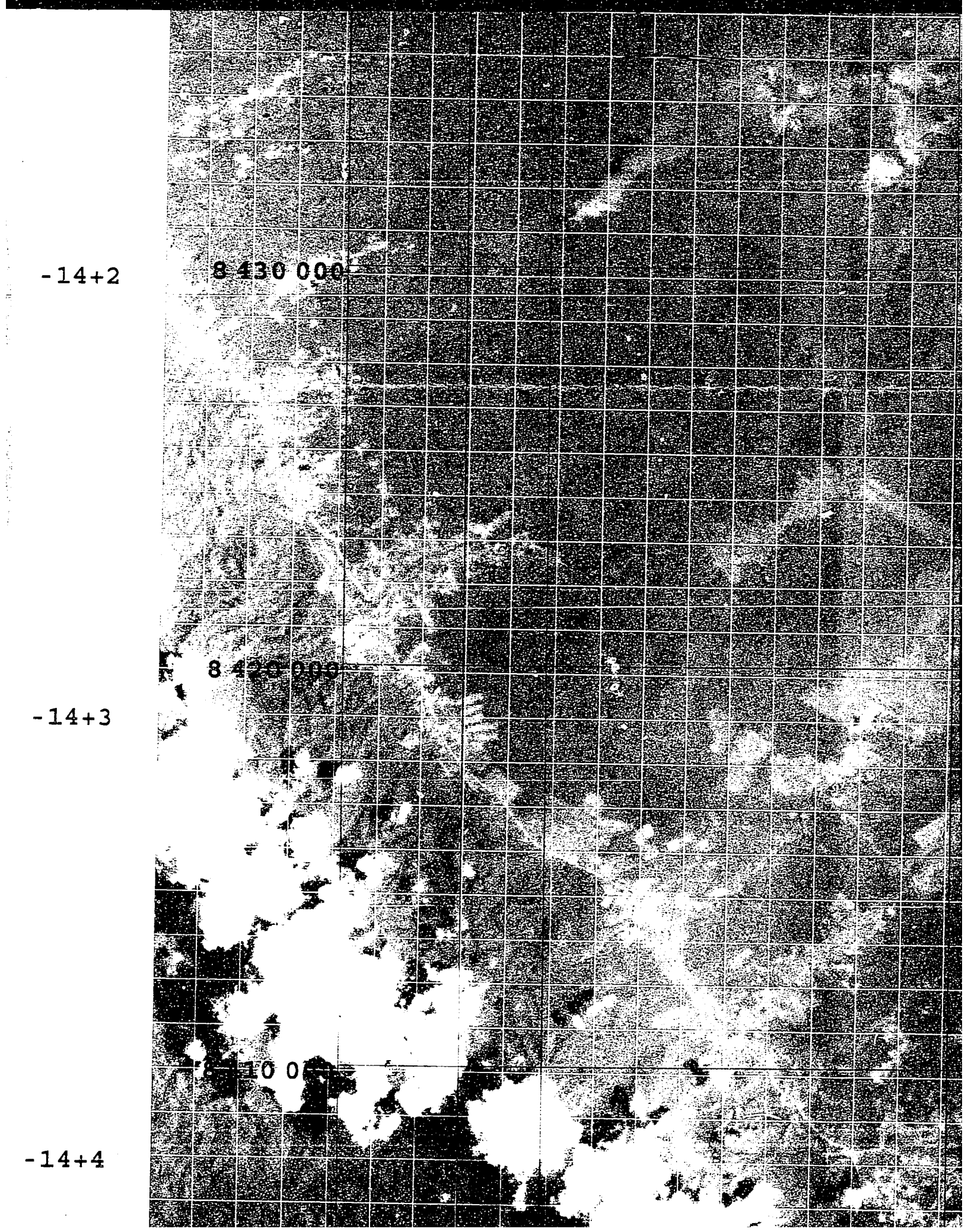
-14+2
8 430 000
8 420 000
-14+3
-14+4

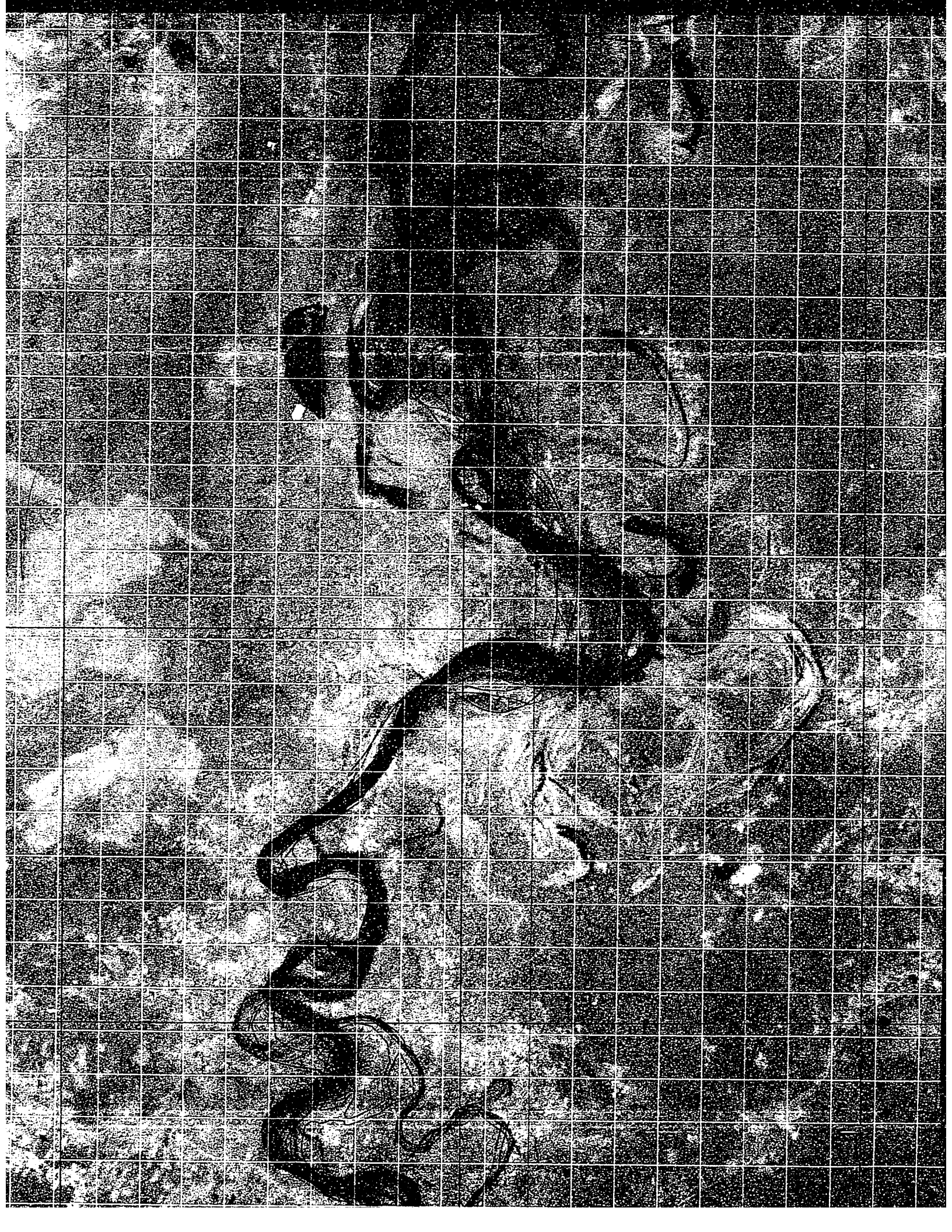

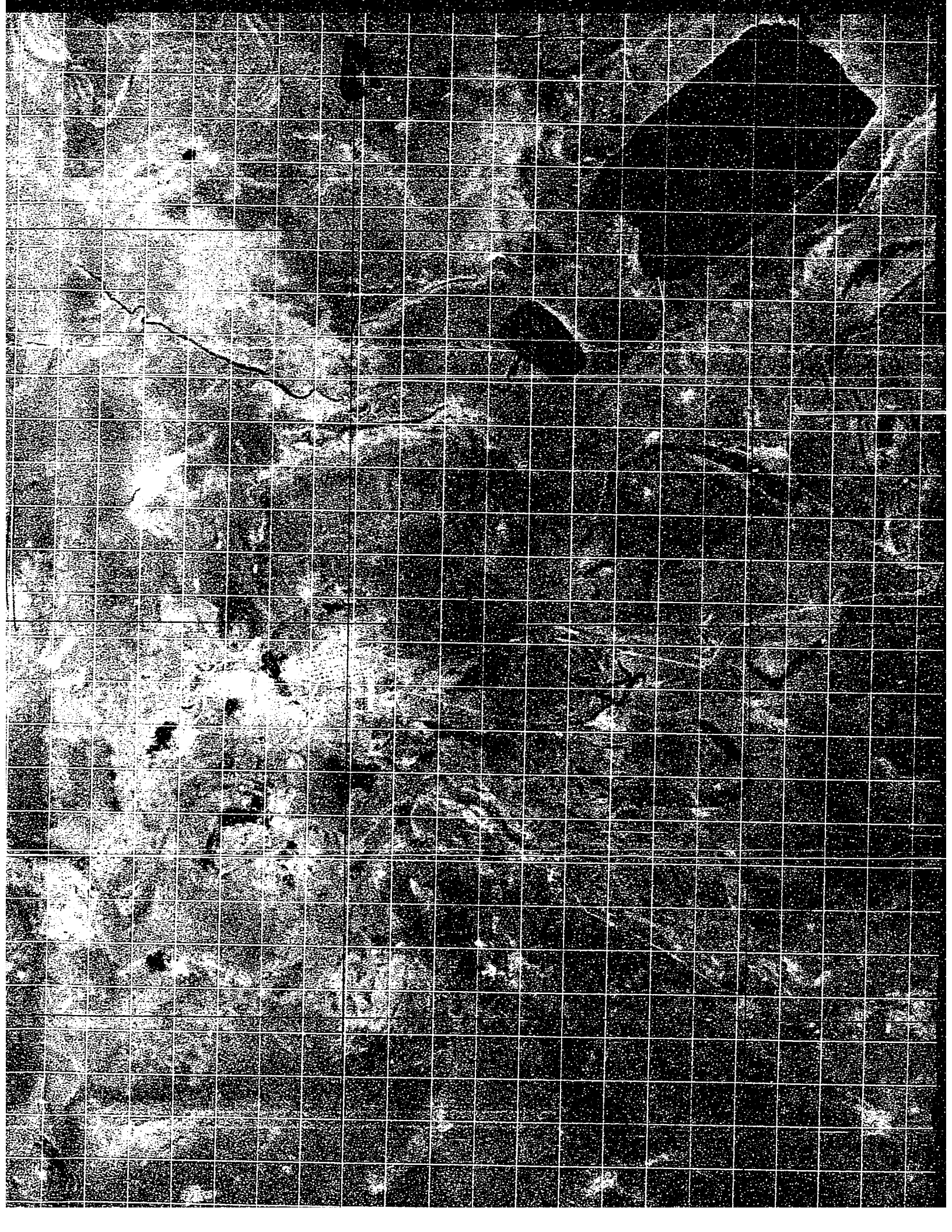

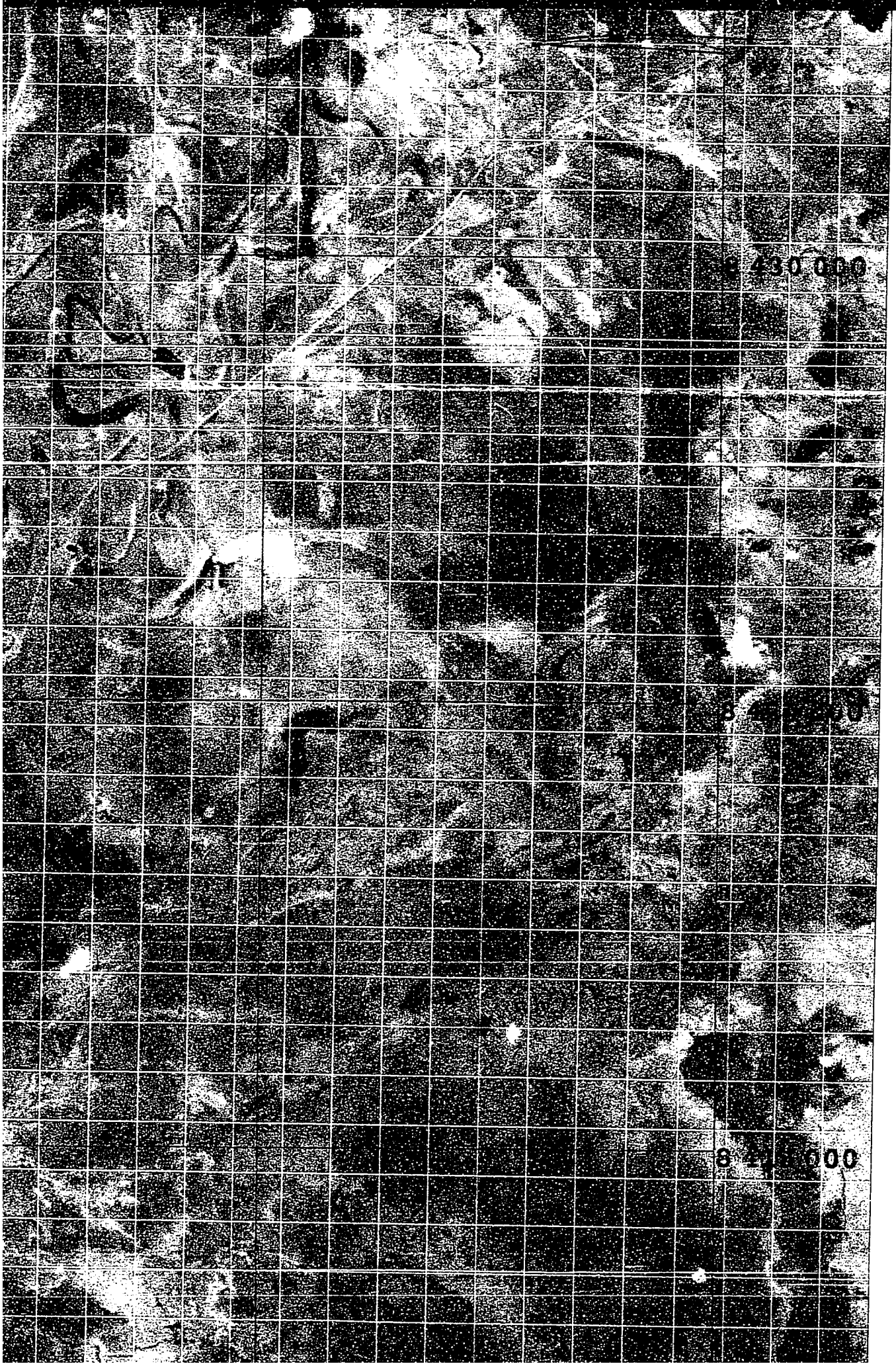
8 430 000
-14+2
-14+3
8 420 000
-14+4

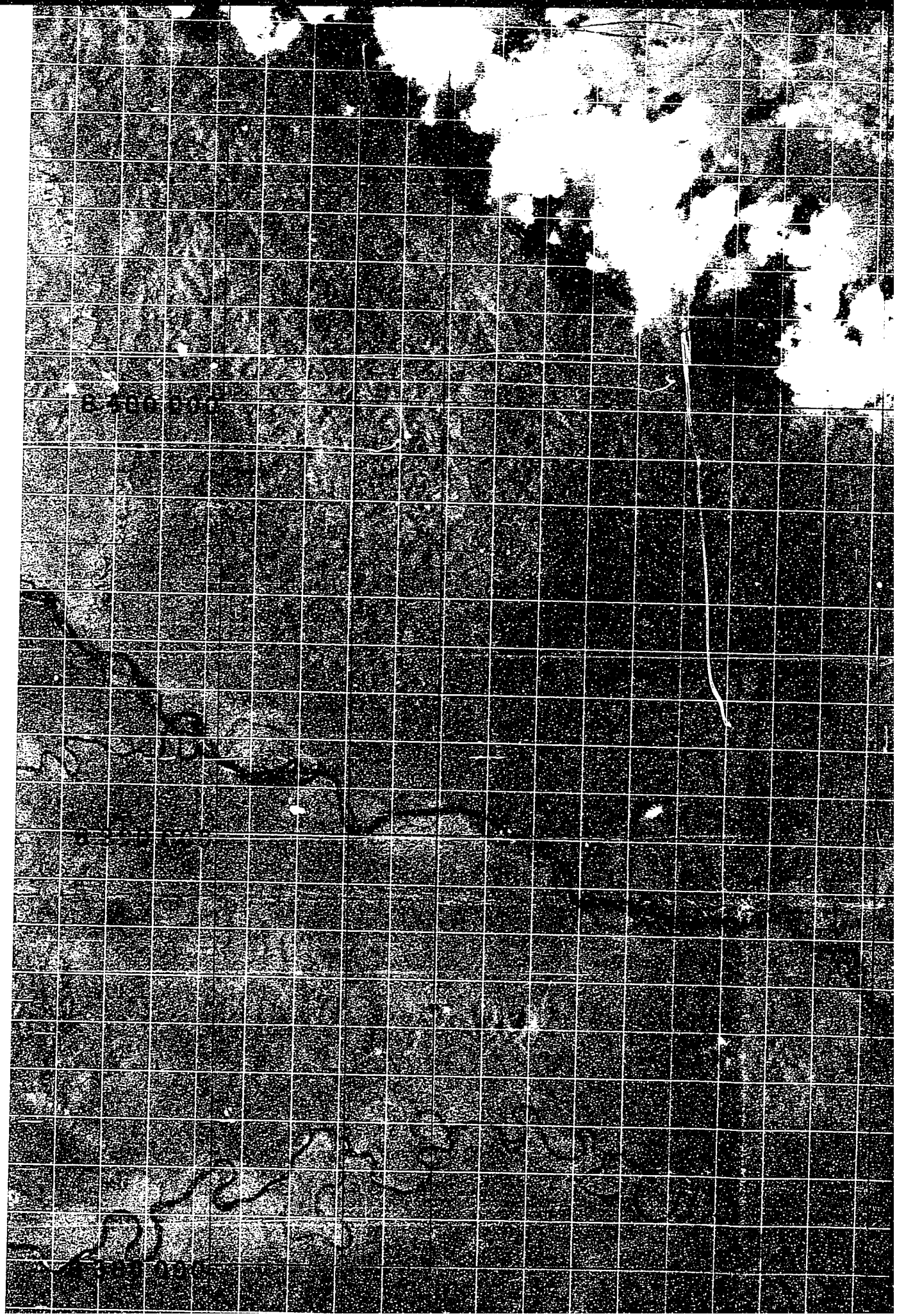
-14+4
-14+5
-14+6

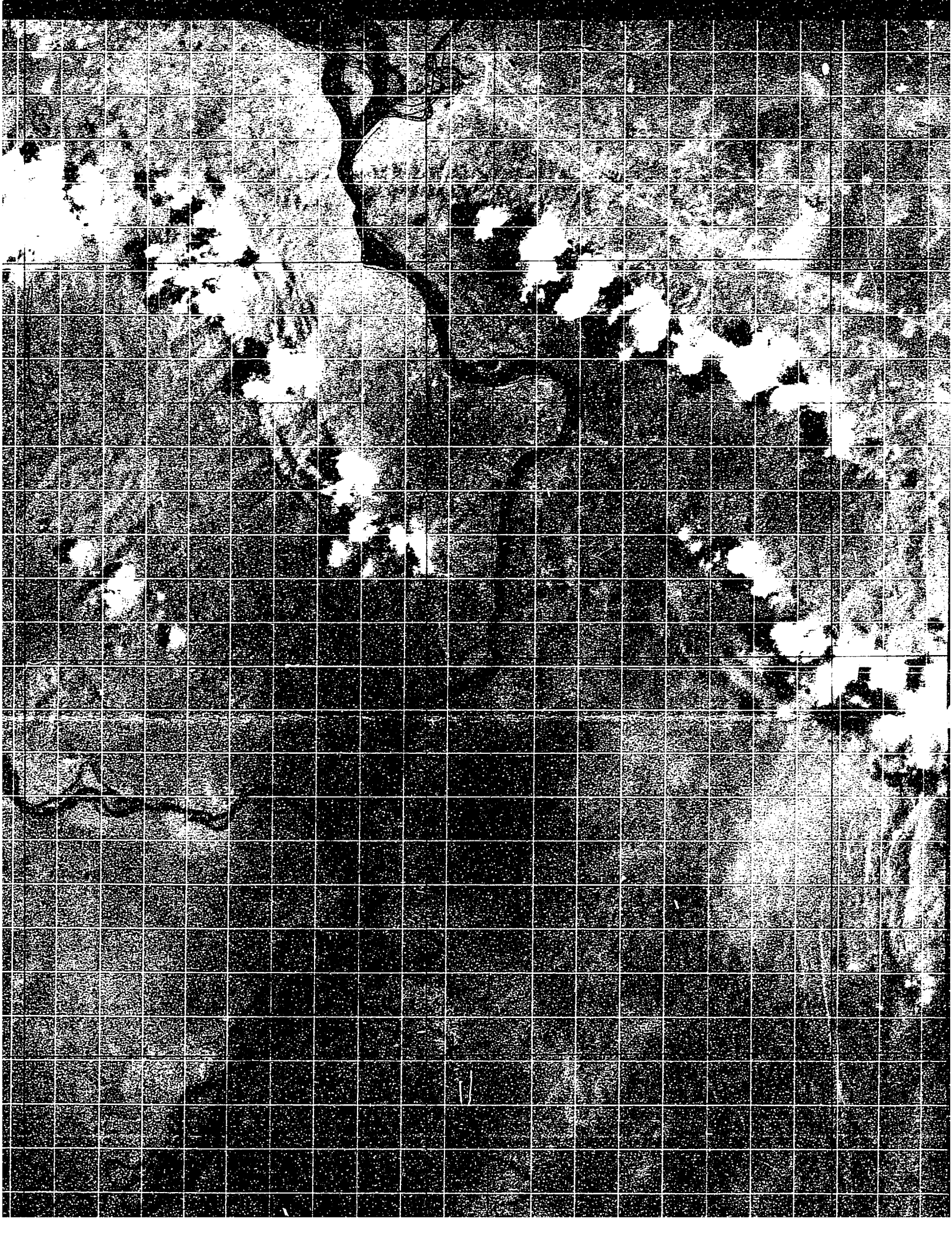

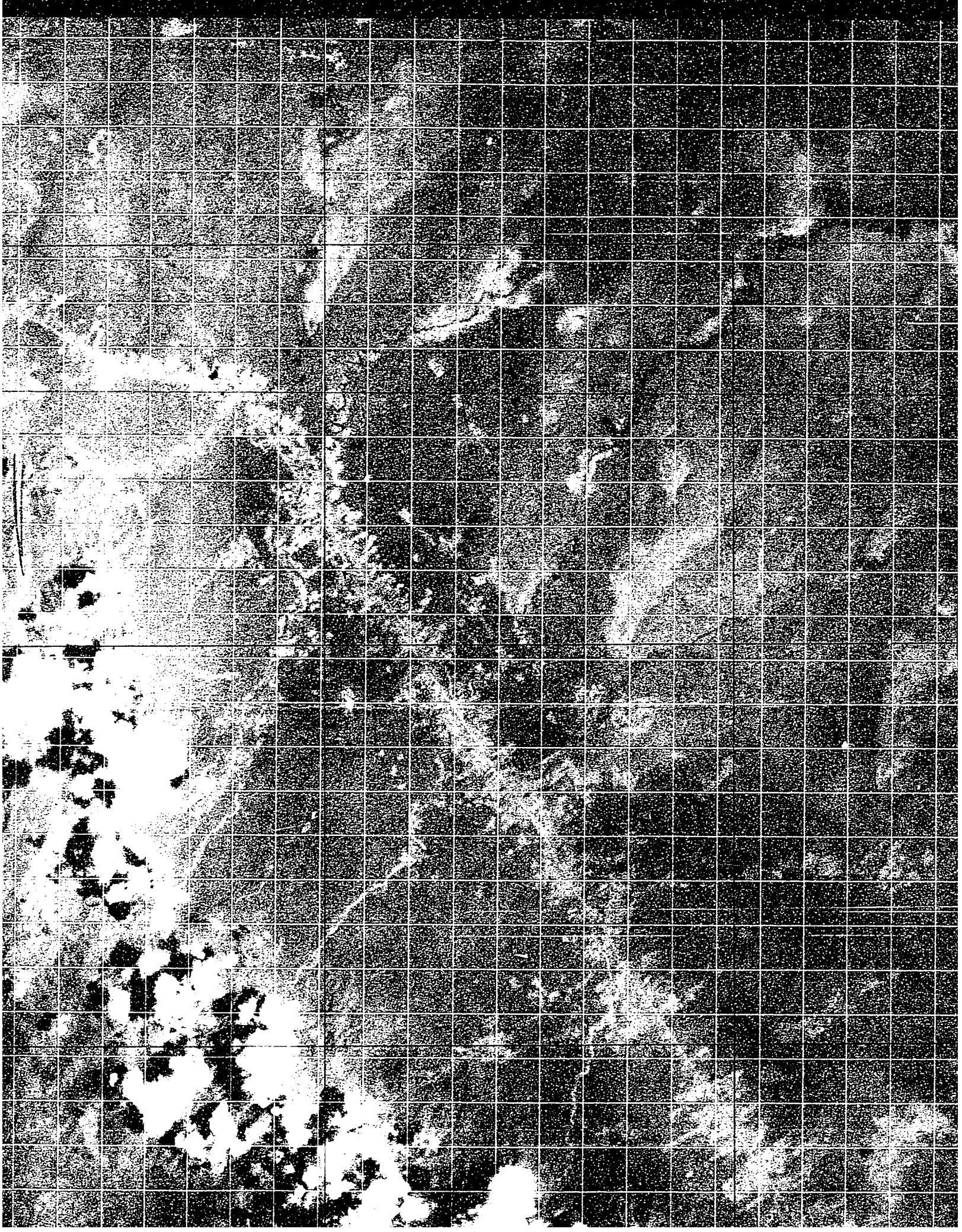

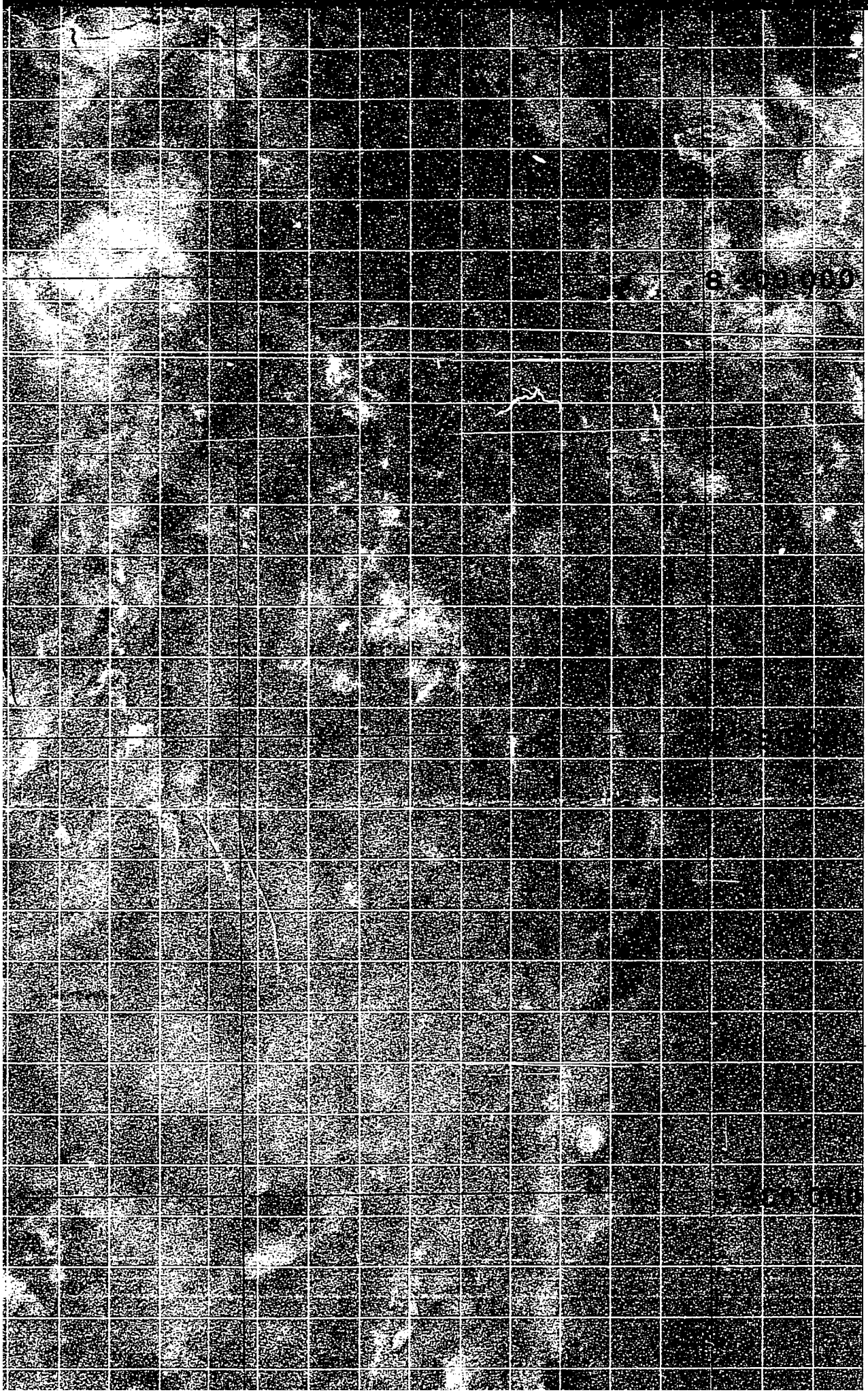
-14+5
-14+6

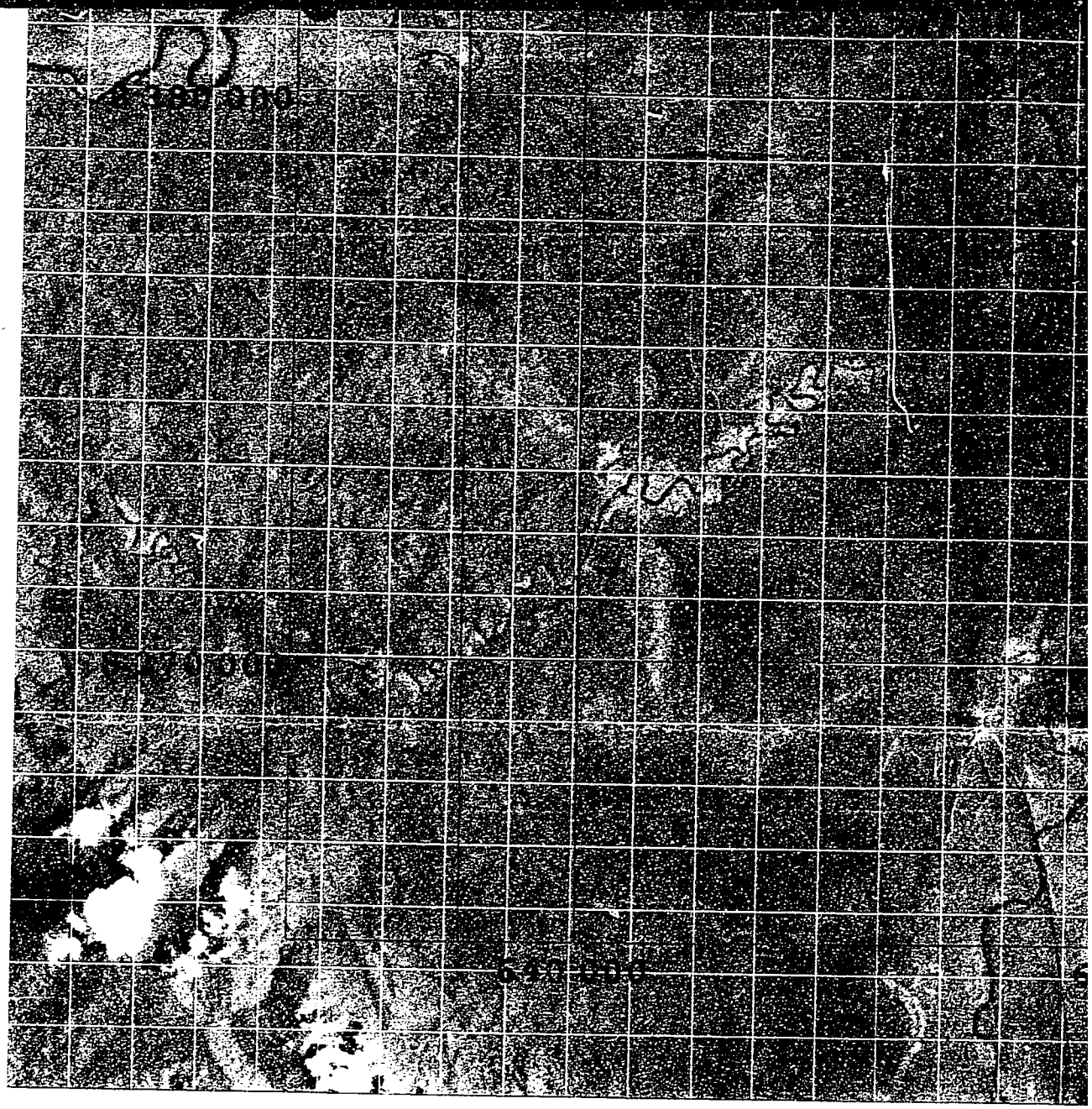

-14+7

-14+8

67+7

1960 channel

1975 channel

1986 channel

1993 channel

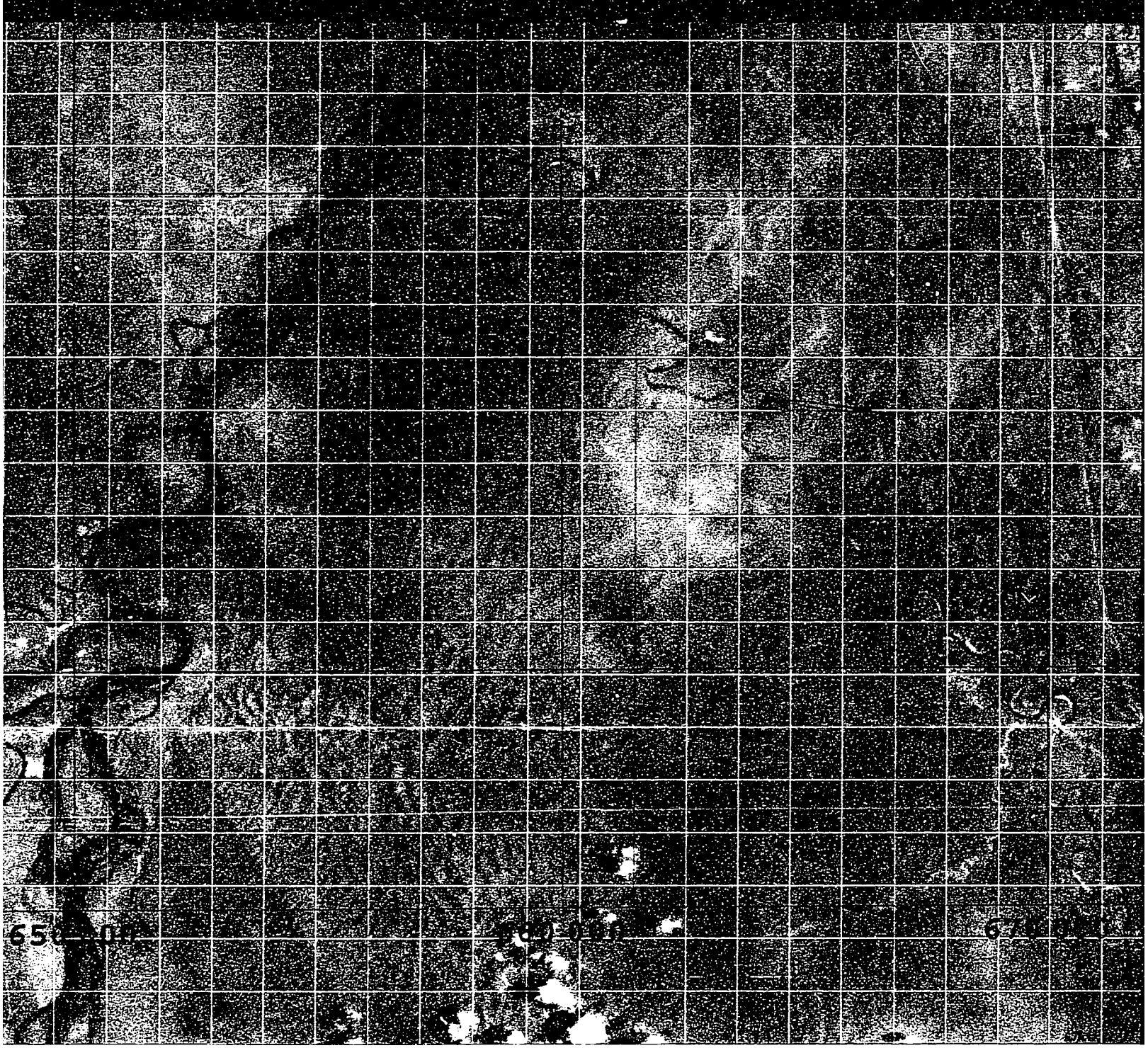

67+6 67+5 67

Base Map: Nov/1999 Land
UTM Zone 19 South
False Color Composite of

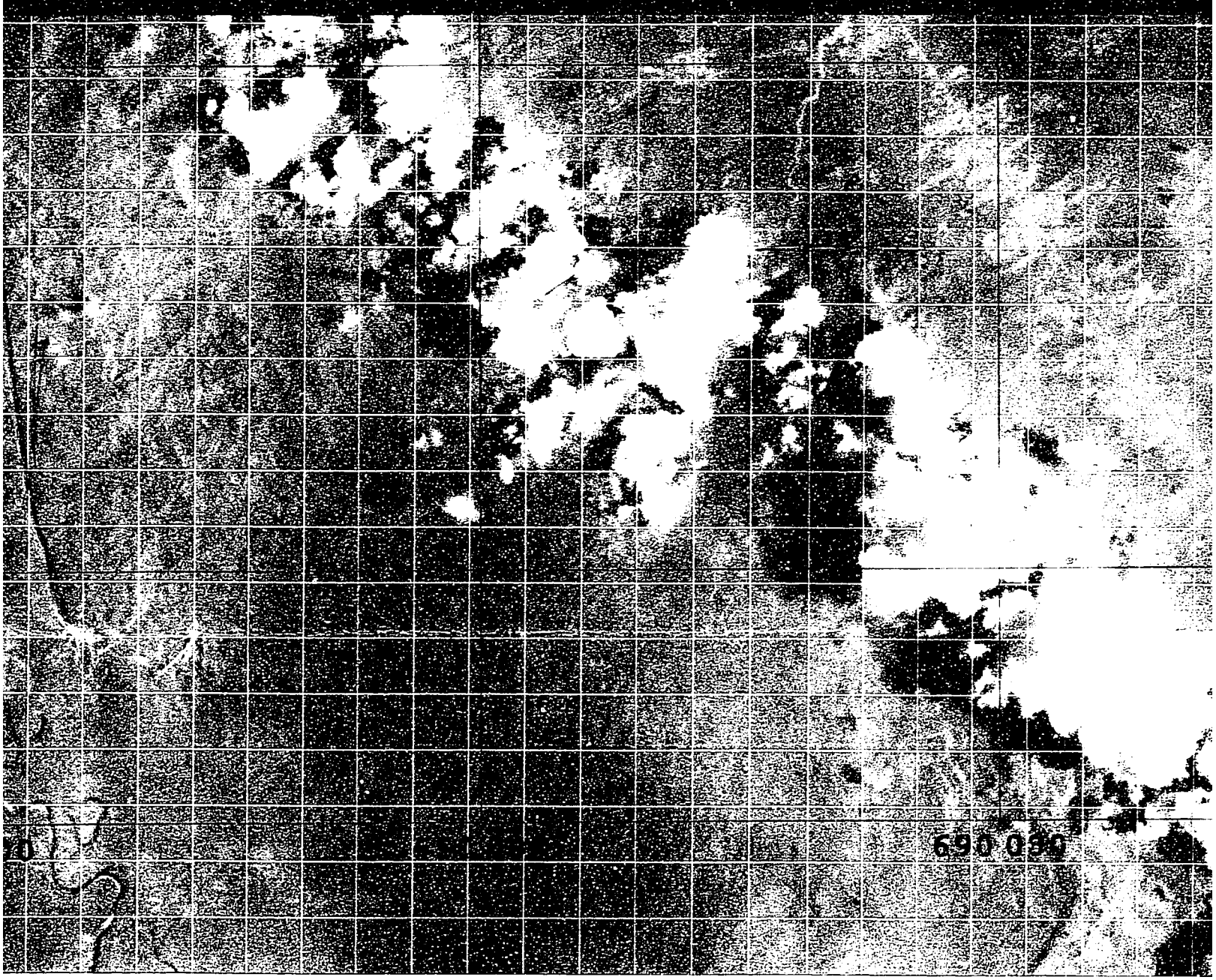

67+4 67+3 67+

Landsat ETM+ Path 1, Row 70

e of Bands 5, 4, and 3